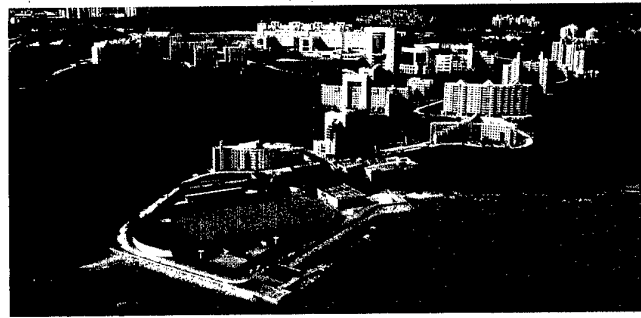


January 9-13, 2000 Hong Kong



Proceedings of

Symposium on
**Energy
Engineering**
in the 21st Century (SEE 2000)

Volume **Three**

DISTRIBUTION STATEMENT A
Approved for Public Release
Distribution Unlimited



Begell House New York, Wallingford (U.K.)

Ping Cheng Editor

Proceedings
of
Symposium on Energy Engineering
in the 21st Century (SEE2000)

Volume 3

Edited by

Ping Cheng
Mechanical Engineering Department
The Hong Kong University of Science and Technology
Clear Water Bay, Kowloon, Hong Kong

Begell House
New York, Wallingford (U.K.)

DISTRIBUTION STATEMENT A
Approved for Public Release
Distribution Unlimited

20000223 143

DTIC QUALITY INSPECTED 1

Library of Congress Cataloging-in-Publication Data

Catalog record is available from the Library of Congress.

This book represents information obtained from authentic and highly regarded sources. Reprinted material is quoted with permission, and sources are indicated. A wide variety of references are listed. Every reasonable effort has been made to give reliable data and information, but the authors and the publisher cannot assume responsibility for the validity of all materials or for the consequences of their use.

All rights reserved. This book, or any parts thereof, may not be reproduced in any form without written consent from the publisher.

Direct all inquiries to Begell House, Inc., 79 Madison Avenue, New York, NY 10016.

© 2000 by Begell House, Inc.

ISBN 1-56700-132-7 (hard cover edition)

Printed in Hong Kong 1 2 3 4 5 6 7 8 9 0

REPORT DOCUMENTATION PAGE					Form Approved OMB No. 0704-0188	
The public reporting burden for this collection of information is estimated to average 1 hour per response, including the time for reviewing instructions, searching existing data sources, gathering and maintaining the data needed, and completing and reviewing the collection of information. Send comments regarding this burden estimate or any other aspect of this collection of information, including suggestions for reducing the burden, to Department of Defense, Washington Headquarters Services, Directorate for Information Operations and Reports (0704-0188), 1215 Jefferson Davis Highway, Suite 1204, Arlington, VA 22202-4302. Respondents should be aware that notwithstanding any other provision of law, no person shall be subject to any penalty for failing to comply with a collection of information if it does not display a currently valid OMB control number.						
1. REPORT DATE (DD-MM-YYYY) 14-02-2000		2. REPORT TYPE Conference Proceedings			3. DATES COVERED (From - To) 9-13 Jan 00	
4. TITLE AND SUBTITLE Proceedings of Symposium on Energy Engineering in the 21 st Century (SEE 2000) (Four Volumes) Vol. 3					5a. CONTRACT NUMBER F6256299M9146	
					5b. GRANT NUMBER	
					5c. PROGRAM ELEMENT NUMBER	
					5d. PROJECT NUMBER	
6. AUTHOR(S) Conference Committee					5e. TASK NUMBER	
					5f. WORK UNIT NUMBER	
7. PERFORMING ORGANIZATION NAME(S) AND ADDRESS(ES) Hong Kong University of S&T Clear Water Bay Hong Kong Hong Kong					8. PERFORMING ORGANIZATION REPORT NUMBER N/A	
9. SPONSORING/MONITORING AGENCY NAME(S) AND ADDRESS(ES) AOARD UNIT 45002 APO AP 96337-5002					10. SPONSOR/MONITOR'S ACRONYM(S) AOARD	
					11. SPONSOR/MONITOR'S REPORT NUMBER(S) CSP-991002	
12. DISTRIBUTION/AVAILABILITY STATEMENT Approved for public release; distribution is unlimited.						
13. SUPPLEMENTARY NOTES						
14. ABSTRACT Volume 1, Page 1 – 406 Includes: Keynote Papers, Forced Convection, Natural Convection, and Boiling and Condensation Volume 2, Page 407 – 903 Includes: Two-Phase Flow, Porous Media, Heat Pipes and Thermosyphons, Conduction and Radiation, Microscale Heat Transfer, Heat Transfer Enhancement, Solar Energy & Nuclear Energy, Thermal Storage, Melting & Solidification Volume 3, Page 904 – 1,345 Includes: Drying & Food Processing, Heat Exchangers, Air-Conditioning and Refrigeration, Cryogenic Engineering, Energy and Environment, Combustion and Fire Volume 4, Page 1,346 – 1,734 Includes: Cycle Analysis, Engine Combustion, Waste Treatment by Thermal Methods, Fuel Cells, Clean Combustion Technology, Coal Combustion						
15. SUBJECT TERMS Fire Suppression						
16. SECURITY CLASSIFICATION OF:			17. LIMITATION OF ABSTRACT	18. NUMBER OF PAGES 1,734	19a. NAME OF RESPONSIBLE PERSON Terence J. Lyons, M.D.	
a. REPORT	b. ABSTRACT	c. THIS PAGE			19b. TELEPHONE NUMBER (Include area code) +81-3-5410-4409	
U	U	U	UU			

FORWARD

The signing of the Montreal Protocol in 1987 and the Kyoto Protocol in 1997 by various nations serves as a reminder once again of the intimate relationship between energy and environment, which will no doubt remain one of the major issues in the 21st Century. This is particularly so in Southeast Asia, where industrial growth has taken place at such a rapid pace during the last two decades. At the same time, research in energy engineering is accelerating in this part of the world. At the Hong Kong University of Science and Technology (HKUST), the Center for Energy and Thermal Systems (CETS) was recently established for the research and development of energy efficient and environmentally benign thermal systems. Thus, it is a privilege for CETS to be able to host the Symposium on Energy Engineering in the 21st Century (SEE2000) on the HKUST campus between 9-13 January 2000, the first international energy engineering conference ever held in Hong Kong.

The aim of this Symposium is to provide a forum for technical interchange in various aspects of energy engineering. The 226 papers (including 11 keynote papers) presented in the 25 technical sessions of the Symposium are published in this proceedings which contains 4 volumes, covering a variety of topics from heat and mass transfer, various energy and thermal systems, to clean combustion technology.

It has been a great pleasure for me to work with Symposium Co-Chairmen Professor Kefa Cen of the Zhejiang University and Professor Patrick Takahashi of the University of Hawaii in the planning of this Symposium. I would like to express my sincere thanks to keynote speakers for their efforts in writing up-to-date review papers, to members of the International Advisory Committee and the Organizing Committee for their enthusiasm in promoting the Symposium, and to members of the Local Committee for their hard work in reviewing the manuscripts. Special thanks are due to Dr. H. H. Qiu (the Symposium Secretariat) and Ms. Lotta Tse for their help in making conference arrangements, as well as to Ms. Ellie Ho, Ms. Ronnie Tse and other clerical staff for their help in the typing of the manuscripts and for the preparation of the proceedings. The generous financial support from the K. C. Wong Education Foundation, U.S. Air Force Asian Office of Aerospace Research and Development, U.S. Army Research Office - Far East, U.S. Office of Naval Research - Asia, and the International Technic HVAC Company are gratefully acknowledged.

Ping Cheng
Symposium Chair

*Hong Kong
January 2000*

SYMPOSIUM CHAIRMAN

Professor Ping Cheng

Department of Mechanical Engineering
Hong Kong University of Science and Technology
Clear Water Bay, Kowloon, Hong Kong
Fax: (852) 2358-1543 E-mail: mepcheng@ust.hk

SYMPOSIUM CO-CHAIRMEN

Professor Kefa Cen

Institute for Thermal Power Engineering
Zhejiang University
Hangzhou 310027, China
Fax: (86) 571-595-1616
E-mail: kfcen@sun.zju.edu.cn

Professor Patrick Takahashi

Hawaii Natural Energy Institute
University of Hawaii
Honolulu, Hawaii 96822, U.S.A.
Fax: (808) 956-2336
E-mail: ptakaha@uhccmvs.uhcc.hawaii.edu

SYMPOSIUM SECRETARIAT

Dr. H. H. Qiu

Department of Mechanical Engineering
Hong Kong University of Science and Technology
Clear Water Bay, Kowloon, Hong Kong
Fax: (852) 2358-1543 E-mail: meqiu@ust.hk

INTERNATIONAL ADVISORY COMMITTEE

Tien, C. L., (Honorary Chairman), University of California, Berkeley
Bull, S. R., National Renewable Energy Laboratory, Golden
Chen, X. J., Xian Jiaotong University, Xian
Chiu, H. H., Cheng Kung University, Tainan
Cotta, R. Federal University of Rio de Janeiro, Rio de Janeiro
De Vahl Davis, G., University of New South Wales, Sydney
Fang, L. J., Industrial Technology Research Institute, Hsinchu
Fletcher, "Skip" L. S., Texas A & M University, College Station
Fujita, Y., Kyushu University, Fukuoka
Goldstein, R., University of Minnesota, Minneapolis
Gori, F., University of Rome, Rome
Hahne, E., University of Stuttgart, Stuttgart
Leontiev, A. I., Moscow State University, Moscow
Martyненко, O. G., Byelorussian Academy of Sciences, Minsk
Mayinger, F., Technical University of Munich, Munich
Mujumdar, A. S., McGill University, Montreal
Ro, S. T., Seoul National University, Seoul
Shi, S. X., Tianjin University, Tianjin
Sidemann, S., Israel Institute of Technology, Haifa
Tanasawa, I., Tokyo University of Agriculture & Technology, Tokyo
Viskanta, R., Purdue University, West Lafayette
Wang, B. X., Tsinghua University, Beijing
Yang, K. T., University of Notre Dame, Notre Dame

ORGANISING COMMITTEE

Auracher, H. L., Technical University of Berlin, Berlin
Cai, R. X., Institute of Engineering Thermophysics, Beijing
Chen, T. S., University of Missouri, Rolla
Faghri, A., University of Connecticut, Storrs
Fujii, T., Kobe University, Kobe
Fukusako, S., Hokkaido University, Sapporo
Groll, M., University of Stuttgart, Stuttgart
Guo, Z. Y., Tsinghua University, Beijing
Howell J., University of Texas, Austin
Inaba, H., Okayama University, Okayama
Kakac, S., University of Miami, Miami
Kashiwagi, T., Tokyo University of Agriculture & Technology, Tokyo
Kaviani, M., University of Michigan, Ann Arbor
Kennedy, L. A., The University of Illinois at Chicago, Chicago
Kim, Jong Hyun, EPRI, Palo Alto
Kurosaki, Y., University of Electro-Communications, Tokyo
Law, C. K., Princeton University, Princeton
Lee, J. S., Seoul National University, Seoul
Lloyd, A. C., Desert Research Institute, Reno
Lou, D. Y. S., University of Nebraska, Lincoln
Minkowycz, W. J., University of Illinois at Chicago, Chicago
Nelson, R. A., Los Alamos National Laboratory, Los Alamos
Ni, M. J., Zhejiang University, Hangzhou
Nishio, S., University of Tokyo, Tokyo
Peng, X. F., Tsinghua University, Beijing
Peterson, G. P., Texas A & M University, College Station
Radebaugh, R., National Institute of Standards and Technology, Boulder
Saitoh, T. S., Tohoku University, Sendai
Serizawa, A., Kyoto University, Kyoto
Shoji, M., University of Tokyo, Tokyo
Son, J. E., Korea Institute of Energy Research, Taejon
Straub, J., Technical University of Munich, Munich
Suzuki, K., Kyoto University, Kyoto
Tong, T. W., Colorado State University, Fort Collins
Wang, C. Y., Pennsylvania State University, College Park

LOCAL COMMITTEE

Hsu, C. T., HKUST
Chao, Y. H., HKUST
Chi, Y., Zhejiang University
Kot, S. C., HKUST
Lee, H. K., HKUST
Qiu, H. H., HKUST
Zhao, T. S., HKUST.

SPONSORS

American Society of Mechanical Engineers
Japanese Society of Mechanical Engineers
Chinese Society of Power Engineering
International Center of Heat and Mass Transfer
K. C. Wong Education Foundation
U.S. Air Force Asian Office of Aerospace Research and Development
U.S. Army Research Office-Far East
U.S. Office of Navy Research-Asia

SUMMARY OF TECHNICAL SESSIONS

Volume 1

- A. Keynote Papers
- B. Forced Convection
- C. Natural Convection
- D. Boiling and Condensation

Volume 2

- E. Two-Phase Flow
- F. Porous Media
- G. Heat Pipes and Thermosyphons
- H. Conduction and Radiation
- I. Microscale Heat Transfer
- J. Heat Transfer Enhancement
- K. Solar Energy & Nuclear Energy
- L. Thermal Storage
- M. Melting and Solidification

Volume 3

- N. Drying and Food Processing
- O. Heat Exchangers
- P. Air-Conditioning and Refrigeration
- Q. Cryogenic Engineering
- R. Energy and Environment
- S. Combustion and Fire

Volume 4

- T. Cycle Analysis
- U. Engine Combustion
- V. Waste Treatment by Thermal Methods
- W. Fuel Cells
- X. Clean Combustion Technology
- Y. Coal Combustion

CONTENTS OF VOLUME 3

	Forward	iii
N.	Drying and Food Processing	904
N1.	Non-Fick Effect in Abnormal High Intense Drying Process of Wet Porous Materials <i>X. Wang, M. H. Shi and W. P. Yu</i>	905
N2.	Osmotic Dehydration Pretreatment in Drying of Fruits and Vegetables <i>Y. K. Pan, L. J. Zhao, Y. Zhang, G. H. Chen and A. S. Mujumdar</i>	910
N3.	Drying of Value-Added Liquid Wastes <i>M Benali, M. Amazouz and T. Kudra</i>	917
N4.	Indirect Drying of Thin-Film Alumina Sludge by Boiling Application on Drum Drying <i>C. Carrere-Gee, D. Lecomte, O. Fudym, P. Arlabosse and B. Ladevie</i>	923
N5.	Application of Chemical Heat Pump Technology to Industrial Drying: A Proposal for a New Chemical Heat Pump Dryer <i>H. Ogura, Hiroyuki Kage, Y. Matsuno and A.S. Mujumdar</i>	932
O.	Heat Exchangers	939
O1.	Coefficient of Heat Transfer in Fin-Tube Heat Exchanger Analysis and the Artificial Neural Networks <i>K. T. Yang, M. Sen, G. Diaz, A. Pacheco-Vega and R. L. McClain</i>	940
O2.	Heat Transfer and Friction Characteristics of Fin-And-Tube Heat Exchangers <i>W. M. Yan and P. J. Sheen</i>	949
O3.	Investigation of Novel Enhanced Heat Transfer Surfaces for Industrial Compact Heat Exchangers <i>R. Mertz and M. Groll</i>	957
O4.	Experimental Investigation of Evaporative Heat Transfer Characteristics in a Small-Diameter Tube Using R-134a <i>Y. W. Hwang, M. S. Kim and S. T. Ro</i>	965
O5.	Optimal Design of Micro Bare-tube Heat Exchanger <i>S. Paitoonsurikarn, N. Kasagi and Y. Suzuki</i>	972
O6.	The Experimental Study of Heat Transfer Enhancement and Pressure Drop Characteristics with Wing-Type Vortex Generators for Staggered Circular Tube Bank Fin Compact Heat Exchanger <i>Y. H. Zhang, Y. X. Dong, Y. G. Mei, Y. Qiu and L. B. Wang</i>	980
O7.	Air-Side Heat Transfer Enhancement Mechanisms of Compact Heat Exchangers with Interrupted Surfaces <i>L. Winston Zhang</i>	989
O8.	Experimental Research of the Plate-Fin Heat Exchanger as an Evaporator in the Room Air-Conditioner <i>X. S. Zhang and L. P. Zhou</i>	997
O9.	The Experimental Study on the Performance of Heat Exchanger with Hydrophobic Surface <i>D. T. Yue, Q. Fei, G.T.Wu, L. J. Chang, J. Huang and B. Z. Ren</i>	1002
O10.	Compact, Double Side Impingement, Air-to-Air Heat Exchanger <i>Z. J. Zuo, E. H. Dubble and S. D. Garner</i>	1007
O11.	Evaporative Heat Transfer in Horizontal Tubes with Strip-Type Inserts Using Refrigerant-600A <i>S. S. Hsieh, K. J. Jang and Y. C. Tsai</i>	1015
P.	Air-Conditioning and Refrigeration	1023
P1.	Numerical Study on a Vapor Flow with Non-Absorbable Gas in the Evaporator-Absorber of an Absorption Chiller <i>H. Suzuki, T. Yamanaka and T. Sugiyama</i>	1024

P2.	Modeling the Thermal Cycle of Dual Compartment Household Refrigerator <i>X. Y. Fu, R. Anderson and A. Miller</i>	1033
P3.	The Development of Energy Efficient Refrigerators by the Industrial Technology and Research Institute <i>J. Y. Sun and J. Y. Lin</i>	1041
P4.	Study of an Auto-Refrigerating Cascade System <i>S. Z. Zhang, G. M. Chen, H. X. Zhang and J. F. Wang</i>	1048
P5.	Performance Study of a Composite Absorbent Block Used for Solar or Waste Heat Powered Refrigeration <i>Z. Y. Liu and Y. Z. Lu</i>	1054
P6.	Analysis of the Thermal Performance of Direct-Contact Air-Conditioning Systems <i>Y. P. Zhang, Y. X. Zhu and Y. Jiang</i>	1059
P7.	Analysis of the Thermal Performance and Energy Saving Effect of Membrane Based Heat Recovery Ventilator <i>Y. P. Zhang, Y. Jiang and L. Z. Zhang</i>	1066
P8.	A Steady State Model for the High-Pressure Side of Unitary Air-Conditioners <i>P. J. Petit and J. P. Meyer</i>	1076
P9.	Development and Experimental Testing of an Enthalpy Recovery Wheel Based on a New Composite Desiccant <i>M. Amazouz, S. Hosatte and R. Cote</i>	1084
P10.	Cooling Requirements for Refrigerated Semi-Trailers Transporting Fresh Fruits and Vegetables <i>C. K. P. Hui, G. S. V. Raghavan and C. Vigneault</i>	1090
P11.	Underground Railway Air Quality and Its Impact on Energy Consumption <i>L. Lee and J. G. Sanchez</i>	1098
P12.	Evaluating Wet Compression in Refrigeration Cycles Working with Pure or Non-Azeotropic Refrigerant Mixtures for Air-Conditioners <i>W. Swanepoel and J. P. Meyer</i>	1105
P13.	Temperature Control in Refrigerated Transport with a Snow Bag <i>V. R. Da Veiga and J. P. Meyer</i>	1114
P14.	An Exergy Analysis of the LiBr-Water Absorption Refrigerating Cycle <i>H. Asano, T. Fujii, X. Wang and Y. Hisazumi</i>	1122
P15.	Thermally Driven High-performance Sorption Heat Pumps <i>H. P. Klein, E. Willers and M. Groll</i>	1130
P16.	Heat and Mass Transfer of a Fluidized Bed Packed with Organic Powder Type Adsorption Material <i>H. Inaba, A. Horibe, K. Kameda, N. Haruki and T. Kida</i>	1138
P17.	Non-Regenerative Multi-Stage and Regenerative Multi-Bed Adsorption Cycles for Low-Temperature Waste Heat Recovery <i>B. B. Saha, A. Akisawa, T. Kashiwagi, K.C. Ng and H. T. Chua</i>	1145
P18.	Study of the Reaction Rate of MH to be Used for Compact MH Refrigeration Systems <i>S. C. Bae, S. Takeguchi, T. Yabe and M. Katsuta</i>	1153
P19.	Performance Comparison and Analysis for Inverter-Driven Air Conditioners Throttling with Electronic Expansion Valve <i>B. F. Yu, Z. G. Wang, and X. Z. Meng</i>	1159
Q:.	Cryogenic Engineering	1163
Q1.	New Results on thermoacoustic Refrigeration with Gas Substance <i>J. V. Lubez, F. J. Jerbi and M. X. Francois</i>	1164
Q2.	Thermoacoustic Streaming on a Cylinder <i>A. Gopinath</i>	1170
Q3.	Experimental Investigation of Cooled Air-Injection in Thermoacoustic Refrigerator <i>T. Hara</i>	1178
Q4.	Analyzing and Verification of Symmetry-Nozzle to Improve the Performance of Pulse Tube Refrigerator <i>L. W. Yang, W. X. Zhu, Y. Zhou and J. T. Liang</i>	1184

Q5.	Transport Phenomena in a Porous Medium Subject to a Compressible Oscillating Flow	1192
	<i>G. Q. Lu and P. Cheng</i>	
Q6.	Analysis of the Valve-Timing Effect on the Performance of a 4.2K Gifford-McMahon Refrigerator	1198
	<i>L. Zhang, X. D. Xu and L. H. Gong</i>	
Q7.	H-Matrix Description of the Performance of Regenerator	1203
	<i>Q. Li, W. Zhang and F. Z. Guo</i>	
Q8.	Displacement of Gas in Pulse Tube of PRT	1208
	<i>Q. Li, Y. Feng and F. Z. Guo</i>	
Q9.	Experimental Investigation of Friction Characteristics of Instrument Ball Bearings in Vacuum and at LHe Temperatures	1212
	<i>X. Z. Li, H. Yang, K. Cheng, Y. W. Liu, Y. Z. Wu and H. D. Denner</i>	
Q10.	Active Network Modeling for Regenerator of Regenerative Cryocooler	1217
	<i>F. Wu, P. G. Deng and X. H. Deng</i>	
R:	Energy and Environment	1225
R1.	A Grand Design of Energy-Efficient Electric Vehicle with Fuel Economy More than 100KM/Liter (Cutting Edge Technologies to Mitigate Urban and Global Warming)	1226
	<i>T. S. Saitoh and D. Ando</i>	
R2.	Improved Modeling of Urban Warming and Numerical Projection to Future Urban Environment in Tokyo	1233
	<i>T. S. Saitoh and N. Yamada</i>	
R3.	Indoor Thermal Environment of Residential Buildings in Large Cities of China	1241
	<i>H. Yoshino and H. Lou</i>	
R4.	Real Time and In-situ Measurement of Particulate Emissions	1250
	<i>N. N. Wang and S. M. Yu</i>	
R5.	Application of Photoenergy on Oxidation of Toxic Nitrite Ion and Hydrogen Generation Using the Rutile Form of TiO_2/Ti Photoelectrode	1257
	<i>C. C. Sun and Tse-Chuan Chou</i>	
S:	Combustion and Fire	1265
S1.	NOx and CO Emissions of Methane/Air Filtration Combustion Waves	1266
	<i>J. P. Bingle, A. V. Saveliev, A. A. Fridman and L. A. Kennedy</i>	
S2.	Acceleration of Flames and Transition From Deflagration to Detonation Due to The Influence of Highly Blocking Obstacles	1273
	<i>C. Gerlach, A. Eder, M. Jordan and F. Mayinger</i>	
S3.	Researches on the Ignition Regulation of the Pulverized Coal-Air Flow in a Tube	1281
	<i>Z. J. Zhou, J. H. Zhou, Q. Yao, X. Y. Cao and K. F. Cen</i>	
S4.	Theoretical and Experimental Study of the Performance of Intumescent Fire-Retardant Materials	1289
	<i>F. B. Cheung, J. H. Koo, Y. C. Shih and B. C. Yang</i>	
S5.	Experimental Observation of Fast Deflagrations and Transition to Detonations in Hydrogen-Air-Mixtures	1296
	<i>A. Eder, C. Gerlach and F. Mayinger</i>	
S6.	The Geometric Appearance of Counterflowing Diffusion Flame Under High Turbulent Intensity	1305
	<i>Y. Q. Xu, H. M. Yang, Y. Liu, W. M. Ma and F. Gu</i>	
S7.	New Concepts and Test Procedures in The Assessment of Hazards Due to Spontaneous Heating of Transported Combustible Solids	1313
	<i>J. C. Jones</i>	
S8.	Trifluoro Methyl Iodide (CF ₃ I) As a Halon 1301 Replacement for Fuel Tank Inertion Applications	1321
	<i>J. A. Vitali and S. R. Vanhorn</i>	
S9.	TWA800 Fuel Tank Combustion and Explosion Mixtures	1327
	<i>F. A. Wyczalek</i>	

S10.	Section Temperature Field Reconstruction From Flame Images Using Algebraic Reconstruction Technique	1333
	<i>F. Wang, Y. Chi, C. Y. Wei, Z. Y. Ma, J. H. Yan, G. Hu and K. F. Cen</i>	
S11.	Experiments and Observations of Interaction of Water Mist with Pool Fires	1340
	<i>X. S. Wang, G. X. Liao, B. Yao, W. C. Fan and X. P. Wu</i>	
Authors Index to Volumes 1-4		xi

N. Drying and Food Processing

NON-FICK EFFECT IN ABNORMAL HIGH INTENSE DRYING PROCESS OF WET POROUS MATERIALS*

Wang Xin Shi Mingheng Yu Weiping

Department of Power Engineering
Southeast University, Nanjing 210096, China
Email: mhshi@seu.edu.cn

Keywords: high intense drying, abnormal mass transfer, non-Fick effect, mass relaxation time

ABSTRACT. Because mass propagation velocity has a finite value in porous media for an unsteady mass transfer process, the hypothesis that mass propagation velocity in mass transfer process is infinite is far away from practical situation for high intense drying process in wet porous materials. Like heat transfer, a description of an unsteady humidity profile in the form of the hyperbolic equation is advanced. From the equation, wave characteristic can be seen in the mass transfer field of inner material. One-dimensional hyperbolic equation of mass transfer for high intense drying process of wet porous materials has been developed in this paper. The non-Fick phenomena in high intense drying process are analyzed by the comparison of the solutions between the Fick equation and the non-Fick equation. The calculating results show that when mass flux or mass transfer coefficient is high, the non-Fick effect is notable and it is not negligible in an intense drying process.

1. INTRODUCTION

When there is mass potential gradient by liquid or gas molecular diffusion, the mass flux will transfer from high potential to low potential. The final result of the process is that concentration or density difference in a system will reach a lowest limit. That is to say, the mass transfer process can be preceded owing to the existence of concentration gradient.

The basic patterns of mass transfer are diffusion (also called frequently molecule mass transfer) and convection mass transfer. Like heat conduction, diffusion mass transfer refers to the phenomena, which is happened because of concentration gradient of components in macroscopically static media or laminar flowing liquid perpendicular to concentration gradient direction.

Generally the mass transfer process can be described by Fick Law. It shows that mass flux J is direct proportional to mass potential gradient $\partial\theta/\partial x$ in transfer direction. That is:

$$J = -\lambda_m \frac{\partial\theta}{\partial x} \quad (1)$$

where, λ_m is mass conductivity of a given material.

However, as for high intense and transient diffusion mass transfer process, which happens in some high technological applications in Energy, Power, Chemical and Environment Engineering, the transfer duration is very short and component A transfers at a finite velocity in component B. Thus Fick Law, which is based on the infinite mass propagation velocity, is not suitable for the mass transfer problem with finite mass propagation velocity. Obviously it affects the further development and application for high intense drying technology. So it has important theoretic significance and academic value to investigate abnormal high intense mass transfer of wet porous materials with considering the non-Fick effect. It also has become a key subject in investigation of mass transfer in porous media[1].

In this paper, the non-Fick phenomena in high intensive drying process are analyzed numerically. By the comparison of the calculated results of the Fick equation and the non-Fick equation, the influences of non-Fick effect are discussed.

* The project supported by National Natural Science Foundation of China (Project Number: 59736130)

2. MATHEMATICAL AND PHYSICAL DESCRIPTION OF NON-FICK EFFECT

As for a transient mass diffusion process, a component diffuses in another component is actually caused by an instantaneous mass disturbance of the component propagating in another component. That is to say, a component diffusing in another component has characteristic of wave propagation in a transient mass transfer process. It is called mass diffusion wave or mass wave. Correspondingly, its moving speed is called mass propagation velocity. The finite mass propagation velocity causes the re-establishment of humidity field, which is later than the change of mass transfer potential. The delaying time is called mass flux relaxation time, in which a quasi-static humidity distribution in the porous media is reached.

Because mass propagation velocity is less than heat propagation velocity in an unsteady drying process, the hypothesis that mass propagation velocity in mass transfer process is infinite is farther away from practical situation than the corresponding hypothesis in heat conduction process for high intense heat and mass transfer process in wet porous materials. Thus the effect of finite mass propagation velocity on mass transfer process should be more obvious than that in heat conduction process.

Considering non-Fick effect caused by finite mass propagation velocity w_m , similar to Cattane-Vernotte equation for heat conduction with finite heat propagation velocity, we can get a transient one-dimensional mass transfer equation. That is:

$$\tau_m \frac{\partial J}{\partial \tau} + J = -\lambda_m \frac{\partial \theta}{\partial x} \quad (2)$$

Compared with conventional Fick Law. A new variation term of diffusion mass flux at a cross-section in relaxation process is added in Eq.2., in which τ_m is mass flux relaxation time, J is mass flux, λ_m is mass conductivity of material, θ is mass transfer potential. In addition,

$$\tau_m = \frac{a_m}{w_m^2} \quad (3)$$

$$a_m = \frac{\lambda_m}{c_m} \quad (4)$$

Where, α_m is mass diffusion coefficient, c_m is specific mass at constant temperature and w_m is mass propagation velocity. Because τ_m is more than τ_q [2], non-Fick effect on mass transfer should be greater than non-Fourier effect on heat transfer in high intense heat and mass transfer process.

Combining Eq.3 with the law of conservation of mass, we can get a one-dimensional transient mass transfer equation with consideration of finite mass propagation velocity:

$$\frac{\partial \theta}{\partial \tau} + \tau_m \frac{\partial^2 \theta}{\partial \tau^2} = a_m \frac{\partial^2 \theta}{\partial x^2} \quad (5)$$

This equation shows that the mass potential field in material will have some wave characteristics after considering finite mass propagation velocity. Usually there are two kinds of limited situations for a transient mass transfer process:

1. When mass disturbance (or boundary conditions) changes relatively slowly and mass flux relaxation time is very short, Eq.5 reduces into conventional Fick Law. In the term of physics, this condition shows that re-establishment of concentration distribution of a component in another component is much quicker than mass disturbance (or boundary condition change). It makes re-establishment of concentration field and mass disturbance are nearly synchronous. Both of them are basically homologous in respect of time. In this case, the influence of instantaneous diffusion mass transfer by non-Fick effect can be negligible.

2. When mass disturbance (or boundary conditions) changes rapidly and mass flux relaxation time is relatively long, the second term of Eq.5 will become greater. It makes possible that the second term and other two terms are in the same order. In this case, non-Fick effect must be considered.

Of course, there are some kinds of conditions between above two limits, for example, although mass flux relaxation time is relatively short, mass disturbance changes rapidly or although mass flux relaxation time long, mass disturbance changes relatively slowly. In these cases, it needs to be analyzed carefully to show whether non-Fick effect should be considered or not.

To analyze the magnitude of the non-Fick effect, we will consider a one-dimensional porous material strip being dried with L in length under two kinds of mass transfer boundary conditions. The mass transfer equation and its specific conditions are as follows:

$$\frac{\partial \theta}{\partial \tau} + \tau_m \frac{\partial^2 \theta}{\partial \tau^2} = a_m \frac{\partial^2 \theta}{\partial x^2} \quad (5)$$

$$\tau = 0, \quad \theta(x, 0) = \theta_0, \quad \left. \frac{\partial \theta}{\partial \tau} \right|_{\tau=0} = 0 \quad (6)$$

$$\tau > 0, \quad -\lambda_m \left. \frac{\partial \theta}{\partial x} \right|_{x=0} = J_0, \quad \theta(l, \tau) = \theta_0 \quad (7)$$

$$\text{Or } \tau > 0, \quad -\lambda_m \left. \frac{\partial \theta}{\partial x} \right|_{x=0} = \alpha_m (\theta|_{x=0} - \theta_\infty), \quad \theta(L, \tau) = \theta_0 \quad (8)$$

where, θ_0 is initial mass transfer potential, θ_∞ is mass transfer potential at infinite distance.

3. CALCULATING RESULTS AND DISCUSS

In order to know the influence of non-Fick effect on concentration field in high intense rapid drying process, the humidity field under constant mass flux and convective mass transfer boundary conditions were calculated. The scheme used in numerical calculation is Von-Neuman form. In the calculation, a set of physical parameters was chosen for a typical wet material. They are: θ_0 , initial relative humidity of material, is 0.5; L , length of material, is 5mm; a_m , mass diffusion coefficient, is $2.8 \times 10^{-6} \text{ m}^2/\text{s}$. The mass flux relaxation time is compared and chosen according to some experimental results of heat flux relaxation time in porous materials [3, 4].

(1) Constant Mass Flux Boundary Condition ($J_{x=0} = \text{Constant}$)

Fig.1 shows a set of relative humidity distribution curves when J_0 is $0.4 \text{ kg}/(\text{m}^2\text{s})$ with $\tau_m = 5\text{s}$ and $\tau_m = 0$ respectively. It can be seen that whether or not considering mass flux relaxation time is very different for relative humidity distribution. There is obvious lag for humidity field re-establishment in porous material for a rapid drying process with considering finite mass propagation velocity. For example, when τ is 10s at $x=1.5\text{mm}$, the relative humidity without non-Fick effect is 0.46 while the one with non-Fick effect is 0.493. It is also shown that the difference is more obvious at the initial time duration. Thus the non-Fick effect should be considered in some rapid drying process, in which the drying time only lasts several seconds. Fig.2 shows another set of relative humidity distribution curves when J_0 is $0.6 \text{ kg}/(\text{m}^2\text{s})$ and other conditions are the same with the Fig.1. When τ is 10s at $x=1.5\text{mm}$, the relative humidity without non-Fick effect is 0.439s and the one with non-Fick effect is 0.489. The relative difference is about 11.3%.

According to these figures, It is clear that the more is mass flux J_0 , the more non-Fick effect is obvious. Furthermore, the relative humidity at given position in the material for $\tau_m = 0$ tends to a constant value after a short time duration and the linear humidity distribution will be existed in the strip. But for $\tau_m \neq 0$, the humidity

variations at given positions will be delayed and their values vary with the time. The wave characteristics are appeared in the humidity distribution curves. This will influence the moisture movement in the rapid drying process.

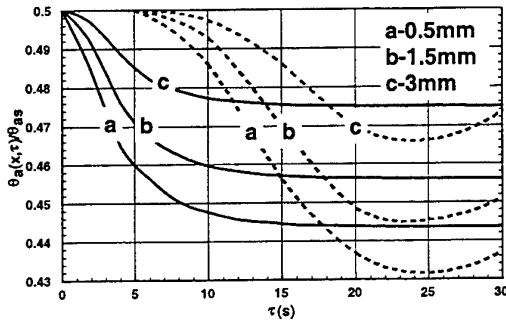


Fig.1 Relative humidity distribution as $J=0.4$ $\text{kg}/(\text{m}^2\text{s})$

----- Non-Fick equation solution ($\tau_m=5\text{s}$)
 _____ Fick equation solution ($\tau_m=0$)

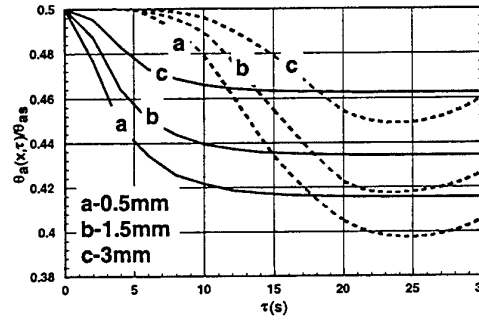


Fig.2 Relative humidity distribution as $J=0.6$ $\text{kg}/(\text{m}^2\text{s})$

----- Non-Fick equation solution ($\tau_m=5\text{s}$)
 _____ Fick equation solution ($\tau_m=0$)

Fig.3 shows relative humidity distribution when mass flux J_0 is $0.4 \text{ kg}/(\text{m}^2\text{s})$ with mass flux relaxation time equal to 5s or 10s respectively. It can be shown that when the mass flux relaxation time is more, the lag phenomena are more obvious in such drying process.

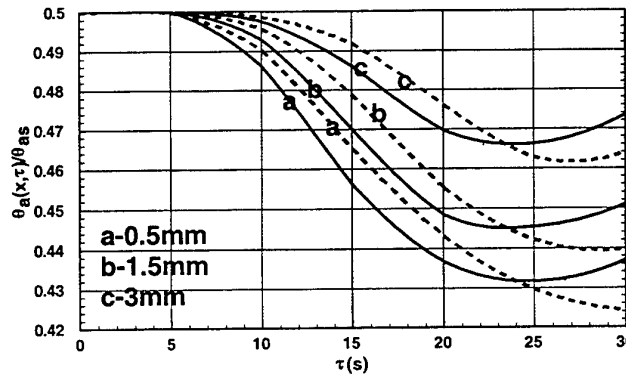


Fig.3 The effect of mass flux relaxation time as $J=0.6 \text{ kg}/(\text{m}^2\text{s})$

----- $\tau_m=10\text{s}$ _____ $\tau_m=5\text{s}$

(2) Convective Mass Transfer Boundar Condition

Fig.4 shows a set of relative humidity distribution curves in an enhanced force convection drying process with or without non-Fick effect. The convective mass transfer coefficient α_m is $0.5/\text{s}$, which corresponds the convective heat transfer coefficient about $400 \text{ W}/(\text{m}^2 \cdot ^\circ\text{C})$ in this convection process.

The calculated results show that the distributions of humidity fields for above two situations are very different. This is caused by the finite mass propagation velocity. For example, when τ is 10s at $x=1.5\text{mm}$, relative humidity without non-Fick effect is 0.481 and the one with non-Fick effect is 0.497. Fig.5 shows another relative set of humidity distribution when convective mass transfer coefficient α_m is $1/\text{s}$, which corresponds the convective heat transfer coefficient about $800 \text{ W}/(\text{m}^2 \cdot ^\circ\text{C})$ as in gas impinging drying process. When τ is 10s at $x=1.5\text{mm}$, relative humidity without non-Fick effect is 0.464 and the one with non-Fick effect is 0.493. The relative error is about 5.9%. Thus the more α_m is, the more non-Fick effect is obvious.

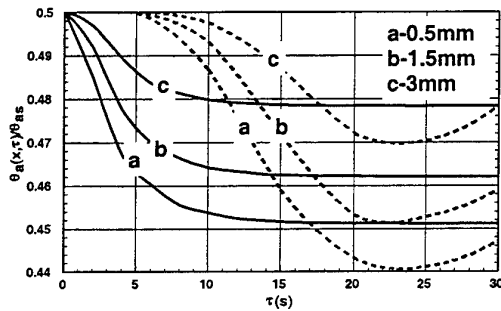


Fig.4 Relative humidity distribution as $\alpha_m=0.5$ m/s
 ----- Non-Fick equation solution ($\tau_m=5s$)
 _____ Fick equation solution ($\tau_m=0$)

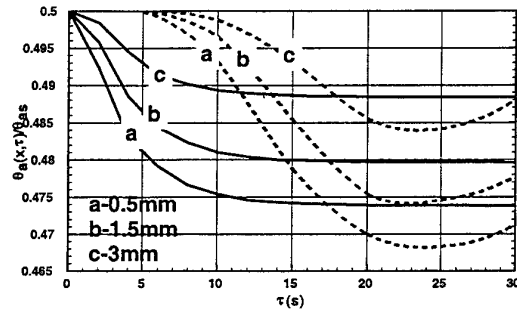


Fig.5 Relative humidity distribution as $\alpha_m=1$ m/s
 ----- Non-Fick equation solution ($\tau_m=5s$)
 _____ Fick equation solution ($\tau_m=0$)

Fig.6 shows relative humidity distribution when convective mass transfer coefficient α_m is 1m/s and mass flux relaxation time is 5s or 10s respectively. From the figure, we can see that with increasing the mass flux relaxation time, the lag phenomena of humidity variation in the material would be more obvious in such drying process. Because the relaxation time τ_m depends on the structure of the porous material, it should be determined experimentally before the design of the corresponding drying porous.

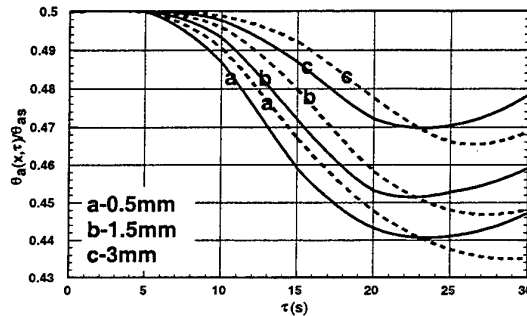


Fig. 6 The effect of mass flux relaxation time $\alpha_m=1$ m/s
 ----- $\tau_m=10s$ _____ $\tau_m=5s$

4. CONCLUSIONS

1. Non-Fick effect caused by finite mass propagation velocity should be considered in high intense rapid drying process of porous material.
2. In the constant mass flux boundary, the non-Fick effect will be obvious when increasing this mass flux, while in the convective mass transfer boundary, the non-Fick effect will be appeared only in very enhanced convective mass transfer process.
3. The finite mass flux relaxation time will causes the lag phenomena of humidity distribution in the material being dried at a high intensive rapid drying process .

REFERENCES

1. M.H.Shi, "Research on Abnormal Heat and Mass Transfer in Porous Media in High Intense Drying Process", proceedings of the 4th Nanjing Engineering Thermal Physics Conference, pp1-7
2. R.T.Lin, Introduction on Heat and Mass Transfer, Science Press (1995)
3. Kaminiski,W.J. Heat Transfer, 1990; 112: 555-560
4. X.G.Liang, Z.Y.Guo, Y.S.Xu, "Instant Heat Conduction Analyses on Sand Particle Stack Bed and Multi-layer Materials", proceedings of Chinese Engineering Thermal Physics Academy Heat and Mass Transfer Academic Conference, Number: 953154: 17-14

OSMOTIC DEHYDRATION PRETREATMENT IN DRYING OF FRUITS AND VEGETABLES

Y.K. Pan*, L.J. Zhao and Y. Zhang

Department of Mechanical Engineering, Tianjin Institute of Light Industry,
300222, Tianjin, China

Tel 86 22 28342052 email panyk@public1.tpt.tj.cn

G.H. Chen

Department of Chemical Engineering, Hong Kong University of Science and Technology
Clear Water Bay, Kowloon, Hong Kong, China
Fax 00852 23580054 email kechengh@ust.hk

A.S. Mujumdar

Department of Chemical Engineering, McGill University
3610 University St., Montreal, Quebec, Canada, H3A, 2B2
Fax (514) 3986678 email arun@chemeng.lan.mcgill.ca

Keywords: osmotic dehydration; vegetable and fruit; nutrition loss; nutrition enrich

ABSTRACT. Several vegetables and fruits, apple, ginger, carrot and pumpkin are dehydrated under various osmotic conditions using sucrose and salt as the permeating agents. The dehydrated materials are then dried. The influence of solute concentration, process temperature and the type of solute on osmotic dehydration and further thermal drying are investigated. The nutrition loss during the osmotic process is measured using carotene as the nutrition index. The effect of calcium chloride present in osmotic solution on the product quality has also been studied. A first order kinetic model is chosen to describe the mass transfer phenomena of the osmotic process. The equilibrium value of water loss, solute gained, kinetic constants K_{WL} and K_{SG} under various conditions are successfully predicted by the model. The relationship between the equilibrium value and four major factors that influence osmotic process of carrot is obtained based on the experimental data. The relations between the loss constant of carotene and the solute concentration in carrot and pumpkin are obtained based on the experimental data. The qualities of dried products are better for the osmotic dehydration pretreated samples than those dried directly.

INTRODUCTION

Osmotic dehydration is a complex dynamic mass transfer process. By putting vegetables and fruit pieces into highly osmotic solution, the water in the cells of the materials permeate into the osmotic solution through the cell membrane due to the high osmotic pressure and low water activity of the osmotic solution. This osmotic dehydration process can reduce the water content of vegetables and fruits by 50%. Since osmotic dehydration is more economical than thermal drying, it is often used as a pretreatment for drying of biological materials.

Osmotic dehydration process is affected by the concentration and the temperature of osmotic solution, the type of osmotic agent, the size of the bio-material and the mixing intensity, etc. In the experiments with apple and kiwi, water loss (WL) and solute gain (SG) are found to increase with the concentration of osmotic solution [1]. An increase in the operating temperature would accelerate the chemical reaction and mass transfer rate but decrease the viscosity of the solution as demonstrated by the results obtained from the osmotic dehydration of pineapple loop in sucrose solution. The time to reach equilibrium was found also shortened significantly due to the increase of solution temperature [2]. The selection of the osmotic agent of food should be made based on the following criteria: having edible taste and acceptable smell, being innocuous, and stable when coexisting with other components in food. The common osmotic agents for dehydration of vegetables and fruits are table salt, sucrose, glucose, fructose, starch, corn syrup, glycerol, and plant hydrogelation colloid. Different osmotic agent behaves differently. A common feature is, however, that low molecular weight osmotic agent performs better than high molecular weight one. The sense organ quality of osmosized product in the mixture of sucrose and table salt is better than either pure sucrose or pure salt solution. Mixtures of low concentration of sucrose and additive salt are usually recommended from the health point of view.

During the osmotic dehydration process, the nature of the bio-material is changed resulting an inevitable loss of nutrition. The characteristics of osmosized material in further drying are deemed to be different from the drying of fresh material. Although there have been a few reports in recent international drying symposium [3-13], there are still many questions remained to be answered especially on the effects of osmotic dehydration on the properties of the dried product. In this paper, we first investigate the influence of the concentration and temperature of the osmotic solution, and the type of osmotic agent on the equilibrium water loss (WL_{∞}) and solute gain (SG_{∞}), water loss rate constant (K_{WL}) and solute gain rate constant (K_{SG}), then identify the differences of drying characteristic of the osmosized material from that of the fresh material, and finally quantify the nutrition loss.

OSMOTIC DEHYDRATION PROCESS

For simplification, only two counter-diffusions are usually assumed to take place in osmotic dehydration with one being the water diffusing out from the inner cell to the surrounding solution and the other being the solute diffusing from the surrounding solution into the cell. The two transfers are independent. Water loss WL (kg/kg fresh material) and solute gain SG (kg/kg fresh material) are the main parameters to consider in this process. They are defined as:

$$WL (\%wb) = \left[(M_o - M_d) - (M_t - M_{td}) \right] / M_o \quad (1)$$

$$SG (\%wb) = (M_{td} - M_d) / M_o \quad (2)$$

where: M_o being the initial mass of material (kg), M_t the mass of material at t time (kg), M_d the initial dry mass of material (kg), and M_{td} the dry mass of material at time t (kg) during osmotic dehydration process.

Experimental data show that WL and SG are of exponential functions with time. Mass transfer can reach its equilibrium when the time of osmotic dehydration process is infinite long. Therefore this process can be described by a first order dynamic model as:

$$d(WL_{\infty} - WL)/dt = K_{WL}(WL_{\infty} - WL) \quad (3)$$

$$\ln(WL_{\infty} - WL) = \ln WL_{\infty} - K_{WL} t \quad (4)$$

$$\text{or } WL = WL_{\infty} (1 - \exp(-K_{WL} t)) \quad (5)$$

Similarly:

$$\ln(SG_{\infty} - SG) = \ln SG_{\infty} - K_{SG} t \quad (6)$$

$$\text{or } SG = SG_{\infty} (1 - \exp(-K_{SG} t)) \quad (7)$$

Eq. (4) and (6) can be used to determine K_{WL} , K_{SG} when WL_{∞} and SG_{∞} are known. WL_{∞} and SG_{∞} are taken as the values of WL and SG when insignificant changes are observed after a sufficiently long period of osmotic dehydration time.

Effect of Osmotic Solution Concentration

Fig. 1 shows the evolution of water contents respectively in carrot and pumpkin slices (3mm in thickness) during osmotic dehydration process using different concentrations of sucrose solution. Detailed experimental conditions and operations are available elsewhere [14]. For carrot dehydration, it needs about 4 hours for WL to reach its equilibrium value. While for pumpkin, the equilibrium is approached after 8 hours of dehydration. Obviously the increase of the sucrose concentration results in not only a faster dehydration rate but also a lower equilibrium water content or a larger WL . Fig. 2 presents the SG values at the same conditions of Fig. 1. It can

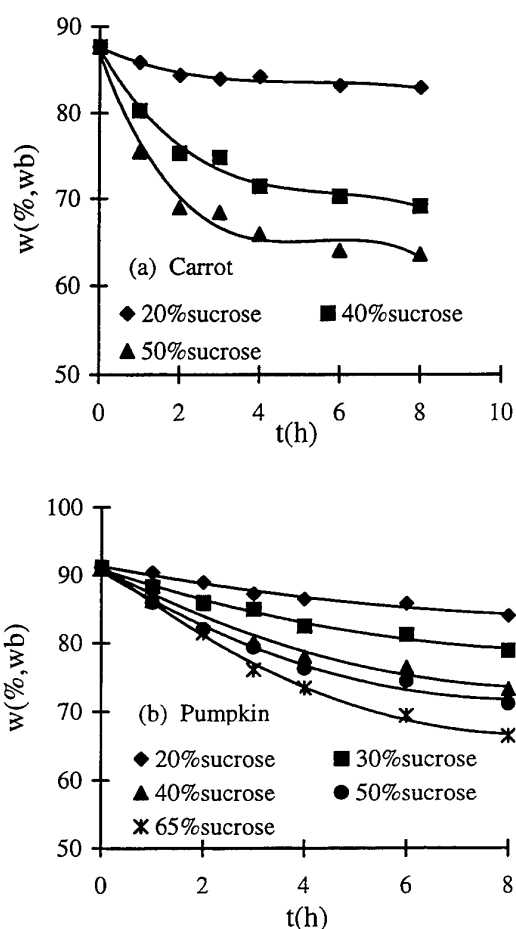


Fig. 1. The decrease of water content with osmotic dehydration time

be seen that the solute gain increases along with the increasing of the osmotic solution concentration in the range of 20% to 50%. Further increase of the solute concentration from 50% to 65% for pumpkin, the solute gain increases initially but shows insignificant difference from that of 50% condition after 4 hours of dehydration. This decrease is resulted from the formation of a protective film on the surface of the material which prevents the solute permeating into the material from the surroundings. Following the analysis mentioned in the previous paragraph, the transfer parameters are obtained as listed in Table 1.

Material	Concentration wt%	WL_{∞} Kg/kg fresh material	K_{WL} h^{-1}	SG_{∞} kg/kg fresh material	K_{SG} h^{-1}
Carrot	20	0.2435	0.4962	0.0258	0.4194
	40	0.4519	0.5937	0.0944	0.4904
	50	0.4528	0.7825	0.1375	0.5336
Pumpkin	20	0.4531	0.3555	0.0506	0.3429
	30	0.5145	0.3993	0.0701	0.3560
	40	0.5640	0.4598	0.0914	0.3720
	50	0.6126	0.5143	0.1064	0.3912
	65	0.6362	0.4215	0.1037	0.4195

Although the equilibrium WL values increase with the solute concentration, the K_{WL} values for pumpkin show a decrease when the solute concentration increases from 50% to 65%. Again this is due to the formation of the dense layer of sucrose on the surface of pumpkin slices and also due to the low diffusivity of water in the highly concentrated sucrose solution. The solute gain rate constant K_{SG} increases with the solute concentration even for 65% condition. This is because K_{SG} not only reflects the mass diffusivity but also includes the concentration gradient effect. The large solute concentration would give a high mass transfer driving force also.

Effect of Osmotic Solution Temperature

Experiments were carried out at ambient temperature, 40 and 50 °C, respectively, using 20% sucrose solution as osmotic agent on 3 mm carrot as well as pumpkin slices. No significant differences were observed either on the water loss or solute gain for both materials.

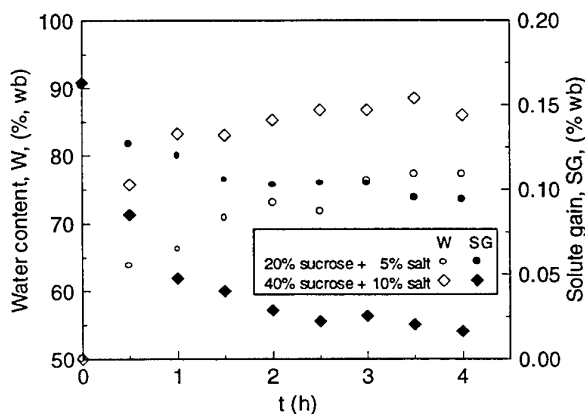


Fig. 3. Variation of water content and solute gain using mixtures of osmotic agents

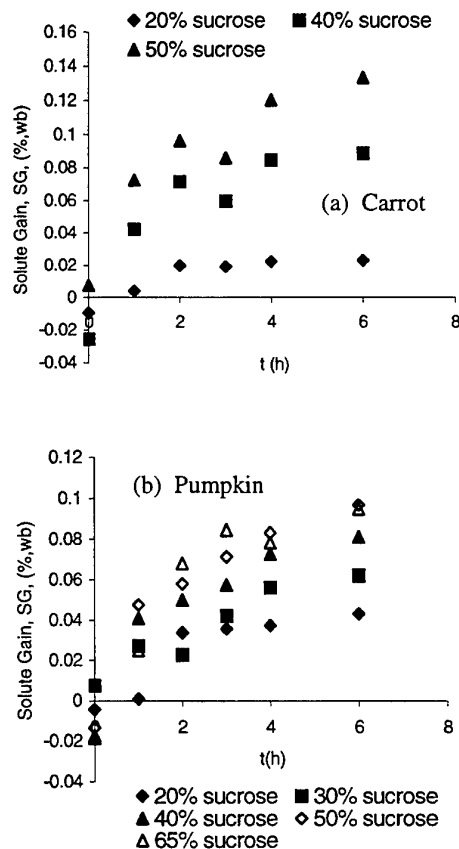


Fig 2. Variation of solute gain with osmotic dehydration time

Effect of Mixture of Osmotic Agents

In order to find the effect of osmotic agent mixtures, 3 mm thick carrot slices were osmosized for 4 hours in the mixtures of sucrose and salt. Fig. 3 shows

that the water losses reach 27% and 35% respectively for 20% sucrose and 40% sucrose mixed with salts. The dehydration is certainly enhanced by the presence of salt comparing with the results shown in Fig. 1 where less than 10% and 20% water loss were observed after the same amount of dehydration time using pure sucrose solution at 20% and 40% concentrations. These differences are supposed to be caused by the increase of the osmotic pressures.

OSMOTIC DEHYDRATION ON THERMAL DRYING CHARACTERISTICS

Fig. 4 shows the drying characteristics of osmosized pumpkin slices in oven. The osmotic pre-treatment not only affects the time required for drying the material, but also changes the drying characteristics significantly. For example, the warm-up period for the three slices treated with high concentration of sucrose is shorter than those treated with low sucrose concentrations including the fresh pumpkin slice without osmotic dehydration pre-treatment. It is interesting to note however that the constant drying rates for the fresh and the pretreated samples are not very different. When the osmotic dehydration temperature increases, a small decrease of the constant rate period is noticed but this small difference does not affect the total drying time significantly. Distinct differences were observed for the samples treated with the solution mixtures as shown in Fig. 5. It is known that the drying characteristics are material dependant, thus different materials may behave differently. However for the same material, the differences noted in Fig. 5 are very impressive.

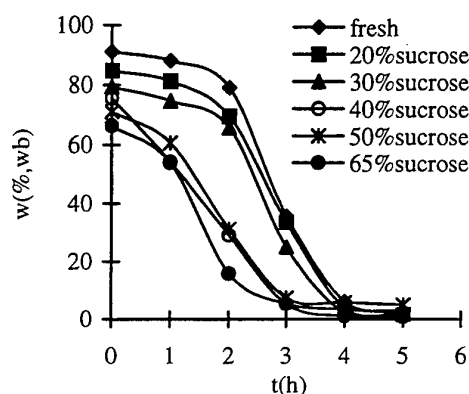


Fig. 4. Effect of osmotic agent concentration on oven drying of pumpkin (85 °C)

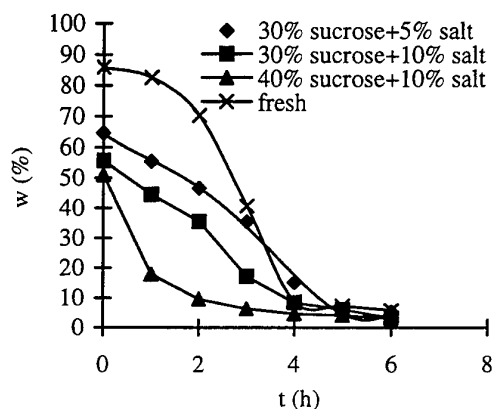


Fig. 5. Effect of osmotic agents on oven drying of ginger (85 °C)

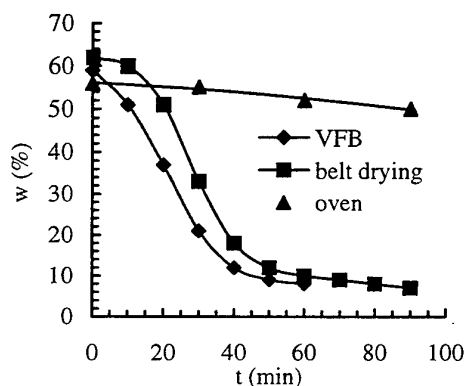


Fig. 6. Comparison of drying processes of osmotic dehydrated carrot (3mm slice, 100 °C)

Further investigation of the osmosis effect on drying characteristic was carried out by drying 3 mm carrot slices in oven, belt dryer and vibrated fluidized bed (VFB) dryer. The slices were osmosized for 4 hours in 50% sucrose solution. The water content of carrot reaches 10% after about 45 minutes of drying in VFB. It takes 60 minutes for the belt dryer to dry the slices to 10% water content. The drying in oven only removes slightly over 5% water in 90 minutes although all the drying temperature was set at 100 °C, Fig. 6. The low drying rate for oven is understandable because the heat transfer was supplied by radiation and hot plate heat conduction with the natural convection contributes insignificantly. In belt drying the hot air flows through the material layer, which increases the contact area between gas and solid. Besides, the material was turned over several

times during the drying process. Thus the mass and heat transfers were intensified. While in VFB the material is always in fluidizing state with no dead volume built by the slices. The fluidized slices also generate high intensity of turbulence around the surface of the slices favoring the transfer process.

It can be seen from Fig. 6 that falling rate periods for VFB as well as belt dryer take nearly half of the drying time. If there is a way to prolong the constant drying rate period, then the total drying time can be shortened significantly. The on set of the falling rate period is marked by the water content at the surface of the material being below its critical value although the inner part of the material may have significantly higher moisture. Tempering can help to uniform the water content of the material and thus brings up the surface water content. In addition, the moisture from inner part of the material can also help to soften the dried shell formed at the material surface. These tempering effects are also beneficial as illustrated in Fig. 7. The drop of water content from 22% to 11% before and after tempering was due to the evaporation of water while the material changes its temperature from 100 °C to ambient condition during the 12 hours tempering process. The final water content of carrot slices was 8.1% after 60 minutes of continuous drying in VFB. For tempering-intermittent drying, the final water content of the dried carrot can be as low as 4.9%, obtained after 55 minutes of VFB drying with the same inlet air temperature of 100 °C. The materials reach 8.1% after only 31 (25 plus 6) minutes of VFB drying when tempering is used. This demonstrates the significant save in energy consumption by using tempering in the VFB drying. The duration of tempering is a factor to consider. For carrot slices, their surfaces are dry and hard at the beginning of tempering but become soft and wet after 6 hours of tempering, which implies that it needs at least 6 hours of tempering for 3 mm carrot slices.

NUTRITION PRESERVATION BY OSMOTIC DEHYDRATION

The nutrition preservation is one of the major concerns in the dehydrated food materials. Unfortunately, there are not many literatures available on such studies of osmotic dehydrated materials. It is believed that any processing of the food dehydration would be accompanied by a loss in nutrition. For osmotic dehydration, this loss is determined by the type of the osmotic agent used, the concentration and the temperature of the osmotic solution, and the thickness of the slices of the material, etc. In this part of the study, effort is focused on the effects of the type of osmotic agent and of the concentration of osmotic solution. Carrot and pumpkin are selected as the testing material due to their rich contents of carotene which is one of the very important nutritious components in vegetables and fruits because it can be transformed into vitamin A during digestion. For the same reason that carotene content is selected as the nutrition index.

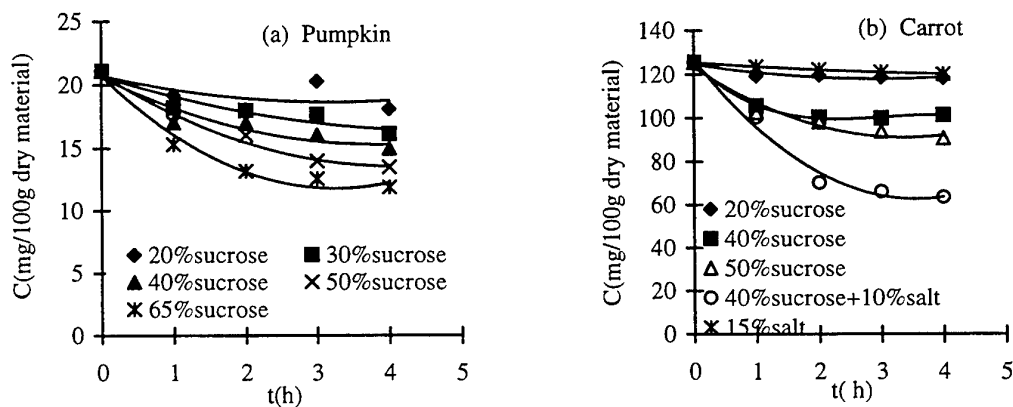


Fig. 8. The change of carotene content under different osmotic dehydration conditions

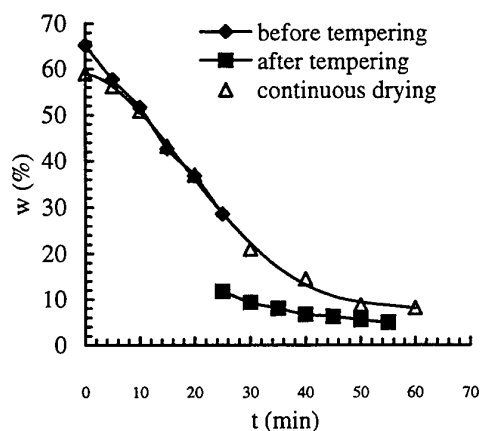


Fig. 7. Comparison between intermittent and continuous drying of osmotic dehydrated carrot (3 mm slice, 100 °C)

Fig. 8 shows the change of carotene content during the osmotic dehydration. It is obvious that the nutrition loss is very remarkable. While the osmotic dehydration was conducted at ambient temperature without excessive supply of oxygen, the loss of carotene cannot be from deterioration commonly resulted from oxidation effect. It is found that the carotene content in the osmotic solution balances that lost from the sliced materials. This suggests that the loss of the nutrition is a direct result of water removal. In fact the carotene loss is found to be directly proportional to water loss or solute gain. Exactly how the carotene ends up in the osmotic solution needs more study. Since the behavior of the change of carotene content is very similar to the change of water content, the variation of carotene content C can be related with dehydration time t in a logarithmic function as:

$$\ln C = -Kt + \ln C_0 \quad (8)$$

With K being the nutrition loss rate constant and C_0 the initial carotene concentration.

Applying Eq. (8) to the dehydration data, K and C_0 can be determined, Table 2. It is found that the nutrition loss constant K is linearly related with the sucrose concentration when there is no presence of salt.

Table 2. Nutrition loss parameters at different osmotic dehydration conditions				
Material	Concentration (wt%)		C_0 mg/100g dry material	K h^{-1}
	Sucrose	Salt		
Pumpkin	20	0	21.0	0.0428
	30	0	20.5	0.0569
	40	0	19.9	0.0749
	50	0	20.0	0.1093
	65	0	18.9	0.1348
Carrot	20	0	124.8	0.0292
	40	0	121.2	0.0536
	50	0	117.6	0.0735
	40	10	117.1	0.1777
	0	15	125.1	0.0108

CONCLUSIONS

The equilibrium water loss and solute gain increase along with the increase of the concentration of sucrose solution up to the value of wt50%. Further increase of concentration of solute would result in a decrease due to the formation of a hard layer around the surface of the samples. The effect of temperature is not remarkable. The addition of salt in the sucrose solution can enhance the osmotic dehydration significantly.

The thermal drying time of the osmosized materials is reduced in comparison with the fresh material. The effect of osmotic agent temperature on thermal drying is not remarkable, thus it is better to conduct the osmosis in room temperature in view of energy saving. The material osmosized by sucrose and salt mixtures shows a significant decrease in drying time. Drying time can be further shortened by using tempering intermittent drying.

Carotene loss is very impressive during osmotic dehydration. It is found to be directly proportional to the water loss or solute gain. The carotene loss rate constant is linearly related with the concentration of sucrose solution without the presence of salt.

REFERENCES

1. N.M.Panagiotou, V.T.Karathanos, Z.B.Maroulis, "Modeling of the Osmotic Dehydration of Fruits", *Drying'98*, v. A, pp.954-961, edited by C.B. Akritidis, D. Marinos-Kouris, G.D. Saravacos, (1998).
2. C.I.Beristain, E.Azuara, R.Cortes, H.S.Garcia, "Mass Transfer During Osmotic Dehydration of Pineapple Rings", *Int. J. of Food Sci. Techn.* v. 25, pp.576-582 (1990).
3. A. Lenart, R. Dabrowska, "Kinetics of Osmotic Dehydration of Apples with Pectin Coatings", *Int. J. Dry Techn.* v. 17, 1359-1374 (1999).
4. D. Torreggiani, E. Forni, A. Maestrelli, F. Quadri, "Influence of Osmotic Dehydration on Texture and Pectic Composition of Kiwifruit Slices", *Int. J. Dry Techn.* v. 17, 1387-1398 (1999).
5. J.M. Barat, A. Albors, A. Chiralt, P. Fito, "Equilibration of Apple Tissue in Osmotic Dehydration Microstructural Changes", *Int. J. Dry Techn.* v. 17, 1375-1386 (1999).
6. A. Peppas, J. Mandala, A.E. Kostaropoulos, G.D. Saravacos, "Influence of Solute Temperature and Concentration on the Combined Osmotic and Air Drying", *Int. J. Dry Techn.* v. 17, 1449-1458 (1999).

7. A. P. Aboim, F. A.R. Oliveira, C. Drumond, J. M.Frias, L. M.Cunha, "Modelling of Water Losses During Osmotic Dehydration Using the Weibull Probabilistic Model:Application of the D-Optimal Design Concept to Improve Parameter Estimation", *Drying'98*, v. A, pp.819-826, edited by C.B. Akritidis, D. Marinos-Kouris, G.D. Saravakos, (1998).
8. N. E. Mavroudis, L. Wadso, V. Gekas, I. Sjöholm, "Shrinkage, Microscopic Studies and Kinetics of Apple Fruit Tissue During Osmotic Dehydration", *Drying'98*, v. A, pp.844-851, edited by C.B. Akritidis, D. Marinos-Kouris, G.D. Saravakos, (1998).
9. M Medina-Vivanco, DJA Sobral, M.D.Hubinger, "Mass Transfer During Dewatering and Salting of Tilapia for Different Volume Brine to Fillets Ratios", *Drying'98*, v. A, pp.852-859, edited by C.B. Akritidis, D. Marinos-Kouris, G.D. Saravakos, (1998).
10. D. Salvatori, A. Andres, A. Chiralt, P. Fito, "Mathematical Modeling of Mass Transfer During Osmotic Dehydration", *Drying'98*, v. A, pp.868-876, edited by C.B. Akritidis, D. Marinos-Kouris, G.D. Saravakos, (1998).
11. A. Albors, D. Salvatori, A. Andres, A. Chiralt, P. Fito, "Influence of the Osmotic Solution Concentration on the Structural and Compositional Profiles in Dehydrated Apple Tissue", *Drying'98*, v. A, pp.877-885, edited by C.B. Akritidis, D. Marinos-Kouris, G.D. Saravakos, (1998).
12. M. Chafer, M.D. Ortola, A. Chiralt, P. Fito, "Osmotic Dehydration of Orange Peel", *Drying'98*, v. A, pp.886-894, edited by C.B. Akritidis, D. Marinos-Kouris, G.D. Saravakos, (1998).
13. B.F.Ozaslan, M.Ozdemir, L.L.Dock, J.D.Floros, "Optimizing the Osmotic Dehydration Process of Green Peppers", *Drying'98*, v. A, pp.946-953, edited by C.B. Akritidis, D. Marinos-Kouris, G.D. Saravakos, (1998).
14. Y. Zhang, "An investigation of osmotic dehydration as the pre-treatment on drying of fruits and vegetables", Master Thesis, Tianjin Institute of Light Industry, China, (1999).

DRYING OF VALUE-ADDED LIQUID WASTES

Marzouk Benali*, Mouloud Amazouz and Tadeusz Kudra

Natural Resources Canada – CANMET/Energy Diversification Research Laboratory
1615, Lionel-Boulet Boulevard, P.O. Box 4800, Varennes (Quebec) J3X 1S6 Canada
Email: mbenali@nrcan.gc.ca; Fax: (450) 652-5994

Keywords: liquid wastes, drying, inert particles, jet-spouted bed

ABSTRACT. The estimated quantity of sludge generated by the Canadian pulp and paper industry in 1995 was about 2.2 million tones of dry solids (tds) while that of municipal and meat-processing sludge was equal to 612,000 and 20,000 tds, respectively. As a result of landfill directives and national legislation which impose minimum solids content of 35% and carbon limit for wastes to be landfilled, major R&D efforts are directed in developing an effective and environmentally acceptable methods of sludge treatment and disposal. Thermal drying could be an attractive solution to sludge disposal especially for complex wastes containing fibres and/or sticky components such as animal fat. Because most of dry wastes have an intrinsic value, they can be beneficially recycled in agriculture, used as a fuel or serve as an inert support in such products as a cat litter. The proposed Jet Spouted Bed Dryer with inert particles (JSBD) is an advanced and energy efficient technology to obtain powders from solutions, slurries and pastes by drying on the surface of inert particles brought into intensive and random motion. The dryer presented here was developed to process otherwise hard-to-dry pulp and paper secondary sludge and meat processing sludge as currently used technologies do not guarantee product of required quality. Experimental results obtained on a 50kW-test bench demonstrate the technical feasibility of drying such sludges, which may contain up to 15% of fibres or up to 60% of fat. Also it is possible to obtain dry product in the form of fine powder with narrow size distribution and with an average particle diameter equal to 40 μm for meat processing sludge, and 136 μm for pulp and paper secondary sludge.

1. INTRODUCTION

In many cases, industrial sludge is disposed of at sanitary landfill sites if it is considered solid waste as defined by applicable environmental legislation, and is not a special or hazardous substance. When landfilled, the process sludge degrades relatively fast and, during biodegradation, releases carbon dioxide, methane and possibly volatile organic compound (VOCs), all of which contribute to the greenhouse effect. To meet international commitments, Canada must significantly reduce its anthropogenic greenhouse gas emissions. To this end, unregulated application of process sludge to land must be reduced to significantly lower emissions of VOCs and methane. Similarly, road transportation of process sludge, which is primarily composed of water, results in exhaust gas emissions. Such emissions could be significantly reduced if the sludges being transported are dried. One of the sludge treatment options is the thermal processing such as drying, which enables reduction of the quantities of sludge to be landfilled, recycling of certain products and even reuse of the dry matter in the form of marketable products such as organic fertilizers produced in the jet spouted bed dryer with inert particles. Another reason to dry sludges is the direct or indirect energy recovery as burning of wet sludge lowers the boiler temperature, hinders combustion and enhances greenhouse gas emissions.

This paper presents the concept and the operation of the JSBD as an energy efficient alternative to convert solids contained in the liquid waste to value-added product. The distinct features of this advanced drying technology are illustrated by results of experiments performed with pulp and paper secondary sludge and meat processing sludge.

2. JET SPOUTED BED DRYER WITH INERT PARTICLES

Principle

The JSBD consists of a conical-cylindrical chamber where a high-velocity gas stream injected at the bottom of the cone brings solid particles into intensive, spout-like motion. As compared to the classical spouted bed, the static bed height of inert particles is reduced to an optimal value ensuring uniform circulation of the particles, especially in the downward zone (Figure 1). As confirmed by Markowski and Kaminski [1], the classical spouted bed and the jet spouted (JSB) behaviour provide a similar cyclic motion of the inert particles. However, the JSB bed operates in a

* Author to whom correspondence should be directed.

fast spouting regime, with a high bed void fraction (typically from 0.85 to 0.95). Therefore, no significant difference is observed between the void fraction of the downward zone (the annulus) and the upward zone (the spout).

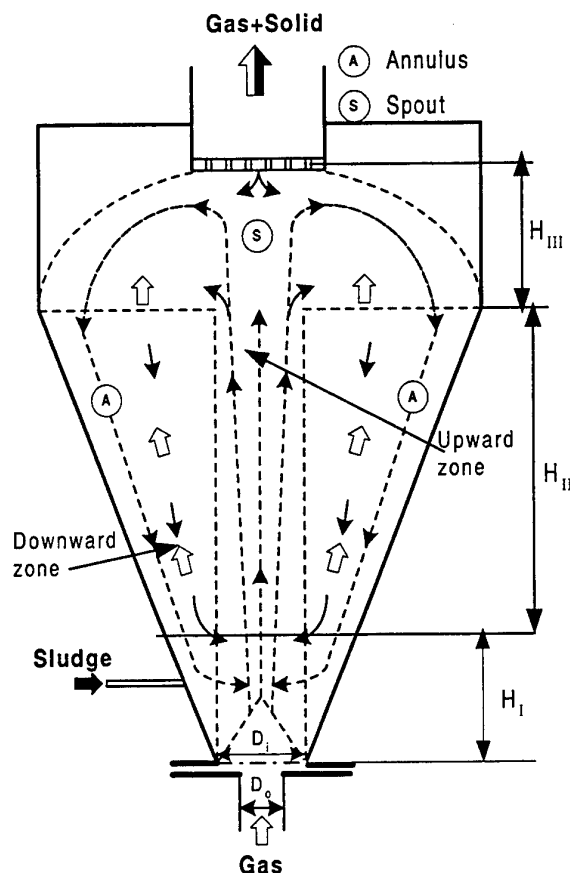


Fig. 1. Principle of jet spouted bed with inert particles

The earliest published studies [1 - 6] on hydrodynamic characteristics and drying in conical spouted beds with inert particles provide some guidance to the process and equipment design. Olazar *et al.* [4] summarized conditions for stable operation of a jet-spouted bed with inert particles as follows:

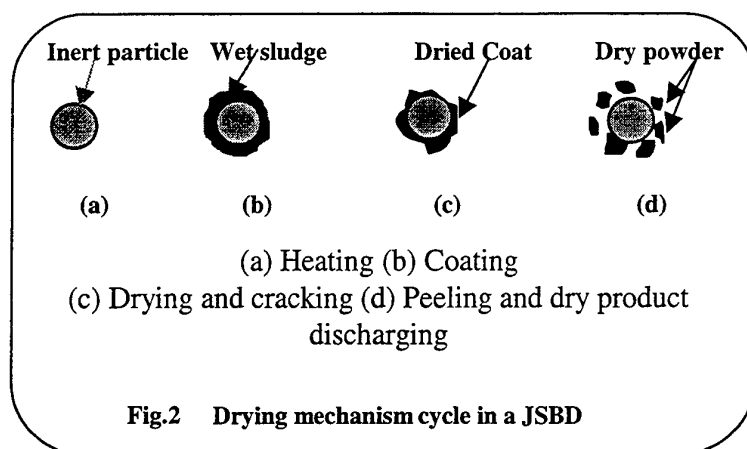
1. D_0/D_1 must be between 1/2 and 5/6,
2. The cone angle must be between 28 and 45°,
3. D_0/d_p has no stability limits: it can be between 1 and 80.

In a standard configuration, the sludge is dispersed into fine droplets and injected into the lower part of the conical drying chamber. Thus the feeding zone (H_I) is set to reduce accumulation of the material within the bed as the hot air stream is in contact with the wettest material. The appropriate height of the feeding zone eliminates thermal damage to the product. Furthermore, this height is closely related to the evaporative capacity of the feeding zone, and to the volume of the JSBD. Drying occurs in the zone defined by the height H_{II} . The separation zone (H_{III}) is located at the fountain of the bed, from which the powdery dry material is carried out of the dryer by exhaust air, and recovered through a discharge section consisting of a cyclone and a bag filter.

Drying Mechanism

In a continuous operation, the spray of fine droplets of dispersed sludge covers the surface of hot inert particles that are heated by convection from the spouting air stream after the period of peeling off the dry material. This wet coat is dried due to convective heat transfer from the upward hot air stream, and due to conduction of heat stored in hot

inert particles. The drying process continues until the moisture content drops to the critical value at which the layer is dry enough to be brittle. The dry layer is then broken and peeled off from the solid surface due to particle-particle collisions, and also due to the collisions with the dryer wall and the overhead screen (abrasion and/or attrition). Therefore, the ideal drying mechanism in a JSBD is divided into four successive steps (Fig.2): (a) heating of inert particles, (b) coating of inert particle, (c) drying and cracking, and (d) peeling and discharging. In a regular operation, coating of particles, drying of the wet coat and product removal-solid heating occur simultaneously, so the dynamic equilibrium between all subsequent stages is established. This results in a steady temperature of the drying material and exhaust air. Stable operation of the dryer is attained when the rate of dry layer removal is at least equal to the feeding rate. Otherwise, build-up of the wet coat on the particle surface and the dryer wall due to adhesion and cohesion can lead to immediate shutdown of the drying process: a choking phenomenon occurs under this condition as in vertical pneumatic transport of solids.



3. EQUIPMENT AND PROCEDURE

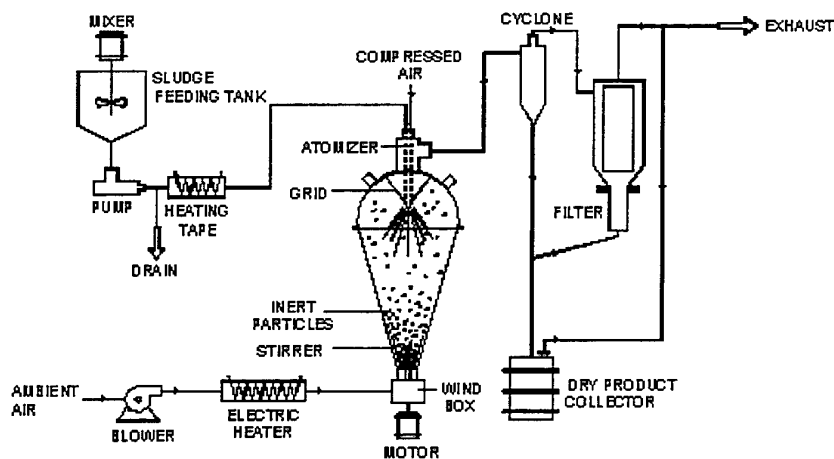


Fig. 3. General view of a jet spouted bed dryer with inert particles

The pilot-scale unit as shown in Fig. 3 consists of the 0.03 m³ JSB dryer equipped with the sludge feeding system, hot air supply and dry product discharge. The height of the conical section is 600 mm with the cone angle of 40°. The spouting hot air is fed through an orifice of 35 mm in diameter, which gives $D_o/D_i = 1/2$. Teflon cubes of 5 mm are used as inert particles. A conical grid located at the top of the disengaging chamber prevents Teflon cubes from being carried away from the dryer. Wet sludge is atomized into droplets (2 - 4 mm) by means of a two-stream pneumatic nozzle located at the central axis of the dryer, 200 mm below the surface of

the static bed of inert particles. A positive displacement pump supplied with a speed control drive achieves the required feed rate of sludge. Dry product is entrained from the exhaust air in a cyclone and a bag filter.

The experiments were carried out for mass of inert particles varied from 4 to 6 kg, inlet air temperature from 180 to 300°C, and feed rate from 5 to 50 kg/h. The spouting velocity was varied from 30 to 45 m/s. Under these conditions the overall pressure drop was within the range from 6.5 to 11.2 kPa. Moisture contents of the wet sludge and the dry product were determined with the OHAUS moisture determination balance (model MB 200). MALVERN-ZETASIZER high sensitivity laser analyser was used to determine the particle size distribution, and microscope Stereo-Master (Fisher Scientific) to quantify fibres.

4. DATA INTERPRETATION

Table 1 summarizes the JSBD operating conditions and the major experimental results. For every experiment the dry product was obtained in the form of fine powder with narrow size distribution (Fig. 4 and 5).

Table 1. Range of Operating Conditions and Experimental Results

Sludge type	Sludge moisture content (%)		Sludge flowrate (L/h)	Air temperature (°C)			Mean particle diameter of dry product (µm)	Impurities
	initial	final		Dryer inlet	In the dryer	Dryer outlet		
Pulp and paper secondary sludge	98	1.5	25	250 to 300	70 to 110	110 to 145	136.0	Cellulose fibres: $(L/d)_m = 60.0$
Meat processing sludge	93	4.0	25	180 to 230	55 to 65	90 to 105	59.5	Bristle $(L/d)_m = 11.4$

In the case of meat processing sludge, the protein content required a lower drying temperature than the pulp and paper secondary sludge. Beyond 65°C, the proteins are denatured and, consequently, their biological value is decreased dramatically. The quality analysis of dry meat processing sludge shows two appearances under different operating conditions: dark brown meaning that the fat content (29.8 – 30.9%) and protein content (18.4 – 27.8%) are highly oxidized and light brown indicating that protein and fat content is not modified. This demonstrates clearly that the oxidation degree of protein and fat depends strongly on the operating parameters of the dryer.

Table 1 shows that the bed temperatures varied from 55 and 110°C being higher than wet bulb temperatures that were in between 50 and 62°C respectively. Such a temperature difference indicates that the fraction of moisture to be removed exists as bound water, and that the conductive heat transfer from inert particle to the wet coat contributes to the drying mechanism. Furthermore, these results confirm the drying mechanism presented in Fig.2 as well as support the hypothesis about the dynamic equilibrium between coating, drying and peeling off due to intensive and continuous recirculation of inert particles in the conical dryer.

It should be noted that beside the "active" component to be dried, the raw material contained solid fibrous impurities. In the case of P&P secondary sludge, the essentially colloidal mixture of clay and polymers contained up to 15% (mass basis) of cellulose fibres whose length varied from 1.0 to 4.5 mm with a mean value of 1.8 mm, and diameter varied from 0.08 to 0.15 mm with a mean value of 0.03 mm. The meat processing sludge contained of about 3% (mass basis) of fibres with length varied from 0.4 to 5.5 mm with a mean value of 1.82 mm, and diameter varied from 0.05 to 0.3 mm with a mean value equal to 0.16 mm. Although these fibres do not contribute significantly to the overall drying kinetics because of evaporation of surface water, they affect

drying characteristics by altering hydrodynamics of the jet spouted bed. In particular, relatively long and flexible cellulose fibres form under certain conditions an elastic and porous shell on the surface of inert particles. This shell might not be broken during particle collision giving rise for build-up of the wet coat and thus clustering of inert particles. In addition, the colloidal matter in the P&P secondary sludge exhibits affinity to cellulose fibres, which may lead finally to agglomeration of the dry material. In contrast, the meat processing sludge does not adhere to the bristle although the fibres may serve as nucleation medium for agglomerates of protein when covered with animal fat.

The specific design of the jet spouted bed dryer ensuring intensive motion of inert particles prevents from cluster formation when drying of P&P sludge containing up to 15% (mass basis) of cellulose fibres although a small fraction (5-10%) of the sludge is retained by the fibres. The fibres contained in the meat processing sludge appear to have no effect on cluster formation, as they are not bound to the dry powder. The presence of fat in meat processing sludge has no effect on dryer operation up to 60% of mass concentration. In both cases, dry powder is free flowing and does not agglomerate during handling.

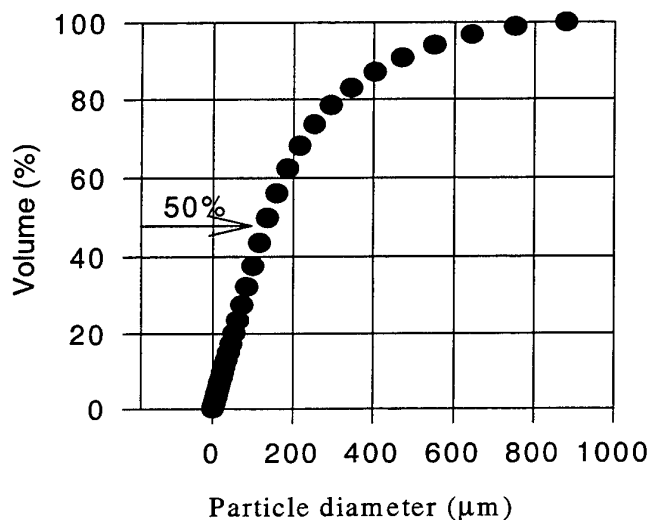


Fig. 4. Particle size distribution of pulp and paper secondary sludge

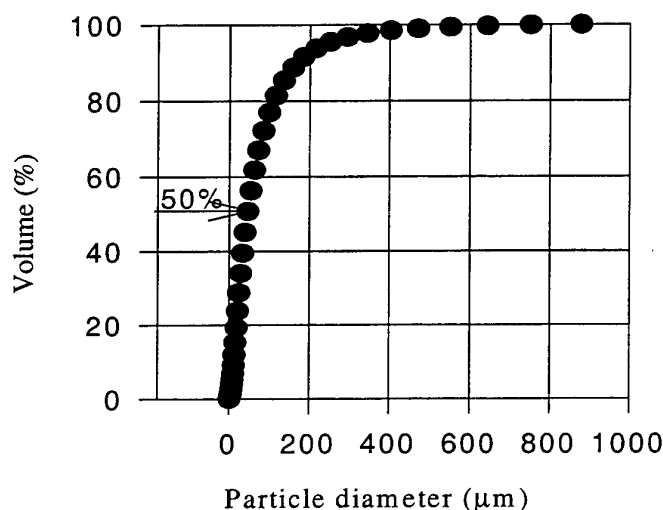


Fig. 5. Particle size distribution of meat processing sludge

5. CONCLUSION

As a result of experiments, the drying of pulp and paper secondary sludge and meat processing sludge can be performed satisfactorily in a JSBD. Moreover, the dry product is obtained in a form of a fine powder and the bed temperature is always higher than wet bulb temperature, which ensures the removal of the bound water and the occurring of the conductive heat transfer between the inert particles and the wet sludge coat.

NOMENCLATURE

D_i : Diameter of the inlet section (spout), m
 D_o : Diameter of the bottom of the bed, m
 d : Diameter of fibres, m
 d_p : Average diameter of inert particle, m
 L : Length of fibres, m
 $(L/d)_m$: Fibre mean length-to-diameter ratio

ACKNOWLEDGMENTS

The authors would like to thank *Gas Technology Canada* for their financial support.

REFERENCES

1. A. Markowski and W. Kaminiski, "Hydrodynamic characteristic of jet-spouted beds", Can. J. Chem. Eng., v.61, pp. 377-383 (1983).
2. K. Kmiec, "The minimum spouting velocity in conical beds", Can. J. Chem. Eng., v.61, pp. 274-280 (1983).
3. Q.T. Pham, "Behaviour of a conical spouted-bed dryer for animal blood", Can. J. Chem. Eng., v.61, pp. 426-434 (1983).
4. A.S. Markowski, "Drying characteristics in a jet-spouted bed dryer", Can. J. Chem. Eng., v.70, pp. 938-944 (1992).
5. M. Olazar, M.J. San José, A.T. Aguayo, J.M. Arandes and J. Bilbao, "Stable operation conditions for gas-solid contact regimes spouted beds", Ind. Chem. Res., v.31, pp. 1784-1792 (1992).
6. H.T. Bi, A. Macchi, J. Chaouki and R. Legros, "Minimum spouting velocity of conical spouted beds", Can. J. Chem. Eng., v.75, pp. 460-465 (1997).

INDIRECT DRYING OF THIN-FILM ALUMINA SLUDGE BY BOILING APPLICATION ON DRUM DRYING

C. Carrère-Gée, D. Lecomte, O. Fudym, P. Arlabosse, B. Ladevie

Ecole des Mines d'Albi, Centre Énergétique – Environnement

Route de Teillet - 81013 Albi - France,

33 (0) 5 63 49 30 93 – lecomte@enstimac.fr

J. Vasseur

ENSIA – INRA – Département Génie Alimentaire, 1 Av. des Olympiades

91305 Massy Cedex - France

Keywords : heat and mass transfer, thin-layer boiling, drum dryer, industrial sludge, inverse conduction problem

ABSTRACT. This work presents a simple method developed for the design of indirect dryers in thin-film by boiling for an alumina sludge treatment. The method developed is based on decoupling of the internal and external transfers. In a first step, external transfers are characterized. A simple experimental device was built up in order both to provide and to estimate the heat flux density at the interface between a hot metallic plate and the drying sample. An analytical direct model is made using the quadripole formalism, and the system transfer function is calculated. The inverse problem is solved using the Beck's sequential function specification method, and the corresponding drying curve is deduced by an energy balance without weighing.

In the second part, the drying of sludge on an electrically heated laboratory drum dryer was studied. The aptitude of sludge to be coated on the cylinder is related to thermal effects. The drying kinetics are obtained by sampling and are compared with those obtained with the first experimental device. The curves are similars whereas the drying time is much longer. A simple model of the drum dryer is developed by taking into account the combined effects of the internal and external transfers. In this case, the importance of the internal transfers, which govern the drying time, are highlighted.

1. INTRODUCTION

A comparative study of dryers technologies currently used for the sludges treatment showed that their development is limited by high energy costs and technological problems [4]. It also directed this work towards indirect drying in thin-film coating. Indirect drying or contact drying, applied to the thermal treatment of sludge presents many advantages : steam and odour confinement, VOC concentration. Drying by boiling in thin-film ensures very high heat flux densities with drying time of a few ten seconds. Among contact drying technologies, drum drying is widely used in the food industry, to treat heat-sensitive products. The product is sprinkled or coated on a hot rotating cylinder. The wall temperature is above boiling temperature. The absence of mixture and agitation constitutes an advantage for viscous products like sludge, enabling a good control of the residence time, the average water content and the thermal efficiency.

A review of drum drying [8], [10], [11] showed that many studies were done on food processing dryer control and internal heat and mass transfer during drying. Little knowledge is exhibited on the external heat and mass transfer rates during coating above boiling temperature. The present study proceeds in two steps:

- *study of the external transfer* between the heated wall and the sludge. A simple and original method is developed to determine the flux density, the wall temperature and thus the thermal resistance at the interface metal/sludge and the drying curves. Since mass balance can't be directly known, a way to estimate the drying rate is to do an energy balance, assuming that the latent heat of vaporization is known. For contact dryer's design, it is important to predict drying rates, but this rate is limited by internal conductive transfers. Internal and external heat transfers are coupled. It is then necessary to find a maximum ideal reference, not driven by internal transfers, but by the intrinsic product's thin film boiling rate.
- *Coupling of the external transfers with the internal transfer:* the review of the drum drying shows that internal heat transfer is largely studied [8], [10], [11]. It is controlled by heat conduction in metal. It can be

associated with external transfer in order to develop a simple analytical resistance model. This model allows to determine the effects of coupled internal and external thermal resistances on the overall drying rate and drying time.

2. CHARACTERIZATION OF EXTERNAL TRANSFERS

Principle of the Experimental Device

It is very difficult to provide and to measure high flux densities (10^5 - 10^6 W.m⁻²) with classical heating systems. For this reason an experimental device was built up in order to provide high flux. The principle of the experiment is to heat up a plate of copper. The heat is stored at a temperature above boiling temperature of water (100°C) and suddenly discharged when the thin-film of the sludge is coated. Initial temperature is provided by placing the plate in a drying convective loop.

The plate must be thick enough in order to store the necessary energy amount for a complete drying by vaporization. It must be highly diffusive in order to ensure high heat flux densities at the interface metal/sludge.

Instrumentation of the Plate

Preliminary tests [5] showed that no direct temperature or heat flux at the interface measure can be made: a sensor located on the front side would perturb the sludge coating or introduce a contact resistance. Thus wall temperature and flux density are estimated using interior location temperature and an inverse heat conduction method.

Two thin thermocouple wires are laid inside the plate, near the surface, and the metal is then dulled. The resulting thermocouple, with separated contacts, is laid in a direction parallel to isothermal curves. With this particular method, the sensor location is precisely known (Fig. 1). Another sensor is laid out on the plate's back side.

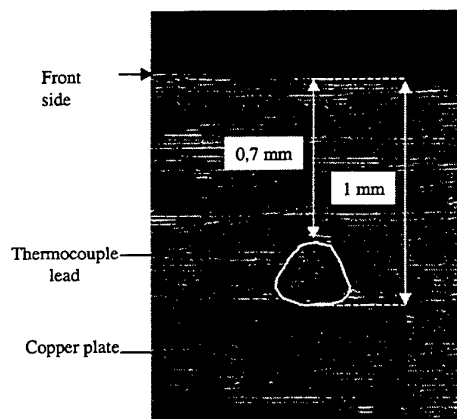


Fig. 1 – Sensor position after dulling

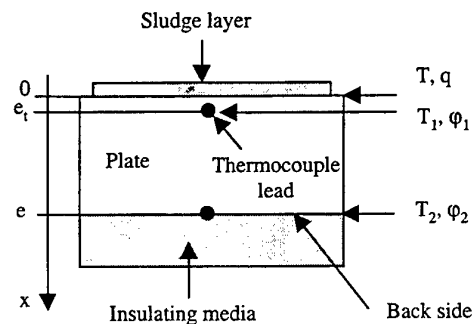


Fig. 2 – Schematic experimental device

Direct Model and Inverse Method

A direct model is built in order to calculate the sensor temperature evolution, when a given heat flux is applied to the plate's surface. The system is shown on Figure 2. An analytical one dimensional conductive model is built, assuming that the plate's back side is insulated. The quadripole formalism [6] is used, and the transfer function $F_1(s)$ between the interface heat flux q and temperature T_1 is calculated.

Heat transfer is here assumed to be purely conductive and the sample homogeneous. To write the previous system in a quadripole form, Laplace transform is applied :

$$\frac{d^2\theta}{dx^2} = \frac{s}{a} \theta \quad (1)$$

with a known heat flux density at the plate surface $x=0$ and insulated back side at $x=e$. The Laplace transformed temperature is defined by: $\theta(x,s) = \int_0^\infty (T(x,t) - T_i) e^{-st} dt$.

Initially, the whole system is assumed to be at uniform temperature T_i and the heat flux is defined by:

$$\phi(x,s) = -\lambda \frac{d\theta(x,s)}{dx} \quad (2)$$

Expressions (1) and (2) are then equivalent to a quadripole presentation [1]:

$$\begin{bmatrix} \theta \\ \phi \end{bmatrix} = \begin{bmatrix} A_1 & B_1 \\ C_1 & D_1 \end{bmatrix} \begin{bmatrix} \theta_1 \\ \phi_1 \end{bmatrix} = \begin{bmatrix} A_1 & B_1 \\ C_1 & D_1 \end{bmatrix} \begin{bmatrix} A_2 & B_2 \\ C_2 & D_2 \end{bmatrix} \begin{bmatrix} \theta_2 \\ 0 \end{bmatrix} \quad (3)$$

The coefficients of the quadripole matrix depend on the thermal properties and on the dimensions of the medium.

It is then easy to determine the transfer functions $F_i(s)$ between the Laplace transformed superficial heat flux ϕ , and the temperatures θ_i to be calculated by

$$\theta_i = F_i(s) \cdot \phi \quad (4)$$

where (i=1,2).

The inverse problem is solved using the Beck's sequential function specification method. The inverse method allows to calculate the superficial heat flux density $q(t)$ from the measured temperatures $Y_1(t)$ at sensor location, and corresponding temperature $T_1(t)$ from the direct model. Inverse transfer function $f_i(t)$ are obtained from $F_i(s)$ through a numerical Laplace inversion [9].

The temperature $T_i(t)$ is then calculated by a convolution product :

$$T_i(t) = \int_0^t q(t-\tau) \cdot f_i(\tau) d\tau \quad (5)$$

Of particular interest is the transfer function between $\phi_1(t)$ and the computed temperature $\theta_1(t)$ at sensor location

$$F_1(s) = \frac{A_2}{C_1 A_2 + D_1 C_2} \quad (6)$$

The insulated boundary condition will be validated from back side measurements Y_2 (T_2 location). Nevertheless, it would be possible to integrate these values in the boundary condition's knowledge.

In the case of one dimensional problem with fast and high heat flux changes, a sequential method is adapted. The function specification method, with a sequential constant heat flux functional form is used [3]. For that method [2], $q(t)$ is approximated in a discrete form.

A thermal resistance, introduced between the sludge and the hot metal, can be introduced:

$$R_{ext}(W, t) = \frac{T(t) - T_b(W)}{q(t)} \quad (7)$$

Heat Flux Estimation, Temperatures and Thermal Resistance Results

Results are presented for thin-film coating of an alumina hydroxyde sludge on copper plate. The water concentration of sludge is identical in both experiments. The analysis of equations 3-6 shows that the thermal properties of the plate should influence the heat transfer.

Estimated superficial heat flux densities are plotted on Figure 3 versus drying time and for different initial temperatures (111-137°C). Two ebullition periods can be observed. A first short period with very high flux ($\approx 4.10^5$ - 10^6 W.m⁻²) followed by a longer period where the flux is several orders of magnitude smaller.

The maximal heat flux decreases with temperature and the duration of the first period increases when the initial temperature of the metal plate decreases.

Measured and estimated temperatures evolution are plotted on Figure 4. The measured sensor temperature Y_1 is perfectly fitted with T_1 , which is a consequence of the chosen inverse method, very close to an exact matching algorithm. More important is the perfect fit between back side measurement Y_2 and computed temperature T_2 , because this means a good agreement between the experiment and the model, and proves the validity of back side insulated boundary condition assumption. Wall temperature T and T_1 are almost identical, due to the low distance between the front side of the plate and the sensor.

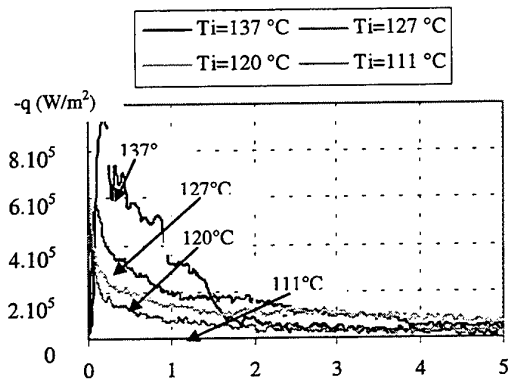


Fig. 3 – Estimated superficial heat flux density $q(t)$

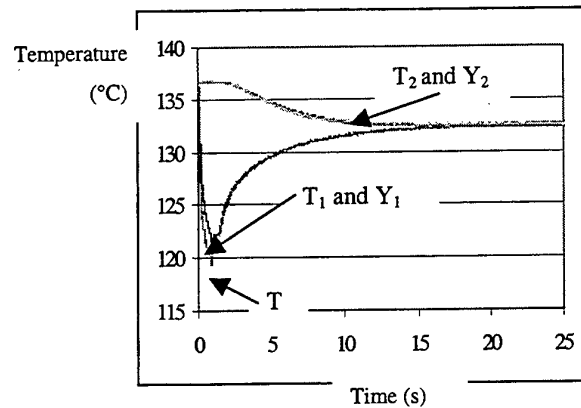


Fig. 4 – Estimated and measured temperatures at $T_i=137^\circ$

Y_1 is submitted to a fast decrease due to sudden boiling phenomena, and the corresponding superficial heat flux density is high. The decrease is stopped when the heat flux intensity falls down while thermal diffusion inside the copper plate tends to its homogenization. When $q(t)$ is close to zero, front side and back side temperatures tend to the same value, corresponding to a quasi-permanent state.

The wall temperature T is always above the product's boiling temperature. Boiling transfer stops probably due to the product structure evolution: a high external thermal resistance is found between the dried product and the plate interface (Fig. 5).

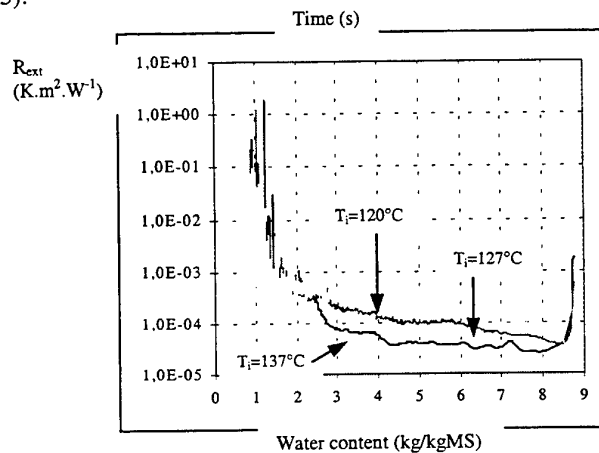


Fig. 5 – External thermal resistance $R_{ext}(W, T_i)$

External thermal resistance reduces when initial temperature of copper increase and increases when water content reduces. The lower the initial temperature is, the more the curves take the form of a sigmoid.

In order to fit these curves, we choose a mathematical relation usually used for the modelling of sorption isotherms with 6 estimated parameters (Table 1):

$$R_{\text{ext}}(W, T_i) = \frac{a_2}{T_i} + b_2 + \frac{R_m W' K e^{\frac{a_1 + b_1}{T_i}}}{(1 - W' K) \left(1 + K W' e^{\frac{a_1 + b_1}{T_i}} - W' K \right)} \quad \text{with} \quad W' = \frac{W_i - W}{W_i} \quad (8)$$

Table 1 – Estimated Coefficients

a_1	b_1	a_2	b_2	R_m	K
$4.23 \cdot 10^4$	$-1.048 \cdot 10^2$	0.196	$-4.431 \cdot 10^{-4}$	1.106	$8.384 \cdot 10^{-5}$

Energy Balance and Drying Curves

Superficial heat flux knowledge can be used to calculate the energy density E lost through the surface :

$$E(t) = \int_0^t q(\tau) d\tau \quad (9)$$

The global energy density lost by the copper plate after a new quasi-permanent state is reached (when front side and back side temperatures are equal to T_f) is:

$$E' = \rho C_p e(T_f - T_i) \quad (10)$$

E' is found to be quite close to $E(t_f)$, where t_f is the final time when $T_1 = T_2 = T_f$. This means that $q(t)$ is the only flux crossing plate walls. This fact confirm the insulated back side assumption, but also seems to prove there are no lateral losses, hence the one dimensional conductive transfer assumption is valid.

It is now possible to calculate the dry matter load:

$$M = \frac{E'}{(W_i - W_f) l_v} \quad (11)$$

with W_i and W_f initial and final moisture content. It is very important to know precisely the dry matter load M , since drying rate is highly dependant on this quantity, and it is not possible to deduce its precise value with direct experimental measurements.

The moisture content $W(t)$, the drying curves, and finally the drying rate can be deduced from equations 9-11:

$$W(t) = W_i - \frac{E(t)}{M \cdot l_v} \quad (12)$$

Drying curves are shown by Figure 6. It is noticeable that boiling thin-layer drying, in that particular case, is very fast, thanks to the non internal transfer limitation. The drying time increases with initial temperature and depends on the dry matter load M .

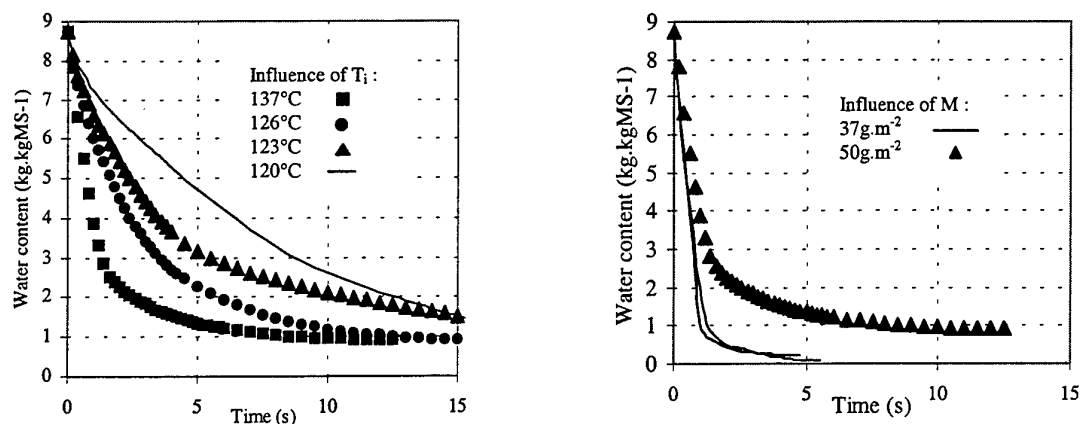


Fig. 6 – Drying curves of alumina sludge

3. DRUM DRYER MODELLING AND EXPERIMENTAL VALIDATION

Experimentation

The drying kinetics are obtained by sampling and can be compared with those obtained with the first experimental device. The curves are similar whereas the drying time is much longer and depend on regulation temperature. The results will be presented in a next section.

Drum Dryer Description

In this part, the drying of alumina sludge on an electrically heated laboratory drum dryer was studied (Fig. 7 and Table 2). The drum dryer (212 mm of diameter and 250 mm of length) is composed of an internal cylinder made of copper (201 mm of diameter and 116,93 mm of length) and of an external layer in stainless steel. The zone of coating is located at the level of the copper cylinder. Twelve cylindrical heating resistances are established uniformly in the copper cylinder. The length of resistances is the same one as the internal copper cylinder. Four probes type Pt100 are set in the copper cylinder. They are positioned between two resistances and are distributed on the circumference of the cylinder. They give the temperature of the center of the zone of coating (in the center of the copper cylinder). A PID controller allows to control its temperature which is limited at 180°C.

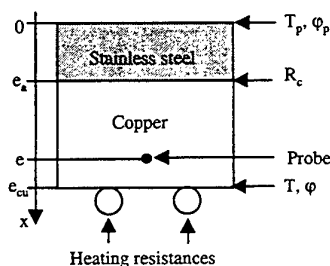


Fig. 7 – Drum dryer schematic description

Table 2 – Dimensions of the Drum Dryer

e_a	5,50 mm
e	15,8 mm
e_{cu}	16,4 mm

Drum Dryer Modelling

The developed model of drum drying is based on thermal resistances in series (fig. 8). This model enables to simulate the heat conduction through various metal layers constituting the laboratory drum dryer. All the energy provided to alumina sludge by the drum dryer makes it possible to vaporize the water contained in sludge.

The mains assumptions for the resistive model are :

- H1 : The sludge temperature and water content in the thickness are considered as means parameters
- H2 : We neglect the heat transfers parallels to the drum dryer generators in front of the axials heat transfers
- H3 : We neglect potentials transfers by convection or radiation

- H4 : Internal thermal resistance of the drum dryer is assumed constant during drying. It take resistance thermal of envelope in steel, the contact resistance between the copper and the stainless steel and the thermal resistance of copper layer into account. Thermal resistances depend on thickness and thermal properties of the metal layer. Thus, internal thermal resistance of the drum dryer is equal to $4.10^{-4} \text{ K.m}^2.\text{W}^{-1}$.
- H5 : In copper, the temperature is assumed homogeneous, constant and equal to regulation temperature. Therefore thermal resistance introduced by copper can be neglected in front of that of stainless steel
- H6 : We will not take wall thermal inertia into account. It is a strong assumption which is not valid in the transient states. Nevertheless, with a view to design, we will preserve this assumption.
- H7 : The expression of $R_{\text{ext}}(W,T)$ is assumed equal to $R_{\text{ext}}(W,T_i)$ founded in the next section with T_i , the initial temperature of the copper plate.

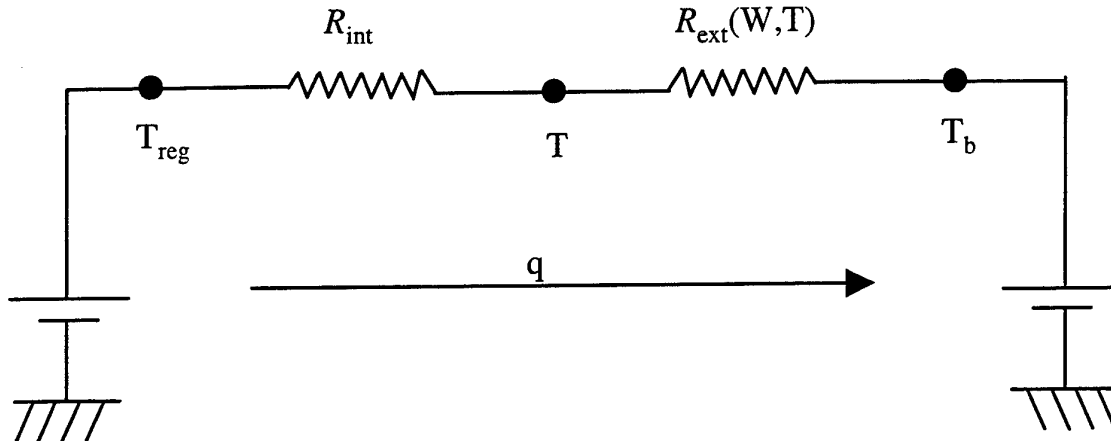


Fig. 8 - Electric equivalent diagram of the drum dryer model

Mathematical Expression of the Drum Dryer Model and Results

The losses being negligible, it is supposed that: $\varphi_p(y) + \varphi_v(y) = 0$ (13)

$$q(y) = \frac{dW}{dy} L_v M = -\varphi_v(y) \quad (14)$$

The relation between heat flux density and the differents temperatures is:

$$q(y) = \frac{T(y) - T_{\text{reg}}}{R_{\text{int}}} = \frac{T_b - T_{\text{reg}}}{R_{\text{int}} + R_{\text{ext}}(W, T_p)} \quad (15)$$

We obtain a system of partial differential equations solved by the method of Runge-Kutta using the function « ode 45 » by MATLAB [7]. For each step, this model calculate the wall temperature (T), the interfacial heat flux density (q), the external thermal resistance (R_{ext}) and the water content of the sludge (W). For $T_{\text{reg}}=140^\circ\text{C}$, the maximum heat flux obtained by drum dryer model (Fig. 9) is about two orders of magnetitude smaller than the maximum heat flux obtained on Figure 3 but the duration of this maximal value is about 10 seconds. The internal thermal resistance is more important that the external thermal resistance until $W=1 \text{ kg.kgMS}^{-1}$ for this simulation (Fig. 10). So, the importance of the internal transfers, which govern the drying time, is highlighted. For this simulation, the drying time is about 15 seconds (Fig. 11). Figure 11 shows the evolution of the reduced water content obtained experimentally and by simulation for $T_{\text{reg}}=140^\circ\text{C}$. Experimental water content is well fitted by thus obtained by simulation. Because of the assumptions on losses by convection negligible, the model is not satisfactory at the end of the drying. The final water content is not the same.

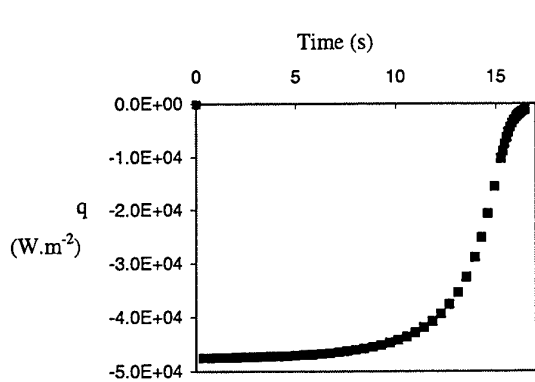


Fig. 9 – Heat flux density evolution versus time for $T_{reg}=140^{\circ}\text{C}$

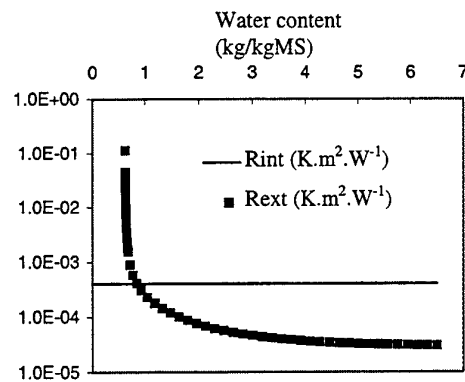


Fig. 10 – Comparaision between R_{ext} and R_{int} for $T_{reg}=140^{\circ}\text{C}$

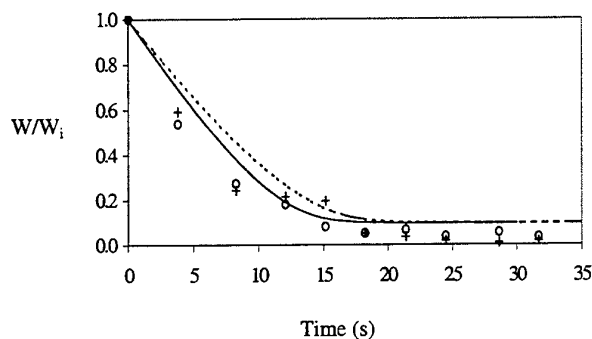


Fig. 11 – Comparison between experimental data and drum dryer model for $T_{reg}=140^{\circ}\text{C}$

4. CONCLUSION

A simple model of the drum dryer is developed by taking the combined effects of the internal and external transfers into account. In this case, the importance of the internal transfers, which govern the drying time, was highlighted. The developed method was largely validated for a type of sludge (alumina hydroxyde sludge) and an electrically laboratory drum dryer. The method developed is for the design of indirect dryers in thin-film by boiling for sludge treatment. Indeed, one of the first prospects would be to apply the method developed with an industrial drum dryer.

NOTATIONS

a	Thermal diffusivity	$\text{m}^2.\text{s}^{-1}$	A, B, C, D	Quadripole elements	-
b	effusivity	$\text{W.m}^{-1}.\text{K}^{-1}.\text{s}^{1/2}$	e	Plate thickness	m
e_a	Stainless steel thickness	m	e_{cu}	Copper thickness	m
e_1	Sensor location	m	E	Energy density	J.m^{-2}
E'	Global energy density	J.m^{-2}	$f(t)$	Inverse transfer function	-
$F(s)$	Transfer function	-	l_v	Water latent heat	J.kg^{-1}
M	Dry matter load	kg.m^{-2}	q	Interfacial heat flux density	W.m^{-2}
R_{int}	Internal thermal resistance	$\text{K.m}^2.\text{W}^{-1}$	R_{ext}	External resistance	$\text{K.m}^2.\text{W}^{-1}$
s	Laplace variable	s^{-1}	t	time	s
T	Temperature	$^{\circ}\text{C}$ or K	T_b	Boiling temperature	$^{\circ}\text{C}$ or K
T_i	Initial temperature	$^{\circ}\text{C}$ or K	T_f	Final temperature	$^{\circ}\text{C}$ or K
T_{reg}	PID controller temperature	$^{\circ}\text{C}$ or K	W	Water content	Kg.kgDM^{-1}
x, y	Spatial variable	m	Y	Measured temperature	$^{\circ}\text{C}$ or K

Greek letters

λ	Thermal conductivity	$\text{W.m}^{-1}.\text{K}^{-1}$	ϕ	Heat flux density	W.m^{-2}
ϕ	Laplace heat flux	-	θ	Laplace temperature	-
ρC_p	Volumic thermal capacity	$\text{J.m}^{-3}.\text{K}^{-1}$			

REFERENCE

1. J.C. Batsale, D.Maillet, A.Degiovanni, 'Extension de la méthode des quadripôles thermiques à l'aide de transformations intégrales: calcul de transfert thermique au travers d'un défaut plan bidimensionnel', Int. J. Heat Mass Transfer, Vol 37, pp 111-127 (1994)
2. J.F. Beck, Nonlinear estimation applied to the nonlinear inverse heat conduction problem, Journal of Heat Mass Transfer, Vol 13, pp 703-716 (1970)
3. J.F. Beck, B. Blackwell, C. St. Clair, Inverse heat condition, ill-posed problems, Wiley-Interscience, New York (1985)
4. C. Carrère-Gée, D. Lecomte, O. Fudym, B. Ladevie, J. Vasseur, 'Determination of heat flux in thin-layer drying of sludges', Proceedings of the 11th International Drying Symposium (IDS'98), Halkidiki, Greece, August 19-22, vol. A, pp. 695-702 (1998)
5. C. Carrère-Gée, *Etude du séchage indirect d'une fine couche de boue d'hydroxyde d'aluminium en ébullition - Application au cylindre sécheur*, PhD Thesis, France (1999)
6. A. Degiovanni, 'Conduction dans un "mur" multicouche avec sources : extension de la notion de quadripôle', Int. J. Heat Mass Transfer, vol 3, pp 553-557 (1988)
7. MATLAB user's guide: The Math Works, Inc.-21 Eliot Street - South Natick, MA 01760 - MOLIER C.B and VAN LOAN C.F.
8. G. Rodriguez, J. Vasseur, G. Trystram, *Automatic control of drum drying of food*, Drying'94, Vol. A, pp. 479-486 (1994)
9. H. Stehfest, 'Remarks on algorithm 368', *Numerical inversion of Laplace transform*, A.C.M, Vol 53, No 10, pp 624 (1970)
10. J. Vasseur, M. Loncin, 'High heat transfer coefficient in thin film drying', Engineering and food, pp. 217-225 (1984)
11. J. Vasseur, *Etude du séchage d'un produit visqueux, en couche mince, sur une paroi chaude, permettant de définir un modèle de séchoir sur cylindre*, PhD Thesis, France (1983)

APPLICATION OF CHEMICAL HEAT PUMP TECHNOLOGY TO INDUSTRIAL DRYING: A PROPOSAL FOR A NEW CHEMICAL HEAT PUMP DRYER

Hironao Ogura, Hiroyuki Kage and Yoshizo Matsuno
Dept. of Applied Chemistry, Kyushu Institute of Technology
Tobata, Kitakyushu 804-8550 JAPAN
Email: ogura@tobata.isc.kyutech.ac.jp; Fax: +81-93-884-3300

Arun S. Mujumdar
Dept. of Chemical Engineering, McGill University
Montreal, Quebec H3A 2B2 CANADA
Email: arun@chemeng.lan.mcgill.ca; Fax: +1-514-398-6678

Keywords: chemical heat pump dryer, energy saving, heat recovery, new system

ABSTRACT. From the viewpoints of energy saving and environmental impact, a Chemical Heat Pump (CHP) system for ecofriendly effective utilization of thermal energy in drying is proposed. The CHP can store thermal energy in the form of chemical energy by an endothermic reaction, and release it at various temperature levels during heat demand by exo/endothermic reactions. As an example, the authors propose a CHP system using the $\text{CaO}/\text{Ca}(\text{OH})_2$ hydration/dehydration reaction for heat storage and cold/hot heat generation. CHPs have potentials for heat recovery and dehumidification in the drying process by heat storage and high-/low-temperature heat release. In this study, we estimate the potential of the CHP application to drying systems for industrial use. Some combined systems of CHP and dryer are proposed as Chemical heat Pump Dryers (CHPD). The potential of the CHPDs are discussed.

1. INTRODUCTION

Drying is a highly energy intensive operation. One option to save energy is the use of a Mechanical Heat Pump (MHP). In many studies of the Heat Pump Dryer (HPD), use of the MHP improved the energy efficiency of dryers. However, the results of those studies are limited to specific conditions. Furthermore, the electric power consumption is high and undesirable working media such as CFC are required.

Here, we propose a new concept: use of a Chemical Heat Pump (CHP) system for ecofriendly effective utilization of thermal energy in thermal drying. The CHP can store thermal energy in the form of chemical energy via an endothermic reaction in a properly designed reactor, and release it at various temperature levels during the heat demand period by exo/endothermic reactions. The CHP basically operates using only thermal energy and does not release any contaminant gases. As an illustration, the authors propose a CHP system using the $\text{CaO}/\text{Ca}(\text{OH})_2$ hydration/dehydration reaction for heat storage and cold/hot heat generation. The CHP operation is validated by experiments and simulations by the authors for KIT and NU in previous studies [1-3].

2. WHAT IS CHEMICAL HEAT PUMP?

Operating Principle of CHP

Fig. 1 shows a typical gas-solid CHP system. The CHP is a closed system, which basically has two reactors connected to each other. The heat storage and release reactions occur at different pressure levels. The low temperature side reactor has a higher reaction equilibrium pressure. The CHP is as studied earlier operates as a batch system with a heat storing step and a heat releasing step.

In the heat storing step, the heat Q_H is stored in the form of thermochemical energy by the decomposition of $\text{AC}(\text{s})$ in the high temperature side reactor. The released gas $\text{C}(\text{g})$ moves into the low temperature side reactor due to the pressure difference between the reactors. The gas $\text{C}(\text{g})$ reacts with $\text{B}(\text{s})$ releasing the low temperature heat Q_L . So long as $\text{A}(\text{s})$ is separated from the gas $\text{C}(\text{g})$, the reaction heat can be stored for any length of time in the form of chemical energy.

In the heat releasing step, the gas $\text{C}(\text{g})$ flows from the low temperature side reactor to the high temperature side reactor by opening a valve (see Fig.1) only due to the pressure difference between the reactors. The exothermic

reaction of A(s) at a high temperature level with C(g) takes place in the high temperature side reactor. The low temperature side reactor stores the low temperature heat QL or is cooled down by releasing its decomposition heat since it is insulated.

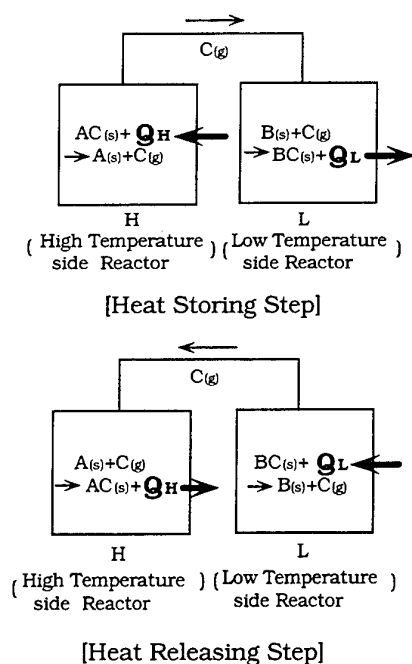


Fig. 1. Schematic diagram of CHP

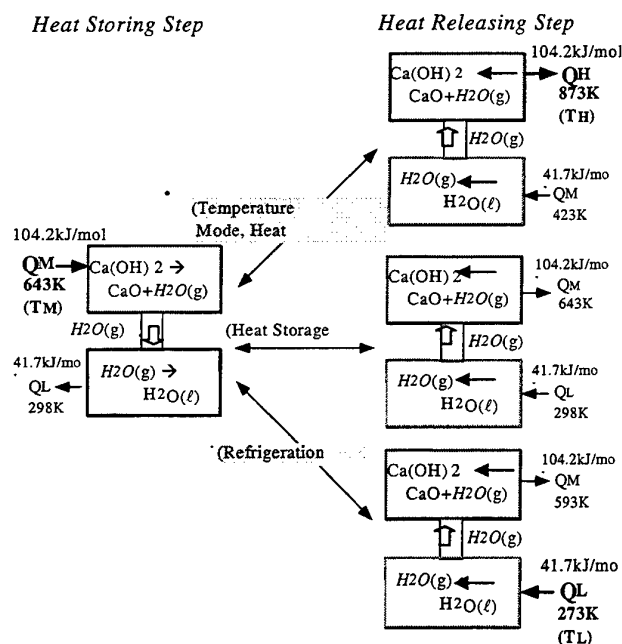


Fig. 2. Operating temperature range of CaO/Ca(OH)₂ CHP

Operating Temperature Range of CHP

CHP has four possible operating modes according to the operating pressure control; they are: heat storage mode, heat enhancement mode, refrigeration mode and temperature upgrade mode. Here, we show the operating temperature range of CHP using the CaO/Ca(OH)₂ hydration/dehydration reaction as an illustration in Fig.2. In this system, a CaO/Ca(OH)₂ reactor is used as a high temperature reactor and an evaporator/condenser is used as a low temperature one. Operating temperature ranges of other type CHPs are depends on their own reaction equilibrium temperatures and pressures.

In the temperature upgrade mode, heat QM is stored at TM in the heat storing step, and high temperature heat QH is released at TH by supplying QM to evaporator in the heat releasing step. In the heat storage mode, heat QM is stored at TM, and the heat is released at the same temperature, TM. In the refrigeration mode, heat QM is stored at TM. We can obtain medium temperature heat QM at TM and cold heat QL at TL in the same heat releasing step. The cold heat QL is generated by releasing its latent heat.

2. POTENTIAL OF CHP APPLICATION TO CONVECTIVE DRYER

Advantages and Limitations of CHP Application to Dryer

From the features of CHP, a CHP has a potential for heat recovery and dehumidification in the drying process by the heat storage and high-/low- temperature heat release. In order to apply CHPs to dryers, thermal energy should be stored in the CHP at first. The exhaust heat from the dryer and the input heat to the dryer can be stored and upgraded in a CHP. Lower temperature level heat such as waste heat from other systems can be used. The stored energy is released from the CHP as "hot" heat for drying. In the case of the refrigeration mode of the CHP, a cold heat can also be released for dehumidification of the exhausted humid air from the dryer.

Many types of CHP systems have been developed in the world. Table 1 shows examples of CHP developed in Japan. These systems basically operate as batch systems. Some gas-liquid reaction systems such as a hydrogen

system can work as continuous systems in combination with a distillation reactor etc. However, the thermal efficiencies of these type systems are low in this stage although they need expensive catalysts.

Table 1 Examples of Chemical Heat Pump developed in Japan

Medium	Reaction	Developer	Scale	Note
Water	$\text{CaO} \rightleftharpoons \text{Ca(OH)}_2$	Nagoya University	Lab	400°C → 600°C
Water	$\text{CaO} \rightleftharpoons \text{Ca(OH)}_2$	Kyushu Inst. of Technology	10MJ (0-10kW)	400°C → 0-350°C
Water	$\text{CaCl}_2 \rightleftharpoons \text{CaCl}_2 \cdot 6\text{H}_2\text{O}$	Meiji University	Lab.	Solar heat Storage
Water	$\text{CaB}_2 \cdot \text{H}_2\text{O} \rightleftharpoons 2\text{CaB}_2 \cdot \text{H}_2\text{O}$	Hitachi Ship Ltd. NEDO	3.5kW	Nighttime Electric Power
Ammonia	$\text{NiCl}_2 \cdot 2\text{NH}_3 \rightleftharpoons \text{NiCl}_2 \cdot 6\text{NH}_3$	I.H.I. NEDO	2.5MJ	200°C Up
Methyl-amine	$\text{CaCl}_2 \cdot 2\text{CH}_3\text{NH}_2 \rightleftharpoons \text{CaCl}_2 \cdot 6\text{CH}_3\text{NH}_2$	Mitsubishi Elec. Osaka University	1kW	Elec. Power → 10°C
Hydrogen	$(\text{CH}_3)_2\text{CO} \rightleftharpoons (\text{CH}_3)_2\text{CHOH}$	Univ. of Tokyo ¹⁾ TU of Agr & Tec JGC Co.	Lab	70°C → 170-230°C
Hydrogen	$\text{C}_6\text{H}_6 \rightleftharpoons \text{C}_6\text{H}_{12}$	TU of Agr & Tec	Lab	200°C → 350°C
Carbon dioxide	$\text{CaO} \rightleftharpoons \text{CaCO}_3$	Nagoya University	Lab	740°C → 970°C

Proposal of Chemical Heat Pump Dryer

In this study, we propose two types of reaction systems of CHP for combining them with a dryer as Chemical Heat Pump Dryer (CHPD). One is a $\text{CaO}/\text{Ca(OH)}_2$ gas-solid reaction system as an example of a batch system. The other is $(\text{CH}_3)_2\text{CO}/(\text{CH}_3)_2\text{CHOH}$ gas-liquid system as an example of a continuous system. There can be several types of CHPDs for each reaction system. We propose three types of CHPD using $\text{CaO}/\text{Ca(OH)}_2$ reaction as shown No. 1 – 3 in Table 2, and two types of CHPD using $(\text{CH}_3)_2\text{CO}/(\text{CH}_3)_2\text{CHOH}$ reaction as shown No. 5, 6 in Table 2. There is no dehumidification option in these systems as these are high temperature dryer systems. The values of the potential energy savings and energy savings are also listed. These values are calculated as follows. The basic efficiencies of the CHPs are based on the studies on $\text{CaO}/\text{Ca(OH)}_2$ CHP by Ogura et al. [1-3] and the studies on $(\text{CH}_3)_2\text{CO}/(\text{CH}_3)_2\text{CHOH}$ CHP by Saito et al. [4,5]. Here, we propose only basic CHPD systems as a preliminary exploratory study of the feasibility of combining CHPs with convective dryers, although many combined systems can be considered in addition to these systems.

Table 2. Examples of the Estimated Potential of Chemical Heat Pump Dryer (CHPD)

No.	Type of Energy Saving	Classification of Dryer	Inlet Air Temp.	Outlet Air Temp.	Applicable CHP	Thermal Efficiency of CHP	Energy Saving of Dryer	Energy Saving of Dryer
1	Heating Up Exhaust Heat	Batch	600 °C	400 °C	$\text{CaO} \rightleftharpoons \text{Ca(OH)}_2$	70 %	42 %	56 %
2	Heating Up Exhaust & Input Heat	Batch	600 °C	400 °C	$\text{CaO} \rightleftharpoons \text{Ca(OH)}_2$	70 %	17 %	40%
3	Storing Exhaust Heat	Batch	370 °C	350 °C	$\text{CaO} \rightleftharpoons \text{Ca(OH)}_2$	70 %	42 %	70%
4	Heating Up Exhaust Heat	Continuous	200 °C	100 °C	$(\text{CH}_3)_2\text{CO} + \text{H}_2 \rightleftharpoons (\text{CH}_3)_2\text{CHOH}$	10 %	9.8%	9.8%
5	Heating Up Exhaust & Input Heat	Continuous	200 °C	100 °C	$(\text{CH}_3)_2\text{CO} + \text{H}_2 \rightleftharpoons (\text{CH}_3)_2\text{CHOH}$	10 %	-	-

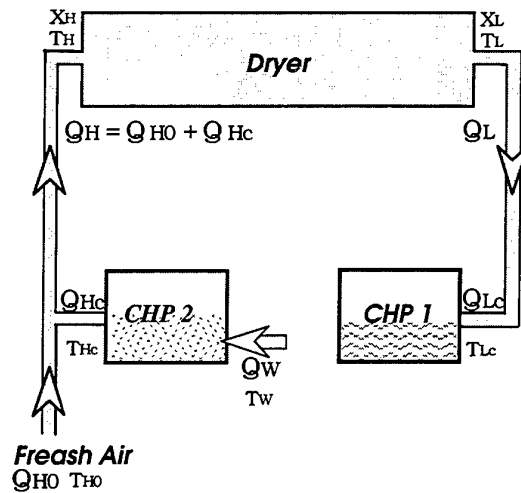


Fig. 3. Schematic diagram of CHPD 1

No. 1 CHPD using CaO/Ca(OH)₂ reaction: heating up exhaust heat from dryer. A schematic diagram for this CHPD is shown in Fig. 3. In this system, hot dry air Q_H at 600 °C goes into the dryer. The exhaust air has energy of Q_L , which has lower temperature of 400 °C and higher humidity. The energy Q_L is stored in CHP1. On the other hand, CHP2 continues to release high temperature heat Q_{Hc} at 600 °C by supplying 150 °C heat Q_W to it. By exchanging CHP1 and CHP2, the stored energy Q_{Lc} in CHP1 is released from CHP2 as temperature upgraded heat Q_{Hc} . In order to make up for the heat consumption by the dryer and the heat loss of CHP, fresh air energy Q_{H0} at T_{H0} is supplied to inlet of the dryer.

Efficiencies of the CaO/Ca(OH)₂CHPD based on our previous studies [1-3] are defined as follows.

$$\text{Thermal efficiency : } \mu_H = \frac{Q_{Hc}}{Q_{Lc}} = 0.7 \quad (1)$$

$$\text{Coefficient of performance : } \text{COP} = \frac{Q_{Hc}}{Q_W} = 2.5 \quad (2)$$

$$\text{Energy efficiency : } \mu_{EX} = \mu_H \frac{(T_{Hc} - T_0)T_{Hc}}{(T_{Lc} - T_0)T_{Lc}} = 1.36 \quad (3)$$

The efficiencies of this CHPD system are defined as follows. These are the ratios of the system consumption to the original dryer consumption.

$$\text{Energy consumption efficiency: } E_H = \frac{Q_{H0} + Q_W}{Q_H} \quad (4)$$

$$\text{Energy consumption efficiency: } E_{EX} = \frac{Q_{H0}(T_{H0} - T_0)/T_{H0} + Q_W(T_W - T_0)/T_W}{Q_H(T_H - T_0)/T_H} \quad (5)$$

An additional condition is defined for this system.

$$Q_H = Q_{H0} + Q_{Hc} \quad (6)$$

The followings are derived from Eqs. 4, 5 with Eqs. 1-3, 6.

$$\text{Energy consumption efficiency: } E_H = 1 - 0.42 \frac{Q_L}{Q_H} \quad (7)$$

$$\text{Energy consumption efficiency: } E_{EX} = 1 - 0.56 \frac{Q_L}{Q_H} \quad (8)$$

From these results, the energy consumption of this CHPD1 system is 42% reduced at maximum when $Q_L/Q_H=1$. Even $Q_H/Q_L=0.5$, the energy consumption is found to be reduced by 21%. The energy consumption is reduced by 56% and 28% in each case.

No. 2 CHPD using CaO/Ca(OH)₂ reaction: heating up exhaust and input heat. The schematic diagram for this CHPS is shown in Fig. 4. This is similar to the CHPS1. The difference is that fresh air energy Q_{L0} at T_{L0} is supplied to the inlet of the CHP1 in order to make up for the heat consumption by the dryer and the heat loss of the CHP.

An additional condition is defined for this system.

$$Q_{Lc} = Q_L + Q_{L0} \quad (9)$$

The following are derived from Eqs. 4, 5 with Eqs. 1-3, 9.

$$\text{Energy consumption efficiency: } E_H = 1.83 - \frac{Q_L}{Q_H} \quad (10)$$

$$\text{Energy consumption efficiency: } E_{EX} = 1.52 - 0.916 \frac{Q_L}{Q_H} \quad (11)$$

From these results, the energy consumption of this CHPD2 is 17% reduced at maximum when $Q_L/Q_H=1$. If $Q_H/Q_L < 0.83$, the consumption energy is not found to be reduced. The energy consumption is reduced by 40% at maximum when $Q_L/Q_H=1$ and 0% reduced when $Q_L/Q_H=0.57$. In this system, the energy consumption is reduced effectively in comparison with the energy consumption because of the use of low temperature heat source Q_{L0} .

No. 3 CHPD using CaO/Ca(OH)₂ reaction: storing exhaust heat. This system is similar to the CHPD1. The difference is that the working energy Q_W is room temperature heat at $T_W = 25^\circ\text{C}$. In this system, Q_H at 370°C goes into the dryer. The output has energy of Q_L , which has lower temperature of 350°C . The energy Q_L is stored to CHP1. In order to store Q_L at 350°C , the condensation heat is released from the CHP1 at 15°C . On the other hand, CHP2 continues to release high temperature heat Q_{Hc} at 370°C by supplying 25°C heat Q_W to it. The following are derived from Eqs. 4, 5 with Eqs. 1-3, 6.

$$\text{Energy consumption efficiency: } E_H = 1 - 0.42 \frac{Q_L}{Q_H} \quad (12)$$

$$\text{Energy consumption efficiency: } E_{EX} = 1 - 0.70 \frac{Q_L}{Q_H} \quad (13)$$

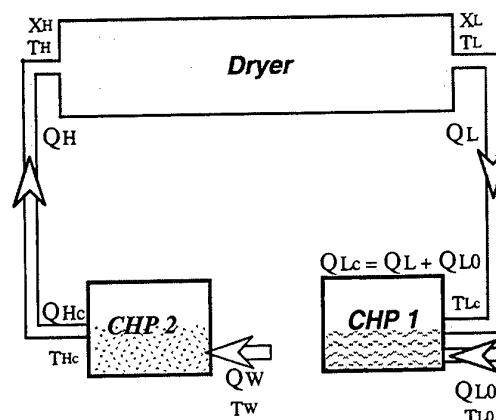


Fig. 4 Schematic diagram of CHPD 2

From these results, the consumption energy of the CHPD3 is same amount of CHPD1. The energy consumption is reduced by 70% at maximum when $Q_L/Q_H=1$ and 35% when $Q_H/Q_L=0.5$. In this system, the energy consumption is more reduced than that of CHPD1 although the consumption energy amount is same. The low energy heat of room temperature heat is used effectively. If we count the room temperature heat as free, the consumption energy efficiency equals the value of consumption energy efficiency.

No. 4 CHPD using $(CH_3)_2CO/(CH_3)_2CHOH$ reaction: heating up exhaust heat. This system is similar to the CHPD1. The difference is that the CHP reaction system is different. In this system, QH at 200 °C goes into the dryer. The exhaust heat has energy of Q_L , which has a lower temperature of 100 °C. The energy Q_L is stored in CHP1. On the other hand, CHP2 continues to release high temperature heat Q_{Hc} at 200 °C by supplying electric power Q_W to it. This system can work continuously by circulating reactant gases and liquids in the CHP. However, the CHP reactivity based on the previous study [5] is very low even with catalysts as follows.

$$\text{Thermal efficiency: } \mu_H = \frac{Q_{Hc}}{Q_{Lc}} = 0.10 \quad (14)$$

$$\text{Coefficient of performance: } COP = \frac{Q_{Hc}}{Q_W} = 50 \quad (15)$$

$$\text{Energy efficiency: } \mu_{EX} = \mu_H \frac{(T_{Hc} - T_0)T_{Hc}}{(T_{Lc} - T_0)T_{Lc}} = 0.18 \quad (16)$$

The followings are derived from Eqs. 4, 5 with Eqs. 6, 14-16.

$$\text{Energy consumption efficiency: } E_H = 1 - 0.098 \frac{Q_L}{Q_H} \quad (17)$$

$$\text{Energy consumption efficiency: } E_{EX} = 1 - 0.098 \frac{Q_L}{Q_H} \quad (18)$$

From these results, the energy consumption of this CHPD is 9.8% reduced even at maximum when $Q_L/Q_H=1$. The energy consumption is also reduced by 9.8% at maximum. In this system, as the thermal efficiency μ_H and the energy efficiency μ_{EX} are very low, the system efficiencies are found to become low although it works continuously. The electric power usage for Q_W is also disadvantage for dryers. Overall, this combination does not appear to have any real potential for application in this stage.

No. 5 CHPD using $(CH_3)_2CO/(CH_3)_2CHOH$ reaction: heating up exhaust and input heat. This system is similar to the CHPD2. The new energy Q_{L0} at T_{L0} is supplied to inlet of the CHP1 in order to make up for the heat consumption by the dryer and the heat loss of the CHP. The following are derived from Eqs. 4, 5 with Eqs. 9, 14-16.

$$\text{Energy consumption efficiency: } E_H = 10.02 - \frac{Q_L}{Q_H} \quad (19)$$

$$\text{Energy consumption efficiency: } E_{EX} = 7.04 - 0.70 \frac{Q_L}{Q_H} \quad (20)$$

From these results, the energy consumption of this CHPD5 is about nine times of the original system even when $Q_L/Q_H=1$. The energy consumption of this CHPD5 is more than six times of the original system even when $Q_L/Q_H=1$. As this system efficiency depends on the thermal efficiency μ_H and the energy efficiency μ_{EX} of the original CHP, the system efficiencies are found to be too low for application to drying operation.

3. POTENTIAL OF CHEMICAL HEAT PUMP DRYER

CHPD Efficiency

As mentioned above, CHPDs can save the consumed energy in drying under special conditions. However, the efficiency of the continuous gas-liquid reaction system is not good because of the low efficiency of the original CHP. In the gas-solid system, it is found to be an effective energy saving system although it is for a batch system. We are designing semi-batch systems or continuous systems by modifying these batch CHP systems. In the continuous systems, some CHPs should operate simultaneously and thermal energy should be exchanged to each other. If the gas-solid systems can work continuously, the system efficiencies of CHPDs should become much higher.

Temperature Range of CHPD

These CHPDs basically work using only thermal energy. So, if we recover waste heat from other system, the total energy consumption efficiency of the combined systems becomes high. In the proposed CHPDs, QH0 and QL0 indicate the heat from other systems. Furthermore, the combined CHPD system is eco-friendly system.

As we proposed basic ideas for CHPDs in this study, the temperature rangess of the CHPDs are high. However, the operating temperature range of CHPD can be modified by the system design, although the operating temperature level of CHP depends on the reaction equilibrium temperature and pressure. Unfortunately, there are not so many CHPs operating at around 200°C which is good temperature for drying. We need to develop the good temperature level CHPDs by new reaction systems or new system designs.

4. CONCLUSIONS

From the viewpoints of energy saving and environmental impact, a Chemical Heat Pump Dryer (CHPD) for eco-friendly effective utilization of thermal energy in drying is proposed with a brief discussion of CHPs and dryers from the viewpoint of their combinations. The efficiencies of five types of CHPD systems were evaluated on the bases of energy and energy consumption. The potential of the energy saving CHPD systems were shown. Currently, only the proposed CHPD systems seem to be feasible. More work is needed to develop the criteria for potential of CHP applications to drying systems. Especially, we need to operate CHPDs continuously with lower air temperatures and humidities for drying of heat-sensitive solids. Different reactor and system designs are needed for the CHPD systems to be applied to continuous drying. Note that justification for a CHPD will ultimately depend on the technoeconomics of the process since it will involve additional investment costs and result in a more complex flowsheet. New CHP reactor designs will be required for coupling with a continuous industrial dryer.

REFERENCES

1. H. Ogura, M. Kanamori, H. Matsuda and M. Hasatani, "High Temperature Heat Storage and Temperature Upgrading by Use of $\text{CaO}/\text{H}_2\text{O}$ and CaO/CO_2 Reactions," Proc. of IAEA Technical Committee Meeting and Workshop on High-Temperature Applications of Nuclear Energy, Oarai-machi, Japan, 95-102 (1992).
2. H. Ogura, S. Fujimoto, H. Iwamoto, H. Kage and Y. Matsuno, Y. Kanamaru, S. Baba, K. Koba, S. Muta and Arun S. Mujumdar, "Reactor Design of $\text{CaO}/\text{H}_2\text{O}/\text{Ca}(\text{OH})_2$ Chemical Heat Pump Unit for Cold/Hot Heat-Generation with Night-Electric Heat-Storage", Proceedings of the 13th International Congress of Chemical and Process Engineering (CHISA'98), August 23-28, Praha, Czech Republic, H7.1 (1998).
3. H. Ogura, S. Fujimoto, H. Iwamoto, H. Kage, Y. Matsuno, Y. Kanamaru and S. Awaya, "Basic Performance of $\text{CaO}/\text{H}_2\text{O}/\text{Ca}(\text{OH})_2$ Chemical Heat Pump Unit for night-Electric Heat-Storage and Cold/Hot Heat-Recovering," Kagaku Kogaku Ronbunshu, 24, 856-861 (1998).
4. Y. Saito, H. Kameyama and Y. Ohida, "Catalyst-assisted chemical heat pump with reaction couple of acetone hydrogenation/ 2-propanol dehydrogenation for upgrading low-level thermal energy", Research of Energy, 11, 549-558 (1987).
5. D. Taneda, I. Yasutomi, S. Shibata and T. Toida, "Studies of 2-propanol/Acetone hydrogen Chemical Heat Pump Characteristics", Kagakukogaku Ronbunshu, 19, 729-735 (1993).

O. Heat Exchangers

COEFFICIENT OF HEAT TRANSFER IN FIN-TUBE HEAT EXCHANGER ANALYSIS AND THE ARTIFICIAL NEURAL NETWORKS

K. T. Yang*, Mihir Sen, Gerardo Diaz,
Arturo Pacheco-Vega and Rodney L. McClain

Hydronics Laboratory, Department of Aerospace and Mechanical Engineering
University of Notre Dame, Notre Dame, IN 46556, USA

*Email: Kwang-Tzu.Yang.1@nd.edu, FAX: 1-(219)-631-8341

Keywords: neural network, correlations, heat exchanger, thermal modeling

ABSTRACT. The use of correlated coefficients of heat transfer from the experimental data has been the universal choice to analyze complex heat transfer processes. Unfortunately, large errors often occur in the application of such coefficients to complex phenomena such as those occurring in compact fin-tube heat exchangers. Basic issues responsible for this difficulty are identified and articulated. An alternative approach of correlating the experimental heat transfer data by the application of artificial neural network (ANN) is presented, and this new approach is shown to possess several inherent advantages not enjoyed by the conventional approach of using correlated heat transfer coefficients, as demonstrated by examples dealing with two fin-tube heat exchangers with different complexities. Also mentioned are further extensions of the ANN approach to the dynamic modeling of heat exchangers and their control.

1. INTRODUCTION

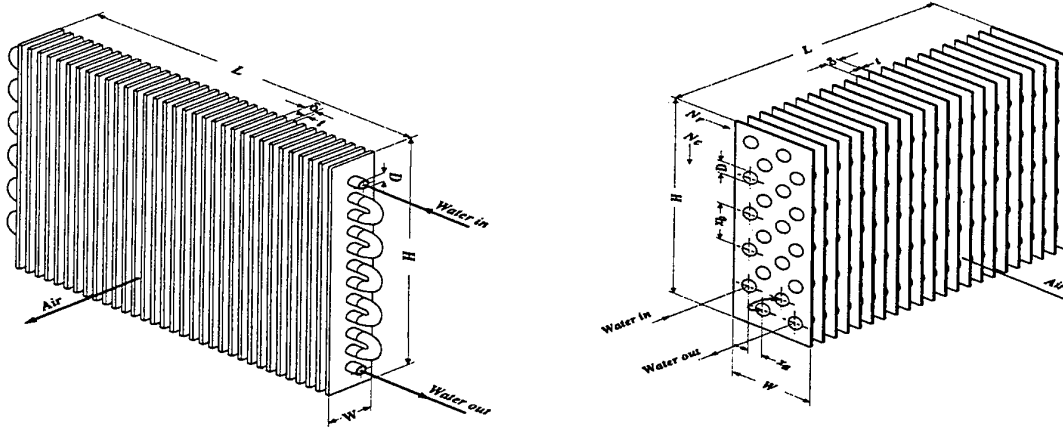
Coefficients of heat transfer, h in W/m^2C , have been widely used in convection analysis, and so much so they are essentially the universal choice as a vehicle to determine heat transfer rates in any convection phenomena. These coefficients are normally calculated from the temperature gradients normal to the heat transfer surface, either based on solutions to the governing energy equations or from the measured normal temperature profiles. The latter are often used in more complex convection phenomena such as in heat exchangers. These coefficients of heat transfer are generally presented in terms of the Nusselt numbers, Nu , as functions of the Reynolds, Re , Grashof, Gr , and Prandtl, Pr numbers, and sometimes also of other dimensionless geometrical and property factors. These are known as the correlation equations, along with validity ranges. The exact forms of such correlation equations are phenomenon dependent, usually based on the dimensional analysis either from known physical parameters in the phenomena or from their mathematical models. In general the Nusselt numbers based on measurements do not exactly coincide with those that can be calculated from the correlation equations, and the differences are normally attributed to uncertainties in the experimental data as well as in the chosen dimensionless parameters. As the complexity of the convection phenomena increases, larger deviations of the calculated data based on the correlations from the experimental results can be expected.

Despite the universal adoption of the analysis of using the correlated coefficients of heat transfer as the basis for determining the heat transfer rates in complex convection phenomena, there are still shortcomings in this approach which in many cases may lead to unsatisfactory predictions of the heat transfer. The basic issues involved have not been identified and studied heretofore in the heat transfer literature, and the difficulty is compounded by the fact that no alternative and better approach is now available. The purpose of this paper is to articulate on these issues, specifically for the popular fin-tube heat exchangers and also to present an alternative approach of correlating the heat transfer data by the application of artificial neural networks (ANN) which will be shown to possess several inherent advantages not enjoyed by the conventional approach.

2. CURRENT USE OF COEFFICIENTS OF HEAT TRANSFER IN FIN-TUBE COMPACT HEAT EXCHANGER ANALYSIS

A typical single-row fin-tube heat exchanger is shown in Fig. 1(a) and the most common application of such a heat exchanger deals with flow of air on the fin-side and single-phase flow of water on the tube-side. Its complexity arises on the tube-side from the entrance-region flow development, secondary flow in the tube bend, flow readjustment downstream of the bend, and possible natural-convection effects, and on the fin-side, from the flow through the fin passages, conduction along the fins, fin-tube interaction, wake flow behind the tube, tube-tube interaction, and also possible natural-convection effects. Despite several recent attempts to analyze the

transport phenomena on the air-side in the fin-tube passages [1,2] and on the water-side due to secondary flow in tube bends [3], both by CFD techniques, such separate analyses still include assumptions and conditions which are not compatible with what exists in the real phenomena, and in addition, no attempt has been made to marry the two analyses to address the real heat-transfer process between the two fluids. On the other hand, obviously there is a need to analyze the heat-transfer performance, and this has been done by the well-known use of two average coefficients of heat transfer, one for the air-side and one for the water-side [4]. The coefficients are then appropriately combined to result in a single overall coefficient of heat transfer to determine the heat transfer rate for the heat exchanger. Thus, it is clear that the accurate determination of the two separate coefficients of heat transfer is crucial to the heat exchanger analysis.



(a) Single-row fin-tube heat exchanger 1.

(b) Multi-row multi-column fin-tube heat exchanger 2.

Figure 1: Schematic of compact heat exchangers.

There is a well-known difficulty in determining the air-side and water-side average coefficients of heat transfer (h_o and h_i) from the experimental data. In a given experiment on a specific heat exchanger, the flow rates of both fluids and the four terminal temperatures can all be measured, and so can be the overall heat transfer rate. For the determination of the two coefficients, we may write [4,5]

$$\frac{1}{U_o A_o} = \frac{\Delta T_m}{Q} = \frac{1}{h_o A_o} + \frac{r_o \ln(A_o / A_i)}{k_t A_o} + \frac{1}{h_i A_i} \quad (1)$$

where U_o is the overall coefficient of heat transfer based on the total fin-side area A_o , A_i is the tube inside area, r_o is the tube outside radius, k_t is the tube thermal conductivity, and ΔT_m is either the usual log-mean temperature difference [4] or some conveniently defined temperature difference. Usually the total fin-side area A_o is given by $A_o = A_t + \eta A_f$ where A_t is the tube outside area, A_f is the total fin surface area which is generally very much larger than A_t , and η is the fin effectiveness. Also the second resistance term on the right-hand side of Eq. (1) is often neglected in view of its small magnitude. Since both h_o and h_i will eventually be determined by the correlations with the experimental data, some specific forms of the correlations must be prescribed and can usually be written as

$$\eta Nu_a = a Re_a^b Pr_a^{1/3}, Nu_w = c Re_w^d Pr_w^{0.3} \quad (2)$$

where the condition that A_t is very small compared to A_f is invoked, and the dimensionless Nusselt, Reynolds, and Prandtl numbers are defined as follows:

$$Nu_a = \frac{h_o \delta}{k_a}, Re_a = \frac{V_a \delta}{\nu_a}, Pr_a = \frac{\nu_a}{\alpha_a}, Nu_w = \frac{h_i D}{k_w}, Re_w = \frac{V_w D}{\nu_w}, Pr_w = \frac{\nu_w}{\alpha_w} \quad (3)$$

where the subscript a and w refer to the air-side and water-side, respectively, V is the average flow velocity, δ is the fin spacing, D is the tube inside diameter, and α , ν and k are the thermal diffusivity, kinematic viscosity and thermal conductivity of the fluids, respectively. Also to simplify the correlations, the exponents on the Prandtl numbers can be prescribed to be those well known in the forced-convection literature [4]. The correlation constants a , b , c , d in the above equations are determined from the experimental data. The well-known difficulty mentioned above is that since it would be difficult in the experiments to measure the tube-wall temperatures, these temperatures are very seldomly measured. Unfortunately as a result, the expressions in Eqs. (2) become coupled and cannot be used to determine the two coefficients separately. The only way out is to carry out a least-square regression analysis to back out the four correlation constants. The two coefficients of heat transfer from Eqs. (2) are first substituted into the simplified Eq. (1), resulting in one single equation containing the four constants, which are then determined by the standard regression analysis from the experimental data.

One example can be given here to illustrate this approach. The heat exchanger considered here, which will be the same one considered later in the artificial neural network (ANN) analysis, is a nominal 457.2 mm (18 in.) \times 609.6 mm (24 in.) fin-tube type manufactured by the Trane Company with a single-row circuit of 12 tubes connected by bends. The experimental data were obtained in an open wind tunnel facility [6,7]. A total of 259 test runs were made, covering laminar, transitional, and turbulent regimes for the water flow. The correlated results are given by Zhao [6] as follows:

$$\eta Nu_a = 0.1368 Re_a^{0.585} Pr_a^{1/3}, Nu_w = 0.01834 Re_w^{0.752} Pr_w^{0.3} \quad (4)$$

applicable for $200 < Re_a < 700$ and $800 < Re_w < 4.5 \times 10^4$. The properties are based on the average of inlet and outlet fluid temperatures. It is important to note that the predictions of the heat transfer rates have an error band of $\pm 10\%$, which are generally considered to be good. This specific variability of the above predictions will be given later in the comparison with that from the new approach of utilizing ANN. Incidentally, improvements of the above approach have also been attempted to capture more of the local heat transfer behaviors [8], but they still have the same shortcomings of the basic approach, as will be discussed in the next section.

3. DEFICIENCIES OF THE COEFFICIENT OF HEAT TRANSFER APPROACH

In the experiments which led to the correlation results as shown in Eqs. (4), the measurement uncertainties were analyzed in some detail and were found to be close to $\pm 0.7\%$ in the heat transfer measurements, as compared to the $\pm 10\%$ from the correlated results. The difference between these two error or uncertainty bands cannot be attributed to the measurement errors alone. Indeed this difference can be traced to the deficiencies associated with the specific correlations. The physics involved in the flow and heat transfer phenomena are known to be extremely complex, and many of the complexities dealing with the nonuniform flow developments in both fluid passages have already been noted. In addition, there are other assumptions that are not entirely valid in the real phenomena. Good examples are the use of average coefficients and constant thermophysical properties. The relatively simple forms as given in Eq. (4) simply cannot be expected to account for all the complexities and nonuniformities in the real physical phenomena. One major difficulty is that there are many additional length scales in the real physics, but not accounted for in the usual correlations. Consequently, this leads to the loss of some of the important physics in the correlated equations, as reflected in the wider error bands of the predicted heat transfer rates.

Another subtle difficulty with the approach using the correlated equations which has not been articulated in the past literature, is that because these two equations are coupled, the least-square regression analysis of the experimental data often lead to non-unique solutions to the four correlation constants. In other words, in the multi-dimensional space for these constants, there are a number of state points for these constants which all represent cases of minimum least-square errors. Consequently they are all local minimums. The fact that nearly only local minimums are obtainable also contributes to the wider error bands of the prediction of heat transfer. Another important consequence of this non-uniqueness issue is that the correlations equations such as those in Eqs. (2) must be used as a pair, and the individual coefficients h_o and h_i in the pair do not have the usual meaning of those corresponding to individual convection phenomena involving any of the two fluids [9].

While the conventional approach can perhaps be improved upon by adding more ratios of length scales to the correlation equation, obtaining the needed additional experimental data, however, may yet reduce the attractiveness of the basic approach. Consequently, every effort should be made to seek alternative methods without most of the shortcomings inherent in the usual correlation approach. A new approach based on the application of artificial neural network (ANN) seems to satisfy all the requirements of such an alternative approach, and is presented here with specific examples. Finally, further extensions of the ANN approach to the dynamic modeling of heat exchangers and their control will also be mentioned.

4. APPLICATION OF ARTIFICIAL NEURAL NETWORK ANALYSIS

Despite the fact that artificial neural networks (ANN) have seen greatly increased applications in recent years in many diverse fields, its application in thermal sciences and engineering, has been comparatively sparse at best, as demonstrated in a very recent review [10]. The technique is rooted in and inspired by the biological network of neurons in the human brain that learns from external experience, handles imprecise information, stores the essential characteristics of the external input, and generalizes previous experience [11]. Since the primary purpose of the present paper is not to give a tutorial on the theory and methodology of ANN, but only to emphasize on the attractiveness of the ANN approach to predict the performance of the fin-tube heat exchangers, only a very brief summary of the ANN technique is given here, and the interested reader is referred to the representative references in [10,12-16] for the basic information.

The fully-connected feedforward ANN configuration has become the most preferred and widely used in many engineering applications [14]. An ANN consists of a series of consecutive layers, each with a number of fully-interconnected nodes which are the artificial neurons. The number of layers and the number of nodes in each layer constitute the basic configuration of the network. In a feedforward network, the connectivity structure is such that the nodes in the first layer known as the input layer are fully connected eventually to those in the final output layer through a series of interim, or hidden layers with hidden nodes of their own. The feedforward process in the network is in accordance with the popular sigmoid activation function which is a generalization of a step function possessing continuous derivatives. The learning or training process carries out the basically massively-parallel computations to recognize the essential pattern that relates the output to the input. It is performed by comparing its output with the data used for training, and using a backward-error propagation algorithm to successively updating the synaptic weights, which are the characteristics of the connections (synapses) of any pair of the connected nodes, and the biases, which are those of individual nodes, until the output values differ little from the experimental data. The synaptic weights and biases both play essential roles in transmitting the signals from node to node and layer to layer through the use of the sigmoid function. A clear explanation of the ANN components, and the general procedure for training and testing the network are presented by Diaz et al. [7].

5. ANN ANALYSIS OF SPECIFIC FIN-TUBE HEAT EXCHANGERS

For the purpose of illustration, the experimental data for two widely used types of fin-tube heat exchangers as shown in Figs. 1 (where H , W and L are the height, width and length of the heat exchanger respectively) are analyzed by the artificial neural network (ANN) approach. The results will be directly compared with those from the coefficient of heat transfer approach. The first Fig. 1(a) is the simpler single-row air-to-water fin-tube heat exchanger manufactured by the Trane Company. A total of 259 test runs were carried out, and in the ANN analysis only 197 runs were used for training the neural network, while the rest were used for testing the predictions. For the ANN analysis, there were four input nodes, corresponding to the normalized air-flow rate m_a , water-flow rate m_w , inlet air temperature T_a^{in} , and inlet water temperature T_w^{in} , and only one single output node for the normalized heat transfer rate Q . It is noted here that no coefficients of heat transfer were used at all in this analysis. Fourteen different ANN configurations, as shown in Table 1, were used to show the error sensitivities to the different configurations. The numerals in the configuration designation refer to the nodes in the successive layers. As an example for the 4-5-2-1-1 configuration, training was carried out to 200,000 cycles, each covering one complete sequence of feedforward and backward-error propagation for all the training data sets. The mean-square errors in the maximum and average errors within each cycle could then be calculated, as shown in Fig. 2. It is seen that the maximum error asymptoted at about 150,000 cycles, while the corresponding level of the average error was reached at about 100,000 cycles. In either case, the error levels were small.

TABLE 1: Comparison of heat transfer rates predicted by different ANN configurations for heat exchanger 1.

Configuration	R	σ
4-1-1	1.02373	0.266
4-2-1	0.98732	0.084
4-5-1	0.99796	0.018
4-1-1-1	1.00065	0.265
4-2-1-1	0.96579	0.089
4-5-1-1	1.00075	0.035
4-5-2-1	1.00400	0.018
4-5-5-1	1.00288	0.015
4-1-1-1-1	0.95743	0.258
4-5-1-1-1	0.99481	0.032
4-5-2-1-1	1.00212	0.018
4-5-5-1-1	1.00214	0.016
4-5-5-2-1	1.00397	0.019
4-5-5-5-1	1.00147	0.022

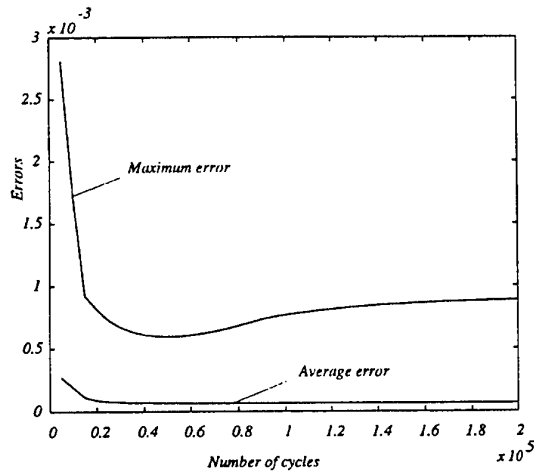


Figure 2: Training error results for configuration 4-5-2-1-1 ANN

After training, the ANN were used to predict the 62 test data sets which were not used in the training process, and the resulting mean R and standard deviations of the errors for each configuration are also shown in Table 1. These quantities are defined as

$$R = \frac{1}{N_p} \sum_{r=1}^{N_p} R_r, \sigma = \sqrt{\frac{1}{N_p} \sum_{r=1}^{N_p} (R_r - R)^2} \quad (5)$$

where R_r is the ratio Q^o/Q^p_{ANN} for run number r , Q^o is the experimental heat transfer rate, and Q^p_{ANN} is the corresponding prediction of the ANN. The quantity R (a mean value of R_r) is an indication of the average accuracy of the prediction, while σ is that of the scatter, both being important to assess the relative success of the ANN analysis. It is seen that the network configuration with R closest to unity is 4-1-1-1, while the network 4-5-5-1 is the one with the smallest σ . It does seem that the criterion on σ is a more important one, since the 4-5-5-1 network has errors confined to less than $\pm 3.7\%$ for all the testing data points, even though most of the scatter lies in the range of less than $\pm 0.7\%$.

With the results now known from the ANN analysis, their comparisons with those from the correlated coefficients of heat transfer as given in Eqs. (4) can be made, and are shown in Fig. 3, where Q^p_{cor} is the predicted heat transfer rate based on the correlations. It is clearly seen that the scatter for the correlation results is in the order of $\pm 10\%$. Even though this result is still considered as good from an application point of view, the ANN results nevertheless is seen to be considerably better at less than $\pm 1.0\%$. Of particular interest is that the error band in the predicted heat transfer rate is now in the range of measurement uncertainties of the experimental data, and thus signifies that most of the physics in the heat transfer behavior of the test heat exchanger is accounted for by the ANN results. It is in a way not surprising, since the massively-parallel processing in the learning process of the ANN is indeed capable of recognizing the functional pattern between the outputs and the input data. Another significant characteristic of the ANN is that in the process of training and testing, no thermophysical properties of the fluids are needed. This is again due to that the effects of properties are part of the physics which eventually affects the heat transfer rate as recognized by the trained ANN. Therefore, the need for good property data is eliminated, along with the needed prescription of a reference temperature to determine the properties.

If the ANN approach is to be a viable one to analyze the performance of any fin-tube heat exchanger, it must also demonstrate its capability in even more complex heat exchanger configurations. For this purpose, the air-

water multi-row multi-column heat exchangers as shown in Fig. 1(b) and studied by McQuiston [17,18] can be used as an example. Since such heat exchangers are normally used for air-cooling purposes, experimental data were obtained for both dry and wet conditions on the air side. Emphasis of the study was placed on the effects of the fin spacing on the air-side coefficients of heat transfer, and on the water side, only high Reynolds-number turbulent-flow conditions were considered so that the two coefficients could be conveniently decoupled. The measurement data were correlated in terms of the air-side heat and mass transfer coefficients in the form of the Colburn's j-factors under different surface conditions. The interested reader is referred to McQuiston [18] for the actual correlations. The rms deviations, in percentages, of the correlated j-factors from those of the measurements are shown in Table 2, where j_s and j_t refer to the sensible and total heat j-factors, respectively, and Q_t is the total heat transfer rate. It is seen that the deviations of the correlated data range from 6 to 15%. Under the dry conditions, the McQuiston correlations were more recently improved by Gray and Webb [19] and the improved results of the corresponding deviations are also shown in Table 2.

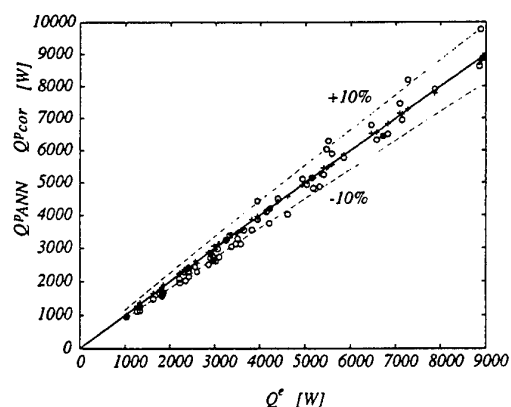


Figure 3: Comparison of 4-5-5-1 ANN (+) and correlation (o) predictions for heat exchanger 1.

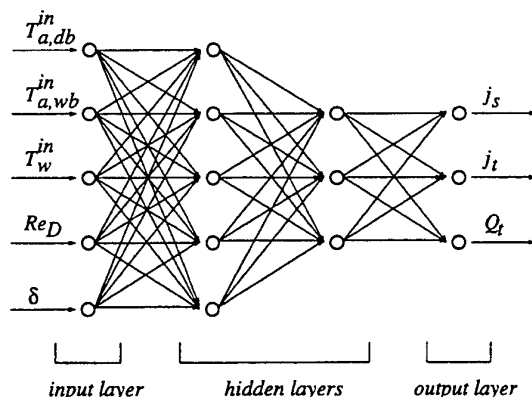


Figure 4: Schematic of a 5-5-3-3 ANN for heat exchanger 2.

TABLE 2: Comparison of percentage errors in j_s , j_t and Q_t predictions between the ANN and standard power-law correlations.

Surface	Method	j_s	j_t	Q_t
Dry	McQuiston	14.57	14.57	6.07
	Gray & Webb	11.62	11.62	4.95
	ANN	1.002	1.002	0.928
Dropwise	McQuiston	8.50	7.55	-
	Gray & Webb	-	-	-
	ANN	3.32	3.87	1.446
Filmwise	McQuiston	9.01	14.98	-
	Gray & Webb	-	-	-
	ANN	2.58	3.15	1.960
Combined	ANN	4.58	5.05	2.69

In the ANN analysis, several neural-network configurations were tried with the best result given by a fully-connected 5-5-3-3 configuration as shown in Fig. 4. The five input nodes correspond to the air-inlet dry-bulb and wet-bulb temperatures, water-inlet temperature, the air-flow Reynolds number, and the fin spacing. Here the actual air-flow rates could have been used just as well instead of the air-flow Reynolds number. The three output nodes are those of j_s , j_t , and Q_t . The j-factors were included only because they could be directly compared to those given by McQuiston [18], and Gray and Webb [19]. A total of 327 experimental data points were reported by McQuiston [17], of which 91 data sets were associated with observed dry conditions, while 117 and 119 data sets were related to dropwise- and filmwise-condensation conditions, respectively. These data sets were

analyzed in two different ways. First, each of the three surface conditions was analyzed separately to train its own ANN. Second, the entire 327 data sets were used to train a single ANN. The purpose here was to determine whether the network trained with separate data sets involving somewhat different physics of dry and condensation processes would perform better or worse than another ANN trained with the complete data sets.

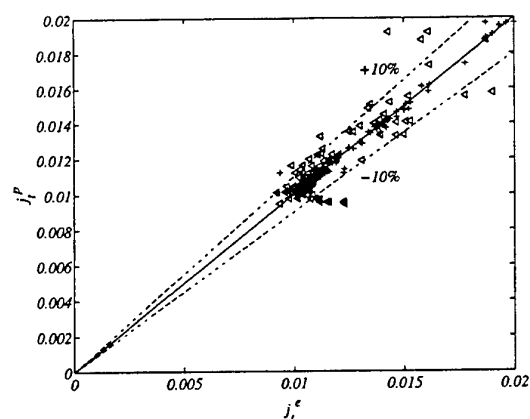


Figure 5: Experimental vs. predicted j_i for heat exchanger 2 with film condensation; ANN (+); McQuiston's correlation (triangle).

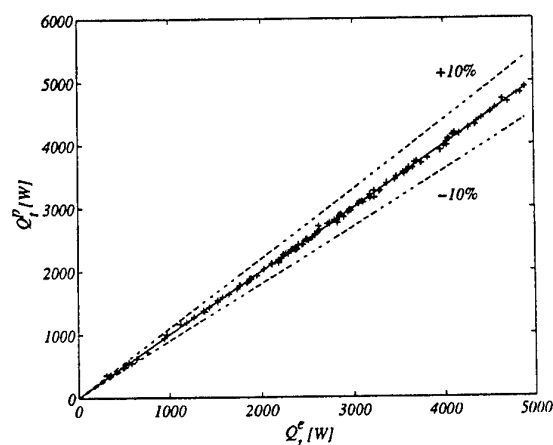


Figure 6: Experimental vs. predicted Q_i for heat exchanger 2 under film condensation.

The results in the rms deviations by those four ANNs are also shown in Table 2, all based on 800,000 training cycles, which were considered more than adequate. For dropwise condensation, the deviations from the ANN analysis is of the order of 3.3% in j_s , 3.9% in j_r , and only 1.4% in the total heat-transfer rates. It is of interest to note that in Q_i , being a physical quantity itself, the ANN better recognized the true relationship between Q_i and the physical input data, and that such a low level of deviations in Q_i is close to the expected uncertainties in the measurements. Similar results can also be seen for the dry-surface and film-condensation conditions. Also, the ANN gives better prediction for dry surfaces than for those that are wet, as the physical phenomena with condensation are more complex. On the other hand, when the ANN is trained with the entire set of data points without differentiating the surface conditions, all deviations tend to increase, indicating that the ANN attempted to negotiate, with more difficulty, the different physics involved. It is even more remarkable to note that even in this case, the predictions of Q_i , which is what the user is ultimately interested in, have deviations only of the order of 2.7%. Also, the above results can be more dramatically seen in the comparisons, for example, of j_i and Q_i under the filmwise-condensation conditions, as respectively shown in Figs. 5 and 6.

6. CONCLUDING REMARKS

Since the fin-tube heat exchangers are indeed complex and no first-principle analysis is now available to predict their heat-transfer performance, it is therefore necessary to utilize the experimental data for correlations and predictions. However, correlations by the usual approach still suffer inherent shortcomings, as reflected in the relatively large deviations from the experimental data in many situations; it has now been demonstrated that the quantitative pattern-recognition capability of ANN offers a much better alternative, and therefore the ANN methodology could and should be much more widely used in many heat-exchanger applications.

Furthermore in a broader context, accurate quantitative modeling in any thermal phenomena, including those in heat exchangers, is the ultimate goal to predict heat transfer rates or other thermal characteristics in relevant applications, and yet such modeling effort could well be very difficult because of the complexity of the associated real phenomenon. In these cases, the correlated experimental data are often used to serve as the thermal model relating the needed outputs to the prescribed inputs. Since the related correlation exercise of the experimental data is none other than an exercise of recognizing the quantitative pattern between the outputs and the inputs and because of the fact that the ANN analysis is seen to represent a powerful, versatile, and accurate method to quantitatively describe (recognize) such patterns, the properly trained neural network itself then

becomes an appropriate thermal model which is much better than other more traditional approaches. Such an ANN model is not written in an equation form, but is represented by a set of synaptic weights and node biases with reference to a specific ANN configuration, and the effort to use the ANN model in applications is just as simple as that in the traditional approaches.

In addition, the powerful capability for pattern recognition in the ANN analysis also suggests that an ANN could be trained to recognize dynamic input-output relations, fundamentally no more difficult than that of training static time-independent ANNs, as recently demonstrated by Diaz et al. [10,20]. The resulting ANN then becomes a dynamic model of the phenomenon, which is in general very difficult to develop in realistic thermal systems. The availability of such ANN dynamic models opens up new avenues of research in applications for which no such models can be developed so far by conventional analysis. A good example, among others, is in the design of robust control strategies for dynamic thermal system applications [21].

There are many other possibilities for the application of the ANN approach, along with other artificial intelligence methodologies, in thermal systems, and it seems that this approach is now receiving ever-increasing attention in the thermal science and system literature [10]. There is no doubt that before long the ANN approach will become established as a perfectly viable methodology to analyze complex thermal-system problems.

ACKNOWLEDGMENT

The authors wish to acknowledge the support of Mr. D. K. Dorini of BRDG-TNDR Corporation for this and related projects in the Hydraulics Laboratory at the University of Notre Dame.

REFERENCES

1. K. Torikoshi, G. Xi, Y. Nakazawa and H. Asano, "Flow and heat transfer performance of a plate-fin and tube heat exchanger, first report: effect of fin pitch," *Proceedings of the Tenth International Heat Transfer Conference*, pp. 411--416, (1994).
2. A. Bastani, M. Fiebig and N.K. Mitra, "Numerical studies of a compact fin tube heat exchanger," in *Design and Operation of Heat Exchangers*, Eds. W. Roetzel, P.J. Heggs, D. Butterworth, Springer-Verlag, Berlin, pp. 154--163 (1992).
3. D.J. Goering, J.A.C. Humphrey and R. Greif, "The dual influence of curvature and buoyancy in fully developed tube flows," *Int. J. Heat and Mass Transfer* Vol. 40, No. 9, pp. 2187--2199 (1997).
4. F.P. Incropera and D.P. DeWitt, *Fundamentals of Heat and Mass Transfer*, John Wiley & Sons (1990).
5. W.M. Kays and A.L. London, *Compact Heat Exchangers*, McGraw-Hill, New York (1984).
6. X. Zhao, *Performance of a Single-Row Heat Exchanger at Low In-Tube Flow Rates*, M.S. Thesis, Department of Aerospace and Mechanical Engineering, University of Notre Dame, Notre Dame, IN (1995).
7. G. Diaz, M. Sen, K.T. Yang and R.L. McClain, "Simulation of Heat Exchanger Performance by Artificial Neural Networks," *Int. J. HVAC&R Research*, Vol. 5, No. 3, pp. 195--208 (1999).
8. S. Kakac and H. Liu, *Heat Exchangers: Selection, Rating, and Thermal Design*, CRC Press, Boca Raton, FL (1998).
9. A. Pacheco-Vega, M. Sen, K.T. Yang, and R.L. McClain, "Genetic-algorithm based prediction of a fin-tube heat exchanger performance," *Proceedings of the 11th International Heat Transfer Conference*, Vol. 6, pp. 137--142 (1998).
10. M. Sen and K.T. Yang, "Applications of artificial neural networks and genetic algorithms in thermal engineering," to appear in *CRC Handbook of Thermal Engineering*, (editor) F. Kreith (1999).
11. F.H. Eeckman (Ed.), *Analysis and modeling of Neural Systems*, Kluwer Academic, Boston, MA (1992).
12. S. Haykin, *Neural Networks: A Comprehensive Foundation*, Macmillan College Publishing Co., New York (1994).
13. R. Schalkoff, *Artificial Neural Networks*, McGraw-Hill Co., New York (1997).
14. P. Zeng, "Neural computing in mechanics," *Appl. Mech. Rev.*, Vol. 51, No. 2, pp. 173--197 (1998).
15. R.L. Mahajan and X.A. Wang, "Neural network models for thermally based microelectronic manufacturing processes," *J. Electrochemical Soc.*, Vol. 140, No. 8, pp. 2287--2293 (1993).
16. A.S. Kelkar, R.L. Mahajan and R.L. Sani, "Real-time physiconeural solutions for MOCVD," *ASME J. Heat Transfer*, Vol. 118, pp. 814--821 (1996).

17. F.C. McQuiston, "Heat, Mass, and Momentum Transfer Data for Five Plate-Fin-Tube Heat Transfer Surfaces," *ASHRAE Transactions*, Vol. 84, Pt. 1, pp. 266--293, (1978).
18. F.C. McQuiston, "Correlation of Heat, Mass, and Momentum Transport Coefficients for Plate-Fin-Tube Heat Transfer Surfaces with Staggered Tube," *ASHRAE Transactions*, Vol. 84, Pt. 1, pp. 294--309, (1978).
19. D.L. Gray and R.L. Webb, "Heat Transfer and Friction Correlations for Plate Finned-Tube Heat Exchangers having Plain Fins," *Proceedings of the 8th International Heat Transfer Conference*, Vol. 6, pp. 2745--2750, (1986).
20. G. Diaz, M. Sen, K.T. Yang, and R.L. McClain, "Artificial Neural Network Simulation of the Dynamic Behavior of Heat Exchangers," *Proceedings of the 7th Latin American Heat and Mass Transfer Conference*, Vol. 1, pp. 23--28, Argentina, (1998).
21. G. Diaz, M. Sen, K.T. Yang and R.L. McClain, "Artificial Neural Network Control of an Experimental Heat Exchanger Facility," *ASME IMECE*, Nashville, Tennessee, (1999).

HEAT TRANSFER AND FRICTION CHARACTERISTICS OF FIN-AND-TUBE HEAT EXCHANGERS

Wei-Mon Yan and Pay-Jen Sheen

Department of Mechanical Engineering, Huafan University

Shih Ting, Taipei, Taiwan 22305

E-mail: wmyan@huafan.hfu.edu.tw

Fax: 886-2-26633847

Keywords: fin-and-tube heat exchangers, heat transfer, friction factor

ABSTRACT. An experimental study has been carried out to investigate the heat transfer and pressure drop characteristics of fin-and-tube exchangers with plate, wavy and louvered fin surfaces. In all, 36 samples of heat exchangers, including 12 plate-fin, 12 wavy-fin and 12 louvered-fin geometries, were tested. Results are presented as plots of friction factor f and Colburn j factor against Reynolds number in the range 300 to 2000. Finally, the various comparison methods were adopted to evaluate the air side performance of the plate, wavy and louver fin heat exchangers. Results show that for comparison using VG-1 criteria, about 40% surface area reduction was found for a louver fin heat exchanger.

NOMENCLATURE

A	area, m^2
C	heat capacity rate, W/K
c_p	Specific heat at constant pressure, $J/(kg \cdot K)$
D_c	fin collar outside diameter, m
D_h	Hydraulic diameter, m
f	Fanning friction factor
F	fin pitch, m
G_c	mass flux of the air based on the minimum flow rate, $kg/(m^2 \cdot s)$
h	heat transfer coefficient, $W/(m^2 \cdot K)$
j	Colburn j factor, $Nu/(Re_{Dc} \cdot Pr^{1/3})$
k	Thermal conductivity, $W/(m \cdot K)$
m	mass flow rate, kg/sec
N	Number of longitudinal tube rows
Nu	Nusselt number, $h \cdot D_c / k$
NTU	Number of transfer units
Pr	Prandtl number, ν/α
Q	Heat transfer rate, W
Re_{Dc}	Reynolds number, $\rho V D_c / \mu$
S_2	heat transfer power per unit temperature difference and per unit core volume, Eq.(11)
S_3	Friction power expenditure per unit core volume, Eq.(12)
T	Temperature, $^{\circ}C$
t	fin thickness, m
U	Overall heat transfer coefficient, $W/(m^2 \cdot K)$
V	Velocity, m/s
Greek letters	
ϵ	heat transfer effectiveness, $\dot{Q}_{avg} / \dot{Q}_{max}$
η	fin efficiency

η_0	Surface effectiveness
μ	Dynamic viscosity of air, Pa·s
ρ	Density of air, kg/m ³
σ	Contraction ratio of cross-sectional area
ΔP	Pressure drop, Pa
Subscripts	
1	air-side inlet
2	air-side outlet
air	air side
ave	Average value
i	tube side
in	Inlet
out	Outlet
w	wall of the tube

1. INTRODUCTION

Heat exchangers with fins and round tubes are widely used in industrial, air-conditioning and refrigeration applications to meet the demand for saving energy and resources. To reduce size and weight of heat exchangers, various fin patterns have been developed to improve the air-side heat transfer performance. Typical fin geometries are plate, wavy and louver fin surfaces. Generally, the complexity of the air flow pattern across the fin-and-tube exchangers makes the numerical simulation very difficult. Accordingly, it is necessary to resort to experimental study. The effects of fin spacing and number of tube rows on the heat transfer were examined by Rich [1, 2]. He concluded that, depending upon the Reynolds number, the average heat transfer coefficient for a deep coil may be higher or lower than that for a shallow. He further concluded that the heat transfer coefficient was essentially independent of the fin spacing. Corrections of Colburn j factor and friction factor f for plain fins were proposed by McQuiston [3] and Gray and Webb [4]. Nayansayan [5] investigated the effects of outer surface geometry on the performance of flat plain fins and round tube heat exchangers with four-row coils. A combined numerical and experimental study of plate-fin and tube heat exchangers was examined by Jang et al. [6]. In their study, the detailed numerical results of pressure drop and heat transfer coefficient are presented. But the experimental results are little. Recently, a systematic study on heat and friction characteristics of plate fin-and-tube heat exchangers was experimentally investigated by Wang et al [7]. In their study, the results are limited to the cases with large fin pitch heat exchangers. Goldstein and Sparrow [8] measured the local and averaged mass transfer coefficients for a wavy finned-tube model using mass transfer technique. They found that the heat transfer is 45% higher than that of plate-fin heat exchanger at $Re=1000$. Beecher and Fagan [9] reported heat transfer data for twenty wavy geometries. Similar studies were also examined experimentally by Mirth and Ramadhyani [10], Wang et al. [11] and Youn et al. [12]. Because the performance of the fin-and-tube heat exchangers is highly dependent on the pattern of fins. The louver surface can break and renew the boundary layer of the air flow. Consequently, higher heat transfer performance is expected as compared the case with plain fins. Kays and London [13] were the first to report heat transfer and pressure drop data on louvered fins. However, the geometries of the test samples do not reflect present industrial designs. Achaichia and Cowell [14, 15] experimentally and numerically examined the heat transfer and pressure drop characteristics of flat tube and louvered fin surfaces. To understand the detailed flow pattern across the fin-and-tube heat exchanger, Webb and Trauger [16] performed a flow visualization study of the louvered fin geometry with a flat tube. An analytical model for prediction of air-side heat exchanger performance of louvered fin geometry was developed by Sahnoun and Webb [17]. Their model is based on boundary layer and channel flow equations, and accounts for the flow efficiency. The studies reviewed above are limited to the results of louver fins with a flat tube. But in the HVAC&R applications, the louver fin-and-tube heat exchangers with round tube are more popular. More recently, experimental studies of heat transfer and friction characteristics of typical louver fin-and-tube heat exchangers were performed by Wang et al. [18, 19]. But in refs. [18, 19], little results are presented in their articles. In addition, the effects of fin spacing and number of tube rows on the heat transfer coefficient and pressure drop do not appear in their studies. Therefore, the extensive experimental results of the louver fin configuration are of importance in the HVAC&R applications. Despite there are numerous experimental data related to the fin-and-tube heat exchangers, however, detailed performance comparisons among these fin patterns are still limited. Therefore, this motivates the present study. The purpose of this work is to quantitatively compared the performance of various fin-and-tube heat exchangers.

2. EXPERIMENTAL APPARATUS

Thirty six heat exchangers of various fin geometries and in staggered configuration with various tube row and fin pitch combinations were examined in this work. A wind tunnel facility similar to the one used in previous fin-and-tube heat exchanger experiments [7, 8, 18, 19] was modified to conduct this study. A schematic diagram of the wind tunnel is shown in Fig.1. the system is designed to suck room air over the finned side of the exchanger by a 3.73 kW centrifugal fan with an inverter while circulating hot water through the tubes. The tunnel was a rectangular duct 60cm×40cm in cross section. To minimize heat loss to the surroundings, the tunnel surface is insulated with a 2cm thick glass-wool layer. Additionally, being supported by stands of perforated steel plates, the tunnel system is evaluated 80cm above the floor level of the laboratory room.

The inlet and exit temperatures across the air side of the heat exchangers are measured by two T-type thermocouple meshes. The inlet measuring mesh consists eight thermocouples while the exit mesh contains twelve thermocouples. These data signals are individually recorded and then averaged. The working medium on the tube side was hot water. The water circulation supplies high-velocity hot water to the tube side. The water is heated by a 80kW electric heater, whose power input is adjustable. Both the inlet and outlet temperatures were measured by two pre-calibrated RTDs (Pt-100Ω) which have an accuracy of 0.1°C. The water flow rate was measured by a calibrated magnetic flow meter with 0.002l/s resolution. During the experiments, the water inlet temperature was kept constant at 60°C with volume flow rate 10l/min. The air pressure drops across the heat exchanger and the nozzle are, respectively, measured by precision differential pressure transducers, reading to 0.1 Pa. The air flow measuring station is a multiple nozzle code tester based on the ASHRAE 41.2 standard [20].

The heat exchanger with specified surface geometry was installed in the test system. In this work, the exchanger height was less than the tunnel dimensions, and the bypass flows was eliminated by a thin layer of foam plastic sandwiched between the edges of the fins and the casing. Upon completion of the hot water side links, the coil was completely insulated with a 3cm thick layer of glass wool. The air flow through the test section was adjusted to a desired value by an converter. In addition, the inlet water was kept at 60°C with a fixed flow rate. If the test system including the air and water sides becomes steady state, the data signals was recorded.

3. ANALYSIS

(A) Pressure Drop

The core friction of the heat exchanger was reduced to obtain the Fanning friction factor f . In the present study, the pressure drop equation proposed by Kays and London [13], including the entrance and exit pressure losses, was used to evaluated the friction factor. The equation is

$$f = \left(\frac{A_c}{A_o} \right) \cdot \left(\frac{\rho_m}{\rho_1} \right) \cdot \left[\frac{2\rho_1 \Delta P}{G_c^2} - (K_c + 1 - \sigma^2) - 2 \left(\frac{\rho_1}{\rho_2} - 1 \right) + (1 - \sigma^2 - K_e) \cdot \left(\frac{\rho_1}{\rho_2} \right) \right] \quad (1)$$

where A_c and A_o are the minimum flow area and total heat transfer area, respectively. K_c and K_e are the inlet and exit heat loss coefficients, respectively, and σ means the ratio of the minimum flow area to the frontal area. The entrance and exit loss coefficients, K_c and K_e , are adopted from Figs. 14-26 from McQuiston and Parker [21].

(B) Heat Transfer

In the study of heat exchanger performance, the Colburn j factor is of interest. To obtain the j factor from the experimental data, the effective-NTU equation with unmixed-unmixed cross flow is employed to determined the UA-value. The ε -NTU relation is [13, 21]

$$\varepsilon = 1 - \exp \frac{NTU^{0.22}}{C \cdot [\exp(-C \cdot NTU^{0.78}) - 1]} \quad (2)$$

where

$$C^* = C_{\min}/C_{\max} = (\dot{m}c_p)_{\text{air}}/(\dot{m}c_p)_{\text{water}} \quad (3)$$

$$\varepsilon = Q_{\text{ave}}/[(\dot{m}c_p)_{\text{air}} \cdot (T_{\text{in,water}} - T_{\text{in,air}})] \quad (4)$$

$$\text{NTU} = UA/C_{\min} \quad (5)$$

The total heat transfer rate Q_{ave} is calculated as the average of the air-and water-side values. With Eqs.(2)-(5), an iterative procedure is needed to obtain the overall heat transfer coefficient UA . The air-side thermal resistance $(1/\eta_o h_o A_o)$ was evaluated by subtracting the water-side and wall thermal resistances from the total thermal resistance, assuming zero water-side fouling resistance. Thus,

$$\left(\frac{1}{\eta_o h_o A_o} \right) = \frac{1}{UA} - \frac{1}{h_i A_i} - \frac{\delta_w}{k_w A_w} \quad (6)$$

Note that the 2nd term of R.H.S. of Eq. (6) indicates the wall-side thermal resistance and the 3rd term means the tube wall resistance. The tube-side heat transfer coefficient, h_i , was calculated by the Petukhov correction for turbulent flow in tubes [22]. This equation is

$$h_i = \left(\frac{k}{D} \right)_i \cdot \text{Re}_i \cdot \text{Pr} \frac{(f_i/2)}{1.07 + 12.7(f_i/2)^{0.5}(\text{Pr}^{2/3} - 1)} \quad (7)$$

with the friction factor given by

$$f_i = 1/[1.58 \ln(\text{Re}_i) - 3.28]^2 \quad (8)$$

The Reynolds number Re_i is about 20000 in the present study. In Eq. (6), the h_o is the air-side heat transfer coefficient and the η_o is the surface effectiveness. The η_o is defined as the actual heat transfer for the fin and base divided by the heat transfer for the fin and base when the fin is at the same base temperature. The detailed evaluation of η_o is available in refs. [7,23]. For the study of performance of heat exchangers, the Colburn j factor is of interest. The j factor is defined as

$$j = \text{Nu}/(\text{Re}_{\text{Dc}} \cdot \text{Pr}^{1/3}) \quad (9)$$

where the Nusselt number is

$$\text{Nu} = h_o D_c / k_{\text{air}} \quad (10)$$

4. RESULTS AND DISCUSSIONS

(A) f and j factors vs. Reynolds Number

The basic surface characteristics of heat exchangers are generally presented in dimensionless form as Fanning friction factor f and the Colburn j factor. Fig. 2 shows the effects of tube row number on the f and j factors against Reynolds number Re_{Dc} . The Reynolds number Re_{Dc} is based on the outer tube diameter (including collar thickness). Consideration of the f and j factors displays that both f and j factors decrease with the increase in Re_{Dc} . Comparison of the results between plate and louver fin heat exchangers shows that larger f and j factors are found for the louver fin heat exchangers.

Fig. 3 presents the effects of fin pitch on the f and j factors for various fin patterns with identical tube row numbers. The fin pitches are 2.0mm, 1.69mm and 1.4mm, respectively. For plate fin heat exchangers, the f and j

factors increase with the decrease in the fin pitch. But for louver fin heat exchangers, the effects of fin pitch on the f and j factors do not show a trend.

(B) ΔP and h vs. Frontal Air Velocity V

In the study of heat exchanger performance, the results of pressure drop ΔP and heat transfer coefficient h are also important for the designers of heat exchangers. Figs. 4 and 5 present the results of ΔP and h against frontal velocity V . As expected, both ΔP and h increase with the frontal air velocity. Additionally, better ΔP and h performances are found for louver fin heat exchangers. In Fig. 4 (a), a larger ΔP is found for a heat exchanger with a greater tube row number. But for heat transfer coefficient h [in Fig. 4 (b)], the effects of tube row number on the h show a insignificant influence. Like the results of fin pitch on the friction factor f , ΔP decreases with the increase in the fin pitch.

(C) Comparison of $\sigma^2 j/f$

Fig. 6 shows the "area goodness factor" comparison vs. the Reynolds number Re_{Dc} for plate, wavy and louver fin exchangers. An overall inspection on Fig. 6 discloses that for 1 tube row number heat exchanger, the wavy fin geometry shows the highest value of $\sigma^2 j/f$ under the same Re_{Dc} , and the plate fin comes in second while the louver fin shows the lowest. But for 2 tube row number heat exchangers, the plate fin surface gives the lowest values of $\sigma^2 j/f$.

(D) Volume Goodness Factor Comparison

In this study, the another comparison of the heat exchanger performance is the volume goodness factor comparison suggested below:

$$S_2 = \frac{c_p \mu \eta_0}{(Pr^{2/3}) \cdot (4\sigma/D_h^2) \cdot j Re} \quad (11)$$

$$S_3 = \frac{\mu^3}{(2\rho^2) \cdot (4\sigma/D_h^2) \cdot f Re^3} \quad (12)$$

where S_2 means the heat transfer power per unit temperature difference and per unit core volume; S_3 indicates the friction power expenditure per unit core volume. From the viewpoint of heat exchanger volume required, a larger S_2 vs. S_3 is better for a designer of heat exchanger. Fig. 7 presents the S_2 vs. S_3 for plate, wavy and louver fin heat exchangers having $F=1.4\text{mm}$ and 2.0mm . It is clear that for a given S_3 , a higher S_2 is found for a case with a lower tube row number. Additionally, a largest S_3 is found for a louver fin surface. This means that a fixed volume of heat exchanger, the louver fin heat exchanger shows a best performance.

(E) Comparison Using VG-1 Criteria

A practical air-side performance may be made using the VG-1 criteria of Webb [24], which measures the possible reduction of surface area. This methodology compares the required total air-side surface area (A) for fixed values of the fan power, heat duty, and temperature difference. Fig. 8 presents the ratio A/A_{plate} against Reynolds number Re_{Dc} . The ratio A/A_{plate} is defined as follows [24]:

$$\frac{A}{A_{plate}} = \left(\frac{f}{f_{plate}} \right)^{1/2} \cdot \left(\frac{j_{plate}}{j} \right)^{3/2} \quad (13)$$

where A_{plate} is the plate fin geometry. As expected, approximately 30% area reduction is seen for the louver fin surface having fin pitch $F=1.4\text{mm}$. For fin pitch $F=2.0\text{mm}$, the louver fins require approximately 40% less than fin surface than the plate fin to yield the same heat transfer performance. This indicates that for the same Reynolds number Re_{Dc} , a larger area reduction is encountered for a system with a larger fin pitch.

5. CONCLUSIONS

An experimental study of the air-side heat transfer and pressure drop characteristics of plate, wavy and louver fin surfaces was carried out. In the present study, 36 samples of plate, wavy and louver fin-and-tube heat exchangers with different fin pitch and tube row number are tested. Various comparison methods have been adopted to evaluate the performance of heat exchanger among various fin surfaces. On the basis of previous discussions, the following conclusions are made:

- (1) At the same Re_{De} , louver fin geometry shows larger values of f and j factors, compared with the plate fin surface.
- (2) At the same frontal velocity, the pressure drop ΔP increases with the increase in the tube row numbers.
- (3) The wavy fin heat exchanger has the highest $\sigma^2 j/f$ ratio for Re_{De} , 1500 among the plate, wavy and louver heat exchangers.
- (4) For volume goodness factor comparison, louver fin heat exchangers have a highest S_2 at a given S_3 .
- (5) For comparison using VG-1 criteria, about 40% surface area reduction was found for a louver fin heat exchanger, relatively to the plate fin heat exchangers. Additionally, the area reduction increases with the fin pitch.

ACKNOWLEDGEMENTS

The support of this work by the National Science Council, R.O.C., under contract No. NSC 87-2212-E211-006 is gratefully acknowledged. Additionally, the valuable suggestions from Dr. C.C. Wang are very much appreciated.

REFERENCES

1. D.G. Rich, The effect of fin spacing on the heat transfer and friction performance of multi-row, plate fin-and-tube heat exchangers. ASHRAE Trans., 1973, 79, 137-145.
2. D.G. Rich, The effect of the number of tube rows on heat transfer performance of smooth plate fin-and-tube heat exchangers. ASHRAE Trans., 1975, 81, 307-317.
3. F.C. McQuiston, Correction of heat, mass and momentum transport coefficients for plate fin-and-tube heat transfer surfaces with staggered tubes. ASHRAE Trans., 1978, 84, 294-309.
4. D.L. Gray and R.L. Webb, Heat transfer and friction corrections for plate fin-and-tube heat exchangers having plain fins. Proc. 8th Int. Heat Transfer Conference, San Francisco, 1986, 2745-2750.
5. N. Kayansayan, Heat transfer characterization of flat plain fins and round tube heat exchangers. Experimental Thermal Fluid Science, 1993, 6, 263-272.
6. J.Y. Jang, M.C. Wu and W.J. Chang, Numerical and experimental studies of three-dimensional plate-fin and tube heat exchangers. Int. J. Heat Mass Transfer, 1996, 39, 3057-3066.
7. C.C. Wang, Y.J. Chang, Y.C. Hsieh and Y.T. Lin, Sensible heat and friction characteristics of plate fin-and-tube heat exchangers having plate fins. Int. J. Refrigeration, 1996, 19, 223-230.
8. L. Goldstein, Jr. and E.M. Sparrow, Experiments on the transfer characteristics of a corrugated fin and tube heat exchanger configuration. ASME J. Heat Transfer, 1976, 98, 26-34.
9. D.T. Beecher and T.J. Fagan, Effects of fin pattern on the air-side heat transfer coefficient in plate finned-tube heat exchangers. ASHRAE Trans., 1987, 93, pt.2, 1961-1984.
10. D.R. Mirth and S. Ramadhyani, Corrections for predicting the air side Nusselt numbers and friction factors in child water cooling coils. Exp. Heat Transfer, 1994, 7, 144-162.
11. C.C. Wang, W.L. Fu and C.T. Chang, Heat transfer and friction characteristics of typical wavy fin-and-tube heat exchanger. Exp. Thermal and Fluid Science, 1997, 14, 174-186.
12. B. Youn, Y.H. Kil, H.Y. Park, K.C. Yoo and Y.S. Kim, Experimental study of pressure drop and heat transfer characteristics of $\phi 10.07$ wave and wave-slit fin-tube heat exchangers with wave depth of 2mm. Proc. 11th Heat Transfer Conference, Kyongju, Korea, 1998, 6, 333-338.
13. W.M. Kays and A.L. London, Compact Heat Exchangers, 3rd ed., McGraw-Hill, New York, 1984.
14. A. Achaichia and T.A. Cowell, Heat transfer and pressure characteristics of flat tube and louvered plate fin surfaces. Exper. Thermal and Fluid science, 1988, 1, 147-157.
15. A. Achaichia and T.A. Cowell, A finite difference analysis of fully developed periodic laminar flow in inclined louver arrays. Proc. 2nd UK National Heat Transfer Conference, Glasgow, U.K. 1988, 2, 883-888.
16. R.L. Webb and P. Trauger, Flow structure in the louvered fin heat exchanger geometry. Exper. Thermal Fluid Science, 1991, 4, 205-217.

17. A. Sahnoun and R.L. Webb, Prediction of heat transfer and friction for the louver fin geometry. ASME J. Heat Transfer, 1992, 114, 893-900.
18. Wang, C.C., Chen, P.Y. and Jang, J.Y., Heat transfer and friction characteristics of convex-louver fin-and-tube heat exchangers. Exp. Heat Transfer, 1996, 9, 61-78.
19. C.C. Wang, K.Y. Chi, Y.J. Chang, An experimental study of heat transfer and friction characteristics of typical louver fin-and-tube heat exchangers. Int. J. Heat Mass Transfer, 1999, 41, 817-822.
20. ASHRAE, ASHRAE Standard 41.2-1987 Standard Methods for Laboratory Air-flow Measurement, 1987.
21. F.C. McQuiston and J.D. Parker, Heating, Ventilation, and Air-conditioning, 4th ed., John Wiley, New York, 1994, Ch. 14, 571.
22. B.S. Petukhov, V.A. Kurganov and A.I. Gladuntsov, Heat transfer in turbulent pipe flow of gases with variable properties. Heat Transfer, Sov. Res., 1973, 5, 109-116.
23. Th.E. Schmidt, Heat transfer calculation for extended surfaces. Refrig. Eng. 1949, 49, 351-357.
24. R.L. Webb, Principles of Enhanced Heat Transfer. John Wiley and Sons, New York, 1994.

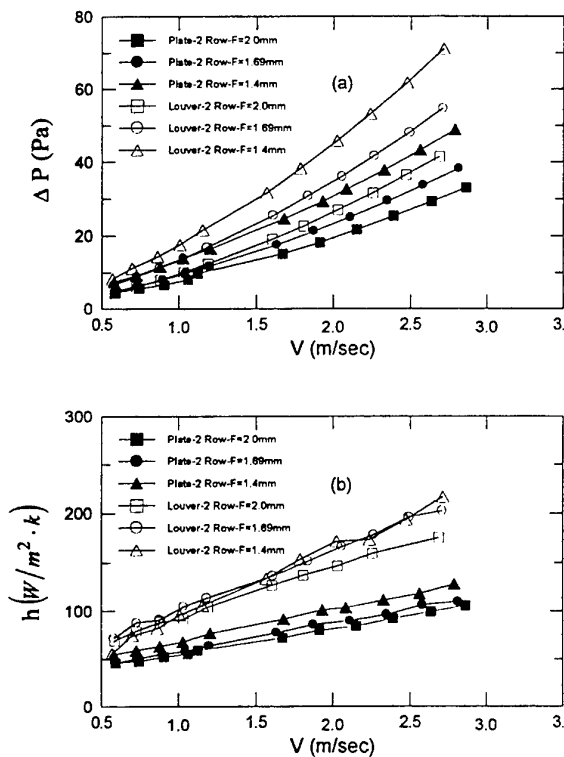


Fig. 5 Effects of fin pitch on the ΔP and h .

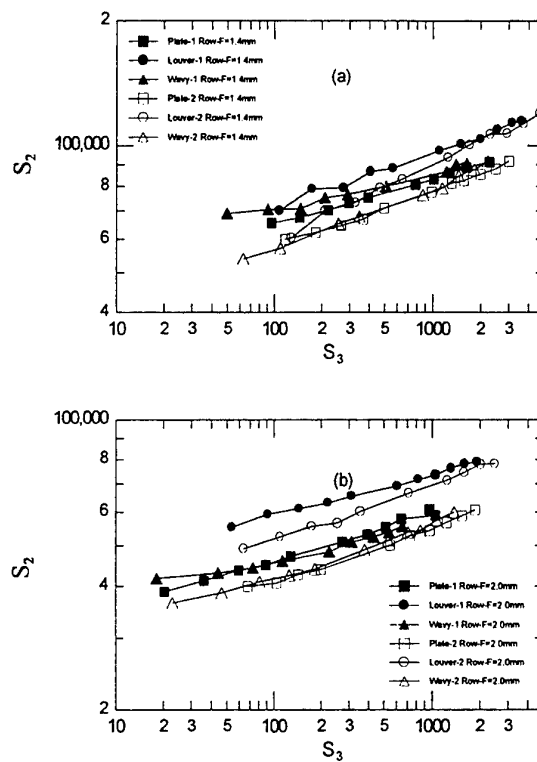


Fig. 7 Volume goodness comparison for 1 and 2 tube row numbers.

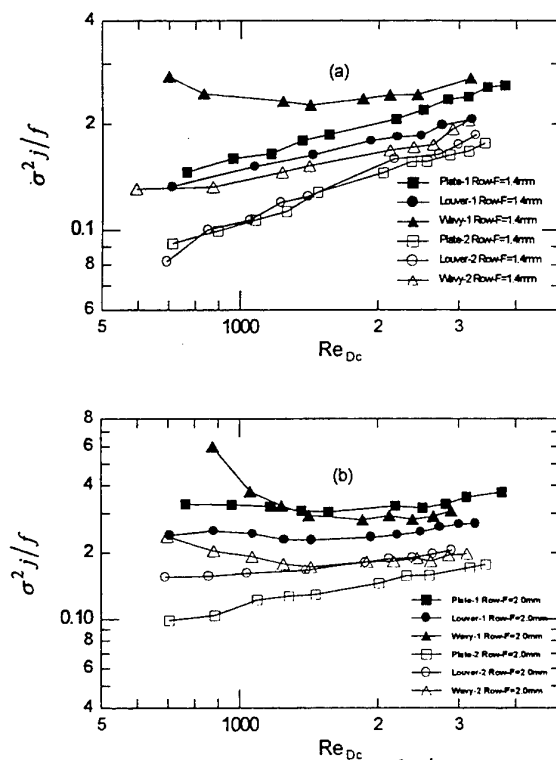


Fig. 6 Comparison of $\sigma^2 j/f$

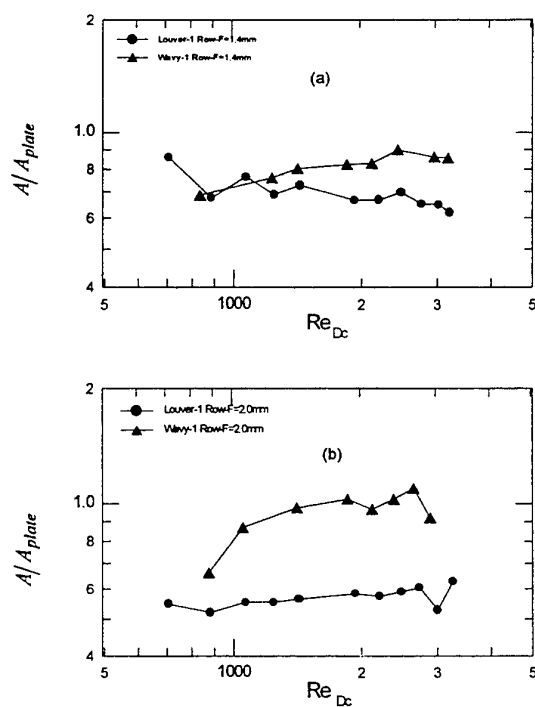


Fig. 8 Ratios of fin surfaces are relative to plate Fin using VG-1 criteria.

INVESTIGATION OF NOVEL ENHANCED HEAT TRANSFER SURFACES FOR INDUSTRIAL COMPACT HEAT EXCHANGERS

Rainer Mertz, Manfred Groll

Institut für Kernenergetik und Energiesysteme (IKE)
(Institute for Nuclear Technology and Energy Systems)
University of Stuttgart
Email: mertz@ike.uni-stuttgart.de; Fax: +49 711 685 2010

Keywords: pool boiling, hydrocarbons, compact heat exchangers,
enhanced heat transfer surfaces, re-entrant cavities

ABSTRACT. To investigate the heat transfer from enhanced evaporation surfaces, various structured tubes, particularly with re-entrant cavities, and one smooth reference surface were tested in the pool boiling mode using the hydrocarbon propane as working fluid. The tubes are made of carbon steel ST35.8. As experimental parameters saturation temperatures between 253 K and 293 K and heat fluxes in the range from 2 kW/m² to 100 kW/m² are employed. For the visualisation of the boiling phenomena and the two-phase flow from the tube surfaces a test rig is employed with a high speed video system. An empirical correlation has been generated to describe the experimental results.

Compared with the smooth reference tube, the structured surfaces with re-entrant cavities show distinct improvements of the heat transfer performance. Particularly for low and medium heat fluxes ($q < 40 \text{ kW/m}^2$), higher heat transfer coefficients of factors up to 3 were observed.

1. INTRODUCTION

The application of compact two-phase heat exchangers (CHEs), particularly in the process industries, has shown that these devices have a number of advantages compared with conventional shell-and-tube heat exchangers. An improved energy efficiency, lower wall superheats, smaller volume and weight are some of them. Besides a reduction of primary energy and raw material consumption for the manufacturing and use of compact heat exchangers, they are also cost-efficient, which is an important factor for their acceptance by the industries.

There is no common definition for a compact heat exchanger. One used classification is the surface/volume ratio of the heat exchangers. But the value for the ratio differs from author to author, one author published a ratio of 700 m²/m³ [1], another author used a ratio of 200 m²/m³ [2]. Recent studies showed, that for compact plate heat exchangers it is possible to reach surface/volume ratios higher than 1000 m²/m³ [3]. However, conventional shell-and-tube heat exchangers, using smooth tubes, will not exceed a surface/volume ratio of 200 m²/m³. Therefore structured tubes have to be used to design compact shell-and-tube heat exchangers, which are of high interest for the chemical and petrochemical industries, e.g. in applications in LNG liquefaction plants.

Compact shell-and-tube heat exchangers employed with low-finned tubes and/or internally finned tubes show distinct thermal and economic advantages compared to heat exchangers with smooth tubes, e.g. the size of the heat exchangers can be reduced by 30% to 75% [4]. So, even if the manufacturing of compact heat exchangers with enhanced tubes is more complex and more expensive than of conventional ones, the reduced size and weight make it possible to use these components cost-effectively for industrial applications [5]. Until now, most compact shell-and-tube heat exchangers are provided with low-finned tubes or tubes with fins modified by rolling, bending or knurling, forming T-fins (Gewa-TWX) or tunnel-and-pore arrangements (Thermoexcel-E, Turbo-B, ECR40).

For further increase of the efficiency and compactness of heat exchangers, new enhanced surfaces with geometries forming re-entrant cavities are investigated at IKE. The pool boiling test are carried out with one smooth reference tube and 4 enhanced tubes in horizontal orientation, all made of carbon steel ST35.8. Results of experiments using tubes made of copper-nickel are available in [6]. As working fluid the hydrocarbon propane was used at saturation temperatures in the range from 253 K to 293 K, and the employed heat flux ranged between 2 kW/m² and 100 kW/m².

The experimental results of the enhanced tubes show higher heat transfer coefficients of factors up to 3, compared with the smooth reference tube, especially for low and medium heat fluxes up to 50 kW/m^2 . For higher heat fluxes, this improvement factor decreases with increasing heat flux. This behaviour, which is not in accordance with the conventional boiling curve, can be explained by an increased vapour production in the small internal channels and cavities, which results in a partial deactivation of the internal heat transfer surface.

To investigate the boiling phenomena and the two-phase flow from the evaporation surfaces, a high speed video system (CCD with 256×256 pixel, 1125 frames/s) is used. The video data are used to evaluate parameters like bubble departure diameter and bubble frequency. For that purpose, the software IKE_DBV for digital image processing was developed at IKE.

Only limited correlations for structured surfaces with re-entrant cavities are available. Some efforts were made by Nakayama et al. [7] and Chien and Webb [8] to correlate the heat transfer coefficients of such geometries, but these empirical correlations are difficult to use. More correlations are available for smooth and low-finned tubes, e.g. by Stephan and Abdelsalam [9], Cooper [10, 11] and Gorenflo [12].

Based on the experimental results obtained with the enhanced heat transfer surfaces, a correlation was generated to predict the heat transfer coefficient [13].

2. EXPERIMENTAL APPARATUS

Due to the used working fluid propane the test rig (Fig. 1) for the experimental investigations had to be designed for high pressures (DN24) and for flammable and explosive liquids. The main components of the test rig are two pressure vessels, viz. a test vessel and a fluid tank for the storage of the working fluid during the time no experiments are carried out. A more detailed description of the experimental apparatus is given in [14]. The high speed video system is shown in Fig. 2.

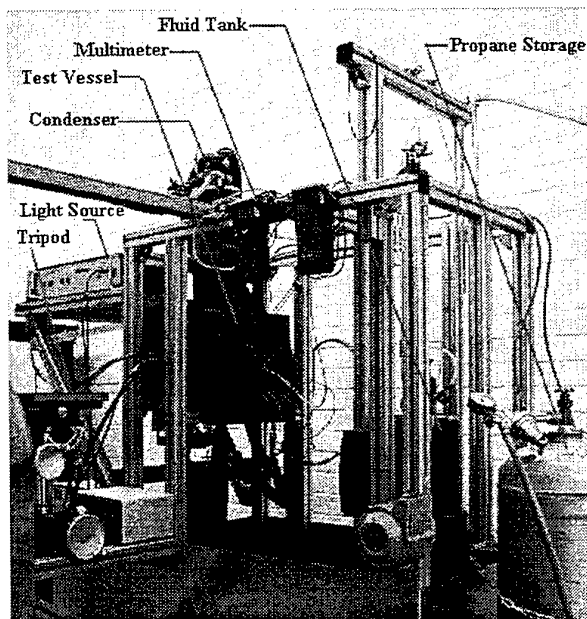


Fig. 1. View of test rig

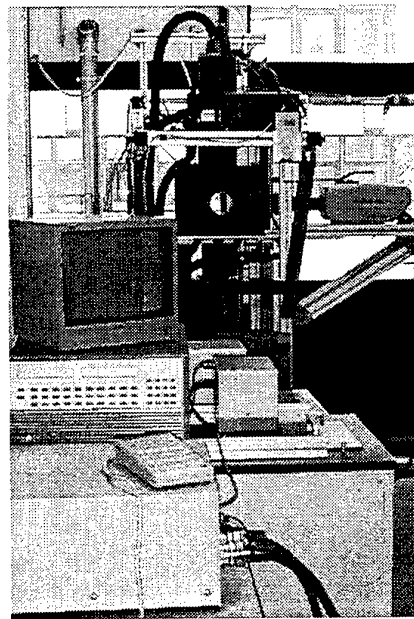


Fig. 2. High Speed Video System

The tubes with the evaporation surfaces are shrunk on a second tube with four grooves on the outer surface for accommodating four thermocouples type K (NiCr-Ni) to measure the wall temperature (Fig. 3).

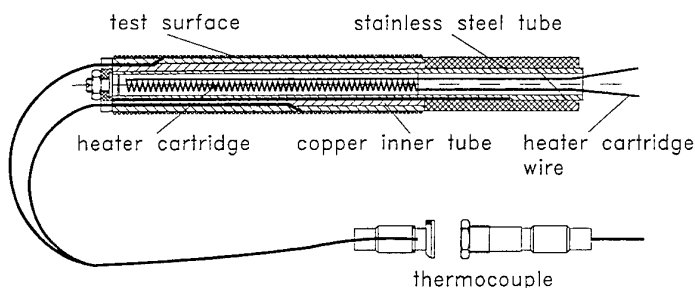


Fig. 3. View of test section

The test section is mounted on a stainless steel tube, which is welded on a removeable flange of the test vessel. This stainless steel tube is closed to the inside of the vessel; it can be provided with a heater cartridge from the outside. This prevents any contact between the heater cartridge and the flammable working fluid.

3. EXPERIMENTAL RESULTS

The experimental results of the investigated tubes are presented in Figs. 4 - 8 as heat transfer coefficient α vs. heat flux q .

Figure 4 shows the experimental results of the smooth reference tube. The obtained heat transfer coefficients are between $0.6 \text{ kW/m}^2\text{K}$ and $11 \text{ kW/m}^2\text{K}$ for employed heat fluxes ranging from 2 kW/m^2 to 100 kW/m^2 . These heat transfer coefficients are used for the calculation of the improvement factors of the different enhanced surfaces. The heat transfer coefficients of the smooth reference tube and the enhanced surfaces are summarized in Table 1.

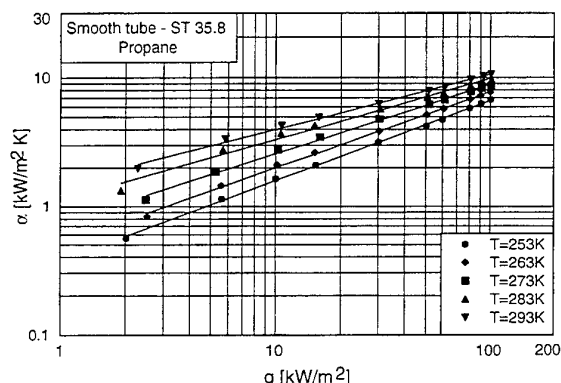


Fig. 4. Smooth tube - ST35.8, working fluid propane

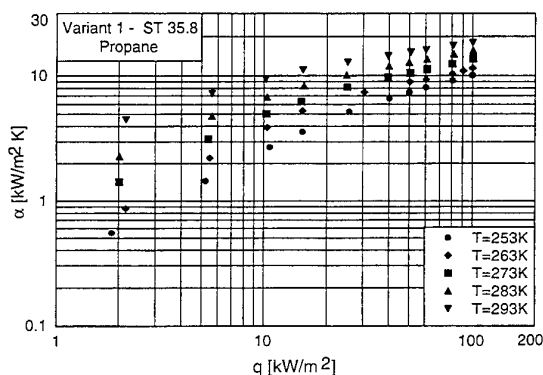


Fig. 5. Enhanced tube variant 1 - ST35.8, working fluid propane

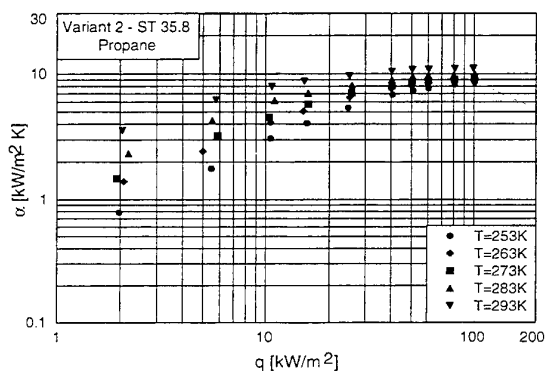


Fig. 6. Enhanced tube variant 2 - ST35.8, working fluid propane

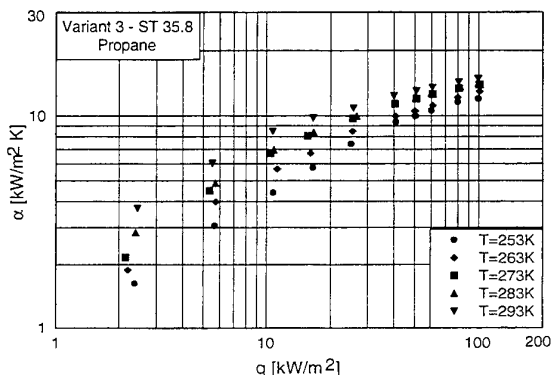


Fig. 7. Enhanced tube variant 3 - ST35.8, working fluid propane

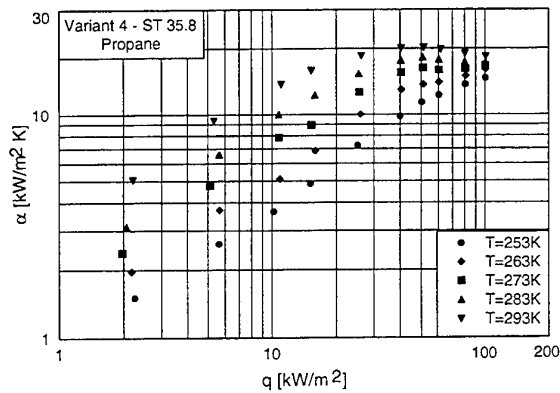


Fig. 8 Enhanced tube variant 4 - ST35.8, working fluid propane

Figure 8 depicts the results of the enhanced tube variant 4. This surface showed the best results with improvement factors over 3, especially for the heat flux range up to 20 kW/m² which is of most interest for industrial applications.

The improvement factors F_i for all enhanced tubes are depicted in Figs. 9 and 10 for saturation temperatures of $T_s = 253$ K and $T_s = 293$ K, respectively. For the lowest investigated temperature $T_s = 253$ K and for low heat fluxes up to 15 kW/m², the enhanced tube variant 3 shows also good results, but this does not hold for higher saturation temperatures. For all other experimental conditions, best results are observed with variant 4.

Table 1 Ranges of heat transfer coefficient α (kW/m²K) of the tested tubes for saturation temperatures of 253 K and 293 K

Heat flux (kW/m²)	2		10		50		100	
Temperature T_s	253 K	293 K	253 K	293 K	253 K	293 K	253 K	293 K
Smooth	0.6	2	1.6	4.2	4.2	7.9	6.8	10.6
Variant 1	0.6	4.5	2.7	9.5	7.4	15.2	10.1	18
Variant 2	0.8	3.6	3.1	7.9	7.3	10.8	8.5	11
Variant 3	1.5	3.5	4.4	8.5	10	13	12	14.9
Variant 4	1.5	5	3.6	13.5	11.3	20	14.6	18.3

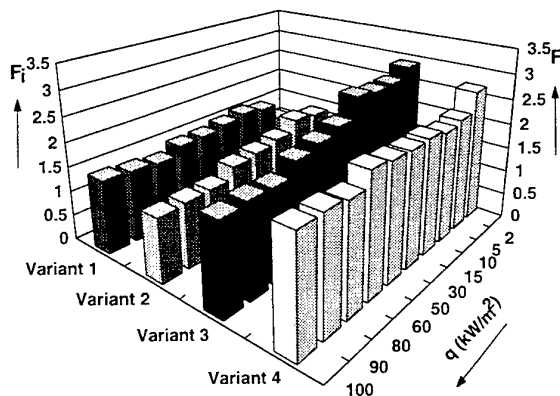


Fig. 9. Improvement factor F_i of the enhanced tubes, saturation temperature $T_s = 253$ K

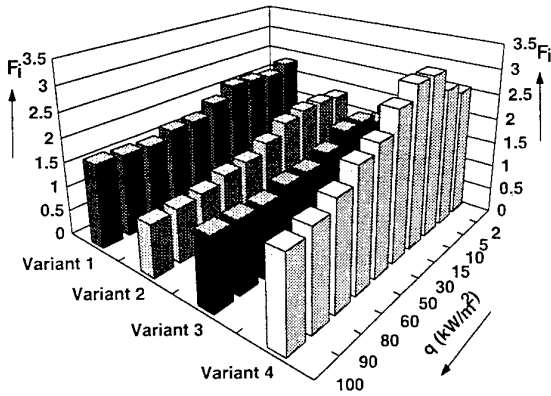


Fig.10. Improvement factor F_i of the enhanced tubes, saturation temperature $T_s = 293$ K

4. VISUALISATION RESULTS

To obtain data about the boiling phenomena and the two-phase flow from the evaporation surfaces, a high speed video system is used to record the boiling behaviour on video tapes. The software IKE_DBV for digital image processing was developed at IKE to analyze video sequences concerning relevant boiling parameters, e.g. the

bubble departure diameter and the bubble frequency. Due to the modular design of the software additional functions can be added and the software can be also used for the evaluation of the results of other visualisation methods (PIV, thermograph images, etc.).

Figure 11 shows one frame of a series and how it is possible to select different observation windows for the analysis of the bubble parameters. Window 1 is used to calculate the bubble velocity (one - dimensional) by identifying the same bubble in two or more frames in a row and measuring the distance between the bubble positions. Because the time step is known by the frame rate, the bubble velocity can be calculated.

The smaller window 2 can be positioned above an active nucleation site and the software recognizes the changing of the grey values if a bubble is passing through the window. The number of recognized bubbles during a known time period gives the bubble frequency.

In parallel, the bubble diameter is determined by investigating the area of the bubble. For the calculation of the bubble departure diameter, a spherical bubble shape is supposed.



Fig. 11. Boiling from an enhanced heat exchanger tube, variant 4, $T_s = 283 \text{ K}$, $q = 2 \text{ KW/m}^2$

A lot of bubbles at a lot of nucleation sites are investigated with statistical methods to obtain average values. For the determination of the bubble frequency for example, a one-dimensional Fast Fourier Analysis (FFT) is carried out. The result of such a FFT is shown in Fig. 12, where three frequencies are emphasized. The first frequency $f_0 = 4 \text{ 1/s}$ is caused by a modulated pedestal signal due to the inhomogeneous illumination in the observation area. The second frequency $f_1 = 13 \text{ 1/s}$ shows the superimposed activation period of the nucleation site, and the third one ($f_2 = 22 \text{ 1/s}$) is the real bubble frequency of the active nucleation site.

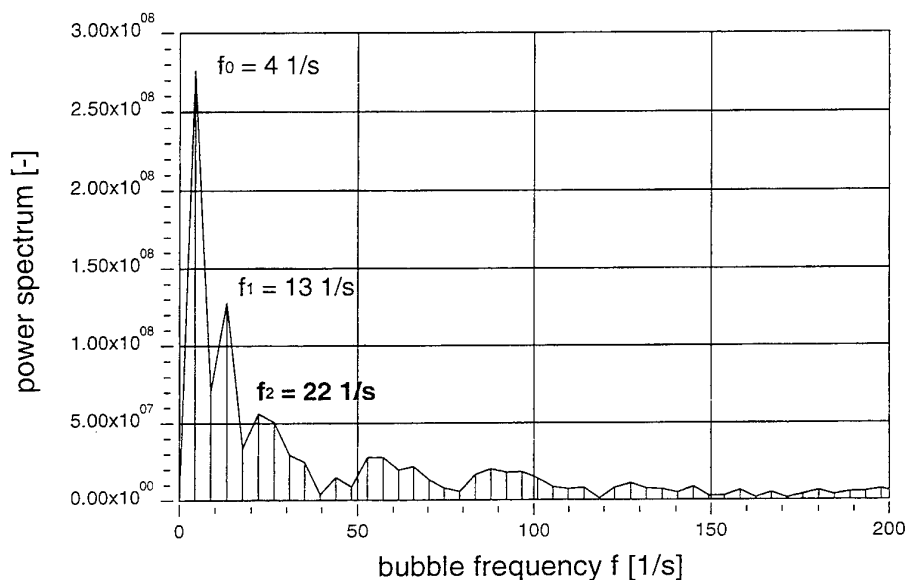


Fig. 12. Bubble frequency obtained with digital image processing software IKE_DBV, enhanced tube variant 4, $T_s = 283 \text{ K}$, $q = 2 \text{ kW/m}^2$

The distribution of the bubble departure diameter and the corresponding Gaussian-fit are depicted in Fig. 13. Most bubbles have a departure diameter in the range from 0.88 mm to 1.16 mm.

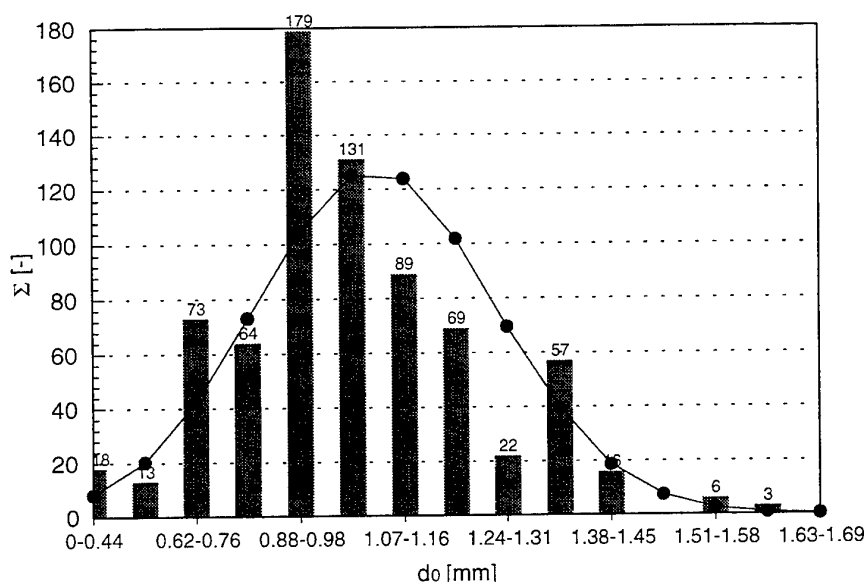


Fig. 13 Bubble departure diameter d_0

5. CORRELATION

The experimental results obtained with the enhanced carbon steel tubes are used to generate a correlation [13]. The well known basic form $\alpha = a q^b$ for predicting the heat transfer coefficient was modified to

$$\alpha = a_0 q^{(a_1 + a_2 \ln q)} \quad (1)$$

A regression analysis was carried out to determine the exponents of the individual terms. Some of the terms are adopted from Stephan and Abdelsalam [9], the ratio of the bubble departure diameter and the pore diameter of the re-entrant cavities are described by Haider [14]. There is still one empirical constant C used. For the carbon steel tubes, $C = 1.0504$ was found.

The variables of equation (1) are described as

$$a_0 = C \left(\frac{d_p^2 (\rho_f - \rho_v) g}{\sigma} \right)^{0.58} \left(\frac{d_0}{d_p} \right)^{3.8649} \left(\frac{p}{p^*} \right)^{1.7942} \left(\frac{\rho_v}{\rho_f} \right)^{-2.666} \left(\frac{a_f^2 \rho_f}{\sigma d_0} \right)^{-0.00797},$$

$$a_1 = 6.844 \cdot 10^{-4} \left(\frac{p}{p^*} \right)^{0.00851} \left(\frac{\rho_v}{\rho_f} \right)^{-0.6758} \left(\frac{c_p T_s d_0^2}{a_f^2} \right)^{0.05997} \left(\frac{\Delta h d_0^2}{a_f^2} \right)^{0.09331}, \quad (2)$$

$$a_2 = -0.1954 \left(\frac{\rho_f - \rho_v}{\rho_f} \right)^{30.3564} \left(\frac{a_f^2 \rho_f}{\sigma d_0} \right)^{0.01441}.$$

A comparison of the experimental results with predicted data is given in Fig. 14. For low and medium heat fluxes, a good comparison is found, but not for higher heat fluxes $q > 50 \text{ kW/m}^2$, where the slope of the heat transfer coefficients start to decrease. Because all data points (from minimum to maximum heat flux) are taken into account for the regression analysis, the accuracy for low heat fluxes is not so good as it could be. However, the accuracy of the correlation can be improved, 1. by using more data points, and 2. if these data points are taken in the range of low heat fluxes, where the correlation fits rather good.

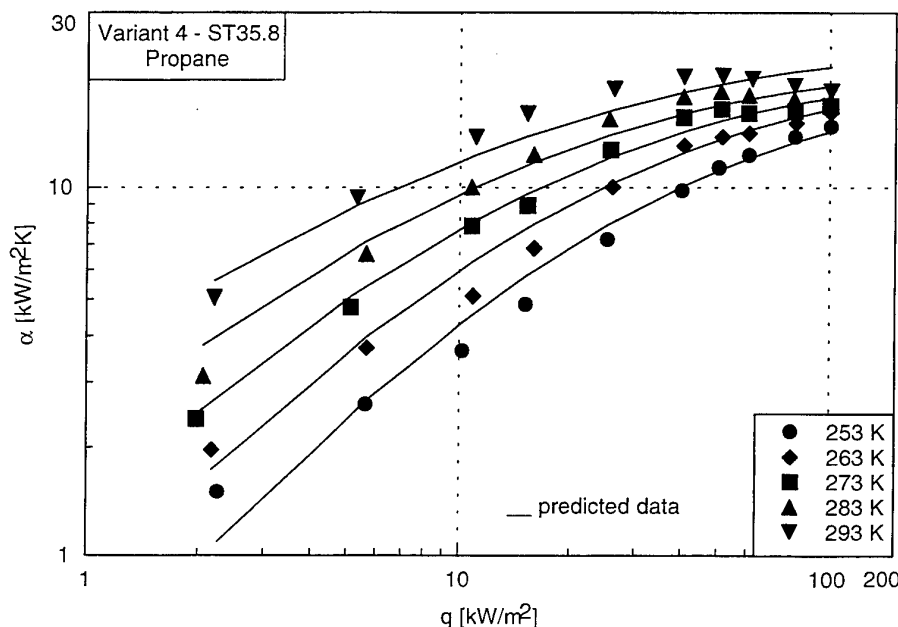


Fig. 14. Comparison of experimental and predicted data, enhanced tube variant 4

6. CONCLUSIONS

The investigation of new enhanced evaporation tubes in the pool boiling mode were carried out with one smooth reference tube and four enhanced tubes with modified low-finned surfaces creating re-entrant cavities. The hydrocarbon propane was used as working fluid at saturation temperatures in the range from 253 K to 293 K and employed heat fluxes between 2 kW/m^2 and 100 kW/m^2 .

The boiling phenomena and the two-phase flow from the heat transfer surfaces are visualised by a high speed video system. The video data are evaluated using the software IKE_DBV for digital image processing to determine boiling parameters like bubble departure diameter and bubble frequency.

The experimental results of all enhanced surfaces show higher heat transfer coefficients than those of the smooth reference tube. Best results are obtained for the enhanced surface variant 4 with improvement factors F_i up to 3. It was shown that the improvement factors of the enhanced surfaces depend on the heat flux and that for higher heat fluxes ($q > 50 \text{ kW/m}^2$) the slope of the heat transfer coefficients decrease, caused by the deactivation of parts of the sub-surface geometries by trapped vapor. But for the heat flux range of industrial interest, up to 20 kW/m^2 , the enhanced surfaces show a very good improvement of the heat transfer.

A correlation was generated to predict the heat transfer coefficients. The theoretical and experimental results show good agreement for low heat fluxes up to 50 kW/m^2 , but the decrease of the slope of the heat transfer coefficients cannot be predicted. Further efforts are necessary to improve the correlation, e.g. by using more experimental data in the heat flux range of interest.

ACKNOWLEDGEMENTS

This research project has been partly funded by the European Union within the frame of the JOULE programme (project no. JOE3-CT97-0061). The support provided by Wieland-Werke AG, Ulm, is gratefully acknowledged.

NOMENCLATURE

a	thermal diffusivity	m ² /s	T	temperature	K
a ₀ , a ₁ , a ₂	variables in eqs. (1), (2)	-	Greek Symbols		
c _p	specific heat capacity	kJ/kg K	α	heat transfer coefficient	kW/m ² K
C	constant in eq. (2)	-	ρ	density	kg/m ³
d ₀	bubble departure diameter	m	σ	surface tension	N/m
d _p	pore diameter	m	Indices		
g	gravitational acceleration	m/s ²	f	fluid	
Δh	latent heat	kJ/kg	s	saturation	
q	heat flux	kW/m ²	v	vapour	
p	pressure	bar			
p _{cr}	critical pressure	bar			
p* = p/p _{cr}	reduced pressure	-			

REFERENCES

1. R.K. Shah and A.C. Mueller, Heat Exchange. *Ullmann's Encyclopedia of Industrial Chemistry*, Vol. B3, Weinheim, Germany, 1988
2. D.A. Reay, Applications of compact heat exchangers. *Advances in Industrial Heat Exchangers*, Birmingham, United Kingdom, 1996
3. B. Thonon, Compact heat exchangers applied to industrial and environmental processes. *Eurotherm Seminar 62*, Grenoble, 1998
4. J.R. Thome, Heat transfer augmentation of shell-and-tube heat exchangers for the chemical processing industry. *2nd European Thermal-Sciences and 14th UIT National Heat Transfer Conference*, Rom, 1996
5. L. Trom, Heat Exchangers: Is it time for a Change? *Chemical Engineering*, pp 70 - 73, Feb.1996
6. R. Mertz and M. Groll, Evaporation heat transfer from enhanced industrial heat exchanger tubes. *Eurotherm Seminar 62*, Grenoble, 1998
7. W. Nakayama, T. Daikoku, H. Kuwahara and T. Nakajima, Dynamic model of enhanced boiling heat transfer on porous surfaces. Part 1: Experimental Investigations, Part 2: Analytical Modeling. *Trans. ASME, J. Heat Transfer*, Vol. 102, No. 3, pp 445-456, 1980
8. L.-H. Chien and R.L. Webb, A nucleate boiling model for structured enhanced surfaces. *Int. J. Heat Mass Transfer*, Vol. 41, No. 14, pp 2183 - 2195, 1998
9. K. Stephan and M. Abdelsalam, Heat transfer correlations for natural convection boiling. *Int. J. Heat Mass Transfer*, Vol 23, pp 73-87, 1980
10. M.G. Cooper, Correlations for nucleate boiling - Formulation using reduced properties. *Physicochem. Hydrodyn.* 3 (2), pp 89-111, 1982
11. M.G. Cooper, Heat flow rates in saturated nucleate pool boiling - A wide-range examination using reduced properties. *Advances in Heat Transfer*, Vol. 16, pp 157-239, 1984
12. D. Gorenflo, *VDI-Wärmeatlas*, 6th Edition, VDI-Verlag Düsseldorf, 1997
13. P. Chatterjee, Nucleate pool boiling from enhanced commercial evaporative tubes. *Master Thesis*, Indian Institute of Technology Kanpur and Institut für Kernenergetik und Energiesysteme, Universität Stuttgart, 1999
14. M. Groll and R. Mertz, Improved evaporation heat transfer surfaces for cost-effective heat exchangers for the process industries, Contract No. JOU2-CT94-0362, *Progress Reports* 1-3, 1994-1995
15. S.I. Haider, A theoretical and experimental study of nucleate pool boiling enhancement of structured surfaces. *Ph.D. Thesis*, Dept. Mechanical Engineering, Penn State University, University Park, PA, 1994

EXPERIMENTAL INVESTIGATION OF EVAPORATIVE HEAT TRANSFER CHARACTERISTICS IN A SMALL-DIAMETER TUBE USING R-134a

Yun-Wook Hwang

Graduate School

Seoul National University

Email: barque@snu.ac.kr, Tel: +82-2-880-1648, Fax: +82-2-883-0179

Min Soo Kim

School of Mechanical and Aerospace Engineering

Seoul National University

Email: minskim@plaza.snu.ac.kr, Tel: +82-2-880-8362, Fax: +82-2-883-0179

Sung Tack Ro

School of Mechanical and Aerospace Engineering

Seoul National University

Email: stro@gong.snu.ac.kr, Tel: +82-2-880-7111, Fax: +82-2-883-0179

Keywords: evaporation, heat transfer coefficient, small-diameter tube, compact heat exchanger, R-134a

ABSTRACT. Evaporative heat transfer characteristics of R-134a in a small diameter tube have been investigated. Stainless steel tube with an inner diameter of 2.2 mm was used as a test section. Test section was uniformly heated by electric current which was applied to the tube wall. The saturation temperature of refrigerant is calculated from the measured saturation pressure by using an equation of state for refrigerant. Inner wall temperature was calculated from measured outer wall temperature, accounting for heat generation in the tube and heat conduction through the tube wall. Mass quality of refrigerant was calculated by considering the heat input to the pre-heater and the test section. Heat fluxes were set at 19, 36, 46, and 64 kW/m², and mass fluxes were set at 380, 470, and 570 kg/m²s for each heat flux condition. From this study, flow patterns in a small-diameter tube were predicted by using flow pattern map, where the flow was presumed to have slug flow pattern for low quality region and to have annular flow pattern for high quality region. Heat transfer coefficients in a small diameter tube have been provided with respect to quality for several mass flux and heat flux conditions. Heat transfer in a small diameter tube is affected by heat flux as well as mass flux for a wide range of mass quality. Finally, the results in this study are compared with Gungor and Winterton correlation, which gives the absolute average deviation of 27%.

NOMENCLATURE

G	mass velocity (kg/m ² s)	r_o	outer radius of tube (mm)
h	heat transfer coefficient (kW/m ² K)	T	temperature (K)
k	thermal conductivity (W/mK)	U_{GS}	superficial velocity of gas phase (m/s)
q''	heat flux (kW/m ²)	U_{LS}	superficial velocity of liquid phase (m/s)
q	heat generation per unit volume (kW/m ³)	x	mass quality
r_i	inner radius of tube (mm)		

Subscripts

l	saturated liquid state	v	saturated vapor state
sat	saturation state	w_i	inner surface of testsection
wo	outer surface of testsection		

1. INTRODUCTION

Due to the rapid industrialization during past decades, serious environmental problems were generated. As the fact is made known that refrigerants such as CFCs and HCFCs deplete stratospheric ozone layer, use of those refrigerants are now being regulated. Therefore, development of new alternative refrigerants and a prompt shift to new refrigerants are required. However, thermodynamic and transport properties of these alternative refrigerants are dissimilar to those of former refrigerants, and thus, system optimization and redesign are mostly

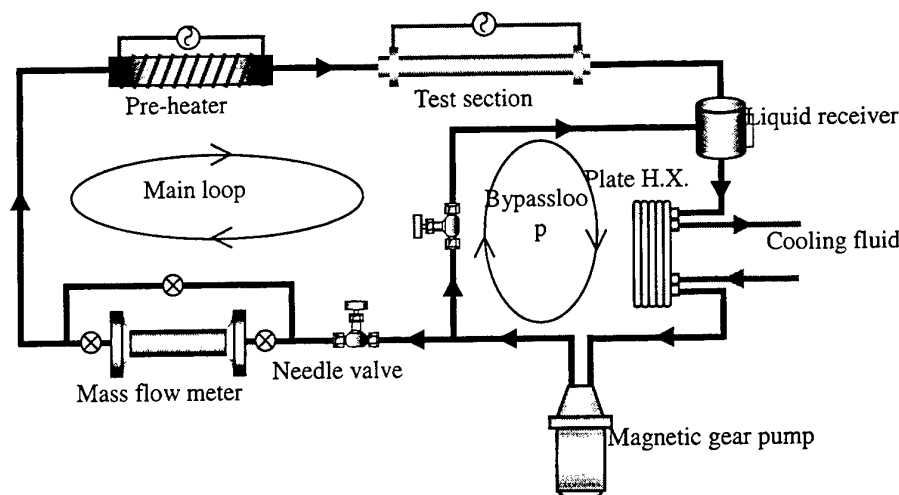


Fig. 1 Schematic diagram of experimental apparatus for evaporative heat transfer test in a small diameter tube.

required in order to get the same or enhanced efficiency and performance. Especially, studies on evaporation and condensation heat transfer characteristics of alternative refrigerants as well as the performance of a refrigeration system should be carried out. Recently, studies on compact heat exchangers as well as heat transfer characteristics of alternative refrigerants have been actively done, which is necessary in a down-sizing of refrigerator and air-conditioner [1,2]. Flow boiling and gas cooling heat transfer in a compact heat exchanger became important, since new high pressure system using CO_2 is developed, where heat exchanger size can be drastically reduced [3]. Wambsganss et al. [4] conducted an experimental study on boiling heat transfer in a tube with inner diameter of 2.92 mm using R-113, and showed the results that heat transfer was much affected by heat flux more than mass flux. Kew and Cornwell [5] conducted the experimental study using R-141b as a boiling fluid, and showed the result that existing flow boiling heat transfer correlations do not predict well with a small diameter tube. In designing a compact heat exchanger, heat transfer characteristics and flow mechanism in a micro or small channel of heat exchanger should be known. Flow pattern, void fraction, pressure loss, and heat transfer characteristics are important parameters in sizing and rating heat exchangers. By knowing heat transfer characteristics which is known as the most important information, heat transfer area and size of heat exchanger can be accurately calculated. There are many studies on a tube whose diameter is about 1 cm, but those on heat transfer in a micro or small diameter tubes are not widely available. In this study, a circular tube with an inner diameter of 2.2 mm will be chosen as a test tube for evaporation heat transfer test.

This paper will present local heat transfer characteristics for R-134a in a small diameter tube according to heat flux, and mass flux conditions. Experimental results of this study will be compared with the correlation (Gungor and Winterton, 1987) [6] which predicts the evaporative heat transfer coefficients in a wide range of mass quality.

2. EXPERIMENTS

Experimental Apparatus

The schematic diagram of experimental apparatus is shown in Fig. 1. The evaporative heat transfer test rig is composed of a magnetic gear pump for refrigerant circulation, a mass flow meter, a pre-heater, a test section, a liquid receiver, and a plate heat exchanger for subcooling the refrigerant. The magnetic gear pump circulates liquid which was subcooled in the plate heat exchanger. The mass flow meter is installed before the pre-heater to measure the flow rate of the refrigerant. The pre-heater is installed to adjust the inlet quality of the refrigerant to the desired value. It is expected that the preheating will change the average temperature of the test section because the test loop is a closed system. Therefore, it is necessary to use the pre-heater and chiller to adjust both the inlet quality and the test section average temperature. The liquid receiver collects the liquid phase refrigerant

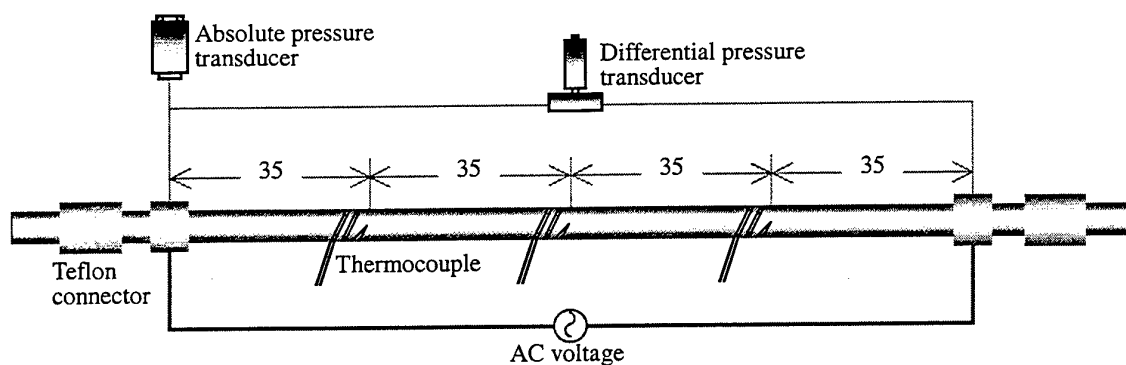


Fig. 2 Representation of the measuring points in the test section.

and adjusts the liquid level which varies due to the volume change in the vapor phase at different test section inlet qualities. Refrigerant, which is from liquid receiver, is subcooled in a plate heat exchanger. Two needle valves are installed at the downstream of magnetic pump to regulate the mass flow rate flowing into the main loop.

The schematic diagram of the test section is represented in Fig. 2. A seamless stainless steel tube is used for test section in order to maintain electrical and thermal uniformity in the test section. The inner and outer diameters of the tube are 2.2 and 3.2 mm, respectively. The heated length of the test section is 140 mm. Heat is transferred to the refrigerant at the test section by applying electric current to the tube, and the transferred heat is measured by a powermeter. Pressure taps are installed at two ends of the heat transfer test section to measure the pressure difference. The pre-heater at the upstream of the test section and liquid receiver after the test section are connected to the test section with teflon connectors to insulate electrically from the test section. T type (copper-constantan) thermocouples to measure the temperatures of the outer wall of the tube are attached at three locations along the tube as shown in Fig. 2.

Test Conditions

Mass flux and heat flux are the major factors which affect evaporative heat transfer. The mass flux was varied from 380 to 570 kg/m²s by using a magnetic pump. The heat flux was set at 19, 36, 46 and 64 kW/m² for each mass flux condition. The test condition in this study represents the heat transfer rate and mass flow rate of commercial air conditioning or heat pump units for small-size domestic use.

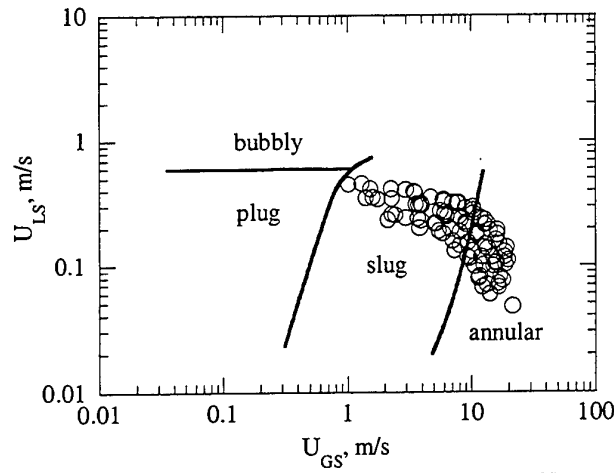
Data Reduction

While the chiller was operated, the desired value of the heat flux was applied gradually to the test section until the steady state was reached. The measured values were transmitted to a personal computer through a multi-channel recorder, using GPIB interface. The transmitted values were shown on a computer monitor with their average values and standard deviation of 30 data sets. The data were saved into a file when the deviations of temperature, mass flux, and pressure were less than 0.1°C, 3 kg/m²s, and 2 kPa, respectively. The saturation temperature of refrigerant was calculated from the measured pressure using REFPROP [7]. The heat transfer coefficient is defined as in equation (1).

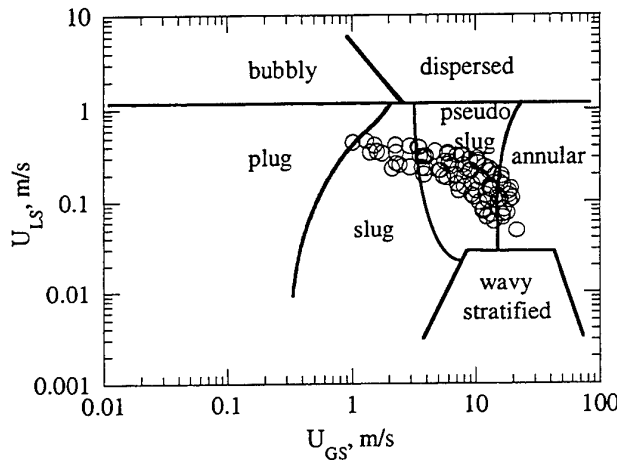
$$h = \frac{q''}{T_{wi} - T_{sat}}, \quad (1)$$

where q'' is the heat flux and T_{wi} is the inner wall temperature calculated from the measured outer wall temperature T_{wo} . The relation between T_{wi} and T_{wo} is obtained by using 1-dimensional conduction equation with heat generation in the tube, which is shown in equation (2).

$$T_{wi} = T(r = r_i) = \frac{\dot{q}r_o^2}{4k} \left(1 - \frac{r_i^2}{r_o^2} \right) + \frac{\dot{q}r_o^2}{2k} \ln \left(\frac{r_i}{r_o} \right) + T_{wo} \quad (2)$$



(a) Flow pattern map by Damianides (1987)



(b) Flow pattern map by Wambsganss et al. (1987)

Fig. 3 The experimental data in flow pattern maps

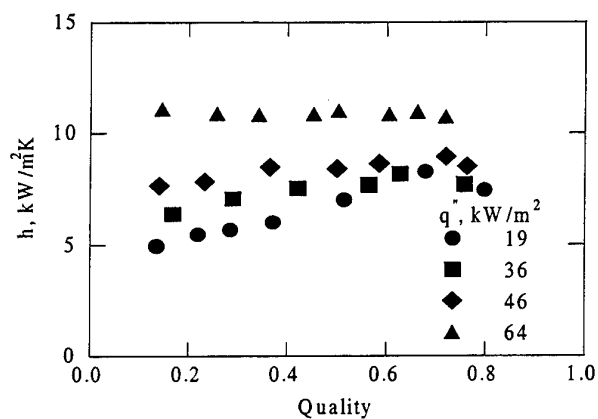
3. RESULTS & DISCUSSION

Figure 3 shows the experimental data in this study with flow pattern maps developed by Damianides [1] and Wambsganss et al. [8]. Those flow pattern maps can be applicable to a mixture of water/air, but here they are used to get the basic information to judge the flow pattern when a mixture of liquid/vapor flows in a small diameter tube. U_{LS} and U_{GS} represent superficial velocities of liquid and gas phase respectively, and they are equal to the values of volumetric flux divided by cross-sectional area of tube as shown in equation (3).

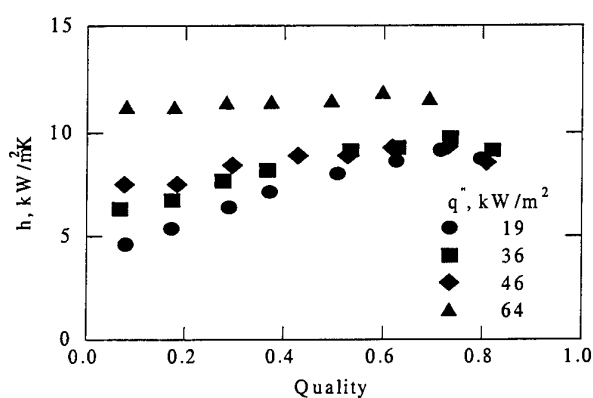
$$U_{LS} = \frac{Q_l}{A} = \frac{G \times (1-x)}{\rho_l}, \quad U_{GS} = \frac{Q_v}{A} = \frac{G \times x}{\rho_v} \quad (3)$$

When evaporation proceeds and mass quality increases, U_{LS} decreases and U_{GS} increases. Therefore, evaporation process is represented from the point with lower U_{GS} and higher U_{LS} to the point with higher U_{GS} and lower U_{LS} for higher mass qualities. Figure 3 shows that flow patterns of experimental data in this study are

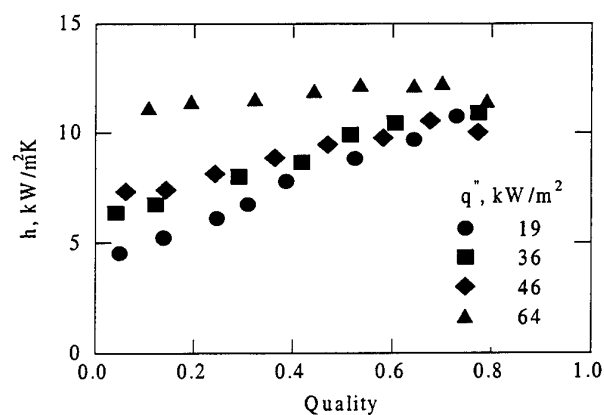
mostly slug and annular flow, or in the transitional area of slug and annular flows. However, it is generally known that when evaporation goes on in a large diameter tube, most of flow patterns are annular flow. This means that evaporation phenomenon in a small diameter tube is different from that in a large diameter tube of a tube nominal diameter of about 1cm.



(a) $G = 380$ kg/m²s



(b) $G = 470$ kg/m²s



(c) $G = 570$ kg/m²s

Fig. 4 Variation of heat transfer coefficients with respect to heat flux

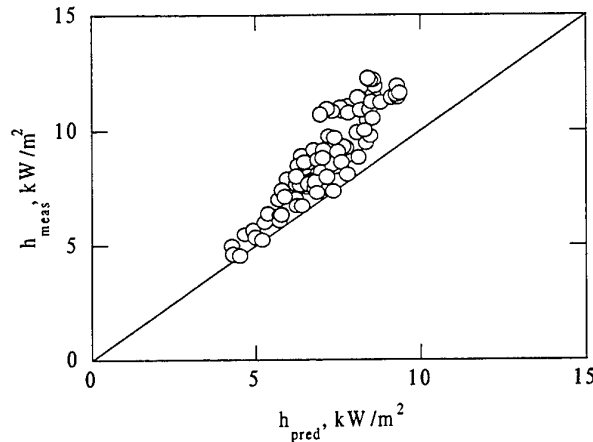


Fig. 5 Comparison of measured heat transfer coefficients with predicted ones by Gungor and Winterton correlation (1987)

Figure 4 shows the variation of heat transfer coefficients with respect to heat flux. In each mass flux condition, the variation of heat transfer coefficient versus quality shows similar trend for the same heat flux. There is a general tendency that the heat transfer coefficient is greater for higher mass flux conditions with increased refrigerant velocity in the tube, which results in vigorous heat removal from the wall. One thing to note is that the magnitude of heat transfer coefficient is affected by the heat flux of the wide range of mass quality. Another characteristic to note is that transition quality does not exist. Generally, in the region of low mass quality, heat transfer coefficient increases as heat flux increases, which means that heat transfer in this region is dominated by heat flux [9]. As refrigerant evaporates, effect of heat flux decreases, and that of mass flux increases, so transition quality exists near the position where mass quality is about 0.2. For convective boiling region in a large diameter tube, heat transfer coefficients hardly change in the region of high mass quality with respect to variation of heat flux. However, heat transfer in a small diameter tube is affected by the heat flux in the region of both low and high mass quality. Figure 3 shows that flow patterns in a small diameter tube are mostly slug or annular, which means that heat transfer in a small diameter tube is affected by heat flux when compared with a large diameter tube.

Boiling number is a dimensionless parameter which shows a ratio of nucleate boiling to convective boiling, and high boiling number means that effect of heat flux is relatively greater than that of mass flux. In case that boiling number is high at each mass flux, heat transfer coefficient changes slightly with respect to variation of mass quality. This is likely to be a direct consequence of dimension of the small diameter tube that allows the crest of a wave on a liquid film to reach the opposite wall, producing a slug of liquid in a situation that would produce stratified or annular flow in a large diameter tube.

Experimental results in this study are compared with the values predicted by Gungor and Winterton correlation, which is applicable in a wide range of mass quality. h_{pred} at x-axis in Fig. 5 is the value predicted by Gungor and Winterton correlation, and h_{meas} at y-axis is the experimental result in this study. Fig. 5 shows that h_{meas} is greater than h_{pred} , and the absolute deviation between the two is 27%. This means that bubbles generated during evaporation are confined to a small diameter tube and make thinner liquid film near the tube wall. These phenomena were also visualized by Fukano and Kariyasaki [10]. And a deviation between h_{meas} and h_{pred} is greater for higher heat flux condition. This implies that it is difficult to predict heat transfer coefficients accurately in a small diameter tube using heat transfer correlation which was formulated with large diameter tubes.

4. CONCLUDING REMARKS

Evaporative heat transfer characteristics in a small diameter tube of HFC refrigerant R-134a have been investigated. Experimental results was compared with a heat transfer correlation of Gungor and Winterton (1987). The conclusions of this study are summarized as follows.

- (1) When experimental results are applied to two phase flow pattern maps by Damianides (1987) and Wambsganss et al. (1991), many experimental data points are located in slug, annular flow, and transitional region of these flow patterns.
- (2) With respect to variation of mass flux, heat transfer coefficient changes slightly in the region of low mass quality. However, it increases in the region of high mass quality. In case that heat flux is high, heat transfer coefficient nearly doesn't change in a wide range of mass quality. Heat transfer in a small diameter tube is affected by heat flux as well as mass flux for a wide range of mass quality.
- (3) Experimental results in this study are compared with the heat transfer coefficient correlation proposed by Gungor and Winterton (1987), and experimental heat transfer coefficients are higher about 27% than those from the correlation.
- (4) From this study, when the compact heat exchanger with small channel or tube is designed, it should be considered that many of flow pattern is slug flow, and heat transfer is affected by heat flux.

ACKNOWLEDGMENTS

This work has been supported by Korea Science and Engineering Foundation (Grant No.: 96-0200-12-1) and by the Institute of Advanced Machinery and Design of Seoul National University.

REFERENCES

1. C. A. Damianides and J. W. Westwater, "Two-Phase Flow Patterns in a Compact Heat Exchanger and in Small Tubes", *In Proc. 2nd UK Nat'l Conf. on Heat Transfer*, v.II, pp.1257-1268 (1988).
2. Y. W. Hwang, S. H. Yoon and M. S. Kim, "A Study of the Characteristics of Evaporative Heat Transfer for R-134a in a Small Diameter Tube", *Proc. of the KSME 1999 Spring Annual Meeting B, Poster Session 260*, April 22-24, pp.572-575, Chon-An, Korea (1999).
3. J. Pettersen, A. Hafner, G. Skaugen and H. Rekstad, *Int. J. Refrig.* v.21, no.3, pp.180-193 (1998).
4. M. W. Wambsganss, D. M. France, J. A. Jendrzejczyk and T. N. Tran, *J. of Heat Transfer* v.115, pp.963-972 (1993).
5. P. A. Kew and K. Cornwell, *Applied Thermal Engineering* v.17, pp.705-715 (1997).
6. K. E. Gungor and R. H. S. Winterton, *Chem. Eng. Res. Des.* v.65, pp.148-156 (1987).
7. M. O. McLinden, S. A. Klein, E. W. Lemmon and A. P. Peskin, Thermodynamic and Transport Properties of Refrigerants and Refrigerant Mixtures (REFPROP), Version 6.0, National Institute of Standards and Technology, Boulder, Colorado, U.S.A. (1998).
8. M. W. Wambsganss, J. A. Jendrzejczyk and D. M. France, *Int. J. Multiphase Flow* v.17, no.3, pp.327-342 (1991).
9. D. S. Jung, M. McLinden, R. Radermacher and D. Didion, *Int. J. Heat Mass Transfer* v.32, no.1, pp.131-145 (1989).
10. T. Fukano and A. Kariyasaki, *Nuclear Engineering and Design* v.141, pp.59-68 (1993).

OPTIMAL DESIGN OF MICRO BARE-TUBE HEAT EXCHANGER

Sawat Paitoonsurikarn, Nobuhide Kasagi, and Yuji Suzuki
Department of Mechanical Engineering, The University of Tokyo
Hongo 7-3-1, Bunkyo-ku, Tokyo, 113-8656, Japan
Email: sawat@thtlab.t.u-tokyo.ac.jp; Fax: +81-(3)-5800-6999

Keywords: compact heat exchanger, tube bank, bare tube, optimum design, simulated annealing technique

ABSTRACT. An optimum design tool based on the simulated annealing technique has been developed for a compact heat exchanger that employs only small diameter tubes without conventional fins, and the performance achieved by the present design is compared to commercially available compact heat exchangers. For all design problems tested, the present heat exchanger design offers a significant degree of improvement in terms of the pumping power, the heat transmission efficiency, and/or the core volume size. The range of tube diameter in the optimum design is found to be 0.3-0.5 mm. Laboratory experiments with a prototype heat exchanger with 0.5 mm OD bare tubes confirm the numerical results.

1. INTRODUCTION

With the growing importance of global environmental problems, efficient energy utilization becomes an ever more urgent target in science and technology. Among diverse elementary techniques to be improved, heat exchanger is one of the major components common in a wide variety of thermal energy handling processes, such as conversion, transport, consumption and storage. Improvement of heat exchanger performance affects both directly and indirectly the performance of various devices and systems, and it would lead to better utility and industrial energy plants, air-conditioning systems, manufacturing processes, transportation systems, and even information devices, all of which should contribute to reduction of emission of greenhouse effect gases. Hence, the present work is aimed at developing an optimum design tool of high-performance heat exchangers. Emphasis is laid upon compact heat exchangers for automobile air-conditioning system.

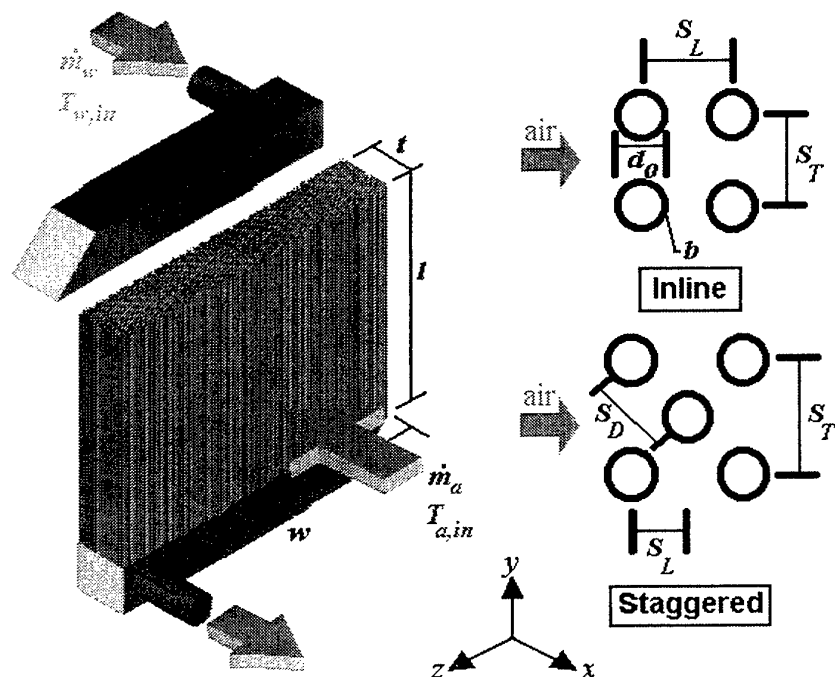


Figure 1. Micro bare-tube heat exchanger.

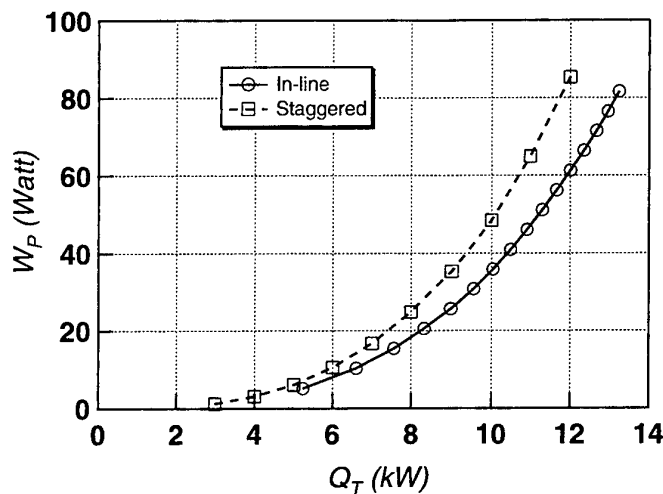


Figure 2. Comparison between in-line and staggered tube arrangements.

Generally, heat transfer enhancement is achieved by employing extended heat transfer surfaces, such as louvered fins and offset-fins. Although the modern heat exchanger performance has been admirably increased with these elaborate heat transfer surfaces, it has also resulted in the increased manufacturing cost due to ad-hoc fabricating processes. Moreover, further improvement in the heat exchanger performance seems to be saturated after a great deal of industrial effort with this sort of sophisticated extended heat transfer surfaces of complex geometry. Alternatively, one would be aware of the fact that, given a Nusselt number ($Nu = hL/k$) for the heat transfer system under study, the heat transfer coefficient h itself would simply increase as the characteristic length scale L is reduced. That is, we might conceive a high performance heat exchanger by reducing the hydraulic diameter of its flow passage.

In the present work, we introduce a new design of compact heat exchanger that consists of many small diameter tubes without any extended surfaces, i.e., *micro bare-tube heat exchanger*. As a result, we meet a large pressure drop across the heat exchanger core. Hence, we should compromise the heat transfer augmentation and pressure penalty. To do this, we have developed an optimum design tool for micro bare-tube heat exchanger, and evaluate its performance in several design cases.

2. DESIGN PROCEDURE

The type of heat exchanger we consider in the present work is a single-pass single-phase air-water crossflow heat exchanger utilized for automobile applications. The heat exchanger core is depicted schematically in Fig. 1 with its design parameters. We considered two kinds of tube arrangements, namely, in-line and staggered arrangements as shown together in Fig. 1. Preliminary calculations, however, showed that the in-line arrangement would be superior to the staggered one for small diameter tubes considered here ($100 < Re_{max} < 1000$). Figure 2 shows the pumping powers W_p required to achieve a specified amount of heat exchange Q_T . It is obvious that the pumping power for the staggered tube bank is larger than that for the in-line one. Therefore, the in-line tube arrangement is employed in all calculations in the present paper.

The basic equations for calculations of heat exchange and pressure drop, and the simulated annealing method are given in the following sections.

Heat Exchange Calculation

In order to calculate the total heat exchange Q_T of heat exchanger, the heat transfer coefficients of water flow inside the tube and air flow across tube bank are estimated by using empirical formulae.

Flow inside tube. Due to very small diameters considered, the tube length to diameter ratio l/d_o is generally

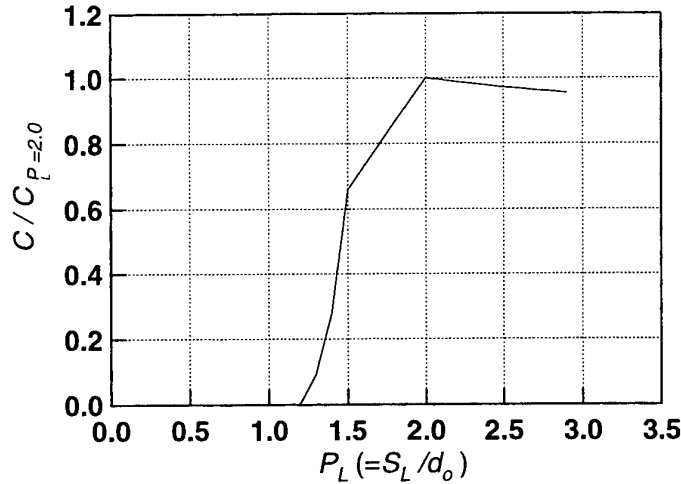


Figure 3. The correction factor for Eq. (2) when $Re_{max} < 1000$.

very large, so that it is reasonable to assume that the flow inside tube is both hydrodynamically and thermally fully-developed. Since the Reynolds number of this flow can be assumed to be less than 2000, the analytical solution of Nusselt number with isothermal wall boundary condition [6] is employed:

$$Nu_i = \frac{h_i d_i}{k_i} = 3.66, \quad (1)$$

where h_i , d_i and k_i are the heat transfer coefficient, tube inner diameter, and fluid thermal conductivity, respectively. Note that, we have assumed the constant tube wall temperature and used Eq. (1), which is not strictly satisfied. However, it is still acceptable because the heat transfer resistance in the water side is much smaller than the air side as shown later.

Flow across tube bank. The Nusselt number for flow across the tube bank is estimated with the following correlation equation given by Zhukauskas [2]:

$$Nu_o = \frac{h_o d_o}{k_o} = C \cdot Re_{max}^m \cdot Pr_f^{0.36} \cdot \left(\frac{Pr_f}{Pr_{wall}} \right)^{0.25}, \quad (2)$$

where h_o , d_o and k_o are the heat transfer coefficient, tube outer diameter, and fluid thermal conductivity, respectively, while Pr_f and Pr_{wall} are the Prandtl numbers evaluated at the bulk temperature and the wall temperature. The Reynolds number Re_{max} is based on the tube outer diameter and the mean velocity at the minimum cross section of the tube bank. Zhukauskas [2] suggested that the values of empirical constants C and m depend only on Re_{max} . However, the use of Eq. (2) at low Re_{max} (< 1000) should result in significant overestimation of Nu , if the effect of pitches of tube bank (S_T, S_L) is not taken into account as can be seen in his experimental data [2]. Therefore, we determine the value of C for various non-dimensional longitudinal pitches $P_L (=S_L/d_o)$ from a series of numerical simulations of flow across a tube bank at $P_T (=S_T/d_o) = 2.0$ with a commercial CFD software package FLUENT/UNS (Fluent Inc.). Figure 3 shows the correction factor for C obtained for the 10-row tube bank at $Re_{max} = 600$ [3].

With the heat transfer coefficients of the flow inside the tube and the flow across the tube bank obtained from Eqs. (1) and (2), we can calculate the overall heat transmission coefficient U by the following equation,

$$\frac{1}{U} = \frac{d_o}{d_i} \cdot \frac{1}{h_i} + \frac{1}{h_o} + \frac{d_o}{k} \cdot \ln \left(\frac{d_o}{d_i} \right), \quad (3)$$

where k is the tube thermal conductivity. In the present work, pure copper is assumed to be the tube material with $k = 401.0$ [W/(m·K)] in all calculations.

Finally, the total heat exchange Q_T can be calculated by using the effectiveness- Ntu method [6]. For crossflow

heat exchanger with both fluid streams unmixed, it yields

$$Q_T = \left(1 - e^{\left[\frac{1}{C_r} Ntu^{0.22} \left[e^{(-C_r \cdot Ntu^{0.78})} - 1 \right] \right]} \right) C_{\min} \Delta T_{\text{inlet}}, \quad (4)$$

where ΔT_{inlet} is the absolute difference in working fluid inlet temperatures. The quantity C_r is the heat capacity ratio defined as $C_r = C_{\min}/C_{\max}$, where C_{\min} and C_{\max} are the smaller and larger values of heat capacities of working fluids, respectively. The Ntu, or number of transfer unit, is defined as $Ntu = UA/C_{\min}$, where U is obtained from Eq. (3) whilst A is the heat exchange area of heat exchanger.

Pressure Drop Calculation

The formulae used for estimating the pressure drop of flow inside the tube and that across the tube bank are summarized below.

Flow inside tube. The core pressure drop of flow inside the tube is calculated by the following formula given by Kays and London [4].

$$\Delta P_{\text{core}} = \frac{\rho u_m^2}{2} \cdot \left(K_c + K_e + c_f \frac{1}{d_i} \right), \quad (5)$$

where c_f is the Darcy friction factor ($= 64/Re$ for fully-developed laminar flow), while K_c and K_e are the core entrance and exit pressure-loss coefficients, respectively. Note that, the friction loss is dominant in the core pressure drop for all cases examined. The total pressure drop including the pressure drop at inlet and outlet manifolds is assumed to be three times the core pressure drop ($\Delta P_i = 3\Delta P_{\text{core}}$).

Flow across tube bank. For the external flow across the tube bank, the empirical equation proposed by Zhukaukas [2] is employed:

$$\Delta P_o = N_L \cdot \chi \cdot \left[\frac{\rho \cdot u_{\max}^2}{2} \right] \cdot f, \quad (6)$$

where the friction factor f and the geometrical correction factor of tube bank χ are given graphically in [2].

Pumping power. The total pumping power can be given as the sum of the pumping power driving the internal (water) and external (air) flows:

$$W_p = \frac{\dot{m}_a \Delta P_o}{\rho_a} + \frac{\dot{m}_w \Delta P_i}{\rho_w}, \quad (7)$$

where \dot{m}_a , \dot{m}_w , ρ_a , ρ_w are the air and water mass flow rates and their densities, respectively.

Simulated Annealing Method

With the above set of equations, design parameters are optimized by using the simulated annealing method [5] in such a way that they should minimize a cost function described below. Both the number of temperature steps and the number of random steps per temperature step are chosen as 10000. The temperature of the system is decreased according to a logarithmic annealing schedule with an arbitrary high starting temperature and the terminal temperature set at $3e-8$.

Table 1. Specification of commercial compact heat exchangers.

	Definition	Q_r (kW)	W_p (W)	w (cm)	l (cm)	t (cm)	V (cm ³)	$T_{w,in}$ (°C)	$T_{a,in}$ (°C)	\dot{m}_a (kg/s)	\dot{m}_w (kg/s)	ΔP_a (Pa)	ΔP_w (kPa)
H1	Air heater	7.0	35.0	20.0	15.0	3.50	1050	80	15	0.116	0.20	343	2.93
H2	Air heater	6.4	21.0	20.0	15.0	2.50	750	80	15	0.116	0.20	196	7.33

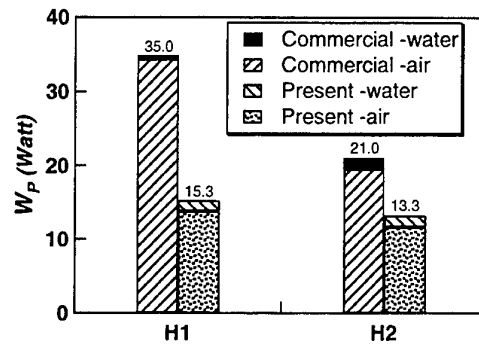


Figure 4. Performance comparison in Case 1.

3. RESULT AND DISCUSSIONS

In order to evaluate the performance of the present design, we refer to typical data from two commercially available louvered-finned tube compact heat exchangers for comparison as shown in Table 1 [7]. For each set of data, we pose three design problems with different cost functions defined as follows.

Optimization Case 1: Minimization of Pumping Power

In this case, the cost function is the total pumping power (W_p) defined by Eq. (7). The core dimension (l, w, t), inlet temperature of both working fluids ($T_{a,in}, T_{w,in}$), and the total heat exchange (Q_T) are set at the same values as the commercial heat exchanger data, while other five parameters, i.e., the tube outer diameter (d_o), the transverse and longitudinal pitches (S_T, S_L), and the required mass flow rates (\dot{m}_a, \dot{m}_w) are simultaneously optimized to obtain minimum W_p .

The comparison of the required pumping power between the optimal micro-bare tube and the commercial heat

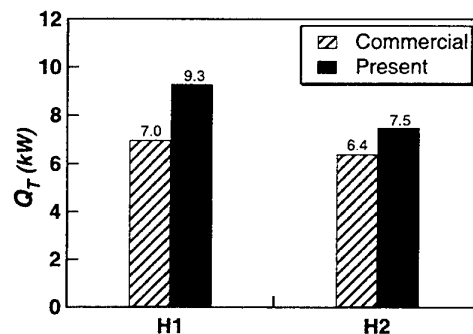


Figure 5. Performance comparison in Case 2.

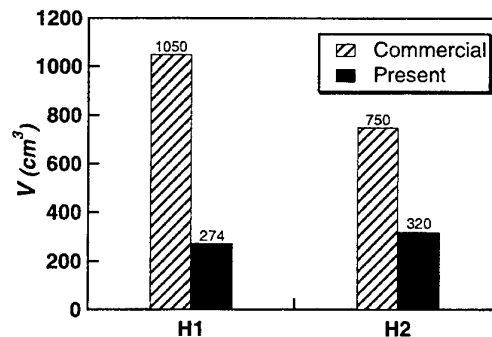


Figure 6. Performance comparison in Case 3.

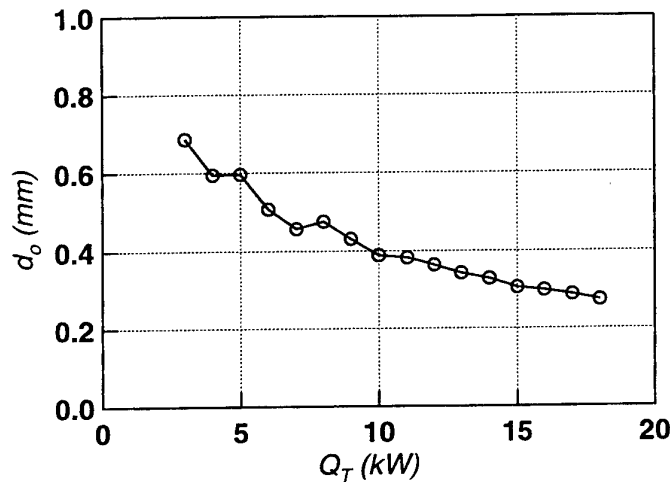


Figure 7. Optimum tube diameter vs total heat exchange for Case 1 (H1).

exchangers is shown in Fig. 4. It is evident that the present design require smaller pumping power than those of the commercial ones, i.e., 63% for H1 and 44% for H2. The optimum tube diameter is found to be around 0.5 [mm] with $P_T = 4.2$ and $P_L = 1.5$. Note that about 90% of W_p is the pumping power on the air side, which is mmajor improvement has been made if compared with the commercial one. On the other hand, the pumping power on the water side is somewhat increased in the present design than in the commercial one.

Optimization Case 2: Maximization of Heat Exchange Rate

In this case, $-Q_T$ is chosen as the cost function to maximize the heat exchange rate. The five parameters, i.e., d_o , S_T , S_L , \dot{m}_a , and \dot{m}_w are simultaneously optimized, while the other parameters including W_p are kept at the same values as the commercial heat exchanger data.

The comparison of total heat exchange rate at the same pumping power is illustrated in Fig. 5. It is obvious that the present design gives higher heat exchange rates, by 33% for H1 and 17% for H2, respectively. The optimum tube diameter is found to be around 0.4 [mm] with $P_T = 4.0$ and $P_L = 1.5$.

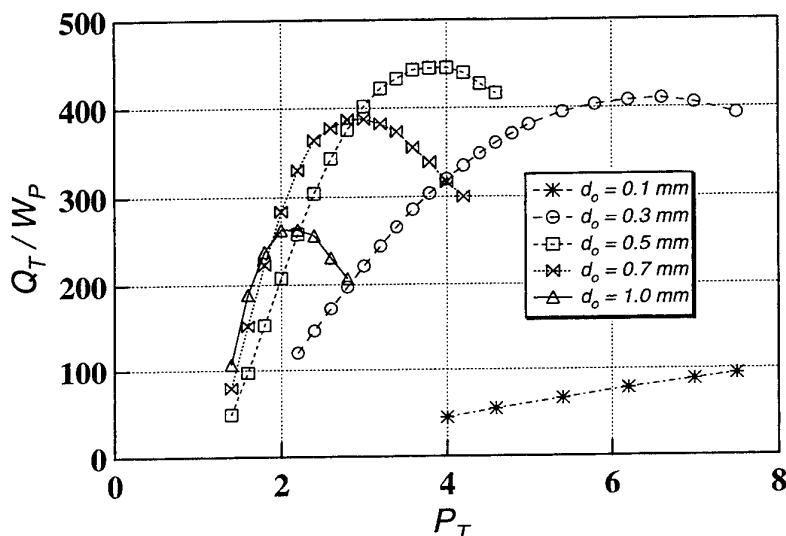


Figure 8. Effect of non-dimensional transverse pitch in Case 1 (H1).

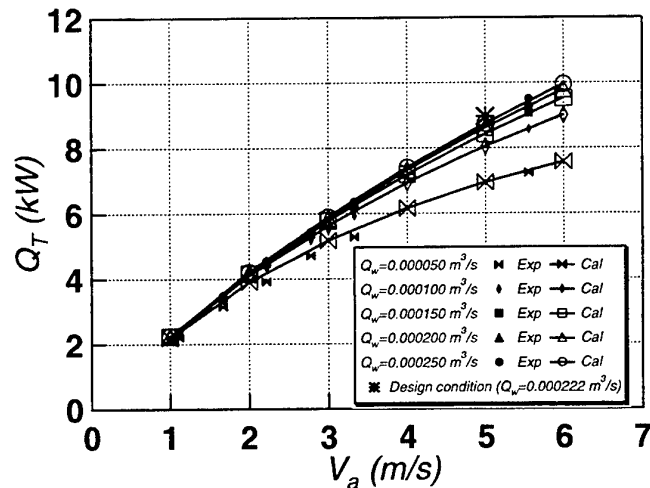


Figure 9. Comparison of total heat transfer between experiment and calculation.

Optimization Case 3: Minimization of Core Volume

In Case 3, we keep the total heat exchange Q_T , the pumping power W_p and also the core width w at the same values of the commercial heat exchanger data, while optimize seven parameters d_o , S_T , S_L , \dot{m}_a , \dot{m}_w , l , and t that would give the minimum core volume ($V = lwt$).

The core volume of the present design is significantly reduced as shown in Fig. 6. The volume optimized is as small as 26% and 43% of those of H1 and H2, respectively. In this case, $d_o \approx 0.3$ [mm], while $P_T \approx 3.0$ and $P_L \approx 2.0$ for the optimal arrangement.

Characteristics of Optimum Designs

Figure 7 shows the optimum tube diameter in Case 1 (H1) for various heat exchange rate Q_T from 3 to 18 kW. The optimum value is about 0.7 [mm] at $Q_T = 3$ [kW] and decreases monotonically with increasing Q_T .

Figure 8 shows Q_T/W_p in Case 1 (H1) as d_o and P_T are changed. For each diameter given, there exists a maximum value at some specific P_T . Although $d_o = 0.1$ [mm] does not show a peak, we estimate it will have one at $P_T > 10$. Note that, at the low value of non-dimensional transverse pitch, the bigger tube is more advantageous than the smaller one. However, the overall maximum value occurs at $P_T \approx 4.0$ when $d_o = 0.5$ [mm] as previously mentioned in the optimization case 1 above.

Validation of the Numerical Results

In order to verify the optimum design in the present work, we constructed a prototype heat exchanger by using the optimum design parameters in Case 2 (H1). A capillary copper tube with outer diameter of 0.5 [mm] and the wall thickness of 0.05 [mm] is employed instead of the actual optimum value ($d_o = 0.4$ [mm]). The non-dimensional transverse and longitudinal pitches in this prototype are 3.7 and 2.0, respectively. The total number of copper tubes used is about 3000.

The total heat transfer of this prototype heat exchanger for various frontal air velocities is shown in Fig. 9. The agreement between experiments and calculations is strikingly good. At the design condition, the actual heat transfer is only 3% less than the predicted value. Note that, the heat transfer coefficient on the water side is around 5000 [W/(m²K)], which is much larger than that for the air side (around 300 [W/(m²K)]).

4. CONCLUSIONS

An optimum design tool for micro bare-tube heat exchanger has been developed by employing empirical formulae and simulated annealing optimization technique. For three optimization cases examined, the present design has significant advantages over typical commercial heat exchanger as summarized below.

Case 1: With the same heat exchange rate and core volume, the pumping power is decreased by 37-56%.

Case 2: With the same pumping power and core volume, the heat exchange rate is increased by 17-33%.

Case 3: With the same heat exchange rate and pumping power, the core volume is decreased by 57-74%.

Note that, in all cases, the present designs require smaller fan power but larger water pumping power than those of the commercial ones in order to achieve the same desired operation condition. The optimum tube outer diameter ranges from 0.3 mm to 0.5 mm in three optimization cases and is found to be decreased gradually with the increase of heat loaded. The performance of the present design is confirmed through physical experiments of a prototype.

ACKNOWLEDGEMENTS

This work is supported by the Proposal-Based New Industry Creative Type Technology Research and Development Promotion Program by NEDO. The authors are grateful to Dr. Ikuta at Calsonic Corp. for the experiment of prototype heat exchanger and valuable discussion during the course of the work.

REFERENCES

1. F. P. Incropera and D. P. De Witt, Introduction to heat transfer 2nd edition, John Wiley & Sons, 1990
2. A. Zhukauskas, Adv. in Heat Transfer, pp. 87- 159, Academic Press, 1987
3. J. Shin, Internal Laboratory Report 9901, Turbulence & Heat Transfer Laboratory, Dept. of Mech. Eng. The University of Tokyo, 1999
4. W. M. Kays and A. L. London, Compact heat exchangers 3rd edition, John Wiley & Sons, 1984
5. W. H. Press, Numerical recipes in Fortran 2nd edition, Cambridge Univ. Press, 1992
6. W. M. Kays and M. E. Crawford, Convective Heat and Mass Transfer 3rd edition, McGraw-Hill, Inc., 1993

THE EXPERIMENTAL STUDY OF HEAT TRANSFER ENHANCEMENT AND PRESSURE DROP CHARACTERISTICS WITH WING-TYPE VORTEX GENERATORS FOR STAGGERED CIRCULAR TUBE BANK FIN COMPACT HEAT EXCHANGER

Y. H. Zhang Y. X. Dong Y. G. Mei Y. Qiu L. B. Wang

Department of Mechanical Engineering
Lanzhou Railway Institute, Lanzhou, Gansu, 730070, P. R. of China
Email: lbwang@mail.gs.cninfo.net; Fax: 86-931-7667661

Keywords: heat /mass transfer enhancement, vortex generators, compact heat exchanger

ABSTRACT. Compact heat exchangers are characterized by high heat duties per unit volume and high heat transfer coefficients. The heat enhancement of wing-type vortex generators (WVGs) with different heights, attack angles and distances between the fins were studied in this report. The staggered circular tube bank fin surface was investigated in detail by changing the angle of attack with $\theta = 25^\circ, 35^\circ, 45^\circ$, the height of wing-type vortex generators with $H=6\text{mm}, 7\text{mm}, 8\text{mm}$, the distance between the fins with $T_p=6\text{mm}, 8\text{mm}, 10\text{mm}$, the diameter of tube is 40mm . The result shows that the friction factor and Nusselt number increased with the increasing of attack angle, height of WVGs and distance of fins, but the Nusselt number does not change much with the attack angle. The WVGs have little heat enhancement to the tube surface; the WVGs have the influence to the other surface forming the channel. In the local mass/heat transfer study, the results show that the heat transfer reverse on the fin behind the tube can be avoided through WVGs.

1. INTRODUCTION

Fin-and-tube heat exchangers are employed in a wide variety of engineering applications, for instance, in air conditioning units, process gas heaters and coolers, compressor inter-coolers and after-coolers, etc. A bank of tubes shares common fins, as shown in Fig.1. Generally, a liquid flows through the tubes, and gas flows through the channels formed by the neighboring fins, around the tube bank. In forced convection heat transfer between a gas and a liquid, the heat transfer coefficient of gas is typically 5-20 percent that of the liquid. The use of extended surfaces will reduce the gas-side thermal resistance. However, the resulting gas-side resistance may still exceed that of liquid, in this case, it will be advantageous to use specially configured extended surfaces which provide increased heat transfer coefficients. Augmentation of heat transfer is of special interest in fin-and-tube heat exchangers channel flows. There the rate of the heat transfer between the fluid and the channel walls deteriorates as the boundary layer grows on the channel wall and the flow tends to become fully developed. To circumvent this difficulty, protrusions in the form of slender wing-lets can be deployed (Fig.2). As shown the base of the wing remains attached to the fin and the apex faces the incoming stream with an angle of attack. With this configuration, the longitudinal vortices are generated along the side edge of the wing-shaped vortex generators (WVGs) due to the pressure difference between the front surface facing the flow and the back surface. These longitudinal vortices, generated by the vortex generators, can be made to disrupt the growth of boundary layer in a channel by exchanging the fluid from the near-wall region with the channel-core region and thus they can serve to enhance the heat transfer rate while producing less of a pressure drop.

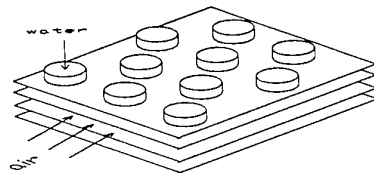


Fig.1 The schematic of a plate-fin tube heat exchanger

In fin-tube heat exchangers the WVGs belong to the category of tertiary surfaces, because they modify the fins. The heat transfer area is not changed for punched WVGs, the area increase is small and negligible for mounted WVGs. Single fin-tube rows were investigated numerically in [1]. Banks of fin-tube elements were studied experimentally in [2], and numerically in [3]. The experimental investigations use a liquid crystal thermography to determine local heat transfer coefficients and a drag

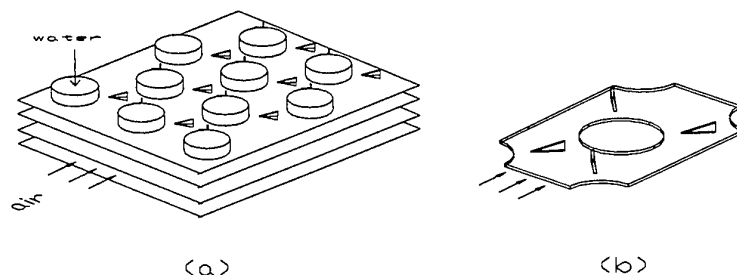


Fig.2 The schematic of a plate-fin tube heat exchanger with WVGs

balance or a pressure transducer to determine drag or pressure loss. In the reference [4], the main points of studies were reviewed, but there have many unclear fields to be explored.

The present paper gives the experimental data for wing-lets vortex generators embedded on the fin surface with different angles of attack, different height and different distance of fins. In order to interpret the mechanism of heat transfer enhancement, local mass /heat transfer coefficients were carried out. Both the average and local characteristics of mass/heat transfer coefficients were experimentally studied, based on the naphthalene sublimation techniques.

2. EXPERIMENTAL APPARATUS AND PROCEDURES

The description of the experimental plates is facilitated by reference to Fig.2, which is a schematic view of the test section. Air from the laboratory room is drawn into the channel formed by the naphthalene plates and no naphthalene plates. The test section has the height of 120mm, wide of 250mm and length of 600mm. The test plates have the dimension as show in Fig.3 and Fig.4. Each test plate has the thickness of about 3mm. The four naphthalene cast plates of A, B, C and D are placed on the two test plates which are mounted on the middle channel of test section. Along the flow direction, there are two naphthalene casting plates arranged as in Fig.3 A and B with WVGs, and as in Fig.4 C and D with no WVGs. Plate A, B, C, and D form the tube-and-fin channel. The two casting naphthalene tubes are shown in Fig.4 (b). The test plates were spaced by the stakes with wide 8mm and variation heights with 6mm, 8mm and 10mm respectively.

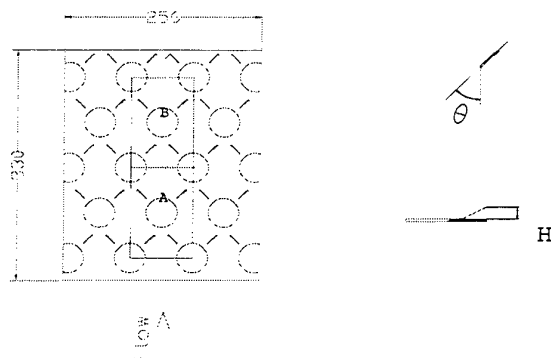


Fig.3 Test plates and configuration of WVGs

To employ the naphthalene sublimation method, naphthalene plates were cast in a specially designed mold

which, together with the casting technique itself, ensured that the plate surface would possess a high degree of flatness. Pains-taking measurements of the surface contour of the naphthalene plates before and after a test run were made with a sensitive dial gage. Corrections were carefully applied to account for natural convection sublimation from the surfaces that occurred during the time required for the contour measurements and for setting up the equipment. The net change in local elevation of the naphthalene surface resulting from the mass transfer during a test run was determined from the contour measurements and the corrections and, from this, the local mass transfer rates and transfer coefficients were evaluated. In addition, the local changes in elevation were integrated over the surface of the plates in order to yield the overall mass transfer. The attentive and fully independent determination of the overall mass transfer was made by directly weighing with a sensitive balance. The results obtained from the surface-integrated local mass transfer and from the balance measurements were compared and found to agree well blow 8 percent. After casting of the naphthalene, the WVGs were mounted on the given position of surface of the naphthalene quickly dry glue with special tool. Using this glue will not cause the damage of the naphthalene surface.

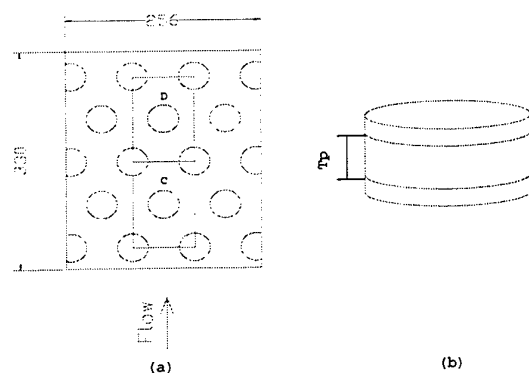


Fig.4 Test plates and tube casting

The contour of naphthalene surface was measured before and after a data run by a precision dial gage whose smallest scale division was 0.001mm. The dial gage was mounted on a fixed strut that over hung a movable coordinate table. The coordinate table enabled the surface to be independently traversed in two directions in the horizontal plane. The traversing was controlled by micrometer head which could be read to 0.05 mm. During the contour measurements, the naphthalene plates were held firmly against the coordinate table by flat springs. Contour measurements were made at as many as discrete locations.

The overall mass transfer was measured with a precision balance capable of discriminating to within 0.1mg for specimens having a mass up to 200g. Measurements of the flow rate through the test section were made with a calibrated Pitot pipe. The temperature of the air entering the test section was sensed by a precision grade laboratory thermometer that could be read to 0.1 deg. C. A digital timer was used to measure the duration of a data run as well as the time required for setting up experiment and for executing the surface contour measurements. The latter times were employed in evaluating natural convection corrections. The pressure drops are measured by the micro pressure gage which with the precision-grade as 0.2 mmH₂O. The parameters of the WVGs and space of fin are presented in Table1, from which it is evident that 30 configurations can be obtained from the combination of different parameters of WVGs, including the no WVGs configurations.

Table 1. Characteristics of the configuration investigated

WVG H / mm	6	7	8
WVG θ	25°	35°	45°
Tp /mm	6	8	10

3. DATA REDUCTION

Mass Transfer-Local Mass Transfer

The surface profile measurements corrected as described in the foregoing paragraphs, yield the surface distribution of the sublimation depth $\delta(x,y)$. Then, using the density ρ_s of the solid naphthalene ($\rho_s=1.145[5]$) and

the measured duration time τ of data run, the local rate of mass transfer per unit area was evaluated from:

$$\dot{m}(x, y) = \rho_s \delta(x, y) / \tau \quad (1)$$

The local mass transfer coefficient K can be defined as

$$\kappa(x, y) = \dot{m}(x, y) / (\rho_{n,w} - \rho_{n,bx}) \quad (2)$$

For determining $\rho_{n,w}$, the vapor pressure-temperature relation for naphthalene can be employed, The vapor pressure correlation [6] is

$$\log_{10} p_{n,w} = 11.55 - 3765 / T_w \quad (3)$$

The perfect gas law, the $\rho_{n,w}$ was defined by

$$\rho_{n,w} = p_{n,w} / (RT_w) \quad (4)$$

The $\rho_{n,bx}$ is calculated by

$$\rho_{n,bx} = \rho_{n,i} + \dot{m}(x) / \dot{Q} \quad (5)$$

where the $\dot{m}(x)$ is defined by

$$\dot{m}(x) = \int_0^x \int_0^B \dot{m}(x, y) dy dx \quad (6)$$

In which \dot{Q} is the volume flow passing through the typical element (such that passing through the channel by the naphthalene plates), B is the width of test plate, x is the direction of main flow. A dimensionless representation can then be made by introducing the local Sherwood number as

$$Sh = KD_h / D \quad D = \nu / S_c,$$

where $S_c = 2.5$ and the kinematic viscosity can be evaluated as that for pure air, D is the diffusion coefficient rate. The hydraulic diameter used in this study is the London and Kay's definition and notation [7]:

$$D_h = 4 \cdot A_c \cdot L / A$$

where A_c is the minimum flow area, L the stream-wise length, and A is the heat transfer area.

Average Mass Transfer

The average mass transfer coefficient \bar{K} of a unit area is evaluated from the sublimated mass Δm and the duration of time τ of the test run by the definition.

$$\bar{K} = \Delta m / (F \cdot \tau \cdot \Delta \rho_m)$$

where F is the transfer area of the naphthalene surface, Δm is the corrected mass of naphthalene, from which the extraneous loss of naphthalene during the auxiliary processes has been excluded, and $\Delta \rho_m$ is the log mean wall-to-bulk naphthalene vapor concentration difference

$$\Delta\rho_m = (\rho_{nw} - \rho_{ni}) \ln((\rho_{nw} - \rho_{ni})/(\rho_{nw} - \rho_{ne})), \quad \rho_{ne} = \rho_{ni} + \Delta m/(\tau \cdot Q)$$

$$\overline{Sh} = \kappa D_a / D, \quad Re = u_{max} \cdot D_h \cdot \rho / \mu$$

In order to generalize the results from naphthalene sublimation to other Schmidt (or Prandtl) numbers, an adequate value of the exponent n in Sc or Pr must be selected. That is to say, both the local and average Sherwood number results can be converted to Nusselt number results by employing the analogy between heat and mass transfer. According to the analogy:

$$Nu = (P_r / S_c)^n \cdot Sh \quad \overline{Nu} = (P_r / S_c)^m \cdot \overline{Sh}$$

The exponents m and n are either $1/3$ or 0.4 . According to the suggestion of [8], a 0.4 power relation of Sc (and Pr) is adopted.

Pressure Drop

The total pressure drop ΔP_t through the test section consists of three components, which are the pressure drop due to friction, that due to inertia losses and the entrance / exit losses. In this paper, an average friction coefficient f is defined as

$$f = \Delta P_t / (\rho u_{max}^2 / 2) \cdot D_h / L$$

4. RESULT AND DISCUSSION

Local Results

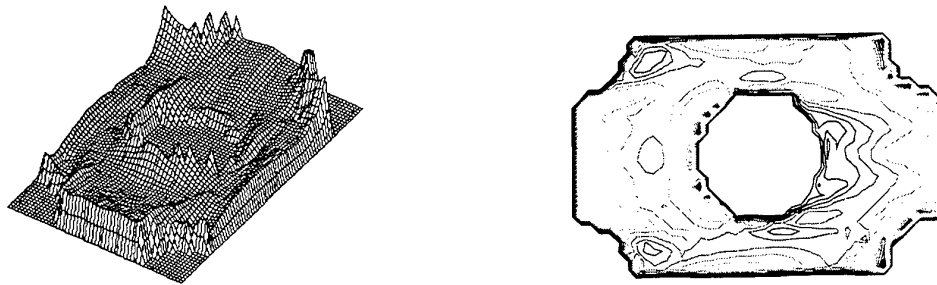


Fig.5 The 3D view and contour line of local transfer coefficients of no enhancement channel

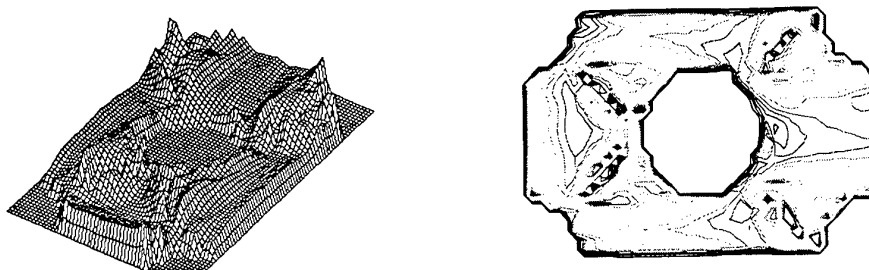


Fig.6 The 3D view and contour line of local transfer coefficients of enhancement channel on the plate with WVGs

Attention will be turned to the heat transfer enhancement mechanisms of WVGs which are operative in the tube-

and-fin surfaces with WVGs, and for this purpose the surface distributions of the local mass transfer coefficients will be presented and discussed. Owing to the complexity of results, such a presentation is very space consuming and will, therefore be limited to at about the same Re number 1678 for two types plate: plates which form the tube-and-fin channel with no WVGs enhancements, plates which form the tube-and-fin channel with WVGs enhancement. As mentioned above, in the channel with WVGs, there have two types of plates, one plate mounted WVGs, and the other plate mounted no WVGs. In Fig. 5, the local Sh number of plate formed the tube-and-fin channel with no WVGs enhancement with Re number 1678 and channel height $T_p=8\text{mm}$ is presented. Fig.5 (a) is the 3D view of the Sh, Fig.5(b) is the contour line of Sh corresponding to the Fig.5(a). Fig.6 and Fig. 7 show the local Sh numbers of plates formed the tube-and fin channel with WVGs enhancement at $Re=1689$ corresponding to the plate with WVGs and plate with no WVGs with parameters of WVGs as $H=6\text{mm}$ $\theta = 25^\circ$ $T_p=6\text{mm}$.

From Fig. 5, we can see the developing mass transfer boundary layers in the forward part of the channel yield relatively high transfer coefficients which decrease in the flow direction. The blockage of the channel by the tube has an upstream influence and causes a span-wise variation of the transfer coefficients. In front of tube, high peak transfer is evidence. This high peak constitutes natural augmentation caused by a vortex system develops in front of the tube and is swept around the side. The region downstream of the tube is one of generally low transfer coefficients, with remarkably low values in the wake. From the contour line, we can see that the low transfer coefficients region is relatively larger than that of Fig. 6 (b), Fig.7 (b). In Fig. 5 it is clear that in the tube sides, there are two symmetrical regions of high transfer coefficient.

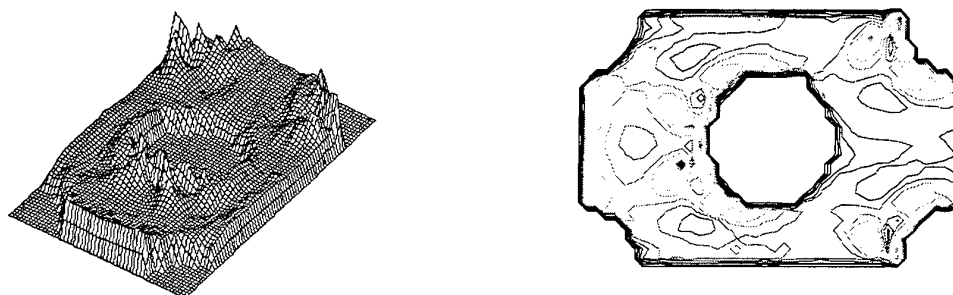


Fig.7 The 3D view and contour line of local transfer coefficients of enhancement channel on the plate with WVGs

From Fig. 6, we can see in the front of WVGs, there have a high peak region of transfer coefficient and also in the back of WVGs. Compared with Fig.5, these regions make the heat transfer increase considerably. The existing of WVGs also makes the transfer coefficient of a part of region of the tube side increase. From these figures, we can see that with WVGs, the area of low transfer coefficient region decreases, that is to say, the vortex generated by WVGs and tube have a great contribution to the increasing transfer coefficient of front of tube region, side region of tube and downstream region.

Besides the enhancement of the plate mounted WVGs, WVGs also have influence to the other plate which formed the channel. These results can be seen from Fig. 7. In Fig. 7 we can see that WVGs also make the transfer coefficient of up plate increase. In the tube wake region, the WVGs make the angle of detach move more behind of tube, from Fig. 6, it is clear that in the wake region are two peaks of transfer coefficients. In front of tube, there are two peaks of transfer coefficient between the weak peaks and front peak of second line tube, there is also a low transfer region.

Average Results

In the presentation of the average results, the Nusselt number of plate A, plate B, plate C, plate D and tube A and tube B are compared firstly, and then the overall average result are presented.

In Fig. 8, Fig.9, Fig. 10, the tube A and tube B, the plate A and plate B, plate C and plate D are compared respectively. From the Fig. 8, Fig. 9 and Fig. 10, it is clear to see that the average Nu of different region has not the same. The Nu of tube A is great than Nu of tube B, the Nu of plate A is great than Nu of plate B, and this is also true to plate C and plate D. In these figures, there is the same trend with the increasing of Re number, the difference of up-stream plate or tube and downstream plate or tube decreases. These results are expected because in reference [9] also find the same trend.

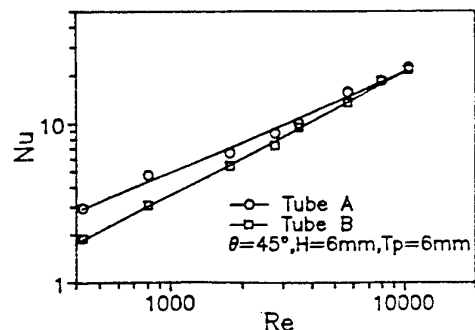


Fig.8 Nu of tube A and tube B

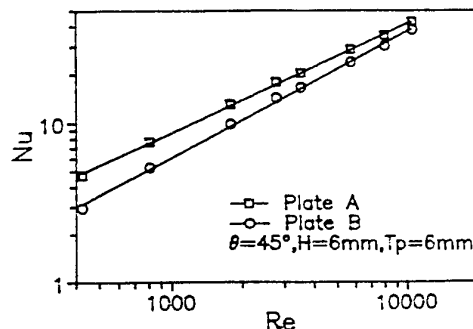


Fig. 9 Nu of plate A and plate B

In Fig. 11, 12 the plate A, C and tube A, the plate B, D and tube B are compared respectively. From the figures, we can see that the average Nusselt number of tube is lower than the plates corresponding to the same up-stream or downstream position. The Nu of plate A with WVGs is greater than Nu of plate C with no WVGs, it is also true to the plates B and D. As mentioned in the local result presentation, the WVGs make contribution to the transfer enhancement of plates formed the tube-and-fin channel, but the intensity is not the same as to the plate with WVGs and plate with no WVGs.

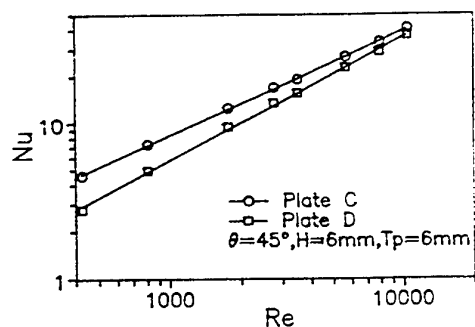


Fig.10 Nu of plate C and plate D

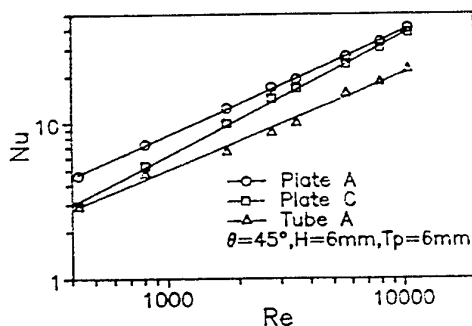


Fig. 11 Nu of plate A, plate C and tube A

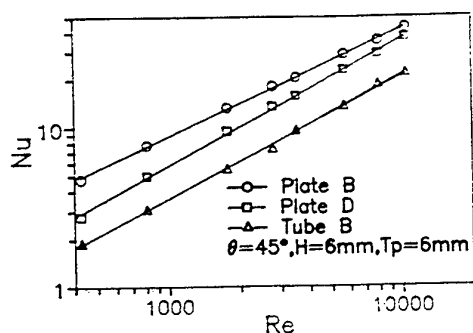


Fig.12 Nu of plate B, plate D and tube B

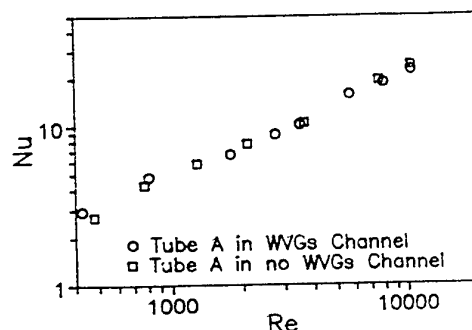


Fig.13 Nu of tube A in two cases (Tp=6mm)

In Fig. 13, the Nusselt numbers of tube A in channel with WVGs and in channel with no WVGs are compared. It can be seen that as to the tube A, the WVGs have little contribution on the heat transfer enhancement. This fact may be account for the longitudinal vortices consists of strong swirling around an axis essentially aligned with the main flow direction, which causes a heavy exchange of core and wall fluid, but it may not enhance the surface which faces to the flow direction.

The overall Nusselt number and friction factor result with respectively to the attack angle, T_p and H are presented in Fig. 14, 15, and 16. From Fig. 14, we can see that, with attack angle increasing, the Nu and f increase, but as to Nu the increasing is very limited. The results in [10] show that with larger angle of attack produce vortices with higher strength which in turn results in improved heat transfer.

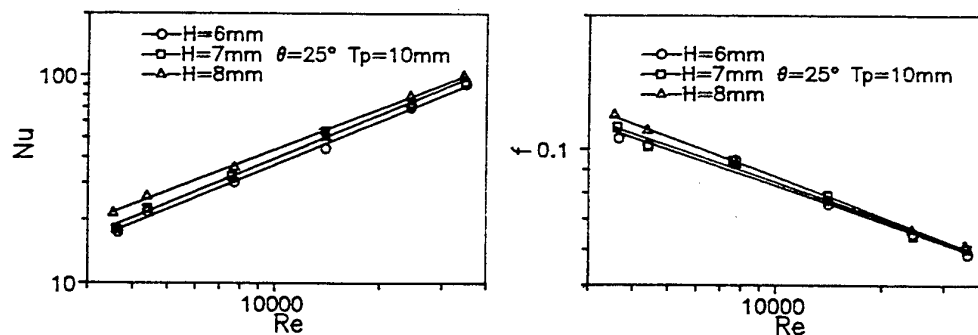


Fig.14 The influence of height of WVGs on overall Nusselt number and friction factor

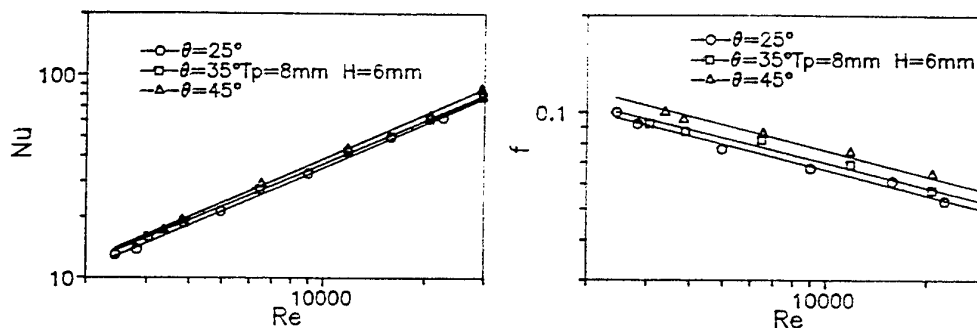


Fig.15 The influence of attack angle of WVGs on overall Nusselt number and friction factor

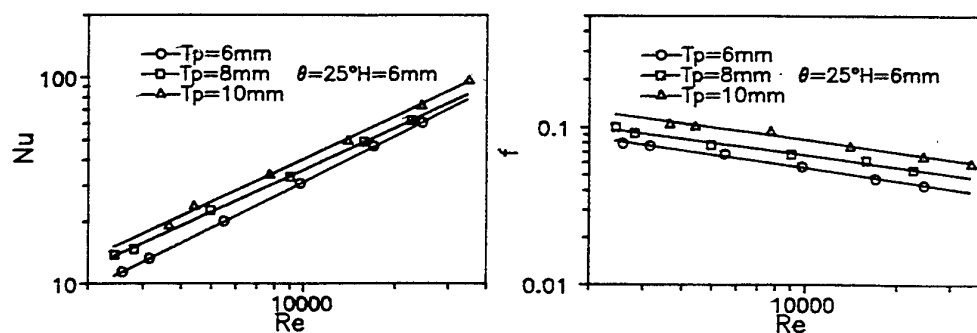


Fig.16 The influence of T_p on overall Nusselt number and friction factor

5. CONCLUSIONS

The results of this investigation have established both the qualitative and quantitative characteristics of the

transfer enhancement of WVGs on the staggered circular tube-and-fin heat exchangers. In the configuration of present investigation, the following results are obtained:

1. With the increasing of attack angle, height of WVGs and the distance between the fins, the Nusselt number and friction factor increase.
2. The WVGs have the enhancement effect not only on the surface of mounted WVGs, but also on the plates with no WVGs formed the channel.
3. The WVGs have litter contribution to the enhancement of the tube in the tube-and-fin channel.
4. In the WVGs enhancement tube-and-fin channel, the upstream plates have greater Nu than that of downstream corresponding.
5. The WVGs will decrease the heat transfer reverse region behind the tube.

REFERENCES

1. M., Fiebig, and N. K., Mitra, and Y., Dong, *HTD*, Vol.201, pp. 7-14, ASME (1992).
2. M., Fiebig, and A., Valencia, and N. K., Mitra, *Proc. 1st International Conference on Aerospace Heat Exchanger Technology*, pp.467-485. Palo Alto (1993).
3. G., Biswas, N. K., Mitra, and M., Fiebig, *Thermophysics Heat Transfer AIAA*, V.3 pp. 447-453 (1989).
4. M., Fiebig, *Enhanced Heat Transfer*, V. 2, pp.43-61 (1995).
5. *Handbook of Chemistry and Physics*, 47th ed., Chemical Rubber Publishing Company, p. C-414 (1966-1967)
6. T. K., Sherwood, and H. S., Jr., Bryant, *J. Chem. Soc.*, Part II, pp. 1690-1692 (1953)
7. W. M., Kays and A. L., London, *Compact Heat Exchangers*, 2nd ed. McGraw-Hill, New York (1964)
8. E. M., Sparrow, and A., Hajiloo, ASME, *Heat Transfer*, Vol. 102, pp. 426-432 (1980).
9. F. E. M., Saboya and E. M., Sparrow, *Int. Heat Mass Transfer* V.19, pp. 41-48 (1976).
10. G. Biswas, P., Deb, and S., Biswas, *ASME Heat Transfer* V.116, pp. 588-597 (1994).

AIR-SIDE HEAT TRANSFER ENHANCEMENT MECHANISMS OF COMPACT HEAT EXCHANGERS WITH INTERRUPTED SURFACES

L. Winston Zhang

Research and Development

Modine Manufacturing Company

Email: l.w.zhang@modine.com, Fax: (414)-636-1424

Keywords: heat exchanger, enhancement, surface interruption, vortex shedding, impingement

Abstract. Air-side heat transfer enhancement mechanisms in three types of interrupted surfaces: parallel-plate, louvered and convex-louvered fins in compact heat exchangers are analyzed. It is found that boundary layer restarting is the major enhancement mechanism in all these interrupted surfaces. Vortex shedding can be generated at sufficiently high Reynolds numbers. However, vortex shedding may or may not provide additional enhancement in heat transfer, depending on the type of interrupted surface employed. Effects of varying geometric parameters have been studied in these interrupted surfaces. In the parallel-plate fins, vortex shedding occurs at much lower Reynolds numbers in the inline and one offset geometry than that in another offset geometry. Different flow characteristics in the louvered fins have been analyzed and the important geometric parameters such as fin pitch to louver pitch ratio have been identified. This study also shows that other mechanisms such as flow impingement seen in convex-louvered fins can provide additional heat transfer enhancement. However, the enhanced heat transfer is usually associated with increased pressure drop penalty, especially, with the more aggressive enhancement mechanisms.

INTRODUCTION

In most liquid-to-air compact heat exchangers, air-side thermal resistance accounts for more than 80% of the total thermal resistance. Thus, heat exchanger design is usually limited by the air-side thermal performance. Various techniques have been applied in industry to enhance air-side heat transfer. The enhancement techniques include employing wavy channels, interrupted surfaces, vortex generators and others. Of particular interest to this study are three types of interrupted surfaces: parallel-plate, louvered and convex-louvered fins.

Surface interruption enhances heat transfer through two major mechanisms for heat transfer enhancement. One is the periodic restarting of boundary layers that prevent the continuous growth of the thermal boundary layers by periodically interrupting them. Thus, the thermal boundary layers are maintained thin and their resistance to heat transfer is reduced. Another important mechanism in these interrupted surfaces is the introduction of flow oscillations in the form of vortex shedding at much lower critical Reynolds numbers than those in the continuous plate fins. In the unsteady flow regime, the unsteady nature of the flow associated with vortex shedding increases frictional loss and form drag due to increased Stokes layer dissipation and Reynolds stresses, resulting in higher pumping power than the continuous plate fins. However, the onset of flow unsteadiness depends very much on the geometry. Thus, the boundary layer restarting and self-sustained flow oscillation in interrupted surfaces simultaneously influence both the overall heat transfer and the pumping power requirements. Additional heat transfer enhancement mechanisms such as flow impingement observed in the convex-louvered fins provide additional enhancement in heat transfer but also increased pressure drop penalty. Therefore, heat exchanger design must carefully consider the impact of these effects on the overall performance of the heat exchanger. In the following sections, the above described air-side heat transfer enhancement mechanisms in three types of interrupted surfaces, parallel-plate, louvered and convex-louvered fins, will be discussed in detail.

PARALLEL-PLATE FINS

There are several types of parallel-plate fins used in compact heat exchangers. The most commonly used in industry is perhaps the offset-strip fin. Figures 1(a) and 1(b) show a typical offset-strip fin heat exchanger and a cross-section of it. There are also other offset patterns for the parallel-plate fins. Figures 2(a-c) show cross-sections of three different types of parallel-plate fins [1]. The inline geometry is the base geometry. Offset-1 is the typical offset-strip fin geometry and it can be obtained by shifting the alternate rows of fins in the inline

geometry by half wavelength in the flow direction. Offset-2 can be obtained by shifting the alternate columns of fins in the inline geometry by half wavelength in the transverse direction.

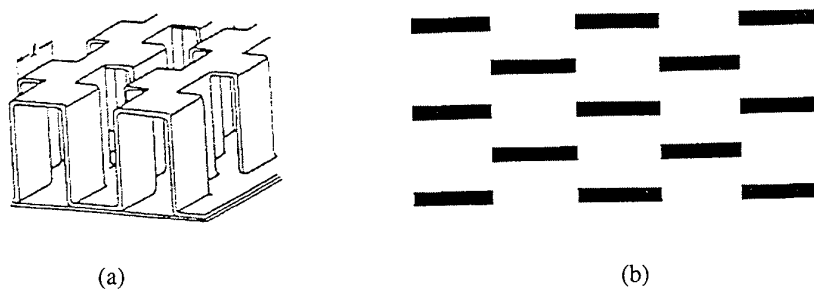


Figure 1. (a) A typical offset-strip fin heat exchanger; (b) a cross-section of an offset-strip fin heat exchanger.

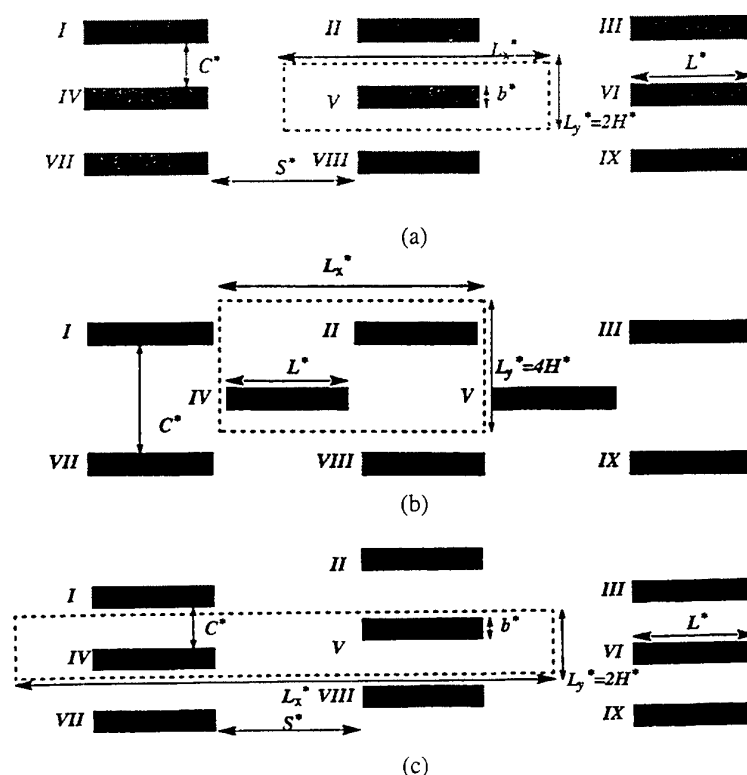


Figure 2. Parallel-plate fin geometries: (a) inline; (b) offset-1; (c) offset-2 [1].

Compact heat exchangers employing parallel-plate fins typically operate in three different flow regimes on the air-side. These flow regimes are steady laminar, periodic unsteady and transition to turbulence as shown in Figure 3 for the inline geometry [2]. It can be seen that significant enhancement in heat transfer can be obtained in both the unsteady laminar and transition to turbulence flow regimes. This also suggests that computations using steady laminar models significantly underpredict both heat transfer and pressure drop of the heat exchanger. Figures 4(a-d) show the flow pattern in an offset-strip fin heat exchanger and the corresponding time variation of the instantaneous Nusselt number, $\langle Nu \rangle$, at four different Reynolds numbers: $Re = 246, 720, 1245$ and 1465 [3]. Here the Reynolds number is defined based on the flow velocity at the minimum cross-section and the hydraulic diameter. The constant $\langle Nu \rangle$ at $Re = 246$ indicates that the flow is steady and laminar. At the next higher Reynolds number of $Re = 720$, the flow has become unsteady with periodic vortex

shedding. As the Reynolds number further increases to $Re = 1245$, a strong secondary low frequency in the time history of Nusselt number has emerged. Vortices can be clearly observed to roll over fin surfaces. When the Reynolds number further increases to $Re = 1465$, the flow has gone through some transition and now it has more than two identifiable frequencies.

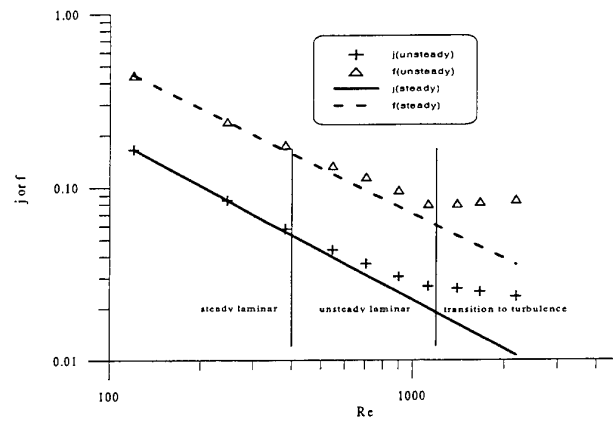


Figure 3. Flow regime map for a typical parallel-plate fin heat exchanger.

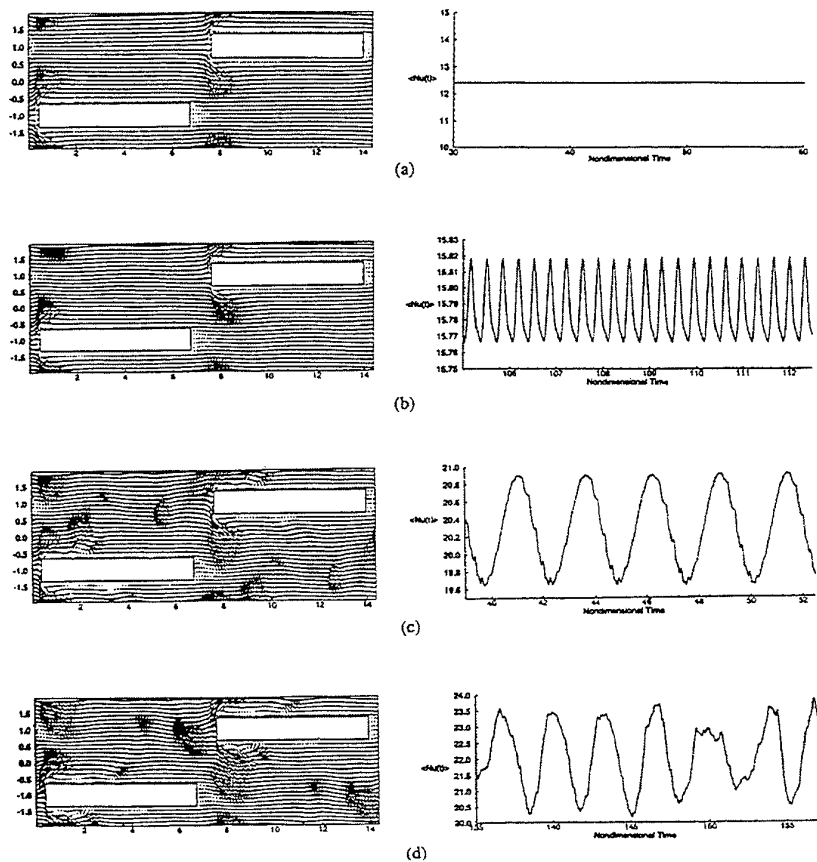


Figure 4. Instantaneous velocity vectors and time history of Nusselt number in an offset-strip fin heat exchanger: (a) $Re = 246$, the flow is steady; (b) $Re = 720$, the flow is unsteady with a single frequency; (c) $Re = 1245$, a secondary low frequency can be observed; (d) $Re = 1465$, the flow is chaotic.

Flow in other parallel-plate fin geometries goes through similar flow regime transitions as the Reynolds number increases. However, the onset Reynolds numbers for flow unsteadiness can be very different for different geometries even when they have exactly the same hydraulic diameter and the same compactness. For example, in the inline geometry, flow becomes unsteady at some Reynolds number between 245 and 381 while flow in the offset-strip geometry (offset-1) becomes unsteady at some higher Reynolds number between 474 and 720. Thus, geometry arrangement of the fins as shown in Figure 2 plays a very important role in determining the heat exchanger air-side thermal performance. This is because the fin geometry can be arranged in certain patterns that generates vortex shedding at low Reynolds numbers, it can be also arranged in other patterns that delays or suppresses vortex shedding. Figure 5 shows the comparisons of the j and friction factors for the different fin

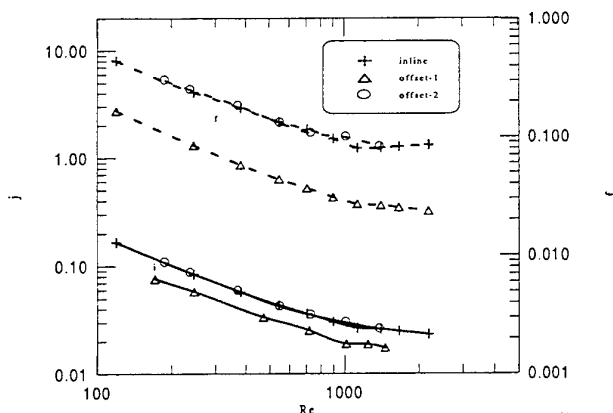


Figure 5. Thermal performance of parallel-plate fins.

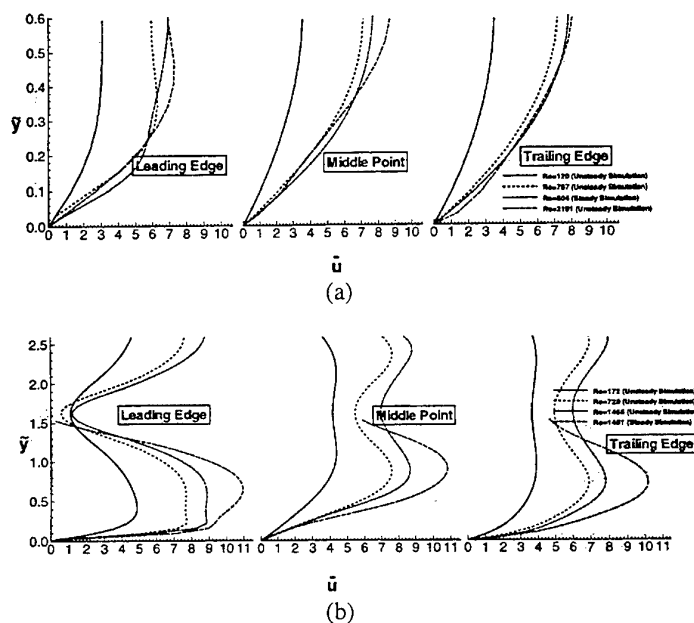


Figure 6. Time-averaged mean velocity profiles as a function of distance away from the top fin surface at three different streamwise locations: (a) inline geometry; (b) offset-1 geometry.

arrangements shown in Figure 2. Note that inline and offset-2 have exactly the same thermal performance with higher heat transfer and pressure drop than the offset-1 geometry. The behavior of the Colburn j and friction factors suggests not only that the offset-2 pattern follows the same flow map of the inline geometry but also that the flow in the inline and offset-2 becomes unsteady and transition to turbulence occurs at lower Reynolds numbers than the offset-1 geometry. A closer examination of the velocity profiles in above fin geometries

indicated that the velocity profiles in offset-1 have been distorted significantly from upstream wakes while such distortions are absent in the inline and offset-2 geometries as shown in Figure 6 [3]. Thus, flow is more restricted and is directed to follow along the channels in offset-1 fin geometry than the other two geometries.

LOUVERED FIN

The next type of interrupted surfaces is the louvered fin widely used in the automotive industry [4, 5]. Figures 7(a) and 7(b) show a typical louvered fin heat exchanger and a cross-section of several louvered fin arrays. The flow map in a louvered fin heat exchanger is significantly different from that of a parallel-plate fin heat exchanger. It has been shown in the past that two major types of flow exist: "duct directed" flow and "louver directed" flow [4]. At low Reynolds numbers, flow bypasses the louver passages due to high viscous resistance inside the louver passages, resulting in the "duct directed" flow. As the Reynolds number increases, the flow is forced to flow along the louver passages, resulting in the "louver directed" flow. Figure 8 shows the Colburn j factors over a wide range of Reynolds numbers. Here the Reynolds number is defined based on the inlet face velocity and the louver pitch. Clearly, three different flow regimes can be observed: "duct directed" flow, transition from "duct directed" to "louver directed" and "louver directed". Typical automotive louvered fin heat exchangers operate in the "louver directed" flow regime [6]. For the "louver directed" flow regime, flow is also highly restricted and is directed to follow along the louver passages as shown in Figure 9, similar to that in offset-1 geometry.

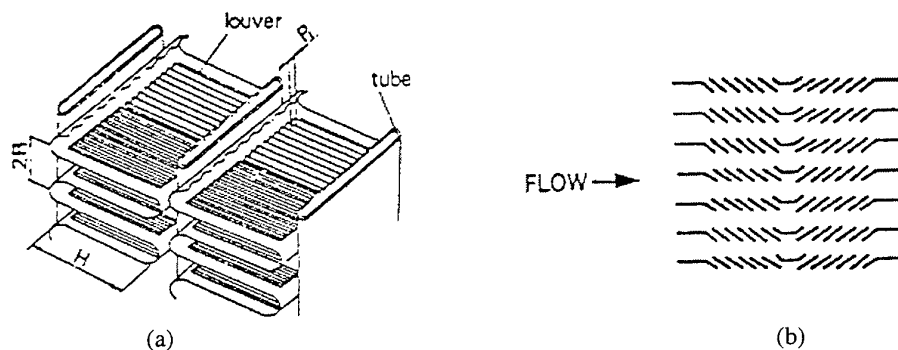


Figure 7. (a) A typical louvered fin heat exchanger; (b) a cross-section of a louvered fin heat exchanger.

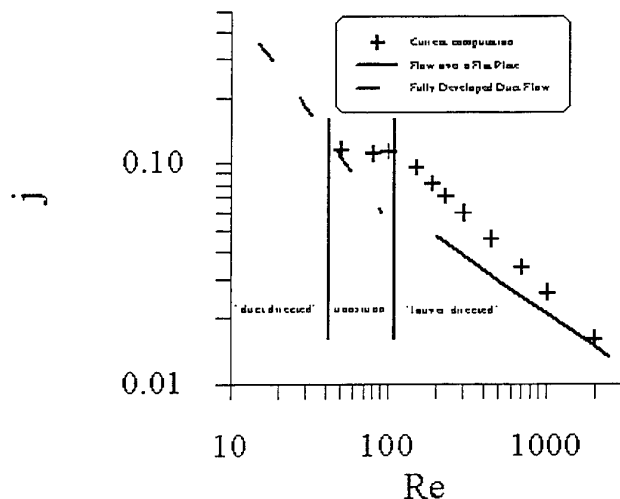


Figure 8. The Colburn j factor versus the Reynolds number for a louvered fin heat exchanger.

Similar to the parallel-plate fins, there are some parameters in a louvered fin heat exchanger that can be varied to help generate vortex shedding. For example, increasing the louver angle, increasing the fin pitch or reducing

the louver pitch. Zhang and Tafti [8] has shown the vortex shedding occurs at significantly lower Reynolds numbers when the fin pitch to the louver pitch ratio has been increased (shown in Figure 10). However, all these only have marginal impact on the overall heat exchanger thermal performance. It is interesting to note that the effect of flow unsteadiness which contributes significantly to the enhancement in heat transfer in parallel-plate fins is nearly absent in the louvered fin heat exchangers as observed in the behavior of the Colburn j factor curve shown in Figure 8.

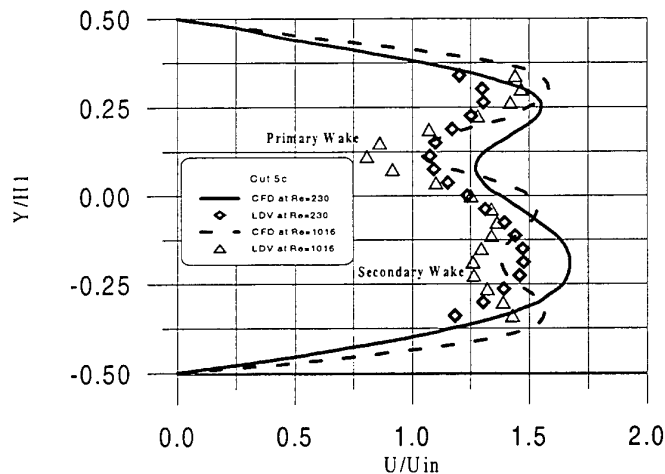


Figure 9. Computed and measured velocity profiles in a louvered fin heat exchanger [7].

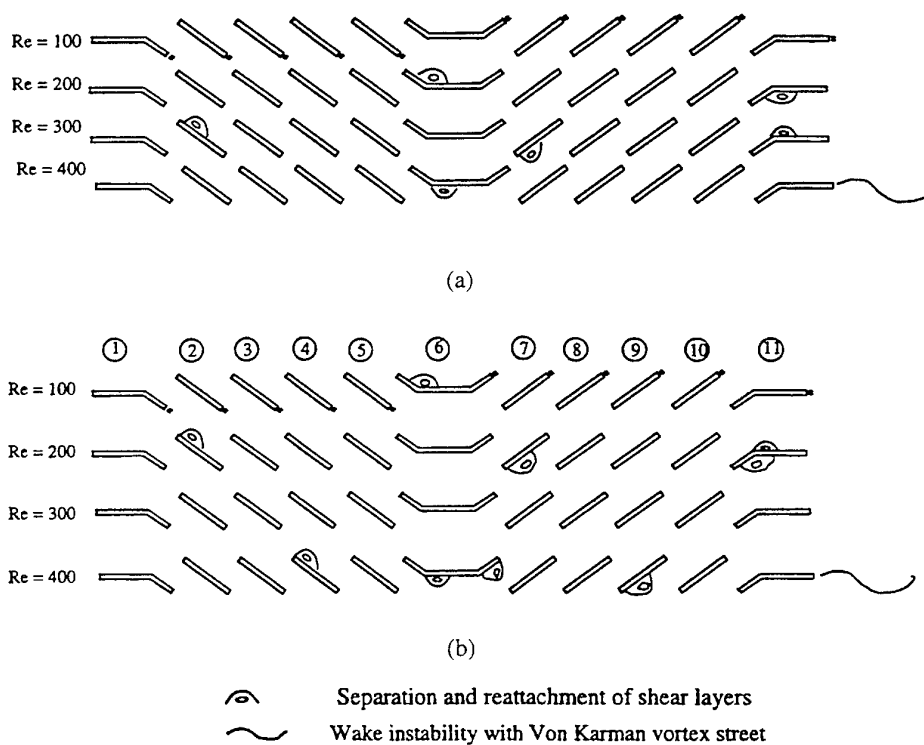


Figure 10. Flow features of a louvered fin array at different F_p/L_p ratios: (a) 1.0; (b) 1.5 [8].

From Figure 10, it can be observed that flow instability occurs initially in the wake region, similar to that of parallel-plate fins at low Reynolds numbers. However, the flow instability in louvered fins does not seem to

move much upstream when the Reynolds number increases as observed in parallel-plate fins [9]. But the upstream vortices that are present in parallel-plate fins that roll on downstream fins (shown in Figure 4) have significantly contributed to the overall heat transfer enhancement in the unsteady flow regime [3]. However, these upstream vortices are nearly absent in a louvered fin heat exchanger under typical operating conditions. Therefore, the wake instability with Von Karman vortex streets in a louvered fin heat exchanger have nearly no impact on the overall heat exchanger thermal performance.

CONVEX-LOUVERED FIN

The last type of interrupted surfaces discussed here is the convex-louvered fin. There is little work available in the literature regarding convex-louvered fin studies [10, 11]. Compared to the corresponding parallel-plate and louvered fins, the convex-louvered fin not only has the boundary layer restarting and self-sustained flow oscillation mechanisms but also it offers an additional heat transfer enhancement through flow impingement. With a finite angle of attack at the leading edge, spanwise vortices are generated at much lower Reynolds numbers than with zero angle of attack as in the case of parallel-plate fins. These spanwise vortices at low Reynolds numbers normally are coherent and offer great advantage in enhancing heat transfer [11].

Figure 11(a) shows the vorticity contours of the standard convex-louvered fin geometry and Figure 11(b) shows the corresponding temperature contours at a Reynolds number (based on the hydraulic diameter) of 3107. This clearly shows that vortices generated from the leading edge of upstream side convect downstream and then impinge on the concave side of convex-louver. Vortices are always generated from the leading edges. This is also different from that in the parallel-plate fin and louvered fin heat exchangers in which instability normally sets in from the trailing edges of fins but move upstream as the Reynolds number increases. The comparison shows that convex-louver fin offers heat transfer enhancement up to 80% over the louvered fin but also the pressure drop penalty can be as much as 300 ~ 400% [11].

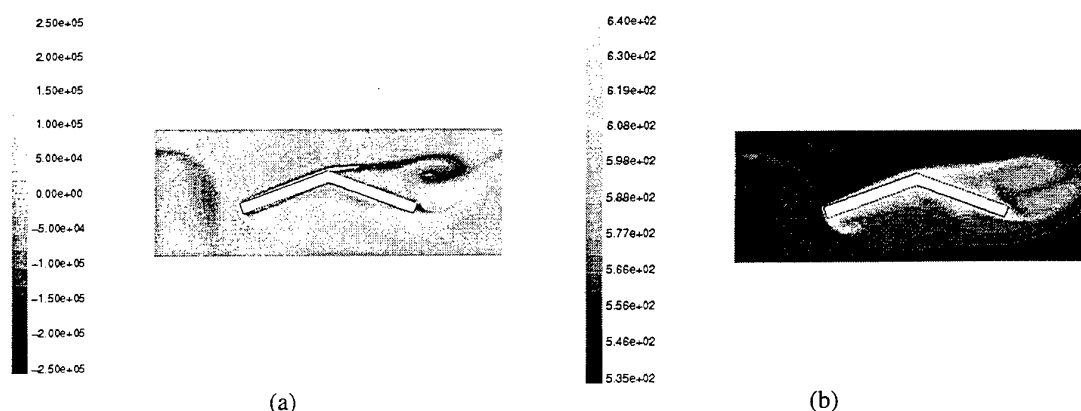


Figure 11. Instantaneous contours of (a) vorticity; (b) temperature of geometry 1 at $Re = 3107$.

CONCLUSION AND PRACTICAL IMPLICATIONS

Air-side heat transfer enhancement mechanisms in three types of interrupted surfaces, parallel-plate, louvered and convex-louvered fins, have been analyzed. It is found that enhancement due to the periodic restarting of boundary layers is present in all these surfaces. Vortex shedding can be generated in these interrupted surfaces at much lower Reynolds numbers than the corresponding continuous plate fins. Geometric arrangement plays a very important role in determining the onset of vortex shedding. However, vortex shedding does not automatically guarantee heat transfer enhancement. To achieve more enhancement, more aggressive mechanisms such as flow impingement can be adopted. But it is shown here both vortex shedding and flow impingement not only increase heat transfer but also impose higher pressure drop penalty. Therefore, it is recommended that thermal design engineers carefully assess the tradeoff between heat transfer and pressure drop in each type of heat transfer surface in order to optimize air-side heat exchanger design for specific applications.

REFERENCES

1. L. W. Zhang, *A Numerical Study of Flow and Heat Transfer in Compact Heat Exchangers*, Ph.D. thesis, University of Illinois at Urbana-Champaign, Urbana, Illinois (1996).
2. L. W. Zhang, D. K. Tafti, F. M. Najjar and S. Balachandar, "Computations of flow and heat transfer in parallel-plate fin heat exchangers on the CM-5: effects of flow unsteadiness and three-dimensionality", *Int. J. Heat Mass Transfer*, v. 40(6), pp. 1325-1341 (1997).
3. L. W. Zhang, S. Balachandar, D. K. Tafti and F. M. Najjar, "Heat transfer enhancement mechanisms in inline and staggered parallel-plate fin heat exchangers", *Int. J. Heat Mass Transfer*, v. 40(10), pp. 2307-2325 (1997).
4. A. Achaichia and T. A. Cowell, "Heat Transfer and Pressure Drop Characteristics of Flat Tube and Louvered Plate Fin Surfaces", *Experimental Thermal Fluid Science*, v. 1, pp. 147-157 (1988).
5. R. L. Webb and P. Trauger, "Flow structure in the louvered fin heat exchanger geometry", *Exp. Thermal Fluid Sci.*, v.4, pp. 205-217 (1991).
6. L. W. Zhang, S. B. Memory, J. P. Wattlelet, M. E. Springer and K. A. Thole, "An Experimental and Computational Study of Flowfields in a Louvered Fin Heat Exchanger", *Proceedings of 4th Vehicle Thermal Management Systems Conference*, Additional Paper No. 5, May 24-26, London, England (1999).
7. M. E. Springer, K. A. Thole, L. W. Zhang, S. B. Memory and J. P. Wattlelet, "A Combined Experimental and Computational Study of Flowfields in Louvered Fin Heat Exchangers", *Proceedings of 1998 ASME Fluids Engineering Division Summer Meeting*, Paper Number FEDSM98-4843, June 21-25, Washington, D. C. (1998).
8. X. Zhang and D. K. Tafti, "Effect of fin pitch on flow and heat transfer in multilouvered fins", (to appear in) *Proceedings of 4th ISHMT/ASME Heat and Mass Transfer Conference*, January 12-15, Pune, India (2000).
9. N. C. DeJong, L. W. Zhang, A. M. Jacobi, S. Balachandar and D. K. Tafti, "A complementary experimental and numerical study of the flow and heat transfer in offset strip-fin heat exchangers", *J. Heat Transfer*, v.120, pp. 690-698 (1998).
10. C. H. Bemisderfer, "Heat transfer: a contemporary analytical tool for developing improved heat transfer surfaces", *ASHRAE Transactions*, v.93(1), pp. 1157-1167 (1987).
11. N. C. DeJong and A. M. Jacobi, "Local flow and heat transfer behavior in convex-louver fin arrays", (in press) *J. Heat Transfer* (1999).

EXPERIMENTAL RESEARCH OF THE PLATE-FIN HEAT EXCHANGER AS AN EVAPORATOR IN THE ROOM AIR-CONDITIONER

Xiaosong Zhang, Leping Zhou

Department of Power Engineering

Southeast University, Nanjing, 210096

Email: zhangxs@public1.ptt.js.cn; Fax: (8625)7712719

Keywords: plate-fin heat exchanger, room air- conditioner, evaporator, R22, experimental research.

ABSTRACT. Experimental research of the plate-fin heat exchanger as an evaporator in a room air-conditioner with R22 was carried out according to the characteristics and requirement of a room air-conditioner. The research emphasizes particularly on the heat transfer and pressure drop characteristics of the heat exchanger, and the comparison with the common heat exchanger. The experimental results show that the heat exchange performance of the plate- fin heat exchanger used in a room air-conditioner is 2 to 3 times higher than that of the conventional one. The research and analysis of the plate-fin heat exchanger are needed for the optimum design of the conventional heat exchanger in a room air-conditioner.

1. INTRODUCTION

As an important component of an air-conditioner, the heat exchanger usually takes the form of tube-fin heat exchanger. However, for the air-conditioner and refrigerating system in vehicles such as automobiles, trains, and ships, tube-fin heat exchanger sometimes is not satisfactory for being less compact. It is also the case of a room air-conditioner for the reason of space and heat transfer coefficient. What is now widely accepted is that heat transfer coefficient should be greatly increased as a result of raising the compactness characteristic; therefore the research of heat exchanger will be needed. But in the case of tube-fin heat exchanger, its compactness characteristic and heat exchange performance cannot be improved too much; plate-fin heat exchanger usually applied in air separating installations has high performance in both aspects mentioned above. Generally its heat exchange area per unit volume is about 2 to 5 times as large as that of tube-fin heat exchanger. But there is little report that it is applied in the room air-conditioners.

To apply plate-fin heat exchanger to air-conditioning and refrigerating systems successfully, more experimental research has to be made. Kays, London and etc. have obtained a large number of experimental data with the performance of heat exchanger and fin surface. Previously, plate-fin heat exchanger was usually used in low-temperature equipment such as air separating installation. So if it is applied to air-conditioners and refrigerating systems, its operating condition is very different from that of low-temperature equipment and existing experimental data cannot be quoted directly. For the above reasons, we have made several simulate test research-using water as actuating medium. In this paper we will show the preliminary experimental research about the ability to apply plate-fin heat exchanger to room air-conditioner.

2. EXPERIMENTAL SYSTEM

To obtain heat exchange data of plate-fin heat exchanger for applications in air-conditioners and refrigerating systems, a set of heat exchanger experimental system has been developed, and the experimental performance of plate-fin heat exchanger as an evaporator in room air-conditioner was made.

2.1 Test Stand System Of Heat Exchanger

This experimental system can provide wide-ranging refrigerant conditions and flow quantities to heat exchange experimental sample. The experimental system includes: 1) heat compressing circulatory system (see Figure 1) which is a heat simulation system providing variable flow quantities of refrigerant to evaporating process or evaporating experimental sample and supplying the required refrigerant operating conditions; 2) air circulatory system (see Figure 2), which can provide required experimental air flow quantity; and 3) data acquisition and computer test and control systems, which can control the conditions automatically, and gather the experimental data.

The air circulatory system is a straight-flow wind tunnel as shown in Figure 2. The air flows through air supply orifice plate of wind tunnel and inlet section, then through the tested heat exchanger, all test elements and instrumentation, and finally is drawn out by an induced-draft fan. The drawn air is then cooled-dehumidified, heated and humidified. Then the required airflow goes back to the air supply chamber through air supply orifice by a forced-draft fan. Changing fan speed through frequency regulator regulates the face velocity of the tested heat exchanger.

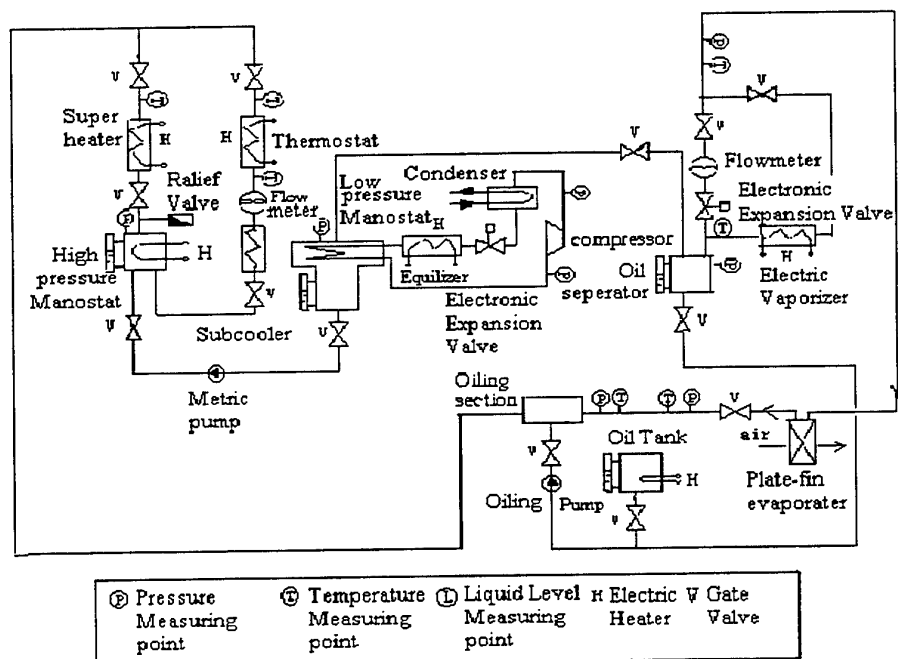


Fig.1 Heat compressing circulatory system

2.2 Experimental Heat Exchanger

To test the practical performance of a plate-fin heat exchanger used in air-conditioning and refrigerating systems, we designed experimental simulate heat exchanger which coordinates with the air system that has existed. Both the airside and refrigerant side of heat exchanger use flat fins. The unitary dimensions are shown in Figure 3 and Table 1. Having considered that convection heat transfer coefficient of refrigerant side is greatly different than that of airside, experimental simulation passage is designed in the ratio 1 to 2.

Table 1. Dimensions of Heat Exchanger

Dimensions	Air side	Refrigerant side
Fin height H (mm)	9.5	4.7
Fin thickness δ (mm)	0.2	0.3
Spacing of fin S (mm)	1.7	2.0
Inner spacing of fin X (mm)	1.5	1.7
Fin inner height Y (mm)	9.3	4.4
Effective length of unit L_e (mm)	110	240
Effective wideness of unit B (mm)	215	80
Equivalent diameter d_e (mm)	0.00258	0.00245
Effective sectional area per passage f_i (m ²)	0.0017648	0.00030
Heat exchanger area per meter per passage A_i (m ²)	2.731	0.488
Ratio of secondary area to total heat exchanger area	0.861	0.721
Total amount of passage	19	20
Effective heat exchanger area of heat exchanger A (m ²)	5.7086	2.34

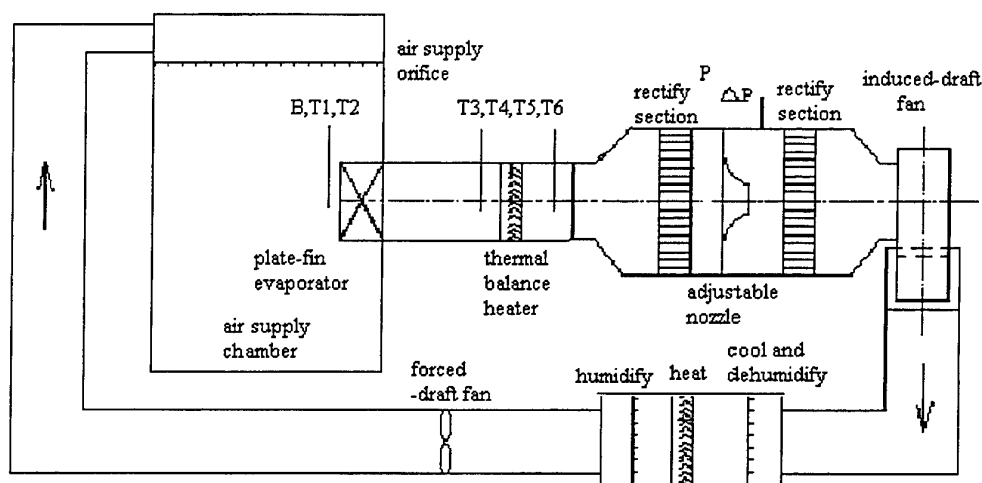


Fig. 2 Air circulatory system

3. EXPERIMENTAL PROCESS

In experimental low-pressure stabilization plant was used to control evaporating pressure, then to regulate evaporating temperature and kept it steady. Electronic expansion valve was used to control degree of superheat in evaporator outlet and kept it steady. The approximate heat-flux density was determined by temperature difference between air and R22. When flow quantity of air side was changed continually (by regulating face velocity), electronic expansion valve regulated its degree of opening automatically to refrigerant flow, then degree of superheat in evaporator outlet was controlled in an allowable range (See Table 2). After the system had become steady, checkpoints of data acquisition system was tested once every 12 seconds. Totally it lasted 12 minutes. Finally the average values were calculated. Through comparing the heat exchange quantity between refrigerant side and airside, we could determine the validity of the experimental results.

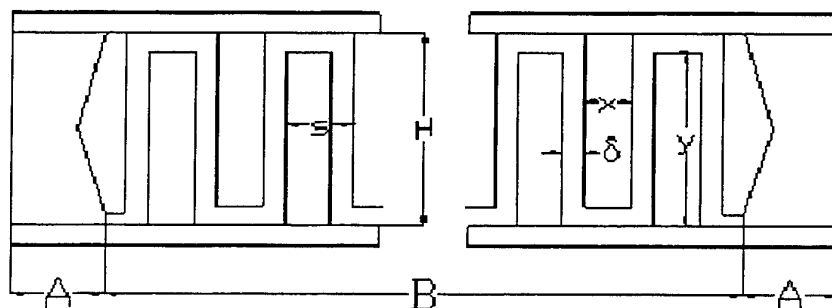


Fig.3. Unit structure size

Table 2. Refrigerant Condition Value Range And Accuracy Of Control

Experimental condition value	value range (°C)	accuracy of control (°C)
Evaporating temperature	0~9	±0.5
Degree of superheat in evaporator outlet	2.2~4.8	±1.0

4. DATA PROCESSING

With outlet temperature and pressure of refrigerant R22 side tested directly, computer software can calculate the enthalpy value. It is stated as:

$$H = f(p, T)$$

Heat exchange quantity is calculated by:

$$Q_r = G\Delta h$$

where G = mass flow rate of refrigerant (kg/s); Heat exchange quantity of airside is tested by 'wind-tunnel calorimeter method'. It is stated as:

$$Q_a = N + \Delta Q$$

where N = electric power of thermal balance heater; ΔQ = modification quantity of 'wind-tunnel calorimeter method'

The judgment on having got steady is stated as:

$$|Q_r + Q_a| / (Q_r + Q_a) \cdot 2 \leq 4\%$$

where $(Q_r + Q_a)/2 = Q_{ave}$, mean heat exchange quantity

Above all, the heat transfer coefficient of heat exchanger is stated as:

$$K = Q_{ave} / (A \cdot \Delta t_m)$$

where A stands for the heat transfer area (m^2) of heat exchanger; $\Delta t_m = |t_{a,ave} - t_r|$, temperature difference between refrigerant side and air side; $t_{a,ave}$, mean temperature of airside; t_r , refrigerant saturation temperature (i.e. evaporating temperature).

5. EXPERIMENTAL RESULTS

Evaporating experiment was carried out with various air velocity while evaporating temperature was controlled at about 0, 6 and 9 °C. As a result, after gathering and handling the effective experimental data, the curve of heat transfer coefficient changing with air velocity was obtained (see Figure 5). After doing return analysis on the experimental data, we can obtain heat exchange criterion equations. They are stated as:

$$K = 22.793(V_w)^{1.84578} \quad (t_e = 0^\circ\text{C})$$

and $K = 27.5993(V_w)^{1.69759} \quad (t_0 = 6^\circ\text{C}).$

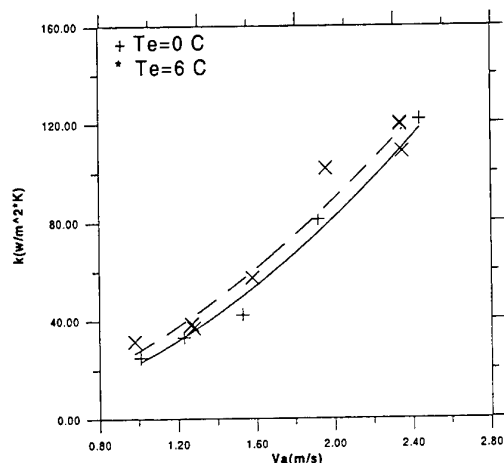


Fig. 5. Evaporating experiment of plate-fin exchanger with R22

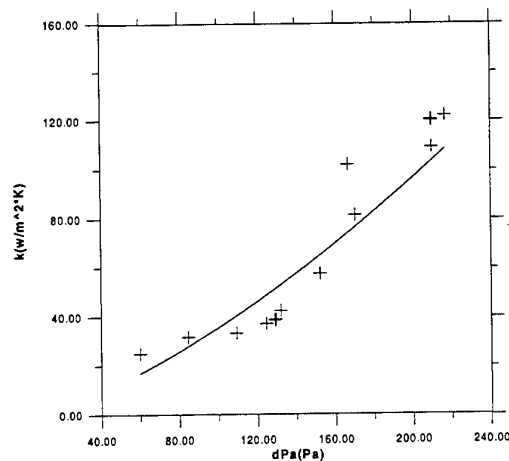


Fig. 6. Evaporating experiment of plate-fin exchanger with R22

From experimental results, we found that heat transfer coefficient of this kind of heat exchanger is relatively high which is generally from 40 to 120 w/(m²k). It is about 2 to 3 times higher than that of the common heat exchanger. Under the same conditions, the heat transfer coefficient of tube-fin heat exchanger is about 30 to 40 w/(m²k) when the logarithmic mean temperature difference is 12 to 14 degree centigrade). This is because the increase of unit heat exchange area of evaporator enhances the heat exchange process. Besides, the experiment in which evaporating temperature is about 9 °C is also made, and the results are similar to those of the above experiments.

Figure 6 shows the experimental data about resistance performance, and the relationship between pressure drop and heat transfer coefficient was obtained as: $k=0.0460126(dp_a)^{1.44287}$. Results show that the absolute value of this experimental sample's pressure drop is relatively high (The relationship of heat transfer coefficient changing with it is shown in Figure). It is because this experimental sample is relatively long, so the absolute value of resistance is high. However, the value does not increase too much, and its resistance coefficient is about one and half times as high as that of the tube-fin heat exchanger. So if the structural design is proper, the high resistance performance will not affect the value of this heat exchanger.

6. CONCLUSIONS

Through the experimental research of plate-fin heat exchanger as an evaporator in room air-conditioner, we have obtained the operating data of plate- fin heat exchanger applied to room air-conditioner and the correlation equations of convection heat exchange performance. The results show that the heat transfer coefficient of plate-fin heat exchanger used in room air-conditioner is about 2 to 3 times higher than that of the common one, with a slight increase in pressure drop of airside.

Experimental results indicate that plate-fin heat exchanger used as an evaporator of air-conditioner is feasible. And, the experimental data and equations about performance of heat exchange and resistance can provide reference for popularizing plate-fin heat exchanger in air-conditioning and refrigerating fields.

We suggest to continue this experiment in future and gaining more experimental data from which more accurate correlation equations about convection heat transfer coefficient can be obtained. We also suggest that by separating the convection heat transfer coefficients of two side flows of heat exchanger so that the accuracy of calculation will be increased. In addition, we should make experimental research of plate-fin heat exchanger applied to air-conditioner system as quickly as possible to accumulate experimental experience.

REFERENCES

1. W.M. Kays and A.L. London, Compact Heat Exchangers, McGraw Hill, New York, (1958).
2. X.S. Zhang, S.H. Li and K.T. Zhao. "The heat transfer characteristics of plate-fin heat exchanger in the field of refrigeration and air-conditioning", Proceeding of ICCR'98, Hangzhou, pp. 324~327. (1998)
3. K.T. Zhao, X.S. Zhang and etc, "The research of refrigerant supply system in heat transfer test stand". *Journal of Southeast University*, Vol.28, No.6, pp 29~33. (1998)
4. B.H. Zhang, X.S. Zhang and K. Du, "Wind-tunnel calorimeter measuring the performance of room air-conditioner", *Journal of Southeast University*, Vol. 24, pp 96~99. (1994)
5. P.L. Chen, X.F. Yue, "Technical manual of refrigeration and air-conditioning", 1990, ISBN 7- 5608- 0594-9/TB-17.
6. S.H. Li, "The experimental research of heat transfer and resistance performance of plate-fin heat exchanger applied in air-conditioning and refrigerating systems", [Academic degree thesis]. Department of Power Engineering, Southeast University, Nanjing, (1997).

THE EXPERIMENTAL STUDY ON THE PERFORMANCE OF HEAT EXCHANGER WITH HYDROPHOBIC SURFACE

Yue Danting Fei Qian Wu Guitao Chang Lijia
College of Marine Engineering, Dalian Maritime University
Dalian 116024 P.R.China
Email: duan@public.wh.hb.cn

Huang Jing Ren Baozhong
Department of Development, Dalian Refrigerator Co., Ltd.
Dalian 116012 P.R.China

Keywords: high hydrophobic coating, heat exchanger, jacket type laboratory, performance experiment

ABSTRACT. The experimental study on the performance of two heat exchangers (model 12-2.2/18, manufactured by Dalian Refrigerator Co., Ltd.) is made in this paper. The two heat exchangers, one is with conventional metal surface, the other is with high hydrophobic surface are contrasted in a jacket type laboratory. Under the dry and wet operating condition and at the vaporizing temperature of 0°C and -5°C, the parameters such as the refrigeration output, the heat transfer coefficient and the velocity of airflow in the airside of the finned tube bundles are measured. The experimental results show that high hydrophobic coating can improve the heat transfer performance of air cooler especially at the wet operating condition and decrease the frost temperature on the cold surface. The theoretical analysis of the mechanism of the drop condensation on the hydrophobic surface is also given in this paper.

1. INTRODUCTION

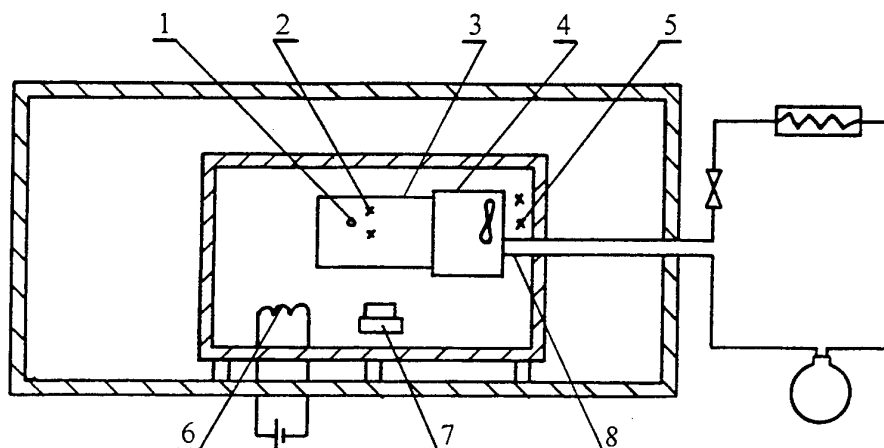
Heat exchanger is one of the most important components of the refrigeration and air-conditioning system. Its performance will directly influence the whole system. The study on the heat exchanger is a very active research area in the field of refrigeration and air-conditioning system. At present, the study on tube heat exchanger is focused on the law of heat transfer and the augment of heat transfer. The heat transfer between the refrigerant and coolant in the refrigeration and air-conditioning system is mostly forced convection heat transfer, therefore the key point to augment the heat transfer is to augment the single-phase fluid convection heat transfer and to augment the condensation and boiling heat transfer. Air-cooled finned tube type heat exchanger is one of the most popular heat exchangers in refrigeration and air-conditioning system. Because the air is condensed on the fin surface during the work time, which is easily forming "Water Bridge", thus the air fluid and the refrigeration output are reduced. At the low temperature, the ventilation resistance will be increased, even the duct between the fins will be blocked because of the frost deposited on the fin surface. Many efforts are made by researchers all over the world to choose different fin parameters to reach the best heat transfer effect [1,2]. For many years the authors have studied the hydrophobic fin surface, changing film condensation to drop condensation in order to improve the heat exchanger performance [3,4]. The high hydrophobic coating with the contact angle of 150° have been developed by the authors. The surface of the heat exchangers (model 12-2.2/18, manufactured by Dalian Refrigerator Co., Ltd.) is coated with the high hydrophobic coating and is contrasted with the same model, conventional metal surface heat exchanger. The experiment is made in a jacket type laboratory in the National Quality Inspecting Center of Cold Storage and Refrigeration Equipment of Agriculture Department. At the vaporizing temperature of 0°C and -5°C, the parameters such as refrigerating output, heat transfer coefficient, the wind velocity on the air side in the finned tubes are measured under the dry and wet operating condition. The theoretical analysis of the mechanism of the drop condensation on the hydrophobic surface is also discussed in this paper.

2. EXPERIMENTAL STUDY

Experimental Instrument

The experiment is made in the jacket type laboratory referring to the standard of ANSI/ASHRAE25-1990. Fig.1 is the schematic of experiment system. The heat exchanger to be measured is mounted the bottom of the cold storage with 1-meter-long of duct in front of it. The electric heater is used to maintain the thermal equilibrium in the cold storage so as to measure the refrigerating output of the air-cooled heat exchanger. The centrifugal

wetting machine is used to maintain the high moisture content in the cold storage.



1. wind velocity measure point 2. exit wind temperature and humidity measure point
3. wind duct 4. heat exchanger to be measured 5. entrance wind temperature and humidity measure point
6. refrigerant temperature measure point 7. centrifugal wetting machine 8. electric heater

Fig.1 Schematic of experiment system

Measurement Apparatus

The temperature measuring system is consisted of SCXI-1001 data collector (manufactured by American National Instrument Co.), HP34970A data collector (manufactured by HP Co.), PCL/GPIB Bus (manufactured by HP Co.) and computers. The copper-constantan thermocouples are used with the range of -210°C - 400°C , the sensitivity of $\pm 0.001^{\circ}\text{C}$ and the precision of 0.6°C .

An electric energy integrated analysis instrument (model DZFG-1, range 0.03-750kW, sensibility 0.001Kw), measures the power of the electric heater.

The wind velocity is measured by a hot bulb electronic wind velocity meter (model QDF-2, range 0-10m/s, precision $\pm 0.1\text{m/s}$).

Experiment Procedure

The air side thermal equilibrium method is used in this experiment. For the coated and metal surface of the heat exchanger, the heat transfer coefficient and the wind velocity on the air side in the finned tubes are measured respectively. The heat exchanger with metal surface is firstly tested, then it is taken off and the one with coated surface is mounted and tested. The vaporizing temperature is 0°C and -5°C under the dry and wet operating condition. The procedure is as follows.

First, the heat transfer coefficient is measured under the dry and wet operating condition referring to the Methods of Testing Forced Convection and Natural Convection Air Coolers for Refrigeration (ANSI/ASHRAE25-1990). Second, starting the wetting machine and wetting, the amount of wetting is constant according to temperature. When the vaporizing temperature is 0°C , the wetting time is 70 minutes and when the vaporizing temperature is -5°C , the wetting time is 130 minutes. The wind velocity is measured. Third, closing the wetting machine. When the thermal equilibrium is reached again, the heat transfer coefficient is measured under the wet operating condition.

Experimental Results

According to the thermal equilibrium in the cold storage, the refrigerating output of the air cooler is

$$Q = K_c(t_o - t_i) + W_c \quad (2.1)$$

where K_c is heat leakage coefficient of cold storage, t_o is the outside temperature of the cold storage, $^{\circ}\text{C}$, t_i is the inside temperature of the cold storage, $^{\circ}\text{C}$, W_c is the total power of the electric heater in the cold storage, (W).

$$k = \frac{Q}{F \cdot \Delta t_m} \quad (2.2)$$

where F is the heat transfer area of the heat exchanger, m^2 , Δt_m is the logarithmic mean temperature difference, $^{\circ}\text{C}$. The calculated heat transfer coefficient of heat exchanger is showed in Table 1.

Table 1 The Calculated Heat Transfer Coefficient of Heat Exchanger

evap. temp. $^{\circ}\text{C}$	indoor temp. $^{\circ}\text{C}$	heat exchanger without coating			heat exchanger with coating		
		dry cond.	wet cond.	decrease	dry cond.	wet cond.	decrease
0	9	33.3	29.0	12.5%	30.3	27.5	9.2%
-5	0	24.8	20.5	17.3%	21.7	20.1	7.3%

In the wetting process, the variety of the wind velocity in the air side heat exchanger is showed in Fig.2 and Fig.3.

When the vaporizing temperature is 0°C , the two heat exchangers are not frosted and the variety of velocity is not clear. The film condensation is occurred on the heat exchanger surface without coating and the heat transfer coefficient is decreased by 12.5%. However the drop rolling and departing is observed on the surface of the other one with hydrophobic coating and the heat transfer coefficient is decreased by 9.2%. When the vaporizing temperature is -5°C and after wetting for 80 minutes, the heat exchanger surface without coating is frosted heavily, the wind velocity is dropped by nearly 60% and the heat transfer coefficient is decreased by 17.3%. However, during the 60 minutes of wetting process, the heat exchanger surface with hydrophobic coating is not frosted. With the wetting process continuing, the surface is frosted slightly. The wind velocity is constant in general and the heat transfer coefficient is decreased only by 7.3%. It can be seen that the heat exchanger performance is improved by high hydrophobic surface coating under the wetting operating condition.

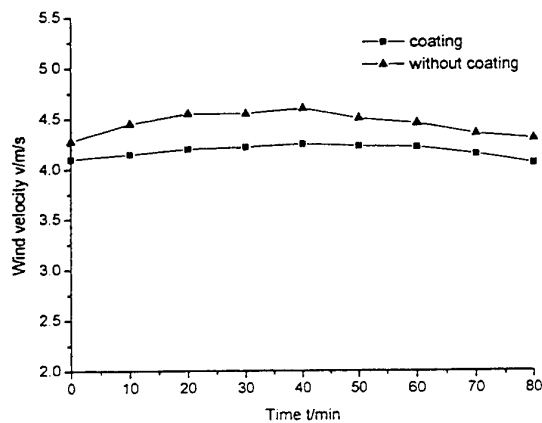


Fig.2 Curves of wind velocity at vaporizing temperature of 0°C

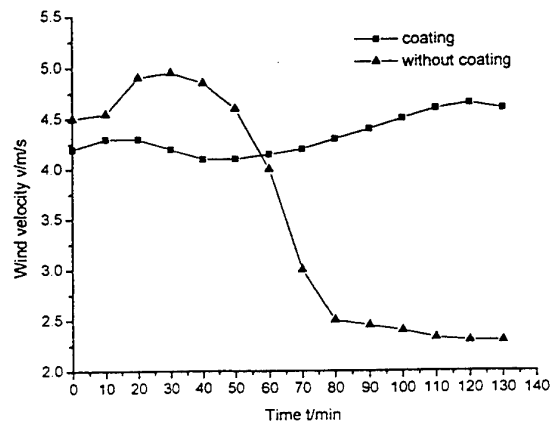


Fig.3 Curves of wind velocity at vaporizing temperature of 0°C

3. THERITICAL ANYLASIS

From the thermodynamics point of view, the vapor condensation or sublimation on the heat exchanger surface can be considered as the process that the system changes from metastable phase (vapor) to stable phase (water or ice). In this process, it is very important that the new phase must occur, the nucleus must be formed. In the

metastable phase, if the nucleus were formed, it would grow simultaneously because the growth process of the new phase is the decrease process of the free enthalpy of the system. In other words, only if the nucleus were formed that the new phase would occurred. Therefore, in order to refrain from forming frost on the heat exchanger surface, we should study the forming rate of the nucleus, find the way to reduce it and make it to the minimum limit.

Assuming the vapor condenses on a cold surface and forms a spherical crown shaped ice crystal, the air is pure and without suspended dust. The system can be considered as a vapor growth system. The difference of the system free enthalpy is described as follow [5]

$$\Delta G = \frac{V_s}{\Omega_s} \Delta g + (F_{vs} \sigma_{vs} + F_{ms} \sigma_{ms} - F_{mv} \sigma_{mv}) \quad (3.1)$$

where Ω_s is the single molecule volume, and V_s is the volume of the spherical crown shaped ice crystal which is given by

$$V_s = \frac{1}{3}(2 - 3\cos\theta + \cos^3\theta)\pi r^3 \quad (3.2)$$

The relationship between the contact angle of ice crystal and the surface θ as well as the three boundary tension σ_{vs} 、 σ_{ms} 、 σ_{mv} is

$$\theta = \frac{\sigma_{mv} - \sigma_{ms}}{\sigma_{vs}} \quad (3.3)$$

The decrease of the free enthalpy Δg produced by the single molecule changed to flat boundary is

$$\Delta g = -kT \ln\left(\frac{p}{p_s}\right) \quad (3.4)$$

where k is Stefan-Boltzmann constant, T is system temperature, p is the vapor pressure of system. p_s is saturation pressure of vapor corresponding to the temperature T of the vapor-ice phase, $\frac{p}{p_s}$ is the ratio of super-saturation. The spherical crown shaped area between the vapor and ice crystal is

$$F_{vs} = 2\pi r^2(1 - \cos\theta) \quad (3.5)$$

where r is the radius of ice crystal.

The boundary area between the surface and ice crystal is

$$F_{ms} = \pi r^2(1 - \cos^2\theta) \quad (3.6)$$

F_{mv} is disappeared boundary between surface and vapor. Combining the equation (3.1) - (3.6) gives [6]

$$\Delta G = \left(-\frac{4\pi r^3 kT}{3\Omega_s} \ln \frac{p}{p_s} + 4\pi r^2 \sigma_{vs}\right) f(\theta) \quad (3.7)$$

$$f(\theta) = \frac{2 - 3\cos\theta + \cos^3\theta}{4} \quad (3.8)$$

For a given temperature and saturation ratio and considering θ as a parameter variable, the curves of ΔG versus r is shown in Fig.4. It can be seen that ΔG has a maximum value ΔG^* when it varies corresponding to the radius r , and this is called the critical radius r^* . The phase change is proceeded along the direction of system free enthalpy drop. For a spherical crown shaped ice crystal of $r < r^*$, the sublimation will not occur, even if the ice crystal deposits on the plate it will disappear because of sublimation. Only If $r > r^*$ will the sublimation occur simultaneously. ΔG^* is an energy obstacle to forming spherical crown shaped crystal nucleus on the plate. The coefficient $f(\theta)$ is the only deviation between the energy obstacle to homogeneously forming nucleus and ΔG_h , that is $\Delta G^* = \Delta G_h f(\theta)$. The scope of the contact angle is $0^\circ \sim 180^\circ$. From the equation (3) we can see that $f(\theta)$ rise from 0 to 1 monotonously, the phase change obstacle energy ΔG^* increases from 0 to ΔG_h . Therefore it can be concluded that enlarging the contact angle and making the surface hydrophobic will enhance the phase change obstacle energy and refrain from frost.

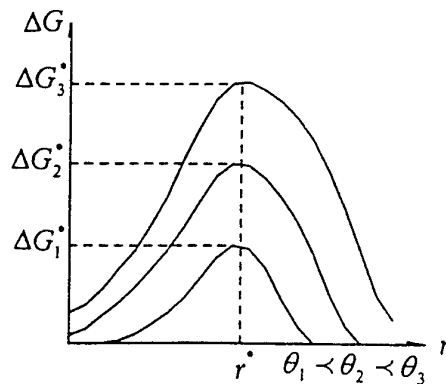


Fig.4 Curves of ΔG corresponding to r

4. CONCLUSION

1. High hydrophobic coating can improve the heat transfer performance of air cooler especially at the wet operating condition.
2. High hydrophobic coating can decrease the frost temperature on the cold surface.

REFERENCES

1. Z.G. Wang and B.F. Yu, *The Journal of Refrigeration* v.18, pp.16-22 (1999).
2. L.C. Thomas, *Heat Transfer*, Prenlice Hall Inc. (1992).
3. D.T. Yue, *Journal of Engineering Thermophysics* v.18, pp529-532 (1997).
4. D.T. Yue, *Journal of Engineering Thermophysics* v.20, pp1-4 (1999).
5. N.B. Min, *Physic Basis of the Crystal Growth*, Shanghai Scientific Press (1982).
6. T. Gu, *Surface Chemistry*, Scientific Press (1994).

COMPACT, DOUBLE SIDE IMPINGEMENT, AIR-TO-AIR HEAT EXCHANGER

Z. J. Zuo, E. H. Dubble and S. D. Garner

Thermacore, Inc.

780 Eden Road

Lancaster, PA 17601, USA

Email: zjz@thermacore.com; Fax: (717) 569-6551

Keywords: double side impingement, air-to-air heat exchanger, cabinet cooling

ABSTRACT. This paper discusses the design, fabrication and testing of a double side impingement air-to-air heat exchanger for cooling of electronic cabinets. Operating principles and advantages of the new heat exchanger concept are discussed, which is followed by descriptions of a theoretical model that can be used to predict the heat exchanger thermal performance. Prototype heat exchanger test results are compared to validate the theoretical model predictions. In addition to thermal tests, environmental tests were also conducted to qualify the heat exchanger for outdoor applications. Procedures of selecting impingement heat exchangers for specific applications are presented at the conclusion of the paper.

1. INTRODUCTION

Cost, size, reliability and thermal performance are four governing factors in choosing air-to-air heat exchangers for cooling electronic cabinets. For many outdoor applications as frequently encountered in the telecommunication industry, heat exchangers must also meet operational requirements under various weather conditions.

Three most common types of air-to-air heat exchangers are Fin-Tube, Plate-Fin and Heat Pipe-Fin heat exchangers that are illustrated in Figure 1 [1, 2]. Depending on the flow directions of the air streams entering the heat exchanger core, a heat exchanger can also be classified as a counter or cross flow heat exchanger. A common feature of the three heat exchangers is that they rely on heat conduction through the fins to extend heat convection surfaces. Therefore, the fin material must have a high thermal conductivity and all joints (such as the fin-tube, plate-fin and heat pipe-fin joints) must have low thermal resistances. These requirements increase the heat exchanger size and manufacturing difficulty and cost.

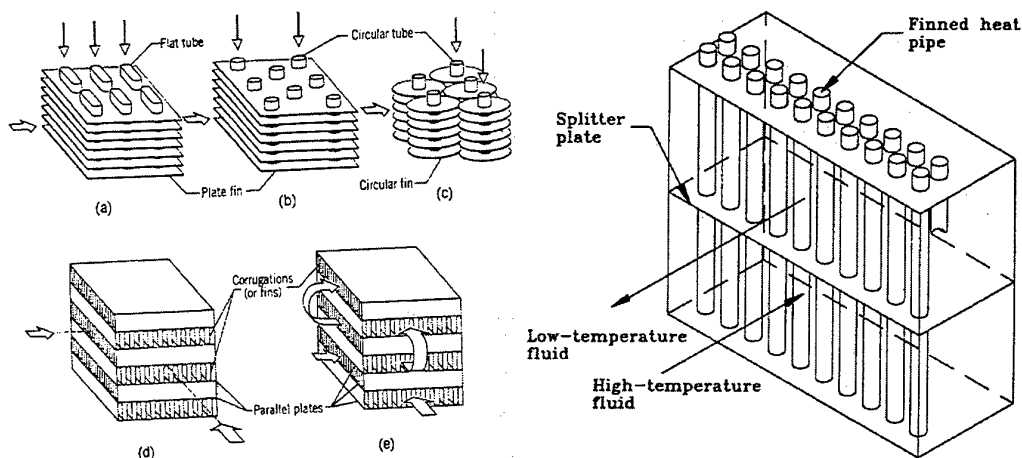


Figure 1. Fin-tube, plate-fin and heat pipe-fin heat exchangers

Impingement jets have been used to achieve enhanced coefficients for heating, cooling, or drying. Applications include tempering of glass plate, annealing of metal sheets, drying of textile and paper products, cooling of gas turbine components, and de-icing of aircraft systems. More recently, impingement jets are used in conjunction with extrusion heat sinks to provide effective cooling of high power chip packages. Many studies have been

conducted to understand the heat transfer enhancement by impinging gas and liquid jets onto various surface configurations [3-5]. Previous applications and studies focused on the single side impingement where a gas or liquid jet impinges onto a surface (from one side) to remove or add heat to that surface. Figure 2 illustrates a typical, single-side impingement heat sink for cooling of electronics.

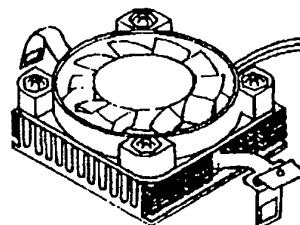


Figure 2. Fan-sink assembly

This paper discusses an innovative, double-side impingement concept that was developed and used by Thermacore, Inc. in a new, HXI series of compact, high performance air-to-air heat exchangers for cooling of electronic cabinets. Principles and advantages of the double side impingement concept are first discussed, which is followed by discussions of the theoretical/design model of the heat exchanger and comparisons with prototype heat exchanger test results. Environmental test results of HXI heat exchangers are also discussed. Finally, procedures of selecting HXI heat exchangers for specific applications are recommended.

2. HXI HEAT EXCHANGER PRINCIPLES AND ADVANTAGES

Figure 3 illustrates the operating principles of a HXI heat exchanger. A folded fin core separates the enclosure inside and outside. A set of inside fans (not shown in Figure 3) draw in the hotter, inside air and blow it toward the fin core. This inside impingement efficiently transfers the heat to the fin core. Similarly, a set of outside fans draw in the cooler, ambient air and blow it toward the outer side of the fin core. This outside impingement efficiently removes the heat from the fin core. The fin core is made of thin material so that the thermal resistance due to heat conduction is negligible. Specially designed core channels and fan housings form the structural frame of the heat exchanger and the NEMA seal between enclosure inside and outside. The double-side air flow impingement technology, along with the structural design and manufacturing techniques, is protected by a pending U.S. patent.

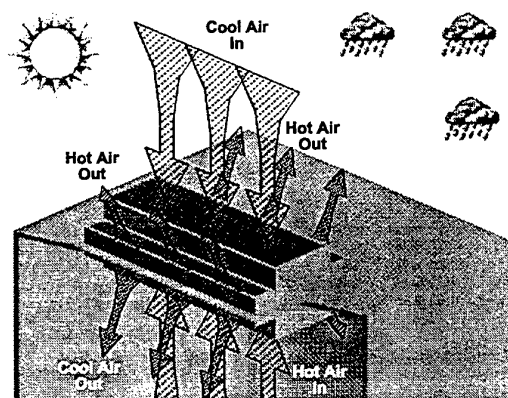


Figure 3. HXI heat exchanger operation

HXI heat exchangers offer five advantages over other types of heat exchangers:

1. Higher heat transfer performance. Double side impingement increases the convective heat transfer coefficient by a factor of 2, compared to counter-flow heat convection. The thin fin core presents negligible thermal resistance, compared to a heat pipe core. Consequently, a HXI heat exchanger offers either improved thermal performance when compared to the same size unit of standard design or reduced heat exchanger size when compared to a standard size unit with the same thermal performance.
2. Lower manufacturing cost. HXI heat exchangers increase thermal performance by using a more efficient, double side impingement flow configuration instead of higher cost blowers or larger size cores. Compared to heat pipe heat exchangers, HXI heat exchangers use fewer components and cost less to manufacture.
3. Higher reliability. Other heat exchangers generally use one high-power blower/fan on each side. Failure of a single fan will cause the entire unit to be non-functional. A HXI heat exchanger uses multiple, lower power fans on each side to improve the reliability and damage resistance. Failure of one fan will reduce the performance but will not cause the entire unit to fail. This is especially beneficial in telecommunication enclosures that may be deployed to remote, less accessible locations.
4. More flexibility in fin material selection. In a HXI heat exchanger, the heat conduction path is across the fin thickness instead of along the fin length/width as in other types of heat exchangers. Therefore, the thermal conductivity of the fin material does not need to be very high, as long as the fin thickness is small. For example, replacing a 0.01" thick aluminum fin core with a plastic fin core results in a <2% performance reduction. This opens the possibility of making all plastic heat exchangers that are light and inexpensive.
5. More tolerant on mechanical/thermal joints. Other types of heat exchangers must transfer heat cross certain joints, which requires the joints to be assembled with materials of high thermal conductivity. HXI heat

exchangers do not have such joints on the heat flow path. The joints in a HXI heat exchanger can be assembled using materials that do not have high thermal conductivity.

Table 1 summarizes the comparisons between HXI heat exchangers and counter flow and heat pipe heat exchangers in terms of dimensions and thermal performance. As shown, HXI heat exchangers outperform counter flow and heat pipe heat exchangers with the comparable dimensions and under the same thermal conditions. HXI-500, 1000 and 1500 refer to heat exchangers with one, two and three pairs of fans, respectively. One pair of fans means one fan on each side of the cabinet inside and outside.

Table 1. Heat Exchanger Comparisons

Product	Dimensions	Performance
HXI-500, double side impingement [6]	14"×10"×7"	0.028W/°C/in ³
HE Series, heat pipe core [7]	29"×10"×3"	0.020W/°C/in ³
HXI-1000, double side impingement [6]	24"×14"×7"	0.021W/°C/in ³
HE Series, heat pipe core [7]	24"×19"×9"	0.012W/°C/in ³
KX Series, counter flow [8]	41"×15"×7"	0.011W/°C/in ³
HXI-1500, double side impingement [6]	24"×14"×7"	0.029W/°C/in ³
KW Series, counter flow [8]	39"×21"×14"	0.006W/°C/in ³

3. THEORETICAL MODEL AND PROTOTYPE TEST RESULTS

Figure 4 shows the domain and coordinates for the theoretical model of a HXI-500 heat exchanger. For heat exchangers with multiple pairs of fans (such as HXI-1000 and HXI-1500), the thermal performance (heat transfer rate) can be calculated by multiplying the HXI-500 performance by the number of fan pairs. The air flow pressure drop is independent of the number of fan pairs.

Each fan can be treated as a round nozzle. The air impingement Nusselt's number can be calculated as [9]:

$$Nu_{\text{impinge}} = Pr^{0.42} \left[2A_r^{1/2} \frac{1 - 2.2A_r^{1/2}}{1 + 0.2(H/D - 6)A_r^{1/2}} \right] \left[2Re_{\text{impinge}}^{1/2} \left(1 + 0.005Re_{\text{impinge}}^{0.55} \right)^{1/2} \right] \quad (1)$$

where Pr , A_r and Re_{impinge} are the air Prandtl number, impingement jet coverage area ($L \times S$) and impingement Reynolds number, respectively. The impingement heat transfer coefficient can be calculated as:

$$h_{\text{impinge}} = Nu_{\text{impinge}} \frac{k}{D} \quad (2)$$

where k is the air thermal conductivity. The impingement thermal conductance is calculated as:

$$U_{\text{impinge}} = h_{\text{impinge}} A_r \quad (3)$$

After impingement, the air flows inside the fin channels towards the exhaust areas. The air flow inside the channels is usually a laminar flow and the Nusselt's number is a constant depending on the channel cross-sectional dimensions. Reference [1] provides a list of Nusselt's numbers for laminar flows in various channels. The air flow thermal conductance can be calculated as:

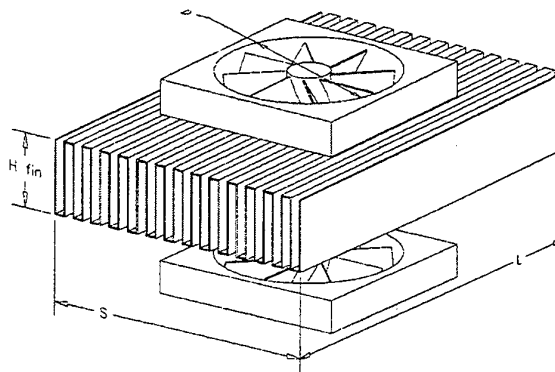


Fig 4. Impingement heat exchanger theoretical model domain and coordinates

$$U_{\text{flow}} = h_{\text{flow}} A_{\text{fin}} \quad (4)$$

where h_{flow} and A_{fin} are the air flow heat transfer coefficient and fin surface area. The fin surface area, A_{fin} , is:

$$A_{\text{fin}} = LH_{\text{fin}}(N_{\text{fin}}S) \quad (5)$$

where H_{fin} and N_{fin} are the fin height and number of fins per inch, respectively.

The total thermal conductance of one side of the heat exchanger is:

$$U_{\text{one_side}} = U_{\text{impinge}} + U_{\text{flow}} \quad (6)$$

Assuming the two sides of the heat exchanger are identical, the overall heat exchanger thermal conductance is:

$$U_{\text{overall}} = \frac{1}{\frac{1}{U_{\text{one_side}}} + \frac{\delta_{\text{fin}}}{k_{\text{fin}} A_{\text{fin}}} + \frac{1}{U_{\text{one_side}}}} \quad (7)$$

where δ_{fin} and k_{fin} are fin material thickness and thermal conductivity, respectively.

The heat transfer rate of the heat exchanger can be calculated as:

$$Q = U_{\text{overall}} \Delta T_m \quad (8)$$

where ΔT_m is the log mean temperature difference between the two air streams and can be calculated as:

$$\Delta T_m = \frac{(T_{h,i} - T_{c,i}) - (T_{h,o} - T_{c,o})}{\ln \left(\frac{T_{h,i} - T_{c,i}}{T_{h,o} - T_{c,o}} \right)} \quad (9)$$

where $T_{h,i}$, $T_{h,o}$, $T_{c,i}$ and $T_{c,o}$ are inlet and outlet temperatures of the hot and cold air streams, respectively.

The air pressure drop consists of three major portions caused by impingement, friction and exhaust. The impingement pressure drop is due to the 90° change in air direction, which can be calculated as:

$$\Delta P_{\text{impinge}} = \frac{1}{2} \rho_{\text{air}} \left(\frac{V_{\text{air}}}{\frac{\pi D^2}{4}} \right)^2 \quad (10)$$

where V_{air} is the air flow rate which should be determined by the total pressure drop according to the fan performance curve (see Figure 5 for the performance curve of a specific fan).

The friction pressure drop is due to the friction between the air flow and the fin surfaces and can be calculated as:

$$\Delta P_{\text{friction}} = \frac{1}{2} \rho_{\text{air}} \left(\frac{V_{\text{air}}}{\frac{1}{N_{\text{fin}}} H_{\text{fin}}} \right)^2 \left(\frac{\frac{L}{2}}{2 \left(\frac{1}{N_{\text{fin}}} + H_{\text{fin}} \right)} \right) f \quad (11)$$

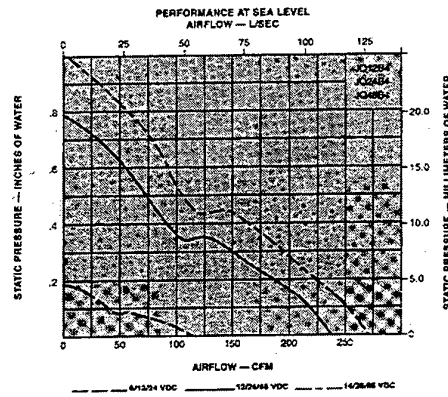


Figure 5. Fan performance curve

where f is the frictional factor that can be estimated as $64/Re_{flow}$ for laminar flows. The air flow Reynolds number is based on the air velocity inside the fin channels and the fin channel cross sectional hydraulic diameter.

The exhaust pressure drop is due to the 90° change in air flow direction and can be calculated as:

$$\Delta P_{\text{exhaust}} = \frac{1}{2} \rho_{\text{air}} \left(\frac{V_{\text{air}}}{\frac{S}{N_{\text{fin}}} H_{\text{fin}}} \right)^2 \quad (12)$$

The above equations along with the fan performance curve (Figure 5 as an example) were implemented in MathCAD for investigation of effects of design parameters including N_{fin} , L , S and V_{air} , etc. Several prototype heat exchangers were designed using the model and tested to verify the model predictions, which is summarized in Table 2.

Table 2. Prototype Heat Exchanger Designs and Performance

	HXI-500	HXI-1000	HXI-1500
Heat exchanger core width (S)	7 inches	10 inches	21 inches
Heat exchanger core height (H_{fin})	2 inches	2 inches	2 inches
Number of fins (N_{fin})	12 fins per inch	12 fins per inch	12 fins per inch
Plenum height (H)	0.5 inch	0.5 inch	0.5 inch
Number of fan pairs	1	2	3
Fan diameter (D)	6 inches	6 inches	6 inches
Fan performance curve	See Figure 5	See Figure 5	See Figure 5
Predicted heat transfer performance (@ 20°C rise above ambient)	500 W	1000 W	1200 W
Measured heat transfer performance (@ 20°C rise above ambient)	470 W	1050 W	1250 W

Table 2 indicates that the theoretical model accurately predicted the performance of double-side impingement heat exchangers. The maximum deviation is within 10%.

4. HXI HEAT EXCHANGER ENVIRONMENTAL TESTING

Figure 6 shows photographs of three standard, double side impingement air-to-air heat exchangers that are presently manufactured by Thermacore: the HXI-500, 1000 and 1500 series. A total of five different power options are offered: 12, 24 and 48VDC, and 110 and 220VAC. Other optional features include the outdoor package and temperature based fan speed controller and air heater.

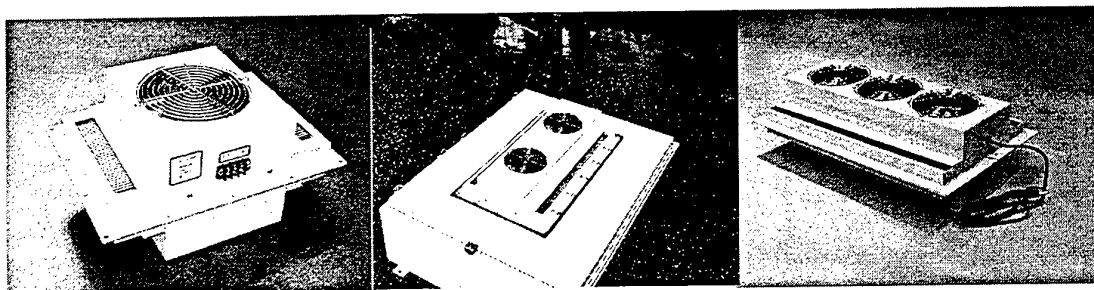


Figure 6. Photographs of HXI-500, 1000 and 1500 heat exchangers

This section summarizes the environmental test results conducted to qualify HXI-heat exchangers (with outdoor packages) for use in various environmental conditions. The environmental tests include Hose-Down Test, Weather Tightness (blowing dust) Test and Salt Fog Corrosion Resistance Test.

The Hose-Down Test was conducted by the Technology Center of Thermacore, Inc. according to NEMA (National Electrical Manufacturers Association) Standards, Section 6.7, for NEMA 4 enclosures. The test sample was a HXI-1000, 230VAC unit. Figure 7 is a photograph of the heat exchanger being tested. The results of three Hose-Down Tests are summarized below.

Test No.	Flow rate	Water inside cabinet
1	75 GPM	0 cc
2	65 GPM	0 cc
3	80 GPM	0 cc

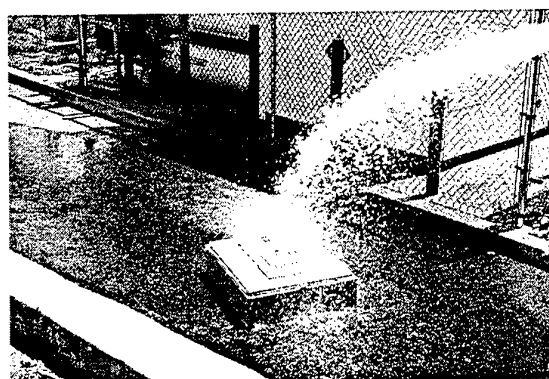


Figure 7. HXI-1000 during Hose-Down Test #3

The Weather Tightness Test was conducted by Marconi Aerospace Electronic Systems, Inc. according to Military Standards, MIL-STD-810E, Method 510.3. Figure 8 is a photograph of the test setup. A HXI-1000 48VDC unit was tested for a total of eighteen hours exposure to blowing dusts. The unit was powered during the last six hours of testing.

No anomalies were observed. All functional testing was reported to be satisfactory. Following exposure, an internal visual inspection of the enclosure revealed no dust penetration through the seal or through the body of the heat exchanger.

The Salt Fog Corrosion Resistance Test was conducted by Marconi Aerospace Electronic Systems, Inc. according to BELLCORE Standards, Section 3.35. A HXI-500 48VDC unit was tested in the salt fog chamber for fourteen consecutive days. The heat exchanger was powered from the start of the test. A Datalogger was used to monitor the time of any fan failure. A synopsis of the test is given below.

Date	Time	Activity/Comments
04/28/99	11:00	Start of test
05/06/99	08:35	One fan stopped operating
05/12/99	13:45	End of test
05/13/99	10:00	Post test inspection

Visual observations after the unit was exposed to salt fog for 14 days:

- No degradation noted.
- Both fans operated properly when 48VDC applied.

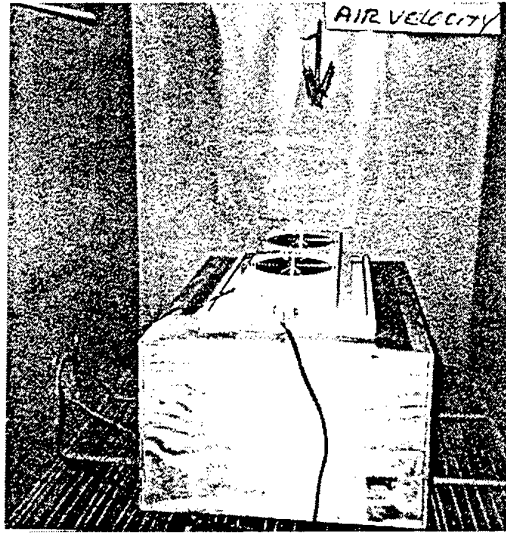


Figure 8. Blowing dust test setup

5. HXI HEAT EXCHANGER SELECTION PROCEDURES

The selection of HXI heat exchangers is application dependent. This section discusses the principles that can be used to select a HXI heat exchanger. Four groups of parameters are required for selecting a HXI heat exchanger:

- (1) Enclosure dimensions including enclosure width, depth and height.
- (2) Maximum heat generation by electronics inside enclosure, Q .
- (3) Maximum enclosure inside air temperature allowed by electronics, T_i .
- (4) Maximum ambient air temperature, T_o .

The following five steps can be used to select a HXI heat exchanger:

Step 1. Determine Heat Dissipation Through Enclosure Surfaces

The heat dissipation through enclosure surfaces is proportional to the enclosure surface area and the temperature difference between enclosure inside and ambient. Assuming natural convection between the enclosure and the

ambient air, the heat dissipation can be estimated as $Q_{\text{loss}} = \left(0.25 \frac{\text{watt}}{\text{m}^2\text{°C}}\right) \cdot A \cdot (T_i - T_o)$, where the enclosure

surface area A is calculated from the enclosure dimensions. The above equation assumes no air circulation inside the enclosure. If there is an internal air circulation, the heat dissipation through the enclosure surfaces should be

calculated as $Q_{\text{loss}} = \left(4.2 \frac{\text{watt}}{\text{m}^2\text{°C}}\right) \cdot A \cdot (T_i - T_o)$.

Step 2. Determine Solar Load (For Outdoor Applications Only)

According to Bellcore standards, solar load can be estimated as $Q_{\text{solar}} = \left(753 \frac{\text{watt}}{\text{m}^2}\right) \times A_{\text{top}}$, where A_{top} is the

top surface area of the enclosure. If a double wall design is used for the enclosure top surface, the solar load is negligible.

Step 3. Determine Total Heat Load on Heat Exchanger

The total heat load on heat exchanger is $Q_{\text{total}} = Q - Q_{\text{loss}} + Q_{\text{solar}}$. If $Q_{\text{total}} \leq 0$ watts, there is no need to use

a heat exchanger. The heat generated by electronics and the solar load are being dissipated through the enclosure wall.

Step 4. Determine Heat Exchanger Operational ΔT

The ΔT across the heat exchanger is the temperature difference between the enclosure inside and the ambient:
 $\Delta T = T_i - T_o$.

Step 5. Choose HXI heat Exchangers According to Total Heat Load and ΔT

With the total heat load (Q_{total}) and operational temperature difference (ΔT) known, the heat exchanger can be determined by looking at the performance curves of the HXI heat exchangers. Figure 9¹ shows performance curves of HXI-500, 1000 and 1500. Each performance curve indicates the heat exchanger's heat dissipation capability at a given operational ΔT . If the total heat load exceeds one HXI heat exchanger's capability, a larger unit or multiple heat exchangers will need to be used.

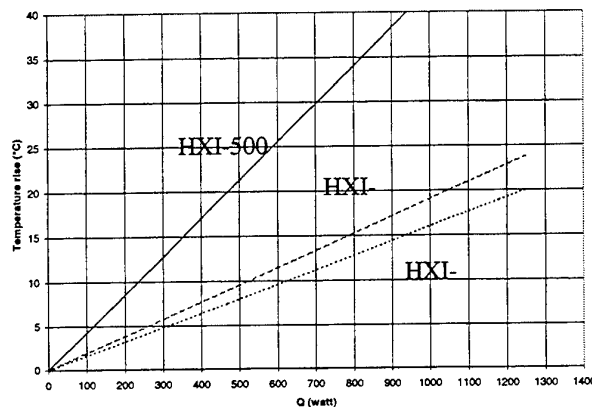


Figure 9. HXI heat exchanger performance

ACKNOWLEDGEMENT

Mr. Jay P. Weaver, of Thermacore, provided technician supports to prototype heat exchanger fabrication and testing. He also provided supports to transition of the heat exchanger design to production.

REFERENCES

1. F. P. Incropera and D. P. DeWitt, *Fundamentals of Heat and Mass Transfer*, 3rd edition, John Wiley & Sons, pp642 (1990)
2. A. Faghri, *Heat Pipe Science and Technology*, Taylor & Francis, pp678 (1995)
3. A.H. Beitelmal, M.A. Saad, C.D. Patel, "Heat Transfer by Air Jet Impinging Obliquely on a Flat Surface", *Proceedings of 1998 ASME International Mechanical Engineering Congress and Exposition*, Anaheim, CA, (1998)
4. V.P. Schroeder and S.V. Garimella "Heat Transfer from a Discrete Heat Source in Confined Air Jet Impingement", *Proceedings of 1998 ASME International Mechanical Engineering Congress and Exposition*, Anaheim, CA, (1998)
5. V.P. Schroeder and S.V. Garimella "Heat Transfer in the Confined Impingement of Multiple Air Jets", *Proceedings of 1998 ASME International Mechanical Engineering Congress and Exposition*, Anaheim, CA, (1998)
6. *HXI Series Low Profile Heat Exchangers*, Thermacore Data Sheet, 1998
7. *Heat Exchanger Catalog*, McLean Midwest, 1998
8. *Heat Exchanger Catalog*, Kooltronics, 1998
9. H. Martin, "Heat and Mass Transfer between Impinging Gas Jets and Solid Surfaces", *Advances in Heat Transfer*, Vol.13, Academic Press, New York (1977)

¹ Based on test results using an INSULATED 38" × 36" × 24" cabinet

EVAPORATIVE HEAT TRANSFER IN HORIZONTAL TUBES WITH STRIP-TYPE INSERTS USING REFRIGERANT-600A

Shou-Shing Hsieh, Kuen-Jang Jang and Yao-Chun Tsai

Department of Mechanical Engineering

National Sun Yat-Sen University

Email: sshsieh@mail.nsysu.edu.tw; Fax: (886)-7-525-4299; Tel: (886)-7-525-2000/4215

Keywords: evaporative heat transfer, horizontal tubes, strip-type inserts, R-600a

ABSTRACT. Results of a study on saturated boiling heat transfer of refrigerant R-600a in horizontal tubes (ID=10.6 mm) with strip-type inserts (longitudinal strip LS and cross-strip CS Inserts) are reported. Local heat transfer coefficients are measured for a range of heat flux (3.86~90 kW/m²), mass velocity (82.3~603.3 kg/m²s), and equilibrium mass quality (≤ 0.8) and the influences were studied. The data were compared with the performance of the corresponding smooth tubes. Enhancement performance ratios are also presented and discussed. Finally, correlations were developed for the evaporation heat transfer coefficients and friction factors for horizontal tubes with strip-type inserts with/without holes using R-600a.

1. INTRODUCTION

A lot of work has been carried out to obtain an understanding of boiling heat transfer from a smooth surface. These fundamental studies clearly brought out the complexities of the flow boiling mechanisms [1]. At present, many aspects of boiling heat transfer on a smooth surface are well explored and reasonably good correlations have been developed for the design of efficient heat exchange equipment. However, there are many saturated flow boiling correlations (over 30) in the literature. Some of the well-known correlations were summarized by Kandlikar [2,3]. With enhanced surfaces, boiling heat transfer is more complicated. Due in part to this complexity, heat transfer in horizontal tubes with strip-type inserts has received less attention than that in smooth tube annuli. The lack of design data for heat transfer coefficients, especially in flow boiling, is now one of the limitations in the design of efficient evaporators for use in the refrigeration and process industries [4].

Numerous test data for flow boiling of new refrigerants are now becoming available in the literature. Using ten electrically heated test sections in series, Hambraeus [5] measured local heat transfer coefficients for R-134a with vapor quality range from 0.1 to 1.0. Wattelet et al. [6] measured heat transfer coefficients rise noticeably with increasing vapor quality while the stratified-wavy data are flat.

Several comprehensive studies have been performed on microfinned tubes [7]. Schlager et al. [8] measured three 12.7 mm OD micro-fin tubes having different helix angles (15 to 25°), the average heat transfer coefficients in the micro-fin tubes, based on a nominal equivalent smooth tube area, were 1.6 to 2.2 times higher than those in smooth tubes. Singh et al. [9] conducted flow boiling observation of R-134a in a microfin tube and showed that at the mass velocity of 100 kg/m²s, a transition from a stratified to annular flow occurred. Recently, Liu [10] experimentally measured the evaporation heat transfer coefficients of R-134a and compared the corresponding values of R-22. This work is a continuation of our previous study regarding evaporative heat transfer and enhancement performance of serpentine tube with strip-type inserts using R-134a [11]. In that paper, the influence of mass velocity, heat flux, and insert type on pressure drop and heat transfer characteristics in a serpentine tube were examined. It was found that flow nucleate boiling is enhanced in terms of a lower wall superheat being required for incipient boiling, and a great number of more stable bubbles exist than in smooth tube. Moreover, the gradual suppression of the nucleation mechanism reduces the heat transfer coefficients with increasing quality.

Although many past studies have examined in-tube evaporative heat transfer enhancement and the associated pressure drop with internally finned tubes. In-tube evaporations with strip-type inserts using R-600a as refrigerant have not been conducted. In addition, the fundamental phenomenon of nucleate boiling from a heated wall subject to a strip-type insert is as yet not well understood for the flow in a horizontal tubes. Attention was given to the heat transfer enhancement as well as pressure drop measurement and to the influences of nucleate flow boiling on the test tubes. Different cases in terms of varied insert type horizontal tubes were tested. To accomplish these tasks, experiments were performed in a horizontal test tube with

longitudinal strip and cross-strip type inserts, 10.6mm inside diameter with refrigerant-600a(R-600a) as the boiling fluid.

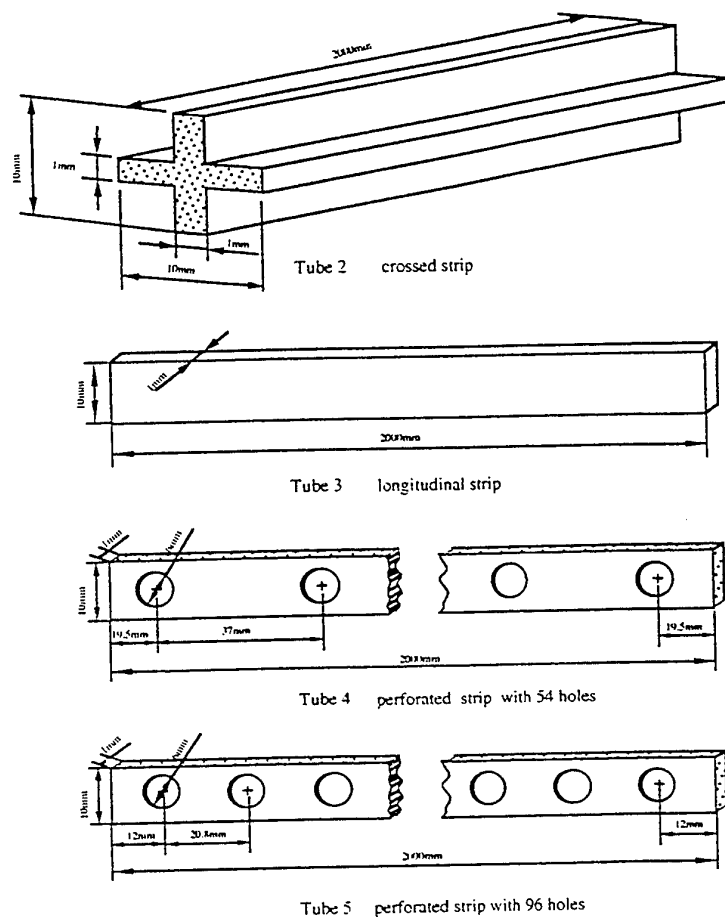


Fig. 1. The geometry of the inserts in present study

In this paper, several correlations related to saturated flow boiling in horizontal tubes with strip-type inserts perforated holes (see Fig. 1 for details) with/without with R-600a will be developed. Over the last few years a large data bank for saturated and subcooled flow boiling in tubes and annuli have been made to fit correlations that cover all the data. In spite of the aim to reduce the number of physical properties required in the correlations and to extend the range of applicability as well as to different types of fluid and to both saturated and subcooled boiling, such correlations are still unavailable in horizontal tubes with inserts.

2. EXPERIMENTAL APPARATUS AND TEST CHANNEL

The heat transfer test apparatus is shown schematically in Fig. 2. It is a closed-loop system that includes a gear pump with variable speed drive, a rotameter, a set of condensers, a preheater, a turbine flowmeter, receiver, water bath and a sight-glass. The liquid receiver allows for stable control of system pressure. The size of the turbine flowmeter was chosen to a certain range of flow rates, from 82.3 to 603.3 kg/ m²s and calibrated with a weighting-technique with stop watch. The estimated uncertainty in measurement of flow rate was ± 1.26 percent.

The test section is also shown schematically in Fig. 2 and consists of a horizontal tube flow channel. It is a copper tube ($k=386$ W/mk) with a total heated length of 2000 mm, and outside and inside diameters of 12.7 mm and 10.6 mm, respectively. Inlet and outlet pressures were measured with a piezo resistive-type transducer, respectively, and differential pressure at a 500mm interval each across the channel is measured with a strain-gage-type transducer. The pressure transducers were calibrated against a known method. The estimated uncertainty in the pressure measurements were $\pm 3.5\%$. Heating was provided by conducting direct current

through electric wire packed into the tube. A two-walled structure(MgO + quartz) was sandwiched between the copper tube and the electric wire as an electrical shield. Quartz was used as an electrical insulation. MgO can distribute heat energy uniformly.

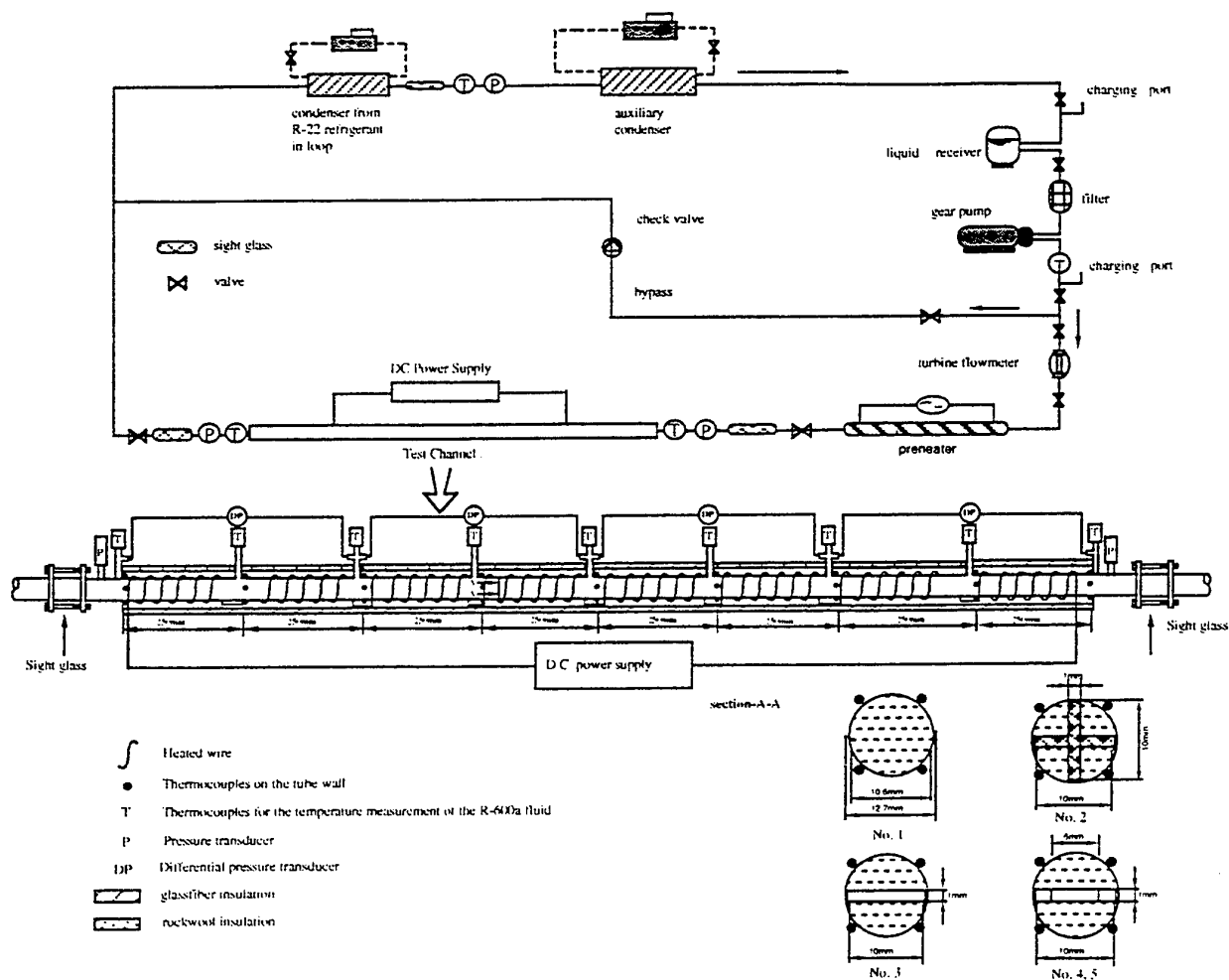


Fig. 2. Schematic of test apparatus and experimental setup

The pre-evaporator preheated R-600a to saturation(within $\pm 0.3^{\circ}\text{C}$). As R-600a flowed through the test section, it was uniformly heated by dc power, provided by a 100v, 550-amp capacity dc rectifier. After exiting the test section, R-600a passed to the R-22 cooled condenser, where it was condensed and subcooled prior to being returned to the pump to complete the circuit.

Intermediate bulk fluid temperatures were obtained by measuring wall temperature at a certain distance (250mm each) along downstream locations(see Fig. 2 for details) with 40 gage Cu-Cn thermocouple through a correction (explained later in the forthcoming section). The wall temperature was measured by four thermocouples circumferentially spaced (90° apart) at these axial downstream locations and an average value was used to calculate the local heat transfer coefficient. The soldering point of the thermocouples to the tube wall was less than 1mm in diameter. It is estimated that the temperature were accurate to within $\pm 0.2^{\circ}\text{C}$. A detailed cross sectional view of the thermocouple setup designed for more accurate temperature measurements was also shown in Fig. 2. Based on calibration of the entire temperature measurement system, including thermocouple and digital voltmeter, the error associated with the temperature data was estimated to be $\pm 0.5^{\circ}\text{C}$. Table 1 shows the ranges of variables over which the experiments were conducted and the associated measurement uncertainties. The error reported in this paper is the absolute value of the maximum expected deviation for the all test runs.

Table 1. Parameters and Measurement Uncertainties

Refrigerant	R-600a				
Single-Phase Forced Convection					
Re	7000~30000				
Boundary Condition	1. Uniform heat flux --- heat transfer coefficient 2. Adiabatic condition --- pressure drop				
Two-Phase Saturated Flow Boiling					
$g(\text{kg/s}\cdot\text{m}^2)$	83, 166, 239, 356, 475, 602				
$q(\text{kw/m}^2)$	9.1, 17.8, 27.6, 31.2				
Quality	0.005 ~ 0.863				
Evaporative temperature	$T_{\text{sat}} = 6^{\circ}\text{C}$				
Test Tube Characteristics					
Tube (No.)	1	2	3	4	5
Tube Type	Smooth	Crossed strip insert	Strip insert	Perforated strip (a)	Perforated strip (b)
Inside diameter (D_i), mm	10.6	10.6	10.6	10.6	10.6
Inside diameter (D_o), mm	12.7	12.7	12.7	12.7	12.7
Hydraulic diameter (D_h), mm	10.6	4.25	6.09	6.35	6.54
Heated length (L), m	2	2	2	2	2
Number of perforation	0	0	0	54	96
Nominal area ($A=\pi D_i L$), m^2	0.0666	0.0666	0.0666	0.0666	0.0666
Internal surface area (A_s), m^2	0.0666	0.1306	0.1026	0.1	0.099

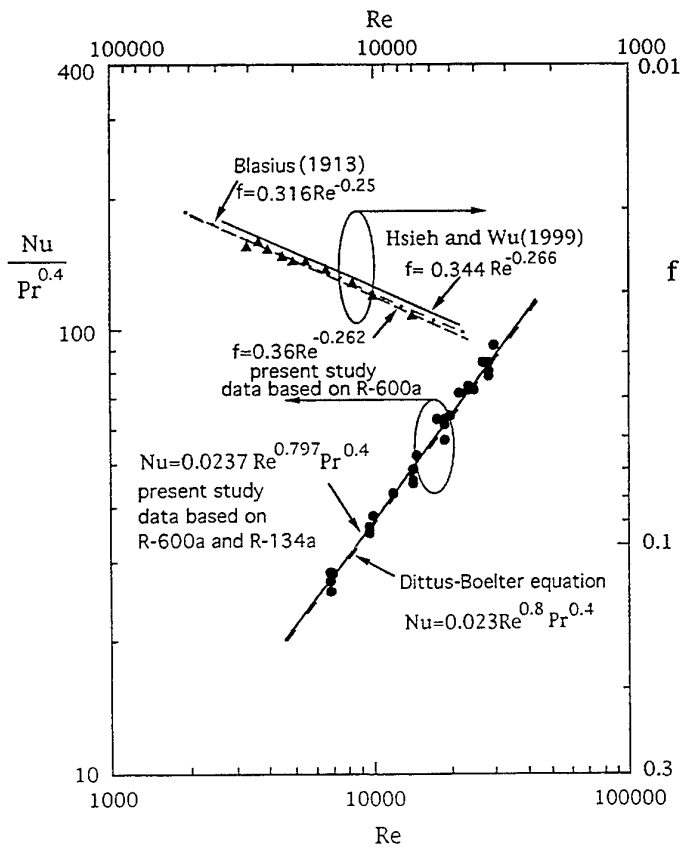


Fig. 3. The measured single-phase heat transfer and pressure drop test

The measured single-phase heat transfer as well as pressure drop approach the well known Dittus-Boelter correlation [12], and Blasius, and Hsieh and Wu(1999) [13] well within $\pm 8.2\%$ and $\pm 9.7\%$ for Nu and f , respectively as shown in Fig. 3. As mentioned earlier, heat loss from the test channel, including end losses, under flow condition was determined as the ratio of the heat flux determined from the liquid enthalpy change divided by the heat flux calculated from the electric power input. The ratio is found to be about 0.91, following by Wambsganss et al. [14]. It was subsequently used to determine the input heat flux for flow boiling experiments.

3. RESULTS AND DISCUSSION

The experimental runs are summarized in Table 2. The flow boiling tests were performed at selected values of mass velocity of 83, 166, 239, 356, 475, and 602 kg/ m²s. The fluid entered the test section as saturated liquid in all tests. The experimental heat flux range from 9.1 to 3.1 kW/ m².

Table 2. Experimental Runs and Test Tube Characteristics of Present Study

Parameters	Uncertainty
Mass velocity, G	$\pm 1.26\%$
Heat flux supplied to test section, q	$\pm 5.15\%$
Heat supplied to the pre-evaporator, Q_p	$\pm 1.01\%$
Average pressure over the test section, \bar{P}	$\pm 0.38\%$
Temperature, T	$\pm 0.1^\circ\text{C}$
Local heat transfer coefficient, h	$\pm 12.86\%$
Two phase friction factor, f_{TP}	$\pm 8.90\%$

Flow Pattern Identification

Application of the flow pattern maps to predict quality at the transition to annular flow indicated that annular flow generally did not start until qualities of 0.6 to 0.8. Figure 4(a) shows the flow pattern map following Taitel and Dukler [16] for the present flow boiling in smooth tubes. It clearly shows that all the tests under study seem in annular and stratified-wavy flow regime. The majority of the boiling data from the smooth tubes used in the present study falls into the annular region, with only a few measurements also falling into stratified-wavy and intermitted flow (slug + plug) pattern regions.

The corresponding plot as shown in Fig. 4(b) shows the local heat transfer coefficient plotted versus vapor quality raises rapidly as its evaporating liquid film thins as $x \geq 0.5$. In the stratified-wavy flow regime ($x < 0.5$), the trend in heat transfer coefficient versus vapor quality is an extension to that for annular flow, where it is termed "partial nucleate boiling," and both forced convection and nucleate boiling are significant. The gradual suppression of the latter leads to a temporary reduction of the local heat transfer coefficients. Later, they will increase until finally merging into a single line with increasing vapor quality, in annular flow regime where is also termed forced convection vaporization region. The map also indicates the influence of stratification at low flow rates (i.e., $G \leq 166$ kg/ m²s) in the present smooth tubes. The visual observation (not shown here) of the flow though the sight glass indicated that for mass velocities less than 166 kg/ m²s, the flow was predominantly stratified, but as the mass velocity increased the flow became annular. The 166 kg/ m²s mass velocity represents the transition value from stratified-wavy flow to annular for the smooth tube studied herein. Although such a plot was made only for smooth tube, the same situation would still expect for tubes with inserts except for the demarcation point (e.g. $x_o = 0.5$ for smooth tube; $x_o < 0.5$ for inserted tubes).

Heat Transfer Results and Augmentation

The effect of tubes with inserts on heat transfer coefficients are shown in Fig. 5 for six different mass velocities at a given heat flux. In general, an increase in mass velocity increases the heat transfer coefficients for all the qualities plotted. For smooth tubes at $G \leq 356$ kg/ m²s, the heat transfer coefficients were observed to be nearly independent of the quality due to the present cases in nucleate boiling. In fact, the data of Figs. 4(b) and 5(a) show dominance of the nucleation mechanisms by virtue of the heat flux dependence and mass velocity independence of the data. In contrast, for tubes with inserts and perforated holes, an increase in the quality increases the heat transfer coefficients for all the mass velocities considered herein. This is because the flow in

the tubes with inserts was in forced convective boiling in which the heat transfer coefficients would increase as the mass velocity increases.

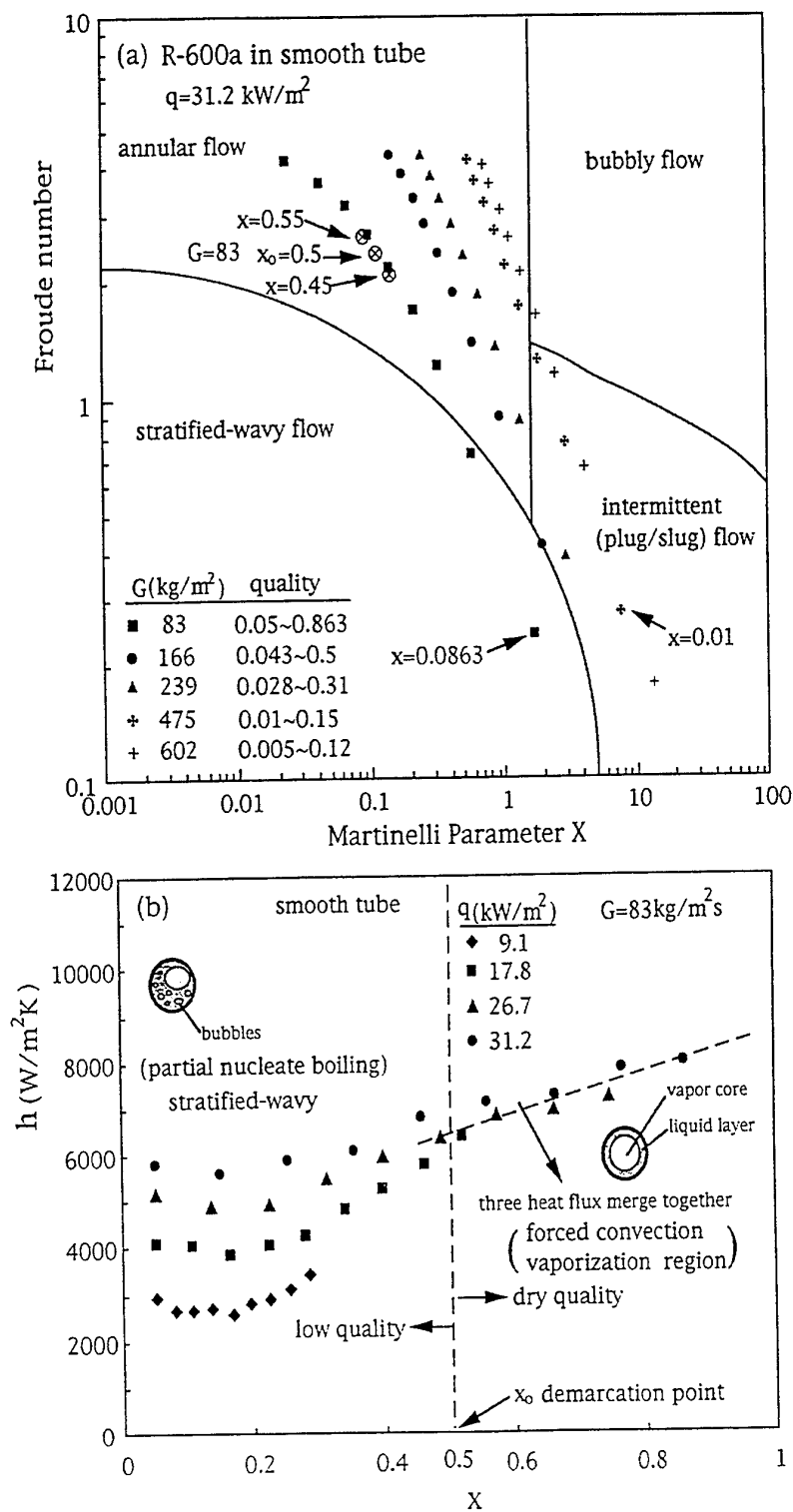


Fig. 4. Flow pattern map and h vs x for different q and G

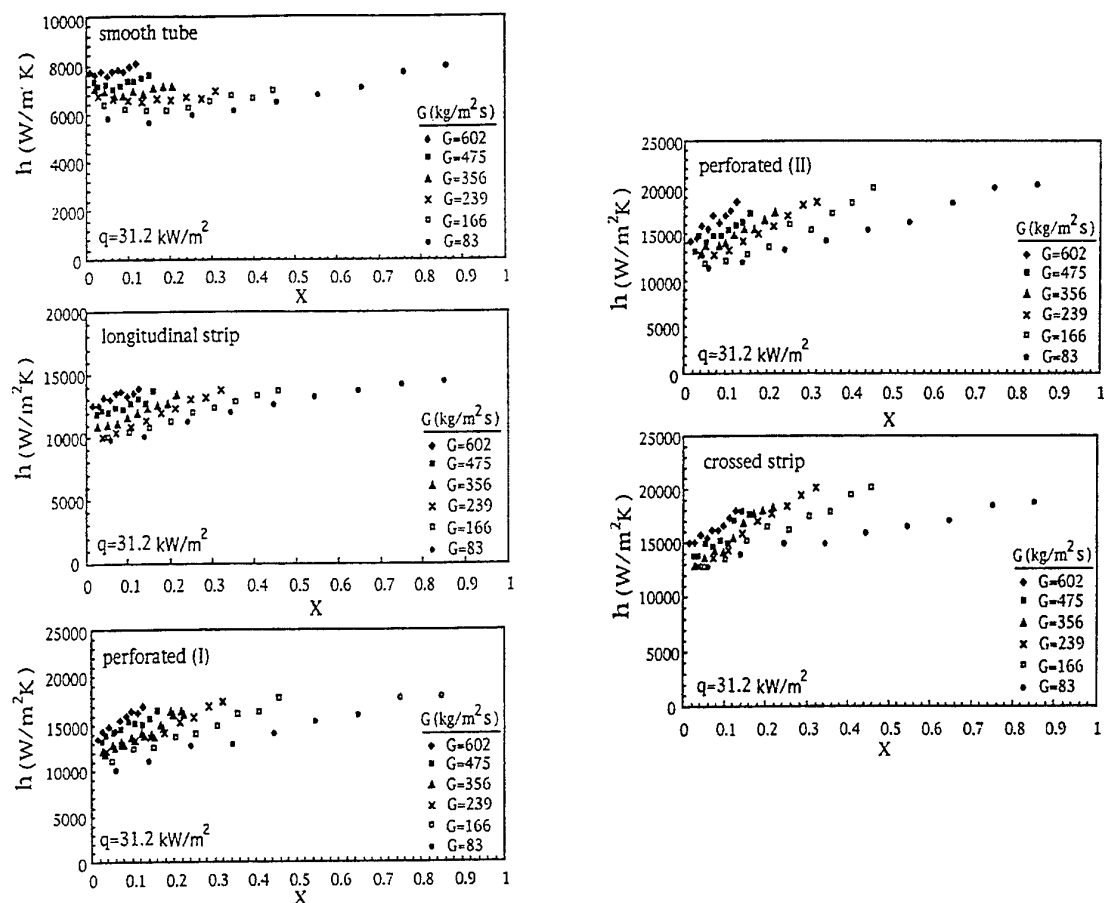


Fig. 5. h versus x for different G at $q=31.2 \text{ kW/m}^2$

Taking a closeup examination of Fig. 5, it is found that the heat transfer coefficient did increase with increasing mass flux at a fixed local mass quality but to a lesser degree than was observed for the smooth tube as evidenced from Fig. 5(a). On the other hand, in spite of the independence of heat flux on h in forced convection vaporization region, the local h depends strongly on the mass flux and the quality as shown in Fig. 5(b)-(e). It is long recognized that heat transfer coefficients are more dependent on heat flux in regions of lower quality ($x < 0.5$), which represents a nucleate boiling region, as compared to a higher quality, which represents a forced convection vaporization region. However, this situation becomes less noted for the tubes with inserts. This indicated that an earlier onset of forced convection vaporization can occur with the inserted tubes as mentioned earlier. At $q=31.2 \text{ kW/m}^2$, the heat transfer coefficients dip (however, not found in the inserted tubes) at a certain quality ($0 < x < 0.1$) and then increase approximately linear with quality with a slow increase rate especially for the smooth tubes. This is because a part of the formed vapor bubbles in the core condense again and the liquid is thereby set into oscillatory motion, which leads to an increase in the heat transfer with the quality. This finding is similar to that of Hsieh et al.. Among four tubes with inserts the tube with crossed strip insert and longitudinal strips with perforated holes have higher heat transfer coefficients at $0 \leq x \leq 0.84$ for all the mass velocities considered under study.

4. CONCLUSION

The present experimental study of saturation flow boiling in five different tubes with / without strips inserts and perforated holes has made it possible to examine for the first time the effect of a number of parameters. The influence of mass flux, heat flux, and type of insert to heat transfer characteristic was examined and discussed. It is found that flow boiling is enhanced in terms of more and stabler bubbles from perforated tubes than from a

tube with strip insert. The present study was in nucleate boiling ($x < 0.5$) and forced convection vaporization regions ($0.5 \leq x \leq 0.84$), respectively depending on the heat flux level. Moreover, the results strongly suggested that the influence due to perforated holes is more pronounced and dominant in forced convection vaporization than that in nucleate boiling region.

NOMENCLATURE

A	cross sectional area of bare tube / or nominal area	Q	electric heat input
D_i	tube inner diameter	P	pressure
D_o	tube outer diameter	q	heat flux
G	mass velocity (flux)	Re	Reynolds number
h	local heat transfer coefficient	Subscripts	
T	temperature	a	enhanced tube
X	Martinelli parameter	h	hydraulic
x	vapor quality	i	inner
x_o	demarcation point vapor quality	o	outer
L_H	heated length	s	smooth tube / surface area

REFERENCES

- 1 J. G. Collier, *Convective Boiling and Condensation*, 2nd ed., McGraw-Hill (1981).
- 2 S. G. Kandlikar, "An Improved Correlation for Predicting Two-Phase Flow Boiling Heat Transfer Coefficient in Horizontal and Vertical Tubes", *Int. Heat Exchangers for Two-Phase Flow Applications*, ASME, New York (1983).
- 3 S. G. Kandlikar, *ASME Journal of Heat Transfer* v.112, pp.219-228 (1990).
- 4 J. R. Thome, *Enhanced Boiling Heat Transfer*, Hemisphere Publishing Corporation (1990).
- 5 K. Hambræus, *Int. J. Refrigeration* v.64, pp.357-362 (1991).
- 6 J. P. Wattelet, J. G. Chato, A. L. Souza, and B. R. Christofferson, *ASHRAE Trans.* v.100, pp.603-615 (1992).
- 7 M. Ito, and H. Kimura, *Bull. Jap. Social Mech. Eng.* v.24, pp.1600-1601 (1979).
- 8 L. M. Schlager, M. B. Pate, and A. E. Bergles, *ASME Journal of Heat Transfer* v.112, pp.1041-1045 (1990).
- 9 A. Singh, M. M. Ohadi, and E. Dessiatoun, *ASME Journal of Heat Transfer* v.118, pp.497-499 (1991).
- 10 X. Liu, *J. of Heat Transfer* v.119, pp.158-163 (1997).
- 11 S. -S. Hsieh, K. -J. Jang, and M. -T. Huang, "Evaporative Heat Transfer and Enhancement Performance of Serpentine Tube with Strip-type Inserts Using Refrigerant-134a", (To appear in *ASME Journal of Heat Transfer*) (1999).
- 12 F. W. Dittus, and L. M. K. Boelter, *Publications on Engineering* v.2, pp.443 (1930).
- 13 S. -S. Hsieh, and F. -Y. Wu, "Turbulent Heat Transfer and Flow Characteristics in a Horizontal Circular Tube with Strip-Type Inserts: Part I – Hydrodynamics", (Submitted to *ASME Journal of Heat Transfer* for publication) (1999).
- 14 M. W. Wambsganss, D. M. France, J. A. Jendrzejczyk, and T. N. Tran, *ASME Journal of Heat Transfer* v.115 pp.963-972 (1993).
- 15 Y. Taitel, and A. E. Dukler, *AIChE J.* v.22, pp.47-55 (1976).

P. Air-Conditioning and Refrigeration

NUMERICAL STUDY ON A VAPOR FLOW WITH NON-ABSORBABLE GAS IN THE EVAPORATOR-ABSORBER OF AN ABSORPTION CHILLER

Hiroshi Suzuki

Graduate School of Science and Technology, Kobe University
Email: hero@cx.kobe-u.ac.jp; Fax: +81-(78)-803-5346

Tomofumi Yamanaka

Graduate School of Cultural Studies and Human Science, Kobe University
Email: CQB03214@nifty.ne.jp

Takahide Sugiyama

Air Conditioning Research and Development Division, Yazaki Corporation
Email: sugiyama.t2@sys.yzk.co.jp; Fax: +81-(53)-461-7111

Keywords: absorption chiller, non-absorbable gas, numerical computation, film theory

ABSTRACT. A two-dimensional numerical study on a vapor flow with non-absorbable gas in the absorber-evaporator of an absorption chiller has been performed to investigate where the non-absorbable gas exists in the device. In a rectangular numerical domain, 80 cylinders for an evaporator and 96 cylinders for an absorber were mounted. The mean concentration of non-absorbable gas was changed from 0 to 10vol% in the computations. From the present results, non-absorbable gas is found mainly to concentrate in the upper region between evaporator and absorber, because the adverse flow is formed in the region. This adverse flow is weakened as the mean concentration of non-absorbable gas increases. Then, the high concentration region of the non-absorbable gas moves toward the absorber. This causes that the gas penetrates deeply into the absorber, and that the decreasing rate increases as the mean concentration increases.

1. INTRODUCTION

An absorption chiller will become one of heat devices paid more attention in the 21st century due to its high efficiency for heat recovery and saving energy resources. This motivates the researchers working on energy and environment to develop ones with high performance, and many works related to material of solution [1,2], to system construction [3] and to absorption enhancement with surfactants [4,5] are reported. In the practical use, however, there is a problem related to non-absorbable gas. Non-absorbable gas is naturally generated in the absorption chiller. Its existence causes low absorption of vapor to the surface of LiBr solution film on the cylinders in the absorber. Then, the development of the suction technology of non-absorbable gas from the evaporator-absorber is required for the recovery of its absorption efficiency.

For this purpose, the concentration distribution of non-absorbable gas in the evaporator-absorber should be investigated, but it is not so easy exactly to know the distribution by experimental works. In this study, numerical simulation technology has been applied to investigate where non-absorbable gas exists in the evaporator-absorber of an absorption chiller.

2. NUMERICAL PROCEDURE

Computational Domain and Governing Equations

In the present computations, only the flow and scalar fields of the water vapor were solved numerically and the thickness of liquid films falling along cylinders was not taken into consideration during solving the vapor flow. The liquid film was treated with the film theory only for determining the boundary condition on the cylinder surface as described in the next section. The computational domain is shown in Figure 1, schematically. The domain includes 176 cylinders. In order to calculate the flow and scalar fields around the cylinder, the multi-grid system [6] in which Cartesian coordinate system is used for main grid system covering all over the domain and cylindrical system for sub-grids assigned in a narrow region around each cylinder was applied as shown in Fig. 2. Then, two kinds of equation sets of two-dimensional, time-dependent momentum, energy and concentration, which correspond to each coordinate system, are used as follows.

Cartesian coordinates:

$$\frac{\partial u}{\partial t} + u \frac{\partial u}{\partial x} + v \frac{\partial u}{\partial y} = -\frac{1}{\rho} \frac{\partial p}{\partial x} + \nu \left[\frac{\partial^2 u}{\partial x^2} + \frac{\partial^2 u}{\partial y^2} \right] \quad (1)$$

$$\frac{\partial v}{\partial t} + u \frac{\partial v}{\partial x} + v \frac{\partial v}{\partial y} = -\frac{1}{\rho} \frac{\partial p}{\partial y} + \nu \left[\frac{\partial^2 v}{\partial x^2} + \frac{\partial^2 v}{\partial y^2} \right] + \frac{g\beta}{c_p} (h - h_0) + g \frac{(1-c)\rho - c\rho_h}{\rho} \quad (2)$$

$$\frac{\partial h}{\partial t} + u \frac{\partial h}{\partial x} + v \frac{\partial h}{\partial y} = a \left[\frac{\partial^2 h}{\partial x^2} + \frac{\partial^2 h}{\partial y^2} \right] \quad (3)$$

$$\frac{\partial c}{\partial t} + u \frac{\partial c}{\partial x} + v \frac{\partial c}{\partial y} = D \left[\frac{\partial^2 c}{\partial x^2} + \frac{\partial^2 c}{\partial y^2} \right] \quad (4)$$

Cylindrical coordinates:

$$\begin{aligned} \frac{\partial u_r}{\partial t} + u_r \frac{\partial u_r}{\partial r} + \frac{v_\theta}{r} \frac{\partial u_r}{\partial \theta} = & -\frac{1}{\rho} \frac{\partial p}{\partial r} + \nu \left[\frac{1}{r} \frac{\partial}{\partial r} \left(r \frac{\partial u_r}{\partial r} \right) + \frac{1}{r^2} \frac{\partial^2 u_r}{\partial \theta^2} \right] - \nu \left[\frac{2}{r^2} \frac{\partial^2 v_\theta}{\partial \theta^2} + \frac{u_r}{r^2} \right] + \frac{v_\theta^2}{r} \\ & + \frac{g\beta}{c_p} (h - h_0) \sin \theta + g \frac{(1-c)\rho - c\rho_h}{\rho} \sin \theta \end{aligned} \quad (5)$$

$$\begin{aligned} \frac{\partial v_\theta}{\partial t} + u_r \frac{\partial v_\theta}{\partial r} + \frac{v_\theta}{r} \frac{\partial v_\theta}{\partial \theta} = & -\frac{1}{\rho} \frac{\partial p}{r \partial \theta} + \nu \left[\frac{1}{r} \frac{\partial}{\partial r} \left(r \frac{\partial v_\theta}{\partial r} \right) + \frac{1}{r^2} \frac{\partial^2 v_\theta}{\partial \theta^2} \right] + \nu \left[\frac{2}{r^2} \frac{\partial^2 u_r}{\partial \theta^2} - \frac{v_\theta}{r^2} \right] - \frac{u_r v_\theta}{r} \\ & + \frac{g\beta}{c_p} (h - h_0) \cos \theta + g \frac{(1-c)\rho - c\rho_h}{\rho} \cos \theta \end{aligned} \quad (6)$$

$$\frac{\partial h}{\partial t} + u_r \frac{\partial h}{\partial r} + \frac{v_\theta}{r} \frac{\partial h}{\partial \theta} = a \left[\frac{1}{r} \frac{\partial}{\partial r} \left(r \frac{\partial h}{\partial r} \right) + \frac{1}{r^2} \frac{\partial^2 h}{\partial \theta^2} \right] \quad (7)$$

$$\frac{\partial c}{\partial t} + u_r \frac{\partial c}{\partial r} + \frac{v_\theta}{r} \frac{\partial c}{\partial \theta} = D \left[\frac{1}{r} \frac{\partial}{\partial r} \left(r \frac{\partial c}{\partial r} \right) + \frac{1}{r^2} \frac{\partial^2 c}{\partial \theta^2} \right] \quad (8)$$

Here, $x[m]$ and $y[m]$ are Cartesian coordinates, and $r[m]$ and $\theta[\text{rad}]$ are cylindrical coordinates assigned around cylinders; θ is defined as the angle from the x -axis. $u[m/s]$ and $v[m/s]$ are the horizontal and vertical velocities, $u_r[m/s]$ and $v_\theta[m/s]$ are the radial and circumferential velocities, and $p[\text{Pa}]$, $h[\text{J/kg}]$ and $c[-]$ are pressure, specific enthalpy and concentration of non-absorbable gas, respectively. $\rho[\text{kg/m}^3]$, $\nu[\text{m}^2/\text{s}]$, $\beta[\text{K}^{-1}]$, $c_p[\text{J/kgK}]$, $a[\text{m}^2/\text{s}]$ are the density, kinematic viscosity, volumetric expansion, specific heat and thermal diffusivity of water vapor and $D[\text{m}^2/\text{s}]$ is the mass diffusivity of non-absorption gas (hydrogen) to the water vapor. $\rho_h[\text{kg/m}^3]$ is the density of hydrogen and $g[\text{m/s}^2]$ is gravitational acceleration. Boussinesq approximation was applied for buoyancy term caused both by temperature and by concentration. All properties were assumed to be constant.

The finite difference equivalents of these equations were numerically solved. The central finite difference for diffusion terms, and the third-order upwind scheme, QUICK [7] for convection terms were respectively applied. Fully implicit form was used for time marching method. The pressure fields were calculated by SIMPLE [8] algorithm.

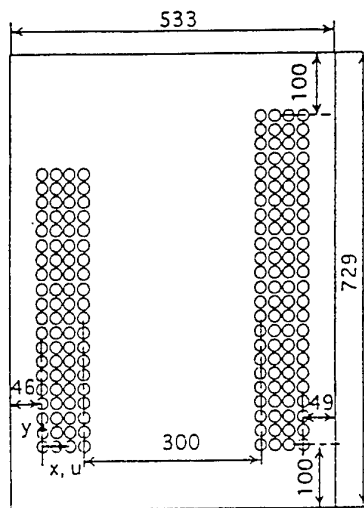


Fig. 1 Computational domain

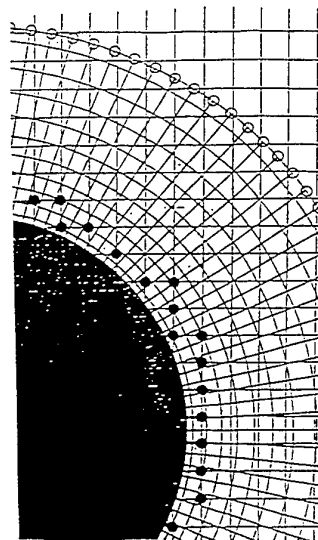


Fig. 2 Multi-grid system

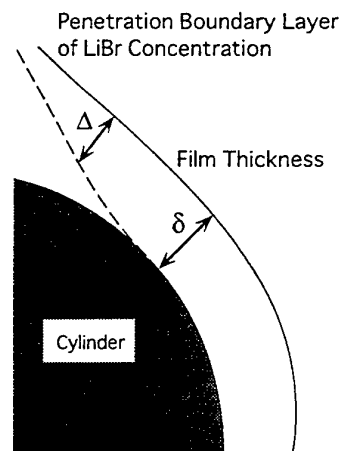


Fig. 3 Liquid film

The domain with 724mm height and 532mm width includes an evaporator and an absorber. They are mounted with a horizontal distance of 300mm, where vapor flows freely. Eighty cylinders with 19mm diameter for the evaporator and 96 cylinders with 19mm diameter for the absorber are mounted in four columns for each device with the pitch-diameter ratio of 1.2 for both horizontal and vertical directions. Grid points totaling 392x888 for Cartesian coordinates and 10x42 in the region with 2.85mm thickness around each cylinder are allocated non-uniformly.

Computational results did not show any unsteadiness though time-dependent equations were solved and total memory was saved within 150MB by the appropriate modeling on the liquid film of LiBr described in the following section. Consequently, computational time could be rather saved. One computation takes only two weeks by using the Pentium II machine of 450Mz with Linux OS and GNU FORTRAN.

Film Theory

For determining the boundary conditions on the surface of cylinders in the absorber, Nusselt's thin film theory was developed for the present situation and applied under saturation condition. Under the situation where the film thickness is very thin compared with the cylinder diameter, the profile of circumferential velocity, U [m/s] in the liquid film is obtained from the film theory as follows.

$$U = \frac{g\delta^2 \sin \phi}{\nu_L} \left\{ \left(\frac{Y}{\delta} \right) - \frac{1}{2} \left(\frac{Y}{\delta} \right)^2 \right\} \quad (9)$$

Here, Y [m] is the normal coordinate from the cylinder surface and ϕ [rad] is the circumferential coordinate defined as the angle from the top of each cylinder. δ [m] is film thickness which is enough thin compared with the cylinder diameter, d [m], and ν_L [m²/s] is the kinematic viscosity of LiBr solution. From the mass balance equation:

$$\frac{d}{d\phi} \int \rho_L U dY = \frac{dm}{2} \quad (10)$$

the circumferential gradient of δ is obtained as follows.

$$\frac{d\delta}{d\phi} = \frac{\nu_L m d}{2\rho_L \delta^2 g \sin \phi} - \frac{\delta}{3 \tan \phi} \quad (11)$$

Here, $m[\text{kg/m}^2\text{s}]$ and $\rho_L[\text{kg/m}^3]$ are the absorption mass flux of vapor into the film surface, which takes positive values for absorption occurrence, and the density of LiBr solution, respectively. At the top point of the cylinder, δ should be infinite, but can be determined at the closest point of the top by using mass flow rate of the LiBr solution with the assumption of $m=0$ at $\phi=0$. If the local value of m can be obtained, δ can be calculated from the top to the bottom of the cylinder.

In this thin film, the profiles of temperature and concentration were assumed to obey with the third order polynomial expression. The concentration of LiBr, $C[\text{wt}\%]$ becomes lower in surface region of the film due to the absorption of vapor. Its distribution might be, however, limited in very thin region from the liquid surface near the top of each cylinder, because its Schmidt number is very high (up to the order 10^3). Then, the

$$C = \begin{cases} C_a & Y < \Delta \\ C_a - E(Y - \delta + \Delta)^3 & Y \geq \Delta \end{cases} \quad \begin{array}{l} \text{penetration boundary layer and its thickness } \Delta[\text{m}] \text{ of LiBr concentration} \\ \text{should be defined as shown in Figure 3. If } \Delta < \delta, \end{array} \quad (12)$$

Otherwise:

$$C = C_a - EY^3 \quad (13)$$

Here, $C_a[\text{wt}\%]$ is concentration on the cylinder surface and $E[\text{wt}\%/\text{m}^3]$ is constant. From the Fick's law on the liquid surface, E is easily determined as follows.

$$E = \frac{100}{3} \frac{m}{\rho_L D_L \Delta^2} \quad (14)$$

where $D_L[\text{m}^2/\text{s}]$ is the mass diffusivity of LiBr in water. This profile of concentration can be substituted to the following balance equation of the concentration.

$$\frac{d}{d\phi} \int_0^\delta \rho_L U C dY = 0 \quad (15)$$

Consequently, the circumferential gradient of Δ or C_a is obtained as a function of m as well as one of δ .

$$\frac{d\Delta}{d\phi} = \frac{9}{10} \frac{D_L \nu_i C_a d}{\Delta g (15\delta^2 - 2\Delta^2) \sin \phi} - \frac{15}{2} \frac{m \nu_i \Delta d}{\rho_L g \delta (15\delta^2 - 2\Delta^2) \sin \phi} + \frac{1}{2} \frac{\Delta (\Delta^2 - 5\delta^2)}{(15\delta^2 - 2\Delta^2) \tan \phi} - \frac{1}{2} \frac{\Delta (15\delta^2 - \Delta^2)}{(15\delta^2 - 2\Delta^2) m} \frac{dm}{d\phi} \quad \Delta < \delta \quad (16)$$

$$\frac{dC_a}{d\phi} = \frac{35}{3} \frac{\delta}{\rho_L D_L} \left(\frac{dm}{d\phi} - \frac{m}{3 \tan \phi} \right) \quad \Delta = \delta \quad (17)$$

At the top of the cylinder, Δ is equal to 0 and C_a is equal to the top concentration at the point where Δ becomes equal to δ . From this upstream condition, Δ or C_a is calculated by this equation if m can be given. The same kind of theory as this on the penetration boundary layer was also considered by Urakawa et al [9], but they assumed parabolic profiles on temperature and concentration. In this situation, the 2nd order gradient of them should be zero on the cylinder surface or outer edge of the penetration boundary layer. Then, the profile should be linear or more than the 3rd order.

For temperature $T[\text{K}]$ profile, the following can be assumed.

$$T = F_1 \left(\frac{Y}{\delta} \right)^3 + F_2 \frac{Y}{\delta} + T_c \quad (18)$$

Here, T_a [K] is wall temperature of the cylinder, and F_1 [-] and F_2 [-] are constants. From the Fourier's law on the film surface, F_2 is obtained with the heat flux q [W/m²] which takes positive values for absorption direction and F_1 as follows.

$$F_2 = \frac{q\delta}{\lambda_L} - 3F_1 \quad (19)$$

Here, λ_L [W/mK] is thermal conductivity of the LiBr solution. In this equation, q includes both absorption heat and conductive heat loss to vapor field around the cylinder.

$$q = mL + \lambda \left. \frac{\partial T}{\partial r} \right|_{r=d/2+\delta} \quad (20)$$

Here, L [J/kg] is latent heat when the vapor is absorbed into LiBr solution. By substituting the temperature profile to the energy balance equation:

$$\frac{d}{d\phi} \int_0^\delta \rho_L c_L U T dY = \frac{d}{2} \left(q - \lambda_L \left. \frac{\partial T}{\partial Y} \right|_{Y=0} \right) \quad (21)$$

the circumferential gradient of F_1 is obtained as a function of q , i.e. m , consequently.

$$\frac{dF_1}{d\phi} = \frac{25}{61} \frac{\delta}{\lambda_L} \left(\frac{dq}{d\phi} - \frac{q}{3 \tan \phi} \right) - \frac{180}{61} \frac{v_L \lambda_L F_1 d}{\rho_L c_L g \delta^4 \sin \phi} \quad (22)$$

Here c_L [J/kg] is specific heat of LiBr solution. The heat flux on the top of the cylinder should be zero because of $m=0$. F_1 can be numerically calculated with this upstream condition toward the bottom of the cylinder if m can be given.

δ , Δ or C_b and F_1 are found to be functions of m in the above theory. Finally, the saturation condition at the liquid surface as the following is used for calculating m .

$$\begin{aligned} T_f &= B_1 + B_2 C_f \\ B_1 &= -70.27 + 0.759 T' \\ B_2 &= 1.82 + 0.00707 T' \\ T' &= \frac{2082}{-159.6 + \sqrt{254.9 + 41.64(7.05 - \log((1 - c_a)p_a/1000))}} - 273.15 \end{aligned} \quad (23)$$

where T_f [K] and C_f [wt%] are the temperature and the concentration on the liquid surface, and p_a [Pa] and c_a [-] are the pressure and the concentration of non-absorbable gas on the liquid surface, respectively. From this relationship between T_f and C_f , m is calculated at each point on the cylinder as follows.

$$m = \frac{2F_1 - T_a + B_1 + B_2 C_a - \lambda \left. \frac{\partial T}{\partial r} \right|_{r=d/2+\delta}}{\frac{\delta L}{\lambda_L} + \frac{100}{3} \frac{B_2 \Delta}{\rho_L D_L}} \quad (24)$$

On the calculation of the vapor flow, film thickness can be assumed to be negligible, so the boundary condition is obtained for radial velocity and enthalpy as follows.

$$u_r|_{r=d/2} = -m/\rho \quad (25)$$

$$h|_{r=d/2} = c_p T_f$$

The liquid droplets falling onto the top row of cylinders in absorber have the uniform temperature and uniform concentration given as inlet conditions. The temperature and the concentration of droplets falling onto the lower cylinder can be assumed to take the same value as ones of the bottom of the upper cylinders and to be uniform. In this way, the temperature and the concentration of the top of each cylinder were changed toward the bottom row.

For the estimation of T_a , heat transfer coefficient on the inner surface of the cylinder is assumed to be uniform and is estimated by using the following Dittus-Beolter's empirical equation on Nusselt number, Nu in a turbulent pipe flow:

$$Nu = 0.023 Re^{0.8} Pr^{0.4} \quad (26)$$

Using the heat flux calculated by the above film theory on each cylinder, the bulk and wall temperatures inside cylinders can be determined from the bottom row, where is the inlet of coolant water, to the top.

For the boundary condition of non-absorbable gas concentration on the cylinder surface, its radial gradient was assumed to be zero when absorption occurs, but the concentration was set to zero if evaporation occurs from the surface of LiBr solution film. The circumferential velocity on the cylinders was assumed to be zero.

For the cylinders in the evaporator, uniform radial velocity which balances to the total mass absorbed in the absorber and uniform temperature evaluated by the saturation condition were given as boundary conditions for saving computational load, briefly. The concentration of non-absorbable gas and the circumferential velocity on the surface were set to zero.

Computational Conditions

The computational conditions and properties are tabulated in Table 1. For the boundary conditions on the solid wall of the vessel, non-slip condition was applied and no gradient conditions for temperature, pressure and concentration were set. In the comparison with experimental data that were measured under almost the same condition as the present computational one, the calculated overall heat transfer coefficient for the case without non-absorbable gas shows the good agreement within 5% difference[10].

Table 1. Computatinal Conditions and Properties

Pressure in evaporator		930 Pa	Surface temperature of cylinders in evaporator		5.12 °C
Water vapor properties			LiBr solution properties		Coolant water conditions
a	$1.38 \times 10^{-3} \text{ m}^2/\text{s}$	c_L	$1.99 \times 10^3 \text{ J/kgK}$	Inlet Temperature	32 °C
c_p	$1.86 \times 10^3 \text{ J/kgK}$	D_L	$1.65 \times 10^{-9} \text{ m}^2/\text{s}$	Density	995 kg/m
b	$3.57 \times 10^{-3} \text{ T}^{-1}$	L	$2.57 \times 10^6 \text{ J/kg}$	Thermal Conductivity	0.618 W/mK
λ	$1.86 \times 10^{-2} \text{ W/mK}$	λ_L	0.433 W/mK	Specific Heat	$4.18 \times 10^3 \text{ J/kgK}$
v	1.14 m ² /s	v_L	$2.91 \times 10^{-6} \text{ m}^2/\text{s}$	Reynolds Number	19300
ρ	$7.26 \times 10^{-3} \text{ kg/m}^3$	ρ_L	$1.67 \times 10^3 \text{ kg/m}^3$	Prantdl number	5.2
LiBr solution conditions			Non-absorbable gas(hydrogen) conditions		
Inlet Temperature	45 °C		D	$5.47 \times 10^{-3} \text{ m}^2/\text{s}$	
Inlet Concentration	58.5wt%		ρ_h	$8.07 \times 10^{-4} \text{ kg/m}^3$	
Mass Flow Rate	$4.42 \times 10^{-2} \text{ kg/s}$		Mean Concentration		0 to 10vol%

3. RESULTS AND DISCUSSION

Figure 4 shows the overall heat transfer coefficient $k[\text{W/m}^2\text{K}]$ on the absorber. k is apparently found to decrease as mean concentration, $c_m[\text{vol}\%]$, of non-absorbable gas increases. This is because the non-absorbable gas concentrated around cylinders in the absorber seriously disturbs absorption. From more careful observation of the figure, the decrease rate of absorption against c_m is found to increase from $c_m=0$ to 3vol%. This implies

the concentration distribution of non-absorbable gas in the evaporator-absorber vessel might be dependent on c_m .

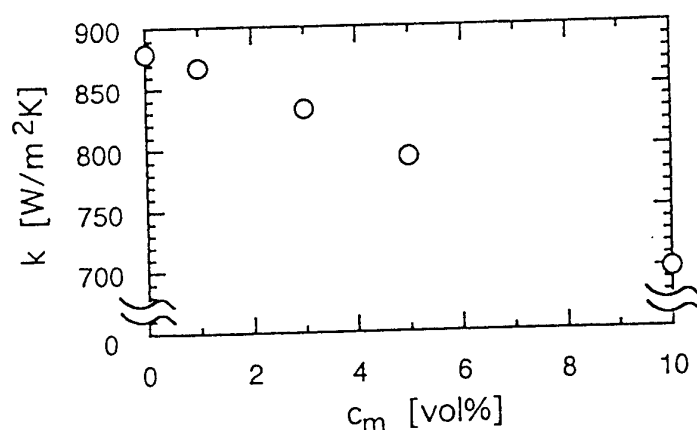


Fig. 4 Overall heat transfer coefficient of the absorber

Before discussing the concentration distribution of non-absorbable gas, the absorption characteristics into the liquid film for each cylinder should be investigated for cases with non-absorbable gas. Figure 5 shows the averaged absorption mass flux of vapor, m_M [kg/m²s], for each cylinder in the absorber. In the figure, the results for cases of $c_m=0, 1$ and 10% are plotted on each row of cylinder array from top to bottom for each column from left to right. m_M for the case of $c_m=0$ takes the highest value at the top row of cylinders and decreases toward the bottom, monotonously. When c_m is low, absorption is affected only for the several cylinders mounted in high position. For the case of $c_m=10\%$, however, the absorption seriously decreases for cylinders mounted for the rows from the top to the middle. On the other hand, m_M sharply increases at a certain row in the middle for each column. This is because the concentration of LiBr is kept high due to low absorption in the upper rows. From these results, the non-absorbable gas could be expected to exist only in the upper region of the absorber, and its existence seriously disturbs absorption in the upper rows of the absorber when c_m becomes high.

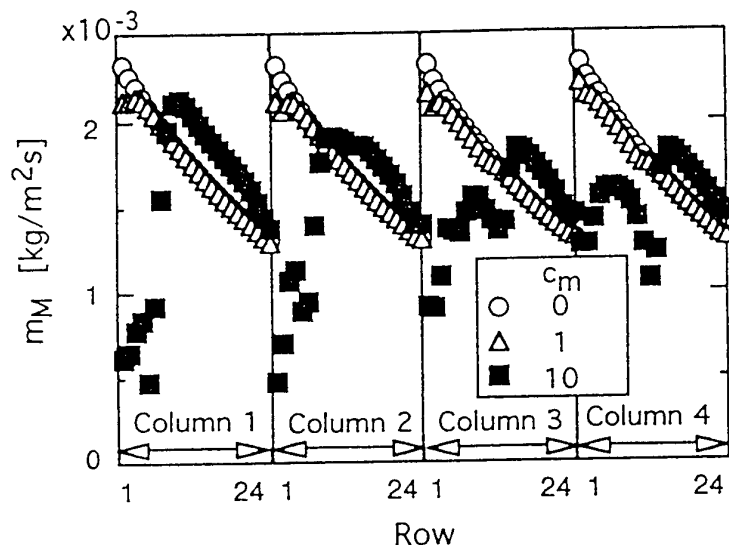


Fig. 5 Mean mass flux around absorber cylinders

Figure 6(a) and (b) show concentration contours for cases of $c_m=1$ and 10vol%, respectively. The dark region in the figure indicates high concentration region of non-absorbable gas. For both cases, non-absorbable gas is found to be mainly concentrated in the upper region between the evaporator and the absorber. The previous analytical works on the effect of non-absorbable gas have been assumed that the gas might drift only around the

cylinders of the absorber [11]. The present work reveals the study on the non-absorbable gas existence location is also important to understand the problem of the absorption disturbance by the non-absorbable gas.

In order to investigate why the non-absorbable gas exists in the region observed in Fig. 6, the horizontal velocity, u , in the mid-plane between the evaporator and absorber for cases of $c_m=0, 1$ and $10\text{vol}\%$ are shown in Figure 7. From the careful observation of the figure, the adverse flow is found to exist in the region where non-absorbable gas is concentrated. The adverse flow caused by the flow recirculation prevents non-absorbable gas from penetrating into the absorber. Then, non-absorbable gas remains to stay in the recirculation region. On the other hand, when the mean concentration of non-absorbable gas is high, a rather amount of non-absorbable gas penetrates into the absorber while most part of the gas still remains around the upper corner of the evaporator. High concentration of non-absorbable gas causes absorption decreases in the region where the gas reaches. Then, mean velocity of vapor flow decreases. This velocity decrease causes recirculation of the flow is weakened. This is the reason for the deep penetration of non-absorbable gas into the absorber. From this difference of the concentration distribution of non-absorbable gas, the decreasing rate of absorption is concluded to increase as c_m increases.

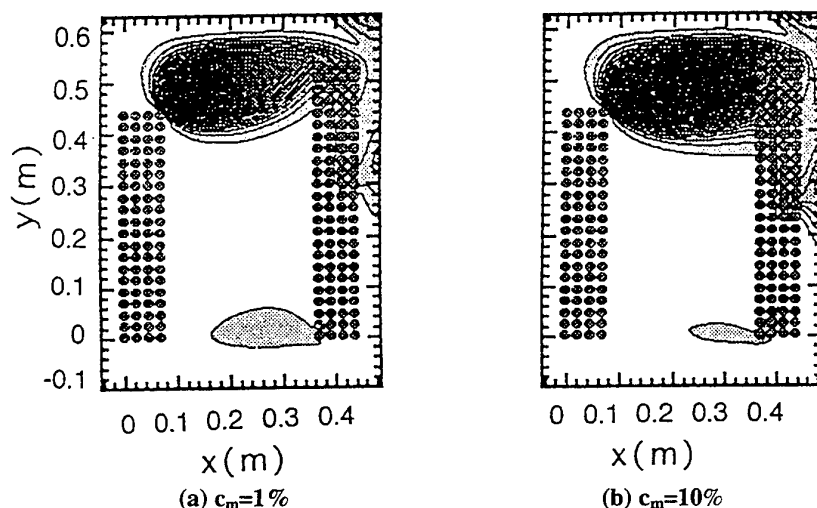


Fig. 6 Concentration Contours of Non-Absorbable Gas

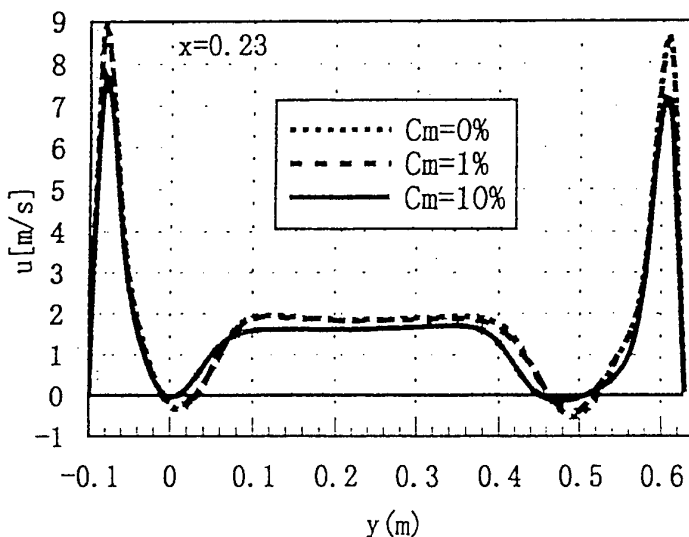


Fig. 7 Horizontal Velocity in the Mid-Plane between Evaporator and Absorber

3. CONCLUSIONS

A numerical study on a vapor flow with non-absorbable gas in the absorber-evaporator of an absorption chiller was performed to investigate where the non-absorbable gas exists in the device, using the film theory developed to model the liquid film on the surface of cylinders in the absorber. The mean concentration of non-absorbable gas was changed from 0 to 10vol% in the computations. From the present results, the following conclusions were obtained.

1. Non-absorbable gas mainly concentrates in the upper region between evaporator and absorber, because the adverse flow is formed in the region.
2. This adverse flow is weakened as the mean concentration of non-absorbable gas increases. Then, the high concentration region of the non-absorbable gas moves toward the absorber.
3. This causes that the gas penetrates deeply into the absorber, and that the decreasing rate increases as the mean concentration increases.

REFERENCES

1. S.B. Raffit, S.E. James and C.W. Wong, *Int. J. Energy Reserch*, v.22, pp.1099-1103(1998).
2. J.-S. Kim, Y. Park and H. Lee, *Applied Thermal Eng.*, v.19, pp.217-225(1999).
3. G.P. Xu, Y.Q. Dai, K.W. Tou and C.P.Tso, *Applied Thermal Eng.*, v.16, pp. 975-987(1996).
4. M. Hozowa, M. Inoue, J. Sato and T. Tsukada, *J. Chem. Eng. Japan*, v.24, pp.209-214(1991).
5. H. Daiguji, E. Hihara and T. Saito, *Int. J. Heat Mass Transfer*, v.40, pp.1743-1752(1997)
6. H. Suzuki, Y. Iwasaki, K. Hara, Prabowo and Y. Kikuchi, *Proc. 10th Int. Sym. Transport Phenomena in Thermal Science & Process Eng.*, v.3, pp.895-900, Kyoto, Japan(1997).
7. B.P. Leonard, *Comput. Meth. Appl. Mech. Eng.*, v.19, pp.59-98(1979).
8. S.V. Patankar and D.B. Spalding, *Int. J. Heat Mass Transfer*, v.15, pp.1787-1806(1972).
9. K. Urakawa, I. Morioka and M. Kiyota, *Trans. JSME, ser.B*, v.52, pp.1766-1771(1986).
10. H. Suzuki, T. Yamanaka and T. Sugiyama, *Proc. 32nd Chemical Engineering of Japan Autumn Meeting*, (1999), to be printed (in Japanese).
11. R. Yang and T.M. Jou, *Int. J. Heat Mass Transfer*, v.41, pp.3657-3668(1998).

MODELING THE THERMAL CYCLE OF A DUAL COMPARTMENT HOUSEHOLD REFRIGERATOR

Xiaoyong Fu, Ron Anderson and Al Miller

Maytag - Galesburg Refrigeration Products

Galesburg, Illinois 61401

Email: xfu@maytag-grp.com; Fax: (309) 345-1702

Keywords: refrigerator, temperature control, heat transfer, cycle

ABSTRACT. A computational model has been developed to simulate the temperature cycles of the freezing and fresh food compartments in a household refrigerator. Modeling consists of two parts coupled with each other: a refrigeration system and a temperature cycle of the refrigerator. The refrigeration system including a compressor, a condenser, an evaporator and a capillary tube is modeled based on performance data measured or provided by the manufacturers. The temperature variation in the refrigerator during a cycle is simulated using the lumped capacitance method. The switching on and off of the compressor is controlled by using a given temperature band of the freezer with the highest temperature for the compressor turning on and the lowest one for turning off. The thermophysical properties of the cabinet of the refrigerator such as the thermal conductance of the walls and heat transfer coefficients on the walls of the cabinet are approximated by a combination of measurements and theoretical calculations. Numerical simulations were carried out for the thermal performance of a 19 cubic foot top mount refrigerator. The model predictions of temperature are validated against the experimental data. The effect of cross ambient temperatures from 21.1 °C (70 °F) to 32.2 °C (90 °F) on the performance of the refrigerator is reported.

NOMENCLATURE

a_i	constants in Eq. (8)	Cycle	per cycle time (min)
b_i	constants in Eq. (9)	Duty cycle	compressor run time per cycle (min)
$c_{p,a}$	air specific heat (J/kg K)		
F_{com}	flag for a compressor (1=on; 0=off)	subscripts:	
h	latent heat (J/kg)	a	refers to air
m	mass flow rate (kg/s)	amb	refers to ambient
P	Power (W)	c	refers to condenser
q	heat rate (W)	e	refers to evaporator
S	heat source (W)	ff	refers to fresh food compartment
T	temperature (°C or °F)	fz	refers to freezing compartment (freezer)
t	time (s)	mol	refers to mullion
UA	overall heat transfer coefficient (W/K)	ret	refers to return
V	volume (m ³)	sup	refers to supply
ρ	density (kg/m ³)		

1. INTRODUCTION

A household refrigerator normally consists of a freezing compartment (freezer) and a fresh food compartment. The cooling capacity for keeping the compartment temperatures below the surrounding temperature is provided by a refrigeration system which primarily consists of a compressor, a condenser, an evaporator and a capillary tube. A schematic diagram of the air flow path in a household refrigerator along with its refrigeration system is shown in Fig. 1. The refrigerant flowing in the refrigeration system goes through a typical vapor compression cycle in which a compressor drives the refrigerant. The refrigerant in the evaporator absorbs heat from the warm air by evaporation. Heat gained by the refrigerant in the evaporator is rejected to the ambience by the condenser. Most of the cooled air flow is delivered to the freezer by a fan with a small fraction of the air flow (less than 10%) to the fresh food compartment since the temperature (0 ± 3 °F or -17.8 ± 1.7 °C) in the freezer is much lower than that (37 ± 3 °F or 2.8 ± 1.7 °C) in the fresh food compartment. The temperature in the freezer is controlled by a thermostat which switches on/off the compressor based on temperature of the thermostat. The fraction of time during which the compressor runs is called a duty cycle. Operation of a damper on the mullion

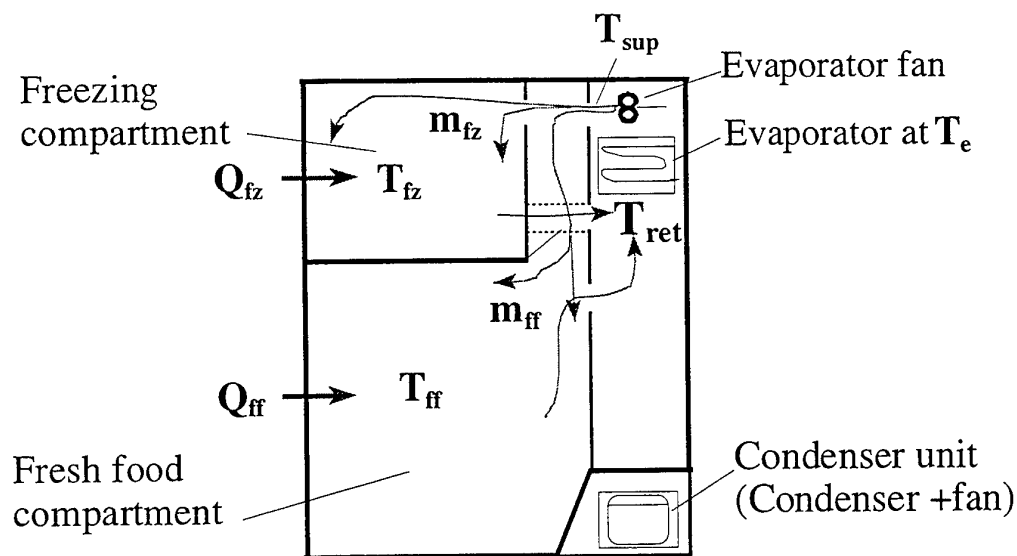


Fig. 1 Schematic side view of a top mount household refrigerator

between the freezer and the fresh food compartment controls the air flow rate delivered to the fresh food compartment, and thus controls the temperature of the fresh food compartment. Therefore, the control methodology for the opening of the damper plays an important role in determining temperature and its variation in the fresh food compartment. Temperature stratification and variation with time in the fresh food compartment strongly influence the quality of the food stored [1].

Increasing effort has been devoted to research and development of temperature control of refrigerators in recent years as health and safety legislation has become more and more restricted. No attention is given to a detailed review on the research of this area in the present paper due to the limitation of the paper length, but some references are listed [2,3,4,5,6,7,8,9].

The objective of the present work is to develop a computational model to simulate transient bulk temperature cycles of the freezing and fresh food compartments in a household refrigerator for a given temperature control. The model can be used to perform a parametric study and the predicted results will provide guidance to achieve an optimal design of the temperature control.

2. MODEL DEVELOPMENT

Detailed simulation of the air temperature performance in a household refrigerator along with its refrigeration system requires deep knowledge of computational fluid dynamics (CFD) and is almost impossible because of complex geometries of airflow and refrigerant flow. Although the air velocity in the refrigerator is much less than the speed of sound, all of the three flow patterns, i.e., the laminar, transient and turbulent flows could exist at different regions along the airflow path. The vapor-liquid two phase flow in the refrigerant presents another challenge for the simulation of the refrigeration system. Some idealized assumptions are always needed in developing a model for the thermal performance of the refrigerator.

A schematic diagram for the airflow path and the refrigerant flow path in a household dual compartment refrigerator is plotted in Fig. 2. The assumptions made in the analysis are as follows: 1) The refrigeration system works under a quasi-steady process; 2) Bulk (average) temperatures are used for the freezer and fresh food

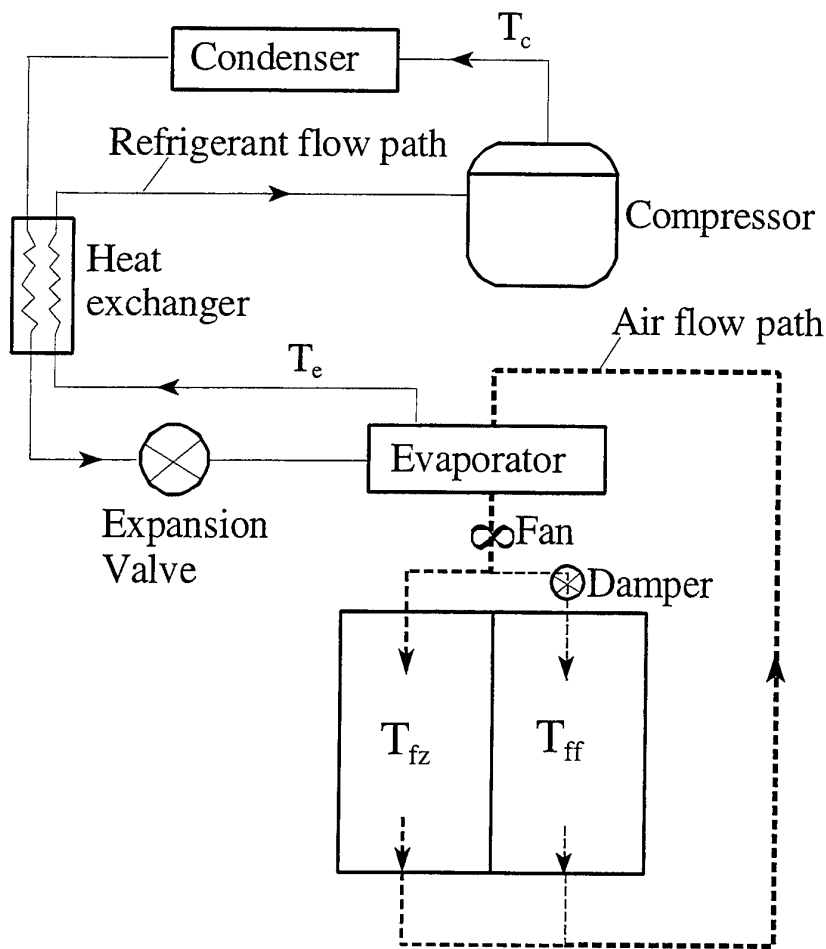


Fig. 2 Schematic diagram of the airflow path and the refrigerant flow path in a household dual compartment refrigerator

compartment; 3) Refrigerant temperature in the condenser is constant and equal to its condensing point; 4) Refrigerant temperature in the evaporator is constant and equal to its boiling point; 5) Overall heat transfer coefficients between the freezer and the ambient, between the fresh food compartment and the ambient, and of the evaporator and of the condenser are constant, respectively.

Application of the energy and mass conservation laws to the model system shown in Figs. 1 and 2 yields the model governing equations. The energy equation for the freezing compartment is

$$m_{fz}(c_{p,a}T_{sup} - c_{p,a}T_{fz})F_{com} - (UA)_{fz}(T_{fz} - T_{amb}) - (UA)_{mol}(T_{fz} - T_{ff}) + S_{fz} = \frac{d}{dt}(V_{fz}\rho_{fz}c_pT_{fz}) \quad (1)$$

The energy equation for the fresh food compartment is

$$m_{ff}(c_{p,a}T_{sup} - c_{p,a}T_{ff})F_{com} - (UA)_{ff}(T_{ff} - T_{amb}) - (UA)_{mol}(T_{ff} - T_{fz}) + S_{ff} = \frac{d}{dt}(V_{ff}\rho_{ff}c_pT_{ff}) \quad (2)$$

The heat transfer equations for the evaporator can be expressed as

$$q_e = (UA)_e \Delta T_e \quad (3)$$

where

$$\Delta T_e = \frac{(T_{sup} - T_e) - (T_{ret} - T_e)}{\ln[(T_{sup} - T_e)/(T_{ret} - T_e)]} \quad (4)$$

and

$$T_{ret} = (m_{fz} c_{p,a} T_{fz} + m_{ff} c_{p,a} T_{ff}) / (m_a c_{p,a}) \quad (5)$$

where $m_a = m_{fz} + m_{ff}$, and

$$m_a c_{p,a} (T_{ret} - T_{sup}) = m_r \Delta h_r \quad (6)$$

$$m_a c_{p,a} (T_{ret} - T_{sup}) = (UA)_e \Delta T_e \quad (7)$$

The compressor performance equations are determined using the compressor performance data at nine operating points (i.e., combination of condenser temperatures of 110, 120 and 130 °F with evaporator temperatures of 0, -10 and -20 °F) provided by the compressor manufacturer, and can be expressed in terms of compressor power consumption or refrigerant mass flow rate as a function of the condenser and evaporator temperatures.

$$P = a_1 + a_2 T_e + a_3 T_e^2 + a_4 T_c + a_5 T_c^2 + a_6 T_e T_c + a_7 T_e^2 T_c + a_8 T_e T_c^2 + a_9 T_e^2 T_c^2 \quad (8)$$

$$m_r = b_1 + b_2 T_e + b_3 T_e^2 + b_4 T_c + b_5 T_c^2 + b_6 T_e T_c + b_7 T_e^2 T_c + b_8 T_e T_c^2 + b_9 T_e^2 T_c^2 \quad (9)$$

The constants applicable to Eqs. (8) and (9) for the compressor are determined by the method of least squares. The heat transfer equation for the condenser is

$$q_c = (UA)_c (T_c - T_{amb}) \quad (10)$$

The heat transfer through the condenser and the heat transfer through the evaporator have a relationship as follows

$$q_c = q_e + P \quad (11)$$

Inspection of the equations, Eqs. (1) to (11), reveals that a number of parameters: overall heat transfer coefficients, thermophysical properties of refrigerant and air, etc. are needed as inputs in the solution of the equations. The required parameters and the sources from which they were taken are discussed in the following paragraph.

The overall heat transfer coefficients (UA) for the freezer, the fresh food compartment, the mullion, the condenser and the evaporator were determined using the computational program, SSRAP which was developed at Maytag Corporation [10] for analysis of the steady state performance of a household refrigerator. The miscellaneous heats generated from a heater (yoder) around the cabinet flange for anti-sweat, an evaporator fan motor, a defrost heater and door leakage were considered as heat sources in Eqs. (1) to (2) and were also determined by the SSRAP. The effective thermal masses or thermal capacities [$V_p c_p$ in Eqs. (1) and (2)] of the compartments consisting of air, shelves, etc. influence the cycle time only, and thus were determined by matching the predicted cycle time to the measured one. The total air flow rate (m_a) was from lab measurements.

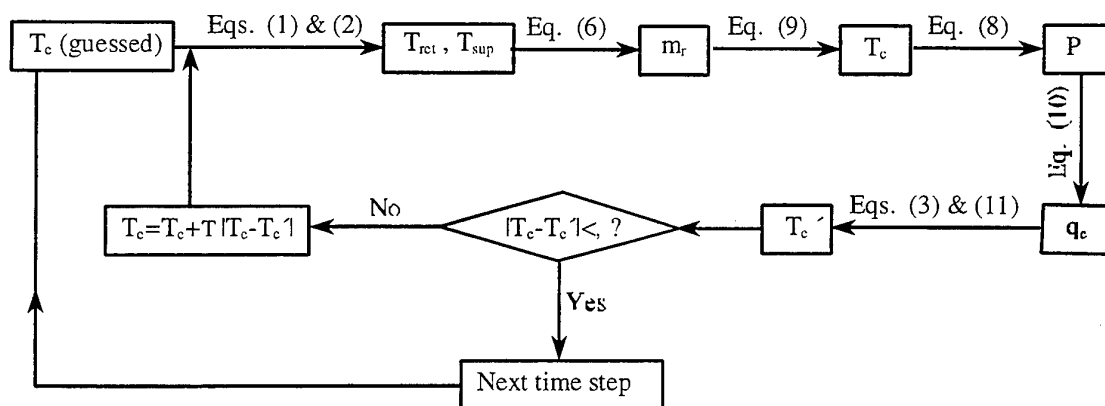


Fig. 3 Computational flow chart

The temperature control band in determining the compressor on/off is specified for a given control bandwidth and a given average freezer temperature over a cycle. The density and the specific heat of the air as a function of the temperature were calculated based on table data of the air properties. The compressor performance data were provided by its manufacturer or measured at Maytag Corporation.

Table 1 Input parameters and results summary for a top mount refrigerator

Input parameters		
Temperature control band:	-7 ~ 8 °F (-21.7 ~ -13.3. °C)	
Control bandwidth:	15 °F (8.3 K)	
Damper air flow rate:	24.4 lb/hr (3.074 x10 ⁻³ kg/s)	
Results summary		
Ambient temperature	90 °F (32.2 °C)	70 °F (21.1 °C)
Average freezer temperature	0.05 °F (-17.8 °C)	0.4 °F (-17.6 °C)
Average fresh food temperature	37 °F (2.8 °C)	36.2 °F (2.3 °C)
Cycle	50 min	46.3 min
Percent run time (=Duty cycle/Cycle)	40%	27%

3. RESULTS AND DISCUSSION

The model Eqs. (1) and (2) were discretized using a fully implicit scheme. A computer program in FORTRAN language was written for solving the equations. A computational flow chart was designed to obtain the convergent solutions (see Fig. 3). The convergence criteria for temperature was set to 0.1 °F (0.06 °C).

Case Study

A 19 cubic foot top mount refrigerator having a freezing compartment and a fresh food compartment was chosen as a base line case study. Portions of the model input parameters are listed in Table 1. The remainder of the model input parameters are not shown in the present paper due to involving the sensitive parameters of the refrigerator of Maytag Corporation. The predicted temperature cycles in the refrigerator for the ambient temperature of 90 °F (32.2 °C) is plotted in Fig. 4. The freezer temperature decreases following the supply air temperature during a duty cycle. During an off cycle, the freezer temperature and the fresh food temperature

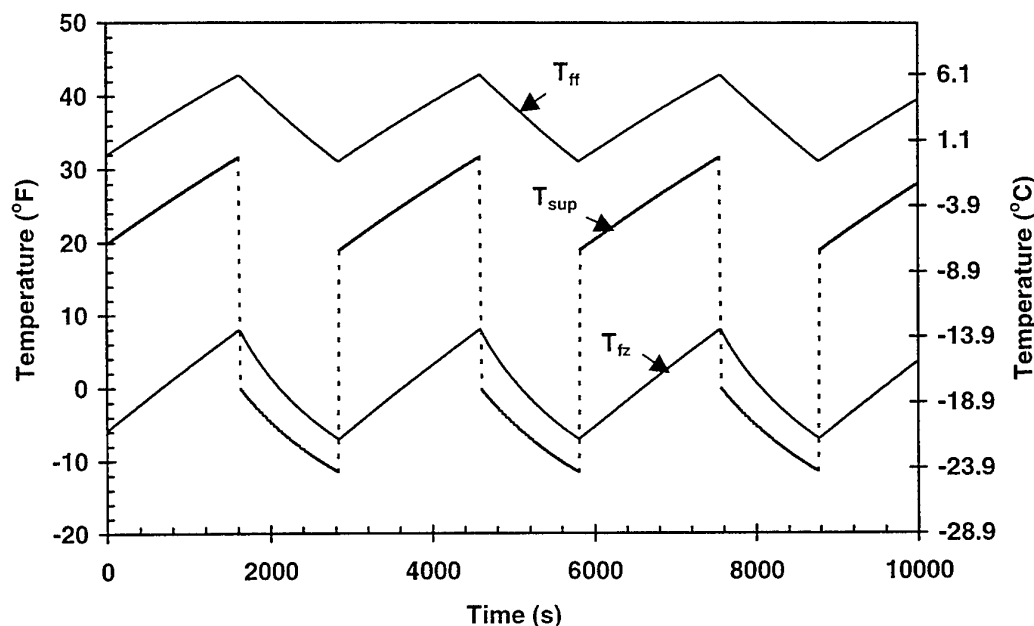


Fig. 4 Temperature cycle in a 19 cubic foot top mount refrigerator for ambient temperature of 90 °F

should increase exponentially according to Eqs. (1) and (2), but they appear to increase linearly with time. This is attributed to the fact that the ratios of the overall heat transfer coefficient to the effective thermal mass $[(UA)_{fz}/(V c_p)_{fz}]$ and $[(UA)_{ff}/(V c_p)_{ff}]$ are very small and equate to 0.2 1/hr and 0.4 1/hr for the freezer and the fresh food compartment, respectively.

Effect of Ambient Temperature

Temperature shift in the compartments with cross ambient temperatures plays an important role in rating the refrigerator performance since the ambient temperature varies normally from day time to night and from one season to another. Temperature cycles in the compartments were simulated for the same refrigerator used in Fig. 4 with the same operating conditions except that the ambient temperature changed from 90 to 70 °F (32.2 to 21.1 °C) and is shown in Fig. 5. Comparison of the temperature performance for the cross ambient temperatures is summarized in Table 1. The temperature shifts in the freezer and the fresh food compartment are 0.4 °F (0.2 °C) and -0.8 °F (0.4 °C), respectively, for the variation in ambient temperature from 90 °F to 70 °F (32.2 to 21.1 °C). This implies a variable temperature control band or a variable air flow rate may be needed to keep constant average temperatures of the compartments for different ambient temperatures. The percent run time decreases significantly by 34% owing to a decrease in the heat transfer from the ambient to the cabinet, which means the power consumption decreases with a decrease in the ambient temperature.

Comparison with Experimental Data

For performance rating of a household refrigerator, the temperature in the cabinet is normally measured using a brass weight thermocouple, which is cylindrical and is around 1 inch in diameter and 1 inch in height. The measured temperature actually is the temperature of the center of the brass weight. Numerical simulations were carried out to study the response of temperature in the center of the brass weight to its surrounding temperature using a two-dimensional model. The detailed numerical approach is skipped in the present paper and referred to elsewhere. The response of temperature in the center of the brass weight to the temperature in the freezer is plotted in Fig. 6 for a side by side refrigerator. A constant heat transfer coefficient between the surface of the brass weight and its surroundings was assumed and was estimated to be of 5 Btu/(hr.ft² °F) [28 W/(m² K)]. The figure shows the peak temperatures in the brass weight center shrink significantly from -6 ~ 5 °F (-21.1 ~ -15 °C)

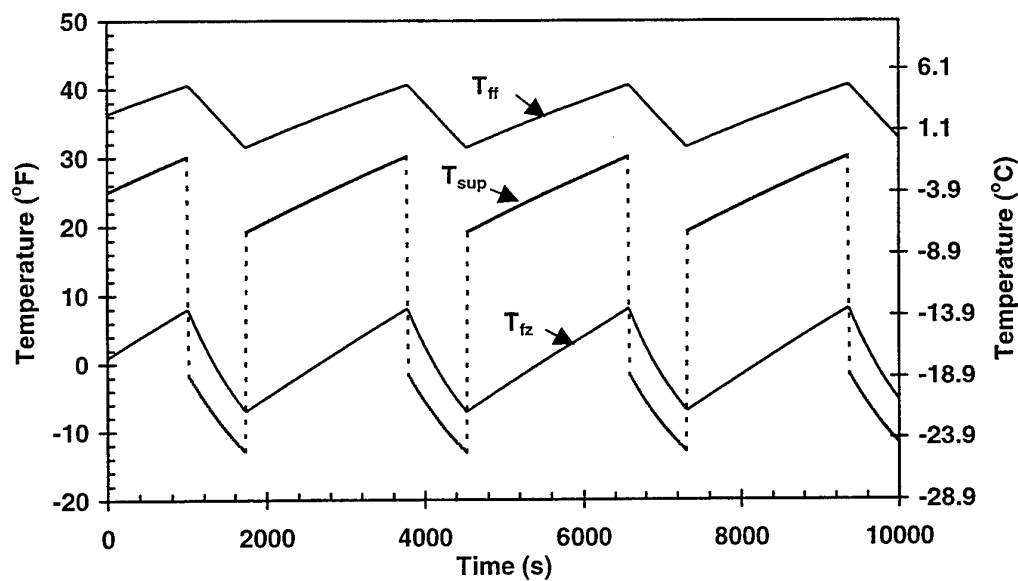


Fig. 5 Temperature cycle in a 19 cubic foot top mount refrigerator for ambient temperature of 70 °F

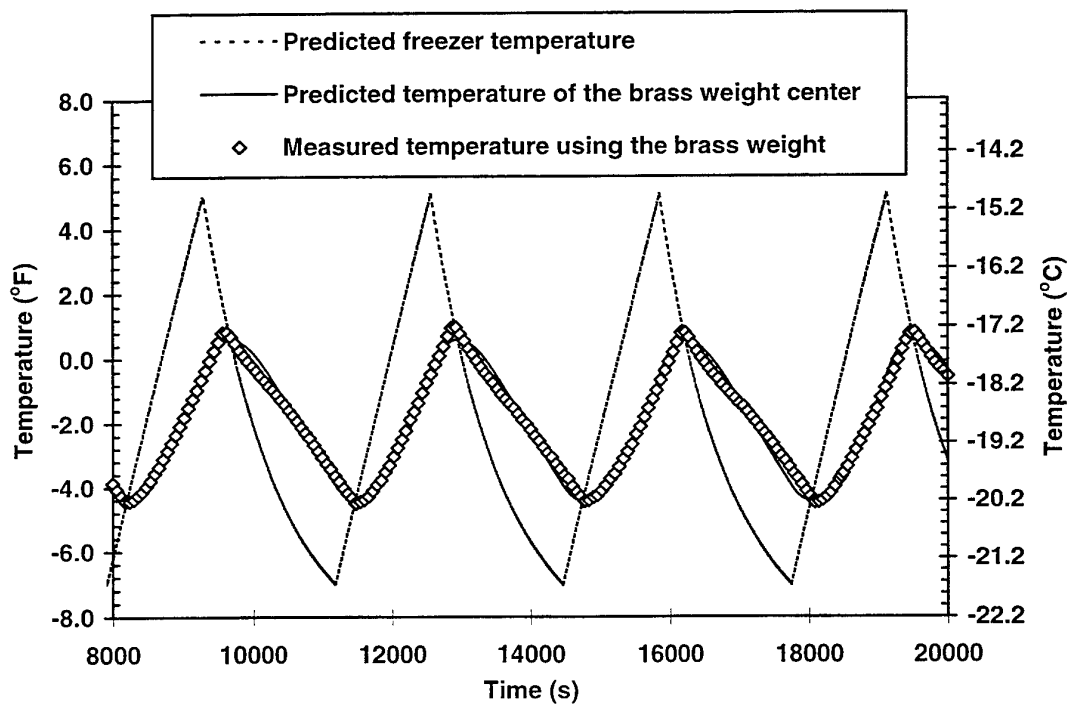


Fig. 6 Comparison of predicted temperature with measurements for a side by side refrigerator

to $-4.4 \sim 0.6$ °F ($-20 \sim -17.4$ °C) due to the thermal mass of the brass weight. The phases of the peak temperatures are delayed around 300 seconds and 400 seconds for the low and high peak temperatures,

respectively, due to the same reason. The variation of measured average freezer temperature in the freezer with time was compared to the predictions (see Fig. 6). It appears that the predictions agree well with the measurements.

Future Work

Future work is recommended as follows: 1) a parameter study such as effects of the temperature control band and bandwidth, air flow rate, the damper control approaches, etc. on the performance of the refrigerator; 2) more experiments for validating the model.

4. CONCLUSIONS

A computational model has been developed to simulate the temperature cycles of the freezing and fresh food compartments in a household refrigerator. Modeling consists of two parts coupled with each other: a refrigeration system and a temperature cycle of the refrigerator. The refrigeration system including a compressor, a condenser, an evaporator and a capillary tube is modeled based on performance data measured or provided by the manufacturers. The temperature variation in the refrigerator during a cycle is simulated using the lumped capacitance method. According to the results discussed, the following conclusions can be reached: 1) The temperatures in the freezing and fresh food compartments decrease following the supply air temperature during a duty cycle, and appear to increase linearly with time during an off cycle; 2) Temperature shifts in the freezer and fresh food compartment exist for the cross ambient temperatures from 90 to 70 °F (32.2 to 21.1 °C) for a fixed temperature control band and a fixed air flow rate of the fresh food compartment. 3) The predicted freezer temperatures agree well with the measurements. 4) A parameter sensitivity study and more experiments for validating the model are recommended for the further study.

REFERENCES

1. *Food Code*, U.S. Department of Health and Human Services, Public Health Service, food and Drug Administration, Washington, DC., USA. (1997).
2. X. Yuan, "Development of a Transient Simulation Model of a Freezer Part I: Model Development", *Proceeding of the int. Refrigeration Conference at Purdue University, W. Lafayette, IN.* pp. 213-218 (1994a).
3. X. Yuan, "Development of a Transient Simulation Model of a Freezer Part II: Comparison of Experimental Data with Model", *Proceeding of the int. Refrigeration Conference at Purdue University, W. Lafayette, IN.* pp. 219-224 (1994b).
4. T. Tiedemann, and H. Kruse, "Simulation of the Transient Behavior of Household Refrigerators and Freezers", *Proceeding of the int. Refrigeration Conference at Purdue University, W. Lafayette, IN.* pp. 191-198 (1994).
5. K. J. Graviss and R. L. Collins, "Strategies for Improving Temperature Control and Energy Use in Household Refrigerators", *Proceeding of the int. Refrigeration Conference at Purdue University, W. Lafayette, IN.* pp. 483-488 (1996).
6. X. Xu and D. Clodic, "Dynamic Simulation Model of a Vapor Compression Domestic Refrigerator Running with R134a", *Proceeding of the int. Refrigeration Conference at Purdue University, W. Lafayette, IN.* pp. 489-494 (1996).
7. E. L. Zapparoli and M. J. S. De Lemos, "Simulation of Transient Response of Domestic Refrigeration System", *Proceeding of the int. Refrigeration Conference at Purdue University, W. Lafayette, IN.* pp. 495-500 (1996).
8. K. J. Graviss and R. L. Collins, "Control of Household Refrigerators Part I: Modeling Temperature Control Performance", *HVAC&R Research*, v. 4, pp. 427-443 (1998).
9. K. J. Graviss and R. L. Collins, "Control of Household Refrigerators Part II: Alternate Control Approaches for Improving Temperature Performance and Reducing Energy Use", *HVAC&R Research*, v. 4, pp. 445-464 (1998).
10. Maytag, "Steady State Refrigeration Analysis Program", Maytag SSRAP user manual, (1996).

THE DEVELOPMENT OF ENERGY EFFICIENT REFRIGERATORS BY THE INDUSTRIAL TECHNOLOGY AND RESEARCH INSTITUTE

Jyi-Yu Sun

Industrial Technology and Research Institute
Energy and Resource Laboratories
Email: f860579@erl.itri.org.tw; Fax: (3) 582-0250

Jian-Yuan Lin

Industrial Technology and Research Institute
Energy and Resource Laboratories
Email: f730633@erl.itri.org.tw; Fax: (3) 582-0250

Keywords: refrigerator, energy-efficient, vacuum insulation panel, compressor

ABSTRACT. The growing concerns over global warming due to greenhouse emission have pushed the appliance industry in Taiwan to further improve energy efficiency of its products. Refrigerator-freezer, as one of the major home appliances, consumes about one-fifth electricity in a household, and its life expectancy could be as long as 10-15 years. In response to expected future regulations to be stricter, several design options were considered for improving the energy efficiency of a conventionally designed domestic refrigerator-freezer. The options, such as cabinet insulation improvements using vacuum insulation panels (VIPs), energy saving defrost control, and high-efficiency compressors were examined in a prototype refrigerator-freezer.

The energy consumption of the original 1997 production refrigerator-freezer was selected as the baseline in order to compare the measured energy savings of each and combined options on the prototype refrigerator-freezer. This study has reached a goal to develop a prototype that has an energy consumption rate of 20% less than the baseline refrigerator-freezer.

1. INTRODUCTION

A refrigeration system can contribute to global warming in two ways: directly through emissions of those refrigerants that are greenhouse gases, and indirectly the carbon dioxide emissions (by burning fossil fuels) associated with energy used to operate refrigeration equipment, such as the domestic refrigerator. As carbon dioxide is the largest contributor to global warming [1,2], to improve energy efficiency of a refrigeration system can consequently reduce the indirect effect.

The growing concerns over global warming due to greenhouse emission have required the appliance industry in Taiwan to consider an enhancement in energy efficiency of its products among all home appliances, refrigerator-freezer (RF) consumes about one-fifth electricity in a household, and its life expectancy could be as long as 10-15 years. It would be decisive to design more efficient RFs in order to reduce energy usage and as result to cut CO₂ emission. In response to expected future regulations to be stricter, several design options were considered for improving the energy efficiency of conventionally designed domestic RFs. Despite domestic RFs have undergone consistent and steady development worldwide over the years, the trend to more efficient refrigerators will continue. On April 23, 1997, the U.S. has already announced new efficiency standards [3] under which refrigerators manufactured after July 1, 2001, will use up to 30 percent less energy. In Europe and Japan similar action are under consideration in order to make more energy-efficient models.

In response to expected future regulations to be stricter, several design options were suggested for improving the energy efficiency of a conventionally designed domestic refrigerator-freezer. These options include substitution of high-efficiency compressor, improved heat transfer in evaporating and condensing units, tighter door gasket to reduce thermal loss, high-efficiency fan motors, better insulation, improved suction line heat transfer, liquid-line off-cycle control, and adaptive defrost control [4, 5]. However, customer expectations and competitive pressures impose constraints on RFs production in Taiwan. The external dimensions, the weight and structure, the ease of operation, and the low selling price are important features for an appliance, such as a RF, that has become a commodity item. Therefore, unless consumers are convinced to pay more for efficiency, it is hard to build models with all improving options added.

The objective of this study is to evaluate available efficiency-enhancing options in order to provide design data for manufacturers in Taiwan to develop their energy-efficient models. The final goal is to cut power consumption of RFs by 40% after the project ends on July 1, 2001. At this current phase, among all those options above, cabinet insulation improvements using vacuum insulation panels (VIPs), energy saving defrost control, and high-efficiency compressors were chosen and examined in a prototype RF system.

2. BACKGROUNDS AND EXPERIMENTAL PLAN

The energy consumption of the original 1997 production RF with a volume of 460 liters was selected as the baseline in order to compare the experimentally measured energy savings of each and combined options on the prototype RF system. Furthermore, the cabinet reverse heat leak test to evaluate the effectiveness of VIPs, and compressor calorimeter test results for currently-used and more efficient compressors were also extensively documented to provide firm basis for the measured energy savings.

The goal for this study was to develop a prototype that has an energy consumption rate of 20% less than the baseline RF. To reach this goal, three options were selected in this study, namely, more efficient compressors, better insulation using VIPs, and more precise defrost control. The background and method to evaluate these options were described as following.

2.1 Compressor Calorimeter Measurements

New compressor developments are leading to considerable efficiency improvements. Nine-point calorimeter measurements were used to determine the performance of several R-134a compressors as options used in the modified units from the baseline RFs. In this procedure, compressor operating characteristics, including refrigeration capacity and EERs (COPs), were determined at each point in a matrix of 110 °F (43.3 °C), 120 °F (48.9 °C), and 130 °F (54.4 °C) condensing temperatures and -20 °F (-28.9 °C), -10 °F (-23.3 °C), and 0 °F (-17.8 °C) evaporating temperatures. Also specified in the test procedure are a 90 °F (32.2 °C) ambient temperature for the compressor, superheating of the suction gas to 90 °F (32.2 °C), and subcooling of the liquid refrigerant line to 90 °F (32.2 °C) before throttled expansion. The nine-point maps generated from the tests were than used as inputs for the design parameters for more efficient RF prototypes.

2.2 Insulation and Its Improvement

In early 1960s rigid urethane foam produced with fluorinated hydrocarbon expanding agents was introduced [6] and had been accepted rapidly until the 1996 ban on the manufacturing of foam-blowing agents containing CFCs. At the present time, RF manufactures in Taiwan uses HCFC-141b as blowing agent, which is considered a transitional blowing agent due to its small ODP (ozone depletion potential). HFC-245fa is the leading non-chlorine solution as blowing agent by the RF manufactures in the U. S., and Cyclopentane is chosen by most European manufactures. Both have energy penalty due to a reduced thermal resistance of the foam [7]. Vacuum insulation, however, can offer several times the insulation value of polyurethane foam [8]. Initially several concerns had to be addressed, such as vacuum reliability, and the weight of the insulation may probably be a disadvantage. Most of these were solved as technology proceeds and European and Japanese makers are now using VIPs (Vacuum Insulation Panels). However, these have not become mass-market production due to the concerns over its cost.

VIPs use various core materials, including fiberglass, silica powder, open-cell rigid polyurethane foam, and open-cell polystyrene foam. ITRI has developed process of making VIPs using rigid polyurethane and polystyrene foam [9,10]. These two types of VIPs together with conventional insulation material using HCFC-141b as blowing agent were evaluated in this study.

Steady state reverse heat leak measurements were performed on the baseline RF cabinets as received and on RF cabinets with VIPs implemented. Heat leak rates under steady state conditions, were measured in watts at various air temperatures inside the RF compartment and various air temperatures (-18, 0, and 32.2°C) maintained by an environmental chamber. Separate heat sources in the form of electrical heaters and small fans controlled with a monitored variac are used in each compartment to obtain similar temperature drops, but opposite in direction, to those seen under normal RF operation. A linear relationship between heat leak rate and temperature difference (Eq. 1) is assumed. Equations obtained through a least-squares fit of the data were used

to calculate the cabinet load arising from heat permeation through walls, doors, and gaskets at operating and ambient temperatures.

$$Q = UA \times T \quad (1)$$

Figure 1 shows the schematic diagram of heat leak test to evaluate the insulation performance. Once VIPs are implemented, a 15-20% improvement in the thermal resistivity of the cabinet was expected as a reasonable design.

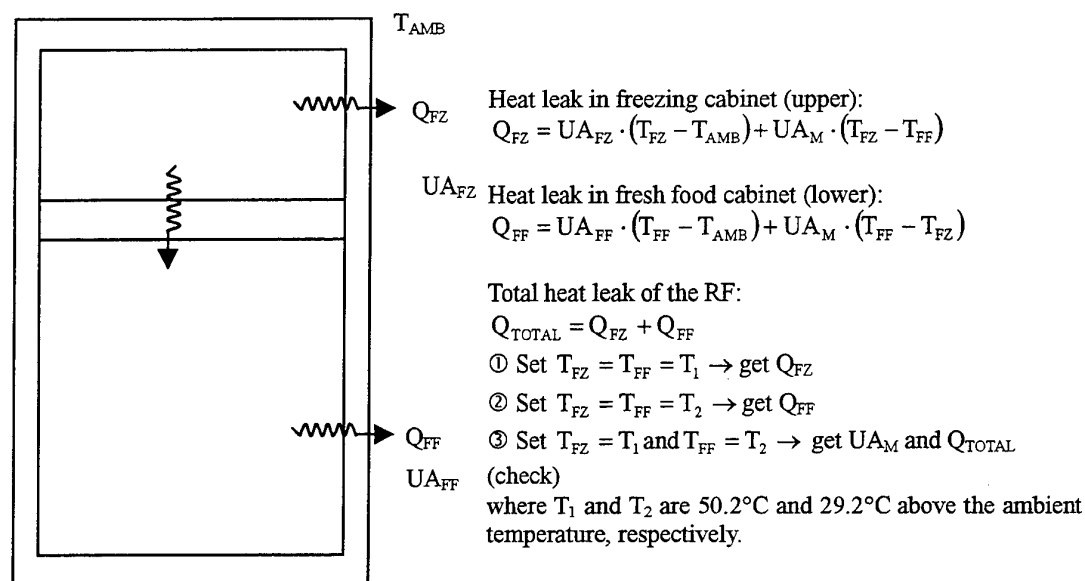


Figure 1. The schematic diagram of cabinet heat leak test for insulation performance

2.3 Defrost Control

Humidity from the airflow within RFs can give rise to the frost formation at evaporators of refrigerant loop. The existence of frost can decrease the rate of heat transfer in two ways. First, the frost growth could introduce additional flow resistance thus decreases the amount of air flow over the coil and thus decrease the heat transfer; and second the frost acts as a thermal barrier to the heat flow [11,12]. Currently, the preferred method for defrosting a RF is to use an electrical heater to heat the evaporator itself, the neighboring surfaces and the air of the evaporator compartment, which usually can exterminate all frost thoroughly. Using electrical heater seems effective, however, the temperature in the RF freezing compartment may deteriorate by a temperature increase as large as $5\text{--}8^\circ\text{C}$ during defrost process, which in turn can become an additional thermal load to the RF.

In the conventional technology, the defrost heater is operated by a timer which is set based on the run time of compressors, and for most climates it may come on much more often than would be required. This conventional technology can not detect the frost formation and improper timing for defrost could occur. Hence, using heater and timer for defrost could lead to unneeded thermal loads to RFs. To avoid this power ineffective consumption, a frost monitor apparatus, which can sense the frost existance and its thickness, was developed to determine when it is necessary to initiate the defrost cycle. In this manner, the defrost heater is only turned on when the frost thickness reaches to a preset value. The performance of this defrost control was evaluated as the fresh-food cabinets of two RFs (both the baseline RF and a RF equipped with this new defrost control) were loaded with two 5-liter barrels of water. The reduction of energy consumption both RFs was then measured to determine the performance of this defrost control apparatus.

3. RESULTS AND DISCUSSIONS

The following options, namely high-efficiency compressors, cabinet insulation improvements using vacuum

insulation panels (VIPs), and energy saving defrost control, were examined and evaluated in prototype RFs. The daily energy consumption rate of RFs applied with each option or combined options were than measured to compare with the original baseline refrigerator-freezer.

3.1 Compressor Calorimeter Tests Results

There were 8 different compressors tested in this study. They were manufactured by A, B, C, and D companies. Compressors were sequenced based on their manufactures and models. Compressor A-1 was used by the baseline RF, compressors A-2 was a new model from the same company. Compressors A and B were considered lower EER models but cheaper. Compressors C and D were considered higher EER models. As specified earlier, 9-point calorimeter tests were performed to evaluate the cooling capacities and EERs for these compressors. The compressor calorimeter test result for compressor A-1 (used in the baseline RF) is listed in Table 1. The compressor calorimeter test result for compressor D-2 (highest EER in this study) is listed in Table 2. For the rest compressors, similar tables, but with different values, could be built for RF system design purpose.

Table 1. Compressor Calorimeter Test Result for Compressor A-1 (Used in the Baseline RF)

Condensing Temperature (°C)		110	120	130
Evaporating Temperature (°C)				
0	Refrigeration Capacity kcal/hr	222.4	245.9	269.1
	E.E.R. kcal/hr-W	0.987	1.104	1.225
-10	Refrigeration Capacity kcal/hr	160.2	178.8	202.7
	E.E.R. kcal/hr-W	0.816	0.928	1.092
-20	Refrigeration Capacity kcal/hr	114.4	125.2	138
	E.E.R. kcal/hr-W	0.672	0.728	0.837

Table 2. Compressor Calorimeter Test Result for Compressor D-2 (Highest EER in this Study)

Condensing Temperature (°C)		110	120	130
Evaporating Temperature (°C)				
0	Refrigeration Capacity kcal/hr	227	251.1	269.7
	E.E.R. kcal/hr-W	1.291	1.462	1.682
-10	Refrigeration Capacity kcal/hr	181.5	196.9	212.8
	E.E.R. kcal/hr-W	1.152	1.249	1.48
-20	Refrigeration Capacity kcal/hr	123.1	136.8	150.2
	E.E.R. kcal/hr-W	0.971	1.093	1.226

Table 3 lists the comparison of refrigeration capacities and EERs from calorimeter test results for various compressors at condensing temperature of 130 °C and evaporating temperature of -10 °C. It can be seen that the compressor used in the baseline RF has the lowest EER value, and using compressors from manufactures C and D can significantly enhance compressor efficiency by 14 to 38%. As compressors in RFs were usually operated with run time of about 50%, there exists plenty of room to raise the energy efficiency of RF system through compressor substitute.

3.2 VIPs Test Results

The performance of VIPs was evaluated through reverse heat leak test as described in Fig. 1. Table 4 shows the thermal conductivity for PU foam blown by HCFC-141b, VIP-PU (with Polyurethane as core foam) and VIP-PS (with polystyrene as core foam) at various operating temperatures. It indicates an increase in thermal conductivity with increasing operating temperatures. This shows that reverse heat leak test may be a little bit conservative in determining the VIPs performance when applying to the normal RF operating condition, especially when ambient temperatures is set above zero.

Table 3. Comparison of Calorimeter Test Results for Various Compressors at Condensing Temperature of 130 °C and Evaporating Temperature of -10 °C

Compressor model	Refrigeration capacity kcal/hr	Deviation from compressor A (%)	E. E.R (kcal/hr-W)	Deviation from compressor A (%)
A-1	202.7	---	1.072	---
A-2	208.5	2.86	1.126	5.04
B	226.5	11.74	1.11	3.54
C-1	188.9	-6.81	1.221	13.9
C-2	205.7	1.48	1.242	15.9
C-3	174.8	-13.76	1.215	13.3
D-1	187.9	-7.3	1.379	28.6
D-2	212.8	4.98	1.48	38.1

Table 5 shows RF reverse heat test results for various insulation conditions. Due to some cooling capacity limitation for the environmental chamber, the ambient temperature can only be set to a value not lower than 15°C, after the baseline unit was run at an ambient temperature of 0°C. As mentioned earlier, this would only bring a more conservative evaluation for insulation effectiveness when evaluation is done under a high ambient temperature. As seen in Table 5 for RF#1, the difference in total heat was about 1% when ambient temperatures were set at 0 and 15°C.

**Table 4. Thermal Conductivity (W/m-K) of Various Insulation Materials
Used in this Study**

Insulation Material	Mean Temperature in Measurement (°C)	0	14.3	27.5
Conventional rigid PU foam		0.021	0.0218	0.0237
VIP-PU (Polyurethane) @10-5 torr		0.0069	0.0073	0.008
VIP-PS (Polystyrene) @ 0.01 torr		0.004	0.0044	0.0047

Table 5. RF Reverse Heat Test Results for Various Insulation Conditions

RF #1-Baseline RF Insulated by Conventional PU Foam with $T_{amb} = 0^{\circ}\text{C}$

Ambient Temperature (°C)	0	0	0
Temperature in freezing cabinet (°C)	29.2	50.2	50.2
Temperature in fresh food cabinet (°C)	29.2	50.2	29.2
Heat leak in freezing cabinet (W)	5.387	26.415	38.925
Heat leak in fresh food cabinet (W)	24.396	55.912	13.176
Total heat leak (W)	29.783	82.327	52.101

RF #1-Baseline RF Insulated by Conventional PU Foam with $T_{amb} = 15^{\circ}\text{C}$

Ambient Temperature (°C)	15	15	15
Temperature in freezing cabinet (°C)	44.2	65.2	65.2
Temperature in fresh food cabinet (°C)	44.2	65.2	44.2
Heat leak in freezing cabinet (W)	5.694	26.754	39.212
Heat leak in fresh food cabinet (W)	24.866	56.478	13.442
Total heat leak (W)	30.56	83.232	52.654

RF #2 – Modified RF Insulated by VIP-PU (20mm)

Ambient Temperature (°C)	15	15	15
Temperature in freezing cabinet (°C)	44.2	65.2	65.2
Temperature in fresh food cabinet (°C)	44.2	65.2	44.2
Heat leak in freezing cabinet (W)	2.67	20.472	31.964
Heat leak in fresh food cabinet (W)	24.443	52.013	12.206
Total heat leak (W)	27.113	72.485	44.17

RF #3 – Modified RF Insulated by VIP-PS (25mm)

Ambient Temperature (°C)	15	15	15
Temperature in freezing cabinet (°C)	44.2	65.2	65.2
Temperature in fresh food cabinet (°C)	44.2	65.2	44.2
Heat leak in freezing cabinet (W)	2.017	18.396	29.675
Heat leak in fresh food cabinet (W)	20.994	46.326	10.552
Total heat leak (W)	23.111	64.722	40.227

The improvement of VIPs on total heat leak rates is listed in Table 6, in which 16.21% and 23.6% can be reached with VIP-PU and VIP-PS, respectively. In our study, only about 12-15% of the total volume of insulation were replaced by VIPs, and the cost increase was kept in a acceptable range.

Table 6. The Improvement of VIPs on Heat Leak Rate

RF model #	1	2 (VIP-PU)	3 (VIP-PU)
Total heat leak (W)	52.654	44.12	40.227
Heat leak Improvement (%)	--	16.21	23.6

3.3 Defrost Control Test Result

The performance of this defrost control was evaluated as the fresh-food cabinets of two RFs (both the baseline RF and a RF equipped with this new defrost control) were each loaded with two 5-liter barrels of water. The daily energy consumption rate for baseline RF and RF with new defrost control were 2.607 kWh and 2.532 kWh, respectively, indicating a 2.88% cut in energy usage.

3.4 Energy Consumption Test Result

Closed-door cumulative daily energy consumption tests were run under 32.2°C and 70% relative humidity environmental condition. Ten RFs, including the baseline RF, were tested to evaluate the effectiveness of each or combined options on energy efficiency enhancement. Test results together with RF description are listed in Table 7. As Table 7 indicates a goal of 20% cut of energy usage can be reached in cases H, I and J.

4. CONCLUSIONS

When applied with better insulation such as VIPs and more efficient compressors (EER greater than 1.2) and probably energy-saving defrost control, a prototype RF can reach to a promising cut of energy consumption rate to the set goal of 20%. The goal of next phase is to continue the development of energy-efficient RFs to get to at least 40% cut of the energy usage from current RFs, which can lead to extensive variety for the manufacturers to choose for their energy-saving models under the consideration of manufacturing cost.

Table 7. Daily Energy Consumption Measurement Results at Various Option Conditions

Case	Description	Consumed Power (kWh/day)		Compressor Run Time %
A	Baseline units	2.509	---	53.1
B	Case A + VIP-PU(20mm)	2.366	5.70%	48.9
C	Case A + VIP-PS(25mm)	2.295	8.53%	47.4
D*	Case A + better defrost control	2.437	2.87%	53.9
E	Case A + 1.242 EER compressor (C-2)	2.338	6.82%	51.6
F	Case A + 1.480 EER compressor (D-2)	2.139	14.75%	50.2
G	Case B + Case E	2.234	10.96%	48
H	Case C + Case F	1.971	21.44%	46.3
I	Case C + 1.215 EER compressor (C-3)	1.96	21.88%	50.7
J*	Case D + Case H	1.92	23.48%	45.2

* readjusted for no-load condition

REFERENCES

1. S.K. Fischer, Total equivalent warming impact: a measure of the global warming impact of CFC alternatives in refrigerating equipment *Int. J. Refrigeration* (1993) 16 423-428.
2. UNEP (United Nations Environment Programme) Technical progress on protecting the ozone layer-report of the refrigeration, air conditioning and heat pumps technical options committee, United Nations, New York.
3. Energy conservation program for consumer products: energy conservation standards for refrigerator-freezers and freezers *US Standards* (1998), Final rule by office of efficiency and renewable energy, DOE.
4. S.H. Hakim, I. Turiel, Cost-Efficiency analysis in support of the energy conservation standards for refrigerator/freezers *ASHRAE* paper n. 4007 (1996).
5. J.R. Sand, et al. Investigation of design options for improving the energy efficiency of conventionally designed RFs *ASHRAE* paper n.94-20-4 (1994).
6. R. E. Knox, Insulation properties of fluorocarbon expanded rigid urethane foam *ASHRAE Trans* (1963) 69 150-159.
7. W. Deeg, et al. Influence of blowing agent selection on foam aging and energy consumption of refrigerators *Proceedings, 49th IATC* (1998) 420-428.
8. D. Simpson, The cooling transition *Appliance* (1998) 55 9 53-61.
9. Tao, W. H., et al. Development of vacuum insulation systems *Proceedings, 37th Annual Polyurethane Technical/Marketing Conference* (1996) 43-47.
10. W.H. Tao, J.Y. Lin, Development of vacuum insulation panel systems *Proceedings, 49th IATC* (1998) 399-410.
11. R.W. Rite, R.R. Crawford, The effect of frost accumulation on the performance of domestic refrigerator-freezer finned-tube evaporator coils *ASHRAE Trans.* (1991) 97 428-437.
12. R.W. Rite, R.R. Crawford, A parametric study of the factors governing the rate of frost accumulation on domestic refrigerator-freezer finned-tube evaporator coils *ASHRAE Trans.* (1991) 97 438-446.

STUDY OF AN AUTO-REFRIGERATING CASCADE SYSTEM¹

Shaozhi Zhang, Guangming Chen, Hongxian Zhang, Jianfeng Wang

Refrigeration and Cryogenic Engineering Institute

Zhejiang University, Hangzhou, 310027, China

Email: enecgm@ dial.zju.edu.cn

Keywords: auto-refrigerating cascade system, thermodynamic analysis, coefficient of performance

ABSTRACT. Low-temperature refrigerating cascade systems are widely used in preservation of biological issues, cooling detectors and providing circumstances for material and component testing. Contrast to some traditional cascade cycles, this paper presents an auto-refrigerating cascade cycle that employs a rectifying column. The rectifying column is used to separate high boiling component and low boiling component. A thermodynamic analysis of the cycle is conducted with R134a/R23 as working fluid. Energy balance equations are established for each component of the system. Some important factors, including composition of the mixture, suction temperature of the compressor and operation pressure of the rectifying column, are analyzed of their impacts on compression ratio and coefficient of performance. The generalized Patel-Teja equation is used to calculate VLE and related thermodynamic properties.

1. INTRODUCTION

Refrigerating cascade systems are usually employed to achieve temperatures below -40°C . According to the temperatures reached, these systems are widely used to preserve biological issues, to cool detectors, to cool cryosurfaces in vacuum deposition chambers for water cryopumping, to provide cooling for materials and component testing. There are two kinds of refrigerating cascade systems. The first kind is made of multiple cycles. As an example, Fig. 1 demonstrates a two-cycle system. The high-temperature cycle circulates the high boiling point refrigerant, such as R22 or R134a, and the low-temperature cycle circulates the low boiling point refrigerant, such as R23. The two cycles are linked with a condenser-evaporator. The disadvantage of this kind of cycle is that it needs two compressors and there are special requirements for the lubrication of the compressor used in the low-temperature cycle. The second kind is called auto-refrigerating cascade system [1-3]. As an example, Fig. 2 demonstrates a system with three phase separators. In this kind of system, a single or multistage compressor circulates a refrigerant mixture. Several partial phase separators and heat exchanger are employed. After each cooling step in an upstream heat exchanger, a phase separator removed the condensate from the vapor stream. The liquid with a reduced pressure mixes with the returning suction stream. The fluid then goes to the next downstream heat exchanger where it evaporates and absorbs heat. The evaporation of the lowest boiling point component provides the cooling capacity. However, since only one phase separator is used to separate one component, the separation process can not be perfect. In order to separate the mixture more perfectly, the author of this paper presents a new cycle that utilizes a rectifying column [4].

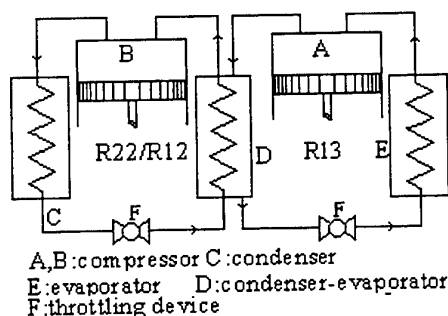


Fig. 1. A two-cycle system

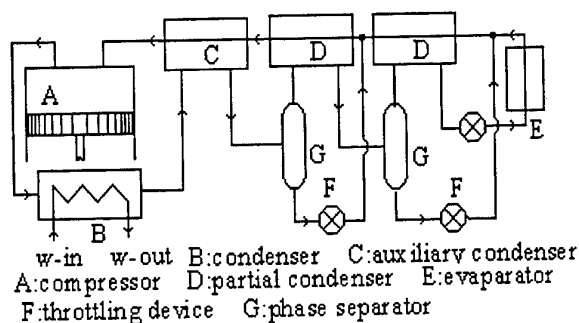


Fig. 2. An auto-refrigerating cascade system with three phase separators

¹ This project is supported by 151 Talent Engineering Foundation of Zhejiang China.

2. AUTO-REFRIGERATING CASCADE CYCLE WITH A RECTIFYING COLUMN

Fig. 3 gives the flowchart of the new cycle. The refrigerant mixture is compressed by a compressor and cooled in condenser where it condenses partially. The mixture then enters into the heat exchanger located in the bottom of the rectifying column to heat the bottom liquid. After throttling, the mixture undergoes a rectification process in the rectifying column. The purified low boiling component vapor flows out from the top of the rectifying column and the liquid rich in high boiling point component flows out from the bottom of the rectifying column. The liquid is cooled by the suction stream and throttled to provide cooling for the operation of the rectifying column and the condensation of the low boiling point component vapor in condenser-evaporator. The condensed low boiling point liquid is then cooled by the return vapor in heat regenerator and throttled to provide the final cooling capacity in evaporator.

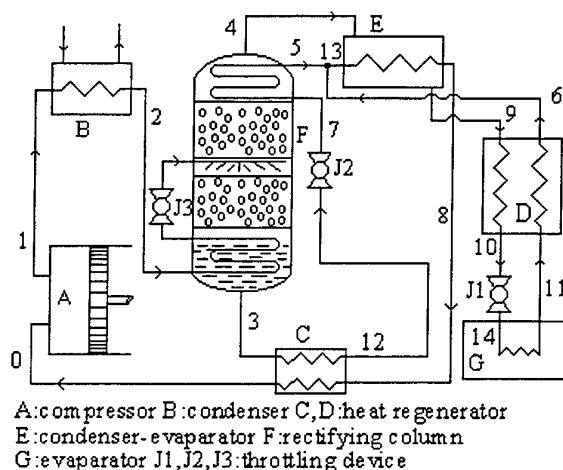


Fig. 3. An auto-refrigerating cascade system with a rectifying column

It can be seen that the main difference between the two cycles shown in Fig. 2 and Fig. 3 is the separation device. The new cycle employs a rectifying column and can offer a better separation of components. The performance of the new cycle is of interest, so in the following we will have a thermodynamic analysis of the cycle to find out the factors that affect the performance.

3. THERMODYNAMIC ANALYSIS OF THE NEW CYCLE

Before the analysis, it is necessary to determine the circulating fluid. In this paper, we choose HFCs mixture as refrigerant. R134a is selected as the high boiling point component and R23 is selected as the low boiling point component. The thermodynamic properties of the refrigerant are calculated with the generalized Patel-Teja equation [5]:

$$p = \frac{RT}{V-b} - \frac{a(T)}{V(V+b) + c(V-b)} \quad (1)$$

$$a(T) = \Omega_a (R^2 T_c^2 / P_c) \alpha(T_r), \quad \alpha(T_r) = [1 + F(1 - T_r^{0.5})]^2 \quad (2)$$

$$b = \Omega_b (RT_c / P_c), \quad c = \Omega_c (RT_c / P_c) \quad (3)$$

where Ω_a, Ω_c are evaluated as follows:

$$\Omega_a = 3\zeta_c^2 + 3(1 - 2\zeta_c)\Omega_b + \Omega_b^2 - \zeta_c^3, \quad \Omega_c = 1 - 3\zeta_c \quad (4)$$

and Ω_b is the smallest positive root of the following cubic equation:

$$\Omega_b^3 + (2 - 3\zeta_c)\Omega_b^2 + 3\zeta_c^2\Omega_b - \zeta_c^3 = 0 \quad (5)$$

For temperatures near or above the critical temperature, ζ_c changes to ζ'_c :

$$\zeta'_c = \zeta_c - 10(\zeta_c - Z_c)(T_r - 0.9), 0.9 < T_r < 1; \quad \zeta'_c = Z_c, T_r \geq 1 \quad (6)$$

For the mixtures the mixing rule is given by:

$$a_m = \sum_{i=1}^n \sum_{j=1}^n a_i a_j x_i x_j (1 - k_{ij}), \quad b_m = \sum_{i=1}^n x_i b_i, \quad c_m = \sum_{i=1}^n x_i c_i \quad (7)$$

where the binary interaction parameter k_{ij} for R134a-R23 is fitted with the experimental data listed in reference [6].

In order to make the analysis feasible, the following assumptions are made:

- 1) The isentropic efficiency of the compression process is 70%. That means the work consumed by an isentropic compression process is 70% of the work consumed by the actual process.
- 2) Pressure drops during the condensing processes and the flowing processes of liquids are neglected. The pressure drops (in kPa) in heat exchangers and ducts are considered as follows:

$$p_{14} - p_{11} = 4, \quad p_{11} - p_6 = 2, \quad p_6 - p_8 = 3, \quad p_8 - p_0 = 1, \quad p_7 - p_5 = 4 \quad (8)$$

The pressure drop along the rectifying column is assumed to 20kPa. That is:

$$p_3 - p_4 = 20 \quad (9)$$

- 3) The liquid out of the bottom of the rectifying column and the vapor out of the top are saturated.
- 4) The vapor at the outlets of the evaporator and the condenser-evaporator is saturated.
- 5) The temperature differences of heat exchangers are fixed or limited as follows:

$$T_6 - T_9 = 5, \quad T_9 - T_8 \geq 3, \quad T_4 - (T_5 + T_7) / 2 \geq 2, \quad T_3 - T_0 \geq 5, \quad T_{12} - T_8 \geq 5, \quad T_2 - T_3 = 5 \quad (10)$$

According the energy balance of the rectifying column and related heat exchangers, the following equations are established:

$$f_L (h_3 - h_{12}) = h_0 - h_8 \quad (11)$$

$$h_2 + f_L h_7 = h_3 + f_L h_5 + (1 - f_L) h_4 \quad (12)$$

$$h_9 - h_{10} = h_6 - h_{11} \quad (13)$$

$$f_L h_5 + (1 - f_L) h_6 - h_8 = (1 - f_L) (h_9 - h_4) \quad (14)$$

where f_L is the ratio of the flow rate of the liquid flowing out of the bottom of the rectifying column to the flow rate of the whole cycle. It can be determined by the continuity of one component as follows:

$$x_2 = f_L x_3 + (1 - f_L) x_4 \quad (15)$$

where x_2, x_3, x_4 refer to the percentage of R134a at state point 2, 3, 4. Provided that the composition of the mixture, the evaporation pressure, the suction temperature and the operation pressure of the rectifying column are given, the discharge pressure of the compressor can be solved with the above given equations. After the

states of the state points in the cycle are determined, the coefficient of performance (COP) can be calculated as follows:

$$\text{COP} = \frac{(1-f_L)(h_{11} - h_{14})}{h_1 - h_0} \quad (16)$$

where h_0, h_1, h_{11}, h_{14} represent the specific enthalpy of state point 0, 1, 11, 14 respectively.

4. RESULTS AND DISCUSSIONS

According to the above assumptions and equations, a program is worked out. Several factors that affect COP and compression ratio, including the composition of the mixture, the suction temperature, the operation pressure of the rectifying column, are investigated while the average evaporation pressure is fixed at 138 kPa and the outlet temperature of the condenser is fixed at 40 °C. The detail is as follows:

4.1 Composition of the Refrigerant Mixture

When the influences of composition are considered, suction temperature is fixed at -5 °C and operation pressure of the column stays at a value where the outlet liquid of the condenser-evaporator is saturated. Fig. 4 displays the curves of COP and compression ratio varying with percentage of R23 in the mixture. As we can see, when the percentage of R23 increases, compression ratio and COP increase at the same time. This can be easily understood. When the quantity of R23 increases, it will be more difficult for the discharge gas to condense and therefore demand higher discharge pressure. On the other hand, the quantity of R23 flowing to the evaporator will also increase and therefore offer a larger cooling capacity. While the percentage of R23 changes from 21% to 27%, COP changes from 0.128 to 0.262 and compression ratio changes from 9.22 to 10.18. Therefore, the composition has a great impact on COP and also impact on compression ratio.

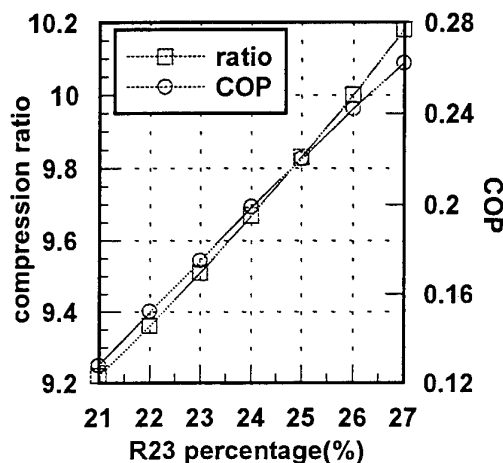


Fig. 4. Effect of composition

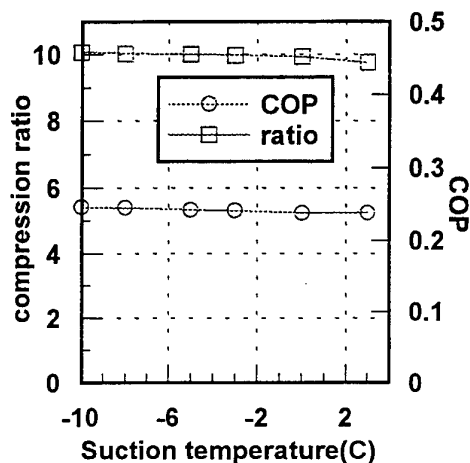


Fig. 5. Effect of suction temperature

4.2 Suction Temperature

When the influences of suction temperature are considered, the percentage of R23 is fixed at 26% and operation pressure of the rectifying column stays at a value where the outlet liquid of the condenser-evaporator is saturated. Raising suction temperature of the compressor will increase recovery of cooling from suction gas. However, the total effect may be difficult to predict qualitatively. Fig. 5 gives the calculated impacts of suction temperature on COP and compression ratio. When suction temperature increases, COP and compression ratio will have a slight decrease. As suction temperature goes up from -10 °C to 3 °C, COP will decrease from 0.246 to 0.238 and compression ratio from 10.07 to 9.75. It can be seen that suction temperature only has a small influence.

4.3 Operation Pressure of the Rectifying Column

When the influences of operation pressure are considered, suction temperature is fixed at -5°C and the percentage of R23 is fixed at 26%. The rectifying process is influenced by operation pressure of the rectifying column. Fig. 6 gives the bubble/dew point curves at 1100 kPa, 1300 kPa and 1500 kPa. It may be a little difficult to see from the figure that the higher, the pressure, the closer the two curves. When the percentage of R23 is 50%, the differences between the dew point and the bubble point are 26.8°C , 25.3°C and 23.9°C corresponding to 1100 kPa, 1300 kPa and 1500 kPa respectively. The closer, the two curves, the smaller of the concentration difference between the liquid and the vapor at equilibrium, the more difficult will be the separation. Therefore, raising operation pressure of the rectifying column will lead to concentration increase of R23 in the outlet liquid of the column and decrease the quantity of R23 flowing to the evaporator and cause COP to fall. This is proved by the calculated result displayed in Fig. 7. When operation pressure increases from 1271 kPa to 1347 kPa, COP decreases from 0.242 to 0.205. At the same time, pressure ratio has a minor decrease from 10.0 to 9.95. The influence of operation pressure is obvious.

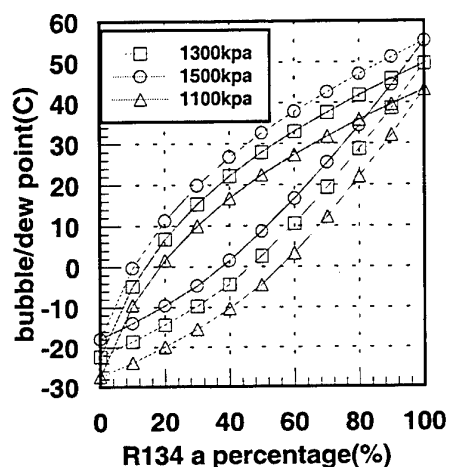


Fig. 6. Dew/bubble point curves of R134a-R23

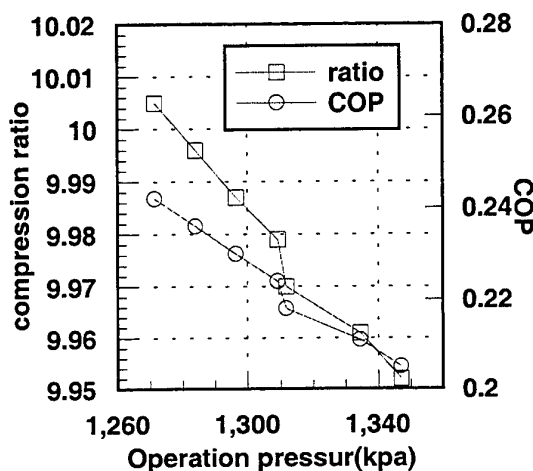


Fig. 7. Effect of operation pressure

5. COMPARISON OF THE NEW CYCLE TO THE TWO-SEPARATOR CYCLE

As mentioned above, the main advantage of the new cycle is that it can offer a lower evaporating temperature. This is further proved by comparison between the new cycle and the two-separator cycle shown in Fig. 2. The analysis of the two-separator cycle was performed. The following assumptions are made:

1. The pressure drop on the high-pressure side is neglected. On the low-pressure side it is considered as:

$$P_{15} - P_{16} = 4, \quad P_{16} - P_{10} = 2.5, \quad P_{10} - P_6 = 2.5, \quad P_6 - P_0 = 1 \quad (17)$$
2. The low-pressure refrigerants at the outlets of the evaporator and the two condenser-evaporators are saturated.
3. The efficiency of the compression process is 70%. That means the work consumed by an isentropic compression process is 70% of the work consumed by the actual process.
4. The temperature differences at the two ends of auxiliary condenser are greater than 5°C and the temperature differences at the four ends of the two condenser-evaporators are greater than 3°C .

For the new cycle, the percentage of R23 in the refrigerant mixture is fixed at 24%. The comparison is made within the following premises:

1. The compression ratio ranges from 9 to 12.
2. The discharge temperature of the compressor is limited below 120°C .
3. The outlet temperature of the condenser stays at 40°C .
4. The pressure at the evaporator inlet is fixed at 140 kPa.

Fig. 8 gives a performance comparison between the two cycles. The average evaporating temperature is defined as the average value of the inlet and the outlet temperature of the evaporator. It can be seen that the lowest temperature the two cycle may reach differs a lot. The new cycle can reach as low as -75.3°C , but the two-

separator cycle can reach only -42.8°C . As to the coefficient of performance, when the average evaporating temperature is -42.8°C , the new cycle's COP is 1.038, but the two-separator cycle's COP is 0.443. Therefore, under the conditions considered in this paper, the new cycle has obvious advantages over the two-separator cycle. The former can not only offer a lower refrigerating temperature but also have a higher COP.

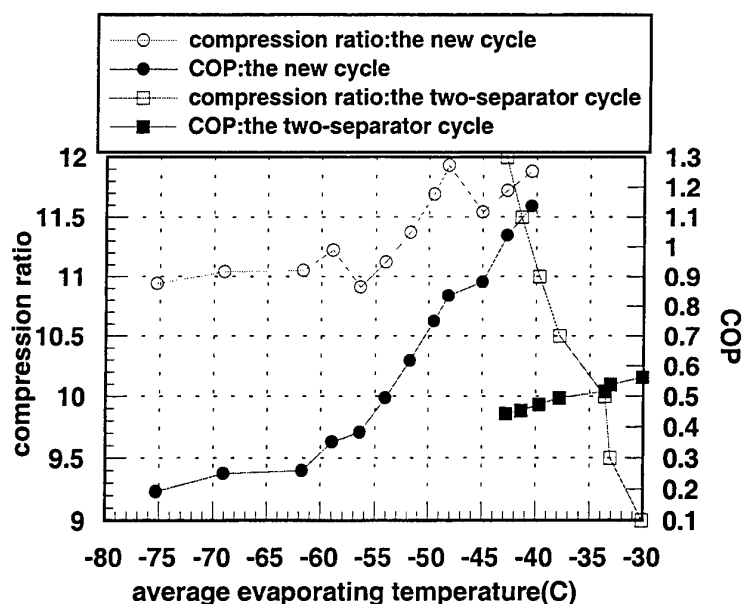


Fig. 8. Comparison between the new cycle and the two-separator cycle

6. SUMMARY

This paper presents a new auto-refrigerating cascade cycle. The cycle uses refrigerant mixture as working fluid and employs only one compressor. A rectifying column is set to separate high boiling point component and low boiling component efficiently. Thermodynamic analysis is carried out with R134a/R23 as refrigerant. Several factors that affect compression ratio and COP are studied. Conclusions are reached as follows:

- 1) As the concentration of low boiling point in the cycling mixture increases, COP and compression ratio will both increase. The composition of the mixture has a large impact on COP and a moderate impact on compression ratio.
- 2) As suction temperature of the compressor increases, COP and compression ratio will decrease. But the impact is not great.
- 3) As operation pressure of the rectifying column increases, COP and compression ratio will decrease. Operation pressure has a moderate impact on COP and a small impact on compression ratio.

Furthermore, a comparison is made between the new cycle and a two-separator cycle. The advantages of the new cycle are obvious. Compared with the two-separator cycle, it can not only reach a lower refrigerating temperature but also have a higher COP.

REFERENCES

1. J.M. Dale, Refrigerant conversion of auto-refrigerating cascade systems, *Int. J. Refrig.* Vol. 20, No. 3, pp. 201-207 (1997).
2. F. Andrija, U.S. patent, 3203194 (1962).
3. J.M. Dale, U.S. patent, 3698202 (1972).
4. G.M. Chen, S.Z. Zhang, J.F. Wang, Y.P. Feng, China patent, 99203770.0 (1999).
5. O.V. José, A generalized Patel-Teja equation of state for polar and nonpolar fluids and their mixtures, *J. Chem. Eng. Japan*, Vol. 23, No. 1, pp. 87-91 (1990).
6. K. Michael, An extension to the UNIFAC group assignment for prediction of vapor-liquid equilibria of mixtures containing refrigerants, *Fluid Phase Equil.*, Vol. 107, pp. 161-188 (1995).

PERFORMANCE STUDY OF A COMPOSITE ADSORBENT BLOCK USED FOR SOLAR OR WASTE HEAT POWERED REFRIGERATION

Zhenyan Liu, Yunzhuang Lu

School of Power and Energy Engineering

Shanghai Jiao Tong University, 200030, P.R.China

Email: zyliu@mail1.sjtu.edu.cn; Fax: (021)62933250

Keywords: composite adsorbent block, thermal conductivity, absorption refrigeration

ABSTRACT. This paper presents a new solid composite adsorbent block after analyzing the influences of some factors on the heat transfer of adsorbent bed. The maximum variation of adsorbate content in a block bed increases about 50 percent compared with that of a grain bed of the same volume, and the thermal conductivity of the block bed is about three times of that of a grain bed by experimental studies. Therefore the performance of adsorbent bed composed of the blocks may have significant improvement compared to that of powder or grain bed. The effective thermal conductivity of the block is also discussed. The application of the solid composite adsorbent block in solar or waste heat powered adsorption refrigeration is discussed, and an solar cooling tube using the blocks as its adsorbent bed which may receive solar energy directly is presented.

1. INTRODUCTION

Because of its simple operation, no pollution, no noise and being possible to utilize low grade thermal energy such as solar energy or industrial waste heat, solid adsorption refrigeration represents promising application prospects in energy saving and environment protect. The adsorption system mainly has only three parts: adsorber, condenser and evaporator. Among them the adsorber is the most important and is researched intensely. In a operation cycle, the adsorber will be heated and cooled alternatively. Thus a good heat exchanger between the adsorbent and the heating fluid is needed. In addition, good thermal conductivity of adsorbent bed is also required. Unfortunately, the heat transfer of adsorbent beds in most current prototypes is very poor, which limits the power density outputted and longer the cycle time.

Much research work on enhancement of the heat transfer of adsorbent bed has been taken recent years [1-6]. In this paper, the influence of some interrelated factors on heat transfer is discussed first. Then a composite adsorbent block with good operation performance will be presented and be studied experimentally. And adsorbent beds composed of the composite blocks will also be investigated.

2. THE FACTORS INFLUENCING THE HEAT TRANSFER OF ADSORBENT BED

Many methods have been proposed to enhance the heat and mass transfer of the adsorbent bed, which can be shown in two sides: improving the thermal conductivity of adsorbent bed, or increasing the heat exchanging area between the adsorbent bed and the heat exchanger, which can be got by using fins and reducing the thickness of the bed. In order to investigate the influence of various factors, such as thermophysical property, adsorption characteristics, contact heat transfer coefficient and geometric shape etc., on heat transfer in adsorbent bed, we have designed two cylindrical adsorbers: one with fins and the other without fins [4]. The adsorbent beds of the adsorber are packed with zeolite grains and are heated by thermal conductive oil. A function F is introduced to indicate the heat transfer coefficient of the adsorber. During the experiment, each time one parameter is changed while the others remain the same. Then the relative variation amount $\Delta F/F$, which determines the influence of the parameter on the heat transfer, can be got. When each parameter is changed by 10 percent, the value of $\Delta F/F$ is shown in Table 1, where λ is equivalent thermal conductivity of adsorbent bed, h is contact heat transfer coefficient between adsorbent bed and fin or exchanger wall, R_i and R_o are internal and external diameter of fin respectively, δ is distance between neighboring fins, and e is copper fin thickness.

Table 1. The Influence of Various Factors on the Heat Transfer of Adsorbent Bed

Factor	λ	h	R_i	R_o	δ	e
$\Delta F/F$	0.20	0.37	0.36	-0.49	-0.80	-0.05

The above data show that for a given working condition, rising λ , h and R_i or lowering R_o and H will obviously improve the heat transfer coefficient; However, change of fin thickness has nearly no influence on that when the diameter of the heat exchanger is not large. In the following, the enhancement of the thermal conductivity of adsorbent bed is concentrated mainly.

3. THE COMPOSITE ADSORBENT BLOCK

The adsorbent is porous medium, so the thermal conductivity of adsorbent bed is considerably low, especially for that packed with grains. For example, the conductivity of a solid carbon grain may reach 0.86 w/m.k , but the average bed thermal conductivity is very poor at about 0.17 w/m.k . Those properties are less for zeolite, which has a grain thermal conductivity and bed thermal conductivity of 0.58 w/m.k and less than 0.09 w/m.k respectively.

To enhance the thermal conductivity of the adsorbent bed, various methods have been proposed. Among them the simplest one is mixing adsorbent grains of different sizes to enhance the packing density [1], but the results are very limited. Another way is mixing the adsorbent grain or powder with material having good thermal conductivity, such as graphite or copper powder [2,3]. The overall thermal conductivity of the adsorbent bed is still not significantly improved even the content of the adding material raises to 25 percent by weight. The reason for this is that the contact between the adsorbent and the adding material is point to point contact, and the contact area needs to be increased. Therefore a more effective way to enhance the conductivity of adsorbent bed is to composite the adsorbent powder with binder to form a solid shape.

The manufacture of a solid composite block must consider the type of the binder and the manufacture process. For the binder selected, it must be sticky first, so as to make the stickiness of the block secure, and it should not block up the microporus of zeolite, which may do harm to the adsorptivity of the adsorbent. In addition, it had better have a good adsorptivity for the adsorbate. Many binders have been tested to form composite adsorbent block, and we find that silica gel or sodium silicate is appropriated be the best for zeolite, either by economic or by preferment consideration.

During the manufacture process of the composite adsorbent block, the weight content of the binder and the pressure under which the block is compressed are the key factors. The binder can enhance the rigidity and thermal conductivity of the block, but it has poorer adsorptivity and a little larger thermal expansion coefficient than zeolite. So the surface of the block is easy to be rough or even has crevices if the binder is added too much.

The block we made has shown good performance on rigidity, adsorptivity and conductivity. In the center of the cylindrical block there is a hollow cylinder as vapor passage. The outer diameter of the block varies from 20mm to 70mm.

4. ADSORPTION AND HEAT TRANSFER PERFORMANCE OF THE COMPOSITE BLOCK

Adsorption Performance

To compare the adsorption performance of composite adsorbent block, 13x zeolite powder and 13x zeolite grain, experiments were done on this samples. To ensure each adsorbent bed having the same area of the surface contacting the adsorbate gas, it is necessary to make each sample have a same shape, so the zeolite powder was compressed in the model by which the block was made, and the grains were put in a frame surrounded with steel net. The initial mass of each sample was 100 game, and the samples were all under equilibrium condition initially.

Figure 1 shows the mass of each sample varied with heating or cooling time. First, the samples were heated in a thermostat whose temperature was kept at 100°C . Then after 8 hours, the samples were taken out to ambient environment. From the figure, we can see that the composite block and the zeolite powder have exactly the same desorption rate and maximum variation of the content of adsorbate in adsorbent, which are both greater than those of zeolite grains. During the adsorption course, the samples have nearly the same adsorption rates at first, but about 4 hours later, the adsorption rate of powder is obviously greater than those of the other two.

For practical utilization, the performance efficiency of a certain volume is more important than that of a certain

mass. Figure 2 shows the adsorption performance of the three samples having a same volume of 100 cm^3 . From the figure, it can see that the composite block has better adsorptivity than zeolite powder and zeolite grains of the same volume. The variation of adsorbate content in composite block increased about 50 percent compared with that of zeolite grain of the same volume.

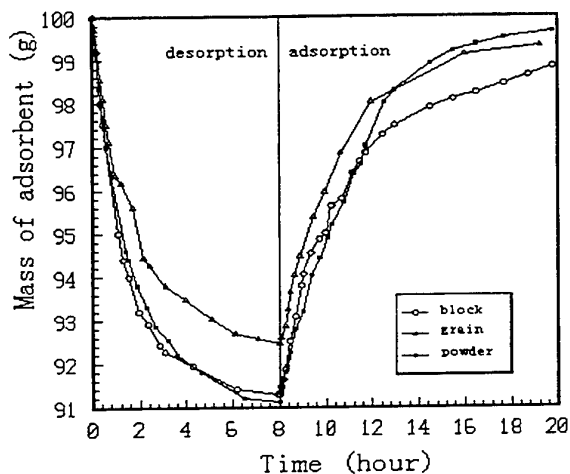


Fig.1. Adsorptivity comparison of the three samples

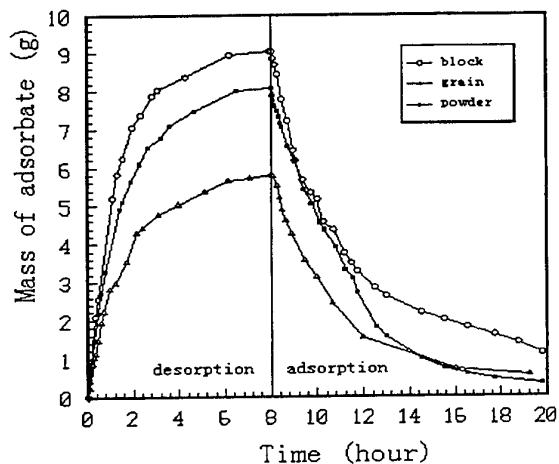


Fig.2. Adsorptivity comparison of the three samples having a same volume of 100 cm^3

Thermal Conductivity

The thermal conductivity of adsorbent bed generally means the real thermal conductivity λ_r , which is defined as the thermal conductivity of the bed without mass transfer or change of adsorbate content. The λ_r mainly depends on adsorbent material and adsorbate content, and it increases slightly when the temperature increases. Figure 3 shows the λ_r of the composite adsorbent block (curve A) compared with other blocks manufactured with other binders, such as calcium chloride, when the temperature is kept at 26°C . The λ_r of the composite block bed is $0.23 \text{ w/m}\cdot\text{k}$ in equilibrium condition, which is about three times of that of a grain bed and four times of that of a powder bed.

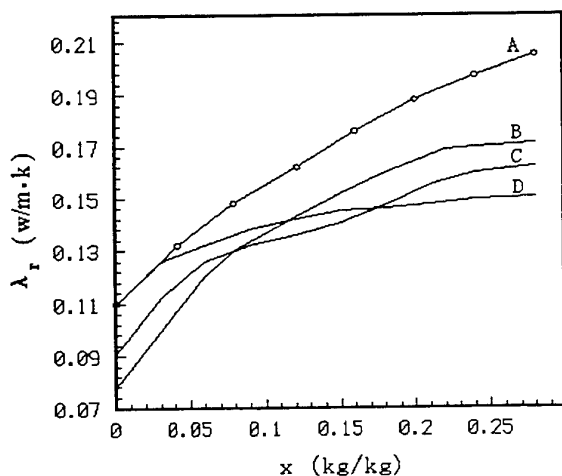


Fig.3. Thermal conductivity of composite adsorbent blocks

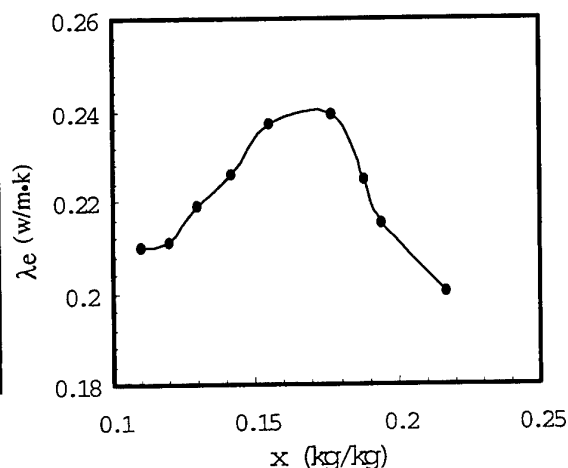


Fig.4. Effective thermal conductivity of the composite adsorbent block

During an operating course, the adsorbate content in adsorbent bed is always changing, and the mass transfer make the thermal conductivity of the bed greater than the real thermal conductivity. The thermal conductivity in such condition is called effective thermal conductivity λ_e , which is a function of λ_r and adsorbate deliverance which is chiefly depends on adsorption rate or desorption rate. Figure 4 shows the λ_e of the composite adsorbent block changing with the adsorbate content x in a adsorption course. It is recommended that the variation of the adsorbate content in a operating course had better in the range of 0.08-0.20, so as to have a better effective thermal conductivity of the adsorbent bed.

5. APPLICATION OF THE COMPOSITE ADSORBENT BLOCK

The composite adsorbent block can be used for either waste heat or solar energy powered adsorption refrigeration. We have designed an adsorbent bed showed as Figure 5. When the zeolite grains in the bed is replaced with the composite adsorbent blocks, and the inner surface of the block is contacted with heating or cooling tube while the outer space of the block is acted as vapor passage. The total heat transfer coefficient will be doubled due to the high conductivity and good contact between the blocks and the heating tubes. So the power output may be greatly raised.

An adsorption solar cooling tube with glass shell showed as Figure 6 is presented by us. The adsorbent bed of the cooling tube is made of the compound adsorbent blocks. In order to absorb solar energy directly through the glass shell, each block is coated with a thin layer of active carbon. So there is no contact thermal resistance between the adsorbent bed and the heat exchanger, which is considerably high in other solar refrigeration systems. Therefor the effectiveness of solar energy utilization is enhanced. The coefficient of performance (COP) of the cooling tube mentioned above may enhanced many time compared with the cooling tube with grain packed bed [7]. Another characteristic of the solar cooling tube is that each cooling tube represents a refrigeration unit. The cooling tube system consisting of many tubes has the advantages of simple structure, low cost, high efficiency and easy maintenance of high vacuum. Experimental results show that the COP of the cooling tube is about 8% without special solar collector in sunny days, when the temperature of the sunny side of the adsorbent bed is only about 75°C. And it will reach 14% if that temperature reaches 100°C.

6. CONCLUSION

A significant improvement in packing density and thermal conductivity in the adsorbent bed can be achieved by replacing the grain packed bed with solid block bed. The solid composite adsorbent block presented has shown good performance on rigidity, adsorptivity and thermal conductivity by experimental studies. The maximum variation of adsorbate content in the composite adsorbent block increases about 50 percent compared with that of grain bed of the same volume. And the thermal conductivity of the block bed is more than twice of that of the grain bed.

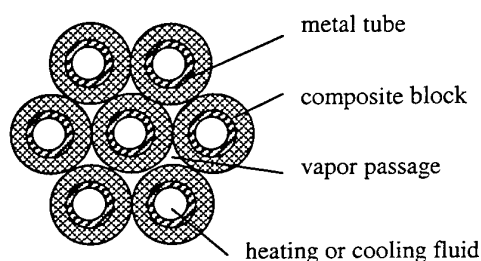


Fig.5. Sketch of an adsorbent bed used for waste heat adsorption refrigeration

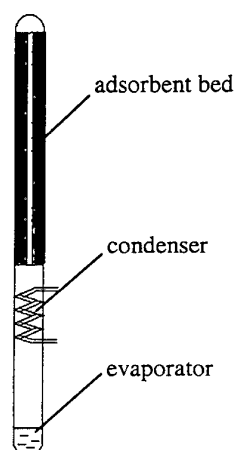


Fig.6. Sketch of the solar cooling tube

The solid composite adsorbent block can be used successfully for solar or waste heat powered adsorption refrigeration. The solar cooling tube using the blocks as its adsorbent bed has the advantages of good thermal conductivity, no contact thermal resistance during heating time and easy maintenance of high vacuum. Experimental results show good coefficient of performance of the solar cooling tube.

REFERENCES

1. J.J.Guillemainot, F.Meunier and J.Pakleza, Heat Mass Transfer v.30, pp.1595-1606 (1990).
2. I.M.Eltom and A.M.Sayigh, Renewable Energy, v.4 (1994).
3. J.J.Guillemainot, A.Choisier and J.B.Chalfen, Heat Recovery System & CHP, v.13, pp.297-300 (1993).
4. Z.Y.Liu and Y.H.Ding, *Proceedings of the 4th Asia Thermophysical Properties Conference*, pp.563-566, Tokyo, Japan (1995).
5. Z.Y.Liu, Z.M.Fu, et al., Thermal Science, v.3, pp.187-190 (1994).
6. G.Restuccia, A.Freni and G.Cacciola, *Proceedings of the International Sorption Heat Pump Conference*, pp.343-347, Munich, Germany (1999).
7. Z.Y.Liu, Y.Z.Lu and J.X.Zhao, Solar Energy Material and Solar Cells, v.52, pp.45-53 (1998).

ANALYSIS OF THE THERMAL PERFORMANCE OF DIRECT-CONTACT AIR-CONDITIONING SYSTEMS

Zhang Yinping, Zhu Yinxing, Jiang Yi

Department of Thermal Engineering, Tsinghua University, Beijing 100084

E-mail: zhangvp@mail.tsinghua.edu.cn ; Fax: (+86) 10 6277 0544

Keywords: heat transfer, air-conditioning, air washer, cooling tower

ABSTRACT. Through theoretical analysis, the thermal performance of direct-contact air-conditioning system was studied. The analysis overcomes some shortcomings of the analysis in 1996 *ASHRAE Systems and Equipment Handbook* and 1997 *ASHRAE Fundamentals Handbook*. The influence of various factors on the characteristics of heat and transfer of such systems was analyzed. A general formula for the heat exchange efficiency of parallel or counter flow direct-contact air-conditioning system was obtained through theoretical analysis, which is with the same type of empirical relations. The heat exchange efficiencies of the processes of cooling and dehumidifying of air by using parallel-flow and counter-flow systems were calculated. Those data agree well with the experimental results in the literature. The analysis method together with some results presented in this paper is helpful to the design, adjusting and simulation of the thermal performance of such systems.

NOMENCLATURE

a	surface area of per water drop, m^2	NTU	the number of transfer units, dimensionless
c_p	specific heat, $J/kg \cdot K$	Nu	the Nusselt number, dimensionless
D	diameter of a water drop, m	Q	heat exchange rate of a system, W
$f(r_w)$	distribution density function of radius of water drops	r_w	radius of a water drop, m
G	mass flow rate of air, kg/s	$r_{w,m}$	mean radius of water drops, m
H	effective height of the system, m	t	temperature, $^{\circ}C$
h	convective heat transfer coefficient, $W/(K \cdot m^2)$	V	effective volume of a system, m^3
h_a	specific enthalpy of moist air, J/kg dry air	v_w	velocity of water drop, m/s
h_s	specific enthalpy of moist air at saturation at thermodynamic wet-bulb temperature, J/kg dry air	v_a	velocity of air through a system, m/s
k	thermal conductivity, $W/(m \cdot K)$	W	humidity ratio, kg of water vapor per kg of dry air, kg/kg
K_M	mass transfer coefficient, $kg/(s \cdot m^2)$	μ	dynamic viscosity, $kg/(s \cdot m)$
L	mass flow rate of water, kg/s	h_m	convective mass transfer coefficient, $kg/(m^2 \cdot s)$
Len	effective length of the system, m	Subscripts	
n	number of water drops from the sprayers per unit time, s^{-1}	1-	inlet
N_d	number of water drops per unit Volume, $1/m^3$	2-	outlet
		a-	air
		w-	water
		wb-	wet bulb
		Constants	
		a_i, b_i, c, c_i	

1. INTRODUCTION

Air-conditioning equipment can be classified as (1) having direct contact between air and water used as a cooling or heating fluid or (2) having the heating or cooling fluid separated from the air stream by a solid wall. Air washers and cooling towers are two typical types of the former.

At present, for a given system, the thermal performance of such equipment under various operative conditions can not be determined theoretically. It has to be determined with experiments. In refs.[2,3], the thermal performance of cooling tower was analyzed. However, the analysis there is not satisfactory because that (i) the

effect of many factors such as radius of water drop etc. on the characteristics of heat and mass transfer of the system was not considered, (2) a general expression for correlation of heat transfer efficiency of such systems was not obtained, (3) for a given system and given operative conditions, the relation of adjustable parameters and various parameters of the outlet fluids was not discussed, which is helpful for adjusting the thermal performance of the systems.

Considering those, from a new point of view, the thermal performance of such systems was theoretically analyzed by us, with which the aforementioned shortcomings of the analysis in refs.[2,3] were overcome. As an illustration, the heat exchange efficiencies of the processes of cooling and dehumidifying of moist air by using counter-flow systems under various operative conditions were calculated. The computed data agree well with the experimental results in the literature. The analysis method together with the results presented in this paper is helpful to the design, adjusting and simulation of the thermal performance of such systems.

2. PHYSICAL MODEL AND DISCUSSION

For the purpose of simplifying the analysis, the following assumptions are made: (1) water drops are spherical, which are distributed homogeneously in a system; (2) during the process of moving of a water drop, its diameter changes a little[2]; (3) the speeds of water drops are equal and constant; (4) the effect of gravity on flow of water drops can be neglected; (5) the Biot number of a water drop $Bi < 0.1$, therefore, the temperature distribution in the drop can be regarded as uniform and the lumped capacitance method can be used[4]; (6) the moist air adjacent to water drops are in equilibrium with water at given temperature and pressure (standard atmosphere pressure), whose specific enthalpy is h_s ; (7) the following dimensionless convective heat transfer correlation $Nu_D = 2 + 0.6 Re_D^{1/2} \cdot Pr^{1/3} = 2 + c_3 Re_D^{1/2} Pr^{1/3}$ is applicable[4]; (8) for the small temperature region ($< 15^\circ C$), h_s can be approximately expressed as follows, $h_s = c_1 \cdot t_w - c_2$; (9) the depth of the system considered is 1 length unit. Besides that, from the point of view of equivalent heat transfer, the mean radius of water drops is defined as follows

$$r_{w,m} = \frac{\int_0^\infty f(r_w) \cdot r_w^3 \cdot dr_w}{\int_0^\infty f(r_w) \cdot r_w^2 \cdot h(r_w) \cdot dr_w} \quad (1)$$

Thus, the effective number of water drops with $r_{w,m}$ produced per second is

$$n = \frac{W}{\frac{4}{3} \pi \cdot r_{w,m}^3 \cdot \rho_w} \quad (2)$$

The density of water drops with $r_{w,m}$ in the system N_d is given by

$$N_d = n \frac{H(\text{or Len})}{v_w} \cdot \frac{1}{H \cdot \text{Len} \cdot 1} = n \frac{1}{v \cdot \text{Len}(\text{or } H) \cdot 1} \quad (3)$$

2.1 Physical Model of Parallel-Flow or Counter-Flow System

2.1.1 Model and analysis. The counter-flow type direct-contact air-conditioning system can be simplified as shown in Fig. 1.

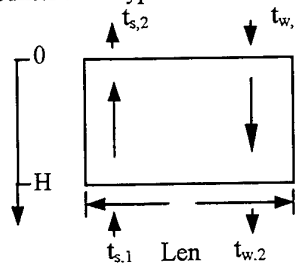


Fig.1 Schematic of a simplified counter-flow system

The basic equations for the process occurring in a controlling layer can be written as

$$\frac{dt_w}{h_s - h_a} = d(NTU) \quad (4)$$

$$L \cdot c_{p,w} \cdot \frac{dt_w}{dy} = G \cdot \frac{dh_a}{dy} \quad (5)$$

where

$$NTU = \frac{k_M \cdot N_d V}{L \cdot c_{p,w}} = \frac{Nu_D \cdot k_a \cdot 3H}{2\rho_w c_{p,w} c_{p,a} r_{w,m}^2 v_w} = f_1[(\rho_a v_{a,w}), r_{w,m}, H / v_w] \quad (6)$$

where $v_{a,w} = v_a + v_w$ (for parallel-flow), $v_{a,w} = |v_a - v_w|$ (for counter-flow).

From eq.(5), we have

$$h_a = h_{a,1} + \frac{L \cdot c_{p,w}}{G} (t_w - t_{w,2}) \quad (7)$$

where $h_{a,1} = c_1 t_{wb,1} - c_2$. Thus, we obtain

$$h_s - h_a = a_0 t_w + a_1 + \frac{L \cdot c_{p,w}}{G} t_{w,2} \quad (8)$$

where $a_0 = c_1 - \frac{L \cdot c_{p,w}}{G} = f_2(L/G)$, $a_1 = -c_1 t_{wb,1}$

Substituting eq.(8) into eq.(4), it yields

$$t_{w,1} - t_{w,2} = (t_{w,2} + \frac{a_1}{a_0} + \frac{L \cdot c_{p,w}}{Ga_0} t_{w,2}) \cdot (e^{a_0 NTU} - 1) \quad (9)$$

Hence, we obtain

$$t_{w,2} = \frac{t_{w,1} + \frac{a_1}{a_0} (1 - e^{a_0 NTU})}{e^{a_0 NTU} + \frac{L \cdot c_{p,w}}{Ga_0} (e^{a_0 NTU} - 1)} \quad (10)$$

Thus

$$t_{w,1} - t_{w,2} = a_2 t_{w,1} + a_3 \quad (11)$$

$$a_2 = \frac{(e^{a_0 NTU} - 1)(1 + \frac{L \cdot c_{p,w}}{Ga_0})}{e^{a_0 NTU} + \frac{L \cdot c_{p,w}}{Ga_0}(e^{a_0 NTU} - 1)} = f_2(a_0, NTU, L/G) \quad (11-a)$$

$$= f_3(L/G, \rho_a v_a, r_{w,m}, H/v_w)$$

$$a_3 = \frac{a_1}{a_0} \cdot \frac{(e^{a_0 NTU} - 1)}{e^{a_0 NTU} + \frac{W \cdot c_{p,w}}{Ga_0}(e^{a_0 NTU} - 1)} = f_4(a_0, a_1, NTU, W/G) \quad (11-b)$$

$$= f_5(L/G, \rho_a v_a, r_{w,m}, t_{wb,1}, H/v_w)$$

Combining eqs.(11), (11-a) and (11-b), it gives

$$Q/L = c_{p,w}(t_{w,1} - t_{w,2})$$

$$= c_{p,w} \cdot t_{w,1} \cdot f_3\left(\frac{L}{G}, \frac{H}{v_w}, r_{w,m}, \rho_a v_a\right) + f_5\left(t_{wb,1}, \frac{L}{G}, \frac{H}{v_w}, r_{w,m}, \rho_a v_a\right) \quad (12)$$

$$= f_6\left(\frac{L}{G}, \frac{H}{v_w}, r_{w,m}, \rho_a v_a, \text{parameters of inlet fluids}\right)$$

For parallel-flow system, similarly to the above, it can yield

$$t_{w,1} - t_{w,2} = t_{w,1} - \frac{c_1 t_{wb,1} + \frac{L}{G} c_{p,w} t_{w,1}}{c_1 + \frac{L}{G} c_{p,w}} \quad (13)$$

$$Q/L = c_{p,w}(t_{w,1} - t_{w,2})$$

$$= f_7\left(\frac{L}{G}, \frac{H}{v_w}, r_{w,m}, \rho_a v_a, \text{parameters of inlet fluids}\right) \quad (14)$$

2.2.2 Discussion (i) Overall heat exchange efficiency of the system and the relating factors. The overall heat exchange efficiency of a cross-flow or parallel-flow system is defined as [1]

$$E = \frac{t_{wb,1} - t_{wb,2} + t_{w,2} - t_{w,1}}{t_{wb,1} - t_{w,1}}$$

Combining eqs.(11), (11-a) and (11-b), and considering

$$\frac{h_{a,2} - h_{a,1}}{t_{w,1} - t_{w,2}} = \frac{L}{G} c_{p,w} \quad (15)$$

$$\frac{c_1(t_{wb,2} - t_{wb,1})}{t_{w,1} - t_{w,2}} = \frac{L}{G} c_{p,w} \quad (16)$$

we have

$$E = \frac{\left(\frac{L}{G} \cdot \frac{c_{p,w}}{c_1} + 1\right) \cdot (t_{w,2} - t_{w,1})}{t_{wb,1} - t_{w,1}} = f_8\left(\frac{L}{G}, \rho_a v_a, r_{w,m}, \frac{H}{v_w}, \text{parameters of inlet fluids}\right) \quad (17)$$

From that, it is seen that the influencing factors of the efficiency are $\frac{L}{G}, \rho_a v_a, r_{w,m}, \frac{H}{v_w}$ and the parameters of inlet fluids. The analysis manifests that $\frac{L}{G}, \rho_a v_a, \frac{H}{v_w} \uparrow, r_{w,m} \downarrow \Rightarrow E \uparrow$.

For a given system, it gives

$$E = f\left(\frac{L}{G}, \rho_a v_a, \frac{H}{v_w}, \text{parameters of inlet fluids}\right) \approx A(\rho_a v_a)^n \cdot \left(\frac{L}{G}\right)^m \quad (18)$$

Eq.(18) presents a general formula of the overall heat exchange efficiency of such systems, which summarizes the common characteristics of available empirical relations. From the analysis, it is seen that, factor A is related to $r_{w,m}$ and H/v_w , in other words, A is determined by the type and dimension of the sprayer used, the pressure of water, the dimension of the system and the parameters of inlet fluids.

(ii) Factors of influencing the parameters of outlet fluids.

Eqs.(10) and (12) describe the effect of various factors on the parameters of outlet fluids and the overall heat transfer rate.

As an illustration, the following operative condition of a cooling tower is considered: $t_{wb,1}=25^\circ\text{C}$, $t_{w,1}=35^\circ\text{C}$. The influences of $r_{w,m}$, L/G , H/v_w and v_w on the heat transfer rate and the temperature of outlet fluids of the cooling tower and the overall heat transfer efficiency are analyzed. The calculated results are shown in Fig.2 through Fig.5. From the figures, it concludes that:

- (i) For given conditions, there is a critical $r_{w,m}$ (nominated as $r_{w,m}^*$). If $r_{w,e} > r_{w,m}^*$, it has strong influence on the heat and mass transfer rate of the system, and the rate decreases with increasing $r_{w,m}$. If $r_{w,m} < r_{w,m}^*$, it hardly influences the heat and mass transfer rate.
- (ii) When $r_{w,m} < r_{w,m}^*$, there is a critical value of L/G (nominated as L/G^*). If $L/G < L/G^*$, it hardly influences the heat and mass transfer rate and vice versa.
- (iii) The overall heat exchange efficiency increases with increasing L/G and decreasing $r_{w,m}$. However, for given conditions, if $L/G > L/G^*$ and $r_{w,m} < r_{w,m}^*$, L/G and $r_{w,m}$ scarcely influence the efficiency of the system.
- (iv) For constant L , G etc., lowering speed of water drops is advantageous to improve the heat transfer rate of the system.
- (v) Increasing the speed of moist air is helpful to improve the heat transfer rate of the system.

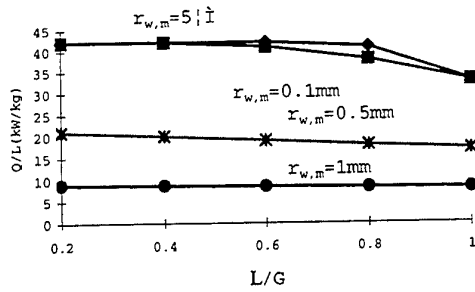


Fig.2 The relation of Q/L versus L/G and $r_{w,m}$ ($H/L=1$, $H/v_w=1$)

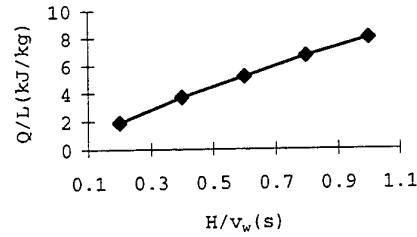


Fig.3 Relation of Q/L versus H/v_w ($L/G=1$, $r_{w,m}=10^{-3} \text{ m}$)

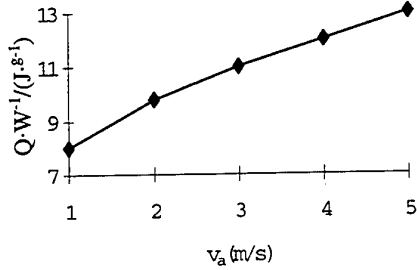


Fig.4 The relation of Q/L versus v_a ($L/G=1$, $r_{w,m}=10^{-3} \text{ m}$)

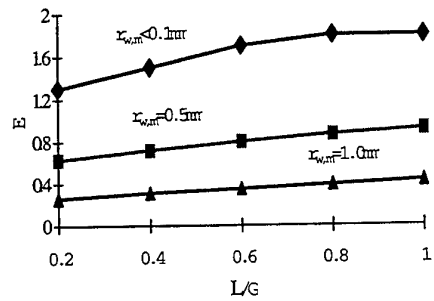


Fig.5 The relation of the overall heat transfer efficiency E versus L/G and $r_{w,e}$

3.COMPARISON WITH EXPERIMENTAL RESULTS

Fig. 6 and Fig. 7 are a comparison of computed results (represented by solid lines) and experimental results [5] (represented by dots) for the efficiency of the cooling and dehumidifying process of moist air in a counter-flow system with single row sprayers. It is shown that they are in good agreement.

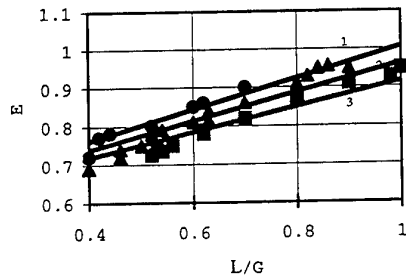


Fig.6 Comparison of the computed results and the experimental results for the efficiency, 1- $\rho_a v_a = 2.8 \text{ kg}/(\text{m}^2 \text{ s})$, 2- $\rho_a v_a = 2.4 \text{ kg}/(\text{m}^2 \text{ s})$, 3- $\rho_a v_a = 2.0 \text{ kg}/(\text{m}^2 \text{ s})$, diameter of sprayer $d_o = 5 \text{ mm}$, $H/v_w = 0.9 \text{ s}$, $r_{w,m} = 0.51 \text{ mm}$, $t_{w,1} = 10^\circ \text{C}$, $t_{s,1} = 20^\circ \text{C}$.

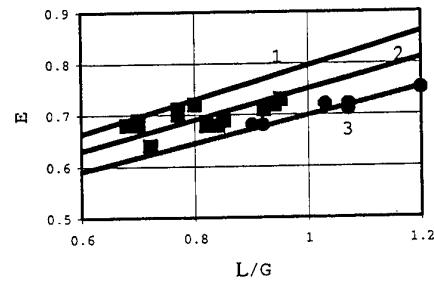


Fig.7 Comparison of the computed results and the experimental results for the efficiency, 1- $\rho_a v_a = 2.35 \text{ (kg}/(\text{m}^2 \text{ s}))$, 2- $\rho_a v_a = 2.0 \text{ (kg}/(\text{m}^2 \text{ s}))$, 3- $\rho_a v_a = 1.6 \text{ (kg}/(\text{m}^2 \text{ s}))$, diameter of sprayer $d_o = 5 \text{ mm}$, $H/v_w = 0.9 \text{ s}$, $r_{w,m} = 0.51 \text{ mm}$, $t_{w,1} = 10^\circ \text{C}$, $t_{s,1} = 20^\circ \text{C}$.

4. CONCLUSIONS

Through theoretical analysis of the thermal performance for direct-contact air-conditioning systems, a general formula for heat exchange efficiency of such systems is obtained, which summarizes the common characteristics of available empirical relations. And the computed results are well validated with experimental results in the literature. With the analysis, the influence of various factors on the efficiency can be clarified and the overall heat exchange rate together with the respective parameters of outlet fluids of the system can be predicted or determined. The results indicate that for a given system and given operative conditions, through theoretical or numerical analysis, the thermal performance of such systems can be estimated. The analysis method together with the some results presented in this paper is useful to the design, adjusting of the thermal performance of such systems.

REFERENCES

1. R. Zhao, C.Y. Fan, D.H. Xue, Y.M. Qian, Air-conditioning, Publishing Company of Chinese Architecture, Beijing, P.R.China, Nov., 1994, pp.60-83(in Chinese).
2. R.A. Parsons(editor), ASHRAE HANDBOOK:1996 HVAC Systems and equipment, Chapter 36, pp.36.1-36.20.
3. R.A. Parsons(editor), ASHRAE HANDBOOK: 1997 Fundamentals Handbook(SI).
4. F.P.Incropera, D.P.DeWitt, Fundamentals of Heat and Mass Transfer(4th Edition), John Wiley & Sons, Inc., 1996, p374.
5. Z.F. Wu, R.G. Zhao,T.Y. Zhao, Heating, Ventilation and Air-conditioning, Beijing Publishing company of Chinese industry(in Chinese), July , 1965, pp.122-124.

ANALYSIS OF THE THERMAL PERFORMANCE AND ENERGY SAVING EFFECT OF MEMBRANE BASED HEAT RECOVERY VENTILATOR

Zhang Yinping, Jiang Yi, Zhang Li Zhi

Department of Thermal Engineering, Tsinghua University, Beijing 100084

E-mail: zhangyp@mail.tsinghua.edu.cn; Fax: +86 10 62770544

Keywords: heat recovery ventilator, heat and mass transfer, water-permeable membrane, energy saving, air-conditioning.

ABSTRACT. The characteristics of heat and mass transfer of water permeable membrane were studied. From the point of view of application of such membrane in heat recovery ventilator(HRV), the selection criterion of the membrane was presented. And a general physical model to analyze the performance of various membranes based HRV was built, with which the effectiveness factors of such HRV was studied and the effect of energy saving of such HRV systems used in an emporium located in Beijing was evaluated. The former was validated with experiments. The results demonstrate the advantages of such system: being able to recover the sensible and latent heat simultaneously, being of high heat and moisture exchange effectiveness, without any mechanical components in it, being able to save energy by using it in air-conditioning system for whole year run. The model and results are helpful for the developing the membrane based heat recovery ventilator.

1. INTRODUCTION

Air-conditioning systems are responsible for a considerable fraction of the total demand for electricity in many countries[1]. In summer, the most widely practiced method of air handling for central air-conditioning system is to use cooling coils. Despite many advantages of cooling coil system, its shortcomings are also obvious: just for the purpose of cooling air, it's not necessary to cool the coolant to 7°C or so in chillers, while in order to dehumidify the air to comfortable level, this temperature is necessary. It means that, for the purpose of dehumidifying air by using cooling coil, COP(coefficient of performance) of a chiller has to be sacrificed, or rather, energy consumption of a cooling coil system tends to be more than that of an independent temperature and humidity control air-conditioning system. Besides that, for independent temperature and humidity control air-conditioning systems, some nature cool sources such as underground water or deep well water can be used to condition the air. Therefore, in recent years, independent humidity control of air-conditioning systems has been an attracting research topic in the field of HVAC(heating, ventilation and air-conditioning). Those researches benefit not only for energy saving but also for environment.

Among the possible methods of independent humidity control, water-permeable membrane based independent humidity control is potentially attractive [2-5] because of its excellent performance and low capital and operating cost[2]. In fact, as one of its applications, applying water-permeable membrane based HRV in fresh air handling unit (AHU) is able to save a lot energy consumption of the system. However, until now the key parameters of influencing the performance of such system and the energy saving effect of using such system have not been clear. In this paper, the aforementioned problems and relating fundamental problems are solved or discussed.

1. PRINCIPLE

2.1 Heat and Mass Transfer Across a Water-Permeable Membrane

Air stream 1 is hot and humid and air stream 2 is relatively dry and cool. They flow across a water-permeable membrane. See Fig.1. Through adsorption of vapor at surface 1 and desorption of water at surface 2, moisture in air stream 1 is transferred to air stream 2. The condition of transferring humidity from surface 1 to surface 2 is only that the water content at surface 1 $C_{s,1}$ is larger than that at surface 2 $C_{s,2}$.

The concentration of water in the solid at the interface may be obtained through use of a property known as the solubility, S . It is defined by the expression[7]

$$C_s = S p_v, \quad (1)$$

where p_v is the partial pressure (bars) of the vapor adjoining the interface; C_s is water content of solid, which can be in units of kilogram of water per kilogram of membrane material, in which case the unit of S must be kilogram of water

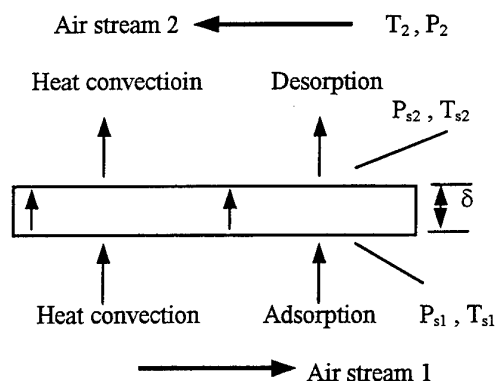


Fig.1 Schematic of heat and mass transfer through the membrane

per kilogram of membrane material per bar partial pressure of vapor. In fact, S is related to T_v (the temperature of vapor adjoining the surface, K), p_v and material. For given material, we have

$$S = (T_v, p_v). \quad (2)$$

For the case shown in Fig.1, at location x , water transfer flux through the membrane M'' can be expressed as follows,

$$M'' = h_m (p_1 - p_{s1}) + \frac{D_{AB}}{\delta} [S(p_{s1}, T_{s1}) p_{s1} - S(p_{s2}, T_{s2}) p_{s2}] + h_m' (p_{s2} - p_2), \quad (3)$$

where h_m and h_m' are heat convective coefficients on surface 1 and 2 [$W/m^2 \cdot K$], respectively, and there is $h_m \approx h_m'$, δ is the thickness of the membrane [m].

And we have

$$S(p_{s1}, T_{s1}) p_{s1} - S(p_{s2}, T_{s2}) p_{s2} = \left\{ S(p_{s1}, T_{s1}) + p_{s2} \left[\frac{\partial S}{\partial p} + \frac{\partial S}{\partial T} \frac{T_{s2} - T_{s1}}{p_{s2} - p_{s1}} \right] \right\} (p_{s1} - p_{s2}) \quad (4)$$

Thus, from eqs.(3) and (4), it yields,

$$\begin{aligned} M'' &= \frac{p_1 - p_2}{\frac{2}{h_m} + \frac{\delta}{D_{AB} \left\{ S(p_{s1}, T_{s1}) + p_{s2} \left[\frac{\partial S}{\partial p} + \frac{\partial S}{\partial T} \frac{T_{s2} - T_{s1}}{p_{s2} - p_{s1}} \right] \right\}}} \\ &= \frac{\frac{h_m}{2} (d_1 - d_2)}{1 + \frac{h_m}{2} \frac{\delta}{D_{AB} \left\{ S(p_{s1}, T_{s1}) + p_{s2} \left[\frac{\partial S}{\partial p} + \frac{\partial S}{\partial T} \frac{T_{s2} - T_{s1}}{p_{s2} - p_{s1}} \right] \right\}}} \\ &= U_m (d_1 - d_2) \end{aligned} \quad (5)$$

$$U_m = \frac{h_m}{2 + \frac{h_m \cdot \delta}{D_{AB} \left\{ S(p_{s1}, T_{s1}) + p_{s2} \left[\frac{\partial S}{\partial p} + \frac{\partial S}{\partial T} \frac{T_{s2} - T_{s1}}{p_{s2} - p_{s1}} \right] \right\}}} \quad (6)$$

where d is water content of air which is in units of kg vapour per kg dry air, D_{AB} is binary diffusion coefficient of water for membrane material whose units are $\text{kg/m} \cdot \text{s}$, h_d is mass convective coefficient corresponding to the case that the driving force of water transfer is expressed as difference of water content of air whose units are $\text{kg} \cdot \text{m}^2/\text{s}$, U_m is overall moisture transfer coefficient whose units are $\text{kg} \cdot \text{m}^2/\text{s}$.

Obviously, for the case that $p_1 > p_2$, from the point of view of improving M'' , the membrane whose D_{AB} , S and $\frac{\partial S}{\partial p}$ ($\frac{\partial S}{\partial p} > 0$) are large and δ , $\left| \frac{\partial S}{\partial T} \right|$ ($\frac{\partial S}{\partial T} < 0$) are small is desirable. This is the criterion of selecting ideal water-permeable membrane for HRV.

From eqs.(5) and (6), it is also seen that: (1) when the thickness of a membrane δ approaches 0, the water transfer through the membrane M'' approaches its maximum,

$$M'' = \frac{h_m(p_1 - p_2)}{2} = \frac{h_d(d_1 - d_2)}{2}, \quad (7)$$

and (2) for the membrane which is not water permeable, M'' is 0 due to D_{AB} is 0 which results in $U_m = 0$.

For heat transfer, we have

$$Q_l/A = M'' \cdot r \quad (8)$$

$$Q_s/A = h(T_1 - T_{s1}) = h(T_{s2} - T_2) = k_m(T_{s1} - T_{s2})/\delta \quad (9)$$

where Q_l , Q_s are latent and sensible heat transfer rates[W], respectively, A is the area of membrane, r is heat of adsorption of water in the membrane material[J/kg], k_m is thermal conductivity of membrane[W/m²·K]. See Fig.1.

From eqs.(8) and (9), it yields:

$$T_{s2} = \frac{1}{2 + \frac{h\delta}{k_m}} \cdot \left(\frac{h\delta}{k_m} \cdot T_2 + T_1 + T_2 - M'' \cdot r \cdot \frac{\delta}{k_m} \right) \quad (10)$$

Similarly to the getting eq.(6), we obtain

$$Q_s/A = U(T_1 - T_2)/\delta, \quad (11)$$

and

$$U = \frac{h}{(2 + \frac{h\delta}{k_m})(T_1 - T_2)} \cdot (T_1 - T_2 - M'' \cdot r \cdot \frac{\delta}{k_m}) \quad (12)$$

By using Chilton-Colburn analogy[7] and from experimental results[8], it is found that

$$h/h_d = \xi c_p, \quad (13)$$

where ξ is a factor, and for a given condition, it is a constant ($1 \leq \xi \leq 1.6$)[8], c_p is specific heat of air.

$$\text{and } U/U_m = \xi \cdot c_p \frac{2 + \frac{h_m \cdot \delta}{D_{AB} \left\{ S(p_{s1}, T_{s1}) + p_{s2} \left[\frac{\partial S}{\partial p} + \frac{\partial S}{\partial T} \frac{T_{s2} - T_{s1}}{p_{s2} - p_{s1}} \right] \right\}}}{\left(2 + \frac{h\delta}{k_m} \right) (T_1 - T_2)} (T_1 - T_2 - M'' \cdot r \cdot \frac{\delta}{k_m}), \quad (14)$$

Eq.(14) is a general expression of U/U_m which is applied for any membrane despite it is water permeable or not. It is easily understood that for water-impermeable membrane, there is $U/U_m=0$.

By using eq.(13), for very thin water-permeable membrane ($\delta \approx 10 \mu\text{m}$), there are: $h\delta/k_m \ll 1$ and

$$M''r \leq \frac{h_m \delta (p_1 - p_2) \cdot r}{2k_m} = \frac{h_d \delta (d_1 - d_2) \cdot r}{2k_m} = \frac{h \cdot \delta \cdot (d_1 - d_2) \cdot r}{2k_m \cdot \xi \cdot c_p} \ll \frac{1}{2} (T_1 + T_2), \quad (15)$$

we have

$$T_{s2} \approx T_{s1} \approx \frac{1}{2} \cdot (T_2 + T_1) \quad (16)$$

$$U/U_m = \xi c_p \quad (17)$$

2.2 The Implementation of HRV in an AHU and Its Operative Principle

A combination of a membrane based heat recovery ventilator(HRV) with an AHU is shown in Fig.2.

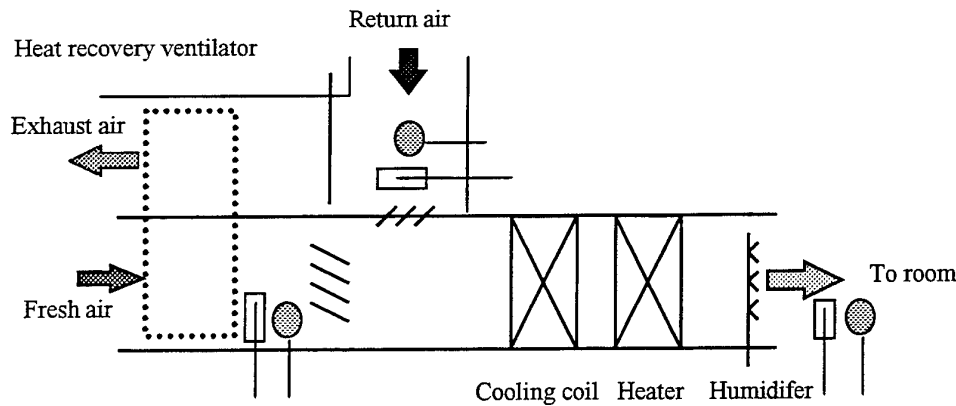


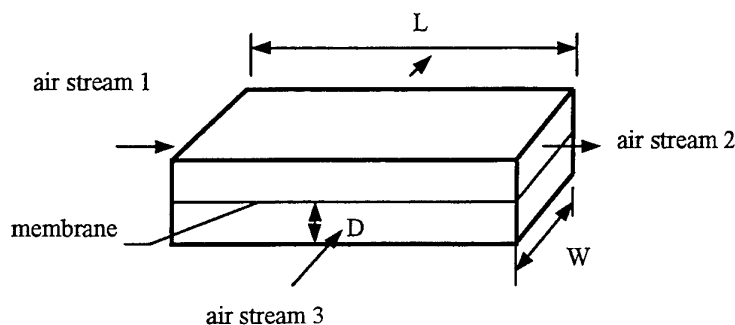
Fig. 2 The combination of HRV and an AHU system

In summer, intake fresh air of the system is hot and humid while return air is relatively cool and dry. By using HRV, through heat and mass transfer between fresh air and return air, fresh air can be partly cooled and dehumidified. In this way, both the sensible heat and the latent heat loads of cooling coils can be reduced. In winter, intake fresh air of the system is cold and dry while return air is hot and relatively humid. Similar to the aforementioned, the loads of heater and humidifier can be reduced. Therefore, compared with conventional AHU, energy consumption can be saved by using such system. It is easily understood that the energy saving effect is related to the thermal performance of buildings and climate conditions.

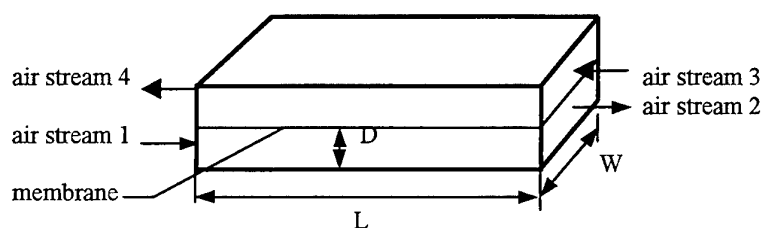
3. MODELS OF HRV SYSTEM AND DISCUSSIONS

3.1 Mathematical Model and Solution

Fig.3 is a conceptual diagram of membrane based HRV. The following assumptions are made to simplify the analysis: (1) heat and mass transfer processes are in steady state; (2) heat conduction in the two air streams is negligible compared to energy transfer by bulk flow; (3) mass diffusion of water vapor in the two air streams is negligible compared to mass transport by bulk flow; (4) heat and mass exchange between the two air streams and the membrane can be represented by convection coefficients; (5) for a membrane made from adsorption material, effective heat and mass transfer coefficients can be used to represent the effects of the porous structured layers on heat and mass exchange between the two air streams and the membrane; (6) heat and mass transfer in the lateral directions of the membrane are negligible; (7) thermodynamic processes are in equilibrium; (8) energy (enthalpy) flux by diffusional transport (perpendicular) in the two air streams is negligible compared to heat convection between the streams and the membrane.



(a) Schematic of a simplified cross flow HRV



(b) Schematic of a simplified counter flow HRV

Fig.3 Schematic of a cross flow and counter flow membrane HRV

For both counter-flow and cross-flow membrane HRV, the governing equations can be written as follows:

$$F_t UA(t_1 - t_4) = Q_s \quad (18)$$

$$G(t_1 - t_2) = Q_s \quad (19)$$

$$G(t_4 - t_3) = Q_s \quad (20)$$

$$F_d U_m A(d_1 - d_4) = M \quad (21)$$

$$M = G(d_1 - d_2) \quad (22)$$

$$M = G(d_4 - d_3) \quad (23)$$

$$U/U_m = \xi c_p \quad (24)$$

$$Q_1 = M \cdot r \quad (25)$$

$$Q_r = Q_1 + Q_s \quad (26)$$

where U is the overall heat transfer coefficient of HRV [$W/m^2 \cdot K$], F_t , F_d are correction factors (for counter-flow HRV, they equal one while for cross-flow HRV, they are smaller than 1 and the value of F_t for a given condition can be found by using the figure of correction factor for a single-pass, cross-flow heat exchanger with both fluids unmixed in ref.[7] which is independent of the specific configuration. Eqs.(18)-(23) implicate that sensible heat and mass transfer are analogies. Accordingly, heat and mass relations for a particular are interchangeable. Based upon that, the value of F_d for a given condition can also be found by using the aforementioned figure in ref.[7].

It should be mentioned that eqs.(18)-(26) form a general mathematical model which is independent of the specific configuration of HRV, the flow type of air (cross-flow or counter-flow) and the membrane material (for different material, just ξ or rather U/U_m is different).

From the equations above, it yields

$$d_2 = (d_3 \cdot F_d \cdot NTU / \xi + d_1) / (1 + F_d \cdot NTU / \xi) \quad (27)$$

$$d_4 = (F_d \cdot NTU / \xi \cdot d_1 + d_3) / (1 + F_d \cdot NTU / \xi) \quad (28)$$

$$t_2 = (t_1 + F_t \cdot NTU \cdot t_3) / (1 + F_t \cdot NTU) \quad (29)$$

$$t_4 = (t_3 + F_t \cdot NTU \cdot t_1) / (1 + F_t \cdot NTU) \quad (30)$$

$$M = F_d \cdot U_m A \frac{d_1 - d_3}{1 + F_d \cdot NTU / \xi} \quad (31)$$

$$Q_s = F_t \cdot UA \frac{t_1 - t_3}{1 + F_t \cdot NTU} \quad (32)$$

$$Q_1 = M \cdot r \quad (33)$$

where $NTU = \frac{UA}{Gc_{p,m}}$, is number of transfer units.

3.2 Thermal-Entry-Region Consideration

Due to the ratio of the length to height of the element is not very large, to obtain heat transfer coefficient, thermal-entry-length has to be taken into account[9].

3.3 Effectiveness of the System

The sensible effectiveness factor of the system is defined as

$$\varepsilon_s = (t_4 - t_3) / (t_1 - t_3) \quad (34)$$

The moisture effectiveness of the system is defined as

$$\varepsilon_t = (d_4 - d_3) / (d_1 - d_3) \quad (35)$$

For cross flow HRV (both fluids unmixed), its effectiveness for heat transfer is written[7]

$$\varepsilon = 1 - \exp[(NTU)^{0.22} (\exp(-(NTU)^{0.78}) - 1)] \quad (36)$$

By using the definition equation of ε , i.e., eq.(35), we obtain

$$\varepsilon_d = 1 - \exp\left[\left(\frac{NTU}{U/U_m}\right)^{0.22} \left(\exp\left(-\left(\frac{NTU}{U/U_m}\right)^{0.78}\right) - 1\right)\right] \quad (37)$$

For thin membrane based HRV, we have

$$\varepsilon_d = 1 - \exp\left[\left(\frac{NTU}{\xi}\right)^{0.22} \left(\exp\left(-\left(\frac{NTU}{\xi}\right)^{0.78}\right) - 1\right)\right] \quad (38)$$

For counter-flow HRV, we have

$$\varepsilon_s = \frac{NTU}{1 + NTU} \quad (39)$$

$$\varepsilon_d = \frac{NTU/\xi}{1 + NTU/\xi} \quad (40)$$

The relation of $\varepsilon_d/\varepsilon_s$ versus U/U_m and NTU is schematically shown in Fig.4.

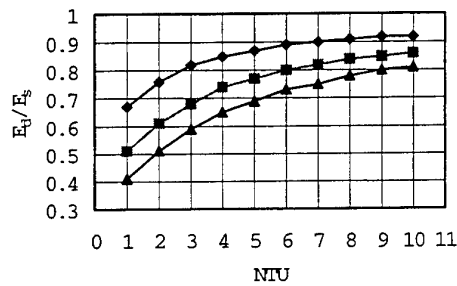


Fig.4 The relation of $\varepsilon_d/\varepsilon_s$ versus U/U_m and NTU

4. COMPARISON OF THE COMPUTED RESULTS WITH EXPERIMENTS

A prototype membrane based HRV was built, in which UTRC-1 water permeable membrane was used. The measured relations of M'' versus $(d_1 - d_3)$ and Q/A versus $(T_1 - T_3)$ were obtained through experiments and are shown in Fig.5 and Fig.6.

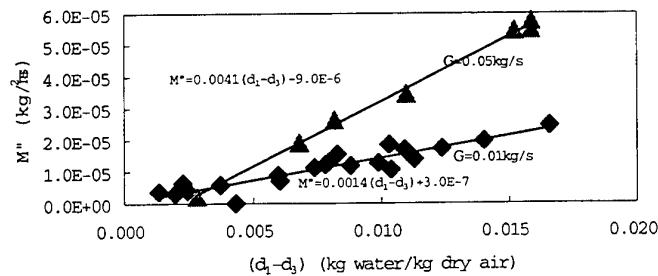


Fig.5 Schematic of the relations of M'' versus $(d_1 - d_3)$

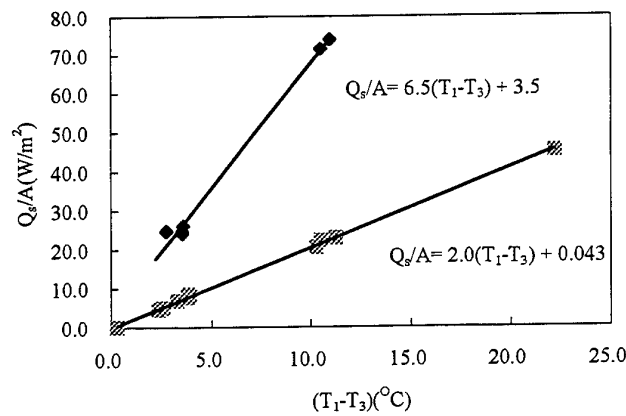


Fig.6 Schematic of the relation of Q_d/A versus $(T_1 - T_3)$

Table.1 lists the comparison of the computed results with experiments. The agreement between both of them is satisfactory, which validates the aforementioned theoretical analysis and model.

Table 1A Comparison of the computed results with experiments ($G=0.01\text{kg/s}$, $A=4.65\text{m}^2$, $D=10\text{mm}$)

Experiment No.	I	J	K	M	O
Experiment Conditions	$T_1 = 35.1^\circ\text{C}$ $\text{RH}_1(\%) = 55.0$ $T_2 = 26.6^\circ\text{C}$ $\text{RH}_2(\%) = 45.4$ $T_3 = 26.6^\circ\text{C}$ $\text{RH}_3(\%) = 15.8$ $T_4 = 31.0^\circ\text{C}$ $\text{RH}_4(\%) = 44.2$	$T_1 = 35.4^\circ\text{C}$ $\text{RH}_1(\%) = 47.2$ $T_2 = 26.1^\circ\text{C}$ $\text{RH}_2(\%) = 44.4$ $T_3 = 24.2^\circ\text{C}$ $\text{RH}_3(\%) = 15.8$ $T_4 = 30.8^\circ\text{C}$ $\text{RH}_4(\%) = 44.2$	$T_1 = 35.4^\circ\text{C}$ $\text{RH}_1(\%) = 40.2$ $T_2 = 26.3^\circ\text{C}$ $\text{RH}_2(\%) = 46.9$ $T_3 = 25.0^\circ\text{C}$ $\text{RH}_3(\%) = 33.6$ $T_4 = 30.8^\circ\text{C}$ $\text{RH}_4(\%) = 37.0$	$T_1 = 28.2^\circ\text{C}$ $\text{RH}_1(\%) = 62.8$ $T_2 = 24.9^\circ\text{C}$ $\text{RH}_2(\%) = 50.1$ $T_3 = 24.3^\circ\text{C}$ $\text{RH}_3(\%) = 36.2$ $T_4 = 26.5^\circ\text{C}$ $\text{RH}_4(\%) = 51.6$	$T_1 = 22.2^\circ\text{C}$ $\text{RH}_1(\%) = 40.3$ $T_2 = 24.2^\circ\text{C}$ $\text{RH}_2(\%) = 29.3$ $T_3 = 24.7^\circ\text{C}$ $\text{RH}_3(\%) = 21.9$ $T_4 = 23.2^\circ\text{C}$ $\text{RH}_4(\%) = 29.9$
Measured ε_d	0.58	0.55	0.54	0.60	0.58
Computed ε_d	0.60	0.60	0.60	0.60	0.60
Measured ε_s	0.72	0.71	0.75	0.74	0.71
Computed ε_s	0.71	0.71	0.71	0.71	0.71
Experiment No.	P	Q	R	U	V
Experiment Conditions	$T_1 = 35.4^\circ\text{C}$ $\text{RH}_1(\%) = 47.2$ $T_2 = 26.1^\circ\text{C}$ $\text{RH}_2(\%) = 44.4$ $T_3 = 24.2^\circ\text{C}$ $\text{RH}_3(\%) = 15.8$ $T_4 = 30.8^\circ\text{C}$ $\text{RH}_4(\%) = 44.2$	$T_1 = 28.2^\circ\text{C}$ $\text{RH}_1(\%) = 41.1$ $T_2 = 25.1^\circ\text{C}$ $\text{RH}_2(\%) = 34.7$ $T_3 = 24.4^\circ\text{C}$ $\text{RH}_3(\%) = 20.2$ $T_4 = 26.6^\circ\text{C}$ $\text{RH}_4(\%) = 29.3$	$T_1 = 28.2^\circ\text{C}$ $\text{RH}_1(\%) = 41.1$ $T_2 = 25.1^\circ\text{C}$ $\text{RH}_2(\%) = 34.7$ $T_3 = 24.4^\circ\text{C}$ $\text{RH}_3(\%) = 20.2$ $T_4 = 26.6^\circ\text{C}$ $\text{RH}_4(\%) = 29.3$	$T_1 = 46.5^\circ\text{C}$ $\text{RH}_1(\%) = 24.8$ $T_2 = 28.0^\circ\text{C}$ $\text{RH}_2(\%) = 49.9$ $T_3 = 24.3^\circ\text{C}$ $\text{RH}_3(\%) = 30.7$ $T_4 = 36.9^\circ\text{C}$ $\text{RH}_4(\%) = 27.7$	$T_1 = 23.6^\circ\text{C}$ $\text{RH}_1(\%) = 33.9$ $T_2 = 23.1^\circ\text{C}$ $\text{RH}_2(\%) = 28.7$ $T_3 = 23.1^\circ\text{C}$ $\text{RH}_3(\%) = 22.1$ $T_4 = 23.4^\circ\text{C}$ $\text{RH}_4(\%) = 26.5$
Measured ε_d	0.54	0.48	0.48	0.48	0.44
Computed ε_d	0.60	0.60	0.60	0.60	0.60
Measured ε_s	0.79	0.73	0.78	0.78	0.80
Computed ε_s	0.71	0.71	0.71	0.71	0.71

Table 1B Experimental results($G=0.05\text{kg/s}$, $A=4.65\text{m}^2$, $D=10\text{mm}$)

Experiment No.	W	Z	AA	AB	AC
Experiment Conditions	$T_1=24.6^\circ\text{C}$ $\text{RH}_1(\%)=34.2$ $T_2=23.2^\circ\text{C}$ $\text{RH}_2(\%)=33.9$ $T_3=22.9^\circ\text{C}$ $\text{RH}_3(\%)=28.9$ $T_4=23.6^\circ\text{C}$ $\text{RH}_4(\%)=30.3$	$T_1=35.2^\circ\text{C}$ $\text{RH}_1(\%)=53.4$ $T_2=28.4^\circ\text{C}$ $\text{RH}_2(\%)=58.5$ $T_3=24.3^\circ\text{C}$ $\text{RH}_3(\%)=17.9$ $T_4=29.9^\circ\text{C}$ $\text{RH}_4(\%)=31.9$	$T_1=27.4^\circ\text{C}$ $\text{RH}_1(\%)=40.3$ $T_2=25.0^\circ\text{C}$ $\text{RH}_2(\%)=38.7$ $T_3=23.8^\circ\text{C}$ $\text{RH}_3(\%)=12.8$ $T_4=25.4^\circ\text{C}$ $\text{RH}_4(\%)=19.7$	$T_1=22.5^\circ\text{C}$ $\text{RH}_1(\%)=63.4$ $T_2=23.7^\circ\text{C}$ $\text{RH}_2(\%)=47.0$ $T_3=24.7^\circ\text{C}$ $\text{RH}_3(\%)=13.5$ $T_4=23.0^\circ\text{C}$ $\text{RH}_4(\%)=30.2$	$T_1=27.5^\circ\text{C}$ $\text{RH}_1(\%)=73.7$ $T_2=25.3^\circ\text{C}$ $\text{RH}_2(\%)=60.6$ $T_3=24.0^\circ\text{C}$ $\text{RH}_3(\%)=10.1$ $T_4=25.5^\circ\text{C}$ $\text{RH}_4(\%)=36.4$
Measured ε_d	0.34	0.32	0.23	0.30	0.35
Computed ε_d	0.35	0.35	0.35	0.35	0.35
Measured ε_s	0.63	0.58	0.56	0.65	0.54
Computed ε_s	0.61	0.61	0.61	0.61	0.61

5. ENERGY SAVING ANALYSIS

Fig.7 and Fig.8 show the air handling process by using an AHU with membrane based HRV in psychrometric diagram (see Fig.2), where R is state point of return air, and F is the state point of fresh air. After passing the HRV, the state point of the intake fresh air is F1. And after mixing with exhaust air from air-conditioned space, the state point of mixed air is F2. If there is no HRV in the system, the state point of outlet air from the mixer is O1. O2 is the state point of outlet air from mixer for the case that only sensible heat recover with same sensible heat exchange effectiveness is adopted. S is the state point of required supply air. From Fig.8 and Fig.9, it is seen that: in winter membrane based HRV is able to simultaneously save energy consumed by heater and humidifier compared with the system without HRV, while sensible HRV can only save the energy consumed by heater but not that by humidifier; Similarly, in summer membrane based HRV can save the energy consumed by cooling coil compared with the system without HRV or can save more energy consumption compared with the system equipped with sensible HRV.

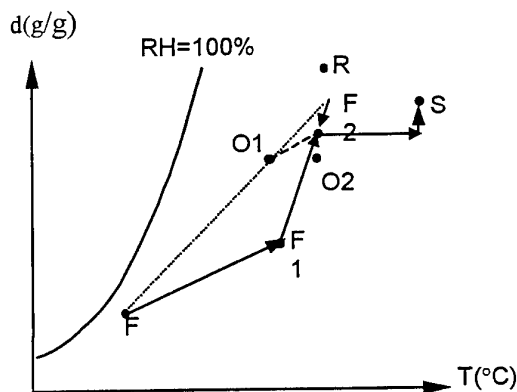


Fig.7 Schematic of air handling processes in winter in psychrometric diagram

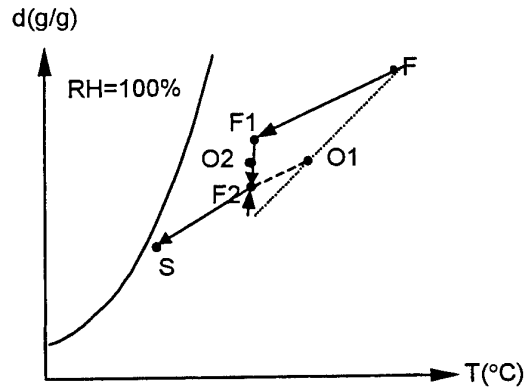


Fig.8 Schematic of air handling processes in summer in psychrometric diagram

In intermediate seasons, it's difficult to show the air handling process in a simple way because the geometric relationship of the state points of fresh air and the return air changes when climate parameters change. As illustration, the energy saving effect of the AHU shown in Fig.2 built in a business building located in Beijing is evaluated. The volumetric fraction of fresh air is kept to be 30% in whole year. With a simulation program named AHU Analysis developed by us, the optimal hourly operative process of the AHU in whole year can be determined. In simulation, the climate data of Beijing are used, and the thermal performance of the business building is calculated by software named DeST developed by us. The computed results are listed in Table.2.

Another paper will describe the details of analyzing the energy consumption of AHU equipped with various HRV in different climate conditions and different type buildings.

Table. 2 Whole year energy saving of using HRV in AHU.

Type of HRV	Sensible HRV	Membrane based HRV
Energy saving	18.0%	23.5%

7. CONCLUSIONS

From the point of view of application of such membrane in heat recovery ventilator(HRV), the selection criterion of the membrane was presented. That is, D_{AB} , S and $\frac{\partial S}{\partial p} (\frac{\partial S}{\partial p} > 0)$ should be large while δ , and

$\left| \frac{\partial S}{\partial T} \right| (\frac{\partial S}{\partial T} < 0)$ should be small.

A general physical model to analyze the performance of various membranes based HRV was built which was validated with experiments. The results demonstrate the advantages of such HRV system: being able to recover the sensible and latent heat simultaneously, being of high heat and moisture exchange effectiveness, without any mechanical components in it, being able to save energy by using it in air-conditioning system for whole year run. The model and results are helpful for the developing the membrane based heat recovery ventilator.

REFERENCES

1. P.Majumdar and M.K.Sarwar, Performance of a desiccant dehumidifier bed with mixed inert and desiccant materials, Energy, Vol.19, No.1, pp.103-116, 1994.
2. U. Sander and H. Janssen, Industrial application of vapor permeation. Journal of Membrane Science, 61, 113-129(1991).
3. S.H. Chen, R.C. Ruaan, and J.Y. Lai, Sorption and transport mechanism of gases in polycarbonate membranes. Journal of Membrane Science, 134, 143-150(1997).
4. U. Bonne, A.W. Deetz, J.H. Lai, D.J. Odde and J.D. Zook, Membrane dehumidification, US Pat., 4915838, 10 April 1990.
5. P. Aranda, W.J. Chen, and C.R. Martin, Water transport across polystyrene-sulfonate/alumina composite membranes. Journal of Membrane Science, 99, 185-195(1995).
6. J.Q. Wang and Z. Li, Synthesis of zeolite membrane and its application in removal of moisture from gases. Membrane Science and Technology, 18, 54-58(1998).
7. F.P. Incropera, D.P. Dewitt, Fundamentals of Heat and Mass Transfer, 4th edition, John Wiley & Sons, New York, USA, 1996.
8. Z.E. Wu, R.Y. Zhao et al., Heating and air-conditioning, Chinese Industrial Publishing Co., Beijing, 1965, pp.100-122, in Chinese.

A STEADY-STATE MODEL FOR THE HIGH-PRESSURE SIDE OF UNITARY AIR-CONDITIONERS

Pascale J. Petit and Josua P. Meyer

Department of Mechanical and Manufacturing Engineering

Rand Afrikaans University

E-mail: pjp@scotty.rau.ac.za; Facsimile: +27 12 326 3375

Keywords: compressor, condenser, temperature, performance, pressure

ABSTRACT. A steady-state model was developed to predict the performance of the high-pressure side of vapour-compression air-conditioning systems. The model consists of two segments; the compressor model and condenser model. The compressor model consists of a single empirical equation, for reciprocating compressors, operating with R-22, and having a cooling capacity from 2.6 to 3.5 kW. An important advantage of the approach is that the compressor performance indexes are based on operating conditions. The condenser model displays an exact method to determine physical dimensions of heat exchangers, and a simple, accurate manner to calculate the heat transfer variables. The correctness of the condensing temperature is obtained by an iterative procedure, using terms from both the compressor and condenser studies. The feasibility of the proposed model is demonstrated via a comparison with experimental data and a simulation study. Results indicate a good correlation between the mathematical model and its counterparts.

1. INTRODUCTION

The shipments of unitary air-conditioners and heat pumps in the United States have been rising steadily from 3.7 million in 1992 to 6.6 million in 1998. According to industry projections, new demand for air-conditioning and refrigeration products by developing countries will increase the global market by an estimated \$150 billion over the next 10 years. The impact of this growth on energy consumption will be significant, and it therefore necessitates the accurate modeling of unitary air-conditioners for optimization, improved energy efficiency, parametric studies and the evaluation of new components.

In recent years, investigations have centered on advanced cycle design for both heat- and work-actuated systems, improved components (including choice of working fluid), and use in a wider range of applications [1]. Concurrently, studies have been undertaken to predict the thermal performance of several variations of heat pumps. Numerous experimental studies, simulation models and computer software have been devised to explain and optimize the process of the vapor-compression refrigeration system.

Consequently, this study proposes a steady-state model that can be used to predict the performance of the high-pressure side (composed of the compressor and condenser) of vapour-compression unitary air-conditioners as function of ambient conditions, compressor operating conditions and geometrical arrangement of the condenser. The emphasis will be on air-conditioners with capillary tubes, operating with R-22, having a cooling capacity of 2.6 to 3.5 kW. At present, these represent the majority of all air-conditioners sold worldwide, even though R-22 is being phased out, due to the Montreal Protocol. Therefore, this work will be of value for the following decade or two, since provision has recently been made for developing countries towards a slower phase out of CFC's and HCFC's. The model integrates the latest and most accurate research published on the performance of air-cooled plate fin-and-tube condensers. The significance of the model is simplicity in execution but not to the disadvantage of accuracy.

2. MODELING OF THE SYSTEM

The system is developed for steady-state operation to allow system energy, pressure and refrigerant mass balances. The execution of the air-conditioner model starts by incorporating selected initial operating conditions of the air-conditioning system, such as the evaporating and condensing temperatures, and superheat value. For this work, ARI conditions for the evaporating temperature (7.2 °C) and condensing temperature (54.4 °C) are used as initial parameters, since most air-conditioning systems operate close to

these values. A superheat value of 11.1 °C is recommended by most manufacturers of compressors, and consequently, was included in this study. In addition, the model requires operating settings as input, namely ambient conditions, for the condenser. The refrigerant cycle is depicted in p-h and T-s diagrams, as shown in Figure 1. The necessary properties were retrieved from the REFPROP computer database [2].

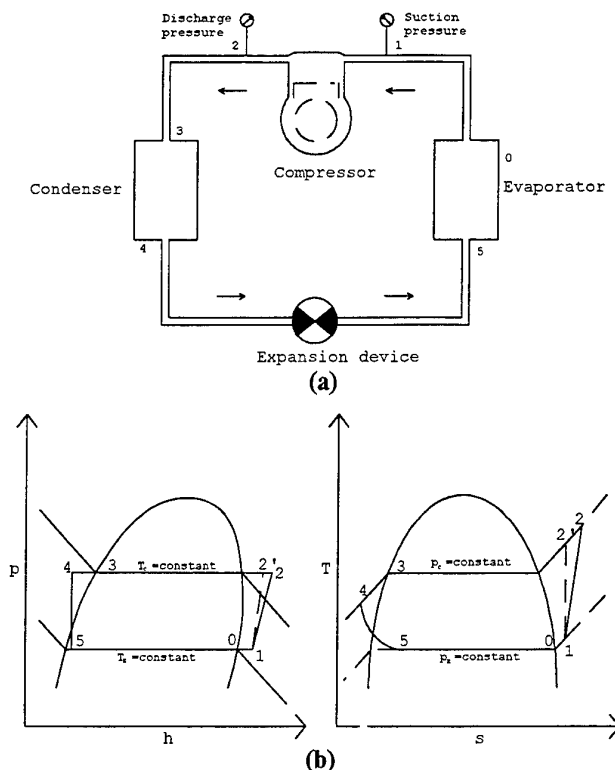


Figure 1. The single-stage vapor-compression cycle: (a) schematic view; (b) p-h and T-s diagrams

3. COMPRESSOR MODEL

In the literature, it is evident that many different models have been to model the performance characteristics of compressors. A different approach can be taken by employing the compressor performance curves provided by most manufacturers. Manufacturers, maintenance and repair personnel have discovered that compressors of various manufacturers could be easily interchanged, without adversely affecting the performance of the air-conditioner, provided the nominal capacity remains the same. In this model, the most important output values are the refrigerant mass flow, input power and outlet temperature for specified evaporating and condensing temperatures/pressures. With the compressor inlet condition known, the refrigerant mass flow, m_r , is given by

$$m_r = E_v \rho_1 V_c N \quad (1)$$

The inlet density can be found since the evaporating temperature and superheat are known at the compressor inlet. The compressor manufacturers usually furnish the remaining variables (i.e.) the cylinder swept volume and reciprocating speed. For hermetically sealed compressors, it is a good assumption to neglect the difference in inlet and outlet velocities, besides assuming adiabatic heat transfer from the compressor dome. Therefore, the input power is

$$W_{act} = m_r (h_2' - h_1) / E_f \quad (2)$$

The outlet temperature is found by knowing the condensing pressure and outlet enthalpy, h_2

$$h_2 = (W_{act} / m_r) + h_1 \quad (3)$$

The isentropic/volumetric efficiency can be expressed by a single formula similar to the polynomial [3].

$$E = C_0 + C_1 T_E + C_2 T_C + C_3 T_E^2 + C_4 T_E T_C + C_5 T_C^2 + C_6 T_E^3 + C_7 T_C T_E^2 + C_8 T_E T_C^2 + C_9 T_C^3 \quad (4)$$

where the coefficients C_0 to C_9 are given in Table 1.

Table 1. Coefficients of the Isentropic and Volumetric Equations

Constants	Isentropic Coefficient	Volumetric Coefficient
C_0	12.78916628	90.8588509815
C_1	-1.71538123537	0.239035154928
C_2	1.9338390985	-0.120092930403
C_3	1.81226082986E-3	5.84251687644E-2
C_4	0.062072771391	1.27526153795E-2
C_5	-2.64785050506E-2	-5.80781577622E-3
C_6	-7.30672209989E-4	-6.69066962859E-4
C_7	-7.14317950575E-4	-2.30174748787E-3
C_8	-3.46060970669E-4	1.83537130424E-4
C_9	7.94178659832E-5	-1.18103716582E-5

Measurements supplied by more than 80% of all compressor manufacturers in the capacity range that is relevant to this study, were obtained. Most manufacturers claim an accuracy of $\pm 5\%$. The given data were the cooling capacity, input power and refrigerant mass flow, as function of several evaporating and condensing temperatures. The volumetric and isentropic efficiencies for all these evaporating and condensing temperatures were determined by placing the efficiencies as the subject of Equations 1 and 2, and substituting the other variables by the manufacturers' data.

Isentropic efficiencies given by Equation 4 gave the best results from different approaches undertaken to generate the results. In the most successful method, the efficiencies were interpolated at four evaporating temperatures, namely -5°C , 0°C , 5°C and 10°C . The condensing temperatures ranged from 26.4°C to 61°C . These values can be expressed by a single matrix equation, namely $A \cdot X = B$. In matrix **A**, the condensing and evaporating temperatures, and their higher order values, are enclosed for the points from the graphical representation. The corresponding efficiencies are entered in matrix labeled **B**. The system is solved to yield the matrix **X**, which contains C_0 to C_9 . The volumetric and isentropic efficiencies of Equation 4 were then used to calculate the refrigerant mass flow according to Equation 1 and the input work according to Equation 2, respectively. These values were compared to the values of the manufacturers, and the results are shown in Figure 2.

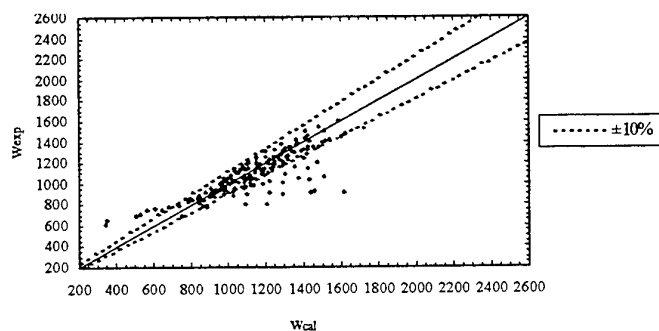


Figure 2a. Comparison between the experimental and calculated actual work

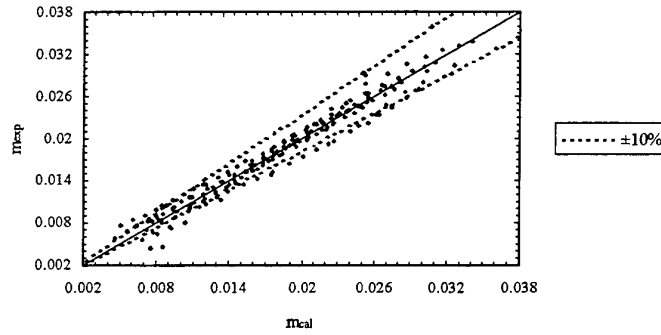


Figure 2b. Comparison between the experimental and calculated refrigerant mass flow

It can be concluded from this figure that the majority of the data, 75% for the mass flow and 80% for the input power, occurs within $\pm 10\%$. However, analyzing the results carefully, most of the points that do not fall within the 10% domain, are extreme operating conditions. This is specifically for compressors functioning to very low evaporating temperatures down to -23°C . These compressors are used for refrigeration besides air-conditioning. If a minimum evaporating temperature of 0°C is considered, together with a maximum condensing temperatures of 60°C , where most air-conditioners are operating, it can be shown that 86% of the refrigerant mass flow and 94% of the input power points fall within the $\pm 10\%$ range.

4. CONDENSER MODEL

Several experimental results and models have been published to model the air-side heat transfer characteristics of plate or wavy fin and tube heat exchangers. Fin efficiencies of several heat exchangers were also determined [4,5,6]. However, in these previous studies, the heat exchanger area is known, and the temperatures and pressures have been measured. However, no research was made simplify the acquisition these terms, nor was any general method derived to calculate the heat transfer variables, in order that they may be applied to other plate fin-and-tube condensers. Therefore, for this model, the basic equation for the total sensible heat transfer of heat exchangers (Equation 5) is expanded, each term is viewed, and resolved into uncomplicated expressions. The results of this technique, undertaken for each variable in Equation 6, are now presented under separate sub-headings.

$$Q = U_o A_o \Delta T_{lm} \quad (5)$$

where

$$U_o = \frac{1}{1/\eta_o (1/h_{o,o}) + (A_o/A_i) (r_{ii}/r_w) \ln(r_o/r_i) + (A_o/A_i) (1/h_{o,i})} \quad (6)$$

4.1 Calculations of Areas A_o and A_i

The total surface area, A_o , of the heat exchanger has been reduced to an association of the surface area of the plates of the condenser, and the 'wetted' area of the tubes.

$$A_o = N_{pl} * (A_{pl} - (N_t * A_{fc,o})) + N_t * (A_w) \quad (7)$$

The tube area, A_w , that is in contact with the incoming air-stream, and the internal area of the tubes A_i are:

$$A_w = (\pi (d_{fc,o}) (N_{pl}(s))) \quad (8)$$

$$A_i = (N_{pl})(s)(\pi * N_t * \text{tube ID}) \quad (9)$$

Therefore, to calculate the overall and inner areas of the heat exchanger, only the number of fins and tubes must be counted. And, the transverse and longitudinal tube pitch, fin dimensions, fin spacing and the tube fin collar and inner diameter are the only measurements required.

4.2 Calculation of the Outer Heat Transfer Coefficient

The air-side heat transfer is realized by solving three non-dimensional factors, namely the Reynolds, Nusselt and Prandtl groups:

$$Re_{fc} = \rho \cdot v_{max} \cdot d_{fc,o} / \mu \quad (10a)$$

where

$$v_{max} = 0.0125 v_i / (0.0125 - d_{fc,o}) \quad (10b)$$

$$Nu = j \cdot Re_{fc} \cdot Pr^{1/3} \quad (11)$$

The Colburn j-factor may be obtained from various correlations [7,8]. The most common configuration is wavy plates, due to the enhanced heat transfer. Applying the correlation by Kim, N.-H. et al. [7],

$$j = 0.394 (Re_{fc})^{-0.357} (P/P_1)^{-0.272} (s/d_o)^{-0.205} (x_g/p_d)^{-0.558} (p_d/s)^{-0.133} \quad (12)$$

Once Equation 11 is solved, the outer heat transfer coefficient is realized as,

$$h_o = Nu \cdot k_a / d_{fc} \quad (13)$$

4.3 Calculation of the Overall Fin Efficiency

The overall efficiency, η_o , is necessary to enumerate the effectiveness of the heat transfer rate, because fins do not have a uniform temperature. The equations for the overall fin efficiency are illustrated by Holman [9], and therefore, shall not be shown here.

4.4 Calculation of the Internal Heat Transfer Coefficient

4.4.1 Desuperheat and subcool regions. The Dittus-Boelter heat transfer correlation for turbulent flow of liquids inside tubes is,

$$Nu = 0.023 Re^{0.8} Pr^{0.3} \quad (14)$$

The internal heat transfer coefficient of desuperheat (point 2' in Figure 1) is

$$h_{i,desuperheat} = Nu \cdot k_r / ID \quad (15)$$

Results for the above two equations were calculated for desuperheat temperatures between 60°C and 175°C, in increments of 5°C, since it is desirable to yield an expression relating the internal heat transfer coefficient as a function of the refrigerant mass flow. The calculations commenced by obtaining values of the mass flow, m_r , of the refrigerant exiting the compressor, using Equation 1. The mass flows range from 20% above and below extreme values of air conditioning operation to moderate activity. The refrigerant properties at the above mentioned temperatures were found in REFPROP [2], and substituted in Equations 14 and 15. These calculations resulted in a series of points, showing the internal heat transfer coefficient versus the refrigerant mass flow rate, for each desuperheat temperature. At each refrigerant mass flow rate, these coefficients were added, averaged and plotted. This established a single equation for the average heat transfer coefficient, as a function of the mass flow per circuit, for the desuperheat region:

$$h_{i,desuperheat} = 1.94E6 (m_r/N_c)^3 - 2.102E5 (m_r/N_c)^2 + 2.33E4 (m_r/N_c) + 33.5 \quad (16)$$

In the subcool region, the calculations to obtain the internal heat transfer coefficient are identical to those for desuperheating. However, the refrigerant properties are obtained at a subcooling temperature of 9.4°C below condensing temperature with REFPROP [2]. The equation for the average heat transfer coefficient, as a function of the mass flow per circuit, for the subcool region is

$$h_{i,subcool} = 2.13E6 (m_r/N_c)^3 - 2.31E5 (m_r/N_c)^2 + 2.56E4 (m_r/N_c) + 36.8 \quad (17)$$

Comparison of Equation 15 and results of Equations 16 and 17, respectively, certified that the equations produced solutions within the 10% of each other.

4.4.1 Two-phase region. An equivalent mathematical method was applied to determine the internal heat transfer coefficient of the two-phase region, lying between points 2 and 3 (Figure 1). The local heat transfer coefficients are obtained between condensing temperatures of 40 and 60°C, and air qualities of 0.05 to 0.9, in increments of 0.05. The calculations are initiated with refrigerant mass flow rates of 0.0083 kg/s to 0.0326 kg/s. Equations for the average local heat transfer coefficient in the two-phase region are determined from five correlations [10,11,12,13,14], since most of them are limited in the range of refrigerant quality. Moreover, differences in flow patterns during measurements prevent any single correlation to be suitable, when applied to another model. Consequently, the resulting calculations offered the following mean local heat transfer coefficients:

$$h_{i,2p} = -3.41E7 (m_r/N_c)^3 + 2.38E6 (m_r/N_c)^2 + 4.43E4 (m_r/N_c) + 654 \quad (18)$$

$$h_{i,2p} = 6120x^3 - 6131x^2 + 3200x + 171 \quad (19)$$

4.5. Condenser Temperature

The final phase required to complete the steady-state model, is to determine the value of the condenser temperature. Previously, this value was assumed to facilitate the development of the compressor and condenser models. A simulation model is created that contains the NTU-method (number of transfer units). Once this has been accomplished, a temperature of condensation is selected. This is denoted as T_c^* . An iterative procedure was executed using arbitrary condenser dimensions and the initial assumed condensing temperature, T_c^* . The repetitions of the loop vary from four to eight loops, depending on how much the original condensing value, T_c^* , departs from the final temperature, T_c . The desired precision required also affects the speed of convergence. Once the correct condenser temperature has been reached, its value remains unchanged, even if additional iterations are conducted. Therefore, the system is considered stable.

5. VALIDATION OF MODEL

A comparison between the mathematical model obtained for the compressor and condenser, and results obtained from the operation of air-conditioners, completes the high-pressure side calculations. Another evaluation method is also employed, namely a simulation software program, HPSIM [15].

The air-conditioners employed to verify this mathematical model, were operated at a high setting for two hours prior to steady-state data collection, inside a 48 m² room with a ceiling height of 2.4 m at an ambient temperature and pressure. After steady-state operation was ensured, individual readings were recorded at 10 minutes intervals, to obtain average readings at a singular atmospheric temperature and pressure. These readings include refrigerant, dry-bulb, wet-bulb air temperatures and pressures, and the air velocity flowing through the evaporator and condenser were also recorded. Measurements also included the total input power of the compressor and the physical dimensions of the evaporator, condenser and pipe elements. The condenser specifications comprised the measuring of the number of circuits, plates, rows and tubes, the longitudinal and transverse tube pitches, fin spacing, fin thickness and the nominal tube diameter.

After the all readings have been collected and averages have been calculated for each quantity, these were entered into the mathematical model and HPSIM. The result yielded the states of the properties for the air and refrigerant at various points in the system. Additional results encompassed flow rates, heat transfers to and from the heat exchangers. Inlet and outlet values of the air and refrigerant related to the condenser were generated. The readings taken from the air-conditioners were also utilised to manually calculate the results. Consequently, the sets of results are evaluated against each other to determine the validity, accuracy and limitations of the steady-state model. The results are not shown in a tabular format, for all air-conditioners, due to space limitations.

6. DISCUSSIONS

From the general data, the compressor performance parameters are well simulated by the mathematical model and HPSIM. The refrigerant mass flow rates of the mathematical model and HPSIM are within 0.001 kg/s from the experiment values. A maximum difference of ± 220 W between HPSIM and the experimental values occur for the input power, since the program calculated the total input power including fans and pumps. Nevertheless, the value obtained by mathematical model was less than 5% from the experimental value. The product of the refrigerant mass transfer and the enthalpy calculates the heat transfer across the evaporator and condenser, individually. The mathematical models overestimated the heat transfer by ± 0.25 kW, while HPSIM underestimated this quantity by ± 0.5 kW. These digressions were less than 12% from the practical amount. The coefficients of performance parameters (COP) showed slightly higher deviations, due to the compounded error that incurs from the relation between the heat transfer and the total input power. However, the deviations for cooling and heating were all less than 15%. The comparisons of the refrigerant properties denoted a maximum divergence of $\pm 20\%$ with the condensing temperatures. The condensing temperature suggested by HPSIM was only $\pm 2\%$ higher than its counterpart from the mathematical model. All other values deviated little from each other. Finally, the overall outer heat transfer coefficients calculated from the practical results and mathematical model were greater than the HPSIM value due to the large value of the simulated outside surface area of the condenser released by HPSIM. The inner heat transfer coefficient was comparable in all three instances.

7. CONCLUSIONS

A mathematical model for the high-pressure side of vapour-compression air-conditioning systems has been developed. The compressor model is based on operating conditions, and generated output values of the refrigerant mass flow, input power and outlet temperatures. Independent variables representing the total sensible heat transfer of a multi-pass, continuous plate fin-and-tube condenser were simplified to simple, precise formulae. A method to determine the correct temperature of the condenser completed the steady-state model. Results of the comparison and simulation ascertained that the mathematical model and HPSIM delivered output values that estimated the experiment data closely.

NOMENCLATURE

English symbols

A	= area (m^2)	P_t	= transverse tube pitch (m)
A_o	= total surface area (m^2)	p	= pressure (kPa)
C_p	= specific heat ($\text{kJ/kg} \cdot ^\circ\text{C}$)	p_d	= fin pattern depth, peak-to-valley excluding fin thickness (m)
d	= tube diameter (m)	Pr	= Prandtl number ($\text{Pr} = C_p \mu / k_a$)
$E_{I \text{ or } V}$	= isentropic or volumetric efficiency	Q_o	= overall heat transfer rate (W)
h	= enthalpy (J/kg)	r	= radius (m)
h_o	= heat transfer coefficient ($\text{W/m}^2 \cdot ^\circ\text{C}$)	Re	= Reynolds number
ID	= internal diameter (m)	s	= entropy ($\text{J/kg} \cdot \text{K}$)
k	= thermal conductivity ($\text{W/m} \cdot \text{K}$)	s	= fin spacing (m)
k_w	= thermal conductivity of wetted surface ($\text{W/m} \cdot \text{K}$)	T	= temperature ($^\circ\text{C}$)
m_r	= refrigerant mass flow (kg/s)	t	= fin thickness (m)
N	= reciprocating speed (rev/s)	U_o	= overall heat transfer coefficient ($\text{W/m}^2 \cdot ^\circ\text{C}$)
N_c	= number of circuits	v	= velocity (m/s)
N_l	= number of longitudinal rows	V_c	= cylinder volume (m^3)
N_{pl}	= number of plates	W_{act}	= actual work (W)
N_t	= number of tubes	x	= vapour quality
Nu	= Nusselt number	x_f	= projected fin pattern length for $\frac{1}{2}$ wave length (m)
OD	= outer diameter (m)		
P_l	= longitudinal tube pitch (m)		

Subscripts and superscripts

1	= air-side inlet	i	= inside or inlet
2	= air-side outlet	l	= liquid
a	= air	max	= maximum
al	= aluminium	o	= outside or outlet
atm	= atmosphere	pl	= plate
C	= condensing	r	= refrigerant
E	= evaporating	tp	= two-phase region
f	= fin	w	= wetted surface
fc	= fin collar		

REFERENCES

1. K., K. Den Braven, Herold, V. Mei, D. O'Neal, and S. Penoncello, Mechanical Engineering Sept. 1993, pp. 98-102 (1993).
2. NIST. Thermodynamic properties of refrigerants and refrigerant mixtures database. *NIST Standard Reference Database 23, Version 4.01* Gaithersburg, MD: National Institute of Standards and Technology, U.S.A. (1993)
3. J.P. Meyer and G.P. Greyvenstein, Energy vol. 16, no. 7, pp. 1039-1044 (1991).
4. F.C. McQuiston, ASHRAE Transactions vol. 81, part 1, pp. 350-355 (1975).
5. A.H. Elmahdy and R.C. Biggs, ASHRAE Transactions vol. 89, part 1A, pp. 135-143 (1983).
6. G. Wu and T.-Y. Bong, ASHRAE Transactions vol. 100, part 1, pp. 367-373 (1994).
7. N.-H. Kim, J.-H. Yun, and R.L. Webb, Journal of Heat Transfer, vol. 119 (Aug.), pp. 560-5671 (1997).
8. C.-C. Wang, Y.-J. Chang, and Kim, Y.-T., International Journal of Refrigeration, vol. 19, no 4, pp 223-230 (1996).
9. J.P. Holman, *Heat Transfer*. London: Mc Graw-Hill. (1992).
10. W.W. Akers, H.A. Deans, and O.K. Crosser, "Condensation heat transfer within horizontal tubes", *Chemical Engineering Progress Symposium Series* vol. 55, no. 29, pp. 151-159. (1959).
11. N.Z. Azer, L.V. Abis, and H.M. Soliman, ASHRAE Transactions vol 78, pp. 135-143 (1972).
12. D.P. Traviss, W.M. Rohsenow, and A.B. Baron, ASHRAE Transactions vol. 79, part 1, pp. 157-165 (1973).
13. A. Cavallini and R. Zecchin, "A dimensionless correlation for heat transfer in forced condensation", *Proceedings of the fifth international heat transfer conference, Japan Society of Mechanical Engineers*, vol. 3, pp. 309-313 (1974).
14. M.M. Shah, International Journal of Heat and Mass Transfer, vol. 22, pp. 547-556 (1979).
15. ENERFLOW Technologies, *HPSIM. Version 1.0*: University of Potchefstroom, South Africa (1994).

DEVELOPMENT AND EXPERIMENTAL TESTING OF AN ENTHALPY RECOVERY WHEEL BASED ON A NEW COMPOSITE DESICCANT

Mouloud Amazouz, Sophie Hosatte

CANMET – Energy Diversification Research Laboratory
1615 Bvd. Lionel-Boulet, Varennes, Québec, J3X 1S6 - Canada
Email: mamazouz@nrcan.gc.ca ; Fax : (+1) 450- 652 5177

Roland Côté

Institut national de la recherche scientifique - Énergie et matériaux
1650 Bvd. Lionel-Boulet, Varennes, Québec, J3X 1S2 – Canada

Keywords: Desiccant, enthalpy, energy recovery ventilator

ABSTRACT. Improved insulation regulations for Canadian houses have made mandatory the use of forced air ventilation systems to maintain indoor air quality. Long term ventilation may nevertheless create uncomfortable indoor air conditions and increase the energy bill when in winter, outside air introduced in the house is cold and dry and in the summer, when it is warm and humid.

The use of a passive heat and humidity exchanger, or enthalpy exchanger, makes it possible to alleviate these problems by a better control of the humidity and temperature levels of the air introduced in the house. The systems are driven by only the temperature and humidity level difference between the fresh airflow entering the house and the exhausted contaminated airflow. Active (gas regenerated) desiccant cooling systems are often used for these passive recovery applications but they are generally costly and overdimensioned.

A new passive and low cost enthalpy exchanger has been developed specifically for these applications and tested successfully. The product is based on the development of a new desiccant material and a new process for direct fabrication into an enthalpy wheel. This enthalpy exchanger presents the same performance as commercially available units, with interesting properties such as frost resistance, an important feature in cold climates.

The paper presents the characteristics of this novel product including its predicted and measured efficiencies.

1. INTRODUCTION

Rotary air to air energy exchangers are used in HVAC (Heating, Ventilation and Air-Conditioning) systems to recover both sensible energy and latent energy from one stream to another. The ability to recover the latent energy represented by the moisture content is of significant interest since it dehumidifies the outdoor air during the cooling season, and humidifies the outdoor air during the heating season. This implies a significant reduction of energy consumption while improving the indoor air quality by controlling the humidity level.

Total energy exchanger wheels consist generally of corrugated substrate impregnated or coated with desiccant material. They are generally in the form of a matrix that provides passages through which air stream can flow. The matrices take generally the form of corrugated sheets alternated with flat sheets wound around a hub (see Figures 1 and 2). When placed between two air streams in counterflow, the wheel enables sensible heat and moisture (latent heat) to be transferred between the two air streams. The portion of the wheel in contact with the hot and humid stream takes up moisture and sensible heat and transfers it to the cooler and dry air streams after half rotation. In the cooling mode, the energy recovery wheel cools and dries the hot, humid incoming air by absorbing its sensible heat and moisture. The energy necessary to further cool and dehumidify the incoming air to the desired conditions is reduced. During the heating season, the energy recovery ventilator (ERV) heats and humidifies the cool and dry incoming air by absorbing and transferring sensible heat and moisture from the warm, humid outgoing air. Thus, the energy required to further heat and humidify the incoming air is reduced.

The optimum rotation speed of these enthalpy wheels is about twenty (20) rpm as known in literature (1). The air passing through the wheel is in contact with the matrix for 1.5 seconds. The sensible heat exchange media and the desiccant must, therefore, be capable of absorbing maximum heat and moisture from one stream and

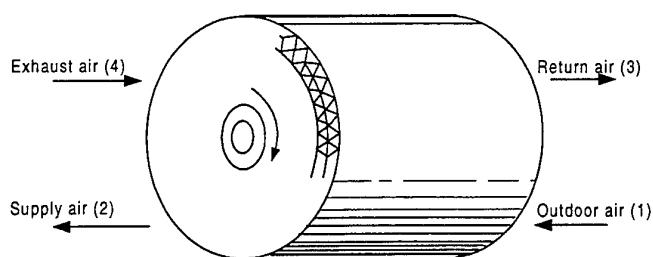


Fig. 1. ERV wheel configuration

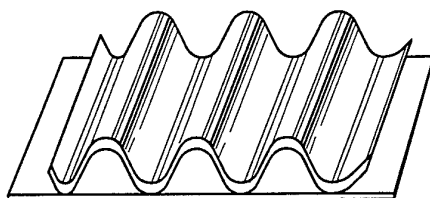


Fig. 2. Corrugated media (flute) geometry

release them to the other stream very quickly. The technology of sensible heat recovery wheels is well developed and heat transfer efficiencies are quite high. It is not the case for moisture or latent heat exchange. The latent heat efficiency and capacity of the matrix depends on the type of desiccant, air temperature and humidity and also the quality of the desiccant deposit on the substrate. Because the moisture transfer is here a surface phenomena, the exposed area of desiccant to the air stream should be as high as possible. This is why the quality of the desiccant to the substrate bonding is of primary importance. Silica gel, lithium chloride and molecular sieves are widely (Collier et al, 1988) used in form of powder for this application. Many techniques of desiccant deposit on different substrates (paper like, aluminium, ceramics,...) are used. Techniques using bonding agents or mixing the desiccant powder to the substrate could suffer from powder deliquescence or inhibition. Manufacturers usually increase the amount of desiccant in order to increase the surface of desiccant available for moisture catching. These techniques are expensive which reduces the penetration of this technology especially in the residential market. It is therefore of premium importance to develop new desiccants and/or new techniques for their deposit in order to lower the manufacturing cost. This paper presents a new technology developed for this aim.

2. TECHNOLOGY DESCRIPTION

Polymer type desiccant material has been chosen because of its ability to be easily modified so that sorption isotherm of desired form and capacity could be obtained. Also, the cost of some commercially available polymers is comparable to the cost of commercial grade silica gel (Czanderna, 1992). Polymers could also be tailored or directly formed in the desired shape. The other advantage of polymers is the possibility of their forming during the process of their deposit on substrates. The cross-linking density of the polymer structure determines the capacity of the desiccant and its sorption isotherm (Buchholz, 1994). The higher is the density of crosslinkage, the lesser is the absorption capacity of the material. The lesser is the capacity of the material, the lesser is its deformation resulting from its swelling. The process of fabrication of polymeric desiccants is well known and more than 300 commercially available polymers have been reported (Czanderna and Thomas, 1986). Some of these polymers could be used in desiccant cooling or enthalpy exchange devices. But no such application has been reported or known. In this work, a promising polymer has been first identified for further development to serve as an optimal desiccant. The material has been chosen for its affinity with cellulose fibres selected among other materials as a substrate. Cellulose based paperboard has been selected for its low cost.

The process of fabrication of the enthalpy wheel is described in a US patent application (Hosatte et al, 1998). A microscopic analysis showed a homogeneous structure in which the substrate composed of fibres is uniformly covered with the desiccant polymer. The optimal amount of desiccant has been determined by performing many

tests in order to obtain the desired capacity with good mechanical resistance; stability and no deliquescence or deformation during cycles of absorption desorption of water vapour. The article possesses also a good fire resistance and other expected properties such as contaminates removal and bactericide effect. The ease of its manufacture and the low cost of the primary materials used make this technology very cost effective, which was the goal, expected in the present work.

3. ERV WHEEL CHARACTERIZATION AND TESTING

Method of Testing and Set-up Description

Sorption isotherms and capacity of the polymer and the composite have been measured during the process of the article optimization. A set-up using thermogravimetric balance technique has been built. Conditioned air (temperature, relative humidity) is introduced through a temperature-controlled measuring chamber in which the desiccant or the composite specimen is suspended to a balance for continuous weighting (Figure 3). Several tests have been performed on the polymer alone and on composite specimens. For each experiment, temperature and relative humidity of the air were kept constant. The weight of the specimen is recorded until it reaches its maximum value corresponding to the capacity of the desiccant at the air conditions. In addition to this characterization, tests of inflammability and cycling effect have been performed along this study. These studies allowed optimizing the desiccant composition and quantity and also the quality of its deposit. Several prototypes have then been built for testing. The effect of desiccant mass proportion in the wheel on the ERV performance has been studied. The prototype performance measurement has been made according to ASHRAE 84-1991 standard method of testing under CSA-C439 norm conditions. Wheels with 304.8 mm (12") diameter and 101.6 mm (4") large mounted on a 50.8 mm (2") diameter hub have been tested under several conditions. Sensible, latent and total efficiencies and pressure losses have been measured.

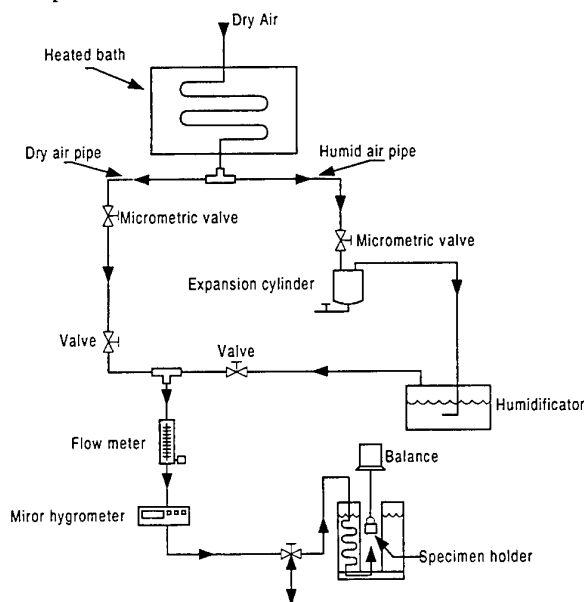


Fig. 3 Desiccant characterization set-up

Results and Discussions

Desiccant sorption isotherm and capacity The polymer isotherm compared to those of the two most popular desiccants (silica gel and molecular sieve) is shown on Figure 4. One can see that the polymer shows higher efficiencies of moisture absorption both at low and high humidity atmospheres. This means that this desiccant is particularly suitable for applications where the air humidity could change continuously. Same results are obtained for the polymer and the composite with 20% desiccant content by mass. This means that the technique of deposit by polymerization is very efficient. Other tests done on humidity cycled specimen showed no capacity decay or change in the isotherm shape even after thousands of cycles. Sorption kinetics have also been measured in order to determine how fast is the water vapour absorption by the desiccant. The result

showed that most of the capacity change is completed within five minutes. Note that the kinetic of sorption is highly dependent on the linear velocity of the air in contact with the desiccant. Figure 5 shows the absorption kinetic of the polymer compared to those of silica gel and zeolite at 1.8 cm/s air velocity for a change in humidity from 30% to 60%. The sorption kinetic of the polymer is faster than that of silica gel and is in the same order that of zeolite. Note that in operation the air velocity is about hundred times higher than it was in experiments. The kinetic is then supposed to be much higher under normal operation.

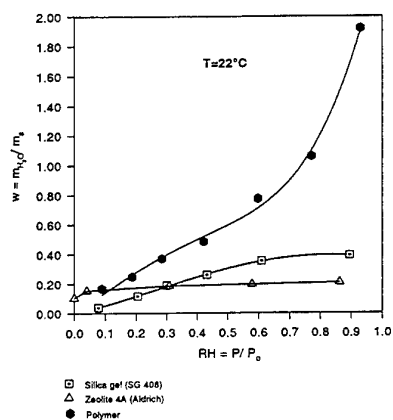


Figure 4. Isotherm sorption of some desiccants

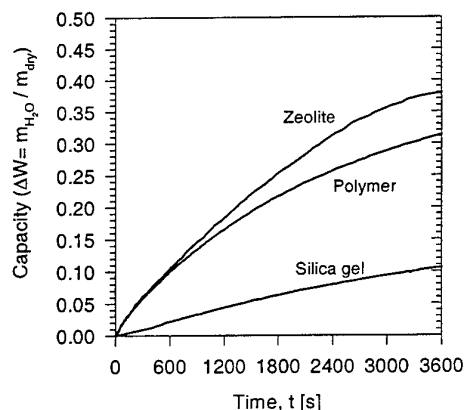


Figure 5. Sorption kinetics of some desiccants (Air velocity: 1.8 cm/s)

ERV's wheel performance The performance of the ERV is given in Table 1. Two winter conditions have been considered (-25°C , 35%RH and 0°C , 35%RH) for the heating mode and one summer condition (35°C , 35%RH) for the cooling season. The flow rate has been kept at 30l/s and the indoor conditions at 22°C , 50%RH. Efficiency is determined by the following equation:

$$\epsilon = \frac{m_e}{m_{\min}} \frac{X_4 - X_3}{X_1 - X_3} = \frac{m_s}{m_{\min}} \frac{X_1 - X_2}{X_1 - X_3}$$

Where X represents the temperature for sensible heat efficiency or the humidity for latent heat efficiency. m_e , m_s and m_{\min} are respectively the return, supply and minimum (m_e or m_s) flow rates. Total heat efficiency is also determined by considering the enthalpy of the air. The indices are given in Figure 2. The results show that the ERV wheel has high efficiency both for sensible and latent heat transfer especially in heating mode with 0°C outside air. The ERV is more efficient or at least equivalent to most of the commercially available enthalpy

wheels. Simulation made with a 3D numerical model (P. Brousseau et al, 1996) gave a value of 80% for both efficiencies for 0°C outside temperature in the heating mode. These efficiencies could be increased with a wider wheel but at an increased cost.

Table 1. Efficiency of the ERV Wheel

Outdoor air conditions	-25°C, 35%RH	0°C, 35%RH	35°C, 35%RH
Sensible heat efficiency (%)	70	81	75
Latent heat efficiency (%)	61	65	68

The effect of desiccant mass content has been studied in order to optimize the wheel. Optimized wheel should have high efficiency, produced at low cost and possess fire resistance capability. Figure 6 shows the effect of the desiccant mass fraction on both the sensible heat and moisture transfer efficiencies. Desiccant mass fraction has been varied from 10% to 20%. The lowest limit is imposed by the fire resistance capability and the highest limit is imposed by deliquescence and cost constraints. The desiccant mass fraction has no effect on the sensible heat transfer efficiency. This result is predictable since the sensible efficiency depends principally on the passageways geometry which remained constant for the range of desiccant contents considered here. In contrary, the latent heat transfer efficiency depends on the desiccant mass fraction. At fractions higher than 12.5%, the latent heat transfer efficiency decreases slightly. At high desiccant mass content, the polymer film becomes thicker allowing the water vapor diffusion resistance to become important despite the celerity of the mass transfer phenomena in this application. Note that the absorption capacity of the ERV increases with the desiccant mass fraction augmentation.

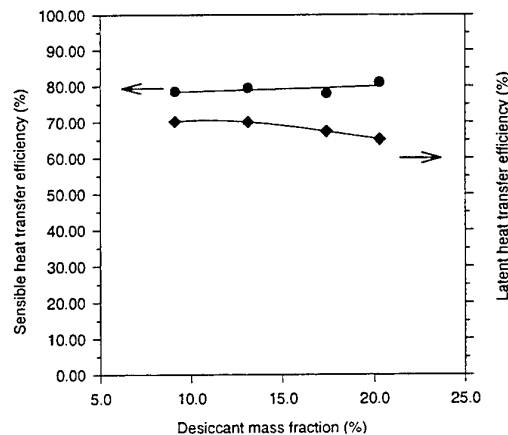


Fig. 6. Effect of desiccant mass fraction on the ERV wheel efficiencies

Impact of the ERV on energy consumption A theoretical estimation of energy savings from an ERV wheel installed in a uni familial residence has been made. The residence with 210 m² is located in the Montreal (Canada) area. Short hot and wet summers and long cold and dry winters characterize Montreal weather. Indoor design conditions are respectively 20°C, 30%RH in winter and 24°C, 50% in summer. The simulation is made by considering constant efficiencies for each season and for 0.3 volume air change per hour. The results gave a 35% energy savings for a whole typical year. The enthalpy ventilator increased the energy savings by 10% compared to a sensible heat only recovery exchanger with the same efficiency. This percentage could be higher in other more humid locations and for higher ventilation rates. The other gain from the ERV is the improvement of the indoor air quality by reducing the number of hours with high humidity ratio (more than 60%). This gain translates into better productivity at work places.

Other characteristics of the ERV wheel

Pressure losses Pressure losses are important for ventilation application. At 30.0 l/s flow rate, the pressure loss was less than 15 Pa (1.5 mm water column), which is relatively low compared to most of the existing ERVs. Figure 7 shows the effect of the flute (the form of the corrugations) geometry on the hydraulic pressure loss for different airflow rates and a 101.6 mm (4 in) wheel width. The corrugations geometry effect is quite important in this application especially in this case where the choice is made in the commercially available paperboard flute geometries for manufacture cost reduction reason.

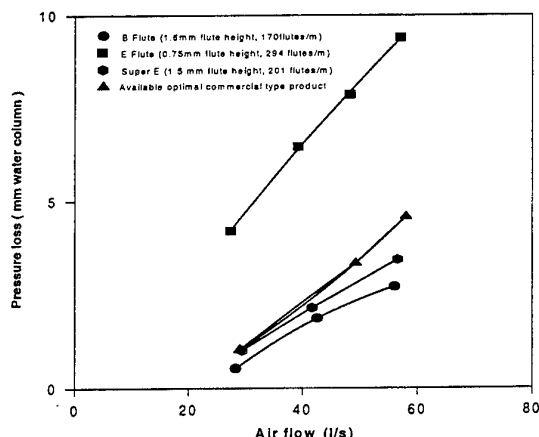


Figure 7. Effect of corrugation geometry on the pressure loss through the ERVs

Long life behaviour Ten prototypes have been installed in residences for one year in order to verify their behaviour in true conditions. The measured performance remained almost unchanged.

Flammability Inflammability is of a big importance for this product since this is of public safety concern. The flammability rating in north America is standardised and the product should satisfy all the UL safety codes (UL94HB, UL900 CLII, and UL723). The composite passed these tests due to the presence of a sufficient amount of fire retardants in the desiccant.

Contaminate transfer Contaminate transfer is one other important issue in ventilation. Contaminates such as CO, CO₂ and formaldehyde, are present in the outdoor air or exhaust air before introducing the air to the room. The new ERV is suspected to have a potential for some contaminates removal but no measurements have been made at this moment. If the contaminate removal potential is demonstrated, the product will contribute to the elimination of the SBS (Syndrome of Sick Building).

4. CONCLUSION

This new composite ERV has a high performance to cost ratio compared to the commercially available enthalpy wheels. The low cost is a very important factor since it will help to widen the market of energy recovery technology. The desiccant used in this composite product presents the advantage of being easily modified, thus, allowing the possibility of optimization for other applications such as dehumidification and desiccant cooling applications.

5. REFERENCES

1. W. M. Kays, A. L. London, Compact Heat Exchangers, McGraw Hill Book, 1984
2. R. K. Collier, R. S. Barlow, F. H. Arnold, An Overview of Open-Cycle Desiccant Cooling Systems and Materials, SERI/TP-631-1065 (1981)
3. W. Czanderna, Desiccant cooling and dehumidification, ASHRAE special publications, 1992, pp. 88.
4. F. L. Buchholz, Keeping dry with superabsorbent polymers, American Chemical Society, Chemtech 1994, pp. 38.
5. W. Czanderna and T.M. Thomas, Advanced desiccant materials research, SERI/PR-255-3102. 1986
6. P. Brousseau, S. Bilodeau, M. Lacroix, Y. Mercadier, Ab-Sorption International conference, Montreal, 96. Pp. 453
7. S. Hosatte, M. Amazouz and R. Côté, 1998, US Patent application

COOLING REQUIREMENTS FOR REFRIGERATED SEMI-TRAILERS TRANSPORTING FRESH FRUITS AND VEGETABLES

Catherine K. P. Hui G.S.V. Raghavan

Department of Agricultural and Biosystems Engineering
Macdonald Campus of McGill University

Email: hui@agreng.lan.mcgill.ca; raghavan@agreng.lan.mcgill.ca; Fax: (514)-398-8387

Clement Vigneault

Horticultural Research and Development Centre
Agriculture and Agri-Food Canada

Email: vigneaultc@em.agr.ca; Fax: (450)-346-7740

Keywords: refrigerated semi-trailer, transport, produce, cooling requirements

ABSTRACT. Fresh fruits and vegetables are perishable products. Their final quality is influenced by several factors such as initial quality, harvest maturity, packaging, physical injuries and pulp temperature. Temperature plays the most important role in the preservation of fresh produce. Its effect is cumulative, hence affecting quality when produce is exposed to temperature variations even for short periods of time. In regions with extensive road networks, refrigerated semi-trailers are used to transport and distribute fresh fruits and vegetables. The semi-trailer is equipped with a refrigeration system to maintain the optimum transit environment of the produce. This paper presents an overview of refrigerated semi-trailers used in the transport of perishable horticultural products. The sources of heat loads inside a refrigerated semi-trailer are identified. A sample calculation of the heat load inside a refrigerated semi-trailer is presented using heat transfer equations. Recommendations on how to minimise the cooling requirements for the refrigeration system will also be made.

1. REFRIGERATED SEMI-TRAILERS

In North America, road transport is the most common method of moving large volumes of fresh produce. In regions where the road network is well developed, road transport is normally used for intra-continental shipments. The reliability of transport equipment, the moderate cost involved and the flexibility to deliver produce to almost any location make road transport the favored method of shipment. Road transport can be combined with rail transport to deliver produce over long distances on land. Refrigerated semi-trailers and intermodal containers are commonly used in road transport.

Refrigerated semi-trailers, often referred to as trailers, can be considered as intermodal transport vehicles. They consist of an insulated rectangular box with wheels in the rear and retractable supports at the front. Uncoupled from the tractors which pull them on the road, trailers can be transported on railroad flatcars (piggyback or trailer-on-flatcar, TOFC) or on sea vessels (roll-on-roll-off or RORO). Refrigerated trailers are available in lengths of 12 m (40 ft), 13.7 m (45 ft), 14.6 m (48 ft) or 16.2 m (53ft) [1].

Fresh fruits and vegetables are perishable and have to be kept at low temperature and high humidity to prolong their shelf life. Modern trailers are usually equipped with mechanical refrigeration having an air circulation system. They may also use liquid ice, liquid N₂, and liquid CO₂ as alternative source of cooling.

Mechanical Refrigeration

Refrigeration systems on trailers are typically driven by diesel engines, with some models having an optional electric motor [3]. Thermostats attached to the refrigeration unit control the cooling rate supplied. Modern refrigerated trailers and containers are equipped with microprocessors to regulate the temperature. These systems are capable of controlling temperature to within $\pm 1^\circ\text{C}$ of the setpoint. To prevent freezing and chilling injury during transport, ASHRAE [3] suggests that thermostats should be set 1 to 2°C higher than the freezing point for cool season vegetables. Recommended thermostat settings for most perishables are listed in ASHRAE [3].

All the components of a mechanical refrigeration system are built into a self-contained unit attached to the front end of the vehicle. The engine, condenser, and other accessories are located on the outside of the front wall, while the evaporator and fans are located inside the trailer walls (Fig. 1).

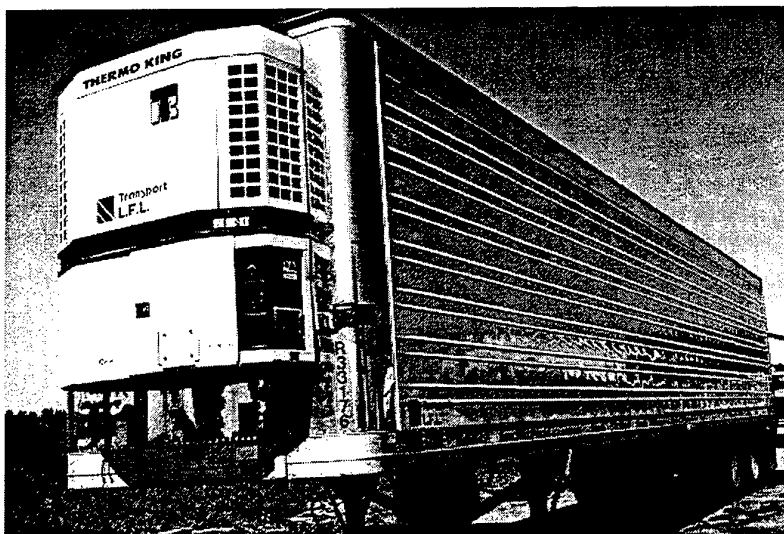


Fig. 1. A refrigerated semi-trailer

Air Circulation System

Air circulation plays an important role in maintaining ideal transport temperature within the trailer. The refrigeration system is useless if cool air is not circulated properly. A poorly designed air circulation system will result in over-warming or over-cooling in different parts of the load. In winter, the air circulation system should circulate warm air around the produce to prevent chilling or freezing injuries. The top-air delivery system usually found in semi-trailers is used to achieve an even distribution of air.

A typical top-air delivery system is composed of an air duct along the ceiling, horizontal floor ducts and a return-air bulkhead (Fig. 2).

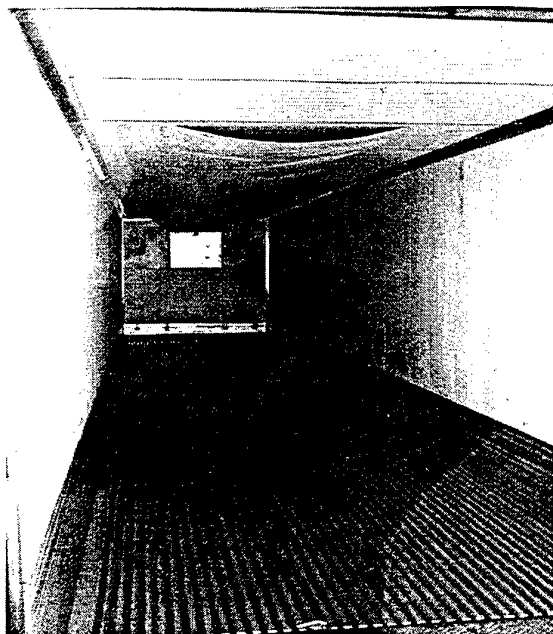


Figure 2. Air circulation system

In this system, the refrigeration unit blows cold air along the ceiling through a duct made of vinyl, canvas or polyethylene. Cold air circulates above the cargo from the front to the rear. Air also flows downward along the sidewalls. Near the rear door, cold air flows downward and return to the refrigeration unit through channels located underneath the cargo. As air reaches the front, it flows upward through the bulkhead into the refrigeration unit.

The use of a bulkhead is recommended to isolate the load from the front wall and prevent it from blocking the return air channel to the refrigeration unit. A frame bulkhead or a solid bulkhead is used. Frame bulkheads prevent the blockage of the return air channel but does not prevent the short-circuiting from the refrigeration unit to the return channel. Solid bulkheads ensure that the air circulates around the cargo rather than short-circuit through the air channel.

2. CALCULATION OF COOLING CAPACITY

In transporting fruits and vegetables, the refrigeration system of the semi-trailer must be capable of removing all external, internal and residual heat loads. The external heat load includes conduction, convection, radiation, and air infiltration through the walls of the semi-trailer. The internal heat load includes field heat that remains within the produce as well as respiratory heat generated by the produce while in transport. The residual heat load includes any heat initially contained within the semi-trailer or any heat load not included as internal or external loads, such as the initial cooling requirement to precool the semi-trailer body, heat in air inside the trailer, and heat from packaging materials.

Conduction and Convection

The heat transfer due to conduction and convection can be calculated by:

$$q_c = \sum UA (T_1 - T_2) \quad (1)$$

where: q_c is the total amount of heat transferred through conduction and convection for the entire semi-trailer, expressed in W. It is equal to the sum of the heat transferred through the different sections of the trailer. U is the overall heat-transfer coefficient expressed in $W/m^2 \cdot K$ for all materials composing one section of the semi-trailer, A is surface area for heat flow of that section expressed in m^2 . $(T_1 - T_2)$ is the temperature gradient across the thickness of that section (walls, rear doors, ceiling or floor), expressed in K.

The overall heat-transfer coefficient of each section is a function of the thermal resistances across the different materials that compose the walls, rear doors, ceiling or floor. In evaluating the performance of insulation materials, it is a common practice in the industry to use the term R-value, which is defined as:

$$R = \frac{\Delta x}{k} \quad (2)$$

where: Δx is the thickness of a material in m, k is the thermal conductivity of that material in $W/m \cdot K$, and R is in $m^2 \cdot K/W$. The overall heat-transfer coefficient is equal to the inverse of the sum of R-values of all materials which make up one section of the semi-trailer.

$$U = \frac{1}{\sum R} \quad (3)$$

Insulating materials used in semi-trailers are of moderate cost, easy to apply, lightweight, have low thermal conductivity, and low moisture permeability and water retention [3]. In addition, the insulation is resistant to fire and extreme temperatures, to cracking, crumbling, shifting, vibration, or any other types of mechanical abrasion [3]. Insulation used for the floor has enough strength to support a forklift or other loading equipment. Any moisture penetration or physical damage decreases the insulation value and since this normally occurs when transport vehicles increase in age, the amount of conduction heat load is generally higher for older vehicles.

Materials for the walls, ceiling and doors. The exterior surfaces of semi-trailers are usually made of aluminum alloy coated with enamel paint. Aluminum lacquer may also be used for coating. Aluminum alloy is highly

conductive. It has a thermal conductivity of 221 W/m·K [2]. The body of semi-trailers normally have 25 to 65 mm thick polyurethane foam insulation [3]. Since the material is foamed-in-place, the contact resistances to the exterior or the interior panel can be considered negligible. Polyurethane foam has a thermal conductivity of 0.022 W/m·K [3]. The interior panels of a semi-trailer are usually made of rigid glass-fiber board. The glass-fiber board has a thermal conductivity of 0.036 W/m·K.

Materials for the floor. The exterior surface of the floor is usually made of galvanized iron or painted mild steel plate. Mild steel plates have a thermal conductivity of 45.3 W/m·K [2]. Polyurethane foam is also used as insulation [3]. The interior surface of the floor is made of molded aluminum alloy. The entire floor is supported on hollow metal beams to increase structural strength.

Outside and inside air films. When refrigerated semi-trailers move on highways, a thin air film layer surrounds the exterior of the vehicle. For vertical and horizontal surfaces, an R-value of 0.044 m²·K/W is associated with the air film when air is moving at 3.4 m/s (12 km/h) [2]. The R-value drops to 0.030 m²·K/W when air moves at 6.7 m/s (24 km/h) [2]. Semi-trailers usually move at speeds of around 25 m/s (90 km/h) or faster on highways. As the R-value decreases with the speed of travel, the R-value of the outside air film is assumed negligible compared to the R-value of the insulating materials. During transport, cool air is also circulated inside the semi-trailer. An air film is created surrounding the interior surfaces of the vehicle. The R-value of this layer can be estimated only if the air speed inside the trailer is known. This air speed is a function of the air flow rate and the cross sectional areas of the space not occupied by produce pallets. The air flow rate and the empty space available for air circulation varies from one situation to another. The air flow rate can be estimated by:

$$Q = V_e A_e \quad (4)$$

where: Q is the airflow rate in m³/s, V_e is the speed of air at the entrance to the evaporator or the exit of the air duct in m/s, and A_e is the corresponding cross-sectional area of the opening in m². Once the air flow rate is known, the air velocity for the inside air film can be estimated by:

$$V_s = \frac{Q}{A_s} \quad (5)$$

where: V_s is the speed of air for the inside air film in m/s, Q is the air flow rate obtained from Eq. 4 in m³/s, A_s is the estimated cross sectional area of the spaces not occupied by produce pallets in m².

Once the air speed of the inside air film is known the R-value of the film can be obtained from tables found in ASHRAE [2].

Infiltration

Infiltration is another source of heat gained from the exterior. Warm air enters the semi-trailer through small holes, cracks, drainage holes and broken door seals. The door openings also significantly increase the refrigeration requirements. The amount of heat loss through infiltration tends to increase with the age of the vehicle. ASHRAE [3] reports that a typical trailer calls for less than 0.001 m³/s (1 L/s) leakage when the trailer has an internal negative pressure of 125 Pa. The sensible heat gain due to air infiltration can be calculated by:

$$q_i = Q \Delta C_{pa} (T_1 - T_2) \quad (6)$$

where: q_i is the heat transfer through infiltration, expressed in W. Q is the infiltration rate in m³/s, Δ is the air density in kg/m³, C_{pa} is the specific heat of air in J/kg·K, and $(T_1 - T_2)$ is the temperature difference between the outside and the inside of the trailer in K.

Solar Radiation

Solar radiation can significantly increase the refrigeration load in a semi-trailer. In 1967, it was found that the

cooling requirement of stationary vehicles increased by 20% when exposed to sunlight for several hours [3]. Using aluminum plates and reflective paints on the exterior of the semi-trailers reduces heat gain through radiation. Frequent cleaning is required to maintain the reflective properties of these surfaces. The amount of heat gained through radiation vary with the type of material, surface condition, surface geometry, solar radiation intensity, wind velocity, cloud cover and air temperature [4]. Radiation is also time and location specific. Therefore, it is difficult to provide any representative value for all cases. Esmay and Dixon [4] and ASHRAE [2] both provide information regarding the radiation heat load.

Field Heat and Respiratory Heat

Precooling is the rapid removal of field heat after harvest. Room cooling, forced-air cooling, hydrocooling, vacuum cooling, and package icing are commonly used to precool horticultural produce [5]. Before shipment, produce should be precooled as near as possible to the recommended storage temperature. Improperly precooled produce requires a higher cooling capacity for the refrigeration system installed in the semi-trailer. Most cooling systems are designed only to maintain the temperature of precooled produce and thus do not have the extra refrigeration capacity to achieve precooling.

The additional amount of heat to be removed from improperly precooled produce is considered as field heat. In addition, loading areas are often at ambient temperature so produce transferred from cold storage to a transport vehicle may gain heat from the surroundings. This heat is also considered as field heat. In some cases, the amount of heat gain is significant, especially when produce is left for long periods of time in the loading area due to delays in the loading process. The amount of field heat can be calculated by:

$$Q_f = m C_p \Delta T \quad (7)$$

where: Q_f is the amount of field heat needed to be removed in kJ, m is the mass of produce inside the trailer in kg, C_p is the specific heat of the produce in kJ/kg.K, and ΔT is the difference between the initial and desired transport temperature for produce in K.

The specific heat of produce above freezing temperatures can be estimated by Siebel's formula:

$$C_p = 0.0335 a + 0.837 \quad (8)$$

where: a is the percent water content of the produce. ASHRAE [3] also provide the a and C_p values for many fruits and vegetables.

Fruits and vegetables respire and continue to respire even after harvest. During respiration, CO_2 , moisture and heat are released. Produce such as asparagus, corn, and strawberries have a higher respiration rate compared to apples, oranges, and potatoes. Highly perishable produce tends to generate more respiratory heat. Furthermore, respiration rate increases with an increase in produce pulp temperature, therefore more heat is released as temperature increases. The amount of respiratory heat load is calculated by:

$$q_r = \frac{H m}{1000} \quad (9)$$

where: q_r is the respiratory heat load in W, H is the heat of respiration in mW/kg and m is the mass of produce in kg.

3. SAMPLE OF CALCULATION

Iceberg lettuce is highly perishable. Its optimum storage and transport conditions are 0°C and 95 to 100% relative humidity [3]. Its freezing point is -0.2°C [3]. Since lettuce is highly susceptible to freezing injury [5] and its optimum storage temperature is close to its freezing point, it is normally vacuum cooled to 1 to 2°C and transported at the same range of temperatures. For a load of 26 pallets of iceberg lettuce transported in a refrigerated semi-trailer, the cargo may have following characteristics:

- 1) Trailer internal dimensions: 2.59 m (102 in) high, 2.44 m (96 in) wide and 16.15 m (53 ft) long.
- 2) Produce boxes dimensions: 0.37 m (14.5 in) high, 0.39 m (15.5 in) wide and 0.60 m (23.5 in) long.

- 3) Produce boxes arrangement: 5 boxes per layer, 6 layers high on each pallet.
- 4) Produce net weight: 22 kg.
- 5) Pallet height: 0.127 m (5 in).
- 6) The inside trailer temperature is 1°C.
- 7) The outside temperature is 30°C.
- 8) The trailer is new, with minimum air infiltration and no damage, all insulation materials are in good condition.
- 9) Trailer is moving at 100 km/h.
- 10) Trailer has a flat floor.
- 11) Cool air is circulated inside the trailer.

Conduction and Convection

The R-value of the inside air film can be estimated as shown in Table 1. Notice that only the space above the pallets is considered available for air circulation.

Table 1. Estimation of the R-value for the Inside Air Film

Average air speed measured at the entrance to the evaporator, V_e	4.20 m/s
Cross-sectional opening at the entrance to the evaporator, A_e	0.10 m ²
Air flow rate inside the trailer, Q (Eq. 4)	0.42 m ³ /s
Internal height of the trailer, h_t	2.59 m
Height of a produce pallet, h_p = produce boxes height + pallet height = (0.37*6 + 0.127)	2.35 m
Empty space above pallet, $H_s = h_t - h_p$	0.24 m
Cross-sectional area of the empty space, $A_s = H_s$ * internal width of trailer	0.59 m ²
Air speed for the inside air film, V_s (Eq. 5)	0.71 m/s
Extrapolated R-value from data given in ASHRAE [2]	0.055 m²·K/W

The material for the walls, ceiling and doors differ from the material for the floor. Therefore, the overall heat transfer coefficient should be evaluated separately as shown in Table 2.

Table 2. Calculations of the Overall Heat-Transfer Coefficients

	Materials	Material thickness Δx (m)	Thermal conductivity k (W/m·K)	R-value (m ² ·K/W)	Equation
walls, ceiling and doors	Outside air film	-	-	negligible	-
	Aluminum alloy	0.002	211	0.0000095	#2
	Polyurethane foam	0.0635	0.022	2.89	#2
	Glass fiberboard	0.003175	0.036	0.088	#2
	Inside air film	-	-	0.055	Table 1
	Contact resistances	-	-	negligible	-
Overall heat-transfer coefficient, $U_{\text{walls, ceiling, door}} = 0.33 \text{ W/m}^2\cdot\text{K}$					#3
floor	Outside air film	-	-	negligible	-
	Mild steel	0.003	45.3	0.000066	#2
	Polyurethane foam	0.0635	0.022	2.89	#2
	Aluminum alloy	0.003	211	0.000014	#2
	Inside air film	-	-	0.055	Table 1
	Contact resistances	-	-	negligible	-
Overall heat-transfer coefficient, $U_{\text{floor}} = 0.34 \text{ W/m}^2\cdot\text{K}$					#3

For an outside temperature $T_1 = 30\text{ }^{\circ}\text{C}$, inside temperature $T_2 = 1\text{ }^{\circ}\text{C}$, $A_{\text{walls, ceiling, door}} = 135.70\text{ m}^2$ and $A_{\text{floor}} = 39.40\text{ m}^2$, the heat transfer through conduction and convection is:

$$\begin{aligned} q_c &= (U_{\text{walls, ceiling, doors}} A_{\text{walls, ceiling, door}} + U_{\text{floor}} A_{\text{floor}}) \cdot (T_1 - T_2) \\ &= (0.33 \cdot 135.70 + 0.34 \cdot 39.40) \cdot (30 - 1) / 1000 \\ &= \underline{1.69\text{ kW}} \end{aligned}$$

Infiltration

For an outside temperature $T_1 = 30\text{ }^{\circ}\text{C}$, inside temperature $T_2 = 1\text{ }^{\circ}\text{C}$, $Q = 0.001\text{ m}^3/\text{s}$, $\Delta = 1.2\text{ kg/m}^3$ and $C_{pa} = 1000\text{ J/kg}\cdot\text{K}$, the heat load for infiltration is:

$$\begin{aligned} q_I &= Q \Delta C_{pa} (T_1 - T_2) \\ &= (0.001 \cdot 1.2 \cdot 1000) \cdot (30 - 1) / 1000 \\ &= \underline{0.0348\text{ kW}} \end{aligned}$$

Field Heat and Respiratory Heat

To verify the importance of precooling the produce and to estimate the amount of extra heat to be removed when produce is not pre-cooled, let's assume two situations. For transporting the same amount of lettuce, lettuce was not pre-cooled and it has an average pulp temperature of 25°C in case 1. In case 2, the lettuce was pre-cooled and its initial pulp temperature was already 1°C . The load will be delivered 72 h later at an average pulp temperature of 1°C in both cases.

The specific heat of iceberg lettuce above freezing is $4.02\text{ kJ/kg}\cdot\text{K}$ [3]. The heat of respiration for lettuce at 1°C is around 32.7 mW/kg [3]. In case 1, the average temperature of lettuce during transport is assumed to be 12°C . The heat of respiration of lettuce at 12°C is around 81.38 mW/kg [3]. The amount of heat load associated with field heat and respiration heat for both cases is summarized in Table 3.

Table 3. Calculations of Field and Respiratory Heat

	Case 1 (non-precooled produce)	Case 2 (precooled produce)	Equation
Mass of produce , $m = 22\text{ kg/box} \cdot 30\text{ box/pallet} \cdot 26\text{ pallets}$	17160 kg	17160 kg	-
Specific heat, C_p	$4.02\text{ kJ/kg}\cdot\text{K}$	$4.02\text{ kJ/kg}\cdot\text{K}$	-
Temperature difference, ΔT	$24\text{ }^{\circ}\text{C}$	$0\text{ }^{\circ}\text{C}$	-
Field heat, Q_f	1655596.8 kJ	0 kJ	#7
Rate of field heat, $q_f = Q_f / (72 \cdot 3600\text{ s})$	6.39 kW	0 kW	-
Heat of respiration, H	81.38 mW/kg	32.7 mW/kg	-
Respiration heat load, q_r	1.40 kW	0.56 kW	#9

The Total Cooling Capacity

The total cooling capacity of the refrigeration system is equal to the sum of the internal, external and residual heat loads. It is summarized in Table 4:

Table 4. Total Amount of Heat Loads

Sources of heat gain	Case 1 (non-precooled produce)	Case 2 (precooled produce)
Conduction and convection (kW)	1.69	1.69
Infiltration (kW)	0.0348	0.0348
Field heat (kW)	6.39	0
Respiration (kW)	1.40	0.56
Total (kW)	9.51	2.28

The cooling capacity would be greater than the one calculated in Table 4 since the calculation did not consider the solar radiation load, the initial cooling requirements to precool the semi-trailer body, the air inside the trailer and

the cargo packaging materials, and the safety factor. As climatic conditions vary from region to region, the specifications required by the users also vary. In the design of mechanical refrigeration systems for semi-trailers, manufacturers normally use computer programs or charts to match the refrigeration unit with the vehicle used for a specific operation.

A few conclusions can still be drawn from the values listed in Table 4. It is clear that if produce is loaded at a temperature higher than its transport temperature, field heat would significantly increase the cooling capacity of the refrigeration system. The amount of respiration would also increase for produce which were not precooled. The amount of heat gain due to air infiltration for new trailers are relatively small. However, if a few cracks or holes were present on the trailer body, the amount of heat gain through infiltration would increase significantly. Age and damage would lower the insulation value of the material therefore the conductive and convective heat gain would increase with usage.

4. RECOMMENDATIONS

To lower the cooling demand from the refrigeration system, the produce should be precooled to its optimum temperature for transport. The trailer and all packaging materials should also be precooled to reduce the residual heat load. The body of the semi-trailer should be well maintained to preserve the thermal properties of the insulation materials. Doors, cracks or holes should be sealed to reduce heat loss through air infiltration. The floor and drains of the semi-trailer should be free of debris to maintain adequate area for air circulation and drainage. The bulkhead and the air delivery duct should be kept in good condition. The exterior of the semi-trailer should be cleaned frequently to preserve the reflective characteristic of its surface, to minimize the amount of radiation heat gain. Travelling at nighttime would also reduce the amount of radiation, conduction and convection heat gain.

ACKNOWLEDGEMENT

The authors wish to acknowledge the financial support provided by Fonds pour la Formation de Chercheurs et l'Aide à la Recherche (Fonds FCAR), Ministère de l'Éducation du Québec (MEQ), and Agriculture and Agri-Food Canada which made this study possible.

REFERENCES

1. B. M. McGregor, *Tropical products transport handbook - Agriculture Handbook No. 668*, Office of Transportation, U.S. Department of Agriculture (1989).
2. ASHRAE, *ASHRAE Fundamentals Handbook (SI)*, American Society of Heating, Refrigerating and Air-Conditioning Engineers Inc. (1997).
3. ASHRAE, *ASHRAE Refrigeration Handbook (SI)*, American Society of Heating, Refrigerating and Air-Conditioning Engineers Inc. (1998).
4. M. L. Esmay and J. E. Dixon, *Environmental control of Agricultural Buildings*, The AVI Publishing Company Inc. (1986).
5. E.H. Hardenburg, A.E. Watada and C.Y. Wang, *The Commercial Storage of Fruits, Vegetables, and Florist and Nursery Stocks - Agriculture Handbook 66*, Agricultural Research Service, U.S. Department of Agriculture (1986).

UNDERGROUND RAILWAY AIR QUALITY AND ITS IMPACT ON ENERGY CONSUMPTION

Leo Lee

Director

Hyder Consulting Limited

3/F, Somerset House, Taikoo Place

979 King's Road, Quarry Bay, Hong Kong, China

Email: llee@hyder.com.hk

J. Greg Sanchez

Ventilation Consultant

9 Thoreau Dr. Plainsboro, NJ 08536, USA

Email: gresanchez@aol.com

Keywords: tunnel ventilation, tunnel air quality, mass transit energy consumption

ABSTRACT. Mass Transit Railway is the backbone of transportation systems for large cities. Many Mass Transit Railways are built underground. The air conditioner (A/C) units onboard the trains intake fresh air from the tunnel for in-cabin ventilation. The in-cabin returned air is discharged back into the tunnel environment. The quantity of "fresh" air intake from the tunnel is controlled in order to reduce the air conditioning load in the train. However, the tunnel air quality will depend on the rate of the train A/C returned air into the tunnel, and the fresh air brought into the tunnel through ventilation shafts, stations, or portals. The air quality in the tunnel will have a direct impact on the in-cabin environment. This may lead to inadequate ventilation in the train and cause discomfort to the weak and elderly people. Because the air intake rate of the train borne A/C units is taken from the tunnel air, the tunnel air quality is of great importance. The air quality also has energy implications. The lower the carbon dioxide (CO₂) ppm requirement, the higher the fresh air rate required. This will increase the train borne A/C unit cooling capacity.

Passenger ridership, train throughput, and the effectiveness of the train-piston action have an impact on the air quality in the tunnel as well. If the tunnel air quality is not enough by means of piston action, fan plants will need to be operated in order to provide the required tunnel air quality for the trains traveling through the tunnel. This brings energy consumption issues in the design of a mass transit system and could represent a big operating factor.

This paper identifies problems, recommends a guideline criterion and proposes a solution to deal with them two environmental control systems for the Hong Kong underground railways. A tunnel ventilation numerical analysis was performed to qualify the recommendations.

1. INTRODUCTION

Many metro trains run in tunnels which are ventilated by mechanical ventilation. Most metro trains are provided with two train borne A/C units per car to provide the comfort of air conditioning to passengers (see Fig. 1). To save energy, only a small percentage of supply air from the train borne A/C unit is outside air (enough to maintain acceptable CO₂ levels in the train cabin), and the majority of the supply air is recirculated in-cabin air. From an air quality point of view, the higher the percentage of outside air, the better the air quality. From an energy consumption point of view, the lower the percentage of outside air, the lower the energy consumption of the A/C units due the enthalpy difference between train cabin air and outside air. These are the contradicting design criteria and it does not help by the fact that passengers on board metro trains varies according to the traffic pattern of the metro system.

Also, the majority of metro systems in tropical region are ventilated by a "closed" ventilation system. A "closed" system refers to a ventilation system which is operated with the ventilation shafts closed in order to save energy. A large percentage of tunnel air in the 'closed' system is recirculated air and therefore is not fresh outside air. If the train borne A/C units were designed to take minimum outside air to satisfy air quality

requirements inside the train cabin, assuming that tunnel air is fresh from outside, then riders would have a problem because the majority of the tunnel air is recirculated air. This air has a poorer quality than the outside air. The end result is that the air quality inside the train cabin is not up to acceptable standard.

The above provide some background information of the paper. The objectives of this paper are as follows:

- Establish the air quality requirements inside a metro system.
- Recommend fresh air rates for train borne A/C units to meet air quality requirements for different type of ventilation systems..
- Identify energy consumption impact for train borne A/C units as a function of fresh air rates.

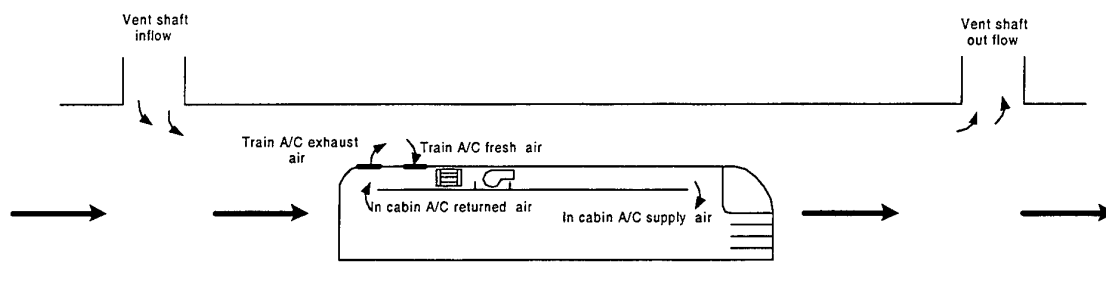


Fig. 1. Tunnel air recirculation schematic

2. RIDERSHIP IMPACT

The underground ventilation requirements to meet air quality criteria are directly proportional to the ridership traveling in a tunnel section. The ridership is a function of the hour of the day. To cope with the ridership demands, mass transit systems dispatch more trains per hour. In Hong Kong, new systems are designed to have a cruise speed of about 80km/h. At this speed, it would take about 45 seconds to travel a kilometre. Typical train dispatch frequency (headway) is on the order 105 seconds to 300 seconds. As the headway becomes smaller, the train piston action increases and more air is pulled down the tunnel. The piston action for train speeds of 60, 80 and 100km/h for various ventilation concepts were studied by Sanchez and Lee [1]. At high train headway (low frequency), and at low train speed, the piston effect is weak and the patrons' exposure time in the tunnel increases. On the other hand, at low train headway (high frequency), and at high train speed, the piston effect is strong and the patron's exposure time in the tunnel is reduced. Furthermore, the longer the travel time and the larger the number of patrons, the greater the concern about tunnel air quality. This paper considered a train-headway of 150 seconds with a traveling speed of 80km/h and 2500 passengers onboard.

The number of patrons has an impact on the air quality because humans inhale air at a rate of approximately 15 breath per minute. Each breath processes about 0.5 L of air. Furthermore, 2500 patrons would exhale 18,750 L of air per minute. Ideally, about 20 percent of the exhaled air is carbon dioxide, which is the amount of oxygen in the atmospheric air. However, it is unlikely that the conversion of oxygen to carbon dioxide be 100 percent. We will assume 4 percent of the exhaled air is converted into carbon dioxide. Therefore, in a 2500-patron train, the patrons would generate about 12.5 L of carbon dioxide per second.

3. CURRENT CO₂ PPM CRITERIA AND STANDARDS

The criterion used to design the ventilation system of a mass transit system plays a key role because it determines the ventilation requirements. There are several recommendations, which are applicable to specific conditions. The ASHRAE- HVAC Applications Handbook [2] recommends 3.57 L/s outside air per person for mass transit systems. ASHRAE Standard 62-1989 [3] recommends 7.14 L/s per person in transportation vehicles; however, it advises that vehicles may require special considerations. For a general office space, ASHRAE Standard 62-1989 recommends outdoor air between 9.52 and 11.76 L/s per person. ASHRAE Standard 62-1989 summarizes the Canadian exposure guidelines for residential indoor air quality. For an acceptable long-term exposure range (ALTER), the Canadian guidelines requires 1.56 L/s per person.

Table 1. Fresh air requirements summary

CO ₂ concentration levels, (ppm)	Fresh air rate (L/s) per person	Fresh air rate (m ³ /s) per train
725	11.76	29.400
825	9.52	23.800
1000	7.14	17.850
1700	3.57	8.925
2200	2.63	6.575
3500	1.56	3.900
5000	1.06	2.650
15000	0.34	0.850

The American Conference of Governmental Industrial Hygienists manual [4] identifies two threshold levels for carbon dioxide: 5000 ppm for Time-Weighted-Average (TWA) for 8-hour day, 40-hour week; 15000 ppm for Short Term Exposure Limits (STEL). STEL is based on a 15-minute TWA and should not be repeated more than 4 times a day and 60 minutes between successive exposure. This corresponds to a fresh air rate of 1.06 L/s per person and 0.34 L/s per person, respectively.

Because elderly people ride the trains, they certainly are to be taken into consideration when establishing an air quality guideline for a mass transit system. Recently, Ninomura and Cohen [5] published a technical article on air quality for the elderly at nursing homes. Although these facilities are designed for a 24-hour operating cycle, it is interesting to note that they design these facilities to meet 7.14 L/s per person, however, this rate may be reduced during periods of less occupancy. Chow [6] has recently studied train vehicle fires for typical Hong Kong's mass transit passenger train vehicles. He considered levels of 2200 ppm of carbon dioxide in his study.

Because the travel time between stations is in the order of 1 to 5 minutes, the authors consider that the Canadian guidelines of 3500 ppm is more than adequate for a mass transit system, such as the Hong Kong MTR. This criterion would be sufficient to meet the TWA threshold level, and since no passengers remain in the system 8 hours, 3500 ppm is conservative.

4. MASS TRANSIT RAILWAY ENVIRONMENT

Many mass transit railway systems in the tropical regions are ventilated by 'closed' system e.g. Hong Kong Mass Transit Railway Kwun Tong Line. During the summer, all tunnel vent shafts will remain closed and the tunnels are ventilated by train-piston effect, which draws cool air from stations to cool the tunnels.

Typically, a station platform design condition is 28°C and the concourse design condition is 30°C with little control on humidity due to the piston effect induced infiltration and exfiltration through station entrances and platforms. The tunnel temperature is designed not to exceed 35°C for normal operation and not to exceed 40°C for congested operation. Owing to the significant difference of outdoor air and station air enthalpy (up to 23 KJ/kg), minimum fresh air, to satisfy air quality standards, is introduced into the station areas to save energy. Also, owing to the inability of the closed system to control exfiltration and infiltration induced by train piston effect, it is not cost effective to lower station temperature to improve passenger comfort.

Recently, due to the pledge to save energy and the general public demand for higher degree of comfort, the previously accepted 'closed' ventilation system is now considered not the most cost effective ventilation system. The latest system adopted is 'open' system with platform screen doors to separate passenger areas and platform trackways, as have been implemented in Hong Kong's Lantau and Airport Line. The platform screen doors enable different temperature zones for trackways and platform areas. Typically, passenger area conditions are 25°C DB; 55% RH, and the trackway temperature is less than or equal to 35°C. For this type of system, trackways are provided with mechanical ventilation and the tunnel vent shafts will remain open for normal operation. Train piston effect will draw air from outside atmosphere and expels tunnel air to outside atmosphere through vent shafts. Typical tunnel temperature $\leq 35^{\circ}\text{C}$ for normal operation & $\leq 40^{\circ}\text{C}$ for congested mode operation. This system will have frequent exchange of tunnel air and outside air. Thanks to the separation

provided by platform screen doors, the station air conditions can be improved without high penalty on energy cost. Overall, it is most cost effective and many new metro systems are adopting this system e.g. Hong Kong Mass Transit Railway Tseung Kwan O Extension and Guangzhou Metro Line 2.

5. IMPACT ON TRAIN BORNE A/C UNITS

A/C units are installed on board metro trains to provide comfort air conditioning for passengers. These A/C units are normally installed at the roof of both ends of each car. These A/C units reject heat to tunnel air through the air cooled condensers. The evaporator fans suck in tunnel air to control CO₂ ppm inside the train cabin to an acceptable level. Tunnel air is required to remove heat rejected by train borne A/C units and also to provide adequate fresh air to control CO₂ ppm inside the train cabin.

Both 'open' and 'closed' systems are able to remove heat rejected by train borne A/C units. However, for 'closed' systems, if a train borne A/C units is designed with the assumption that tunnel air is fresh air, this may lead to unacceptable high CO₂ ppm in the train cabin. This is true because tunnel air quality is the same (except temperatures) as station recirculated air and therefore is not as good as outside air to control CO₂ ppm in train cabin. For 'closed' system more 'fresh' air is required.

For 'open' system, there is frequent exchange of tunnel air and outside air, therefore air quality of tunnel air is almost as good as outside air. Train borne A/C units using tunnel air to control CO₂ ppm inside train saloon is considered appropriate for 'open' system and no extra 'fresh' air is required.

6. VENTILATION CONCEPTS

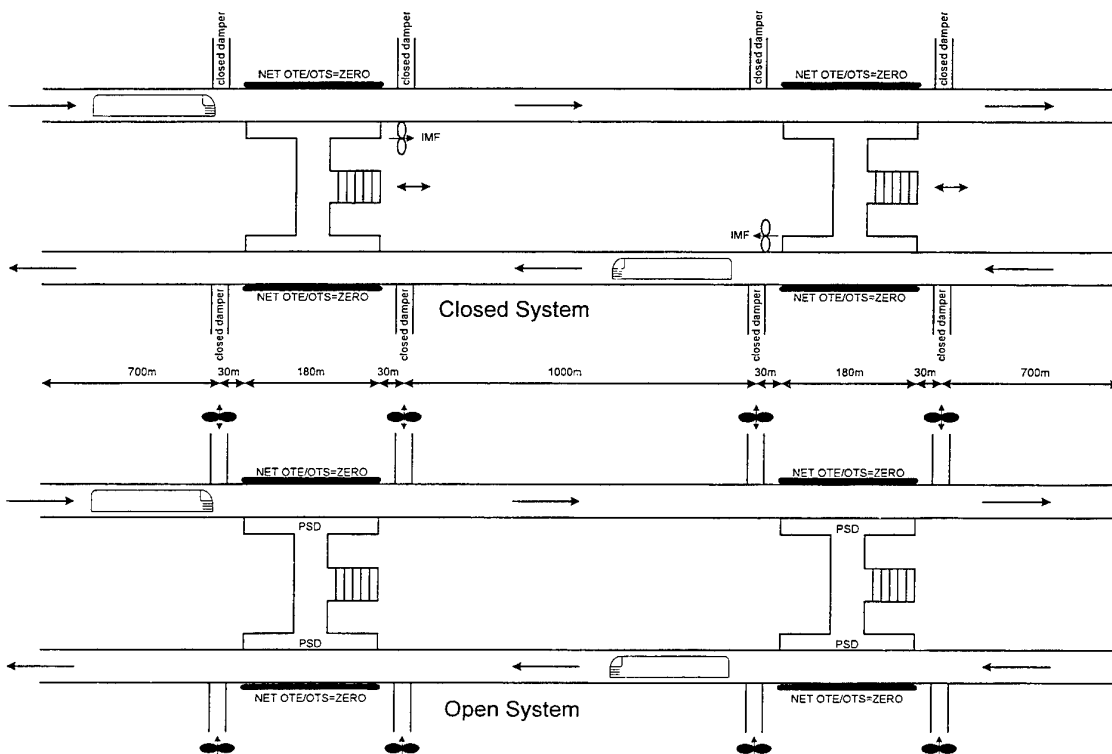


Fig. 2 Layout of "Open" and "Closed" tunnel ventilation systems

Two ventilation concepts were investigated: a closed and an open system. Figure 2 illustrates both concepts. Hong Kong's Mass Transit Rail is designed providing air conditioning at the stations. In a closed system, the tunnel ventilation dampers are closed to preserve the cool temperature and to minimize the mixing with hot

outside air. This is an alternative that restricts the inflow of outside fresh air into the tunnel and depends on the amount of fresh air introduced by the station and dissipated down the tunnel. In the new systems, the stations have been designed with platform screen doors which reduced the leakage of the station air conditioning into the tunnel and the tunnel ventilation dampers are open to allow the train piston action ventilate the tunnels. The advantage of this method is that the trains are now supplied with outside air directly through the tunnel ventilation shaft.

To analyse the impact these two ventilation concepts have on tunnel air quality, the Subway Environment Simulation (SES) computer program [7] was used to model both system for a two-station configuration. Figure 3 shows the average air flows over a full headway in the tunnel and through the station entrance for a closed system. Since the dampers do not shut completely the vent shaft, some small leakage is observed in the tunnel. The air flows shown due to the train-piston action indicate that it is expected to have an average of $32 \text{ m}^3/\text{s}$ inflow from ambient. This represents the load added unto the station air conditioning unit. On the other hand, $22 \text{ m}^3/\text{s}$ out flow to ambient. This represents the cooled station air lost to ambient. The platform indicates that between 2 to $8 \text{ m}^3/\text{s}$ of air are added from the station to the tunnels. This may not be enough fresh air and people may not feel comfortable in the long run.

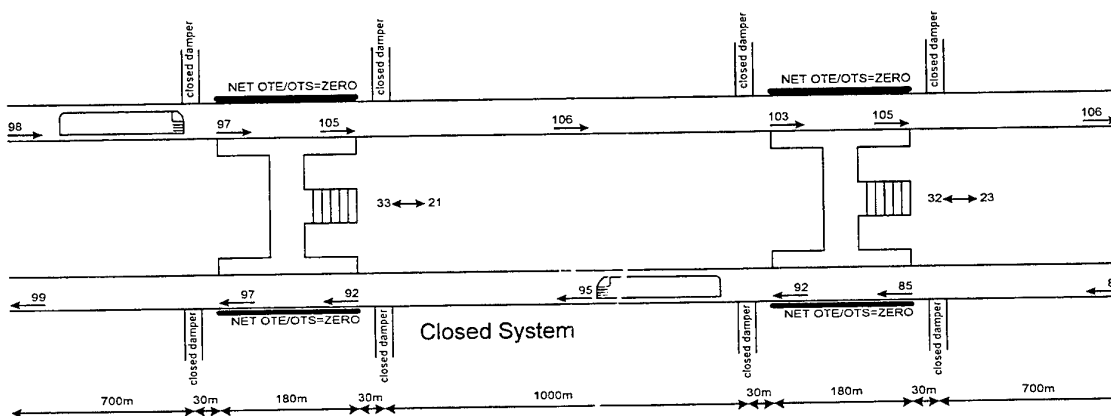


Fig. 3 SES results for a "Closed" system

Figure 4 shows the average air flows for an open system. It can be noticed that there is very little loss through the station entrance and the platform screen doors. However, the average net effect of the air drawn from outside through the open damper is between 8 to $14 \text{ m}^3/\text{s}$. This is certainly a big improvement because more fresh air is directly provided to the tunnel and the station loads are reduced.

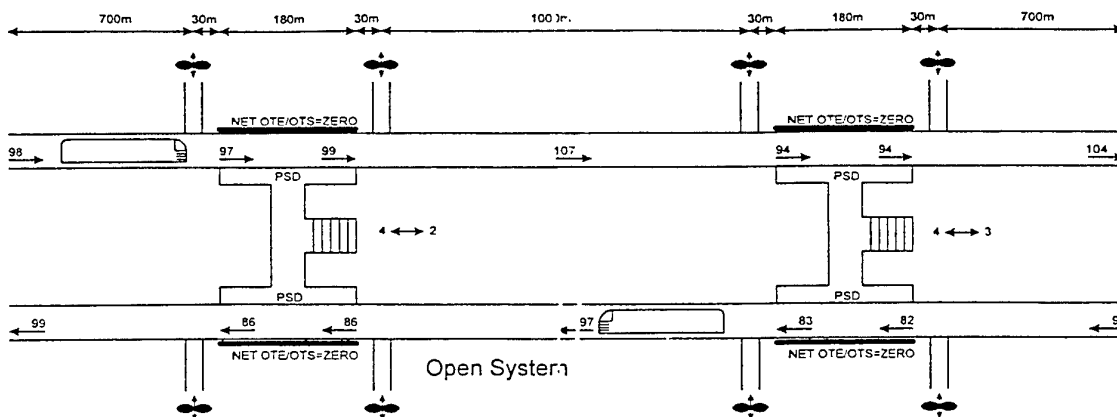


Fig. 4 SES results for an "Open" system

7. ENERGY CONSUMPTION

Closed System

For a closed system, a typical MTRC station is designed with a total station air conditioner supply rate of about $120 \text{ m}^3/\text{s}$, of which $8 \text{ m}^3/\text{s}$ air fresh air. Let's consider the station design first. If we assumed that a station was designed to hold 1250 people, and the ASHRAE Standard 62-1989 [3] general recommendation of 1000 ppm (7.14 L/s of air per person) were applied, the fresh air requirements would be $8.9 \text{ m}^3/\text{s}$ for the station. The $8 \text{ m}^3/\text{s}$ handled by the current station design is enough to meet this criterion. However, based on the SES results, the station inflow through the entrance was $33 \text{ m}^3/\text{s}$. On the average, the station platforms felt between 9 and $13 \text{ m}^3/\text{s}$. Using the highest figure of the two, the station air conditioning system handles $8 \text{ m}^3/\text{s}$ of fresh air plus $13 \text{ m}^3/\text{s}$ coming from the entrances. This certainly increases the load in the system. However, if we were to adopt 3500 ppm (1.56 L/s of air per person), only $1.95 \text{ m}^3/\text{s}$ fresh air would be required. Since $13 \text{ m}^3/\text{s}$ of fresh air being supplied through the station entrance, the $1.95 \text{ m}^3/\text{s}$ could be waived and the station loads would be reduced significantly.

However, for a closed system, the major problem exists in the tunnel and not in the station, since the station air will be distributed throughout the tunnel by the train piston action. Following the same assumptions and SES results as just above, $21 \text{ m}^3/\text{s}$ of fresh air are provided to the station through the supply air and the station entrances. If we assumed that half corresponds to each platform, each platform will have about $10.5 \text{ m}^3/\text{s}$ of fresh air. This would correspond to a CO_2 concentration of 895 ppm. Furthermore, this will represent the initial tunnel CO_2 background concentration. Therefore, with this background, we would need $119 \text{ m}^3/\text{s}$ of additional fresh air to meet 1000 ppm in the train cabin. If we adopted the 3500 ppm recommendation, only and additional $4.8 \text{ m}^3/\text{s}$ of fresh air would be required. This is a more reasonable requirement, which can be achieved through the implementation of impulse fans. Nevertheless, it would add load to the station air conditioning system.

Open System

For an open system, the station design becomes independent to some degree from the tunnel ventilation (some infiltration from the tunnel still couples the station and the tunnel ventilation systems). For the open system, the station design can be isolated from the tunnel. If we were to use the same typical number as for the closed system ($120 \text{ m}^3/\text{s}$ of supply and $8 \text{ m}^3/\text{s}$ of fresh air), the station would then satisfy ASHRAE Standard 62-1989 [3] recommendation of 1000 ppm. The SES results showed that the station infiltration through the entrances is very minimal for an open system. Thus the station air conditioning will need to handle outside air through the cooling coils. If we were to adopt 3500 ppm recommendation, only $1.95 \text{ m}^3/\text{s}$ of fresh air would be required. This would reduce the station energy consumption significantly.

In the tunnel, however, the station trackway is equipped with an overhead exhaust ($60 \text{ m}^3/\text{s}$ typical), which removes hot air from the trackway, and an overhead supply system ($54 \text{ m}^3/\text{s}$ typical), which provides fresh make up air to the tunnel. In addition, the tunnel air flows predicted by the SES simulation for an open system report for one section of the tunnel with a total tunnel air flow of $107 \text{ m}^3/\text{s}$ and $8 \text{ m}^3/\text{s}$ of fresh air through the ventilation shaft due to train piston action. This indicates that of the $107 \text{ m}^3/\text{s}$ tunnel air flow, $62 \text{ m}^3/\text{s}$ is fresh air (58 percent). This is more than enough fresh air to meet any air quality standard. Furthermore, the air quality for an open system is very good.

Train Borne A/C Unit

A typical train car is equipped with an 80 kW cooling capacity. To maintain the temperature conditions in the cabin, the enthalpy difference between the tunnel air and the cabin air is 39 kJ/kg . Chow [6] assumed $0.9 \text{ m}^3/\text{s}$ of fresh air per train car to maintain 2200 ppm CO_2 concentration in the cabin. Chow assumed that the tunnel air quality was very close to ambient conditions (This is only true for an open system). This resulted in 34.7 kW due to the outside air, which represents 43 percent of the air cooling load. This is a very significant figure.

In a closed system, the tunnel initial air quality condition is important. The discussion above has shown that this is not the case for a closed system. As a matter of fact, the tunnel background could be about 895 ppm. Based on this background condition, the train would need $9.57 \text{ m}^3/\text{s}$ of fresh air. This will add about 25 percent to the train cooling capacity. However, if the criterion were changed to 3500 ppm, only $4.8 \text{ m}^3/\text{s}$ would be needed per train and the load due to the fresh air would be reduced by 33 percent.

On the other hand, for an open system, it is safe to assume that outside air is fresh at the ambient background level. For this condition, to maintain 2200 ppm CO₂ concentration in the cabin would require 6.58 m³/s per train. If we were to adopt the 3500 ppm recommendation, only 3.9 m³/s per train would be required. This would represent 45 percent reduction in the cooling load due to outside air.

8. CONCLUSIONS

This paper has addressed the air quality issue for mass transit systems. This topic has never been presented being concerned with the exposure of the passengers and energy consumption. It has been presented that mass transit systems are environments with a very short-term exposure. Various guidelines have been studied and it is recommended that mass transit systems be designed using 3500 ppm of CO₂. Because passengers are not exposed for long periods of time and because the mass transit systems are very dynamic environments, we feel the old design criterion can be refined. This would impact the energy consumption of mass transit systems for both open and closed ventilation systems. It would also reduce the train borne A/C unit cooling load. This paper also points out that the implementation of open systems have great advantages both on the air quality control and the energy consumption of the mass transit system. On the other hand, the closed systems still need some additional ventilation to maintain good air quality of its recirculated tunnel air. This can be accomplished by installing impulse or jet fans.

REFERENCES

1. G. Sanchez and L. Lee, "Alternatives to Control Tunnel Temperatures in Hong Kong", Proceedings of International Conference on Tunnel Control and Instrumentation and Communications Systems for Tunnels, pp.73-83, organised by Independent Technical Conferences Ltd, 8-9 February 1999, Hong Kong, China.
2. 1999 ASHRAE Handbook, HVAC Applications, Chapter 12.
3. ASHRAE. 1989, Ventilation for acceptable indoor air quality. Standard 62-1989.
4. ACGIH. 1992. Industrial ventilation: A manual of recommended practice, 21st ed. American Conference of Governmental Industrial Hygienists, Cincinnati, OH.
5. P. T. Ninomura and M. H. Cohen, "IAQ in Nursing Homes", ASHRAE Journal, pp.34-38, February 1999.
6. W. K. Chow, "Study on Passenger Train Vehicle Fires", Proceeding of Institution of Mechanical Engineers, Vol. 211, Part F, 1997.
7. USDOT, "Subway Environmental Design Handbook, Volume II, Subway Environmental Simulation Computer Program, SES Version 4.0, Part I, User's Manual", FTA-MA-26-7022-97-1, 1997.

EVALUATING WET COMPRESSION IN REFRIGERATION CYCLES WORKING WITH PURE OR NON-AZEOTROPIC REFRIGERANT MIXTURES FOR AIR-CONDITIONERS

Wayne Swanepoel

Research Group for Cooling and Heating Technology,
Department of Mechanical and Manufacturing Engineering
Rand Afrikaans University
Email: waynes@yebo.co.za Fax: +27 16 889 3011

J.P. Meyer

Research Group for Cooling and Heating Technology,
Department of Mechanical and Manufacturing Engineering, Laboratory for Energy,
Rand Afrikaans University, P.O. Box 524, Auckland Park, 2006, South Africa
Email: jpm@ingl.rau.ac.za Fax: +27 11 489 2607

Keywords: wet compression, dry compression, refrigeration cycle, pure refrigerant, non-azeotropic refrigerant

ABSTRACT. Wet compression versus dry compression in refrigeration cycles working with pure refrigerants or non-azeotropic mixtures is investigated in this paper. In total 34 pure refrigerants as well as 31 non-azeotropic binary mixtures are considered. This resulted in approximately 300 different mixtures being analysed. The pure refrigerants and refrigerant mixtures were analysed for one cooling application, namely that of spatial air conditioning at an evaporating temperature of 7°C, and a condensing temperature of 50°C. The investigation was conducted with cycle analyses calculating performances at different wet and dry compressor inlet values. Use was made of thermodynamic refrigerant properties calculated from a computer database. It was concluded that for both pure and non-azeotropic refrigerants analysed, all those with re-entrant saturation vapour lines produce better cooling COP's when the refrigerant is superheated before entering the compressor. Only a few of the refrigerants with bell-shaped T-s curves consistently produce higher cooling COP's when wet compression is used. However, their cooling capacities decreased while the compressor displacement rates increased. It was concluded that in general dry compression is more favourable than wet compression. From the exceptions that do exist, some manage to produce relatively high COP_c's while retaining competitive cooling capacities. A by-product of this study is that, from the vast amount of refrigerant mixtures analysed, valuable knowledge was gathered regarding refrigerants not commonly used in the applications considered.

1. INTRODUCTION

Background

The Montreal Protocol is an international agreement designed to protect the stratospheric ozone layer against substances that deplete the ozone layer. The treaty was originally signed in 1987 and substantially amended a few times. The Montreal Protocol was the dawn of a new age for industries, including the air conditioning and refrigerating industry which were consuming and producing these compounds. Short to medium term alternatives (HCFC's) were almost readily available, but the industry was continuously faced with the challenge of finding suitable replacements for ozone depleting compounds. Although numerous studies have revealed various possibilities, the search for a more efficient, cheaper and safer refrigerant is a never-ending one. The reason for this statement is partly due to the fact that, although refrigerants are used in a pure state, research revealed that mixtures of refrigerants can reveal some interesting results as well. This provides an extra degree of freedom and literally thousands of new refrigerants can be "formed". Since the advent of the Montreal Protocol, much work has been done in an attempt to find replacements for CFC's. These include studies on pure refrigerants, as well as mixtures of refrigerants [2 to 12].

These refrigerants can be divided into two main groups, azeotropes and non-azeotropes. The major difference between the two groups can best be explained by referring to Fig.1. The standard vapour-compression cycles for the two different groups of refrigerants are presented for negligible pressure drop. The main difference, as can be seen in the figure, lies in the region underneath the saturation curve. Evaporation and condensation of a non-azeotropic mixture takes place at non-constant temperature, unlike that of the pure refrigerants at constant pressure. A mixture of two refrigerants leads to a supplementary degree of freedom in refrigeration systems during evaporation and condensation. A pure refrigerant in the two-phase region has only one degree of freedom: the temperature is a function of the pressure only. A non-azeotropic mixture possesses two degrees of freedom: the temperature is a function of both the pressure and of the liquid concentration. For this reason, when using non-azeotropes, the exchanging of heat coincides with a drop in temperature at a constant pressure as shown in Fig.1b. Due to the fact that the different parts of the mixtures exhibit different evaporating and condensing temperatures, this temperature glide is common among mixtures of refrigerants.

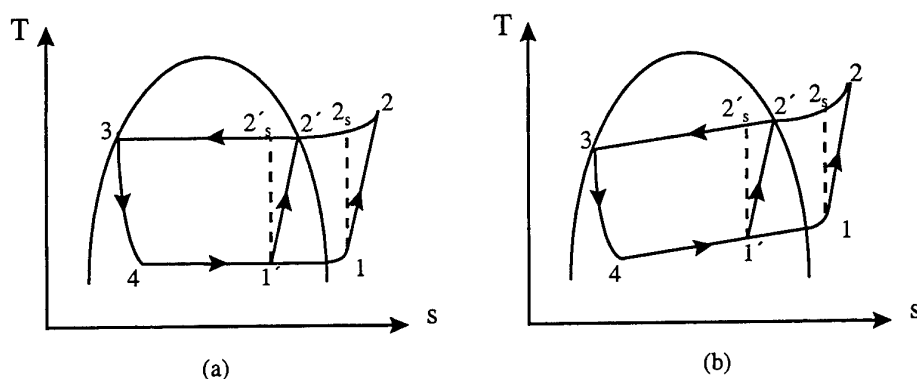


Fig.1. Vapour-compression cycle for wet ($1'$ to $2'$) and dry (1 to 2) compression for a (a) pure refrigerant and a (b) non-azeotropic refrigerant mixture

The compression process¹³, $1'$ to $2'$, in Fig.1. is called wet compression because the entire process occurs in the mixture region with droplets of liquid present. Although wet compression is likely to damage compressors that are currently used in industry, advancements are made rapidly in materials, lubricants and new types of compressors. It would therefore not be farfetched to hope that wet compression might be a practical reality in the near future.

Points 1 to 2 in Fig.1. represent dry compression, which takes place with no droplets of liquid present. The refrigerant that is compressed via a dry compression process, ends up in a superheated phase. A cycle using dry compression is called the Rankine cycle and this has been the norm for vapour-compression cycles up to date. The advantages are obvious if one recognises that wet compression brings the Rankine cycle closer to the ideal Carnot cycle for pure refrigerants and closer to the Lorentz cycle for non-azeotropic refrigerants.

Previous work. Itard [14] investigated wet compression versus dry compression in heat pumps working with pure refrigerants or non-azeotropic mixtures. From his study he found that the principle of wet compression seems attractive to pure refrigerants, but particularly attractive to non-azeotropic refrigerants. Only three pure refrigerants were considered, namely: R12, R123 and NH_3 . Non-azeotropic refrigerants were limited to $\text{NH}_3/\text{H}_2\text{O}$ on a mass ratio of 80%/20%.

Purpose of this study. It is the purpose of this paper to consider more refrigerants- 34 pure refrigerants as well as 31 non-azeotropic binary mixtures at different concentrations. One cooling application is considered in this paper,

namely that of spatial air conditioning at an evaporating temperature of 7°C, and a condensing temperature of 50°C. These temperatures represent typical evaporation and condensing temperatures used in practice. The non-azeotropic mixtures were analysed using a dew point temperature of 50°C and the bubble temperature was kept constant at 7°C.

2. CYCLE ANALYSIS

Seeing that this study focuses on wet compression, it inevitably implies that many calculations will be done based on data from within the two- phase region. It is as a result of this that the evaluation takes place over a wide spectrum of compressor inlet vapour qualities. This quality ranges from 0.3 to 1.0 in increments of 0.1, and for superheat values of 10°C and 20°C.

For this type of study, accurate thermodynamic refrigerant properties are essential for pure refrigerants as well as for mixtures. To calculate these properties is very time-consuming. Therefore, use was made of the NIST [15] REFPROP database. Although some of the refrigerants have already been phased out by the Montreal Protocol, they were included in this study so that the results could be compared to the refrigerants which over the years developed as the "favourites" and benchmarks for certain applications.

The specific work done by the compressor, specific cooling capacity, COP_c , refrigerant circulated for one kilowatt of cooling and compressor displacement per kilowatt of cooling, were calculated for each of the refrigerants for the different compressor inlet qualities discussed previously. A compressor isentropic efficiency of 75% was used and the condenser sub-cooling was assumed to be zero. Isenthalpic expansion was also used for all refrigerants and zero pressure drop was assumed through the condenser and evaporator.

The performance of the different refrigerants for air conditioning applications were calculated as follows (referring to Fig.1):

The specific work done by the compressor for dry or superheated compression is calculated as

$$w = h_2 - h_1 \quad (1)$$

The specific work done by the compressor for wet compression is calculated as

$$w = h_{2'} - h_1 \quad (2)$$

The value of $h_{1'}$ is calculated on the evaporating pressure line as

$$h_{1'}(x) = h_f + x(h_g - h_f) \quad (3)$$

The specific cooling capacity for dry compression is calculated as

$$q = h_1 - h_4 \quad (4)$$

while the specific cooling capacity for wet compression is calculated as

$$q = h_{1'} - h_4 \quad (5)$$

The cooling coefficient of performance for dry compression is

$$COP = (h_1 - h_4)/(h_2 - h_1) \quad (6)$$

The cooling coefficient of performance for wet compression is calculated as

$$\text{COP} = (h_1 - h_4)/(h_2 - h_1) \quad (7)$$

The required refrigerant mass flow for 1 kW of cooling for dry compression is calculated as

$$m_r = 1/(h_1 - h_4) \quad (8)$$

The required refrigerant mass flow for 1 kW of cooling for wet compression is calculated as

$$m_r = 1/(h_1 - h_4) \quad (9)$$

The required compressor displacement rate per kilowatt of cooling for dry compression is calculated as

$$V = (1/(h_1 - h_4))\rho * 1000 \quad (10)$$

The required compressor displacement rate per kilowatt of cooling for wet compression is calculated as

$$V = (1/(h_1 - h_4))\rho * 1000 \quad (11)$$

The compressor discharge temperature was also obtained from the condensing pressure and enthalpy at point 2.

3. RESULTS

General Findings

All the refrigerants, pure and non-azeotropic, could be divided into two groups according to their T-s graphs (temperature-entropy graphs). Two shapes were identified: those with bell-shaped curves as in Fig.2. and those with re-entrant saturated vapour lines as in Fig.3.

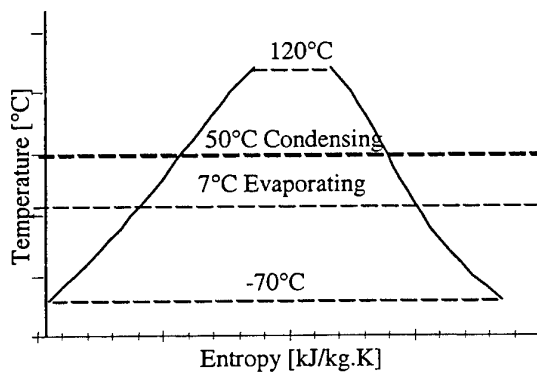


Fig.2. The T-s graph of NH₃ as an example of a bell- shaped curve

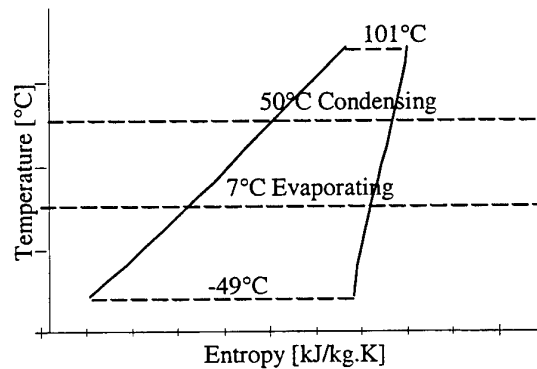


Fig.3. The T-s graph of RC318 as an example of a curve with a re- entrant saturated vapour line

From the pure refrigerants with bell-shaped T-s graphs, only R32 and NH_3 produce higher COP_c 's when wet compression is used. Wet compression, however, reduces the cooling capacity and increases the compressor displacement.

The majority of non-azeotropic mixtures belong to the family with bell-shaped curves. As was found with pure refrigerants, none of the mixtures with re-entrant saturation vapour line on the T-s curve produce better results with the use of wet compression. The only mixtures that respond favourably to wet compression, come out of the bell-shaped T-s curve family. Again, wet compression reduces the cooling capacity and increases the compressor displacement.

Non-azeotropic refrigerant mixtures tend to gain more from wet compression than pure refrigerants.

Pure Refrigerants

The highest COP_c value, that of ammonia, is obtained through the process of wet compression. A COP_c value of 4.28 at a vapour quality of 0.9 is 7.2% higher than the COP_c value of 3.99 at 10°C . Ammonia's specific cooling capacity decreased with 14.3% against the 16.8% decrease considering R32. Wet compression of ammonia doesn't affect the required compressor displacement rate to acquire 1kW of cooling.

It should be noted that although the COP_c values increase substantially, the specific cooling capacity decreases. In the case of R32 the required compressor displacement rate to acquire 1kW of cooling increases with 3.1%. This means that for wet compression more of the refrigerant is needed to have the same cooling effect obtained from dry compression, which may require larger and more expensive compressors.

Binary Non-Azeotropic Refrigerant Mixtures

The analysis of a non-azeotropic yields different results to that of a pure refrigerant. This is due to the fact that a mixture of two refrigerants can produce many different refrigerants by just changing the mass ratio. In this study, the mass ratio was changed over the entire spectrum of the different components of a mixture, but at intervals of 10% at a time. A total of 31 binary refrigerant mixtures were analysed in this way, resulting in 279 different mixtures being analysed.

As with pure refrigerants, the specific cooling capacity decreases and the compressor displacement increases with the use of wet compression as can be expected. It was found, however, that for some refrigerant mixtures, for example R32/R143 (0.3/0.7), the compressor displacement reaches a relative low value at approximately the same vapour quality where the maximum COP_c is reached. It is interesting to note that this phenomenon occurs especially in refrigerant mixtures that produce higher COP values with wet compression. The opposite also seems true: refrigerant mixtures for which the compressor displacement decreases when it is superheated, do not tend to enjoy the advantages of wet compression.

The highest percentage improvement in COP_c , 11.6%, is found through the process of wet compression when considering R12/R152a (0.5/0.5) at a vapour quality of 0.9. A COP_c value of 4.45 at a vapour quality of 0.9 is 11.6% higher than the COP_c value of 3.99 at 10°C superheat, and 3.9% higher than the 4.28 of Ammonia (best performing pure refrigerant) at the same vapour quality. The specific cooling capacity decreased with 18.3%, while the required compressor displacement rate to acquire 1kW of cooling increased with 10.5%.

Temperature glide: The higher the temperature glide, the higher the COP_c . This seems obvious if one is reminded that the evaporator outlet temperature is then closer to the condenser inlet temperature on the Temperature-Entropy diagram. This results in less work required from the compressor.

The top performing refrigerants are summarised in Tables 1 and 2. In both the tables the non-azeotropic mixtures were divided into three categories according to the amount of temperature glide displayed by each of them. A "low temperature glide" is defined by a refrigerant having a temperature glide that lies between 0°C and 5°C . A "medium

temperature glide" is defined by a refrigerant having a temperature glide that lies between 5°C and 10°C. A refrigerant that has a temperature glide higher than 10°C falls in the "high temperature glide" category. All the refrigerants were divided into groups of "phased-out", "temporarily acceptable" and "acceptable" refrigerants. These three groups correspond to the groups identified by the Montreal Protocol: "phased-out" refrigerants being CFC's or similar refrigerants phased-out since January 1996, "temporarily acceptable" refrigerants being HCFC's or similar refrigerants that will be phased-out in future under the Montreal Protocol, and "acceptable" refrigerants being those deemed acceptable for use in future. The phased-out refrigerants are analysed but omitted here for obvious reasons, while Table 1 lists the temporarily acceptable refrigerant mixtures and Table 2 shows the acceptable refrigerant mixtures.

Table 1 The Highest COP_c Values for Each of the Three Levels of Temperature Glides, Considering Only Temporarily Acceptable Refrigerant Mixtures. The First Value in Each Block is the COP_c (With the Relevant Inlet Vapour Quality in Brackets), the Second is the Specific Cooling Capacity (kJ/kg) and the Third is the Compressor Displacement per Kilowatt Cooling (litre/s)

Temporarily acceptable refrigerant mixtures					
Low Temperature Glide (0°C-5°C)		Medium Temperature Glide (5°C-10°C)		High Temperature Glide (>10°C)	
R22/R134a (0.7/0.3) 1.15	4.890(0.9) 123.8 0.295	R22/R142b (0.3/0.7) 9.97	6.056(20SH) 195.4 0.368	R123/R134a (0.6/0.4) 26.98	14.07(10SH) 191.4 0.44
R22/R124 (0.1/0.9) 4.45	4.887(0.9) 103.1 0.539	R22/R142b (0.6/0.4) 9.01	5.880(0.9) 153.4 0.291	R123/R134a (0.8/0.2) 25.26	13.24(10SH) 185.3 0.614

Table 2 The Highest COP_c Values for Each of the Three Levels of Temperature Glides, Considering Only Acceptable Refrigerant Mixtures. The First Value in Each Block is the COP_c (With the Relevant Inlet Vapour Quality in Brackets), the Second is the Specific Cooling Capacity (kJ/kg) and the Third is the Compressor Displacement per Kilowatt Cooling (litre/s)

Acceptable refrigerant mixtures					
Low Temperature Glide (0°C-5°C)		Medium Temperature Glide (5°C-10°C)		High Temperature Glide (>10°C)	
R218/RC318 (0.9/0.1) 2.78	5.96(20SH) 60.9 0.398	R143/R143a (0.9/0.1) 9.94	6.588(0.9) 215.9 0.611	R32/R143 (0.3/0.7) 25.85	13.0(0.8) 238.1 0.235
R125/R143a (0.8/0.2) 0.08	5.087(20SH) 103.1 0.238	R125/R143 (0.1/0.9) 9.64	5.873(1.0) 239.6 0.615	R32/R143 (0.4/0.6) 26.42	12.69(1.0) 308.0 0.198

Environmental impact: Two criteria are instrumental in determining the impact a certain refrigerant has on the environment, namely its ozone depletion potential (ODP) and its global warming potential (GWP). Cavallini¹⁹ identified a possible working region for refrigerants after the phase-out of CFC's. This working region includes refrigerants with an ODP of less than 0.1 (with R11 given a value of one as the norm) and a GWP of less than 4000 (with reference to CO₂, with an Integration Time Horizon of 100 years). With the phase-out of HCFC's, this window will shrink to a single line, which will only include refrigerants with zero ODP, while the GWP will be limited, given the current global warming issue.

It seems that for respectively low and medium temperature glide mixtures, R22/R134a (0.7/0.3) and R22/R142b (0.3/0.7) provide medium term solutions. Obviously R22/R142b is chosen above R22/R134a seeing that its COP_c is 24% and its specific cooling capacity 58% higher than the same values of R22/R134a. Unfortunately, though, the required compressor displacement rate increased by 25%.

Comparing high with medium temperature glide, the COP_c value of 14.07 recorded for R123/R134a (0.6/0.4) is more than double than the COP_c of R22/R142b. Unfortunately, for R123/R134a, the required compressor displacement rate is 20% higher, and the specific cooling capacity 2% lower.

It seems that concentrations of R290/R600 possess the best combination of the thermodynamic characteristics. It provides both a high COP_c as well as a high specific cooling capacity. Unfortunately this mixture carries a high risk of flammability.

From the refrigerant components considered the majority was classified A1 and A2. The only exceptions were R123 (B1), R290 (A3) and R600 (A3). For this reason, note should be taken of the hazards presented by mixtures of R123/R134a and R290/R600.

4. CONCLUSIONS

The top performing non-azeotropic mixtures produce higher COP_c 's than the top performing pure refrigerants. It should be kept in mind, however, that this conclusion is based on the method of comparison between non-azeotropes and pure refrigerants chosen for this study. The chosen method of comparison is that the evaporation and condensation temperatures chosen for the evaluation of a pure refrigerant, are retained as respectively bubble point and dew point temperatures for the evaluation of the non-azeotropic mixture. Other methods of comparison may lead to different results.

After analysing the 34 pure refrigerants it was concluded that all of them can be divided into two distinctive groups, depending on the shape of their temperature entropy curves. Two common shapes were identified: a bell shape and a re-entrant curve. From the 34 pure refrigerants analysed, all those with re-entrant saturated vapour lines produce better COP_c 's when the refrigerant is superheated before entering the compressor. Only two of the refrigerants (R32 and NH_3) with bell-shaped T-s curves, consistently produce higher COP_c 's when wet compression is used. It can therefore be concluded that in general it has been found that wet compression is not attractive when pure refrigerants are used.

As with pure refrigerants, non-azeotropic refrigerant mixtures were also divided into two groups according to the shape of their T-s curves. All the refrigerant mixtures with a re-entrant saturation vapour line on the T-s curve produced better COP_c values when the refrigerant was superheated before entering the compressor. From the group of refrigerant mixtures with bell-shaped T-s curves, quite a few were identified that produce better COP_c values through the process of wet compression. It seemed that especially R11/R114, R32/R142b, R32/R142b and R32/R143 performed better under wet compression conditions. The use of wet compression unfortunately also resulted in a drop in cooling capacity and in some cases, an increase in the compressor displacement. Again, a refrigerant with a bell-shaped T-s curve did not automatically perform better with wet compression. To conclude, mention was made of the advantages of wet compression on the discharge temperature and the effect it has on compressor life.

Reviewing the binary non-azeotropic mixtures analysed, it seems from a COP_c point of view that for air conditioning, the following refrigerant mixtures consistently respond favourably to wet compression: R11/R114, R12/R22, R124/R125, R142b/R143a, R143/R143a, R22/R134a, R22/R142b, R22/R152a, R22/R218, R32/R124, R32/R125, R32/R134, R32/R143, R32/R152a, R32/R42b, R22/R124, R22/R143 and R134a/R124. As with pure refrigerants, the specific cooling capacity decreases and the compressor displacement increases with the use of wet compression as can be expected. It was found, however, that for some refrigerant mixtures, for example R32/R143 (0.3/0.7), the compressor displacement reaches a relative low value at approximately the same vapour quality where

the maximum COP_c is reached. It is interesting to note that this phenomenon occurs especially in refrigerant mixtures that produce higher COP_c values with wet compression. It is recommended that this phenomenon be investigated more closely. The opposite also seems true: refrigerant mixtures for which the compressor displacement decreases when it is superheated, do not tend to enjoy the advantages of wet compression. It was found that only 1.1% of all the refrigerant mixtures considered produced higher COP_c through the process of wet compression.

It was also found that the temperature glide of each refrigerant mixture plays an important role in how it will perform. It was possible to define an accurate approximation of the COP_c as a function of the temperature glide for all the refrigerant mixtures considered. The approximation has an average error of 7%.

The refrigerant mixtures were grouped into three different temperature glide categories, depending on its type of temperature glide distribution. The highest COP_c obtained with a low temperature glide was for R218/RC318 (0.9/0.1). R143/R143a (0.9/0.1) topped the chart for the medium temperature glide whilst R123/R134a (0.6/0.4) outperformed the rest in the high temperature glide category. Although the COP_c values were not so spectacular, they are a great improvement on the values for pure refrigerants.

The impact of the refrigerants on the environment was also taken into account. Three types of refrigerants were identified: phased-out refrigerants, refrigerants that are temporarily acceptable and acceptable refrigerants. With the phased-out refrigerants ignored, the temporarily acceptable mixtures with the best combination of high COP_c and cooling capacity were R22/R134a (0.7/0.3) for low, R22/R142b (0.3/0.7) for medium and R123/R134a (0.6/0.4) for high temperature glide categories. R22/R134a was compressed at a vapour quality of 0.9, R22/R142b at 20SH and R123/R134a at 10SH. The long-term acceptable refrigerant mixtures were R32/R152a (0.1/0.9) for low, R32/R152a (0.4/0.6) for medium and R32/R143 (0.4/0.6) for high temperature glide categories. All three refrigerants were compressed at a vapour quality of 1.0.

The top performing refrigerant mixtures were also evaluated for flammability and toxicity using the ASHRAE 34-1992 Standard [21]. Only mixtures of R123/R134a and R290/R600 were identified as exceptional hazards regarding flammability and toxicity.

A final look at the top performing refrigerant mixtures revealed that only 27% of the refrigerant mixtures in the low and medium temperature glide categories prefer the process of wet compression. Only 10% of the refrigerant mixtures in the high temperature glide category prefer the process of wet compression.

Non-azeotropic mixtures tend to gain more from wet compression than pure refrigerants when considering the COP_c values. Unfortunately, though, the cooling capacities decrease in general. Another advantage of some of the non-azeotropes is that the compressor displacement does not necessarily increase substantially when wet compression is applied.

REFERENCES

1. F.S. Rowland, Stratospheric ozone depletion: identifying the problem and the solution, *ASHRAE Journal*, (September 1997), pp. 29-31.
2. A. Cavallini, Working fluids for mechanical refrigeration, *International Journal of Refrigeration*, (1996), 19(8), 485-496.
3. G. Lorentzen, The use of natural refrigerants: a complete solution to the CFC/HCFC predicament, *International Journal of Refrigeration*, (1995) 18(3), 190-197.
4. R.N. Richardson, J.S. Butterworth, The performance of propane/isobutane mixtures in a vapour-compression refrigeration system, *International Journal of Refrigeration* (1995) 18(1), 58-62.
5. M.V. Rane, R. Radermacher, Feasibility study of a two stage vapour-compression heat pump with ammonia-water solution circuits: experimental results, *International Journal of Refrigeration*, (1993) 16 (4), 258-264.

6. J.R. Sand, S.K. Fischer, Screening analysis for chlorine-free alternative refrigerants to replace R-22 in air-conditioning applications, *ASHRAE Technical Data Bulletin*, (1993) 9(4), 12-20.
7. P.A. Domanski, D.A. Didion, Thermodynamic evaluation of R-22 alternative refrigerants and refrigerant mixtures, *ASHRAE Technical Data Bulletin*, (1993) 9(4), 21-33.
8. S.N. Kondepudi, Drop-in testing of R-32 blends as R-22 alternatives in a split-system air conditioner, *ASHRAE Technical Data Bulletin* (1993) 9(4), 40-47.
9. K.S. Sanvordenker, Experimental evaluation of an R-32/R-134a blend as a near drop-in substitute for R-22, *ASHRAE Technical Data Bulletin* (1993) 9(4), 34-39.
10. M.W. Spatz, J. Zheng, R-22 Alternative refrigerants: performance in unitary equipment, *ASHRAE Technical Data Bulletin* (1993) 9(4), 48-54.
11. J.W. Linton, W.K. Snelson, P.F. Hearty, Triebe, A.R. System performance of near azeotropic mixtures of R-134a and R-152a, *ASHRAE Technical Data Bulletin*, (1993) 9(4), 55-60.
12. R. Radermacher, D. Jung, Theoretical analysis of replacement refrigerants for residential uses, *ASHRAE Technical Data Bulletin* (1993) 9(4), 1-11.
13. W.F. Stoecker, J.W. Jones, *Refrigeration and Air Conditioning*, McGraw-Hill, 3rd ed. (1982) 193-195.
14. L.C.M. Itard, Wet compression versus dry compression in heat pumps working with pure refrigerants or non-azeotropic mixtures, *International Journal of Refrigeration* (1995) 18(7) 495-504.
15. NIST REFPROP Standard Reference Database 23. NIST Thermodynamic properties of refrigerants and refrigerant mixtures Version 4.0, *Thermophysics Division, National Institute of Standards and Technology*, (November 1993) Gaithersburg, MD 20899.
16. H. Kruse, M. Kuever, U. Guast, M. Schroeder, B. Upmeyer, Theoretical and Experimental Investigations of Advantageous Refrigerant Mixture Applications, *ASHRAE Technical Data Bulletin* (1985), 96-131.
17. M. Nagel, K. Bier, Vapour-liquid equilibrium of ternary mixtures of the refrigerants R32, R125, and R134a, *International Journal of Refrigeration*, (1995), 18(8), 534-543.
18. A. Cavallini, CFC and HCFC substitution – short-and long-term solutions, *IIR Bullitin*, (1994), 94(6), 2-15.
19. J.M. Calm, D.A. Didion, Trade-offs in refrigerant selections: past, present and future Refrigerants for the 21st Century (1997), 6-19.
20. K.S. Sanvordenker, Status of CFC and HCFC alternatives *Refrigerants for the 21st Century* (1997), 111-116 trade-offs in refrigerant selections: past, present and future.
21. ASHRAE Standard 34-1992 *Number Designation and Safety Classification of Refrigerants*, American Society of Heating, Refrigeration and Air-Conditioning Engineers, Inc., Atlanta, GA, USA (1992), 1-9.

NOMENCLATURE

COP _c	Coefficient of performance for cooling	T _{evap}	Evaporation temperature (K)
h	Specific enthalpy (J kg ⁻¹)	T _g	Temperature glide (K)
h _f	Specific enthalpy at saturated liquid qualities (J kg ⁻¹)	V	Compressor displacement rate for each kilowatt of cooling (m ³ s ⁻¹)
h _g	Specific enthalpy at saturated vapour qualities (J kg ⁻¹)	w	Specific work (J kg ⁻¹)
m _r	Refrigerant mass flow for each kilowatt of cooling (kg s ⁻¹)	x	Vapour quality
q	Specific cooling capacity (J kg ⁻¹)	ρ	Refrigerant density (kg m ⁻³)
s	Specific entropy (J kg ⁻¹ K ⁻¹) or isentropic point in figures	η _c	Compressor isentropic efficiency
T _{cond}	Condensation temperature (K)		

TEMPERATURE CONTROL IN REFRIGERATED TRANSPORT WITH A SNOW BAG

W. R. Da Veiga and J. P. Meyer

Department of Mechanical and Manufacturing Engineering

Rand Afrikaans University

Email: jpm@ing1.rau.ac.za; Fax (+27-11)-489-2532

Keywords: snow shooting, snow bag, transport refrigeration, carbon dioxide, CO₂

ABSTRACT. Snow shooting is a recently patented process that is used in refrigerated transport. Pressurised liquid carbon dioxide is injected via a "snow" lance into a permeable snow bag mounted near the ceiling of the insulated container. The decrease in pressure causes the liquid carbon dioxide to convert to "snow" and vapour inside the snow bag. It is the purpose of the paper to develop a model that can be used to predict the heat transfer and more specifically the heat transfer coefficient of a snow bag. This model could then be used to predict the amount of snow and/or size of the snow bag for a given size of body and heat load. This is done with experimental and theoretical energy balances over the container walls and the snow bag.

1. INTRODUCTION

Countries with a warm climate and high ambient temperatures require careful temperature control of all perishable products from producer to consumer. Should the cold chain be broken, spoilage of food products will occur mainly through microbial growth such as bacteria, yeast and mould. Wide temperature fluctuations will also affect the quality of the frozen and chilled foods during transportation. The demands placed on the refrigerated transport industry over the last decade has increased as more is understood about the importance of cargo temperature maintenance.

Refrigerated transport equipment [1], can be broadly classified by the type of refrigeration system used. These types are ventilation, product subcooling, water ice, dry ice (carbon dioxide), liquid nitrogen or liquid carbon dioxide spray, eutectic plates for holdover, mechanical refrigeration and snow shooting. Mechanical refrigeration and snow shooting will now be discussed.

Mechanical refrigeration

Many styles of independent engine and/or electric motor driven mechanical refrigerating units are available and constitute the most popular application for both trucks and trailers. More than 90% of the refrigerated transport industry use mechanical refrigeration (vapour compression of refrigerant gases, mostly ozone destroying CFC's and HCFC's) of one type or another. Steps are however being taken to use more environmentally friendly refrigerants. Usually it is a one-piece, plug type, self-contained unit mounted in an opening in the front wall of the vehicle. The condensing section on the outside and the evaporator section on the inside are separated by an insulated plug that attaches to the vehicle wall and supports the various parts of the refrigerating unit. Most evaporators can be defrosted automatically by the hot-gas method. Most units are thermostatically controlled, starting and stopping or reducing speed as refrigeration needs arise.

Snow shooting

Snow shooting should not be confused with liquid carbon dioxide spray. It is a new technology on which no literature has been published as far as could be determined. It has been recently patented in South Africa². After loading the cargo into the insulated body, the doors are closed and the pressurised liquid carbon dioxide (R-744) at a pressure of 2 MPa (gauge) is injected via a "snow" lance into a permeable snow bag mounted near the ceiling of the insulated container (Figure 1). As is shown in Figure 2 the decrease in pressure causes the liquid carbon dioxide to convert to "snow" and vapour inside the snow bag. At an atmospheric pressure of 101.325 kPa one kilogram of liquid carbon dioxide expands to form 0.54 kg of gas at a temperature of approximately -78.5°C and an enthalpy of 47 kJ/kg as well as 0.46 kg of solid snow, also at a temperature of -78.5°C, but with an enthalpy value of 640 kJ/kg. This results in 8% of the cooling capacity in a gas phase and 92% in a solid phase.

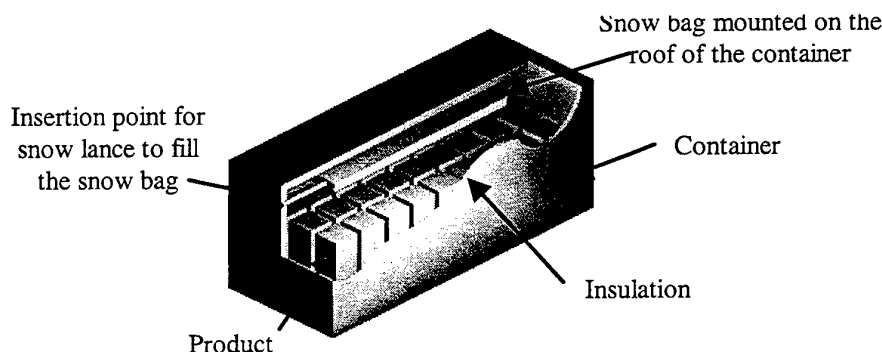


Fig. 1. Container with snow bag

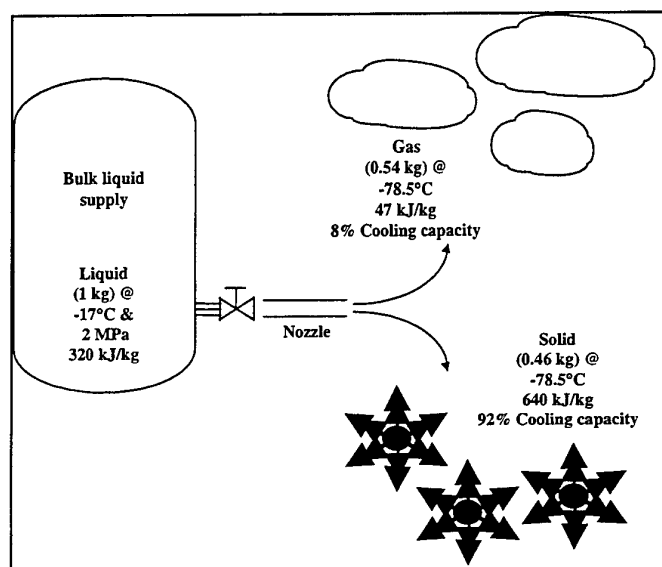


Fig. 2. Carbon dioxide snow formation

The snow bag is designed so that only the snow particles are retained, thus allowing the cold vapour to escape and pre-cool the container walls and product. The permeable snow bag acts as a phase separator, separating the carbon dioxide snow from the gas. The snow in the snow bag sublimates to cold carbon dioxide gas, flows down the cargo keeping it cold. The snow is not in direct contact with the product or the container walls, therefore this method can be used for most chilled as well as frozen products. Semi-compaction of the solid carbon dioxide snow phase occurs during charging, which reduces the sublimation rate of the snow, resulting in a more controlled release of the refrigeration capacity.

Snow shooting compared to direct injection into the snow bag results in limited thermal shock on the transport container or vehicle walls because of the containment of the snow within the snow bag. Therefore, a more uniform time versus temperature profile within the transport container or vehicle and cargo is obtained because of the relatively low rate of "snow" sublimation and separation of the snow from the cargo.

A further advantage of using snow shooting is that the inert carbon dioxide atmosphere reduces all bacterial activity in the cargo and hence snow shooting is intrinsically hygienic. In addition, the cargo is reliably kept at or below the temperature at which it is loaded into the truck. Another advantage is that the cold carbon dioxide is twice as dense as normal air and this dense gas quickly sinks and a natural thermal convection pattern is set up. There is therefore no need for a forced draft that assures a negligible weight loss due to dehydration of fresh

produce. It compares very favourably to the typical two percent per 24 hour weight loss that occurs with mechanical refrigeration units that blow dry air past the fresh produce and pick up its moisture.

Snow shooting releases carbon dioxide to the atmosphere that contributes to global warming. However, the carbon dioxide used in South Africa where the process was developed is a by-product from chemical plants that releases it to the atmosphere. The process of liquifying and storing the carbon dioxide before it is used for snow shooting among others therefore does not directly increase global warming but delays it.

The amount of snow injected into the snow bag determines the length of time that the cargo may be maintained at its loaded temperature. This is established from experience with similarly insulated and sized vehicles.

Some of the advantages of snow shooting against mechanical refrigeration are: A small capital investment is needed as no refrigeration unit is required. The simpler design results in almost no maintenance costs; less dehydration of product occurs due to the absence of forced air circulation; the equipment is easier to install; no downtime is needed due to defrost cycles; faster cool down of internal structure; easier cleaning and maintenance; shorter delivery and installation time of equipment; it is environmentally friendly, no CFC's or HCFC's are released and no noise pollution occurs; less wear-and-tear on vehicle itself because the bag is much lighter than a mechanical refrigeration unit and therefore results in a higher payload. No personnel discomfort during off-loading due to the absence of forced air circulation and a higher payload since this method is lighter than a mechanical refrigeration unit.

Some of the disadvantages of snow shooting are: The single, most important health hazard that carbon dioxide presents is the risk of suffocation: by excluding oxygen from the lungs, the necessary precautions must therefore be taken when the doors of the delivery vehicle are opened.

Carbon dioxide is normally stored as a cold liquid at 2 MPa (gauge) pressure and at -17°C . To maintain these conditions and prevent loss through evaporation, special vessels are needed to store the very cold liquid. These are designed to limit the heat exchange between air and the cold liquid. They are double skinned and filled with an expanded insulant. The small losses due to the heat in-leak of the vessel are taken care of by a small integral mechanical refrigeration unit. The refrigeration unit recondenses the evaporated carbon dioxide back into a liquid, thus reducing the pressure in the vessel. The capital cost and running cost of this "plant" is therefore a disadvantage.

It is important to ensure that the correct amount of snow is added for the duration of the journey (too much will increase the operating cost and too little will prevent the refrigeration effect) - this factor can be complicated by non-constant journey times and vehicle breakdowns. Additional leftover snow at the end of the journey is of little practical use. The COP of snow shooting is lower than that of mechanical refrigeration and therefore results in higher operating costs. Snow-shooting is not a cost-effective means of lowering the temperature of the product. It is best used to maintain product temperatures. Products that need to respire during transit such as fruit or vegetables should be transported with caution, as prolonged exposure to high concentrations of carbon dioxide could cause spoilage.

The process of snow formation can be represented on a temperature entropy graph as can be seen in Figure 3. This graph was compiled from thermodynamic data given in reference [3] which based entropy and enthalpy on 0 for the perfect crystal at -273.15°C . The expansion was assumed to be an adiabatic constant enthalpy process from point 1 (liquid CO_2) to point 2 (mixture of gas and solid). The conversion rate efficiency using the snow bag is very close to the theoretical value of 50% (compared to the measured value of 46%), i.e., one kilogram carbon dioxide theoretically converts to 0.5 kg carbon dioxide snow. There is a slight (± 0.3 to $\pm 0.7\%$) decrease in percentage solid mass formed at 80 kPa atmospheric pressures compared to 101.325 kPa depending on the starting liquid pressure.

Presently the size of the snow bag and length of filling for a particular journey is determined through practical experience with similarly insulated and sized vehicles. This is no cost effective and sufficient to answer to the needs of different customers. It is the purpose of this paper to develop a model that can be used to predict the

heat transfer and more specifically the heat transfer coefficient of a snow bag. This model could then be used to predict the amount of snow and/or size of the snow bag for a given size of body and heat load.

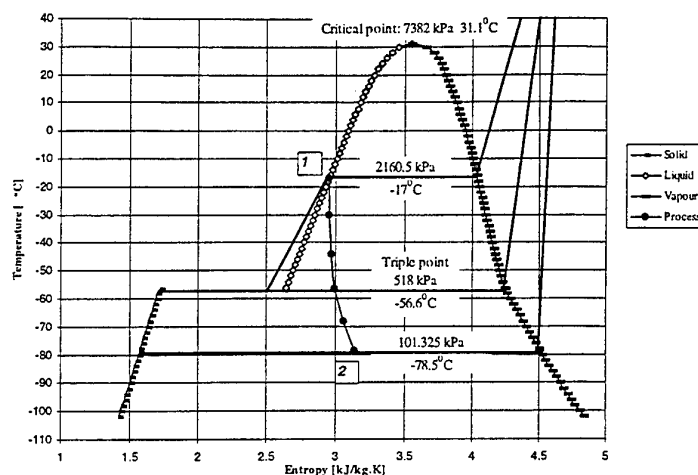


Fig. 3. Snow shooting process (from point 1 to 2) represented on a temperature entropy graph of carbon dioxide

The layout of the paper is as follows. Firstly the overall heat transfer coefficient of the container will be calculated after which the heat transfer coefficient of the snow will be calculated. Both named coefficients are calculated with experimental work. Thereafter the heat transfer coefficient of the snow is calculated with theoretical equations and compared to the previous calculated heat transfer coefficient.

2. EXPERIMENTAL WORK

The container used is a thermal insulated container used for transport. The snow bag construction is mounted to the roof of the container with the shade netting material used as the phase separator (snow bag). K-type thermocouples are positioned on the inner and outer face of each wall to determine the temperature on the inside and outside respectively. The thermocouples used are calibrated to an accuracy of $\pm 0.5^\circ\text{C}$.

For heating the inside of the container six 1 kW electric heating elements are placed at even intervals inside the container. In order to measure the heat load inserted into the container via the heating elements a kilowatt-hour meter is connected on the power supply line of the heating elements. Four fans are placed inside the container to circulate the air if a uniform temperature inside the container is required.

The snow bag construction is suspended with two s-type load cells from the roof to measure the weight of the snow inside the snow bag. Three depth gauges are positioned at the top of the container to measure the height of the snow in the snow bag at different positions during the experiment without opening the doors of the container.

The container and snow bag dimensions and the position of the thermocouples, elements, fans, depth gauges and load cells are shown in Figure 4.

The overall heat transfer coefficient of the container is determined by heating the inside of the container until a temperature difference of approximately 50°C between inside and outside is reached. With a constant temperature difference an energy balance (Equation 1 and 2) is used to calculate the overall heat transfer coefficient of the container walls.

$$Q_i = Q_t + mC_p\Delta T/t$$

$$\therefore Q_i = UA(T_{ia} - T_s) + mC_p(T_{i2} - T_{i1})/t \quad (1)$$

$$\text{where } T_{ia} = (T_{i2} + T_{i1})/2 \quad (2)$$

The heat transfer coefficient of the snow in the snow bag can thereafter be calculated with Equation 3 and 4. The area of the snow is determined with the height of the snow measured with the dept gauges on the roof. The heat transferred rate of the snow calculated in Equation 3 is checked by using the sublimation rate of the snow determined from the load cell readings according to Equation 5.

$$Q_l + Q_t = Q_s + mC_p \Delta T/t$$

$$\therefore Q_l + UA(T_a - T_{ia}) = h_s A_s (T_{ia} - T_s) + mC_p (T_{i2} - T_{i1})/t \quad (3)$$

$$\text{where } T_{ia} = (T_{i2} + T_{i1})/2 \quad (4)$$

$$Q_{lc} = \Delta m_i (h_g - h_i)/t \quad (5)$$

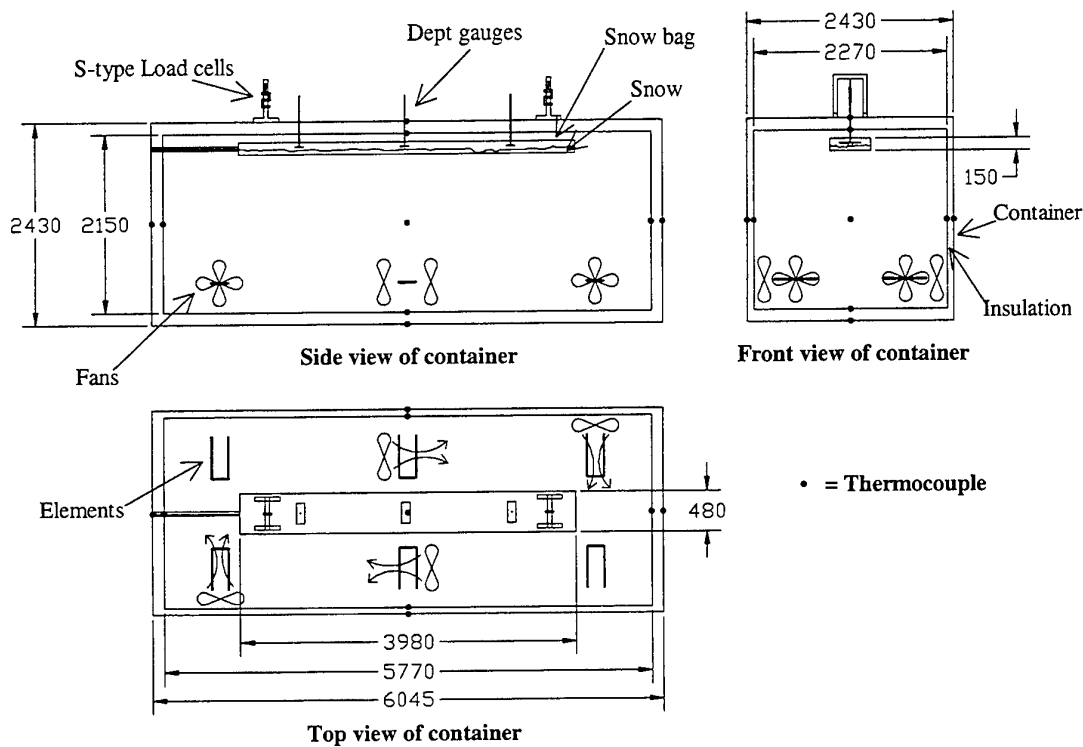


Fig. 4. Diagrammatic view of the container

3. THEORETICAL HEAT TRANSFER COEFFICIENT

The equations used to find the theoretical heat transfer coefficient of the snow are obtained from reference [4]. In the equations all the properties are calculated at the film temperature defined in Equation 6. The snow bag is separated into three different sections according to the orientation of the surface and the way the free convection gas moves over the surface. For the sides and points the characteristic length, Rayleigh number, Nusselt number and heat transfer coefficient are calculated with Equation 7, 9, 10 and 13 respectively. For the top the characteristic length, Rayleigh number, Nusselt number and heat transfer coefficient are calculated with Equation 8, 9, 11 and 13 respectively. For the bottom the characteristic length, Rayleigh number, Nusselt number and heat

transfer coefficient are calculated with Equation 8, 9, 12 and 13 respectively.

$$T_f = (T_{ia} + T_s) / 2 \quad (6)$$

$$L_c = h_{av} \quad (7)$$

$$L_c = \frac{A_s}{P} \quad (8)$$

$$Ra_L = \frac{g\beta(T_s - T_{ia})L_c^3}{\nu\alpha} \quad (9)$$

$$Nu_L = 0.68 + \frac{0.670Ra_L^{1/4}}{[1 + (0.492/Pr)^{9/16}]^{1/4}} \quad Ra_L \leq 10^9 \quad (10)$$

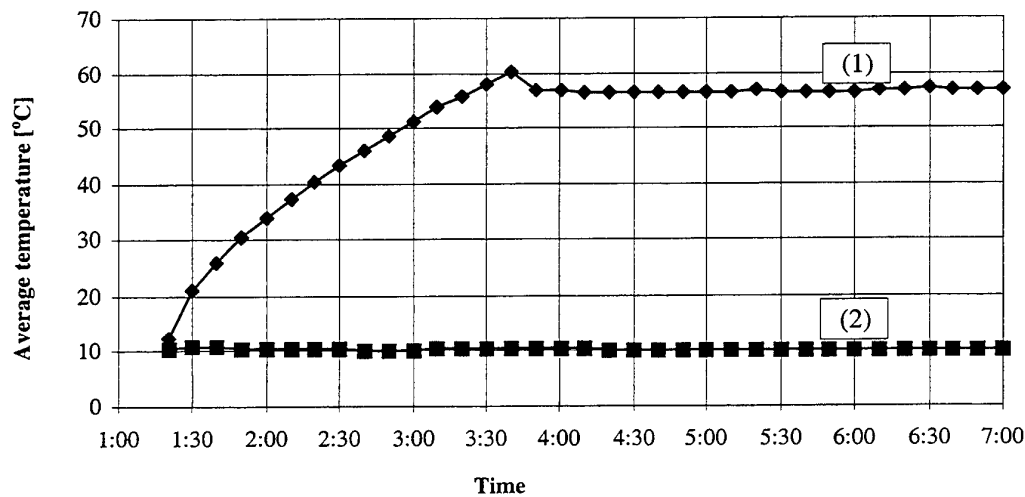
$$Nu_L = 0.27Ra_L^{1/4} \quad 10^5 \leq Ra_L \leq 10^{10} \quad (11)$$

$$Nu_L = 0.15Ra_L^{1/3} \quad 10^7 \leq Ra_L \leq 10^{11} \quad (12)$$

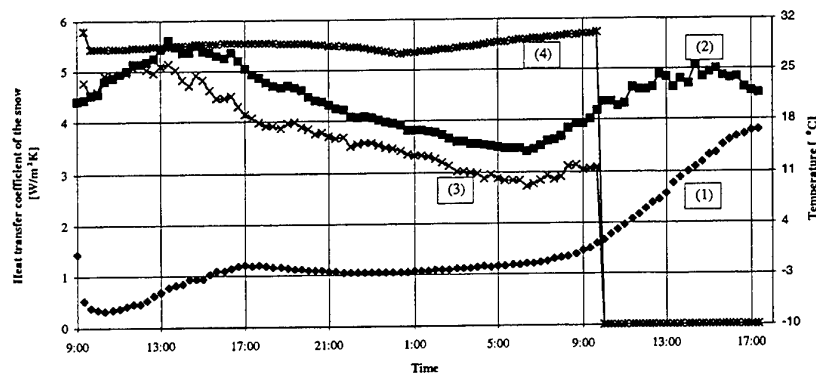
$$h_s = \frac{k}{L_c} Nu_L \quad (13)$$

4. RESULTS

The overall heat transfer coefficient of the container is determined with the temperature inside the container stabilising with approximately a 50°C temperature difference between the inside and outside of the container. Graph 1 shows the temperature curves of the inside and ambient temperatures. The product of UA is determined to be 45 W/K. The heat transfer coefficient of the snow in the snow bag is determined experimentally and theoretically and shown in Graph 2. The corresponding temperatures inside and outside the container are also shown on Graph 2.



Graph 1. Average inner (1) and ambient (2) temperature versus time with four elements and fans switched off at 3:50 am



Graph 2. Average inner (1), ambient (2) temperature, experimental (3) and theoretical (4) heat transfer coefficient of the snow versus time

5. DISCUSSION OF RESULTS

The product of the overall heat transfer coefficient and the area of the container (UA) determined to be 45 W/K can unfortunately not be verified theoretically because of deterioration of the container insulation and damage to the container itself. Fortunately the verification of the energy balance with the load cells also verifies this result. The verification of the heat transferred rate of the snow with the load cells result in an error of 12%, which is accurate for an energy balance.

The average difference between the experimental and the theoretical calculated heat transfer coefficient of the snow is 19%. The reason for this can be explained by the fact that the equations used to calculate the theoretical heat transfer coefficient describes a flat surface with free natural convection. In the snow sublimation this is not 100% the case since:

1. The snow bag creates a boundary between the free stream and the snow and therefore cause unnatural flow patterns.
2. The bag is close to the roof, therefore at the top there is not a free stream flow.
3. A critical reason is that a layer of ice forms on the snow bag from the moist air. This creates an insulation layer that prevents the snow from sublimating.
4. The free stream temperature around the snow bag was assumed to be constant. Actually there is a temperature gradient (warmer at the top side than the bottom side since the cold CO_2 moves down).
5. 100% CO_2 was assumed around the snow bag while it was actually a mixture of CO_2 and air.

The first four reasons will give a higher theoretical than experimental value since they all create restriction for natural convection to take place. Through calculations it is seen that the fifth reason actually gives a slight increase in theoretical heat transfer coefficient of the snow.

5. CONCLUSION

With an average difference of 19% between the theoretical and experimental heat transfer coefficient it can be concluded that the theoretical equations can be used as a first order estimation to calculate the amount of snow needed for a specific journey. However more experiments have to be done, perhaps in conjunction with finite element analysis to achieve more accurate results. Finite element analysis can be used to take into consideration the insulation layer created by the ice and the snow bag as well as the temperature gradient inside the container. A further advantage is that actual products can be simulated to increase the value of the results obtained.

NOMENCLATURE

A area of the container used in experiments [m^2]

A_s	area of the snow in the snow bag [m^2]
α	thermal diffusivity [m^2/s]
β	volumetric thermal expansion coefficient [K^{-1}]
C_p	specific heat at constant pressure [$J/kg.K$]
g	gravitational acceleration [m/s^2]
h_{av}	average height of the snow in the snow bag [m]
h_g	enthalpy of saturated vapour [kJ/kg]
h_s	enthalpy of saturated solid [kJ/kg]
h_i	heat transfer coefficient of the snow in the snow bag [$W/m^2.K$]
k	thermal conductivity [$W/m.K$]
L_c	characteristic length [m]
m	mass of carbon dioxide gas in container [kg]
m_t	total mass of snow bag construction and snow [kg]
Nu_L	Nusselt number based on the characteristic length
Pr	Prandtl number
P	perimeter of surface area [m]
ρ	density of carbon dioxide [kg/m^3]
Q_l	product heat load [W]
Q_{lc}	heat transferred rate of snow calculated with load cells [W]
Q_s	heat transferred rate of snow [W]
Q_t	heat transmitted through container walls [W]
Ra_L	Rayleigh number based on the characteristic length
T_a	ambient temperature outside the container [$^{\circ}C$]
T_f	film temperature [$^{\circ}C$]
T_{i1}	temperature inside the container at a given instant [$^{\circ}C$]
T_{i2}	temperature inside the container after a certain period [$^{\circ}C$]
T_{ia}	average temperature inside the container [$^{\circ}C$]
T_s	temperature of snow in the snow bag [$^{\circ}C$]
t	time in which temperature change [s]
U	overall heat transfer coefficient of the container walls [$W/m^2.K$]
ν	kinematic viscosity [m^2/s]

REFERENCES

1. ASHRAE 1994 *ASHRAE Handbook Fundamentals SI edn* pp. 27.3-27.5 (1994).
2. Patent number 91/5027 hold by *African Oxygen Limited*, South Africa
3. Compressed Gas Association Inc., *Carbon Dioxide*, 4th edition USA pp. 7 (1984).
4. Incropera FP & DeWitt DP, *Introduction to Heat Transfer*, John Wiley & Sons Inc. (1996).

AN EXERGY ANALYSIS OF THE LiBr-WATER ABSORPTION REFRIGERATING CYCLE

Hitoshi Asano, Terushige Fujii, and Xiao Wang
Department of Mechanical Engineering, Kobe University
E-mail: asano@mech.kobe-u.ac.jp; Fax: +81-78-803-6122

Yoshinori Hisazumi
Engineering Department, Osaka Gas Co., Ltd.
E-mail: yoshinori-hisazumi@osakagas.co.jp; Fax: +81-6-6231-1062

Keywords; exergy analysis, COP, LiBr-water absorption cycle, single-effect, double-effect

ABSTRACT. It is important to use the waste heat efficiently for energy saving. An absorption cycle is efficient as the thermal utilizing equipment of the waste heat. In order to improve the performance of absorption cycle for the various operating conditions, it is important to analyze the exergy loss in each component and evaluate not only the quantity but also the quality of heat flow. In this paper, an exergy analysis of the single- and double-effect LiBr-water absorption refrigerating cycles whose heat source are a saturated steam at the pressure of 800 kPa is carried out, and the exergy loss in each component is obtained. As a result, it is shown that the exergy coefficients and COP of the single-effect absorption cycle are about 17% and 80 %, and those of the double-effect cycle are about 30 and 140 %, respectively.

NOMENCLATURE

C	: Solution concentration [wt%]	Subscripts	
e	: Specific exergy [kJ/kg]	A	: Absorber
E	: Exergy loss [kW]	C	: Condenser
h	: Specific enthalpy [kJ/kg]	E	: Evaporator
Δh_L	: Latent heat [kJ/kg]	HX	: Solution heat exchanger
m	: Mass flow rate [kg/s]	HR	: High temp. regenerator
Q	: Heat flow [kW]	LR	: Low temp. regenerator
s	: Specific entropy [kJ/kg]	R	: Regenerator
T	: Temperature [°C]	T	: Throttle
x	: Quality of steam		
η	: Exergy coefficient		

1. INTRODUCTION

The promotion of the useful utilization of the waste heat from factories and the municipal solid waste-burned boiler and so on is the efficient way for the energy saving and the solution of the global environmental problems. An absorption refrigerating system is efficient as the thermal utilizing equipment of the waste heat. On the other hand, because an absorption system uses not the ozone-depleting chlorofluorocarbons (CFCs) and hydrochlorofluorocarbons (HCFCs) with the high greenhouse effect but the natural refrigerant of water or ammonia, the interest in the absorption system is growing.

Wardono and Nelson [1] simulated a double-effect LiBr/water absorption cooling system, and presented the effect of the heat transfer area of the solution heat exchanger and the inlet temperature of heat source on the COP (coefficient of performance). The maximum value of the COP was between 1.4 and 1.5 at the temperature of the heat source of 145 °C. Schweigler et al. [2] constructed and tested the prototype of a single-effect/double-lift LiBr absorption system with a cooling capacity of about 400 kW for district heating networks. The COP was about 0.7 and was the same as a normal single-effect system, but it was shown that the single-effect/double-lift system could be operated with lower temperature heat than a single-effect system. There are many previous works for various type absorption cycle (e.g., Grossman et al.[3], Wardono and Nelson [2]), but all of these studies are based on the quantity of energy. In order to design the absorption cycle driven by the waste heat under the various conditions, it is necessary to evaluate the quality of energy, that is, exergy flow, and clarify the loss in each component.

In this study, the numerical calculations on the exergy flow in the single- and double-effect LiBr-water absorption refrigerating systems whose heat source are the saturated steam of 800kPa were carried out, and the COP, the exergy coefficient, and the exergy loss in each component were evaluated.

2. MODEL DESCRIPTION

Schematic diagrams of a single- and double-effect LiBr-water absorption refrigerating cycles are shown in Figs. 1 (a) and (b), respectively. A single-effect system (Fig.1 (a)) consists of heat exchangers, a throttle, and a solution pump. In the regenerator, LiBr solution is heated by a saturated steam heat source, and the superheated refrigerant steam is generated. This steam is condensed to a saturated liquid in the condenser, using a cooling water fed out from the absorber. The water is decompressed through a expansion valve, evaporates at low

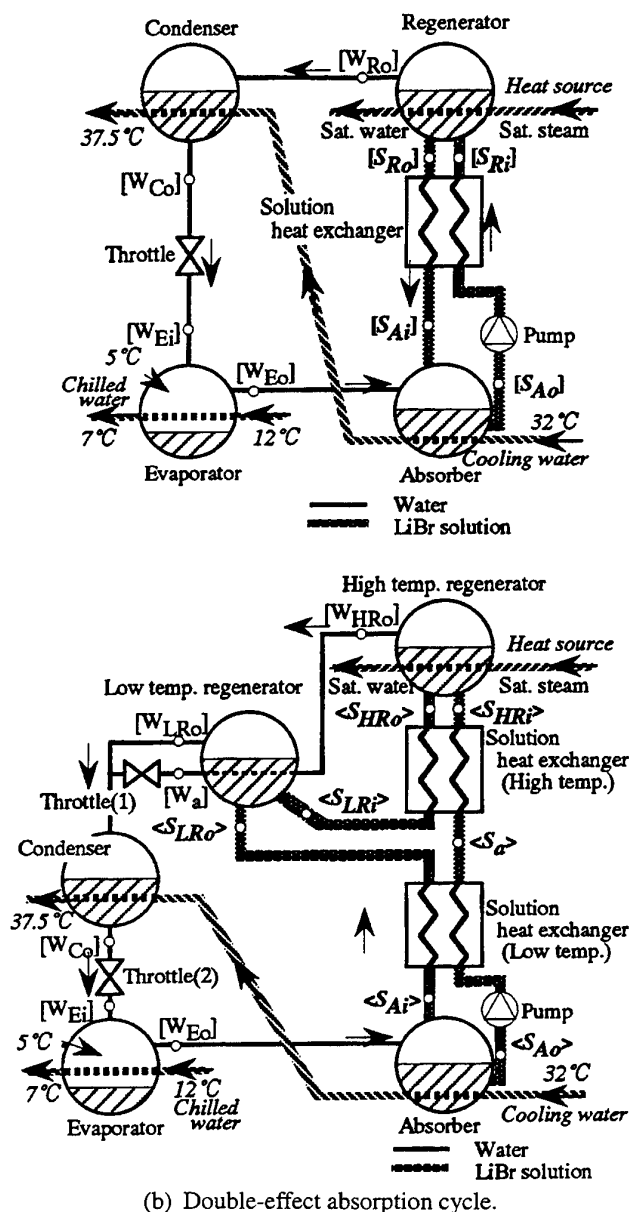


Fig. 1 Schematic diagram of absorption cycle.

temperature in the evaporator, and cools a chilled water. The steam is led to the absorber and absorbed by the high concentration solution with the cooling by cooling water. The low concentration solution is led to the regenerator through a solution heat exchanger by the solution pump. On the other hand, a double-effect system (Fig.1 (b)) has two regenerators and two solution heat exchangers. The superheated steam generated in the high temperature regenerator condenses in the low temperature regenerator, which uses the heat of condensation to generate superheated refrigerant steam in the low temperature regenerator.

Figure 2 shows schematic diagrams of the single- and double-effect absorption processes in the Dühring chart, respectively. For a high temperature heat source, the double-effect cycle is more efficient than a single-effect cycle.

In this study, the following assumptions were made.

- Heat loss in each component, the solution pump work and pressure loss in pipe elements are neglected.
- The outlet condition of the refrigerant of the condenser and the evaporator are saturated water and steam, respectively.
- In the regenerator and absorber, the solution is at the equilibrium state related on the pressure and the solution temperature.
- A saturated steam which is used as the heat source become a saturated water in the regenerator.
- The minimum terminal temperature difference of the solution heat exchanger is 5K. The temperature differences in the condenser, the evaporator, the absorber, and the regenerator, are 2 to 3 K.

The calculation was carried out under the constant condition of the cooling load, the cooling water temperature, the chilled water temperature, and the evaporating temperature as shown in Table 1.

Table 1. Calculating Conditions

Cooling load	100 USRT (=352 kW)	
Cooling water temperature	inlet	32°C
	outlet	37.5°C
Chilled water temperature	inlet	12°C
	outlet	7°C
Evaporating temperature	5°C	

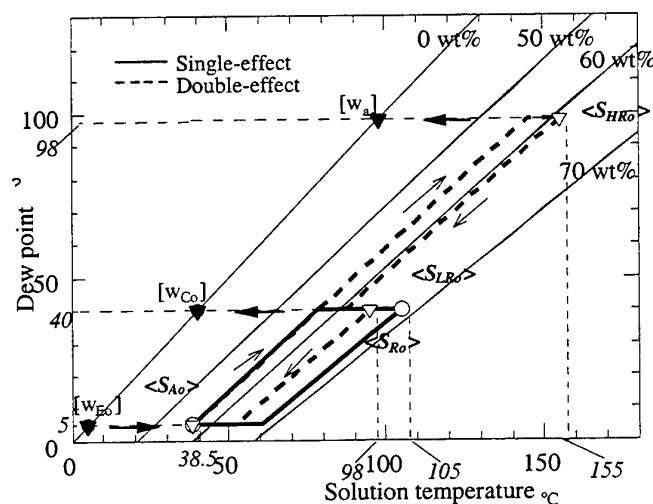


Fig.2 Single- and double-effect absorption cycle in Dühring

3. THERMOPHYSICAL PROPERTIES OF WORKING FLUIDS

Water and LiBr solution are used as the refrigerant and the absorption liquid, respectively. The thermophysical properties of water were those given in the ASME steam table. The specific enthalpy and the boiling point of

the LiBr solution, that is the dühling chart, were those given by McNeely[5]. The specific entropy of the LiBr solution was that given by Koehler et al.[6]. Specific enthalpy, h , entropy, s , and exergy, e , of the LiBr solution are shown in Figs. 3 (a) to (c), respectively. Here, the specific exergy is defined as the following equation.

$$e = h - h_0 - T_0 \times (s - s_0) \quad (1)$$

where T_0 , s_0 is the normalized value of temperature and entropy based on the external condition. Here, the condition of the cooling water at the inlet of the absorber is used, that is, the temperature T_0 is 32 °C and the pressure is 100 kPa. The enthalpy and the entropy of the LiBr solution increase with the temperature. In the concentration range over 50 wt% that is in the range of the ordinary use, the enthalpy increases slightly, but the entropy decreases with the increase of the concentration. The exergy increases with the concentration in this range. The dependence of the exergy on the concentration is greater than that on the temperature.

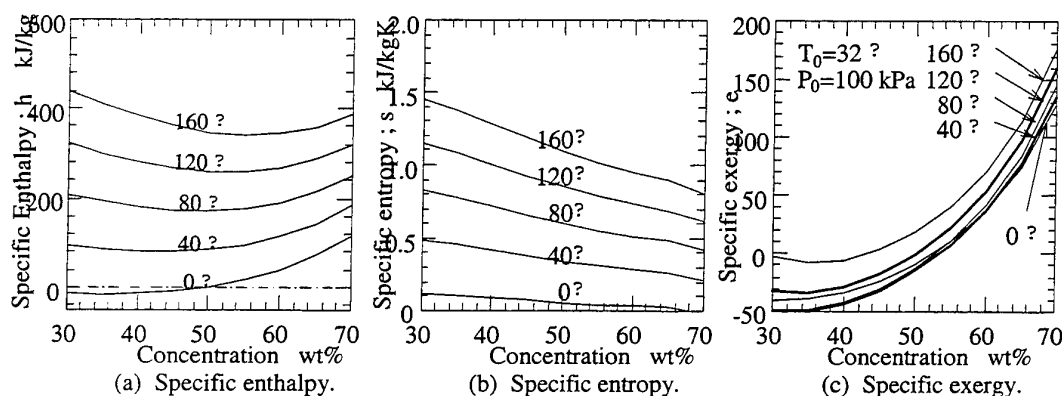


Fig.3 Thermophysical properties of LiBr-water

4. RESULTS AND DISCUSSIONS

4.1 Single-Effect Absorption Cycle.

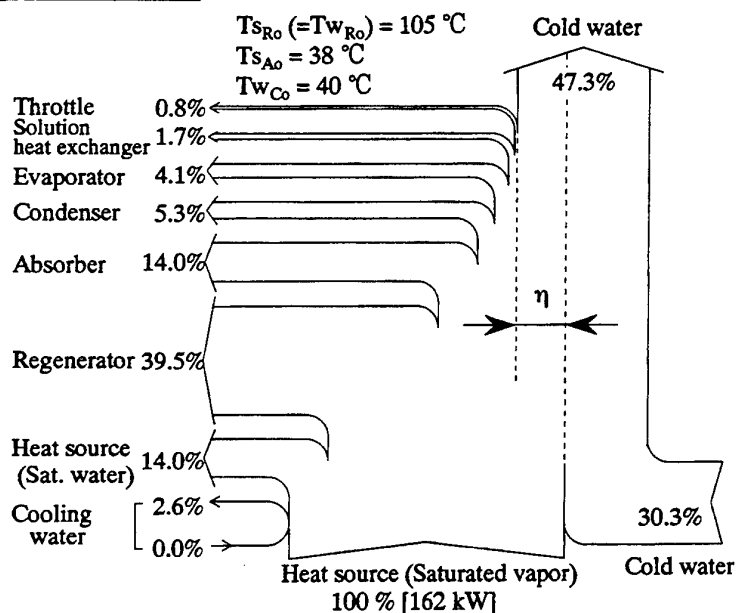


Fig. 4 Flow diagram of exergy of single-effect absorption cycle.

a. Energy flow Figure 4 shows the exergy flow chart of the single-effect absorption cycle with the heat source temperature of 170.4°C at the pressure of 800 kPa. The steam temperature exhausted from the regenerator that is equivalent to the solution temperature in the regenerator is 105 °C. The solution temperature in the absorber is 38.5 °C, so the concentration of the lean solution was 57 wt%. In this figure, the width of each flow is corresponding to the proportion of the exergy input of the steam as the heat source, that is, the width for each component shows the magnitude of the exergy loss. The effective exergy that is the increase in exergy of the chilled water, is about 17.0 % in the single-effect absorption cycle. In this paper, this value is defined as an exergy coefficient, η .

$$\eta = \frac{\text{Effective exergy}}{\text{Exergy input}} = \frac{\Delta e_{\text{chilled water}} \times m_{\text{chilled water}}}{e_{i(\text{heat source})} \times m_{\text{heat source}}} \quad (2)$$

where e is the specific exergy (kJ/kg), Δe is the exergy difference (kJ/kg), and m is the mass flow rate (kg/s). About 14 % of the exergy input is drained with saturated water. The exergy loss of the regenerator is the highest, 39.5 %, of all components because of the large temperature difference between the heat source and the solution in the regenerator. The loss in the absorber is 14.0 %.

b. Effect of condensing temperature on the cycle performance

The effect of the condensing temperature, T_{wCo} , on the cycle performance and exergy loss is shown in Fig.5. Only T_{wCo} is varied from 35 °C to 60 °C. The other conditions are the same as those in Fig.4. The coefficient of performance, COP, is defined as the ratio of cooling load to heat input.

$$\text{COP} = \frac{\text{Cooling load}}{\text{Heat input}} = \frac{\Delta h_{\text{chilled water}} \times m_{\text{chilled water}}}{\Delta h_{L(\text{heat source})} \times m_{\text{heat source}}} \quad (3)$$

where Δh is the difference of specific enthalpy (kJ/kg), and Δh_L is the latent heat (kJ/kg). The COP is about 78 % at the condensing temperature of 40 °C.

For a constant solution temperature in the regenerator, the concentration difference of solution decreases with the increase of the condensing

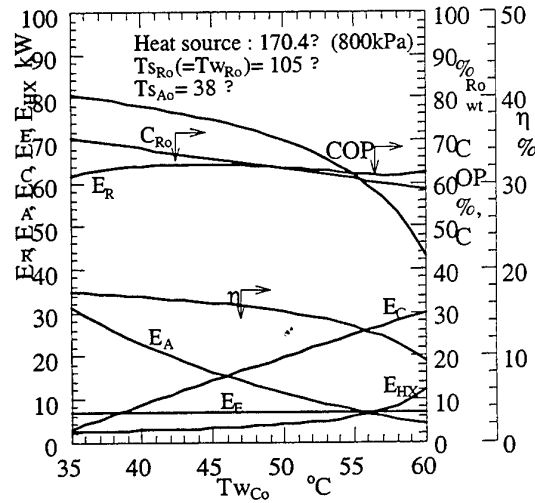


Fig.5 Effect of condensing temperature

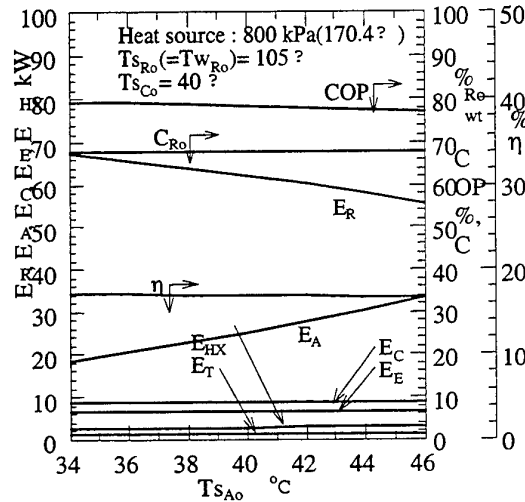


Fig.6 Effect of solution temperature in absorber

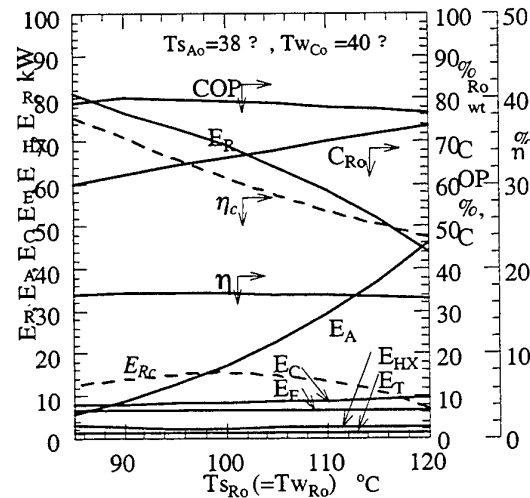


Fig.7 Effect of solution temperature in regenerator

temperature. So the loss in the absorber decreases owing to the decrease of the exergy of the rich solution flowing into the absorber. On the other hand, with the increase of $T_{w_{CO}}$, the loss in the condenser increases owing to the increase of temperature difference between the refrigerant and the cooling water. As the result, the COP and the exergy coefficient increase with the decrease of $T_{w_{CO}}$.

c. Effect of solution temperature in absorber The effect of the solution temperature in the absorber $T_{s_{AO}}$ is shown in Fig. 6. With the increase of $T_{s_{AO}}$, the loss of the absorber increases and that of the regenerator decreases. The effects of $T_{s_{AO}}$ on the COP and the exergy coefficient are little.

d. Effect of solution temperature in regenerator The steam generated in the regenerator is superheated because the solution temperature is higher than the dew point temperature corresponding to the pressure. The respective values calculated are shown in Fig.7 by bold lines under the constant condition of the heat source temperature of 170.4 °C. The broken lines show the results obtained in the case that the temperature difference between the solution and the heat source in the regenerator is 3K, where, in particular, the exergy coefficient and the exergy loss in the regenerator are shown as η_c and E_{RC} . For the constant heat source, the effect of the solution temperature in the regenerator on the COP and the exergy coefficient are a little. Those values of the COP and η are about 80 % and 17%, respectively. However, by using the low level temperature heat source, the exergy coefficient is improved to 38% at the heat source temperature of 88 °C.

4.2 Double-Effect Absorption Cycle.

a. Exergy flow Figure 8 shows the exergy flow chart of the double effect absorption cycle with the heat source temperature of 170.4 °C and the pressure of 800 kPa. The solution temperature in the regenerator and the absorber are 105 °C and 38.5 °C, respectively. For this double-effect absorption cycle, the exergy coefficient η is 23.6%. The summation of the exergy losses of the regenerators is 11.9 % and is lower than that in a single -effect cycle. For the double-effect cycle, the losses of the absorber and the throttle(1) indicated in Fig.1(b) are larger, 14.8 and 12.9%.

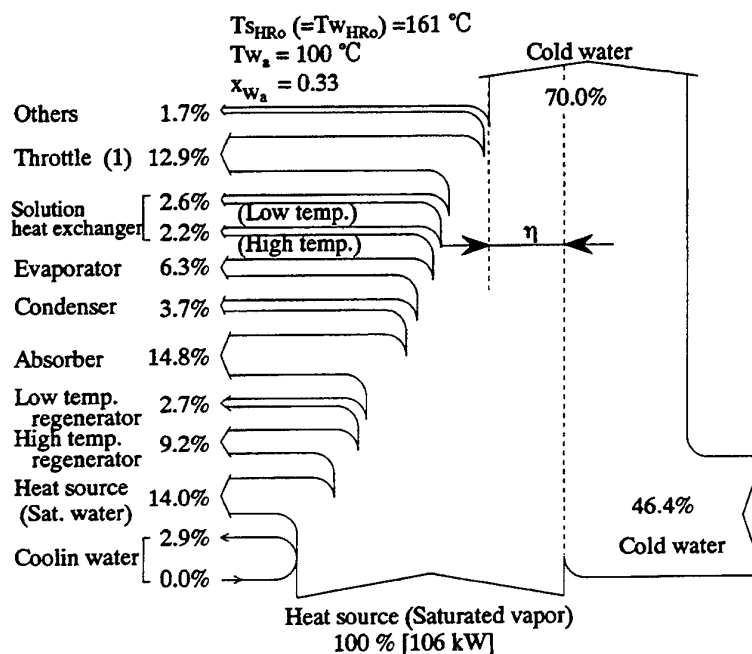


Fig. 8 Flow diagram of exergy of double-effect absorption cycle.

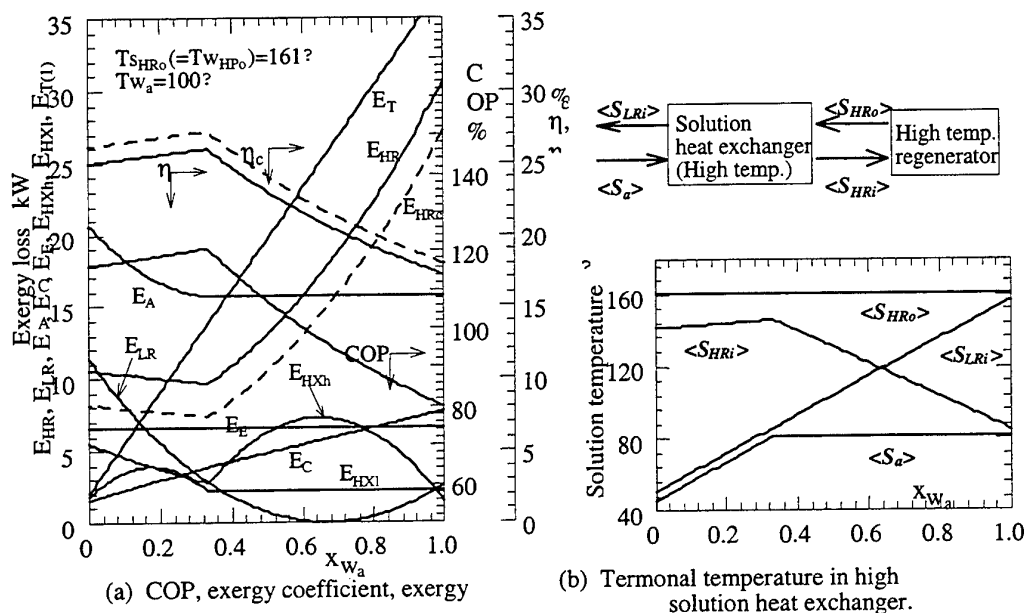


Fig.9 Effect of steam quality of the flow of [Wa]

b. Effect of heat input of low temperature regenerator

Figures 9(a) and (b) show the effect of the steam quality of the flow [Wa] indicated in Fig.1(b) on the cycle performance and the terminal temperatures of the high temperature solution heat exchanger, respectively. The decrease of the quality means the increase of heat transfer rate of the low temperature regenerator and the high temperature solution heat exchanger. It can be seen that there is an optimum condition for the COP and the exergy coefficient against the quality of [Wa]. This condition is achieved by adjusting the heat transfer rate of the solution heat exchanger and the low temperature regenerator. It is necessary to design the terminal temperature differences of the two solution heat exchangers as the minimum value of 5K.

The calculated results of the COP and the exergy coefficient for the varied solution temperature in the high temperature regenerator are shown in Fig.10. In the case that the temperature of [Wa] is constant, the maximum values of the COP and the exergy coefficient increase with the decrease of the solution temperature in the high temperature, and the quality in the maximum value decreases.

The maximum value of the exergy coefficient obtained in Fig. 10 is plotted against the solution temperature in the high temperature regenerator in Fig.11 as a parameter of the steam temperature of the flow "Wa". It can be seen that there is an optimum temperature of T_{Wa} for the temperature of T_{SHRo} , and the maximum value of exergy coefficient is about 30 % for the heat source whose temperature is 170.4 °C. However, if the low level temperature heat source that is fit for the solution temperature in the high temperature regenerator is available, the exergy coefficient is improved to 37% at the heat source temperature of 138 °C.

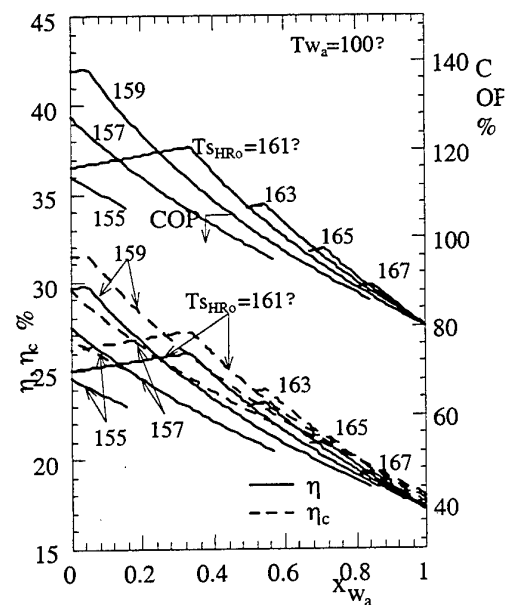


Fig.10 Effect of solution temperature in high temperature regenerator

5 CONCLUSIONS

An analysis based on the heat quality, that is the exergy, was carried out on the single- and double effect LiBr/water absorption refrigerating system with the cooling load of 100 USRT(352 kW) using the saturated steam as the driving heat source. The conclusions are as follows.

- (1) For a single-effect cycle, the effects of the condensing temperature, the solution temperature in a regenerator, and an absorber on the COP are shown.
- (2) The exergy coefficient η for the constant heat source has a quantitative tendency same as the COP. However, if the heat source whose temperature is 3K greater than the solution temperature in the regenerator is available, η increases with a decreasing temperature of heat source.
- (3) For a double-effect cycle, there is an optimum condition of the temperature in low temperature regenerator for the temperature in the high temperature regenerator. It is necessary to optimize the heat transfer rate of the high temperature solution heat exchanger.
- (4) When the temperature of heat source is constant at 170.4 °C, the maximum value of the COPs for the single- and double-effect cycles are 80% and 140 %, respectively. And exergy coefficients for each cycle are 17 % and 30%, respectively.

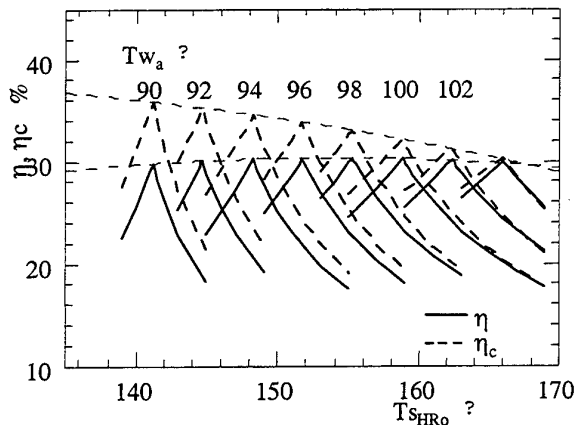


Fig.11 Optimum condition for exergy coefficient

REFERENCES

1. B. Wardono, and R. M. Nelson, "Simulation of a 20-ton LiBr/H₂O Absorption Cooling System.", ASHRAE Trans. , vol.102, Pt.1, (1996), p. 96.
2. C. J. Schweinger, P. Riesch, S. Demmel and G. Alefeld, "A New Absorption Chiller to Establish Combined Cold, Heat, and Power Generation Utilizing Low-Temperature Heat", ASHRAE Trans., vol. 102, Pt. 1, (1996), p. 1118.
3. G. Grossman, M. Wilk and R. C. DeVault, "Simulation and Performance Analysis of Triple-Effect Absorption Cycles.", ASRAE Trans., vol. 100, Pt.1, (1994), p.452.
4. B. Wardono, and R. M. Nelson, "Simulation of a Solar-Assisted LiBr/H₂O Cooling System.", ASHRAE Trans. , vol.102, Pt.1, (1996), p. 104.
5. L. A. McNeely, "Thermodynamic Properties of Aqueous Solutions of lithium Bromide.", ASHRAE Trans., vol. 85, Pt.1, (1979), p.413.
6. W. J. Koehler, W. E. Ibele, J. Soltes and E. R. Winter, "Entropy Calculations for Lithium Bromide Aqueous Solutions and Approximation Equation.", ASHRAE Trans., vol. 93, Pt.2, (1987), p.2379.

THERMALLY DRIVEN HIGH-PERFORMANCE SORPTION HEAT PUMPS

Hans-Peter Klein, Eike Willers, Manfred Groll
Institute for Nuclear Technology and Energy Systems
University of Stuttgart
Email: h.klein@ike.uni-stuttgart.de; Fax: (49) 711-685-2010

Keywords: metal hydride, sorption heat pump, air-conditioning

ABSTRACT. Sorption Heat Pumps are promising devices for the rational and environmentally friendly use of energy. The commonly used working pairs have no Ozone layer Depletion Potential (ODP) and a negligible Global Warming Potential (GWP). In the field of liquid sorption, lithium bromide-water (LiBr-H₂O) and water-ammonia (H₂O-NH₃) machines are commercialized, while among the solid sorption machines only silicagel-water devices are produced in small series. To cover a larger fraction of the potential market, sorption devices need to have a performance close to the overall performance of compression devices, taking into account the efficiency of electricity generation. This is possible by coupling systems operating with different working pairs. A topping cycle allowing its waste heat to drive a bottoming device increases the efficiency significantly, and thus contributes to a higher competitiveness of the sorption technology. Some materials have the potential to be used in a topping cycle for providing simultaneously cold and high temperature waste heat to a bottoming cycle. Suitable materials are ammonia salts and metal hydrides, which cover a large temperature range from very low to very high temperatures. Favourable materials for bottoming cycles are silicagel-water and lithium bromide-water. In this paper various combinations of topping/bottoming cycles and machine schemes are compared.

1. INTRODUCTION

Over the last years, various thermally driven sorption machines using different working pairs have been investigated with respect to cooling and heating applications. They can be attractive systems for the rational and environmentally friendly use of energy, especially if the driving heat is low grade or waste heat. Sorption machines can be divided into two groups, the liquid sorption and the solid sorption systems. Examples for liquid sorption systems are lithium bromide-water or water-ammonia. Examples for solid sorption systems are silicagel-water, zeolite-water, salt-ammonia or metal-hydrogen. The currently developed or commercially produced systems have, however, low efficiencies compared to commercially available compression systems, even when more complex machine schemes like double-stage or triple-effect are used. To cover a larger fraction of the potential market, sorption devices need to have a performance close to the overall performance of compression devices, taking into account the efficiency of electricity generation. This is possible with multi-effect systems, which means the coupling of different sorption systems. Therefore a sorption system, capable of producing heat and cold is used as a topping cycle, delivering its released heat at sufficiently high temperature as driving heat to another sorption system that acts as bottoming cycle. However, if sorption systems with different working pairs are coupled, some points have to be considered. The most important one is the temperature at which the topping systems releases the heat that is used for driving the bottoming system and if there is a temperature drop during the cycle time. Other questions are, whether the coupled systems are continuously or periodically operating systems and whether the heat exchange between them should be realized directly with a heat exchanger or employing a heat storage system.

Typical applications for sorption systems are deep-freezing, ice-making, air-conditioning or heat pumping [1]. Examples of sorption systems have been described in [1,2,3] and the coupling of a ammonia-salt and metal hydride system has been discussed in [4], showing a high flexibility concerning temperature range and part load behaviour. In this paper we will focus on cold production for air-conditioning purposes with water as heat transfer fluid for the cold source. The low temperature waste heat of the systems is released to the environment. Therefore the internal operating temperatures (temperatures of the reaction beds) can be set to 2 to 7 °C for cold production and 30 to 35 °C for the temperature of the low temperature heat source.

2. DESIGN OF METAL HYDRIDE HEAT PUMPS

Some metals, respectively metal alloys, are able to form metal hydrides by uptaking hydrogen. This reaction is reversible and heat is released during the absorption of hydrogen while during the desorption of hydrogen heat

has to be provided to the hydride. This allows the use of metal hydrides in heat storage systems or in sorption heat pump systems providing heat and/or cold. Various metal hydride systems have been investigated [5], especially with respect to their application as air-conditioning systems. The great advantage of these systems is, that they are adjustable to a wide range of temperature profile demands, because metal hydrides are available with equilibrium temperatures (for 1 bar pressure) between 160 and 800 K.

Single-Stage System

The simplest machine scheme of a metal hydride heat pump is the single-stage system. It comprises two pairs of reactors, containing two different metal hydrides A and B (Fig. 1). In each pair, the hydrides A and B are coupled on the hydrogen side. One pair is at a high pressure level, the other at a low pressure level. In this system, a driving heat of temperature T_H is used to desorb hydrogen from reactor A1 which is absorbed in reactor B1 thereby providing heat at a temperature T_M . Simultaneously cold of temperature T_C is used to desorb hydrogen from reactor B2 which is absorbed in reactor A2 again providing heat at a temperature T_M . This system operates quasi-continuously with two half-cycles. Between these two half-cycles, hydride A1 has to be cooled from T_H to T_M and hydride A2 has to be heated from T_M to T_H , hydride B1 has to be cooled from T_M to T_C and hydride B2 has to be heated from T_C to T_M . Owing to this periodic absorption-desorption process, the performance of the system can be increased by internal heat recovery. For example, before applying the driving heat Q_H to hydride A2 and generating the useful heat Q_{M1} , one can separate the heat source and sink from the reactors and pump the heat transfer fluid in a closed loop through the reactors A1 and A2. This internal heat recovery becomes the more important the higher the temperature lift of one hydride is. The internal heat recovery rate cannot be higher than 50 %. However, the sensible heat of the hydride A1 that is cooled down to $(T_H+T_M)/2$ is still used for providing Q_{M1} . Theoretical cooling temperatures between 10 °C and -50 °C can be obtained with the single stage system. For air-conditioning purposes, temperatures between 7 and 2 °C are suitable. The driving temperatures have not to be very high (e.g. 90 to 130 °C).

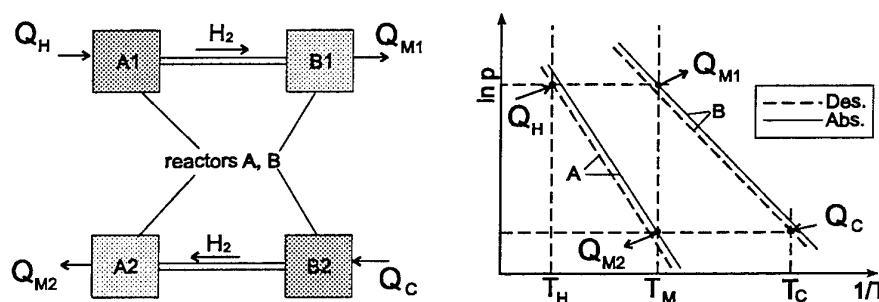


Fig. 1. The metal hydride single-stage system

For COP calculation, the amounts of heat transferred to or from the reaction beds have to be determined. In the case of the single-stage system, they correspond exactly to the heat that is delivered to the system by the heat exchangers, if the thermal losses through tubing between the reaction beds and heat exchangers are neglected.

The calculation is based on an internal heat recovery rate ϕ and an exchange of n_{H_2} moles of hydrogen. Thus the amount of driving heat is

$$Q_H = n_{H_2} * \Delta H_{A,DES} + (1 - \phi) * c_{P,RB} * m_{RB} * (T_H - T_M) \quad (1)$$

the amount of useful cold is

$$Q_C = n_{H_2} * \Delta H_{B,DES} + (1 - \phi) * c_{P,RB} * m_{RB} * (T_M - T_C) \quad (2)$$

and the amount of useful heat is

$$Q_M = n_H 2 * \Delta H_{A,ABS} + (1-\phi) * C_{P,RE} * m_{RB} * (T_H - T_M) \quad (3)$$

$$+ n_H 2 * \Delta H_{B,ABS} - (1-\phi) * C_{P,RE} * m_{RB} * (T_M - T_C)$$

Double-Stage System

Another metal hydride system is the double-stage system. It employs three different metal hydrides A, B and C. In a special star-scheme design (Fig. 2), there are six interconnected reactors (A1, A2, B1, B2, C1, C2). Each hydride is connected with the other two hydrides on the hydrogen side. All reactors are simultaneously in operation. Between each pair of coupled reactors there is one hydrogen valve. The star-scheme operates in two half-cycles and allows a quasi-continuous cold and heat generation. Three different temperature levels are at least necessary: T_H as heat source (driving heat), T_M as heat sink (useful heat) and T_C as low temperature heat source (useful cold). This system is appropriate for high COPs. There is a large temperature difference required between T_H and T_M . In each half-cycle, driving heat is put in once, useful heat is generated three times and useful cold is obtained twice. The van't Hoff diagram of the double-stage system is shown in Fig. 3.

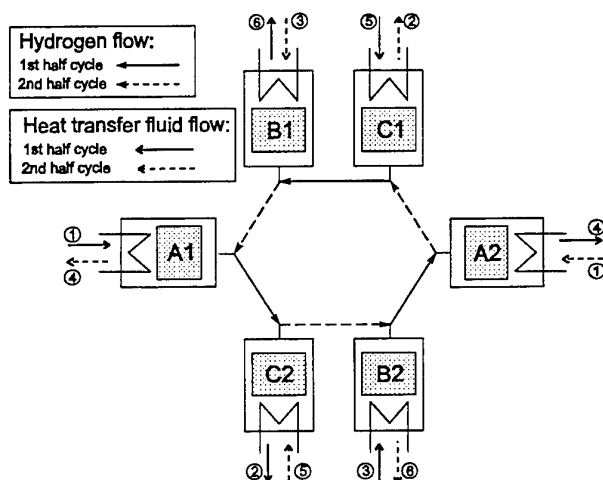


Fig. 2. The double-stage star-scheme

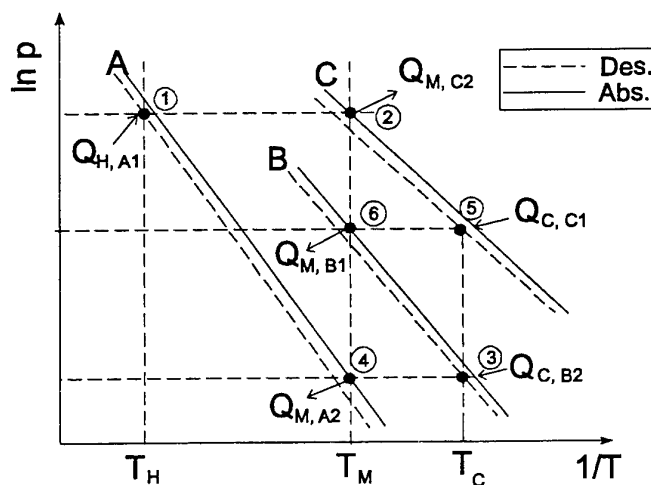


Fig. 3. The van't Hoff diagram of the double-stage star-scheme

In the first half cycle, the hydride A1 is desorbed by the driving heat $Q_{H, A1}$ at temperature T_H . It is coupled on the hydrogen side with hydride C2 where the absorption heat $Q_{M, C2}$ at temperature T_M is released. Hydride B2 is desorbed by the heat $Q_{C, B2}$ (useful cold) at temperature T_C . It is coupled on the hydrogen side with hydride A2 where the absorption heat $Q_{M, A2}$ at temperature T_M is released. Hydride C1 is also desorbed by the heat input $Q_{C, C1}$ at temperature T_C . It is coupled on the hydrogen side with hydride B1 where the absorption heat $Q_{M, B1}$ at temperature T_M is released. After the first half-cycle an internal heat recovery between A1 and A2, between B1 and B2 and between C1 and C2 takes place. Now the hydrogen valves and fluid valves are switched and the second half-cycle with the following processes starts

A2 desorbs by $Q_{H, A2}$ at T_H and C1 absorbs $Q_{M, C1}$ at T_M .

B1 desorbs by $Q_{C, B1}$ at T_C and A1 absorbs $Q_{M, A1}$ at T_M .

C2 desorbs by $Q_{C, C2}$ at T_C and B2 absorbs $Q_{M, B1}$ at T_M .

Because there is always a large difference between the highest and the lowest temperature level, it is very difficult to find a suitable heat transfer fluid which covers the whole temperature range and provides good heat transfer and thermodynamic characteristics. For the cold side (hydrides B and C), water or water-glycol are the best solutions as heat transfer fluid, while oil is more appropriate for the hot side (hydride A). For COP calculation, the amounts of heat transferred to or from the reaction beds have to be calculated. The amount of driving heat is

$$Q_H = n_{H_2} * \Delta H_{A,DES} + (1 - \phi) * c_{P, RB, A} * m_{RB, A} * (T_H - T_M) \quad (4)$$

the amount of useful cold is

$$Q_C = n_{H_2} * \Delta H_{B,DES} - (1 - \phi) * c_{P, RB, B} * m_{RB, B} * (T_M - T_C) \\ + n_{H_2} * \Delta H_{C,DES} - (1 - \phi) * c_{P, RB, C} * m_{RB, C} * (T_M - T_C) \quad (5)$$

and the amount of useful heat is

$$Q_M = n_{H_2} * \Delta H_{A,DES} - (1 - \phi) * c_{P, RB, A} * m_{RB, A} * (T_H - T_C) \\ + n_{H_2} * \Delta H_{B,DES} - (1 - \phi) * c_{P, RB, B} * m_{RB, B} * (T_M - T_C) \\ + n_{H_2} * \Delta H_{C,DES} - (1 - \phi) * c_{P, RB, C} * m_{RB, C} * (T_M - T_C) \quad (6)$$

Double-Effect System

The double-effect system requires 3 different metal hydrides (A, B, C) in four reactors (A, B, C₁, C₂) and four different temperature levels. As shown in Fig. 4, the reactors C₁ and B, respectively C₂ and A, are coupled on the hydrogen side.

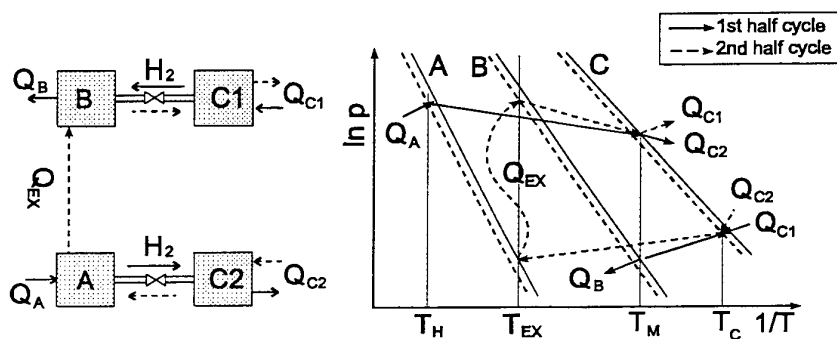


Fig. 4. The double-effect system

In the first half-cycle, A is desorbed by the driving heat input at temperature T_H , while C_2 produces heat at temperature T_M . At the same time, C_1 takes up desorption heat (cold) at the low temperature T_C , while the released hydrogen is taken up by B which releases heat at temperature T_M . After an internal heat recovery, the second half-cycle starts. C_2 is desorbed by the cold input at T_C . The released hydrogen is taken up by A, which releases the heat Q_{EX} at temperature T_{EX} . This heat is completely used for the desorption of B, which is coupled with the absorbing C_1 that releases heat at temperature T_M . During one full cycle, driving heat has to be put in once, useful cold is produced twice and useful heat is generated three times. The amount of driving heat is

$$Q_H = n_{H_2} * \Delta H_{A,DES} + (1 - \phi) * c_{P,RB,A} * m_{RB,A} * (T_H - T_{EX}) \quad (7)$$

the amount of useful cold is

$$Q_C = n_{H_2} * \Delta H_{C1,DES} - (1 - \phi) * c_{P,RB,C1} * m_{RB,C1} * (T_M - T_C) \\ + n_{H_2} * \Delta H_{C2,DES} - (1 - \phi) * c_{P,RB,C2} * m_{RB,C2} * (T_M - T_C) \quad (8)$$

and the amount of useful heat is

$$Q_C = n_{H_2} * \Delta H_{B,DES} - (1 - \phi) * c_{P,RB,B} * m_{RB,B} * (T_{EX} - T_M) \\ + n_{H_2} * \Delta H_{C1,DES} - (1 - \phi) * c_{P,RB,C1} * m_{RB,C1} * (T_M - T_C) \\ + n_{H_2} * \Delta H_{C2,DES} - (1 - \phi) * c_{P,RB,C2} * m_{RB,C2} * (T_M - T_C) \quad (9)$$

Driving Temperatures and Coefficients of Performance

The usefulness of the discussed machine schemes with metal hydrides for topping and bottoming cycles will be evaluated. The COP for cooling (Coefficient of Performance) of a coupled sorption system comprises of two parts. The first is the COP for cooling of the topping cycle and the second is the COP for cooling of the bottoming cycle multiplied with the COP for heating, in the following referred to as COA (Coefficient of Heat Amplification), of the topping cycle, thus leading to:

$$COP_{OVERALL} = COP^{TOPPING} + COP^{BOTTOMING} * COP^{TOPPING} \quad (10)$$

The individual COPs and COAs have to be discussed as a function of related temperatures (Table 1).

Table 1. Temperatures and COPs of metal hydride systems

	Bottoming Cycle				Topping Cycle			
	Single-Stage		Double-Stage	Double-Effect	Single-Stage	Double-Stage	Double-Effect	Triple-Effect
T_H [°C]	95	105	165	160	245	280	370	360
COP	0.65	0.7	1.1	1.2	0.5	0.95	0.9	1.2
T_M [°C]					85	100	100	100
COA					1.3	0.85	0.8	0.8

From the description of the different metal hydride machine schemes it is obvious, that not all metal hydride schemes can be used as a bottoming cycle in a coupled system. Double-stage and double-effect systems need a minimum driving temperature of at least 160 °C. Triple-effect or multi-hydride systems need at least 240 °C. There are some other sorption systems which can provide those temperatures, but their efficiencies for cooling

as well as heat pumping are rather low. Therefore only single-stage systems are suitable for the use as a bottoming cycle. Those single-stage systems can be operated with driving temperatures between 90 and 130 °C; the maximum COPs that can be obtained are in the range of 0.5 to 0.7. Therefore the topping cycle must have a COP of around 0.8 and a COA of 1.1 to obtain an overall efficiency for cooling of 1.6. But again it is difficult to design a sorption system which fulfills these conditions.

If, on the other hand, the use of metal hydride systems as a topping cycle is considered, the results are more promising. The requirements are a high temperature of the released heat and either a very good COP or a very good COA. In principle, every machine scheme can be used as topping cycle. However, if a single-stage system is used, there are no hydrides available which can deliver good efficiencies for the given thermal boundary conditions, and at the same time operate at pressure levels below 100 bar. Multi-hydride systems have also some disadvantages. The heat is not released at a constant temperature and the maximum COPs are around 0.9. To get good COAs, the driving temperature has to be in the range of 400 to 500 °C which is difficult to handle with oil as heat transfer fluid. However, double-effect, triple-effect and double-stage systems or their combinations can fulfill the requirements for topping cycles.

3. COUPLED SORPTION SYSTEMS

Metal Hydrides for Bottoming Cycles

Sorption systems like lithium bromide-water, silicagel-water, zeolite-water and salt-ammonia have the same problems like metal hydride systems, when they are used as topping cycles, i.e. if heat at a temperature above 150 °C should be released. Then the COPs and COAs are rather low. Therefore the bottoming cycle should have a driving temperature as low as possible. Then, e.g. for driving temperatures of 95 to 105 °C, a metal hydride single-stage system can have COPs of 0.65 to 0.7 and would be a suitable candidate as a bottoming cycle. The calculation of these values has taken into account the thermal masses of the used hydrides and an internal heat recovery of 40 %. Heat losses, the thermal masses of reactors, heat transfer fluids and hydrogen have not been considered.

Zeolite-water or salt-ammonia systems can be used as topping cycles. A zeolite-water system with a driving temperature of 310 °C, providing heat at a temperature of 100 °C can reach a COP of 0.53 and a COA of 1.53. Coupling with an appropriate metal hydride system with a driving temperature of 95 °C and a COP of 0.65 could result in an overall COP of 1.53. With the same metal hydride system, a salt-ammonia system with a driving temperature of 290 °C and a COP of 0.25 and a COA of 1.17 can reach an overall COP of 1.05 (Table 2).

Table 2. Overall COPs for metal hydride bottoming cycles

Metal Hydride Single-Stage $T_H=95^{\circ}\text{C}$ COP=0.65	Zeolite-Water $T_H=310^{\circ}\text{C}$ $T_M=100^{\circ}\text{C}$	Salt-Ammonia $T_H=290^{\circ}\text{C}$ $T_M=100^{\circ}\text{C}$
COP	0.53	0.25
COA	1.53	1.17
COP _{OVERALL}	1.53	1.01

Metal Hydrides for Topping Cycles

If metal hydride systems are used as topping cycles, silicagel-water or lithium bromide-water can be used as bottoming cycles. For example, silicagel-water systems can be driven with a temperature between 80 to 100 °C providing a COP between 0.5 and 0.65, lithium bromide-water systems can reach COPs up to 0.75 within the same driving temperature ranges. A metal hydride double-stage system with a driving temperature of 280 °C and a temperature of the released heat of 100 °C can provide a COP of 0.95 and a COA of 0.85. With the above-mentioned silicagel-water bottoming system that have a COP of 0.63 for a driving temperature of 95 °C, an

overall COP of 1.49 can be reached. With the lithium bromide-water system that has a COP of 0.7 at a driving temperature of 95 °C, an overall COP of 1.55 can be reached. If instead of the double-stage metal hydride system a double-effect system is used with a driving temperature of 370 °C, a temperature of the released heat of 100 °C and COP=0.9 and COA=0.8, the overall COP of a coupled hydride-silicagel system would reach 1.4, and the overall COP of a coupled hydride-lithium bromide system would reach 1.45. If a triple-effect metal hydride system is used with a driving temperature of 360 °C, a temperature of the released heat of again 100°C and a COP of 1.2 and a COA of 0.8, then it is possible to reach an overall COP of 1.7 for a silicagel bottoming cycle and an overall COP 1.75 of for a lithium bromide bottoming cycle (Table 3).

Table 3. Overall COPs for metal hydride topping cycles

COP _{OVERALL}	Double-Stage T _H =280°C COP=0.95 COA=0.85	Double-Effect T _H =370°C COP=0.9 COA=0.8	Triple-Effect T _H =360°C COP=1.2 COA=0.8
Silicagel-Water T _H = 95°C COP=0.63	1.49	1.4	1.7
Lithium Bromide-Water T _H = 95°C COP=0.7	1.55	1.45	1.75

4. COUPLING PROBLEMS

Through the coupling of different sorption systems, it is possible to obtain very good COPs for cooling. However, there are some points that have to be considered. If the temperature of the heat output of the topping cycle varies over the cycle time, there can be the problem that the COP of the bottoming cycle also varies because most of the sorption systems can't provide a constant COP if either the driving temperature or the temperatures of the heat sink and cold source vary. Even if those temperatures can be held constant, it is still possible that the performance decreases towards the end of the cycle, since the reaction enthalpy is not only a function of temperature and pressure but also a function of the concentration of the solvent. It can also occur that the sorption reaction slows down at the end of a cycle due to reaction kinetics. Another point is the kind of operation of a system. Metal hydride and salt-ammonia systems are operated periodically. That means, during the internal heat recovery between two half-cycles, there is no cold and heat output. On the other hand, a continuously operated system like lithium bromide-water needs a continuous driving heat input to maintain cold production. Therefore the coupling of systems with different operation modes requires a heat storage system. If two sorption systems with the same operation mode are coupled, their half-cycle times have to be adjusted very carefully to each other.

5. CONCLUSION

With the coupling of two different types of sorption systems it is possible to obtain an overall cooling efficiency, which is in the range of commercially available compression cooling devices, if the efficiency of electricity generation is considered. The best use of metal hydride systems in such coupled systems is as topping cycle. From the examined systems, the most promising one can reach a cooling efficiency of 1.2 and an efficiency for heat pumping of 0.8. The temperature of the output heat is around 100 °C. Therefore it is possible to use the released heat to drive a single-effect lithium bromide-water absorption cooling device or a silicagel-water adsorption cooling device and obtain overall cooling efficiencies of about 1.75 respectively 1.7. Still further research is required with respect to the optimization of the individual systems and for the realization of the practical coupling of two systems.

ACKNOWLEDGEMENT

This work is financially supported by the Commission of the European Union in the frame of the JOULE-III-programme 'Non-Nuclear Energy'.

NOMENCLATURE

c_p	specific heat capacity	$J\ kg^{-1}\ K^{-1}$
COA	coeff. of performance, heating	
COP	coeff. of performance, cooling	
HTF	heat transfer fluid	
m	mass	kg
n	number of moles	
Q	heat	J
T	temperature	K, °C

Indices

A	reactor A
Abs	absorption
B	reactor B
C	reactor C
C	cooling
Des	desorption
EX	internal heat exchange
H	driving
M	heating
RB	reaction bed

Greek letters

ΔH	reaction enthalpy	$J\ mol^{-1}$
ΔT	temperature difference	K
ϕ	internal heat recovery rate	%

REFERENCES

- 1 M. Pons et al., "Thermodynamic based Comparison of Sorption Systems for Cooling and Heat Pumping", Int. J. Refr., n.22, pp.5-17 (1999).
- 2 P.Lamp and F. Ziegler, "Comparison of different Liquid and Solid Sorption Systems with Respect to Low Temperature Driving Heat", *Proc. Int. Conf. Absorption Heat Pumps, v.1, pp.269-276, Montreal (1996).*
- 3 F. Ziegler et al., "A Contribution to the Evaluation of the Economic Perspectives of Absorption Chillers", Int. J. Refr., n.22, pp.47-58, (1999).
- 4 E. Willers and M. Groll, "Coupled Ammonia Salt/Metal Hydride System for Heat and Cold Management in Buildings", *Proc. Int. Symp. Air-Conditioning in High Rise Buildings, v.2, pp.521-526, Shanghai (1997).*
- 5 E. Willers and M. Groll, "Evaluation of Metal Hydride Machines for Heat Pumping and Cooling Applications", Int. J. Refr., n.22, pp.67-76 (1999).

HEAT AND MASS TRANSFER OF A FLUIDIZED BED PACKED WITH ORGANIC POWDER TYPE ADSORPTION MATERIAL

Hideo Inaba, Akihiko Horibe,
Kiyohiro Kameda and Naoto Haruki

The graduate School of Natural Science and Technology
Okayama University
Email: inaba@mech.okayama-u.ac.jp; Fax : (086)-251-8266

Takahisa Kida

Japan Exran kogyo Co. Ltd.
Email: kida@exlan.co.jp; Fax : (086)-942-9853

Keywords: organic adsorbent, sodium polyacrylate, water vapor, fluidized bed,
transient adsorption characteristics

ABSTRACT. The present paper has dealt with the transient adsorption characteristics of the organic powder type adsorbent in a fluidized bed. The organic powder type adsorbent was made from the bridged complex of sodium polyacrylate and its diameter ranged from 30 μm to 48 μm . The measured results of adsorption isotherm equilibrium revealed that the mass ratio of the present organic adsorbent adsorbed water-vapor to the adsorbent dried were 1.3 to 2.3 times larger than that of silica gel adsorbent in the relative air humidity range from 3 to 80%. The humid air was used as a working fluid for transient experiments. The test organic powder type adsorbent was fluidized in a rectangular vessel by flowing the air from its bottom. The adsorption rate of water-vapor and the variation of the air temperature in the adsorbent bed with time were measured under various inlet air temperatures and humidity and air flow rates. The completion time for the adsorption process was increased with decreasing air temperature and increasing the relative air humidity and the air flow rate. It was observed that the adsorption process of passing a moist air into the organic adsorbent bed was the isoenthalpy change. The data of Sherwood number for mass transfer in the present adsorption experiments were correlated by means of modified Reynolds number, Schmidt number and other non-dimensional parameters.

1. INTRODUCTION

In recent years, the rapid increase of energy demand has been brought about by increasing energy usage in people's living and transportation categories. The major part of thermal energy demanded for domestic air heating and cooling and hot water supply was classified as a low temperature energy below 100 °C. On the other hand, the dependency on the fossil fuel, which produces the green house gas, has been increasing at its low price. One of the settlements of this problem is to utilize effectively the abundant waste heat energy at low temperature, which has been produced in the manufacturing and peoples' living processes. This type of the unused heat energy has been classified into hopefully new energy source, which is cost free and harmless to the environment. Therefore, one of the candidate heat conversion machines, which is suitable to low temperature heat source and has lesser load on the environment, is an adsorption refrigerator instead of a vapor compression refrigerator or heat pump using harmful refrigerants. The inorganic adsorbents such as silica gel and zeolite etc. have been used in general for an adsorption refrigerator. However, this adsorption heat cycle has been pervaded to a lesser extent due to degradation phenomenon of powdering the inorganic adsorbents caused by expansion and shrinkage of the adsorbents under the adsorption and desorption processes.

One of the suitable adsorbents for solving this problem against the inorganic adsorbents is an organic adsorbent like adsorption polymers. One of the candidate adsorption polymers is a bridged complex of sodium polyacrylate. This bridged complex containing the carboxyl group as water vapor adsorption site has abilities to have larger adsorption capacity as compared with silica gel.

The objective of this paper is to reveal the static and dynamic characteristics of powder type organic adsorbent of the bridged complex of sodium polyacrylate. The physical properties and adsorption isotherm equilibrium have been investigated as the static characteristics of the present adsorbent. The transient adsorption characteristics of the present organic powder type adsorbents have been examined by flowing the moist air into

the fluidized bed packed with them.

2. DESCRIPTION OF POWDER TYPE SODIUM POLYACRYLATE AS AN ORGANIC ADSORBENT

Figure 1 shows the adsorption isotherm of the present adsorbent for various temperatures. Where p_w/p_s means the relative humidity, p_w corresponds to the water vapor pressure and p_s corresponds to the water vapor saturation pressure, m_w/m_o means the mass ratio of adsorbed water vapor, m_w to the dried polymer adsorbent, m_o . In Fig.2, it is noticed that the data of m_w/m_o for the present powder type adsorbent are 1.3 to 2.3 time greater than those for silica gel indicated by hatching line at 30°C. It is also seen that the data of m_w/m_o for the present adsorbent increase with an increase of p_w/p_s , and its increasing rate of m_w/m_o is remarkable in the range of $p_w/p_s > 0.6$.

The following correlation equation of m_w/m_o was derived in terms of the relative humidity, p_w/p_s and the temperature ratio of T/T_o ($T_o = 273.15$ K) within the relative deviation of $\pm 9.8\%$ by using the least mean squares method.

$$m_w/m_o = 0.635 \times (p_w/p_s)^{0.800} (T/T_o)^{-1.53} \quad (1)$$

Applicable ranges in Eq.(1) are as follows:

$$p_w/p_s = 0.02 \sim 0.88 \text{ and } T/T_o = 1.02 \sim 1.36 \text{ } (\theta = 5 \sim 70^\circ\text{C}).$$

Figure 2 presents the relationship between the average diameter d_m of the present powder adsorbents and m_w/m_o . From the data of d_m in Fig.3, it is revealed that the d_m increases monotonously with increasing m_w/m_o due to the expansion of the present organic adsorbent by adsorbing water vapor. The correlation equation of d_m was expressed in terms of m_w/m_o within the relative deviation of ± 3 as follows;

$$d_m = 31.0 \times (m_w/m_o) + 30.1 \times 10^{-6} \quad (2)$$

Applicable range in Eq.(2) is $m_w/m_o = 0 \sim 0.8$.

3. TRANSIENT ADSORPTION CHARACTERISTICS OF THE POWDER TYPE ORGANIC ADSORBENT

Experimental apparatus and procedure

Transient adsorption experiments were carried out by passing the moist air into the fluidized rectangular bed as indicated in Fig.3, which showed the schematic diagram for the experimental apparatus. The experimental apparatus consisted of an air compressor and air flow meter as air supply control system, after-cooler, air purifier, air moisture and temperature controllers as air quality control system, and the fluidized rectangular bed packed with the present powder type organic adsorbent. The temperature and relative humidity of moist air as a adsorbate in the present experiments could be controlled in the ranges of $\theta = 10 \sim 70^\circ\text{C}$ and $p_w/p_s = 0.02$ (2%RH) ~ 0.8 (80%RH), respectively. The compressed air at a desired pressure from an oil-less air compressor (a regular output power of 2.5 kW, a maximum output pressure of 0.81 MPa and a maximum air flow rate of $4 \times 10^{-3} \text{ m}^3/\text{s}$) went through the air purifier after controlling air flow rate with a flow control valve. The air purifier system was composed of an air filter capable of eliminating the dust over $0.3\mu\text{m}$ in diameter and micro-mist-filter capable of eliminating the fine dust over $0.01\mu\text{m}$ in diameter. The moisture and temperature of the purified air could be controlled by the moisture and temperature control units. The moisture control unit consisted of the dehumidifier made of fine polymer films capable of obtaining dry air, the humidifier capable of water-vapor saturation air and two adjusting valves for the air flow rate control. The air was humidified at a water-vapor saturation condition of the desired temperature by passing air bubbles into the humidifier, which consisted of the hot water layer in a cylindrical vessel packed with fine spherical balls as a air bubble distributor. The temperature of the hot water in the humidifier could be controlled by adjusting output electric power of an electric heater with a PID control unit. In the case of low humidity experiments, the film dehumidifier was used to control the air humidity. While the air humidity control for high humidity experiments was performed by using together the humidifier and the dehumidifier. The air temperature control unit consisted of a cylindrical stainless steel vessel covered with the thermal insulation material and an electric heater (maximum electric

output of 1.5 kW), and its air temperature was adjusted at the desired temperature by using a PID controller. The flow rate of the air was measured with a rota-meter (measuring range of 1.2 ~ 6.0 m³/s, measuring accuracy of ± 0.05 m³/s).

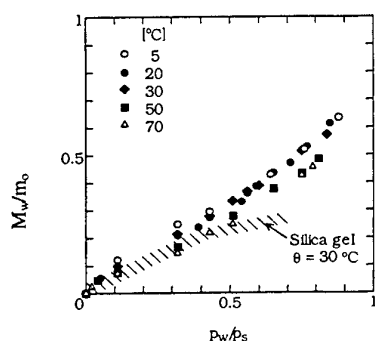


Fig. 1. Adsorption isotherm

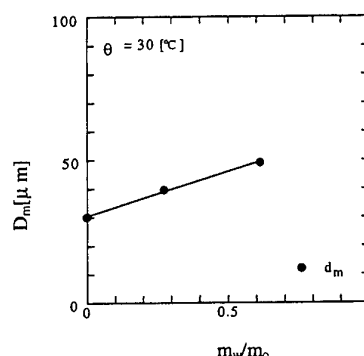


Fig. 2. Variations of dimensions of adsorbent with m_w/m_0

The fluidized rectangular bed packed with the present powder type adsorbent as shown in Fig. 4 was constructed by a transparent acrylic resin plate (5 mm in thickness), whose inside dimensions were 450 mm in height x 150 mm in depth x 150 mm in width. The fluidized rectangular bed was covered with thermal insulation material of 50 mm in thickness to avoid the heat-loss from the bed to the environment. The air flow could be uniformly distributed in the fluidized bed by using the film distributor made of polymer film-filter (pore size of 2 μ m) which was mounted on the bottom of the bed. The same type of polymer-film-filter was set at the upper part of the fluidized bed to avoid flowing out the powder type adsorbent. The temperature, humidity and pressure of the humid air in the inlet and outlet of the fluidized bed were measured with K type thermocouples (0.1 mm in diameter, measuring accuracy of ± 0.1 °C), static electricity type hygrometers (measuring accuracy of ± 0.5 %RH) and mano-meters (measuring accuracy of ± 2 Pa), respectively. The temperature distribution of the air in the fluidized bed was measured with four T type thermocouples set in the bed, and the heat-loss from the bed to the environment was measured by the heat flow meter (measuring accuracy of ± 10 W/m²) mounted on the

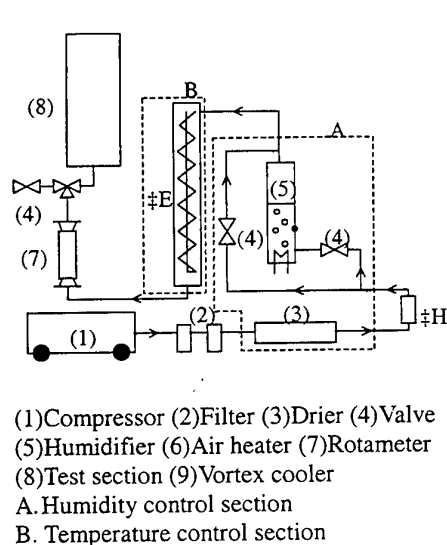


Fig. 3. Schematic diagram of apparatus

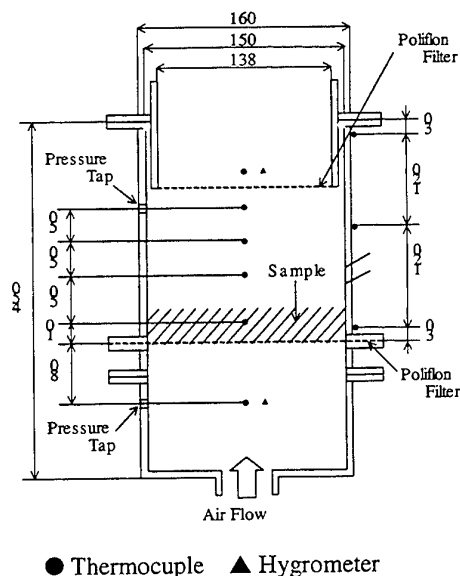


Fig. 4. Detail of test section

outside wall of the rectangular bed. The maximum ratio of the heat-loss to the total heat input to the fluidized bed was estimated to be not more than 2%. The amount of adsorbed water vapor into the adsorbent was

evaluated at a certain time interval by comparing the total mass of the test adsorbent adsorbed water vapor, which was sampled by about 0.5 g from a small port drilled in the side wall of the fluidized bed and the mass of the same sampled adsorbent dried at 120 °C during 48 hours in a dry oven. Those masses were measured with a precision electric balancer (measuring accuracy of ± 5 mg). During sampling the adsorbent from the fluidized bed, the airflow in the bed was stopped by operating the three-way valve. All data of temperatures and humidity were recorded with a data acquisition system consisted of a personal computer. The time interval for data record was controlled during the experiments according to experimental conditions.

Pressure Drop Characteristics of the Fluidized Bed Packed With the Powder Type Organic Adsorbent

Figure 5 shows the variation of pressure drop Δp of the fluidized bed packed with the powder type organic adsorbent in an initial height of 0.01 m with superficial air flow velocity u_o for two air relative humidities of $p_w/p_s = 0.05$ and 0.6. Here, the air relative humidity p_w/p_s means the air humidity condition when the adsorbent reaches the adsorption equilibrium. The solid and the dotted lines in Fig.5 are derived from the previous correlation equations of the fixed bed [2] and the fluidized bed [3]. The pressure drop Δp is the net pressure loss of the fluidized bed, which could be estimated by subtracting both pressure losses of two fine film filters set between the fluidized bed from the total pressure loss of the test rectangular vessel. From the results of Fig.5, it is revealed that the pressure drop data of the present adsorbent remain constant against the superficial air flow velocity, and the data (closed circle) under the almost dry air condition of $p_w/p_s = 0.05$ are consistent with the previous correlation curve indicated by the dotted line. While the pressure drop data for $p_w/p_s = 0.6$ are over by about 60 Pa as compared with the previous correlation curve for the fluidized bed. This behavior might be explained by the fact that the flow drag resistance was increased with increasing the air humidity due to the increase in density of the adsorbent particles and adhesive force (aggregation force) of the adsorbent particle surface adsorbed water vapor. In Fig.5, it is found that the value of Δp under the fluidized condition is lower by one figure than that under the fixed bed condition. This result of pressure drop would be allowed to perform the adsorption operation under the low pressure difference condition.

Experimental Results and Discussion of Transient Characteristics of the Fluidized Bed Packed with the Powder Type Adsorbent

Fig.6 presents the relation of the moist air temperatures θ , the relative humidity p_w/p_s and the mass ratio of the adsorbent adsorbed water vapor to the dried adsorbent with time at a superficial air flow velocity of $u_o = 0.037$ m/s, temperature of $\theta_{in} = 30$ °C and a relative humidity of $p_w/p_s = 0.6$. Other experimental conditions are described in Fig.6. From the results of Fig.6, it is found that the relative humidity of the moist air, p_w/p_s , at the exit of the fluidized bed decreases drastically immediately after starting the experiment, subsequently it increases sharply until $t = 5$ hours, consequently it reaches the air relative humidity at the inlet of the fluidized bed at about $t = 15$ hours. Regarding the amount of mass ratio of the adsorbed water vapor m_w/m_o , the value of m_w/m_o increases drastically in a couple of minutes after starting the experiment due to large humidity difference between the inlet moist air and the adsorption site, and then it increases gradually with time since the humidity difference between them decreases little by little. While, with regard to the temperature of the moist air, it is seen that the moist air temperature θ_{out} at the exit of the fluidized bed rises sharply in a couple of minutes after starting the experiment and it falls gradually with time. This time history of the moist air temperature θ_{out} would be brought about by the heat generation from the adsorbent as above-mentioned in terms of the variation in the amount of the water vapor adsorbed into the adsorbent. Concerning the time history of the temperature θ_{test} of the moist air under the fluidized condition at the upside position of 10 mm from the bottom of the fluidized bed, it is observed that the value of θ_{test} increases sharply by about 10 °C immediately after starting the test run and then it decreased gradually with time until it reaches the inlet air temperature. The completion time t_f for the adsorption process was defined as the period of time when the accumulated amount of water vapor adsorbed to the test adsorbent with time reaches 80 % of the total amount of adsorbed water vapor, which could be estimated by the correlation equation (1) for the adsorption isotherm. For the experimental condition in Fig.6, the value of t_f was equal to 6.19 hours.

Figure 7 shows the variations of integrated enthalpies of moist air with time, that is, $\Sigma H_{in}\Delta t$ and $\Sigma H_{out}\Delta t$ at both the inlet and outlet of the fluidized bed and the integrated enthalpy of the heat-loss to the environment, $\Sigma \Delta H_{loss}\Delta t$, and enthalpy changes in the test adsorbent, ΔH_p , the fluidized bed vessel, ΔH_c and the adsorbed water vapor, ΔH_w under the same experimental conditions as indicated in Fig.6. From the results of Fig.7, it is revealed that the enthalpy of inlet moist air is almost equal to that of outlet moist air. This adsorption process might be supposed to be an isenthalpy change since both enthalpies of inlet and outlet moist air are second orders of

magnitude greater than enthalpy changes obtained for the test adsorbent, the adsorbed water vapor, the fluidized bed vessel and the heat loss to the environment. It is also seen that the enthalpy of the adsorbent increases slightly with time due to the large amount of heat generated by adsorption process and then it decreases gradually with time, finally it reaches the thermal equilibrium of $\Delta H_p = 0$. It is understood that the enthalpy of the adsorbed water vapor increases markedly at the first stage due to heat generation from the adsorbent and then its increasing rate decreases gradually with time. While the enthalpy of the fluidized bed vessel increases to a great extent at the beginning due to the heat gain from the adsorption heat of the adsorbent, and then it decreases drastically due to the heat loss to the environment.

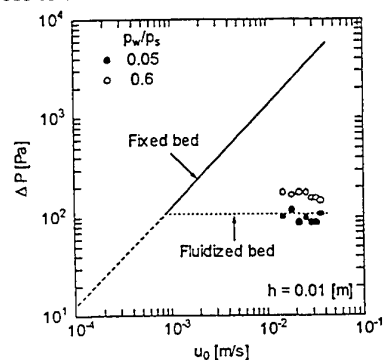


Fig.5. Variation of ΔP with u_0

The time histories of temperature θ , the relative humidity p_w/p_s and mass ratio of the adsorbent adsorbed water vapor, m_w/m_0 in the case of low superficial air flow velocity $u_0 = 0.014$ m/s are presented in Fig.8. Regarding the time history of the moist air temperatures, it is found that the maximum outlet temperature θ_{out} of flowing air for $u_0 = 0.014$ m/s is by about 2°C lower than that in the case of high superficial air flow velocity of $u_0 = 0.037$ m/s as shown in Fig.6. This decrease of the maximum temperature rise for the low air flow velocity could be explained by the fact that the reduction of heat generation in the adsorption process was brought by decreasing water vapor supply to the adsorbent and mass transfer coefficient with a decrease in the moist air velocity. With respect to the amount of adsorbed water vapor, it is seen that the increasing rate of m_w/m_0 with time for $u_0 = 0.014$ m/s is lesser than that for high air flow velocity $u_0 = 0.037$ m/s. The completion time t_f of adsorption process in the case of lower air flow velocity $u_0 = 0.014$ m/s stands at about 10.1 hours.

Figure 9 shows the variations of the moist air temperature θ , p_w/p_s and m_w/m_0 with time for fluidized bed height of $h = 2.5$ mm instead of $h = 10$ mm in Fig.6. From the results of Fig.9, it is revealed that the outlet air temperature θ_{out} for $h = 2.5$ mm reaches the same maximum one as for $h = 10$ mm, however it's maximum temperature for $h = 2.5$ mm appears at shorter time than that for $h = 10$ mm. This decrease of time period for smaller fluidized bed height could be explained by the fact that the water vapor supply per unit volume of the adsorbent was increased and the heat capacity of the adsorbent was decreased with a decrease in the fluidized bed height, that is, the adsorbent volume. The completion time of adsorption process for $h = 2.5$ mm is shortened at $t_f = 1.98$ hours as compared with that for $h = 10$ mm ($t_f = 6.19$ hours).

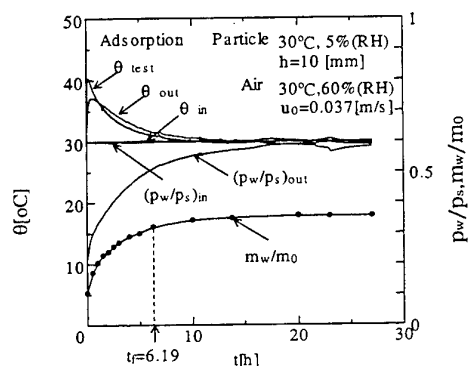


Fig.6. Time histories of measured quantities

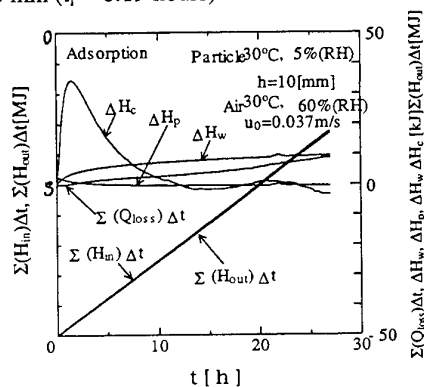


Fig.7. Time histories of measured quantities

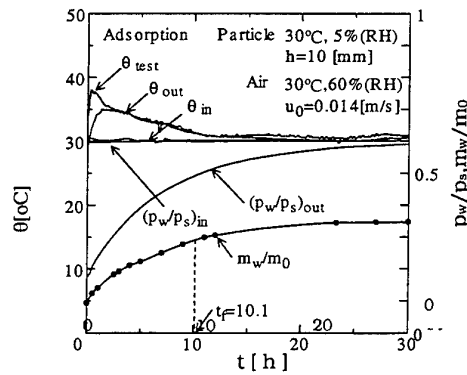


Fig.8. Time histories of measured quantities

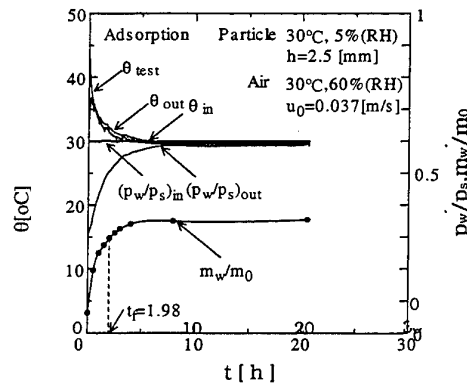


Fig.9. Time histories of measured quantities

Data Reduction for Completion Time of Mass Transfer and Adsorption Process

In general, it is difficult to correlate the present data for the transient adsorption experiments by the previous data reduction method for mass transfer based on the steady state experiment since the amount of adsorbed water vapor and the air humidity and temperature in the fluidized bed vary markedly with time. Therefore, the data reduction in the present study has been performed by the effective mass transfer coefficient h_m^* proposed by reference [2], which was defined by the time and space average value of the completion time period in adsorption process and at measuring positions in the fluidized bed as follows:

$$h_m^* = (\Delta m_w)_t / (t_f \cdot S_p (\rho_{in} - \rho_{wp})) \quad (3)$$

where, S_p : surface area of the powder type adsorbent, ρ_{in} and ρ_{wp} : density of moist air at inlet of the fluidized bed and near the surface of the adsorbent, respectively. Non-dimensional completion time of adsorption process T^* and the modified Sherwood number Sh^* of mass transfer coefficient are defined by two following equations.

$$T^* = Dt_f / d_m^2 \quad (4)$$

$$Sh^* = h_m^* d_m / D \quad (5)$$

The other non-dimensional parameters are defined as follows:

$$\text{Reynolds number } Re = u_o d_m / \nu_a \quad (6)$$

Mass ratio of the adsorbent adsorbed water vapor;

$$\Delta(m_w/m_o) = (m_w/m_o)_f - (m_w/m_o)_o \quad (7)$$

$$\text{Modified Stefan number } Ste^* = H_{in}/r \quad (8)$$

$$\text{Schmidt number } Sc = \nu_a / D \quad (9)$$

Where, ν_a : kinematic viscosity of air, H_{in} : enthalpy of inlet moist air, r : adsorption heat (water vapor condensed heat), D : molecular diffusion coefficient, d_m : average diameter of the adsorbent particle diameters at the starting and finishing of the experiment.

Figure 10 presents the variation of non-dimensional completion time T^* with Reynolds number Re for various p_w/p_s and h/d_m . From the results of Fig.10, it is revealed that the value of T^* decreases with an increase in Re due to an increase in the amount of water vapor supply and the mass transfer coefficient with increasing moist air flow velocity. While, it is also found that the value of T^* increases with increasing p_w/p_s and h/d_m . The data of non-dimensional completion time T^* were correlated by means of Re , $\Delta(m_w/m_o)$, h/d_m and Ste^* with standard deviation of $\pm 12\%$ by using method of least squares as follows:

$$T^* = 3.0 \times 10^4 \Delta(m_w/m_o)^{0.60} Re^{-0.64} (h/d_m)^{0.91} Ste^{*-1.7} \quad (10)$$

Applicable ranges in Eq.(10): $\Delta(m_w/m_o) = 0.0453 \sim 0.482$, $Re = 0.029 \sim 0.097$, $h/d_m = 70 \sim 420$ and $Ste^* = 0.1 \sim 0.14$.

Figure 11 shows the relationship between the modified Sherwood number $Sh^*/Sc^{1/3}$ and Reynolds number Re for various p_w/p_s and h/d_m . The dependence of Sc on Sh^* was dealt as a proportion of $Sc^{1/3}$ proposed by previous report [3]. In Fig.11, it is seen that the data of $Sh^*/Sc^{1/3}$ increase with an increase in Re because of an increase in mass transfer coefficient in relation with mass boundary layer thickness. While, it is also found that the values of $Sh^*/Sc^{1/3}$ decrease with increasing p_w/p_s and h/d_m . From these results, the data of Sh^* were correlated by means of those non-dimensional parameters with the standard deviation of $\pm 14.8\%$ as follows:

$$Sh^* = 1.0 \times 10^{-6} \Delta(m_w/m_o)^{-0.27} Re^{0.7} (h/d_m)^{-0.88} Ste^{*-4.1} Sc^{1/3} \quad (11)$$

Applicable ranges in Eq.(11): $\Delta(m_w/m_o) = 0.0453 \sim 0.482$, $Re = 0.029 \sim 0.097$, $h/d_m = 70 \sim 420$ and $Ste^* = 0.1 \sim 0.14$.

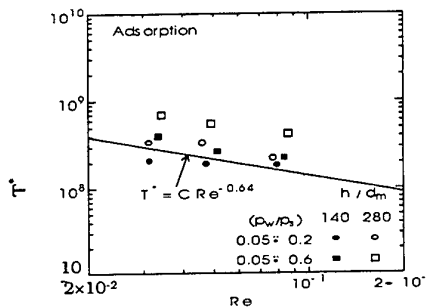


Fig.10.Variation of T^* with Re

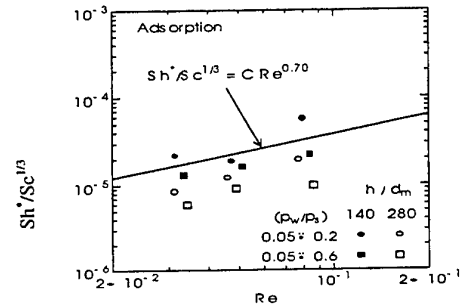


Fig.11.Variation of Sh^* with Re

4. CONCLUDING REMARKS

The experimental investigation was carried out to observe the transient adsorption characteristics of the organic powder type adsorbent made from the bridged complex of sodium polyacrylate in a fluidized bed. Consequently, some conclusions were obtained as follows:

- (1) The measured results of adsorption isotherm equilibrium revealed that the mass ratio of the present organic adsorbent adsorbed water-vapor to the dried one was 1.3 to 2.3 times larger than that of silica gel adsorbent in the relative air humidity range from 3 to 80%. Moreover, it was found that the present organic adsorbent was markedly dependent on the relative air humidity while to a lesser extent dependent on temperature in the low temperature range of $10^\circ\text{C} \sim 30^\circ\text{C}$.
- (2) Concerning the transient experiments, it was found that the pressure loss under the fluidized condition was lower by one figure than that under the fixed bed condition. It was also observed that the adsorption process of passing the moist air into the organic adsorbent bed was the isoenthalpy change.
- (3) The data of the modified Sherwood number and non-dimensional time of the adsorption process were correlated by means of modified Reynolds number, Schmidt number, mass ratio of adsorbed water vapor to the adsorbent, non-dimensional dimension of the fluidized bed height and modified Stefan number.

REFERENCES

1. H.Inaba, Thermal Science and Engineering v.6, no.1, pp.11-18(1998).
2. W.M.Rosenow, et al., Handbook of Heat Transfer Applications, 2nd Ed., McGraw-Hill Inc. (1985).
3. S.Ergan, Chem. Engng. Prog., v.48, pp.88-92(1952).
4. A.Fedorov and R. Viskanta, J. The Heat Transfer Society of Japan, v.36, no.142, pp.4-11(1997).
5. H.Sakurai, Adsorption Engineering, Kyoritsu Pub. Co.(1977).

NON-REGENERATIVE MULTI-STAGE AND REGENERATIVE MULTI-BED ADSORPTION CYCLES FOR LOW-TEMPERATURE WASTE HEAT RECOVERY

Bidyut Baran Saha, Atsushi Akisawa, Takao Kashiwagi

Mechanical Systems Engineering, Tokyo University of Agriculture & Technology
2-24-16 Naka-machi, Koganei-shi, Tokyo 184-8588, Japan.
E-mail: bidyut@cc.tuat.ac.jp, Fax: (81)-42-388-7012

Kim Choon Ng, Hui Tong Chua

Department of Mechanical and Production Engineering
National University of Singapore, 10 Kent Ridge Crescent, S (119260), Singapore
E-mail: mpengkc@nus.edu.sg, Fax: (65)-779-1459

Keywords: adsorption, multi-stage, multi-bed, silica gel, waste heat utilization

ABSTRACT. This study aims at clarifying the possible operating temperature ranges for silica gel-water adsorption refrigeration cycles, driven by near-ambient temperature waste heat sources (between 40 and 90 °C) with relatively small regenerating temperature lifts (10 to 60K). To exploit waste heat or renewable energy of temperature below 60 °C, staged-regeneration is necessary. A two-stage cycle, which can be operated effectively with 55 °C in combination with a 30 °C cooling source is introduced and compared with a conventional (single-stage) cycle. These cycles are evaluated in terms of cooling capacity, COP and their operational viability with near ambient temperature driving heat sources. By cycle simulation, it is found that the single-stage cycle yields better cooling capacity and COP in comparison with the two-stage cycle for ΔT_{regen} (heat source - heat sink temperature) higher than 35K. The advantage of two-stage cycle lies in its capacity to be operational with small ΔT_{regen} so that low grade waste heat sources can be exploited effectively. The use of multiple beds (more than two) will increase performance. To extract as much enthalpy as possible from waste heat sources of temperature above 65 °C, a multi-bed, single-stage regenerative adsorption chiller is introduced. Simulation results show that for the same waste heat source flow rate and inlet temperature, a single-stage, 4-bed chiller generates 70% more cooling capacity than a single-stage, 2-bed chiller. A 6-bed chiller in turn generates 40% more than a 4-bed chiller. Since the beds can be triggered into operation sequentially during start-up, the risk of ice formation in the evaporator is greatly reduced compared with that of a 2-bed chiller. Another significant advantage of multi-bed regenerative adsorption chiller is that it will minimize the chilled water temperature fluctuation so that a downstream temperature-smoothing device may be downsized or even eliminated in applications where tighter temperature control may be required. Depending on solar radiation or waste heat availability, suitable multi-stage chillers or single-stage, multi-bed chillers can be selected for optimal operation.

1. INTRODUCTION

The severity of the ozone layer destruction problem due partly to CFCs and HCFCs has been calling for rapid developments in freon-free air conditioning technologies. With regard to energy use, global warming prevention has been requiring a thorough revision of energy utilization practices towards greater efficiency. From this perspective, interest in adsorption systems has been increased as they do not use ozone depleting substances as refrigerants and nor do need electricity or fossil fuels as driving sources. Several heat-pumping and refrigeration applications have been studied using various adsorbent and adsorbate pairs. Some representative examples are given in Table 1. Most of the cycles mentioned in Table 1 require medium and/or high temperature heat sources to as the driving sources. However, silica gel-water and active carbon-methanol adsorption cycles have a distinct advantage over other systems in their ability to be driven by heat of relatively low, near-ambient temperatures, so that waste heat below 100 °C can be recovered, which is highly desirable. In this study, silica gel-water has been chosen as the adsorbent-refrigerant pair because the regeneration temperature of silica gel is lower than that of active carbon; and water has a large latent heat of vaporization.

The primary objective of this paper is to clarify the possible operating temperature ranges for silica gel-water adsorption cycles. In order to utilize near environment temperature heat sources between 50 °C and 70 °C with a cooling source of 30 °C, a two-stage, four-bed, non-regenerative adsorption cycle is introduced and its performance is compared with that of conventional cycle. The secondary goal is to explore the possibility of

improving the recovery efficiency of waste heat between 70 °C and 90 °C to useful cooling by introducing single-stage, four-bed, regenerative adsorption cycle. The latter cycle also minimizes the delivered chilled water temperature fluctuations.

Table 1. Developments in Adsorption Heat Pump Systems (Typical Achievements)

Adsorbent/adsorbate	System type	Source	Remarks
Activated carbon/ Ammonia	Regenerative system	J.A. Jones [1]	4 bed system
Activated carbon/ Methanol	Regenerative system	Pons and Guilleminot [2]	Solar driven ice maker
Calcium chloride/ Methanol	Intermittent adsorption system	Lai et al. 1993 [3]	Chemical heat pump
Complex compounds/Salts	Intermittent adsorption system	Beijer and Horsman [4]	Promising uses: vehicles and residential air conditioning
Ditto	Regenerative system	Miles and Shelton [5]	Thermal wave system; $T_{\text{regeneration}}$ is very high
Silica gel/water	Intermittent adsorption system, single stage	Saha et al. [6] and Boelman et al. [7]	Waste heat driven cycle; Heat of adsorption Q_{st} = 2800 kJ/kg
Silica gel/water	Intermittent adsorption system, three stage	Saha et al. [8]	Waste heat driven cycle; $T_{\text{regeneration}}$ is very low
Zeolite/ammonia	Intermittent system	Critoph and Turner [9]	$T_{\text{regeneration}}$ is very high
Zeolite/water	Cascaded adsorption system	Douss and Meunier [10]	Application: heating; Heat of adsorption Q_{st} = 3700 kJ/kg
Zeolite composites/ Water	Intermittent adsorption system	Guilleminot et al. [11]	Composites: (a) 65% zeolite + 35% metallic foam and (b) 70% zeolite + 30% natural expanded graphite

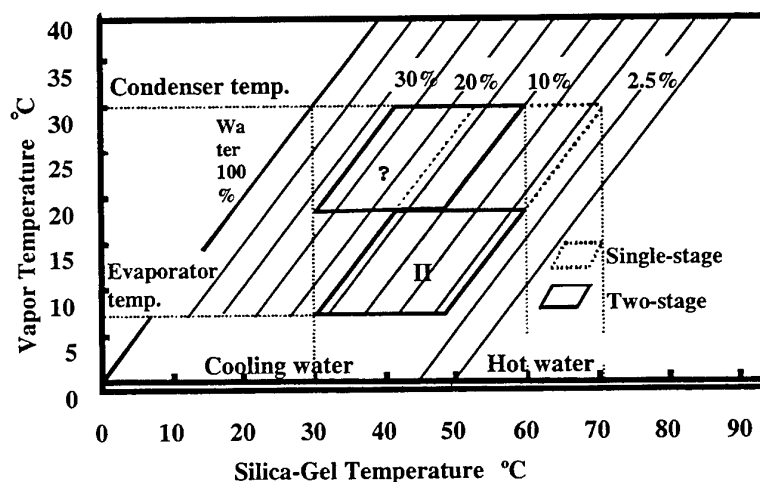


Fig. 1. Conceptual Dühring diagram for conventional and two-stage cycles

2. WORKING PRINCIPLES

As can be seen from the conceptual Dühring diagram (Fig. 1), a conventional silica gel-water cycle will not be

operational with 50 °C driving heat source if the heat sink is at 30 °C or more. For practical utilization of these temperatures (50 to 70 °C) to produce effective cooling, a two-stage adsorption cycle is introduced. As can be seen from Fig. 1, the two-stage cycle allows the reduced ΔT_{regen} of the adsorbent ($T_{\text{des}} - T_{\text{ads}}$) by splitting the evaporating temperature lift ($T_{\text{cond}} - T_{\text{eva}}$) into two smaller lifts. Refrigerant (water vapor) pressures thus rises into two progressive steps from evaporation to condensation level. In order to attain this objective, the introduction of two additional reactors is necessary, as shown in Fig. 3.

Conventional Adsorption Cycle

Conventional silica gel-water cycle consists of four heat exchangers, namely, a condenser, an evaporator and a pair of sorption elements. The adsorbent is packed in the sorption elements, which undergoes alternate heating and cooling to allow refrigerant desorption and adsorption. Figure 2 illustrates the process. Refrigerant is evaporated at evaporation temperature with heat input Q_{eva} from the chilled water. Adsorber (HX2) adsorbs it. Adsorption continues until the gel reaches strong concentration of water. The adsorption temperature determines concentration at which coolant (cooling water) removes the adsorption heat Q_{ads} . Desorber (HX1) is heated up to desorption temperature by driving heat Q_{des} . It is connected to condenser via valve 1. Desorbed refrigerant vapor is condensed inside the condenser. The condensate heat Q_{cond} removes by the coolant. The resulting condensate flows back to the evaporator to complete the prescribed cycle of duration 420 s. A short cycle of duration 30 s was introduced by closing all valves so that no evaporation occurs. A complete reverse cycle was followed thereafter by changing the modes of all valves.

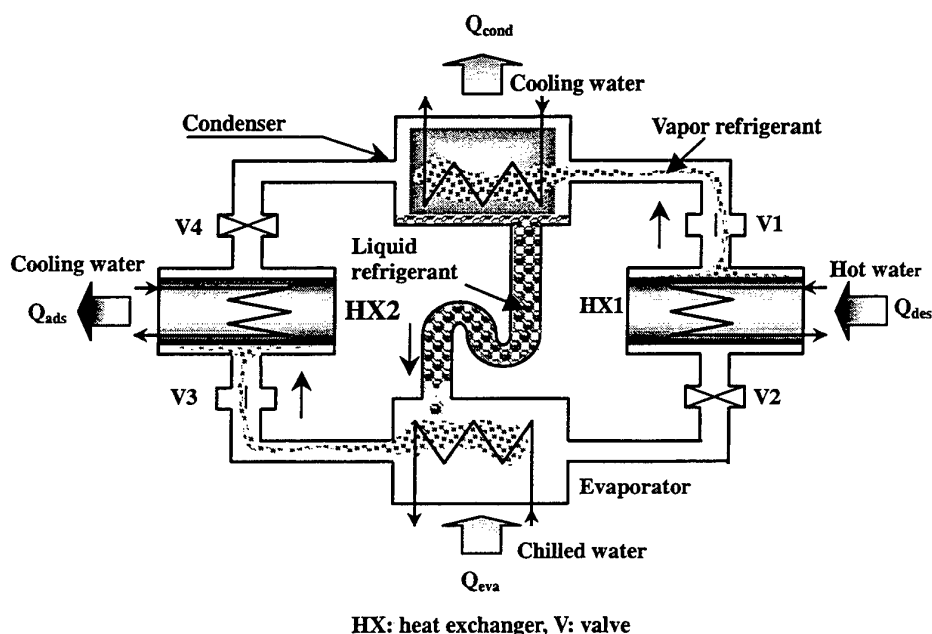


Fig. 2. A schematic diagram of the conventional adsorption chiller

Non-Regenerative, Multi-Stage Cycle

As shown in Fig. 3, two-stage cycle comprises of a condenser, an evaporator and two pairs of sorption elements. In the cycle, valves 1, 3 and 5 are open to allow refrigerant flow between heat exchangers. The desorbers (HX1 and HX4) are heated by hot water while adsorbers (HX2 and HX3) are cooled by coolant. Refrigerant is evaporated at evaporation temperature with heat input Q_{eva} from the chilled water and adsorbed by adsorber 2 (HX2). Adsorber 3 (HX3) adsorbed refrigerant from desorber 4 (HX4). Desorbers are heated up to the desorption temperature by driving heat Q_{des} . Desorber 1 (HX1) is connected to the condenser via valve 1, where the desorbed refrigerant vapor is condensed at condensation temperature. Coolant removes the condensation heat Q_{cond} . The evaporator is fed by the liquid condensate to complete the cycle. The pre-heating/pre-cooling cycle and reverse adsorption/desorption cycle are similar in principle to those of the conventional cycle.

Regenerative, Single-Stage, Multi-Bed Cycles

The proposed four-bed regenerative strategy is an extension from the conventional two-bed operation. In the conventional chiller, the inherent restriction in the number of beds resulted in significant temperature fluctuation in all components. On top of the fluctuation of the chilled water temperature, the peak temperature of the condenser outlet temperature that follows shortly after bed switching adds on to the instantaneous load of the cooling tower [7]. The four-bed scheme [12] will serve to significantly reduce the peak temperatures in both the evaporator and condenser. The second objective is to improve the recovery efficiency of waste heat to useful cooling. Such low temperature, industrial waste heat (typically below 90 °C) is commonly purged into the environment. The enthalpy of such waste heat relative to that of the environment represents a fixed energy expenditure waiting to be tapped for productive uses. Using such waste heat to serially heat the desorber of a string of two-bed adsorption chillers signifies a move towards better utilizing this fixed amount of energy expenditure. However, such a master-and-slave configuration for the string of adsorption chillers represents an under-utilization of these downstream adsorption chillers. The proposed scheme will be shown to eliminate such rigid configurations. Furthermore, with the condenser water peak temperature slashed, the condenser and adsorber could then be cooled in series, just as in a conventional absorption chiller. Table 2 and Fig. 4 depict the energy utilization schedule and flow configuration for a 4-bed chiller respectively. By capitalizing on the phase difference between the two pairs of beds, the heat source from a hotter desorber can be used to regenerate another cooler desorber before being purged. Similarly, the coolant from a cooler adsorber can be used to further cool a hotter adsorber before being sent back to the cooling tower.

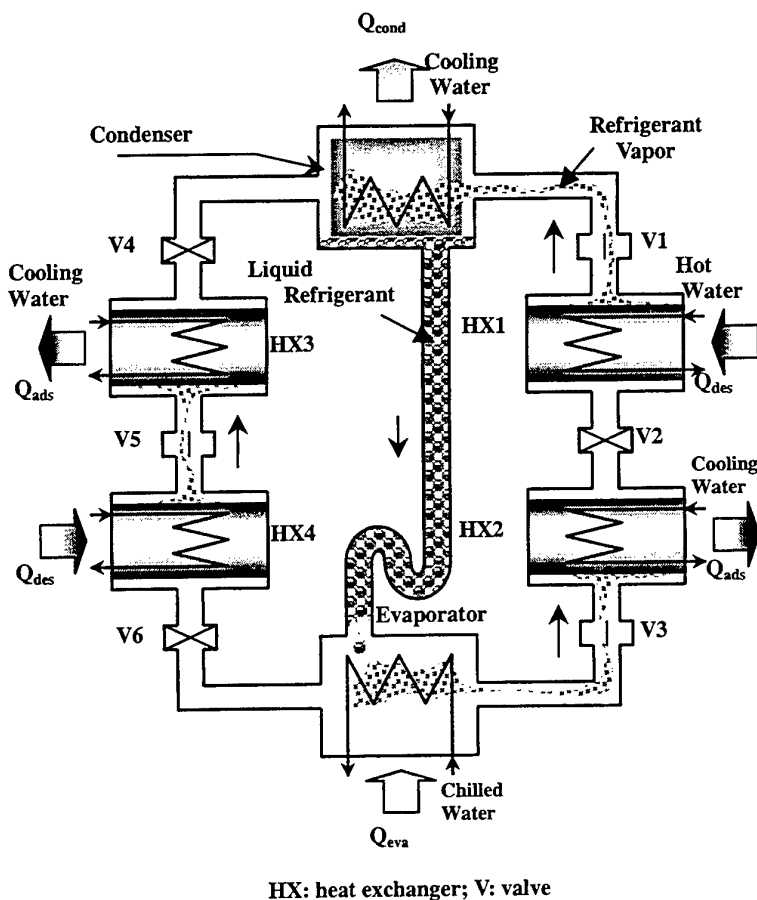


Fig. 3. A schematic diagram of the two-stage adsorption chiller

Table 2. Energy Utilization Schedule for a Four-Bed Chiller over Two Cycles

Bed 1	sw	ads (2)	ads (1)	sw	des (2)	des (1)
Bed 2	des (1)	Sw	ads (2)	ads (1)	sw	des (2)
Bed 3	sw	des (2)	des (1)	sw	ads (2)	ads (1)
Bed 4	ads (1)	sw	des (2)	des (1)	sw	ads (2)

Legend:
ads: adsorber; des: desorber
sw: switching from adsorber to desorber, and receiving heating stream from des (1) or switching from desorber to adsorber, and receiving cooling stream from ads (1)
(1): this refers to the situation when the bed receives either cooling stream from the condenser or heating stream directly from the heat source.
(2): this refers to the situation when the bed receives either cooling stream from ads (1) or heating stream from des (1).
Note: The width of each box is a not-to-scale indication of the relative time duration.

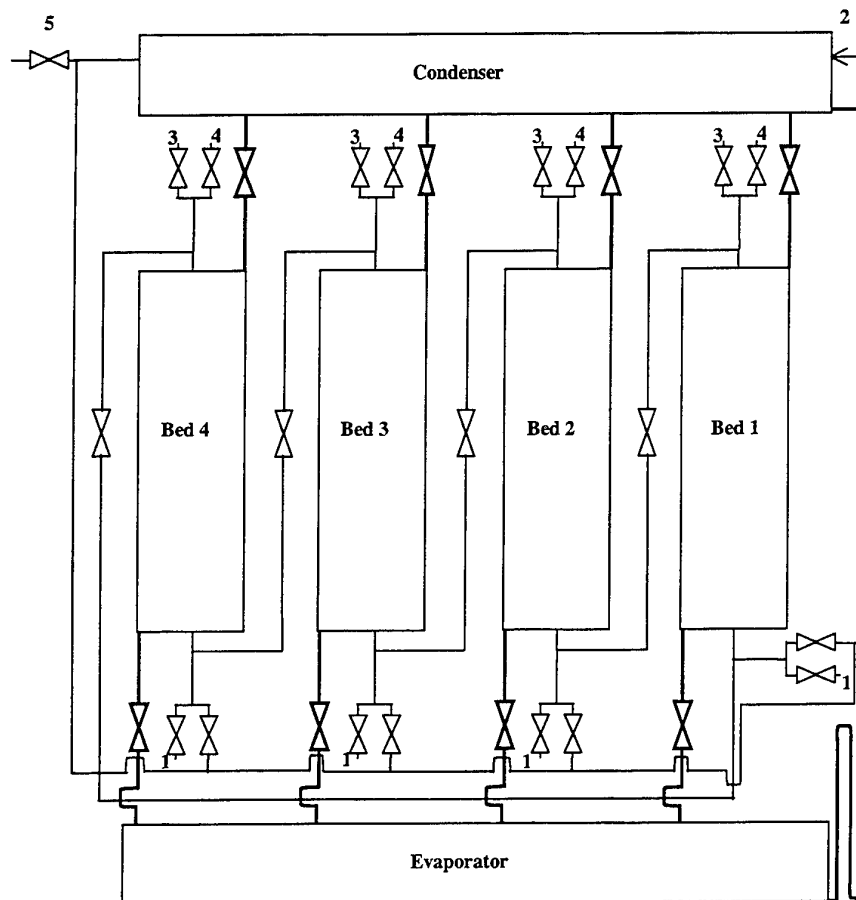


Fig. 4. A schematic diagram of the adsorption chiller in a 4-bed regenerative strategy

Fluid flow between beds has been depicted as top-down. 1 refers to waste heat stream inlet, 2 refers to coolant inlet, 3 refers to waste heat stream outlet, 4 refers to coolant outlet, and 5 refers to the excess coolant outlet port. The bold lines depict the refrigerant circuit, while the thin lines depict the coolant and heat source circuit.

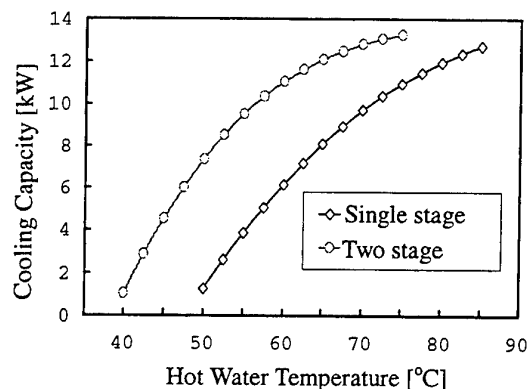


Fig. 5(a) Cooling capacity as a function of hot water temperature.

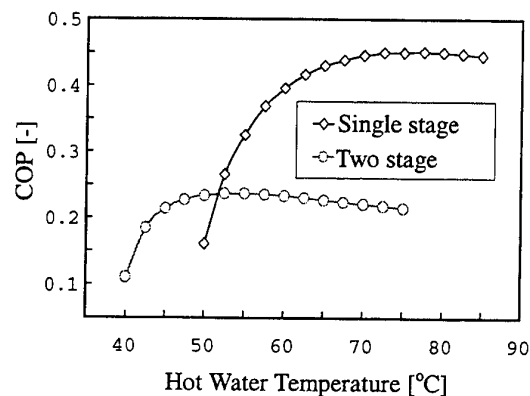


Fig. 5(b) COP as a function of hot water temperature.

3. RESULTS AND DISCUSSIONS

In order to clarify the practical operational limits and also the performance characteristics, cycle simulation runs were performed for conventional and two-stage chillers. Since the main objective of conventional and staged chillers is to use low temperature waste heat as the driving source, the investigation was conducted for hot water between 40 and 85 °C with cooling water of 30 °C.

Hot Water Temperature Effect on Cooling Capacity and COP

Figures 5(a) and (b) show the effect of hot water temperature on cooling capacity and COP. For a fixed cooling source of temperature 30 °C, the cooling capacity increases as the hot water temperatures increase for both conventional and two-stage chillers. This can be attributed to the fact that an increasing amount of refrigerant is desorbed occurs with higher driving source temperature. The COP peaks between 45 and 50 °C for the advanced cycle, while it increases almost uniformly with the increase of hot water temperature for the conventional cycle. When the hot water temperature is less than 54 °C, COP values of the conventional cycle are lower than those of the two-stage cycle. This suggests that the conventional cycle will not be able to operate effectively when ΔT_{regen} becomes less than 16K.

Performance Modeling of Multi-Bed Chillers

The non-dimensional cycle averaged cooling power is defined as

$$\overline{Q}_{\text{evap}} = \omega \frac{dM_{\text{chilled}}}{dt} c_{\text{chilled}}^{\text{in}} \int_0^1 (\Theta_{\text{chilled}}^{\text{in}} - \Theta_{\text{chilled}}^{\text{out}}) d\tau \quad (1)$$

As this part of the present study is focusing on the utilization of waste heat before it is ultimately purged to the environment, its enthalpy relative to that of the environment can be viewed as being a fixed energy input into a system. Consequently, maximizing cooling capacity rather than the conventional coefficient of performance may be more pertinent. Thus, the following conversion efficiency is accordingly defined:

$$\eta = \frac{\frac{dM_{\text{chilled}}}{dt} c_{\text{chilled}}^{\text{in}} \int_0^1 (\Theta_{\text{chilled}}^{\text{in}} - \Theta_{\text{chilled}}^{\text{out}}) d\tau}{\frac{dM_{\text{heating}}}{dt} c_{\text{heating}}^{\text{in}}} \quad (2)$$

The environment temperature has been selected to be $T_{\text{cond}}^{\text{in}}$. Detail description of the mathematical equations can be found in [13].

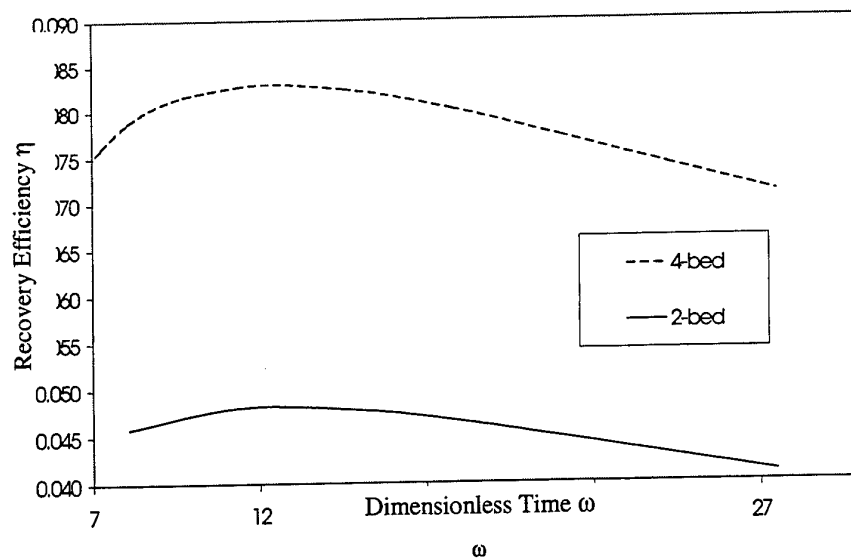


Fig. 6. Comparison of recovery efficiency between conventional and 4-bed chillers.

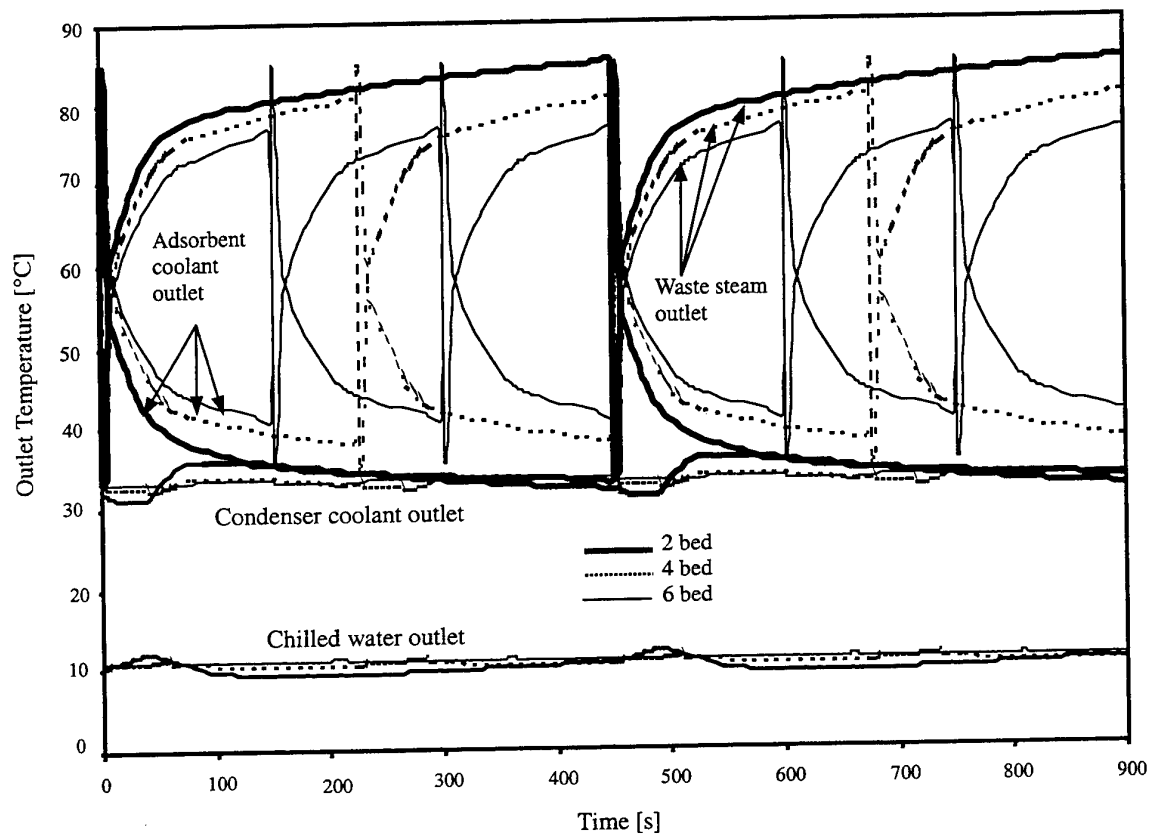


Fig. 7. Temperature profiles of conventional and multi-bed chillers.

Figure 6 shows the recovery efficiency, η of the 2-bed and 4-bed chillers as a function of dimensionless cycle time, ω . The recovery efficiency of the 2-bed chiller at a standard rated ω of 14.55 (corresponding to cycle time of 450 s) is 0.0478. From 2 to 4-beds, the recovery efficiency is boosted by 70%. One could anticipate that the recovery efficiency improves with the number of beds, but this has to be balanced with the construction costs. Figure 7 illustrates the dimensionless outlet temperatures for the coolants, waste steam and delivered chilled water during dynamic steady state. Waste heat outlet temperature generally decreases with the number of beds, representing a better utilization of waste heat before it purged to the environment. The condenser coolant temperature for the conventional chiller is significantly reduced, rendering it suitable for subsequent cooling of the adsorbers. In the case of multi-bed chillers, the delivered chilled water temperature tends to be smoothened. This may lead to the elimination of downstream cooling devices for demanding process cooling and dehumidification. With the same amount of resource commitment, delivered chilled water temperature and cycle average cooling capacity necessarily drop but at a rate slower than the reduction in heat source and coolant flow rate, resulting in improved recovery efficiency.

4. CONCLUSIONS

The following conclusions can be drawn:

1. The main advantage in the two-stage cycle is its ability to utilize low temperature waste heat (40 to 75 °C) as the driving heat sources. This chiller is operational with a regenerating temperature lift as small as 10K.
2. With relatively higher driving source temperatures (above 54 °C), the conventional cycle yields better performance in comparison to the two-stage cycle.
3. It is possible to significantly improve the recovery efficiency of low-grade waste heat sources via a single-stage, 4-bed regenerating scheme. A single-stage, 4-bed chiller improves the recovery efficiency by 70% over that of a conventional chiller. This ensures the enthalpy of waste steam relative to the ambient is better utilized before being purged eventually.
4. In the case of multi-bed regenerative chillers, the delivered chilled water temperature tends to be smoothened. This prevents a sudden temperature drop in the evaporator, reducing the risk of ice formation. This suggests that the downstream temperature smoothening device may be downsized or eliminated for the application of cooling.
5. From the above perspectives, the use of unexploited low-temperature waste heat may offer an attractive possibility for improving energy efficiency.

REFERENCES

1. J.A. Jones, *Proceedings of the International Absorption Heat Pump Conference, ASME-AES*, v. 31, pp. 449-455, edited by Radermacher et al., New Orleans, USA (1994).
2. M. Pons and J.J. Guilleminot, *Trans. of the ASME J. Solar Energy Engineering*, v. 108, pp. 332-337 (1986).
3. H. Lai, C. Li, D. Zheng and J. Fu, *Proceedings of the International Absorption Heat Pump Conference, ASME-AES*, v. 31, pp. 440-445, edited by Radermacher et al., New Orleans, USA (1994).
4. H.A. Beijer and J.W.K. Horsman, *Proceedings of the International Absorption Heat Pump Conference, ASME-AES*, v. 31, pp. 457-462, edited by Radermacher et al., New Orleans, USA (1994).
5. D.J. Miles and S.V. Shelton, *Applied Thermal Engineering*, v. 16, No. 5, pp. 389-394 (1996).
6. B.B. Saha, E.C. Boelman and T. Kashiwagi, *ASHRAE Transactions*, v. 101, No. 1, pp. 348-357 (1995).
7. E.C. Boelman, B.B. Saha and T. Kashiwagi, *ASHRAE Transactions*, v. 101, No. 1, pp. 358-366 (1995).
8. B.B. Saha and T. Kashiwagi, *ASHRAE Transactions*, v. 103, No. 2, pp. 50-58 (1997).
9. R.E. Critoph and H.L. Turner, *Proceedings of the International Conference on Pompes a Chaleur Chimiques de Hautes Performances*, Perpignan, France, pp. 202-211 (1988).
10. N. Douss and F. Meunier, *Chemical Engineering Science*, v. 44, No. 2, pp. 225-235 (1989).
11. J.J. Guilleminot, J.B. Chalfen and A. Choisier, *Proceedings of the International Absorption Heat Pump Conference, ASME-AES*, v. 31, pp. 401-406, edited by Radermacher et al., New Orleans, USA (1994).
12. H.T. Chua, K.C. Ng, A. Malek, A. Akisawa, T. Kashiwagi and B.B. Saha, *International Journal of Refrigeration*, (in press 1999).
13. H.T. Chua, K.C. Ng, A. Malek, A. Akisawa, T. Kashiwagi and B.B. Saha, *Proceedings of the International Sorption Heat Pump Conference*, pp. 187-192, edited by Schweigler et al., Munich Germany (1999).

STUDY OF THE REACTION RATE OF MH_{High} (MHTAL HYDRIDE: $Ti_{0.18}Zr_{0.84}Cr_{1.0}Fe_{0.7}Mn_{0.3}Cu_{0.057}$) TO BE USED FOR COMPACT MH REFRIGERAION SYSTEMS

Sang-Chul BAE*, Shinsuke TAKEGUCHI**, Takahiro YABE**

Department of Mechanical Engineering
Waseda University, Graduate School of Science and Engineering
*Email: 697a5031@mn.waseda.ac.jp; Fax: +81-3-5286-3251

Masafumi KATSUTA**

Department of Mechanical Engineering
Waseda University, School of Science and Engineering
Email: katsuta@mn.waseda.ac.jp; Fax: +81-3-5286-3251

Keywords: reaction rate, plateau pressure, rate-controlling step, reacted fraction

ABSTRACT. Our purpose is to develop the compact MH refrigeration system for the vending machine and the show case, and to attain a refrigeration temperature of 243 K by using a heat source of about 423K. The reaction rate of the MH to use for the heat source, MH_{High} is studied first though the MH refrigeration system consists of two MHs, one is used for the heat source and the other is used for the cooling load extracting. As for the reaction rate in the hydriding process, initially, a rapid surface reaction, governed by the relation $1-(1-F)^{1/3} = k_h t$. After the MH surface has been covered by hydride, the reaction becomes diffusion controlled with the relation $1-3(1-F')^{2/3} + 2(1-F') = k'_h t$. The reaction rates, k_h , k'_h are exponentially proportional to the pressure difference and increase with temperature. And, As for the dehydriding process, it is found out that the rate-controlling step is uniquely diffusion reaction. The dehydriding reaction rate is exponentially proportional to the pressure difference and the initial reacted fraction, and increases with temperature. Finally, on the basis of these experimental results, the brand new rate correlations are reasonably derived. The calculated results are in agreement with the experimental ones.

1. INTRODUCTION AND EXPERIMENTAL METHODS

We must saturate the next heat flow equation [1] to design a heat exchanger to use for the MH refrigerator.

$$\frac{\Delta H_{c\infty} \times dF}{201.6 \, dt} = \frac{\lambda S}{\delta} (\theta - \theta_A) + C \frac{dT}{dt} \quad (1)$$

where $\lambda S/\delta$ is the heat transfer factor (λ , S and δ are the MH effective conductivity, area and thickness respectively), C is a heat capacity of a system and dF/dt is the reaction rate. First, our interests focused to the determination of the reaction rate, dF/dt in the heat flow equation [1]. The dF/dt of MH_{High} is studied in this paper. The schematic diagram of the Sievert's type of experimental facility is shown in Fig.1. It is composed of gas supply system, gas release system, reactor and reservoir tank. Particularly, the heat capacity of reactor is enlarged, and an approximate isothermal condition is created to identify the intrinsic reaction rate. The each experimental run is started after repeating the activation treatment 10 times. The Japan Steel Works (J.S.W) offered the MH_{High} used for us with this research.

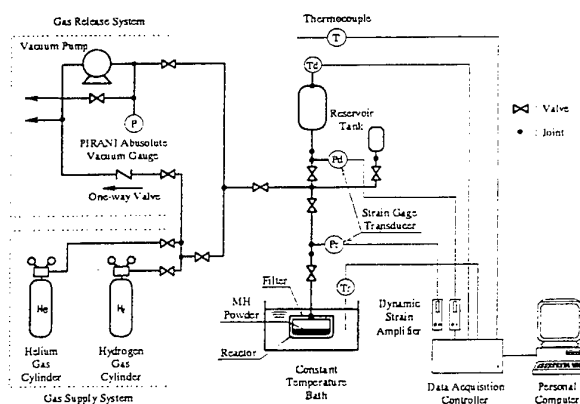


Fig. 1. Experimental facility

2. EXPERIMENTAL RESULTS

2.1 The Radius And The Packing Density Of MH Particles

The surface area radius r_s and the volume radius r_d of MH particles after the activation are measured by using the scanning electron microscope (SEM). To determine the surface rate equation 4 and the diffusion rate equation 5, these measured r_s and r_d are substituted, respectively. In addition, the r_s and r_d before activation are also measured. They are shown in the table 1. As for MH particles size, it is understood that it is atomized down to about 1/40 by the activation.

Table 1. Mean Radius Of MH Before And After Activation

	Before Activation	After Activation
Surface Radius r_s	0.2017 mm	4.373 μm
Volume Radius r_d	0.2192 mm	5.295 μm

The packing density has the next assumptions, and it is defined. 1) MH particle is made a globular form. 2) 1 MH particle is being charged in the cube which makes the diameter of the particle one side. The packing density is 3.665 g/cc by the above assumptions.

2.2 The Reaction Rate Of Hydriding Process

2.2.1 The pressure difference dependency. The reacted fraction F at constant temperature (303K), as a function of time t , is shown in Fig. 2. Fig. 3 shows the relations between dF/dt and the reacted fraction F . A relatively rapid reaction rate takes place for values of the reacted fraction F up to about 0.3. It is evident that a hydrogen diffusion plays a minor role during this stage, as that part of the alloy not covered by hydride is always in contact with hydrogen. The surface reaction is therefore postulated as the rate-controlling step. After the alloy particles have been completely covered by a hydride layer, the transport of materials through the layer by diffusion becomes rate-controlling step. At this stage, the reaction rate decreases and becomes slow.

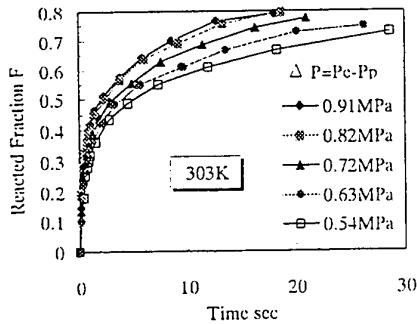


Fig. 2. Hydriding reacted fraction vs. time

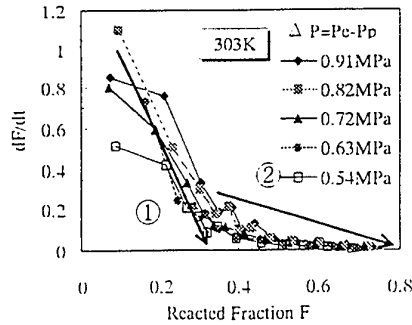


Fig. 3. Hydriding rate-controlling step

After various trials, we reached the result that k_h , k'_h of MH_{High} are governed by the following expressions [2,3].

Surface reaction: $1-(1-F)^{1/3}=k_h t$ (2)

Diffusion reaction: $1-3(1-F')^{2/3}+2(1-F')-k'_h t$ (3)

And, we suppose that k_h , k'_h are the functions of pressure difference ΔP ($\Delta P = P_e - P_p$, P_e is the equilibrium hydrogen pressure, P_p is the plateau pressure), temperature T , particle size, and the packing density ρ such as equations (4), (5). These functional relationships are experimentally investigated.

$$k_h = k_s g(P_e, P_p) h(T) / R \rho r_s \quad (4)$$

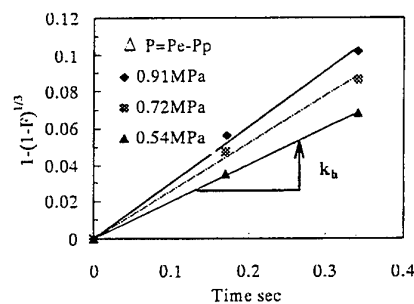
$$k'_h = 6 D e_h g'(P_e, P_p) h'(T) / R \rho r_d^2 \quad (5)$$

where k_s is a rate constant in cm/s, $D e_h$ is a diffusion coefficient in cm^2/s .

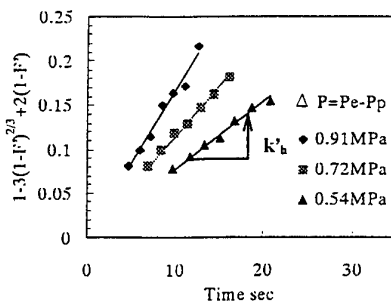
Plots of $1-(1-F)^{1/3}$ and $1-3(1-F')^{2/3}+2(1-F')$ at constant temperature (303K), as a function of time, are shown in Fig. 4. k_h , k'_h are given by the slope of the straight lines shown in Fig. 4. As ΔP becomes larger, it can confirm that enhanced k_h , k'_h are observed. The experimental data are possible to correlate by using the following exponential approximation [4,5] as function of ΔP among the present approximations.

Surface reaction: $k_h = 0.2662(P_e - P_p)^{0.5836}$ (6)

Diffusion reaction: $k'_h = 0.01818(P_e - P_p)^{1.615}$ (7)



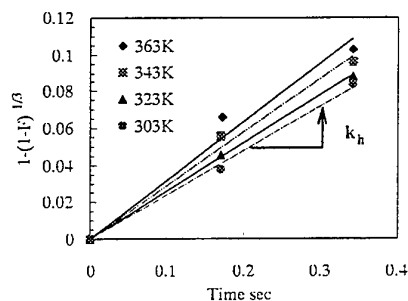
(a) Surface reaction



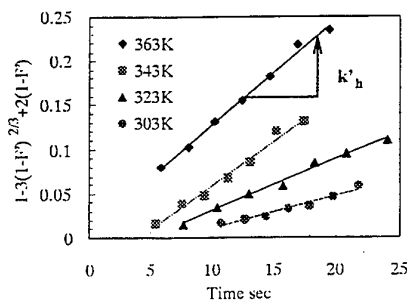
(b) Diffusion reaction

Fig. 4. $f(F)$ as function of time at 303 K

2.2.2 The temperature dependency. Fig. 5 shows the plots of $1-(1-F)^{1/3}$ and $1-3(1-F')^{2/3}+2(1-F')$ as a function of time at constant ΔP . k_h , k'_h are given by the slope of the straight lines shown in Fig. 5. k_h , k'_h become higher with increasing temperature. After various trials, the temperature dependency of k_h , k'_h can be represented by the Arrhenius expressions [6,7] and activation energies also obtain as shown in equations (8), (9).



(a) Surface reaction



(b) Diffusion reaction

Fig. 5. $f(F)$ as function of time at $\Delta P = 0.63$ MPa

Surface reaction: $k_h = 0.2605 \exp(-545.7/RT)$, $E_{hs} = 545.7 \text{ J/molH}_2$ (8)

Diffusion reaction: $k'_h = 0.7000 \exp(-1.214 \times 10^4/RT)$, $E_{hd} = 1.214 \times 10^4 \text{ J/molH}_2$ (9)

The constants $k_s = 1.653 \times 10^{-2}$ and $De_h = 1.425 \times 10^{-6}$ in the equations (4) and (5) are sought by using the above results. Therefore, the brand new rate correlations of hydriding process is expressed as follows.

Surface reaction step ($F < 0.3$),

$$1 - (1 - F)^{1/3} = k_h t$$

$$k_h = (1.653 \times 10^{-2} / R p r_s) (P_e - P_p)^{0.5836} \exp(-545.7 / RT) \quad (10)$$

Diffusion reaction step ($F > 0.3$),

$$1 - 3(1 - F')^{2/3} + 2(1 - F') = k'_h t \quad (11)$$

$$k'_h = (6 \times 1.425 \times 10^{-6} / R p r_d^2) (P_e - P_p)^{1.615} \exp(-1.214 \times 10^4 / RT)$$

where $F' = F - F_0 / 1 - F_0$, $F_0 = 0.3$, and F_0 is a reacted fraction which diffusion reaction starts at.

2.3 The Reaction Rate Of Dehydriding Process

2.3.1 The pressure difference dependency. The reacted fraction F at constant temperature (433 K), as a function of time t , is shown in Fig.6. Fig.7 shows the relations between the reaction rate dF/dt and the reacted fraction F , and it is found out that the dehydriding process is dominated by a unique rate-controlling step.

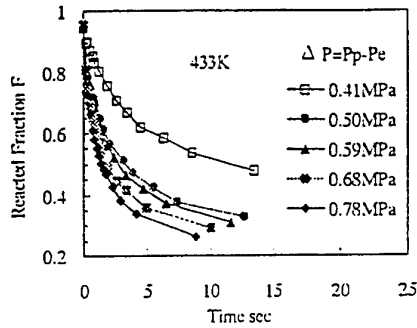


Fig. 6. Dehydriding reacted fraction vs. time

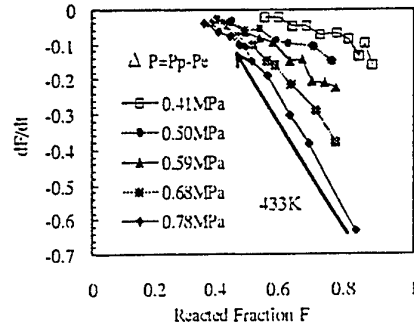


Fig. 7. Dehydriding rate-controlling step

About the dehydriding process the relations of the reacted fraction F vs. time t are expressed with the Equation (3). Therefore, the dehydriding process is considered only to be controlled by the diffusion. But, the F' of Equation (3) is calculated as $F' = F_1 - F$. F_1 is an initial reacted fraction in the dehydriding process. The dehydriding experiments begin from the condition of the hydride every time. However, because it is difficult to keep the initial reacted fraction F_1 as every run, this effect should be taken into account to the dehydriding process. Therefore, as for the dehydriding process, we propose Equation (12) by introducing the c_1^{nc} term which relates to F_1 .

$$k'_d = (6De_d / R p r_d^2) g'(P_p, P_e) h'(T) c_1^{nc} \quad (12)$$

where c_1 is the initial composition of the dehydriding process in wt. %.

Plots of $1 - 3(1 - F')^{2/3} + 2(1 - F')$ at constant temperature (433K), as a function of time, are shown in Fig. 8. The reaction rates k'_d are given by the slopes of the straight lines shown in Fig. 8. The qualitative trend of k'_d on ΔP is almost similar as those of k_s , k'_s . The expression of experimental data is also possible by the exponential function [4,5] of the pressure difference ΔP such as:

$$k'_d = 0.08470 (P_p - P_e)^{1.803} \quad (13)$$

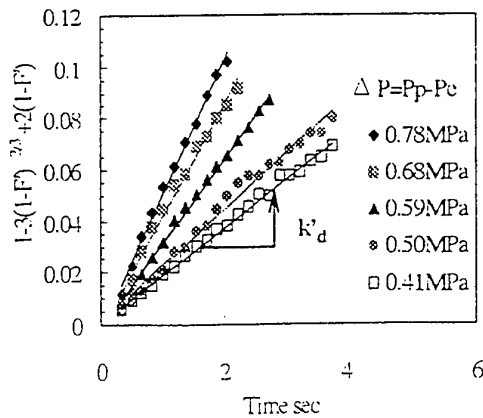


Fig. 8. $f(F)$ as function of time at 433 K

2.3.2 The temperature and the initial reacted fraction dependency. A plot of the reaction rate k'_d at the constant temperature (403 K), at the constant ΔP (0.41 MPa), as a function of initial composition c_1 , is shown in Fig. 9.

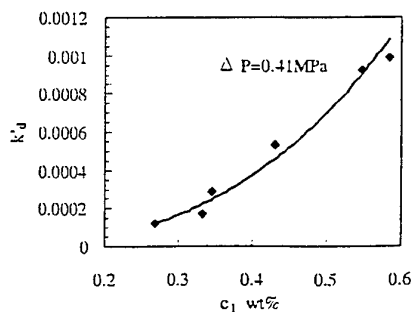


Fig. 9. Dependency of initial composition at 403 K

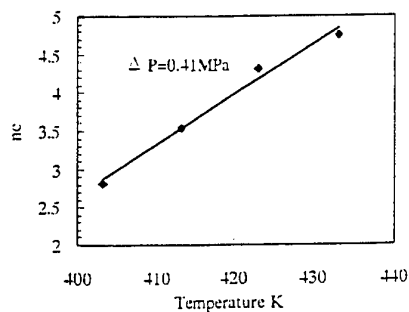


Fig. 10. Nc vs. temperature

The expression of experimental data is possible by the exponential function of the c_1 such as Equation (14). And, the relation of the nc vs. the temperature at constant ΔP (0.41 MPa) is illustrated in Fig. 10.

$$k'_d \propto c_1^{nc} = 0.004948c_1^{2.815} = 0.004948c_1^{0.06559T-23.58} \quad (14)$$

The Arrhenius plot [6,7] for the apparent rate constant defined as the k'_d / c_1^{nc} at the constant ΔP (0.41 MPa) is shown in Fig. 11. The activation energy of dehydriding process E_{dd} is found to be 7.102×10^4 J/mol. From the above, The constant De_d of the Equation (12) is 62.07. Therefore it can get the brand new rate equation of the dehydriding process as follows.

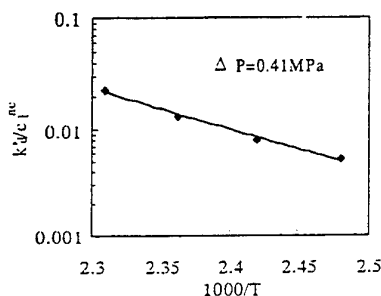


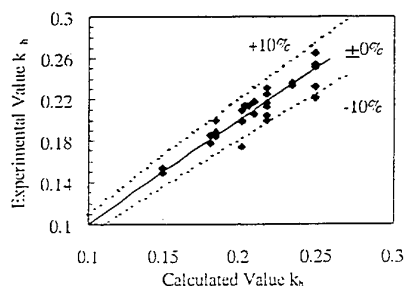
Fig. 11. Arrhenius plot of dehydriding process

$$1 - 3(1 - F')^{2/3} + 2(1 - F') = k'_d t$$

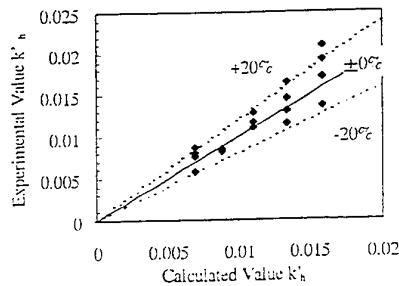
$$k'_d = (6 \times 62.07 / R p r_d^2 (P_p - P_e))^{1.803} \exp(-7.102 \times 10^4 / RT) c_1^{0.06559T-23.58} \quad (15)$$

2.4 Consideration

2.4.1 Hydriding process. Fig. 12 is the graphs of the experimental reaction rates vs. the calculated reaction rates at hydriding process. As for the surface reaction step, the reproduction of experimental value is made by the brand new rate Equation (10) in the error within $\pm 10\%$. And, about the diffusion reaction step, the reproduction of experimental value is made by the brand new rate Equation (11) in the error within $\pm 20\%$.



(a) Surface reaction



(b) Diffusion reaction

Fig. 12. Calculated data vs. experimental data at hydriding process

2.4.2 Dehydriding process. About the dehydriding process, it is understood that the reproduction of experimental data is made by the brand new rate Equation (15) in the error within $\pm 15\%$ from the comparison.

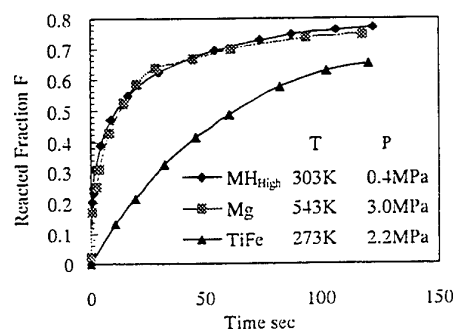


Fig. 13. Comparison with other MHs

2.4.3 The other MHs. Fig. 13 is a plot of the reacted fraction F vs. time for MH_{High} which shows a similar behavior to that of Mg alloy. When an experiment condition is compared, the condition of MH_{High} is the low temperature and the low pressure more. It is understood how the reaction rate of MH_{High} is fast when it thinks about our results of the effect of the temperature and the pressure. The reaction rates of MH_{High} are sufficiently fast to use it for the MH refrigeration system which is our target.

3. CONCLUSIONS

In the initial stage of the hydriding process of MH_{High} ($F < 0.3$) the rate-controlling step is a surface reaction. And, at a later stage of the hydriding process ($F > 0.3$) the diffusion reaction is the rate controlling step. As for the dehydriding process, it is understood that only diffusion reaction is the rate-controlling step. The reaction rates are exponentially proportional to the pressure difference and increases with temperature. The experimental reaction rates of MH_{High} are represented by the brand new rate correlations in the error within $\pm 20\%$. The reaction rates of MH_{High} are sufficiently fast to use it for the MH refrigeration system which is our target.

REFERENCES

1. P.S. Rudman, *Journal of the Less-Common Metals*, v. 89, pp. 93-110 (1983).
2. C.M. Stander, *Physic. Chemie Neue Folge*, pp. 229-238 (1977).
3. Octave Levenspiel, *Chemical Reaction Engineering*, John Wiley & Sons, Inc., (1972).
4. N. Komazaki and S. Suda, *Journal of the Less-Common Metals*, v. 89, pp. 127-132 (1983).
5. S. Suda, N. Kobayashi and K. Yoshida, *Journal of the Less-Common Metals*, v. 73, pp. 119-126 (1980).
6. X.L. Wang and S. Suda, *Journal of the Less-Common Metals*, v. 159, pp. 83-90 (1990).
7. S. Han and J. Y. Lee, *Journal of the Less-Common Metals*, v. 128, pp. 155-165 (1987).

ACKNOWLEDGEMENTS

This work has been partially funded by Waseda Advanced Research Institute of Science and Engineering.

PERFORMANCE COMPARISON AND ANALYSIS FOR INVERTER-DRIVEN AIR CONDITIONERS THROTTLING WITH ELECTRONIC EXPANSION VALVE

Yu Bingfeng Wang Zhigang Meng Xiangzhao

School of Energy and Power Engineering
Xi'an Jiaotong University, Xi'an 710049, P.R.China

Keywords: electronic expansion valve, capillary tube, performance

ABSTRACT. In this paper, the performances variation of a refrigerating system of the small capacity inverter-driven air conditioner at the different operating frequencies using the electronic expansion valve and capillary tube individually are analyzed. The mathematical models and the steady model of the refrigerating system which have been verified by the experiments. The analysis shows that more advantages could be obtained for the air conditioner with the electronic expansion valve at the frequencies of 20Hz-120Hz, however, the air conditioner applying the capillary tube has the acceptable performance in the major frequency range of 40Hz-80Hz at the most time so that it is feasible for the small capacity inverter-driven air conditioner to employ the capillary tube as the throttling device.

INTRODUCTION

The recent development for improving the performance of air conditioners is the capacity adjustment with the variable load using the combination of the inverter-driven compressor and electronic expansion valve (EEV). The wide adjusting range of the refrigerant mass flow rate is required for the capacity modulation of inverter-driven air conditioners. The EEV has the characteristics of the large scope of the mass flow rate adjustment, high controlling accuracy, and suitable for the artificial intelligence control, which can change the flow rate according to the varying load so that the performance property of the refrigerating system is obviously better than that with the other types of throttling devices. It is ideal that EEV is applied to the inverter-driven air conditioner without consideration of other factors such as cost. However, the inverter-driven air conditioner operates in some frequency range at the most time, and the capillary tube is more available and cheaper, it is of great importance that the performance comparison and the analysis for the small capacity inverter-driven air conditioner throttling with EEV and capillary tube are carried out so as to decide if the capillary tube could be adopted in the small capacity inverter-driven air conditioner.

MATHEMATICAL MODEL OF EEV

For the power-operated type electronic expansion valve (EEV), the equation of the mass flow rate through EEV can be expressed by

$$M = \varepsilon \alpha F_o \sqrt{2\rho(P_1 - P_2)} \quad (1)$$

where F_o represents the opening area of the electronic expansion valve; ε is expansion correction coefficient which is relevant to the factors such as the relative difference of the pressure before-and-after the orifice-plate, the ratio of the hole cross section area. α , the mass flow rate coefficient, has the relation to the structure of the throttling device, the method of pressure measuring intake, and also the ratio of the hole cross section area to the pipe cross section area. Under normal conditions the value of $\varepsilon \alpha$ is achieved from the experiments or numerical computation. In this paper, The experiments for EEV were carried out in a standard rig of air conditioner performance. The test environment temperatures are: for indoor, 27 C (DB), 19 C (WB), for outdoor, 35 C (DB), 24 C (WB). The sensors and the flowmeters for measuring temperatures and pressures are installed at the entrance and exit locations of the refrigerating system parts, and also at the air side. After the testing conditions are fixed, the experimental system implements the data collection, communication, computation, and control output automatically. The computing results based on the testing are shown in Fig.1 and Fig.2. Fig.1 shows that the curve of the relationship between $\alpha \cdot \varepsilon$ and the driving impulse number of EEV and Fig.2 indicates the relationship between $\alpha \cdot \varepsilon$ and the quality at outlet of EEV.

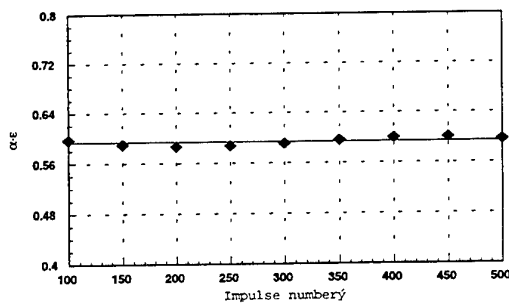


Fig.1. Curve of $\alpha \cdot \varepsilon$ versus driving impulse number

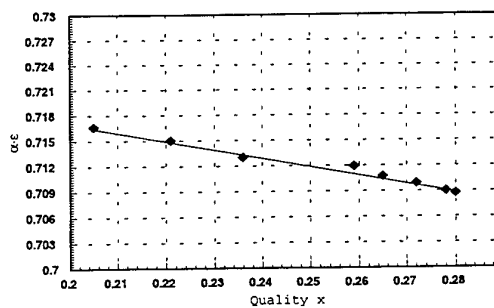


Fig.2. Curve of $\alpha \cdot \varepsilon$ versus quality at outlet

Applying the least square regression method, the following expression could be obtained from the curve shown in Fig.2:

$$\alpha \cdot \varepsilon = 0.75 - 0.1407x \quad (2)$$

Fig.3 is the schematic of the structure of the cone-type valve investigated in this paper. Its flow area can be obtained with the following equation:

$$A = \pi \cdot h \cdot \sin \frac{\beta}{2} \left(d - \frac{1}{2} h \cdot \sin \beta \right) \quad (3)$$

where h is the open extent of the needle valve, d is the hole diameter of the valve, and β is the needle valve angle. If $A_{\max} = \frac{1}{4} \pi d^2$ and $\beta = 36^\circ$, then

$$\frac{A}{A_{\max}} = \frac{2.568 - \frac{h}{h_{\max}}}{1.568} \times \frac{h}{h_{\max}} \quad (4)$$

According to equation (4), the flow area of the throttling hole at any impulse number could be evaluated.

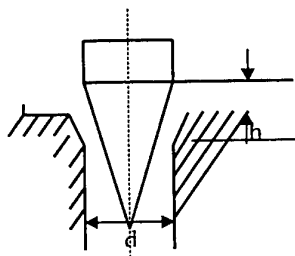


Fig.3. Schematic of the structure of cone valve

REFRIGERATING PERFORMANCE

The frequency variation range of the inverter-driven air conditioner is rather large, e.g. 20Hz-120Hz. In this paper the computation simulation is employed to the investigation which has been verified by the experiments. The integrated simulation program is composed of the models of the refrigerating compressor, condenser, evaporator, connecting pipes, accumulator, and also EEV presented in this paper. It is used in the computation for the 1.5HP small power inverter-driven air conditioner and the curves of the refrigeration system performance

are achieved at the different driving impulse numbers of the EEV and variable power frequencies of the compressor. In this investigation the LAM type EEV made by FUJIKOKIMFC CO. LTD is applied. The other considerations for the simulation conditions are: indoor air flow rate 500m³/h outdoor air flow rate 1580m³/h indoor temperatures: 27 C (DB) and 19 C (DB), outdoor temperatures: 35 C (DB) and 24 C (WB). The relationship between the refrigerating capacity and the power-supply frequency of the compressor is given in Fig.4. It can be understood from Fig.4 that the refrigerating capacity of the system increases gradually with the operating frequency rising from 20Hz to 120 Hz. When the driving impulse number EEV grows from 300 to 500, the increasing tendency of the system refrigerating capacity is more obvious. Moreover, with the impulse number getting higher from 100 to 500, the refrigerating capacity rises first but then decreases, and there exists a peak value for all the frequencies. The relative impulse number to the largest refrigerating capacity increases with the growing frequency. Fig.5 shows the curves of system EER changes with the power-supply frequencies of the compressor at the various driving impulse numbers of EEV. From Fig.5, it can be noticed that EER of the air conditioner rises first but then decrease, and there also is a crest value at the various impulse numbers. With the impulse number increases from 100 to 500, the EER rises first but then decreases, and there exists a peak value for all frequencies, and the relative impulse number to the best EER of the air conditioner is getting bigger with the growing frequency. From Fig.5, there is an intercross of EER curves for the frequencies of 20Hz and 40Hz respectively at the impulse number of about 270. The reason for this intercross is that the outlet superheat degree of the evaporator at 20 Hz and the frequency number of 270 is 0, while the enhancement of the refrigerating capacity with the increase of the impulse number is small but the power consumption is bigger so that the EER will decrease.

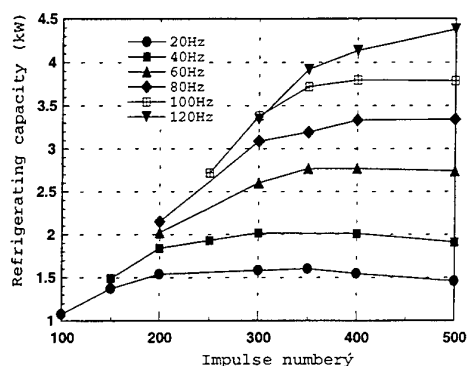


Fig.4. Curve of refrigerating capacity versus driving impulse number

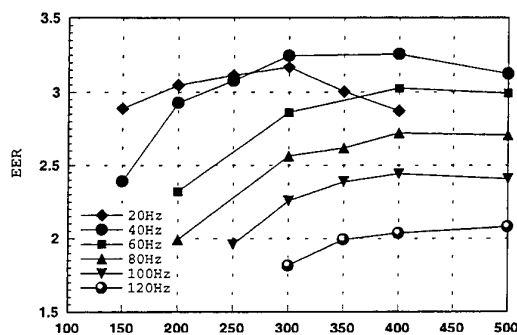


Fig.5. Curve of EER versus driving impulse number

COMPARISON OF REFRIGERATING PERFORMANCE OF THE INVERTER-DRIVEN AIR CONDITIONER WITH EEV AND THE CAPILLARY TUBE

Based on the reference[2] and the computing results in this investigation, a comparison of EER and the refrigerating capacity of the inverter-driven air conditioner with EEV and the capillary tube respectively are shown in Fig.6. and Fig.7.

Fig.6 indicates the comparison of the refrigerating capacity of the inverter-driven air conditioner using EEV and the capillary tube individually while the comparison of EER is given in Fig. 7. From Fig. 6 and Fig.7 it is found out that the system performance with EEV can be guaranteed to be better than that with the capillary tube at all frequencies by adjusting the driving impulse to change the throttling passage area and the refrigerant flow rate. The refrigerating capacity of the air conditioner applying EEV is higher than that with the capillary tube by 14.6% (144W) at the lower frequency of 20Hz and higher by 17%(635W) at higher frequency of 120Hz, while is higher only by 5%(116W) at the frequency of 80Hz. The advantage of the system refrigerating capacity using EEV to be the throttling device at both lower and higher frequencies is more obvious than that using the capillary tube. Also it can be seen from Fig.7 that the EER of the inverter-driven air conditioner using EEV is higher than that with the capillary tube by 10%(0.284)

at the lower frequency of 20Hz and higher by 16%(0.28) at the higher frequency of 120Hz, while is higher only by 6%(0.16) at the frequency of 80Hz. The more advantage of the system EER using EEV to be throttling device at both lower and higher frequencies can be obtained. However, the refrigerating performance of the inverter-driven air conditioner can be acceptable at the normal frequency range from 40Hz to 80Hz.

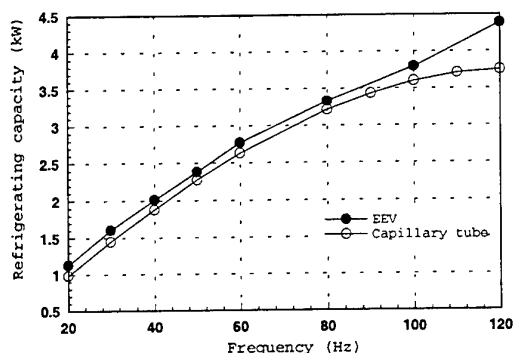


Fig.6. Comparison of the refrigerating capacity

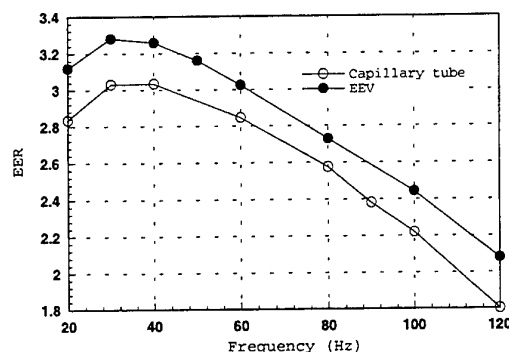


Fig.7. Comparison of EER

CONCLUSION

For 1.5HP inverter-driven air conditioner, the simulation analysis to the performance applying the electronic expansion valve is carried out using the mathematical model of the refrigerating system which has been verified by the experiments. The performance curves are achieved at the different power-supply frequencies of the compressor and the various driving impulse number (opening extent) of EEV. The comparison of the performance between the inverter-driven air conditioner with the capillary tube and that with EEV is pursued. The analysis reveals that the performance of the inverter-driven air conditioner with EEV is always better than that with the capillary tube and the advantages are more distinct at both lower and higher frequencies. The inverter-driven air conditioner employing the capillary tube to be the throttling device has an acceptable refrigerating performance which indicates that it is feasible for the small refrigerating capacity inverter-driven air conditioner to adopt the capillary tube.

REFERENCES

1. B. F. Yu, Z. G. Wang and X. M. He, "The Influence of the Refrigerant Charge on the Refrigerating Performance and Its Determining Principle for Inverter-driven Air Conditioner", *Fluid Machinery* v.26, No. 9, pp.52-56 (1998)
2. B. F. Yu, Z. G. Wang and X.M. He, "The Analysis of the Performance for the Small Refrigerating Capacity Inverter-driven Air Conditioner with Single Capillary Tube", *Fluid Machinery* v.26, No. 12, pp.47-50 (1998)
3. Z.Y. Zhang, *Refrigeration Principle and Its Devices*, Machinery Industry Press.(1991)
4. W. Q. Tao, *Numerical Heat Transfer*. Xi'an Jiaotong University Press. (1988)

NOMENCLATURE

ε	Expansion correction coefficient	ρ	Density of refrigerant at the entrance of electronic expansion valve(kg/m ³)
α	Mass flow rate coefficient	F_0	Passage area of electronic expansion valve(m ²)
P_1	Pressure at the entrance of electronic expansion valve(bar)	x	Quality of refrigerant at the exit of electronic expansion valve
P_2	Pressure at the exit of electronic expansion valve(bar)		

Q. Cryogenic Engineering

NEW RESULTS ON THERMOACOUSTIC REFRIGERATION WITH GAS SUBSTANCE

Jean Valentin Lubiez, Fathi Jebali Jerbi and Maurice Xavier Francois
LIMSI BP 133 91403 Orsay Cedex France
Email: jebali@limsi.fr; Fax: (33) 1 69 85 80 88

Keywords: thermoacoustic, regenerator, network, heat engines

ABSTRACT. A thermoacoustic refrigerator working with nitrogen gas is investigated near the resonance condition. The gas oscillations with frequencies varying from 5 to 80 Hz are produced by a mechanical driver mounted at one end of the resonant tube containing the heat exchangers (cold and hot) and the regenerator (parallel stack of plates). Detailed experimental data of oscillating pressure amplitude and phase shift at two locations of the resonant tube are given as a function of the driving frequency for a fixed gas mean pressure. These results, compared with the analytical prediction derived from the network theory, show a good agreement. Once the acoustical properties (acoustic pressure and velocity) have been determined, the energy flow (heat and work) is then calculated along the resonant tube and the heat flux pumped at the cold end of the stack, Q_c , is deduced as function of the working frequency for various temperature differences between heat exchangers, ΔT . These calculations show a good agreement with the experimental results which put forward a maximum heat pumping close to the resonance condition.

1. INTRODUCTION

Increasing interest for environment protection and requirement of simplicity for heat engines give new goals for researches on energy conversion processes such as thermoacoustics. In particular, thermoacoustic refrigerators achieve these goals by using no harmful fluids with no moving parts [1]. In this paper we intend to present some results on the thermoacoustic refrigeration using a resonant tube refrigerator working with nitrogen gas. We point out that the aim of this work is not to propose a high efficiency prototype of engine, but to give more quantitative analysis of this energy conversion process. In this heat engine, acoustic power is used to pump heat from a low temperature source (cold heat exchanger) to a high temperature source (hot heat exchanger). These work and heat flows and their mutual conversion occur in the regenerator consisting of two thermodynamic media: the oscillating fluid and the solid plates (matrix). When operating conditions are near resonance, which is the case of the actual investigation, spacing between the plates is of the same order of the thermal penetration depth, δ_k , and therefore the contribution of the standing wave to the energy conversion is much more important than that of the progressive wave.

In previous works [2,3], it has been shown that the heat flux and the work flux can be expressed in terms of pressure oscillation and velocity. These oscillating variables can be calculated by using a linear network approach [4,5]. Each element of the engine is represented by an active or a passive circuit depending on whether it is subjected to a temperature gradient or not. Hence, the stack, being placed between two heat exchangers, acts as an active network whose current gain, E , depends on the axial temperature gradient while the hot and the cold heat exchangers, as well as the resonator, assumed to be isothermal, act as passive circuits. Inside the stack, physical properties such as ambient density, viscosity, sound speed, thermal conductivity, etc., are temperature dependent and thus depend on location. The stack network is then divided into a series of elementary circuits to take into account the local fluid thermodynamic properties.

Once the acoustical elements (impedance, admittance and current gain) of an elementary circuit have been determined, the oscillating pressure and velocity are deduced at this location. Then, the acoustic power, the heat flux and therefore the total energy flow are calculated as function of these parameters. From the energy balance, the local temperature gradient is then corrected, and this operation is recurred until convergence. Hence, one can calculate step by step, the heat flux pumped at the cold end of the stack, Q_c . Another aim of this paper is to carry out new experimental results on the thermoacoustic heat pumping and to analyze these results on the ground of the above mentioned calculations. In the actual work, we will present the experimental dependence of the acoustic pressure and the heat flux pumped at the cold end of the stack as functions of the working frequency.

2. EXPERIMENTAL SET-UP AND PROCEDURE

The experimental set-up (Fig. 1) consists of an acoustic driver, a regenerator, two heat exchangers and a resonator tube ending by a splaying. The acoustic source is a mechanical driver using a mobile piston of 100 mm diameter and whose full stroke can reach 8 mm. This system allows to generate acoustic waves of frequency varying from 5 to 70 Hz and of hundreds mbars pressure amplitude. A cone-shaped duct of 124 mm length allows to avoid an abrupt transition between the driver and the resonator. Note that in order to avoid the seal problems, a clearance between the piston and the driver wall inner side have been provided for. The resonator is 36 mm diameter and 1.995 m length brass ending by 100 mm splaying allowing to reduce the resonance frequency (53 Hz). The regenerator is a Mylar parallel plates-stack of 0.15 m length. The plates are of 0.2 mm thickness and are spaced 0.7 mm apart. The two heat exchangers consist of parallel copper plates of 0.2 mm thickness and of 0.8 mm spacing. The hot heat exchanger is held at the room temperature by water circulating through a collar surrounding the copper plates. The cold heat exchanger is encircled by a screwed copper ring around which a wire, of 23 Ω electrical resistance, has been wound in order to measure the refrigeration power, Q_c . The temperature difference between the hot and the cold ends of the stack are measured by two thermocouples inserted between the plates of this latter.

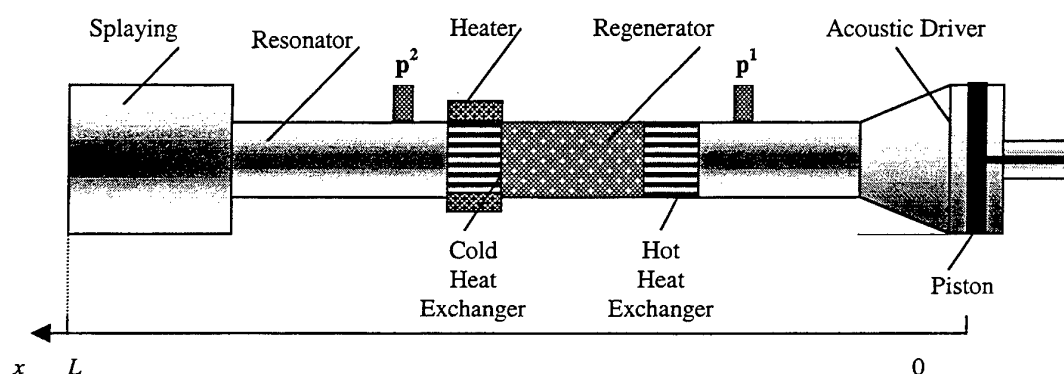


Fig. 1 Experimental set-up

The acoustic pressures are measured by two piezoelectric transducers of 80 pC/bar sensitivity and of 70 kHz natural frequency, mounted on upstream and downstream side of the regenerator. These pressures, $p^1(t)$ and $p^2(t)$, are recorded during two seconds with a sampling frequency of 1 kHz and then processed to obtain their Fourier transforms, respectively, $p^1(f)$ and $p^2(f)$, f being the working frequency. The experiment consists in starting the acoustic source for a fixed mean pressure, p_0 , and a fixed frequency, f , leading to a thermoacoustic effect (cooling at the cold heat exchanger). Then one supply the heater with an electrical current and held a chosen temperature gradient between the stack ends. Taking into account the heat losses through the regenerator, the surrounding thermal insulation and the resonator walls, one can measure the pumped heat at the cold heat exchanger.

3. THEORETICAL BACKGROUND

Acoustic Field

Using one-dimensional network model, an infinitesimal line section of length dx , situated at a location x , is represented, when it is submitted to a longitudinal temperature gradient, by an active circuit having an impedance, $z(x) dx$, an admittance, $y(x) dx$, and a current gain constant, $e(x) dx$. Expressing the acoustic power variation dI/dx in the stack, one can obtain the following set of transmission line equations:

$$\frac{dp_1}{dx} = -z(x) q_1 \quad (1)$$

$$\frac{dq_1}{dx} = -y(x)p_1 + e(x)q_1 \quad (2)$$

where p_1 is the first order acoustic pressure which is assumed to be homogeneous over the cross section and $q_1 = A_f u_1$ is the volumetric velocity, u_1 being the first order spatial average of the axial component velocity and A_f being the fluid cross section. The impedance and the admittance per unit length are given respectively by [6]

$$z = \frac{1}{A_f} \frac{j\omega\rho_0}{1-f_v} \quad (3)$$

$$y = \frac{j\omega A_f}{\rho_0 c^2} [1 + (\gamma - 1)f_\alpha] \quad (4)$$

where $j = \sqrt{-1}$, ρ_0 , c and γ are respectively the density, sound velocity and specific heats ratio of fluid, ω is the radian frequency, f_v and f_α are respectively the viscous and the thermal dissipation function depending on the medium geometry and are detailed in above reference. The constant $e(x)$ characterises the attenuation (or the gain) of the volumetric velocity which arises when the longitudinal temperature gradient dT_0/dx is nonzero. It can be written as:

$$e = \beta \frac{dT_0}{dx} f_{vk} \quad (5)$$

where β is the fluid isobaric thermal expansion coefficient and f_{vk} is a factor taking into account geometry and both thermal and viscous dissipations [6].

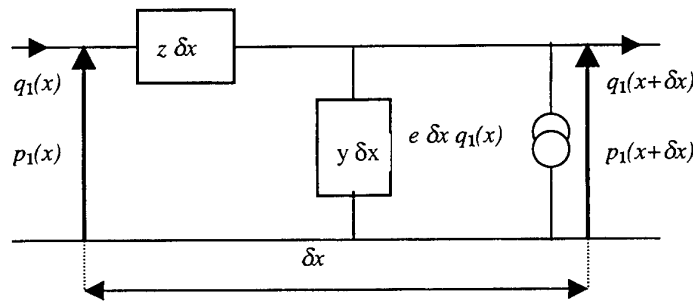


Fig. 2 Active network

Dividing the whole system into N elementary circuits, of length δx (Fig. 2), the above equations lead to the transmission equations system within a circuit k

$$\begin{bmatrix} p_1^k \\ q_1^k \end{bmatrix} = H^k \begin{bmatrix} p_1^{k-1} \\ q_1^{k-1} \end{bmatrix} \quad (6)$$

and therefore for the line of length L , one obtains:

$$\begin{bmatrix} p_1^N \\ q_1^N \end{bmatrix} = \prod_{k=1}^N H^k \begin{bmatrix} p_1^0 \\ q_1^0 \end{bmatrix} \quad (7)$$

where H^k is the transfer matrix of the circuit k given by:

$$H^k = \begin{bmatrix} 1 & \frac{z_k \delta x}{1 + e_k \delta x} \\ \frac{y_k \delta x}{1 + e_k \delta x} & 1 \\ 1 + e_k \delta x & 1 + e_k \delta x \end{bmatrix} \quad (8)$$

Then, taking into account the boundary conditions: $q_1(x=0) = j\omega l A_f e^{j\omega t}$ at the piston location, with l being the piston stroke, and $q_1(x=L) = 0$ at the tube closed end, one can calculate step by step the acoustic pressure and velocity along the whole engine. Note that in this calculation, the transfer matrix H^k depends on the location: for the regenerator and for heat exchangers, which are made of N_p parallel plates stacks, the equivalent impedance and admittance of these circuits are those of circuits of N_p parallel impedance and admittance. On the other hand, for the resonator tube and for heat exchangers, which are assumed to be isothermal, the current gain constant vanishes and therefore their circuits become passive.

Work and Heat Fluxes

According to Tominaga model [3], the energy flux per unit area due to fluid oscillations in the stack (or regenerator) region is equal to enthalpy flow:

$$\rho_0 \langle \langle h_1 \cdot u_1 \rangle_t \rangle_r = \tilde{Q} + I \quad (9)$$

where $\tilde{Q} = \rho_0 T_0 \langle \langle s_1 \cdot u_1 \rangle_t \rangle_r$ is the heat flux due to fluid oscillation and $I = \langle \langle p_1 \cdot u_1 \rangle_t \rangle_r$ is the work flux., s_1 and h_1 being respectively the oscillating entropy and enthalpy. Symbols $\langle \cdot \rangle_t$ and $\langle \cdot \rangle_r$ indicate respectively time average and space average of the quantity in the bracket. Note that the heat flux due to fluid oscillation, \tilde{Q} , consists of three components whose expressions have been developed in reference 3: a standing and progressive parts, Q_{stand} and Q_{prog} and heat loss in the regenerator, Q_D . In a resonant tube stack, Q_{stand} is dominant while it is Q_{prog} in a good regenerator. On the other hand, The work flux per unit area can be expressed as a function of acoustic pressure and velocity amplitudes as follows:

$$I = \frac{1}{2} |p_1| |u_1| \cos \Phi \quad (10)$$

where Φ is the phase between p_1 and u_1 . The total energy flux, which consists of the work flux, I , the heat flux due to fluid oscillation, \tilde{Q} , and the heat conduction flux $Q_{cd} = -\lambda_s \nabla T_0$ through the solid matrix, is constant along the stack:

$$E = (I + \tilde{Q}) A_f + Q_{cd} A_s = C_{st} \quad (11)$$

where subscript s indicates the solid medium (one notes that the heat conduction in fluid is much less than that in solid medium). Then, the total heat flux $\tilde{Q} A_f + Q_{cd} A_s$ at the stack cold end position yields the pumped heat at the cold heat exchanger, Q_c . For experimental comparison, this refrigeration load (in Watts) can be determined taking into account both the heat losses through the cold heat exchanger due to viscous dissipation, and the heat leaks through the surrounding thermal insulation and the resonator walls:

$$Q_c = Q_{elec} + Q_{loss} + Q_{leak} \quad (12)$$

3. RESULTS AND COMPARAISON BETWEEN THEORY AND EXPERIMENTS

An example of our results on the ratio of two acoustic pressures, p_1^1 and p_1^2 , (transfer function) evaluated at the locations $x_1 = 190$ mm and $x_2 = 765$ mm as a function of frequency and for mean pressure $p_0 = 1$ bar, is shown in

Fig. 3. The solid lines are the theoretical predictions using network model as explained in the above section. These results show a good agreement between theory and experiments for amplitude (Fig. 3.a) as well as for phase (Fig. 3.b).

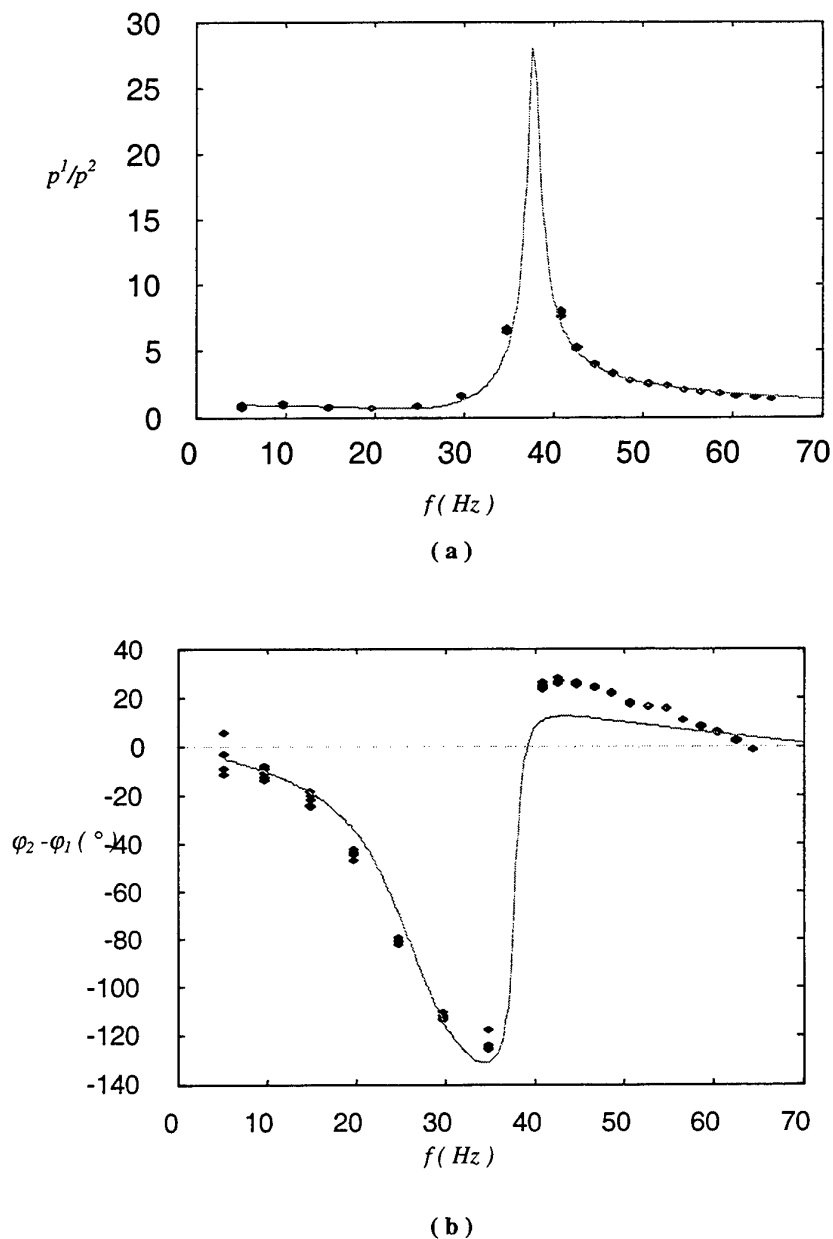


Fig. 3 Transfer function between two pressures transducers as a function of frequency

However, note that if one plots the absolute pressures, the results show that the experimental values are systematically lower than the theoretical ones. This discrepancy is due very probably to the indetermination of the acoustic driver characteristics. Indeed, as mentioned in section 2., a clearance between the piston and the driver wall have been provided for, in order to avoid the seal problems, which affects the acoustic field in the system by reducing the pressure. This clearance can be represented by an impedance which could be introduced in the total circuit, and therefore, its effect could be taken into account in the heat and work fluxes calculations.

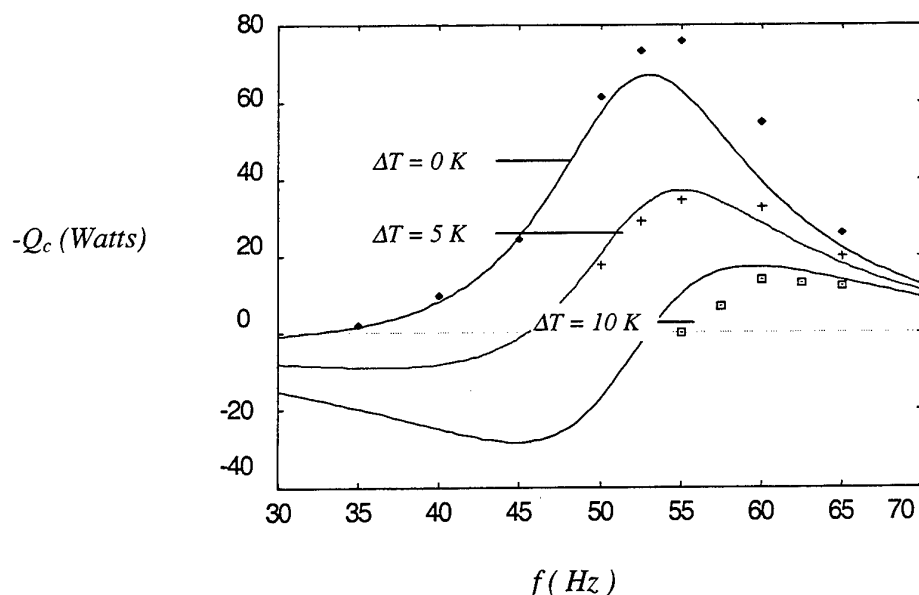


Fig. 4 Refrigeration power as a function of frequency

In Fig. 4, we have plotted an example of our results on the refrigeration power, $-Q_c$, as a function of the working frequency for various temperature differences between the two stack ends ($\Delta T = 0$ K, $\Delta T = 5$ K and $\Delta T = 10$ K) at a fixed mean pressure ($p_0 = 2.5$ bars). Note that the results corresponding to $\Delta T = 0$ K are obtained by supplying the cold heat exchanger with an electrical power until reaching zero temperature difference. These results show, on one hand, a good agreement between theory and experiment, and on the other hand, a maximum refrigeration power close to the resonance. In particular, for $\Delta T = 0$ K, the maximum refrigeration power is situated at the resonance (53 Hz). This could be explained as follows: when the temperature difference between the two heat exchangers is zero, the local temperature gradients in the stack region are in their turn close to zero. The heat losses in the stack (Q_D and Q_{cd}) are then non-existent and, therefore, the total heat flux consists of Q_{stand} which is maximal at the resonance (the progressive component is much lower than the standing one in our system). For non-zero temperature differences, the heat losses increase with ΔT (they are proportional to temperature gradients) and therefore the pumped heat decreases.

4. CONCLUSION

We have presented some experimental results on thermoacoustic refrigeration occurring in a resonant tube filled with nitrogen gas. They are in good agreement with models based on a network and thermodynamic approaches. It is shown, in particular, that the heat losses depend on both the frequency and the temperature difference between the two stack ends, and the maximum heat pumping occurs close to the resonance condition. The network and the thermodynamic approaches allow us to determine a parametric analysis of the performance of the refrigerator.

REFERENCES

1. G. W. Swift, "Thermoacoustic Engines", *J. Acoust. Soc. Am.*, v84, (4), (1988).
2. W. P. Arnott et al., "General Formulation of Thermoacoustics for Stacks Having Arbitrarily Shaped Pore Cross Sections", *J. Acoust. Soc. Am.*, v90, (6), (1991).
3. A. Tominaga, "Thermodynamic aspects of thermoacoustic theory", *Cryogenics*, v35 (7), 427-440, (1995).
4. F. Z. Guo et al., "Flow Characteristics of a Cyclic Flow Regenerator", *Cryogenics*, v27, 152-155, (1987).
5. J. H. Xiao and F. Z. Guo, "Analytical Network Model on the Flow and Thermal Characteristics of Cyclic Flow Cryogenic Regenerators", *Cryogenics*, v28, 762-769, (1988).
6. G. W. Swift, "Thermoacoustic Engines and Refrigerators", Short Course on Thermoacoustics, Berlin version (1999).

THERMOACOUSTIC STREAMING ON A CYLINDER

Ashok Gopinath

Department of Mechanical Engineering
Naval Postgraduate School, Code ME
Monterey, California 93943, USA
E-mail: gopinath@nps.navy.mil

Keywords: thermoacoustics, time-averaged effects, streaming, thermodynamic moduli

Abstract. The fundamental problem of thermoacoustic streaming on a cylinder in a strong standing acoustic field has been treated analytically. The cylinder is taken to be located at the velocity antinode of the plane standing wave, and also assumed to be compact ($ak \ll 1$). Only the high frequency limit is considered here for which the Stokes oscillatory boundary layer thickness is much smaller than the cylinder radius, and the dissipative effects in the boundary layer are more pronounced. It is found that the phased interaction of the first-order harmonic quantities in the boundary layer is capable of introducing a second-order time-averaged temperature distribution, in addition to the well known second-order time-averaged fluid motion. The associated steady temperature gradients cause localized heating and cooling effects over the surface of the cylinder, even in the complete absence of any externally applied temperature gradient. The role of little known second-order thermodynamic moduli is pointed out, which however do not contribute to this phenomenon for the case of an ideal gas host fluid. Results for this time-averaged thermal effect are presented and discussed with possible application to the acoustic heating of a suspension of small particles.

1. INTRODUCTION

Thermoacoustic streaming, by analogy with acoustic streaming, refers to the phenomenon of secondary time-independent thermal effects that may be induced by the nonlinear interactions of primary time-harmonic flow variables, such as in an acoustic field. Such thermal effects in an oscillatory flow field can either be generated in the bulk of the fluid, or more significantly, in the oscillatory shear layers where it interacts with rigid boundaries. This paper deals with the latter situation of thermoacoustic streaming induced in the oscillatory boundary layers on a rigid and compact cylinder located at the velocity antinode of a monochromatic plane standing acoustic field.

Such phenomena were originally treated by Rott [1, 2], and Merkli & Thomann [3], and in the past decade or so have generated much interest from the view point of applicability to thermoacoustic engines, as reviewed, for instance, by Swift [4, 5]. A more recent treatment of the problem along with a survey of the relevant literature in the field has also been provided by Gopinath et al.[6]. A related problem of time-averaged streaming fluid motion around a sphere (positioned at a velocity *node*) may be found in a recent paper by Zhao et al.[7].

The layout of the paper is as follows: the governing equations and solution procedure are outlined in § 2 and § 3. The leading order solution is laid out in § 4 and compressibility corrections are added in § 5. The second-order thermoacoustic streaming solution is then developed in § 6, along with a brief analysis of the role of second-order thermodynamic moduli. The paper ends with a presentation and discussion of the results in § 7.

2. GOVERNING EQUATIONS

Consider the initial quiescent state of the fluid, at rest, characterized by a mean pressure, p_m , density, ρ_m , and temperature, T_m . Now in the presence of a plane standing sound field, the governing equations are developed for the velocity (\mathbf{u}^*) and temperature (T^*) distributions in the fluid around a long rigid

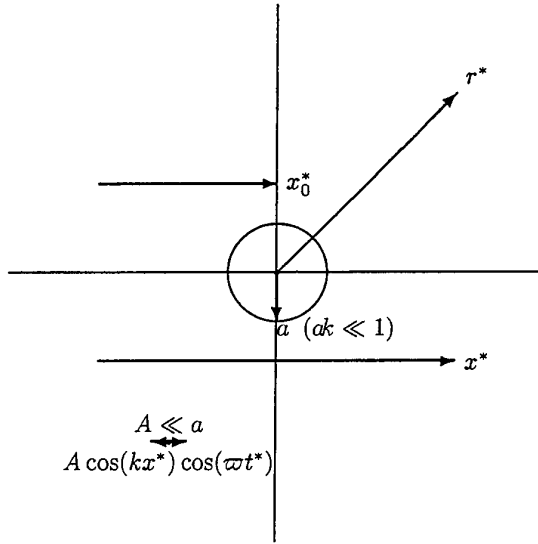


Figure 1: Definition sketch of the problem showing the cylinder position and the coordinate system

circular cylinder of radius, a , located at the velocity antinode of the standing wave – see Figure 1 for a definition sketch of the problem. In what follows, a superscript $*$ denotes dimensional quantities, a subscript m denotes the mean quiescent state, while variables in **boldface** represent vector quantities. The cylinder is located at $x^* = x_0^*$ and the standing wave velocity distribution in the immediate vicinity of the cylinder is taken to be of the form

$$u_x^* = U_0 \cos(kx_0^*) \cos(\omega t^*) \quad (1)$$

where $U_0 = A\omega$ is the velocity amplitude, $k = 2\pi/\lambda$ the wave number, ω the radian frequency, t^* the time, and x^* the coordinate measured from the velocity antinode of the standing wave (cf. Figure 1) in the (r, ϑ) plane along the $\vartheta = 0$ direction which coincides with the axis of fluid oscillation (ϑ is as usual measured counter-clockwise from this axis). Here we are concerned with the case of the cylinder positioned at the velocity peak for which $x_0^* = 0$. We choose a cylindrical coordinate system (r^*, ϑ, z^*) , with origin at the center of the cylinder, and axis normal to the direction of oscillation. The fluid velocity $(u_r^*, u_\vartheta^*, 0)$ is sought in the following form

$$\mathbf{u}^* = \nabla^* \times (\hat{\mathbf{i}}_z \psi^*) \quad (2)$$

where ψ is the stream function representing the velocity field assumed incompressible for the case of a compact cylinder ($ak \ll 1$) in a small amplitude sound field ($A/a \ll 1$), which together ensures that their product, the Mach number ($\alpha = Ak$), is also small. Since the focus of this study is on thermoacoustic effects in the fluid, to simplify the analysis, the rigid cylinder is taken to be isothermal at the temperature T_m , and with a heat capacity large enough to thermally decouple it from the fluid. For the more general case it would be a straightforward matter to extend this analysis to a conjugate problem involving coupling with heat transfer in the cylinder as well, as has been treated elsewhere [6], although in a different context.

In the presence of the acoustic field, the (dependent) flow variables are defined as disturbance quantities from the quiescent mean and non-dimensionalized as follows

$$\tau = \omega t^*, \quad x = kx^*, \quad r = \frac{r^*}{a}, \quad \mathbf{u} = \frac{\mathbf{u}^*}{U_0}, \quad \psi = \frac{\psi^*}{U_0 a}, \quad \nabla \equiv a \nabla^* \quad (3a)$$

$$\rho = \frac{(\rho^* - \rho_m)}{\Delta \rho_{ref}}, \quad p = \frac{(p^* - p_m)}{\Delta p_{ref}}, \quad \theta = \frac{(T^* - T_m)}{\Delta T_{ref}} \quad (3b)$$

$$\Delta \rho_{ref} = \alpha \rho_m, \quad \Delta p_{ref} = \alpha \rho_m c_m^2, \quad \Delta T_{ref} = \alpha T_m \left(\frac{c_m^2}{c_p T_m} \right) \quad (3c)$$

along with the definitions $c_m = \varpi/k$ being the *adiabatic* speed of sound in the quiescent state, γ the ratio of specific heats, and $\alpha = U_0/c_m = Ak$ the Mach number (also called the wave-slope parameter). In terms of the above dimensionless variables the velocity components are given by

$$u_\vartheta = -\frac{\partial \psi}{\partial r}, \quad u_r = \frac{1}{r} \frac{\partial \psi}{\partial \vartheta} \quad (4)$$

and the dimensionless vorticity defined as $\omega = \nabla \times \mathbf{u}$, with components $(0, 0, \omega_z)$ is given by

$$\omega_z = -\nabla^2 \psi \quad (5)$$

For the other flow variables, the governing equations of mass, momentum and energy (ignoring higher order terms in view of $ak, \alpha \ll 1$) are given by ([8])

$$\nabla \cdot \mathbf{u} = 0 \quad (6)$$

$$\left[\frac{\partial \mathbf{u}}{\partial \tau} + \varepsilon (\mathbf{u} \cdot \nabla) \mathbf{u} \right] = -\frac{1}{ak} \nabla p + \frac{1}{M^2} \left[\nabla^2 \mathbf{u} + \left(\frac{1}{3} + \frac{K}{\mu_v} \right) \nabla (\nabla \cdot \mathbf{u}) \right] \quad (7)$$

$$\left[\frac{\partial \theta}{\partial \tau} + \varepsilon (\mathbf{u} \cdot \nabla) \theta \right] = \frac{1}{\sigma M^2} \nabla^2 \theta + \beta T^* \left[\frac{\partial p}{\partial \tau} + \varepsilon (\mathbf{u} \cdot \nabla) p \right] + \frac{\varepsilon ak}{M^2} \chi \quad (8)$$

and need to be solved together with a suitable equation of state relating the pressure, density and temperature disturbances which in general may be expressed as follows

$$\Delta \rho^* = \left(\frac{\partial \rho^*}{\partial p^*} \right)_{T^*} \Delta p^* + \left(\frac{\partial \rho^*}{\partial T^*} \right)_{p^*} \Delta T^* \quad (9)$$

In the above equations μ_v is the dynamic (first coefficient of) viscosity of the fluid, while K is the bulk viscosity, and the thermodynamic modulus β is the familiar (first) coefficient of thermal expansion defined (in dimensional terms) as

$$\beta = -\frac{\hat{\beta}}{\rho^*} \quad \text{where } \hat{\beta} = \left(\frac{\partial \rho^*}{\partial T^*} \right)_{p^*} \quad (10)$$

In (8) σ represents the Prandtl number, and the last term χ represents the viscous dissipation terms defined in the usual manner as

$$\chi = 2 \left[\left(\frac{\partial u_r}{\partial r} \right)^2 + \left(\frac{1}{r} \frac{\partial u_\vartheta}{\partial \vartheta} + \frac{u_r}{r} \right)^2 \right] + \left[\frac{\partial u_\vartheta}{\partial r} - \frac{u_\vartheta}{r} + \frac{1}{r} \frac{\partial u_r}{\partial \vartheta} \right]^2 + \left(\frac{K}{\mu_v} - \frac{2}{3} \right) [\nabla \cdot \mathbf{u}]^2 \quad (11)$$

The associated boundary conditions are

$$\mathbf{u} = 0, \quad \theta = 0 \quad \text{on} \quad r = 1 \quad (12)$$

$$|\mathbf{u}|_x = \cos \tau, \quad \theta = 0 \quad \text{as} \quad r \rightarrow \infty \quad (13)$$

The dimensionless parameters that emerge are $\varepsilon = U_0/a\varpi = A/a$ which is called the amplitude parameter, while $M^2 = a^2\varpi/\nu = 2a^2/\delta_\nu^2$ is the frequency parameter, where $\delta_\nu = \sqrt{2\nu/\varpi}$ is representative of the well known Stokes boundary layer thickness, and $\nu = \mu_v/\rho_m$ is the kinematic viscosity of the fluid. As noted earlier, of particular concern here are cases of $\varepsilon \ll 1$ for which the flow is nominally

attached and laminar, and of $M^2 \gg 1$ for which the boundary layer induced thermoacoustic phenomena of interest are most pronounced. Under these conditions the leading order flow has a well known Stokes boundary layer behavior, and the problem is analytically amenable to a perturbation analysis. Note that the Mach number, α , may be expressed as $\alpha = \varepsilon ak$ whereby the ordering of the different parameters being considered in this study may be summarized as follows

$$\alpha \ll \varepsilon \ll 1 \ll M \ll \frac{1}{ak} \quad (14)$$

from which it is clear that although ε and ak are both small, they could be of comparable magnitude.

3. SOLUTION PROCEDURE

The solution for the different flow variables ($\psi, \omega, \mathbf{u}, \theta, p, \rho$) is sought in a perturbation series of the form

$$\mathbf{u} = \mathbf{u}_0 + \varepsilon \mathbf{u}_1 + \dots \quad (15)$$

where in general the dependent variables are solved as complex quantities, although their physically meaningful real parts are, of course, understood. For a typical variable, such as $\mathbf{u}(r, \vartheta, \tau)$ for instance, the solution is represented by the real part $\Re \{ \bar{\mathbf{u}}(r, \vartheta) e^{in\tau} \}$, where $\bar{\mathbf{u}}(r, \vartheta)$ is the "complex amplitude", and integer $n \geq 0$ represents the n^{th} harmonic. The focus in this study is on the leading order first harmonic contributions which eventually contribute to the time-averaged thermoacoustic streaming effect of interest.

For the case of $M^2 \gg 1$ being treated, in anticipation of the importance of the flow mechanics in the large gradient narrow Stokes boundary layer region where the time-averaged effects of primary interest are engendered, suitable boundary layer variables for this inner region are also defined as follows

$$\eta = \frac{M}{\sqrt{2}} (r - 1), \quad \Omega_z, \Psi(\eta, \vartheta, \tau) = \frac{M}{\sqrt{2}} \omega_z, \psi(r, \vartheta, \tau), \quad \Theta(\eta, \vartheta, \tau) \equiv \theta(r, \vartheta, \tau) \quad (16a)$$

$$\mathcal{U}_\vartheta(\eta, \vartheta, \tau) \equiv u_\vartheta(r, \vartheta, \tau), \quad \mathcal{U}_\eta(\eta, \vartheta, \tau) = \frac{M}{\sqrt{2}} u_r(r, \vartheta, \tau), \quad \varrho, \varrho(\eta, \vartheta, \tau) \equiv p, \rho(r, \vartheta, \tau) \quad (16b)$$

4. THE LEADING ORDER SOLUTION

The leading order velocity contribution corresponding to ψ_0 in (15) is $\mathbf{u}_0 = \nabla \times (\hat{\mathbf{i}}_z \psi_0)$, and is solenoidal by definition. The corresponding stream function is given by the solution of

$$\frac{\partial}{\partial \tau} (\nabla^2 \psi_0) = \frac{1}{M^2} \nabla^4 \psi_0 \quad (17)$$

and has been shown (Riley [9], Amin [10], Watson [11]) to be

$$\psi_0 = \left[r - \frac{1}{r} \frac{K_2(\tilde{M})}{K_0(\tilde{M})} + \frac{2}{\tilde{M}} \frac{K_1(\tilde{M}r)}{K_0(\tilde{M})} \right] \sin \vartheta e^{i\tau} \quad (18)$$

where $\tilde{M}^2 = iM^2$, and the K_n represent modified Bessel's functions of the second kind of integer order n . In terms of the boundary layer variables for the inner region in (16) for the case of $M^2 \gg 1$, the above leading order stream function becomes,

$$\Psi_0 = 2 \left[\eta - \frac{1}{2}(1-i) \left(1 - e^{-\eta(1+i)} \right) \right] (1 + O(M^{-1})) \sin \vartheta e^{i\tau} \quad (19)$$

and the corresponding leading order velocity components it predicts are

$$\mathcal{U}_{0,\vartheta} = -2 \left[1 - e^{-\eta(1+i)} \right] (1 + O(M^{-1})) \sin \vartheta e^{i\tau} \quad (20a)$$

$$\mathcal{U}_{0,\eta} = 2 \left[\eta - \frac{1}{2}(1-i) \left(1 - e^{-\eta(1+i)} \right) \right] (1 + O(M^{-1})) \cos \vartheta e^{i\tau} \quad (20b)$$

5. COMPRESSIBILITY CORRECTIONS

An $O(1)$ balance of the energy equation (8) in the inner Stokes layer region yields

$$\frac{\partial \Theta_0}{\partial \tau} = \frac{1}{2\sigma} \frac{\partial^2 \Theta_0}{\partial \eta^2} + \beta_m T_m \frac{\partial \wp_0}{\partial \tau} \quad (21)$$

where \wp_0 the leading order pressure in the inner region is uniform across the boundary layer. Using $\Theta_0 = \bar{\Theta}_0 e^{i\tau}$, and $\wp_0 = \bar{\wp}_0 e^{i\tau}$, the solution of (21) subject to $\Theta_0 = 0$ at $\eta = 0$ in (12) is

$$\bar{\Theta}_0 = \beta_m T_m \bar{\wp}_0 \left[1 - e^{-\eta \sqrt{\sigma}(1+i)} \right] \quad (22)$$

The leading order density term $\varrho_0 = \bar{\varrho}_0 e^{i\tau}$ can now be obtained in terms of \wp_0 and Θ_0 from the equation of state in (9) to yield

$$\varrho_0 = \gamma \wp_0 - \beta_m T_m \frac{c_m^2}{c_p T_m} \Theta_0 \quad (23a)$$

$$\bar{\varrho}_0 = \bar{\wp}_0 \left[\gamma - B \left(1 - e^{-\eta \sqrt{\sigma}(1+i)} \right) \right] \quad (23b)$$

wherein it can be shown from Maxwell's generalized thermodynamic relations that the parameter $B = (\beta_m T_m)^2 (c_m^2 / c_p T_m)^2 \equiv (\gamma - 1)$. Then at the outer edge of the boundary layer region the density is given by

$$\varrho_0|_{\eta \rightarrow \infty} = (\gamma - B) \wp_0 = \wp_0 \quad (24)$$

as should be the case to match with the density distribution in the outer region.

To determine the pressure distribution, \wp_0 , for use in (22) and (23) above, we consider a leading order balance of the ϑ -component of the momentum equation in the inner boundary layer region which gives

$$\frac{\partial \mathcal{U}_{0,\vartheta}}{\partial \tau} = -\frac{1}{ak} \frac{\partial \wp_0}{\partial \vartheta} + \frac{1}{2} \frac{\partial^2 \mathcal{U}_{0,\vartheta}}{\partial \eta^2} \quad (25)$$

Using the solution for $\bar{\mathcal{U}}_{0,\vartheta}$ from (20a) in (25) we find that

$$\bar{\wp}_0 = 2i ak \cos \vartheta \quad (26)$$

which indicates a small $O(ak)$ correction to the nodal value of the pressure attributable to the presence of the compact cylinder at the velocity antinode ($x_0 = 0$). It is worth noting here that although the compressibility corrections to the boundary layer velocity, \mathcal{U}_0 in (20), are in general $O(ak)$, for the case of the cylinder located at the velocity antinode ($x_0 = 0$) being treated here, these corrections are of $O(ak)^2$ and smaller than the $O(ak)$ accuracy level of this analysis and are hence being ignored.

6. THE THERMOACOUSTIC STREAMING EFFECT

Having determined the leading first order quantities, attention is now turned to determine the primary quantity of interest in this study, i.e. the time-averaged thermoacoustic streaming effect generated in the inner boundary layer region on the cylinder. This time-independent thermal effect is induced as a result of the interaction of the first harmonics, and can be determined by an $O(\varepsilon)$ balance of the energy equation (8) in terms of the boundary layer variables (16) of the inner region as follows

$$\begin{aligned} \left[\frac{\partial \Theta_1}{\partial \tau} + ak \varrho_0 \frac{\partial \Theta_0}{\partial \tau} \right] + \left[\mathcal{U}_{0,\vartheta} \frac{\partial \Theta_0}{\partial \vartheta} + \mathcal{U}_{0,\eta} \frac{\partial \Theta_0}{\partial \eta} \right] &= \frac{1}{2\sigma} \frac{\partial^2 \Theta_1}{\partial \eta^2} + \\ \left[(\beta T^*)_\varepsilon \frac{\partial \wp_0}{\partial \tau} + \beta_m T_m \frac{\partial \wp_1}{\partial \tau} \right] + \beta_m T_m \left[\mathcal{U}_{0,\vartheta} \frac{\partial \wp_0}{\partial \vartheta} + \mathcal{U}_{0,\eta} \frac{\partial \wp_0}{\partial \eta} \right] &+ \frac{1}{2} ak \left(\frac{\partial \mathcal{U}_{0,\vartheta}}{\partial \eta} \right)^2 \end{aligned} \quad (27)$$

where higher order terms in powers of $O(1/M)$ have been ignored, and the last term above represents the only surviving contribution from the viscous dissipation effect in (11).

In view of the above arguments, the solution for the $O(\varepsilon)$ term Θ_1 is sought in the form

$$\Theta_1(r, \vartheta, \tau) = \Theta_{10}(r, \vartheta) + \bar{\Theta}_{12}(r, \vartheta) e^{2i\tau} \quad (28)$$

as a sum of a time-independent term, $\Theta_{10}(r, \vartheta)$, and a second harmonic, $\bar{\Theta}_{12}(r, \vartheta, \tau)$. Noting that to leading order $\partial \varphi_0 / \partial \eta = 0$ in (27), the governing equation for the time-independent term of interest is

$$\begin{aligned} \frac{1}{2\sigma} \frac{\partial^2 \Theta_{10}}{\partial \eta^2} &= ak \left\langle \varrho_0 \frac{\partial \Theta_0}{\partial \tau} \right\rangle + \left\langle \left[\mathcal{U}_{0,\vartheta} \frac{\partial \Theta_0}{\partial \vartheta} + \mathcal{U}_{0,\eta} \frac{\partial \Theta_0}{\partial \eta} \right] \right\rangle \\ &- \left\langle (\beta T^*)_\varepsilon \frac{\partial \varphi_0}{\partial \tau} \right\rangle - \beta_m T_m \left\langle \mathcal{U}_{0,\vartheta} \frac{\partial \varphi_0}{\partial \vartheta} \right\rangle - \frac{1}{2} ak \left\langle \left(\frac{\partial \mathcal{U}_{0,\vartheta}}{\partial \eta} \right)^2 \right\rangle \end{aligned} \quad (29)$$

subject to $\Theta_{10} = 0$ at $\eta = 0$ in (12), where the angle brackets $\langle \dots \rangle$ denote a time average of the enclosed quantities.

6.1. THE $(\beta T^*)_\varepsilon$ CORRECTION

Before solving for Θ_{10} it becomes necessary to consider the term representing higher order thermal expansion effects of $O(\varepsilon)$ which in anticipation has been denoted by $(\beta T^*)_\varepsilon$ in (27,29). This arises since βT^* can be expanded as

$$\beta T^* = \left\{ \beta_m + \left(\frac{\partial \beta}{\partial p^*} \right) \Delta p^* + \left(\frac{\partial \beta}{\partial T^*} \right) \Delta T^* \right\} \{T_m + \Delta T^*\} + \dots \quad (30)$$

which after some manipulation can be shown to simplify to

$$\frac{\beta T^*}{\beta_m T_m} = 1 - \varepsilon ak \left[\varrho_0 + \Theta_0 \frac{(\gamma - 1)}{\beta_m T_m} \beta_m^{(2P)} - \varphi_0 \frac{K_s}{p_m} \beta_m^{(2T)} \right] + O(\alpha^2) \quad (31)$$

where $K_s = \rho_m c_m^2$ is the adiabatic bulk modulus ($K_s = \gamma p_m$ for an ideal gas), and $\beta_m^{(2P)}$ and $\beta_m^{(2T)}$ represent second-order thermodynamic moduli which in view of $\hat{\beta}$ in (10) are defined as

$$\beta_m^{(2P)} = \frac{1}{\beta_m T_m} \left[\frac{T_m}{\rho_m \beta_m} \left(\frac{\partial \hat{\beta}}{\partial T^*} \right)_{p^*, m} - 1 \right] \quad (= 1 \text{ for an ideal gas}) \quad (32a)$$

$$\beta_m^{(2T)} = -\frac{p_m}{\rho_m \beta_m} \left(\frac{\partial \hat{\beta}}{\partial p^*} \right)_{T^*, m} \quad (= 1 \text{ for an ideal gas}) \quad (32b)$$

Using the results for ϱ_0 and Θ_0 from (22) and (23) in (31), $(\beta T^*)_\varepsilon$, the desired $O(\varepsilon)$ correction to βT^* can be expressed as

$$(\beta T^*)_\varepsilon = -ak \beta_m T_m \bar{\varphi}_0 e^{i\tau} \left[\left(\gamma - \frac{K_s}{p_m} \beta_m^{(2T)} \right) + (\gamma - 1) (\beta_m^{(2P)} - 1) (1 - e^{-\eta \sqrt{\sigma}(1+i)}) \right] \quad (33)$$

from which it becomes clear that it is only the second of the two terms in [...] proportional to $(\beta_m^{(2P)} - 1)$ that is capable of making a nonzero time-averaged contribution through the $\langle (\beta T^*)_\varepsilon (\partial \varphi_0 / \partial \tau) \rangle$ term in (29). However for the case of an ideal gas, $(\beta T^*)_\varepsilon$ vanishes by virtue of (32), and there is no contribution to the time-averaged thermoacoustic effect through these second order thermal expansion coefficients.

7. RESULTS AND DISCUSSION

Although the development so far has been applicable to the general case of any fluid (gas or liquid), owing to the unknown values of the second-order thermodynamic moduli from (32) present in the final

solution form, in what follows in the remainder of the paper the analysis will be restricted to the case of ideal gases ($\beta_m T_m = 1, \sigma < 1$) which proves sufficient to provide the desired physical insight into the thermoacoustic streaming effect induced in the dissipative boundary layers on the cylinder.

The leading order first harmonic results for the various flow variables from (20), (22), (23) and (26) are substituted in (29), and the equation integrated twice (subject to (12)) to arrive at the steady temperature distribution in the boundary layer region. In view of (22), (23) and (26), we may note that the contribution from the $ak \langle \rho_0 \partial \Theta_0 / \partial \tau \rangle$ term in (29) will be of $O(ak)^3$, and can hence be neglected for consistency with the $O(ak)$ accuracy level of this analysis which all the remaining terms in (29) satisfy.

One integration of (29) yields the time-averaged temperature gradient in the fluid in the inner region. The resulting expression is unwieldy and has not been reproduced here, except to note that of particular concern is the temperature gradient it predicts at the wall-fluid boundary $\eta = 0$ which is given by

$$\left(\frac{\partial \Theta_{10}}{\partial \eta} \right)_{\eta=0} = ak \sigma \left[1 - \cos 2\vartheta \left\{ 1 + \frac{2}{\sqrt{\sigma}} \left(\frac{1 + \sqrt{\sigma}}{1 + \sigma} \right) \right\} \right] \quad (34)$$

and indicates a cooling of the cylinder in the vicinity of the end-points $\vartheta = 0, \pi$, and heating in the vicinity of $\vartheta = \pi/2$. The temperature gradient in (34) can be integrated over the angle, ϑ , to determine the radial heat transfer rate per unit length of the cylinder as

$$q'_r = -(ak \sigma \pi) q_r^* \quad \text{where} \quad (35a)$$

$$q_r^* = \left(\frac{P_0}{\gamma p_m} \right)^2 \frac{(\gamma - 1) c_m k_c T_m}{\sqrt{\nu \omega / 2}} \quad (35b)$$

where the Mach number $\alpha = (P_0 / \gamma p_m)$ for a standing sound wave, with $P_0 = \rho_m U_0 c_m$ being the pressure amplitude of the wave, and k_c the thermal conductivity of the fluid. The negative sign on q'_r in (35) clearly indicates a *net heating* of the cylinder, despite both angular heating and cooling variations over the circumference as indicated by (34).

A second integration of (29) yields the time-averaged temperature distribution of the fluid in the inner region which can be expressed as

$$\Theta_{10}(\eta, \vartheta; ak, \sigma, \gamma) = ak \phi(\eta, \vartheta; \sigma, \gamma) \quad (36)$$

by virtue of direct proportionality to ak . Although the actual magnitude of this temperature is not as important as its gradient (and associated heat transfer rates as discussed above in (34) and (35)), it nonetheless provides the necessary condition for matching with the temperature solution in the outer region as

$$\Theta_{10}|_{\eta \rightarrow \infty} = \frac{ak}{2(\sigma + 1)^2} [(\sigma + 2)(\sigma + 1)(\sigma - 1) - \cos 2\vartheta (\sigma^3 + 2\sigma^2 + 15\sigma + 6)] \quad (37)$$

The complete expression for the temperature distribution itself (ϕ in (36)) is too long-winded and hence not reproduced here, but instead presented below as plots in Figs. 2 and 3 for the representative case of air with $(\sigma, \gamma) = (0.7, 1.4)$. Figure 2 shows the variation of ϕ with (η, ϑ) , and clearly shows the nonzero matching value at the outer edge of the inner region as $\eta \rightarrow \infty$. Figure 3 shows the same variation but for clarity has been presented only for selected values of the angle, ϑ .

In conclusion, it is noted that it would be useful to generalize the above analysis for the case of the cylinder positioned anywhere along the standing wave, and to also further account for the ignored higher order correction terms to obtain a more complete and accurate description of the thermoacoustics.

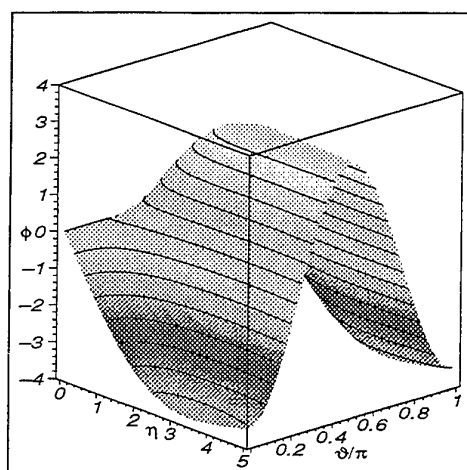


Figure 2: A plot of $\phi(\eta, \vartheta)$ in (36) for the case of air, $(\sigma, \gamma) = (0.7, 1.4)$.

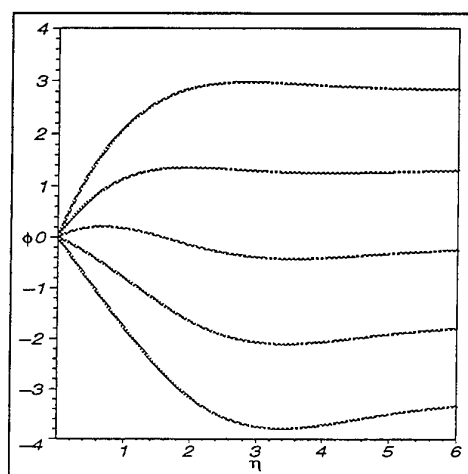


Figure 3: A plot of $\phi(\eta, \vartheta)$ in (36) for the case of air for different angular locations, $\vartheta = \pi/2, \pi/3, \pi/4, \pi/6, 0$ (from top to bottom respectively).

REFERENCES

1. N. Rott. The heating effect connected with non-linear oscillations in a resonance tube. *J. Appl. Math. Phys. (ZAMP)*, 25:619–634, 1974.
2. N. Rott. Thermoacoustics. *Adv. Appl. Mech.*, 20:135–175, 1980.
3. P. Merkli and H. Thomann. Thermoacoustic effects in a resonance tube. *J. Fluid Mech.*, 70:161–177, 1975.
4. G. W. Swift. Thermoacoustic engines. *J. Acoust. Soc. Am.*, 84(4):1145–1180, Oct. 1988.
5. G. W. Swift. Thermoacoustic engines and refrigerators. *Physics Today*, 48(7):22–28, July 1995.
6. A. Gopinath, N. L. Tait, and S. L. Garrett. Thermoacoustic streaming in a resonant channel: the time-averaged temperature distribution. *J. Acoust. Soc. Am.*, 103(3):1388–1405, March 1998.
7. H. Zhao, S. S. Sadhal, and E. H. Trinh. Singular perturbation analysis of an acoustically levitated sphere: Flow about the velocity node. *due to appear in J. Acoust. Soc. Am.*, 1999.
8. L. C. Burmeister. *Convective Heat Transfer*, chapter 2, pages 12–51. Wiley-Interscience. John Wiley & Sons Inc., New York, 2nd edition, 1993.
9. N. Riley. Oscillatory viscous flows. Review and extension. *IMA J. Appl. Math.*, 3:419–434, 1967.
10. N. Amin. Low-frequency oscillations of a cylinder in a viscous fluid. *Quart. J. Mech. Appl. Math.*, 41(2):195–201, 1988.
11. E. J. Watson. Slow oscillations of a circular cylinder or sphere in a viscous fluid. *Quart. J. Mech. Appl. Math.*, 45(2):263–275, 1992.

EXPERIMENTAL INVESTIGATION OF COOLED AIR INJECTION IN THERMOACOUSTIC REFRIGERATOR

T. Hara

Department of Systems Engineering, Nippon Institute of Technology
Miyashiro, Saitama, 345-8501 Japan

Email: hara@leo.nit.ac.jp; Phone: +81-480-33-7719; Fax: +81-480-33-7745

Keywords: thermoacoustics, refrigeration, air-conditioner, air injection, acoustic streaming

ABSTRACT. Experimental investigation was conducted on the phenomenon of cooled air injection from a thermoacoustic refrigerator. The location of the stack, the diameter and the position of the air outlet hole, and electrical thermal input were varied in the experiments. Axial pressure distribution in the resonance tube was measured by a movable pressure transducer along the tube axis. Refrigeration capacity was measured with electrical thermal input. Air, a working gas in the tube in this experiment, was cooled by thermoacoustic phenomena and was naturally flown out through the outlet hole near the pressure antinode. Ambient air was flown in through the inlet hole near the pressure node. The air streams naturally flowed in and out through the holes without any one-way valve.

1. INTRODUCTION

Chlorofluorocarbons (CFCs) have long been used in almost all refrigerator/freezers and commercial residential air conditioning applications as working fluids for the vapor compression refrigeration cycle. That situation however is now about to change dramatically. CFCs were found to be destroying the Earth's protective ozone layer, and the production of CFCs has now been prohibited in the world. Alternative compounds such as HCFCs and HFCs have problems associated with their pollution potential, their toxicity and their incompatibility with lubricants. Thermoacoustic refrigeration has been thought one of new systems which can operate with natural working fluid.

A schematic diagram of a simple, one-quarter wavelength, $\lambda/4$, thermoacoustic refrigerator is shown in Figure 1. The loudspeaker at the left sets up the standing wave within the gas-filled tube. Its frequency is chosen so that the loudspeaker excites the fundamental ($\lambda/4$) resonance of the tube. The termination at the right-hand end of the tube is rigid, so the longitudinal particle velocity at the rigid end is zero (a velocity node) and the acoustical pressure variation is at a maximum (a pressure antinode). At the loudspeaker end of the tube, there is an acoustic pressure node and a particle velocity antinode. An acoustic pressure node and a particle velocity antinode are at the left end of the tube. Near the right-hand end is a stack of plates (the stack). The spacing of the stack is made close enough for heat to be easily transferred between the gas and the plate, and wide enough for the gas to move easily back and forth through the stack in the tube.

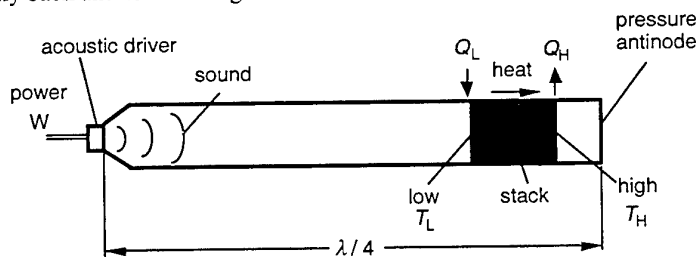


Figure 1: Schematic diagram of thermoacoustic refrigeration

The mechanism is visualized in Figure 2. In the first part of this four step cycle, the working fluid is transported along the plate from position X' to position X'' , and is heated by adiabatic compression from a temperature of T_1' to T_1'' . The adiabatic gas law provides the relationship between the change in gas pressure and the associated change in temperature. Hence, at its present location ($T_1'' > T_2''$), it is now at a higher temperature than the plate. In the second step, the warmer gas parcel transfers an amount of heat to the plate at constant pressure, and its temperature decreases to that of the plate T_2'' . In the third step, the working fluid is transported back along the plate to position X'' and is cooled by adiabatic expansion to a temperature T_2' . This temperature is lower than

the original temperature at location X' . In the fourth step, the gas parcel absorbs an amount of heat from the plate. This raises its temperature back to its original value T_1' . Heat has been transported up to a determined temperature gradient by sound. Figure 3 shows the cycle followed by a typical mass of gas.

Carnot cycle, the most efficient possible cycle between two temperatures, would consist of a reversible adiabatic compression, a reversible isothermal compression, a reversible adiabatic expansion, and a reversible isothermal expansion, completing the cycle. In a sense, the thermoacoustic refrigeration cycle exists between the Brayton cycle and the Carnot cycle because the heat transfer process deviates from constant pressure change to constant temperature change by the heat transfer between gas and stack in the compression and expansion. This cycle would be more efficient than the Brayton cycle, if we could control the rate of heat transfer between the stack and the gas.

Thermoacoustic refrigeration has been investigated and examined from the early 1980s. Wheatley et al. (1983) showed phenomena in thermoacoustics and acoustical heat engines. Swift (1988) reviewed the fundamentals of thermoacoustic engines, by analysis, intuition and examples. Garrett and Hofler (1992) showed that thermoacoustics offered COPs competitive edge on conventional refrigerators by using resonant high amplitude sound to pump heat.

It is the purpose of this paper to investigate the flow rate and temperature difference of outlet air through the hole near the antinode. Refrigeration capacity was calculated by the experimental data and discussed on the relation of air flow rate and axial pressure distribution in the tube.

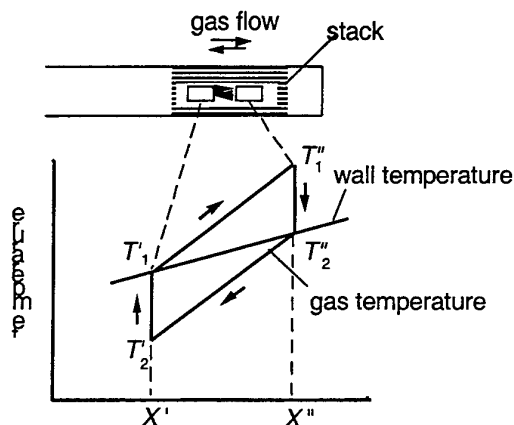


Figure 2: Principle of thermoacoustic refrigeration

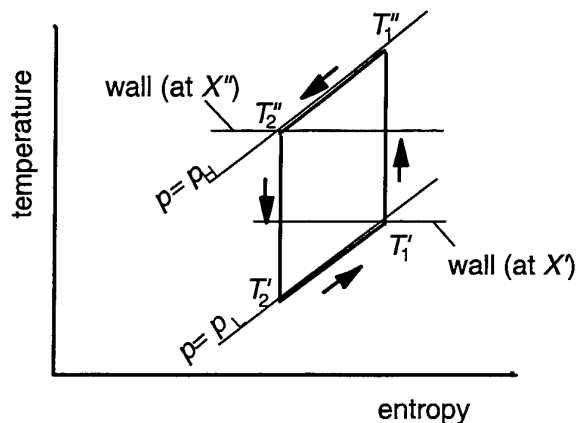


Figure 3: Temperature-entropy diagram

2. EXPERIMENTAL APPARATUS AND PROCEDURE

Experiments were done with two experimental apparatus for two kinds of tube lengths equivalent to each resonance frequency. The first experimental apparatus was made for measuring outlet air flow rate with a tube which was 400 mm in length and 30 mm in internal diameter. The length was equivalent to $\lambda/4$ of the sound wave. It is shown in Figure 4. The apparatus was made with a horizontal brass tube which was closed at one end and attached to the acoustic driver at the other end. The acoustic driver was a full-range speaker. The air outlet hole was drilled near the end of the stack where the pressure amplitude was large since pressure antinode was at the closed end. The stack was made of a bundle of glass tubes. The glass tubes were 1.2 mm in diameter and 50 mm in length. About 500 pieces of the glass tubes were bound for the stack.

Configuration and location of the air outlet hole is shown in Figure 5. The diameter of the outlet hole was varied from 0.4 to 2.0 mm. The position of the hole was varied axially from 90 to 360 mm from the acoustic driver to the closed end of the tube.

The second experiment was conducted with the long tube equivalent to $3\lambda/4$ of the sound wave. The tube was 1500 mm long and 30 mm in diameter, as shown in Figure 6. The stack was located near the pressure antinode. It was about $1/3$ the length from the right side of the tube. Outlet hole was set near the right side (cold side) of the stack. In this experiment, inlet hole was also set at the pressure node in order to measure the evacuated air flow rate into the tube. Outlet hole was made by a ceramic tube of which inner diameter was varied from 0.4 to 1.6 mm at 30 mm of the length. The inlet hole was made by a ceramic tube of which inner diameter was 2.0 mm. Any valve was not used along the tube. Sound pressure in the tube was measured with a small pressure transducer which was 0.6 mm thick and 4.5 mm in diameter. It was a type of vapor-deposition semiconductor strain-gauge. It was set at the top of a 4 mm diameter tube and moved axially back and forth in the tube to measure axial pressure distribution. It is shown in Figure 7.

In these experiments, air at atmospheric pressure was used as a working fluid. Air temperature at the outlet hole, temperature of the cold and hot side heat exchangers at both side of the stack and ambient temperature were measured by thermocouples. They were Copper-Constantan wire which were 0.2 mm in diameter with enamel insulation. The air flow rate was measured by a flowmeter with bubbly film of soap.

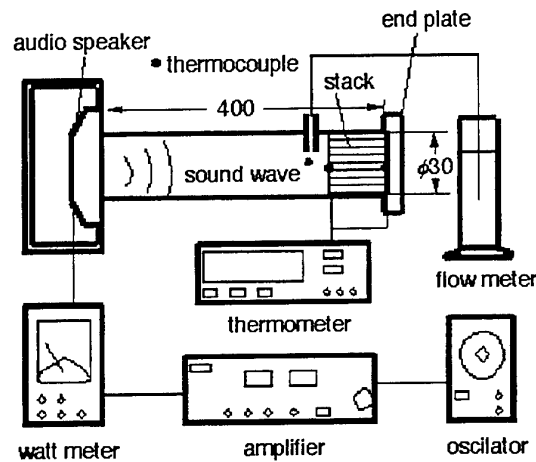


Figure 4: First experimental apparatus for $\lambda/4$ length of pressure wave

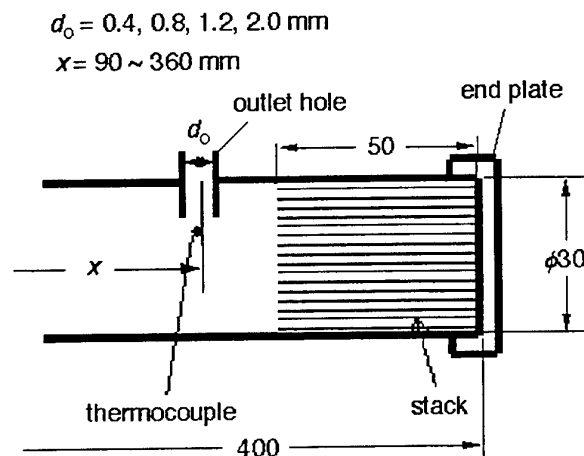


Figure 5: Configuration and location of air outlet hole

3. EXPERIMENTAL RESULTS AND DISCUSSION

In the first experiments, proper position of the air outlet hole was examined. Figure 8 shows a relation of air flow rate and position of air outlet hole. It was shown that air flow rate was maximized at $x = 350$ mm, which was equivalent to the left side (cold side) of the stack. When hole position was nearer to the left end of the tube, the air flow rate decreased and finally became negative. This means that air was evacuated near the pressure node.

The flow rate also decreased inside of the stack since the flow resistance through the stack was large. Air flow rate was found to be maximum at the left side of the stack. Figure 9 shows the temperature difference and input power to the acoustic driver. Temperature difference ΔT at the vertical axis was defined as follows,

$$\Delta T = T_a - T \quad (1)$$

where stack T_a is an ambient temperature and T is the air temperature adjacent to the cold side of the stack. These terms are also used in the following sections.

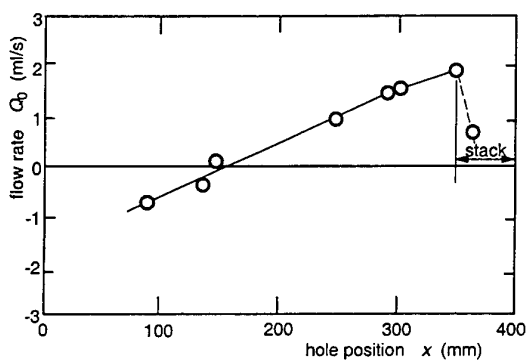


Figure 8: Hole position and air flow rate

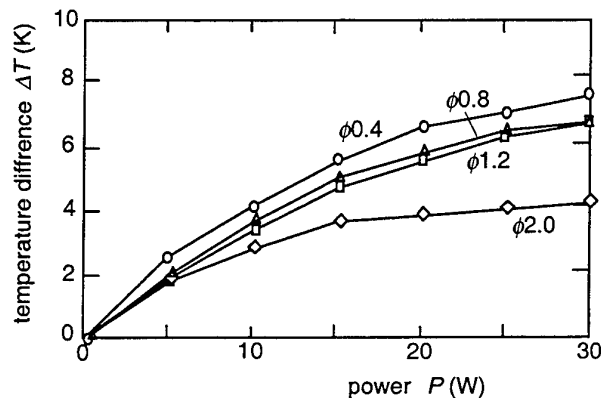


Figure 9: Temperature difference and input power

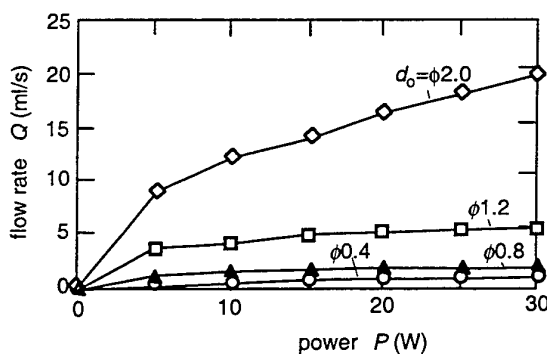


Figure 10: Air flow rate and input power

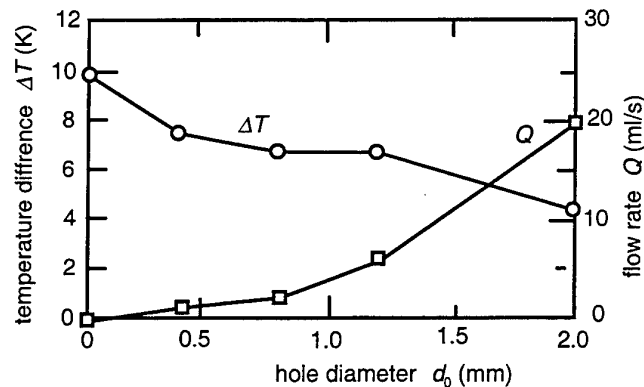


Figure 11: Temperature difference and flow rate

Figure 10 shows the relation of outlet flow rate and input power. Figure 11 shows the relation of temperature difference and hole diameter and that of flow rate and hole diameter. Temperature difference decreased and flow rate increased with the inner diameter.

In the second experiment with a long tube, pressure distribution was measured in order to know resonant state. Figure 12 shows the axial distribution of pressure amplitude in a resonance tube. The calculated result is shown in the figure by a dotted line. It was calculated when the reflection coefficient was 0.6. Standing wave of $3\frac{1}{4}$ was found to be formed in the tube. Figure 13 shows the temperature difference between the hot side and cold side of the stack when the stack was moved axially along the tube. Temperature difference of the speaker (left) side increased to maximum with the increase of distance from the speaker end and decreased to minimum when stack was near the closed end (right side of the tube).

Figure 14 shows the change of the temperature difference and outlet flow rate when outlet nozzle diameter changed. When outlet nozzle diameter increased, outlet air flow rate increased while the temperature difference. Figure 14 shows the change of the temperature difference and outlet flow rate when outlet nozzle diameter changed. When outlet nozzle diameter increased, outlet air flow rate increased while the temperature difference decreased. Cooling capacity was calculated and the result was shown in Figure 15. Cooling capacity was at maximum when the outlet Nozzle diameter was 1,1 mm in this experiment.

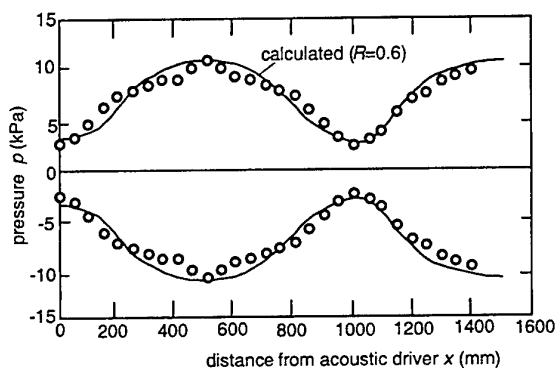


Figure 12: Axial pressure distribution

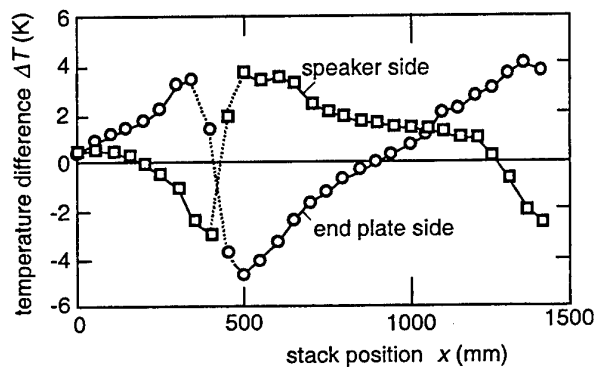


Figure 13: Temperatures difference at both side of the stack

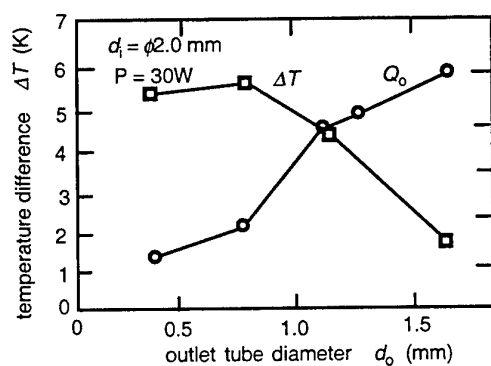


Figure 14: Temperature difference and outlet air flow rate

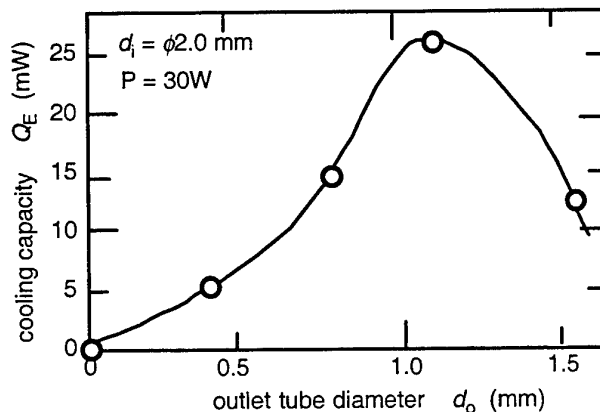


Figure 15: Cooling capacity and outlet nozzle diameter

3 CONCLUSION

An experimental investigation was carried out on the effects of the stack in a thermoacoustic resonance tube. The following results were obtained.

1. Cooled air naturally flowed out through a hole near the pressure antinode. Ambient air was naturally

- evacuated through the inlet hole near the pressure node. A one-way valve was not needed.
- 2) Outlet air flow rate was at a maximum when the outlet hole was located at the end of the stack.
 - 3) Temperature difference (difference from the ambient temperature) was smaller with the inner diameter of the outlet hole larger. Air flow rate was larger with the diameter was larger.

ACKNOWLEDGMENTS

The authors acknowledge the support of the students, K.Nagaya, J. Higurashi, T. Sano, S. Tsuchiya and M. Tsuchiya for their assistance in the experiments and measurements.

NOMENCLATURE

d	tube diameter	(mm)
Q	air flow rate	(ml/s)
T	temperature	(K)
ΔT	temperature difference from an ambient temperature	(K)
f	acoustic frequency	(s ⁻¹)
Greek		
λ	wave length	(m)
ρ	air density	(kg/m ³)
suffix		
i	inlet	
o	outlet	

REFERENCES

1. S.L. Garret, and T.J. Hofler., December 1992, Thermoacoustic refrigeration, *ASHRAE Journal*:: p. 28-36.
2. T. Hara, et al., 1995, Temperature distribution in a thermoacoustic refrigerator, *Proceeding of the Asia-Pacific Conference on the Built Environment*, Vol. 1: p. 152-159.
3. T. Hara, et al., 1997, Experimental studies on thermoacoustic refrigeration, *Proceeding of the Conference of Experimental Heat Transfer, Fluid Mechanics and Thermodynamics*, Vol. 4: p. 2451-2457.
4. G.W. Swift, 1988, Thermoacoustic engines, *Journal of Acoustic Society of America*, Vol. 84, No. 4: p.1145-1180.
5. J. Wheatley, T. Hofler, G.W. Swift, and A. Migliori, 1983, An intrinsically irreversible thermoacoustic heat engine, *Journal of Acoustic Society of America*, Vol. 74: p. 153-170.
6. J. Wheatly, T. Hofler, G.W. Swift, and A. Migliori, 1985, Understanding some simple phenomena in thermoacoustics with applications to acoustical heat engines, *American Journal of Physics*, Vol. 53, No. 2: p. 147-162.

ANALYZING AND VERIFICATION OF SYMMETRY-NOZZLE TO IMPROVE THE PERFORMANCE OF PULSE TUBE REFRIGERATOR

Luwei Yang, Wenxiu Zhu, Yuan Zhou, Jingtao Liang
Cryogenic Laboratory, Chinese Academy of Sciences
Beijing Post Box 2711, 100080, P.R.C.
Fax: (8610) 6256.4049 E-mail: lwyang@cl.cryo.ac.cn

Keywords: pulse tube refrigerator, symmetry nozzle, orifice, theory refrigeration

ABSTRACT. For the development of practical products, valves such as orifice, double-inlet and multi-bypass in the pulse tube refrigerators, should be replaced by other more reliable structures. Potential choices are long thin tube, orifice or nozzle. In this paper, the difference between nozzle flow and orifice flow is analyzed. Their similarities are that they result in a similar reciprocal movement at hot end of the pulse tube; their differences are that their flow rates have different characteristics. According to state-flow theory, nozzle flow coefficient has a positive feedback to flow rate while orifice has no relation to flow rate generally. Further analysis shows this feature of nozzle will result in large refrigeration with the same pressure ratio and reservoir coefficient, which explains the reason that even lower temperature and a larger refrigeration amount can be obtained when symmetry-nozzle is used instead of orifice. Experiments of miniature pulse tube refrigerator show that symmetry-nozzle instead of check valves can improve the performance of pulse tube refrigerator effectively, which is also verified by calculation. But with Re number increasing, this advantage becomes unclear. This is explained both in analysis and in low frequency experiments.

1. INTRODUCTION

During recent ten years, pulse tube refrigerator develops quickly, and it has been put into use because of its very good performance. Its mechanism to acquire cooling capacity is also very special. As shown in Figure 1, a simple pulse tube cooler consists of compressor 1, regenerator 2, multi-bypass valve 3, cold tip 4, double-inlet valve 5, pulse tube 6, hot end 7, orifice valve 8, reservoir 9. There is only one moving part at room temperature, that is the compressor, which can be placed at a rather remote distance from the other parts. And for the other parts, they can be coupled together to form an integral unit.

In pulse tube refrigerators, there are adjusting valves, such as multi-bypass 3, double-inlet 5 and orifice valve 8 in Figure 1. But in practical products, these valves are not suitable, because they may become unstable when they stay unchanged for a long time. A potential method is to replace these valves with orifice, or long tube of small diameter (inertance tube). Generally we may not adopt symmetry-nozzle or convergent-divergent nozzle. However, in fact, this is a very good method.

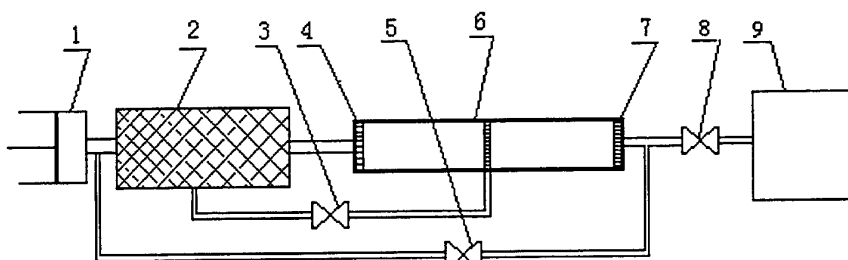


Fig.1 Main components of a pulse tube cooler

1 compressor 2 regenerator 3 multi-bypass valve 4 cold tip 5 double-inlet valve
6 pulse tube 7 hot end 8 orifice valve 9 reservoir

Generally, orifice, long thin tube, or check valve will get similar results if they are optimized. But there are differences. And in this paper, difference between nozzle and orifice or valve is given. This difference makes the performance different under some condition.

2. ANALYSIS

Essence of Orifice flow

First let us analyze the function of orifice or needle valve that connect reservoir and pulse tube. There are potentially three parts of gas oscillation in pulse tube, which was analyzed in reference [1] for the first time. The first part is the oscillating gas in and out cold tip; the second is the gas that oscillating in pulse tube always; the third is the gas in and out of pulse tube hot end and reservoir. Thus the function of orifice is to control the flow amount of gas in and out of pulse tube and reservoir. Here the largest amplitude of part 3 is assumed to be L3. In this meaning, whether we use orifice or symmetry-nozzle, the amplitude of L3 should not change or change little. In other words, if L3 is kept to be a certain value, different kind of resistance devices will not result in much difference, and the refrigeration temperature should be of no large difference.

But the different flow characteristics of different devices coupled with refrigeration mechanism may reach obviously different results.

Difference of Orifice Flow and Nozzle Flow

As to orifice or nozzle flow due to pressure difference, steady flow rate is determined by:

$$\dot{m} = \alpha \cdot \epsilon \cdot \frac{\pi d^2}{4} \sqrt{2\rho_h(p_h - p_l)} \quad (1)$$

where α is flow coefficient, which is determined by version of channel, d/D (d is smallest diameter; D is the large diameter beside d), Re (Reynolds's number), ϵ is flow expansion coefficient, which shows the compressibility of gas and $\epsilon=1$ for incompressible fluid. According to equation (1), if α and ϵ stay unchanged though they have different values because of different flow channels, a suitable adjustable value of diameter d will keep third part of gas in pulse tube "L3" changing little. Then almost same refrigeration results can be obtained for different resistance devices. In theory, α and ϵ keep unchanged with a given pressure difference of $p_h - p_l$; but in reality, because pressure wave in pulse tube is oscillating constantly, α may change.

Take the orifice in Fig. 1 and relatives parameters into consideration, according to Bernoulli equation[2], flow through the orifice or nozzle can be written as:

$$\frac{v_h^2}{2g} + \frac{p_h}{\rho_h g} = \frac{v_0^2}{2g} + \frac{p_0}{\rho_0 g} + h_{j0} = \frac{v_l^2}{2g} + \frac{p_l}{\rho_l g} + h_j \quad (2)$$

where h_j is hydraulic loss due to tube length or sharp change of flow channel, and $\rho_h g h_j$ means pressure loss.

In equation (2), considering that the flow area is large before and after the orifice, and v_h, v_l is small and can be omitted, we have:

$$\frac{p_h}{\rho_h g} = \frac{v_0^2}{2g} + \frac{p_0}{\rho_0 g} + h_{j0} = \frac{p_l}{\rho_l g} + h_j \quad (3)$$

$$h_j = \frac{p_h}{\rho_h g} - \frac{p_l}{\rho_l g} \quad (4)$$

The definition for hydraulic loss is as follows:

For major loss due to tube length:

$$h_j = \lambda \cdot \frac{L}{d} \cdot \frac{v^2}{2g} \quad (5)$$

where λ is friction factor, L is tube length and d is tube diameter .

For minor loss due to sharp change of flow channel

$$h_j = \xi \frac{v^2}{2g} \quad (6)$$

where ξ is minor loss coefficient.

From equation (4) and (6), we can get:

$$\xi \frac{v_0^2}{2g} = \frac{p_h}{\rho_h g} - \frac{p_l}{\rho_l g} \quad (7)$$

$$\rho_0^2 v_0^2 A^2 = A^2 \cdot 2\rho_0 \left(\frac{p_h \rho_0}{\rho_h} - \frac{p_l \rho_0}{\rho_l} \right) / \xi \quad (8)$$

and introducing ε to make $\rho_h = \rho_l = \rho_0$ when gas compressibility is considered, we get:

$$m = \rho_0 v_0 A = A \cdot \varepsilon \cdot \sqrt{1/\xi} \cdot \sqrt{2\rho_h(p_h - p_l)} \quad (9)$$

Comparing equation (1) and (10) will make:

$$\alpha = \sqrt{1/\xi} \quad (10)$$

According to equation (10), flow coefficient α is mainly determined by minor loss coefficient ξ . Then let's analyze the difference of minor loss coefficient ξ for different devices.

In Figure 2, four typical flow resistance devices are given. They are orifice, check valve, divergent tube and convergent tube. According to reference [2], their minor loss coefficients for steady state flow are listed in table 1. From the table, we can find that minor loss coefficients of orifice and needle valve are determined solely by geometry. This is because the flow is unstable due to irregular or sharp flow area change, and the effect of Re number is negligible. But for divergent tube and convergent tube, friction factor λ has an evident effect on minor loss coefficient ξ .

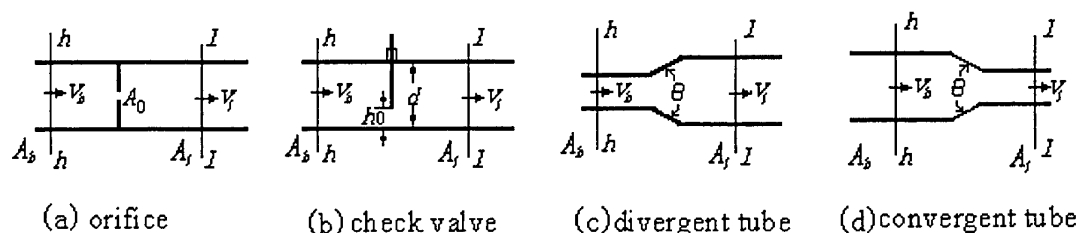


Fig.2 Four typical flow device

Such phenomenon is also introduced elsewhere. For example in reference [3], three kind of flow meter devices, orifice, nozzle, venturi tube (similar to symmetry-nozzle) are introduced. The result in Reference [3] is shown in Figure 3. For orifice, the flow coefficient α is inversely proportional to Re number and α has a relatively small value; on the other hand, for nozzle or venturi tube, the flow coefficient α is proportional to Re number. But here is no value for α after $Re < 1000$ in reference [3].

Table 1 Flow characteristics of different resistance devices

Version	ξ							$h_j = \xi \frac{v_1^2}{2g}$
Orifice	$\xi = \left(\frac{A_0}{nA_h} - 1\right)^2, n = 0.57 + \frac{0.043}{1.1 - A_0/A_h}$							$h_j = \xi \frac{v_1^2}{2g}$
Check valve	h_0/d	8/8	6/8	4/8	3/8	2/8	1/8	$h_j = \xi \frac{v_1^2}{2g}$
	ξ	0.11	0.26	2.06	5.52	17.0	97.8	
Divergent	$\xi = k \left(\frac{A_1}{A_h} - 1\right)^2 + \frac{\lambda}{8 \operatorname{tg}(\theta/2)} \left[\left(\frac{A_1}{A_h}\right)^2 - 1\right]$							$h_j = \xi \frac{v_1^2}{2g}$
	θ	8°	10°	12°	15°	20°	25°	
	k	0.14	0.16	0.22	0.30	0.42	0.62	
Convergent	$\xi = k \left(\frac{1}{n} - 1\right)^2 + \frac{\lambda}{8 \operatorname{tg}(\theta/2)} \left[1 - \left(\frac{A_1}{A_h}\right)^2\right], n = 0.57 + \frac{0.043}{1.1 - A_1/A_h}$							$h_j = \xi \frac{v_1^2}{2g}$
	θ	10°	20°	40°	80°	100°	120°	
	k	0.40	0.25	0.20	0.30	0.40	0.60	

Note: n contraction coefficient due to flow area further decreasing after smallest point.
k correction coefficient determined by flow channel inclination θ .

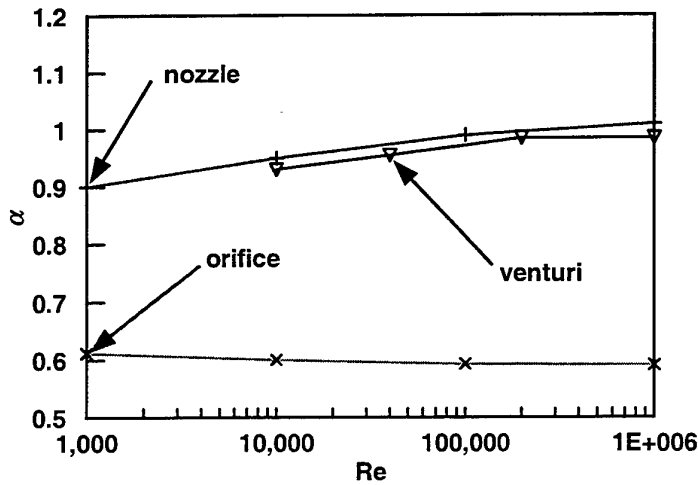


Fig. 3 Flow coefficient change with Re number

In order to take into consideration the effect of friction factor λ on flow, let's think about its value. λ is mainly determined by Reynolds number[2, 3]:

$$\operatorname{Re} < 2000, \lambda = 64 / \operatorname{Re}, \quad (11)$$

$$\operatorname{Re} > 2000, \lambda = \frac{0.3164}{\operatorname{Re}^{0.25}} \quad (12)$$

$$\text{where } \operatorname{Re} = vd/\nu \quad (13)$$

Equations (11, 12, 13) mean that when Re increases, λ is decreasing. In other words, a large flow rate results in a smaller value of λ . According to table 1, this means that in divergent and convergent tube, minor loss coefficient ξ changes with the flow rate. With a larger flow rate, the flow coefficient α may increase and result in an even larger flow rate; on the other hand, if the flow rate is very small, flow coefficient α may be even smaller.

With the definition of ξ_1, ξ_2 , let's compare the contribution of friction factor λ to general minor loss coefficient ξ for divergent flow:

$$\xi_1 = k \left(\frac{A_1}{A_h} - 1 \right)^2 \quad (15)$$

$$\xi_2 = \frac{\lambda}{8 \lg(\theta/2)} \left[\left(\frac{A_1}{A_h} \right)^2 - 1 \right] \quad (16)$$

Assuming $\frac{A_1}{A_h} = 10$, a comparison of ξ_2/ξ_1 with Re and θ is shown in Figure 3. In calculation, λ adopts the larger value in equation (11), (12). As shown in Figure 3, in laminar flow scope of $Re < 2000$, ξ_2/ξ_1 has a large value. This means that friction factor has an evident effect.

Nozzle with such kind flow characteristics will result in a larger cooling capacity than orifice and check valve.

But further explanation needs to be combined with refrigeration analysis.

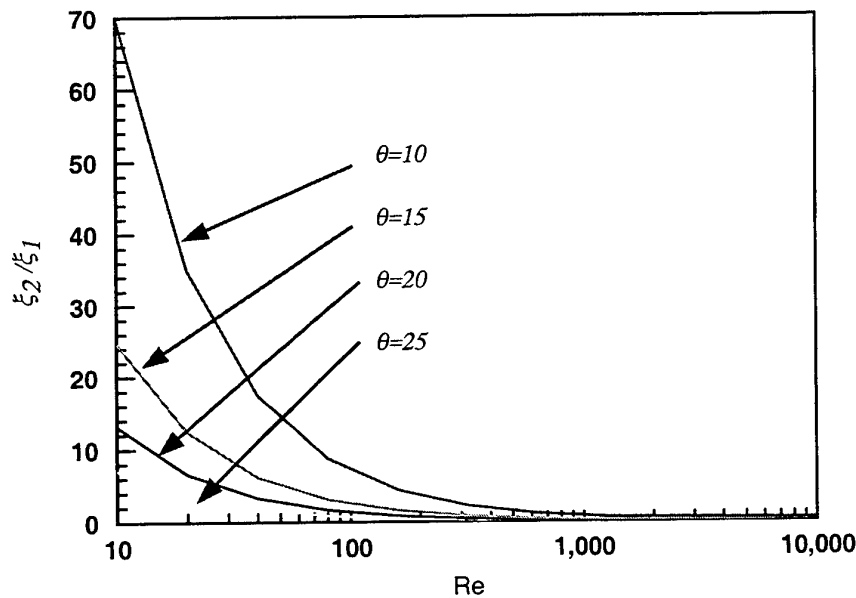


Figure 4 Effect of Re number on minor loss

Refrigeration Capacity

For pressure wave of any form, assuming that orifice has a constant coefficient c_1 , this coefficient includes effect of α, ε, A , and flow rate of orifice is assumed to be:

$$\dot{m}_1 = c_1 X(p_{pt}, p_r) \quad (17)$$

where p_{pt} is the pressure in pulse tube, p_r is the pressure in reservoir,

Theoretical largest refrigeration capacity is as follow [4]:

For differential form:

$$\begin{aligned} dq_c &= RT_0 \ln(p_{pt}/p_r) m_1 dt \\ &= RT_0 \ln(p_{pt}/p_r) \cdot c_1 X(p_{pt}, p_r) dt \end{aligned} \quad (18)$$

For unit time with frequency f :

$$\dot{Q}_c = fRT_0 c_1 \int_0^{\tau} \ln(p_{pt}/p_r) X(p_{pt}, p_r) dt \quad (19)$$

The maximum mass m_0 that flows into reservoir is:

$$m_0 = \int_0^{\tau/2} c_1 \cdot X(p_{pt}, p_r) dt \quad (20)$$

From equation (18) and (19), we can find that there are two important parameters affecting theoretical refrigeration: pressure ratio and mass flow rate. With the same mass amount, a large pressure ratio results in a large refrigeration; with the same pressure ratio, a large mass amount results in a large refrigeration. Upper analysis shows that "L3" determines the total mass amount m_0 , and this is limited to a suitable value. And pressure ratio is mainly determined by compressor swept volume, and is not easy to increase. Thus in theory, "L3" and pressure ratio is predetermined when compressor and structure are determined. But if the mass flow in equation (18, 19) is larger when pressure differences are large and smaller when pressure differences are small while m_0 is constant, total refrigeration will increase. Considering this, the merit of symmetry-nozzle become evident.

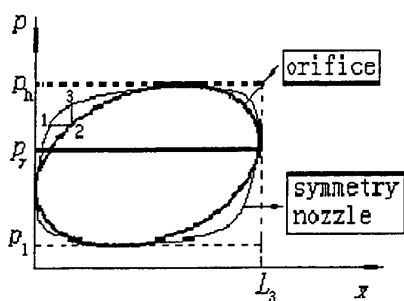


Fig. 5 Difference between orifice and nozzle

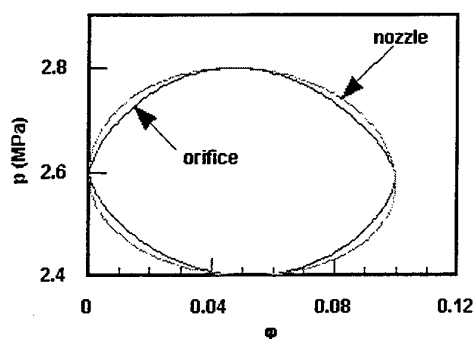


Fig. 6 Calculated difference between orifice and for nozzle

According to table 1 and Figure 4, when pressure difference and Re number are small, large λ results in a larger ξ and flow rate decreases; and when pressure difference and Re number are large, λ becomes small and flow rate increases. This means that more gas flows in and out when pressure differences are large while total amount m_0 is the same. This automatic positive feedback of symmetry-nozzle may result in about 3-5 percent larger refrigeration.

Fig. 5 gives an explanation to this. With same "L3" and same pressure ratio p_h / p_l , comparatively larger circle area can be gained with symmetry-nozzle than with orifice. First compare point 1 and 2 where high pressure is the same, because orifice has a large flow rate, x is larger than that of symmetry-nozzle. Then compare point 2 and 3 where x is same, because symmetry-nozzle has small flow rate at small pressure differences, the pressure in pulse tube is higher than that of orifice when mass amount reaches this point. There are similar conditions at other three places when pulse tube pressure nears reservoir pressure. Thus an evident area increasing is acquired in Fig. 5.

Based on upper analysis and relative parameters, a simulation [4, 5] is done to reveal the extent of difference between orifice and nozzle. Fig. 6 gives a typical result. The curve of nozzle is outside of the orifice, which is just like the analysis results in Fig.5. Calculation shows that a theoretical cooling power of about 5% can be gained according to the experiment condition in Table 2. This equals to 0.1W cooling power or 3-5K temperature difference. But for low frequency experiments, where pressure ratio is large and Re number is large, the difference between orifice and nozzle is limited to 1%.

3. EXPERIMENT

Table 2 gives a comparison between results of using symmetry-nozzle and orifice in miniature pulse tube cooler experiments. In experiments, pulse tube cooler is driven by a 0.79 cm^3 linear compressor. The pressure difference in pulse tube is about 0.3-0.4MPa, and calculated maximum Re number is limited to 1500. Table 2 shows that, whether there is double-inlet or not, 3-5K lower temperature is acquired with symmetry nozzle than with check valve.

Table 2 Comparison between results of using needle valves and symmetry nozzle

Filling pressure	$p_{ave} = 2.0\text{MPa}$		$p_{ave} = 2.6\text{MPa}$	
Version	Orifice	Double-inlet	Orifice	Double-inlet
Needle valve	132.0K	128.5K	124.0K	119.5K
Symmetry nozzle	129.0K	124.0K	121.0K	116.5K

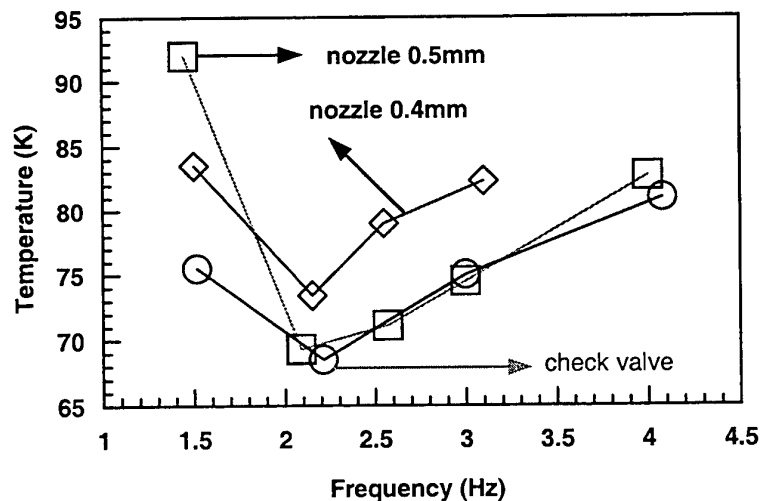


Fig.7 Experiment results of low frequency pulse tube refrigerator

In further research, low frequency experiments with 1KW G-M compressor and rotary valve are done to reveal the effect of nozzle. In experiments, pressure difference in pulse tube was about 0.6-0.8MPa, and pressure ratio was generally greater than 1.6. Several nozzles were used to compare with check valve. The experiment results are shown in Fig. 7. Two nozzles with diameter of 0.5mm and 0.4mm were used. Evidently, both two have a lowest temperature with change of frequency. But temperature with 0.4mm was higher. A check valve was also used. At every point, its temperature was adjusted to reach the lowest temperature. Comparing 0.5mm nozzle

with check valve showed that there were little differences from 2Hz to 3Hz. This means that replacing check valve by suitable nozzle will result in similar result. At the same time, experiments show that symmetry-nozzle to improve the performance at low frequency is limited by its special condition.

Now let's come to the beginning of this paper. If we replace check valve with long thin tube, similar result will be gained, because tube flow coefficient will also be effected by Re number. This can partly explain the reason that long thin tube is more and more used in pulse tube refrigerator in the place of orifice.

4. CONCLUSION

Analysis of orifice and symmetry-nozzle shows that their flow features are different: for symmetry-nozzle, because of positive feedback of flow rate on flow rate, at low-pressure difference, the flow rate is small comparing to orifice condition. These results in larger refrigeration when total gas amount flowing in and out of reservoir keeps unchanged or change little, and a better performance can be obtained with symmetry-nozzle in comparison with needle valve or orifice. The essence of this improvement should attribute to phase relation change of pressure and mass flow rate. But for low frequency experiments with a G-M compressor and a rotary valve, improvement is not evident.

ACKNOWLEDGEMENT

National Superconductor Center of China and National Nature Science Foundation of China support this research.

REFERENCES

1. S. Zhu, P. Wu and Z. Chen, Double inlet pulse tube refrigerator--An important improvement, *Cryogenics*, V.30, pp.514-520 (1990).
2. H.J. Jiang, *Flow Mechanics*, Higher Education Publication in Chinese, 1985, p.308.
3. R.W. Fox, and A.T. McDonald, *Introduction to fluid mechanics*, John Wiley & Sons, Inc, 1978, pp. 449-459.
4. L. Yang, Research of pulse tube refrigeration mechanism and practical development, Post-doctor Research Report, 1998.10, Institute of Mechanics, Chinese academy of Sciences.
5. L. Yang, S.Y. Bian, J.T. Liang, Y. Zhou, Code simulation and verification of pulse tube refrigerator, *Chinese J. of Cryogenics*, No.5, pp.1-6 (1997).

TRANSPORT PHENOMENA IN A CAPILLARY-TUBE SUBJECTED TO A COMPRESSIBLE OSCILLATING FLOW

Guoqiang Lu* Ping Cheng**

Department of Mechanical Engineering
Hong Kong University of Science & Technology
Clear Water Bay, Kowloon, HongKong

*Email: melgq@ust.hk **Email: mepcheng@ust.hk Fax: (852)23581543

Keywords: Transport phenomena, Porous medium, Compressible, Oscillating flow

ABSTRACT In this paper, we analyzed the transport phenomena in a porous medium subjected to a compressible oscillating flow by a capillary-tube model. It is found that momentum transport of a compressible oscillating flow in a capillary-tube follows the Darcy law and an expression for the permeability can be identified. In addition, a closed form analytical expression of the Nusselt number for solid-fluid interfacial heat transfer has been obtained by analyzing the energy equation.

INTRODUCTION

In the literatures, transport phenomena in the porous medium have been investigated extensively. Tong and London [1] measured the friction coefficient and interfacial heat transfer coefficient in the porous medium with steady flows. Tanaika and Yamashita [2], Hsu, Fu and Cheng [3] investigated transport phenomena in the porous medium with oscillating flows. However all of these previous work were based on an incompressible model. In order to analyze the performance of a regenerator in the Stirling refrigerator or the pulse tube refrigerator, it is necessary to investigate the transport phenomena in the porous medium subjected to a compressible oscillating flow.

In this paper, we analyze the transport phenomena of a compressible oscillating flow in a porous medium based on a capillary-tube model. We simplify the governing equations of the physical phenomena based on the thermoacoustic theory, which was first discussed by Rott [4], extensively reviewed by Swift [5], and further investigated by Xiao [6]. The present paper will focus on the transport phenomena. It is found that momentum transport of a compressible oscillating flow in a capillary-tube follows the Darcy law and the permeability is identified. A theoretical expression of the Nusselt number for the solid/fluid interface can be obtained by analyzing the energy transport phenomena.

PHYSIC MODEL

As shown in Fig.1, we study the transport phenomena of a compressible oscillating flow in a capillary-tube with outer radius of R_o and inner radius of R_i .

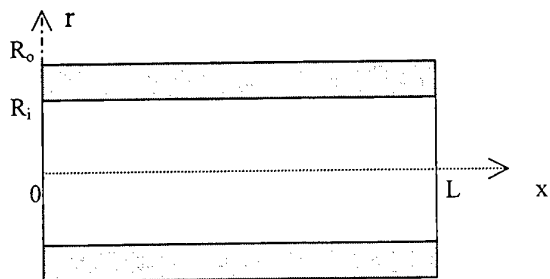


Fig.1 Schematic diagram

We consider the case that the tube is insulated outside and there is a steady axial temperature gradient existing due to compressible effect. Following the assumptions in [4-6], we assume that: (1) the radial gradient of the pressure is neglected throughout the tube; (2) the radial variations of the average

temperature and of the viscosity and thermal diffusivities of the solid and the fluid are neglected; (3) axial heat conduction and friction in the x-direction are ignored; (4) the average oscillating velocity of the fluid equals to zero. The governing equations of the first-order acoustic quantities such as velocity and temperatures of the fluid and solid are given as follows:

$$\frac{\partial u^*}{\partial t^*} = -\frac{1}{\rho_0} \frac{\partial p^*}{\partial x^*} + \nu_0 \frac{1}{r^*} \frac{\partial}{\partial r^*} \left(r^* \frac{\partial u^*}{\partial r^*} \right) \quad (1)$$

$$\frac{\partial T^*}{\partial t^*} + u^* \frac{\partial T_0}{\partial x^*} = \frac{1}{\rho_0 C_{p,0}} \frac{\partial p^*}{\partial t^*} + a_0 \frac{1}{r^*} \frac{\partial}{\partial r^*} \left(r^* \frac{\partial T^*}{\partial r^*} \right) \quad (2)$$

$$\frac{\partial T_s^*}{\partial t^*} = a_{s,0} \frac{1}{r^*} \frac{\partial}{\partial r^*} \left(r^* \frac{\partial T_s^*}{\partial r^*} \right) \quad (3)$$

with boundary conditions given by:

$$r^* = 0 \quad \frac{\partial u^*}{\partial r^*} = 0 \quad \frac{\partial T^*}{\partial r^*} = 0 \quad (4)$$

$$r^* = R_i \quad u^* = 0 \quad T^* = T_s^* \quad k \frac{\partial T^*}{\partial r^*} = k_s \frac{\partial T_s^*}{\partial r^*} \quad (5)$$

$$r^* = R_o \quad \frac{\partial T_s^*}{\partial r^*} = 0 \quad (6)$$

where p , T , u , ρ are pressure, temperature, velocity and density, respectively. Coefficients ν_0 , $C_{p,0}$, k , α_0 and $\alpha_{s,0}$ denote the kinematic viscosity, thermal capacity, thermal conductivity, thermal diffusivities of the fluid and the solid. Subscript "s" denotes solid phase and subscript "0" denotes cycle-average quantity that is independent of time and radial coordinate. Superscript "*" denotes dimensional quantity.

For the first-order acoustic quantities, we take the form of time derivative of the quantities as $\partial/\partial t = i\omega$, here i is unit complex number and ω is angular velocity. We can normalize the above governing equations to a dimensionless form by scaling the radial coordinate by the inner radius R_i , the axial coordinate by the tube length L , time by the $1/\omega$, pressure by the local cycle-average pressure $p_0 = R\rho_0 T_0$, temperature by the local cycle-average temperature T_0 , velocity by the local speed of sound $a = \sqrt{\gamma RT_0}$ where γ is the ratio of specific heats and R is the gas constant. It follows that

$$iu = -\frac{a}{\omega L \gamma} \frac{\partial p}{\partial x} + \frac{\nu_0}{\omega R_i^2} \frac{1}{r} \frac{\partial}{\partial r} \left(r \frac{\partial u}{\partial r} \right) \quad (7)$$

$$iT + \frac{a}{\omega L} \frac{1}{T_0} \frac{dT_0}{dx} u = \frac{\gamma-1}{\gamma} ip + \frac{\alpha_0}{\omega R_i^2} \frac{1}{r} \frac{\partial}{\partial r} \left(r \frac{\partial T}{\partial r} \right) \quad (8)$$

$$iT_s = \frac{\alpha_{s,0}}{\omega R_i^2} \frac{1}{r} \frac{\partial}{\partial r} \left(r \frac{\partial T_s}{\partial r} \right) \quad (9)$$

with boundary conditions:

$$r = 0 \quad \frac{\partial T}{\partial r} = 0 \quad \frac{\partial u}{\partial r} = 0 \quad (10)$$

$$r = 1 \quad u = 0 \quad T = T_s \quad k \frac{\partial T}{\partial r} = k_s \frac{\partial T_s}{\partial r} \quad (11)$$

$$r = \Delta = \frac{R_o}{R_i} \quad \frac{\partial T_s}{\partial r} = 0 \quad (12)$$

We now can solve the above equations subject to the boundary conditions. One should be reminded that only real parts of the complex quantities, which are to be solved, have physical significance in the above equations.

MOMENTUM TRANSPORT

The solution of Eq.(7) with the aids of Eqs.(10-11) is:

$$u = \frac{ai}{\omega L \gamma} \frac{\partial p}{\partial x} \left\{ 1 - \frac{J_0(\eta)}{J_0(\eta_0)} \right\} \quad (13)$$

where $J_0(\eta_0)$ is the Bessel function of the first kind of order zero, $\eta_0 = (i-1) \frac{R_i}{\delta_v}$ and $\eta = \eta_0 r$, in

which $\delta_v = \left(\frac{2\nu_0}{\omega} \right)^{1/2}$ is the fluid's viscous penetration depth. The dimensional form of Eq.(13) was also given in [4].

Define cross-section area average quantities as $\bar{\Omega} = \frac{1}{A_0} \int \Omega dA$. Here Ω is a certain physical quantity and A_0 is cross-section area. Then Eq.(13) leads to:

$$\bar{u} = \left\{ 1 - \frac{2}{\eta_0} \frac{J_1(\eta_0)}{J_0(\eta_0)} \right\} \frac{ai}{\omega L \gamma} \frac{\partial p}{\partial x} \quad (14)$$

where $J_1(\eta_0)$ is the Bessel function of the first kind of order one. One should be reminded that $\partial p / \partial x$ is independent of radial coordinate in the above equation. Recalling the Darcy law in a porous medium is given by:

$$u^* = - \frac{K}{\mu} \frac{\partial p^*}{\partial x^*} \quad (15)$$

where K is the permeability and μ is viscosity of fluid. Comparing Eq.(14) and Eq.(15), we find that they are of the same form, which indicates that the momentum transport in a capillary-tube subjected to a compressible oscillating flow also follows Darcy law. Normalizing Eq.(15) by the same scales as we discussed before and compare to Eq.(14), we have:

$$K = \left\{ \frac{2i}{\eta_0} \frac{J_1(\eta_0)}{J_0(\eta_0)} - i \right\} \frac{\nu_0}{\omega} \quad (16)$$

The variation of $K / \left(\frac{\nu_0}{\omega} \right)$ with respect to R_i / δ_v is shown in Fig.2. We can see that when

R_i / δ_v approaches to zero, the complex modulus and phase angle of $K / \left(\frac{\nu_0}{\omega} \right)$ also approach to zero.

Physically, if the inner diameter R_i approaches to zero, then the permeability K also approaches to zero when the fluid's viscous penetration depth δ_v holds a certain values. It is also shown in Fig.5 that the

values of $K / \left(\frac{\nu_0}{\omega} \right)$ are almost independent of R_i / δ_v when $R_i / \delta_v \gg 1$, and the limit case is

$\lim_{\eta_0 \rightarrow \infty} K / \left(\frac{\nu_0}{\omega} \right) = -i$ which implies that the cross-sectional velocity has a phase lag of 90° from that of

pressure gradient when $R_i / \delta_v \gg 1$.

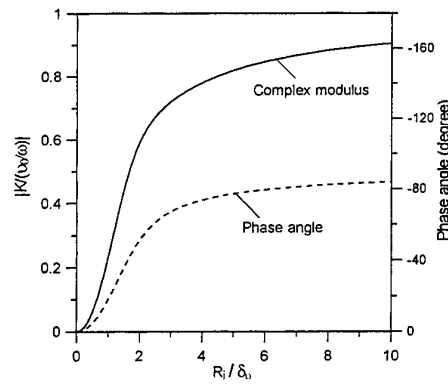


Fig.2 The variation of $K/\left(\frac{v_0}{\omega}\right)$ with respect to R_i/δ_o

ENERGY TRANSPORT

The interfacial heat transfer coefficient h between the solid phase and the fluid phase is:

$$h = \frac{k \left(\frac{\partial T^*}{\partial r^*} \right)_{r^*=R_i}}{\bar{T}_s - \bar{T}} = \frac{k}{R_i} \frac{\left(\frac{\partial T}{\partial r} \right)_{r=1}}{\bar{T}_s - \bar{T}} \quad (17)$$

where \bar{T}_s and \bar{T} are the cross-sectional area averaged temperatures of the solid phase and the fluid phase respectively. A cross-sectional averaging of Eqs.(8)-(9) leads to:

$$i\bar{T} + \frac{a}{\omega L} \frac{1}{T_0} \frac{dT_0}{dx} \bar{u} = \frac{\gamma-1}{\gamma} p + \frac{2\alpha_{s,0}}{\omega R_i^2} \left(\frac{\partial T}{\partial r} \right)_{r=1} \quad (18)$$

$$i\bar{T}_s = -\frac{2\alpha_{s,0}}{\omega(R_o^2 - R_i^2)} \left(\frac{\partial T_s}{\partial r} \right)_{r=1} = -\frac{2\alpha_{s,0}}{\omega(R_o^2 - R_i^2)} \frac{k}{k_s} \left(\frac{\partial T}{\partial r} \right)_{r=1} \quad (19)$$

where we have used the boundary condition of Eq.(11) in Eq.(19). Defining Nusselt number

$Nu = \frac{2hR_i}{k}$ and substituting Eqs.(17)-(19), we have:

$$\frac{1}{Nu} = \frac{i\alpha_{s,0}}{\omega(R_o^2 - R_i^2)} \frac{k}{k_{s,0}} + \frac{i\alpha_o}{\omega R_i^2} - \frac{\frac{\gamma-1}{2\gamma} p + \frac{ia}{2\omega L} \frac{1}{T_0} \frac{dT_0}{dx} \bar{u}}{\left(\frac{\partial T}{\partial r} \right)_{r=1}} \quad (20)$$

Now we return our attention to Eqs.(7)-(12), the temperature of the fluid can be solved and the solution is:

$$T = \left[\frac{b_1}{1-\sigma^2} \frac{J_0(\sigma\eta)}{J_0(\sigma\eta_0)} - \frac{\sigma^2}{1-\sigma^2} \frac{J_0(\eta)}{J_0(\eta_0)} - 1 \right] \frac{1}{\gamma} \left(\frac{a}{\omega L} \right)^2 \frac{\partial p}{\partial x} \frac{1}{T_0} \frac{dT_0}{dx} + \left[1 - \frac{1}{1-b_2} \frac{J_0(\sigma\eta)}{J_0(\sigma\eta_0)} \right] \frac{\gamma-1}{\gamma} p \quad (21)$$

where b_1 and b_2 are given as follows:

$$b_1 = \frac{\frac{\sigma J_1(\eta_0)}{J_0(\eta_0)} \left[\frac{Y_1(\sigma_s \Delta \eta_0)}{J_1(\sigma_s \Delta \eta_0)} J_0(\sigma_s \eta_0) - Y_0(\sigma_s \eta_0) \right] - \varepsilon \left[\frac{Y_1(\sigma_s \Delta \eta_0)}{J_1(\sigma_s \Delta \eta_0)} J_1(\sigma_s \eta_0) - Y_1(\sigma_s \eta_0) \right]}{\frac{J_1(\sigma \eta_0)}{J_0(\sigma \eta_0)} \left[\frac{Y_1(\sigma_s \Delta \eta_0)}{J_1(\sigma_s \Delta \eta_0)} J_0(\sigma_s \eta_0) - Y_0(\sigma_s \eta_0) \right] - \varepsilon \left[\frac{Y_1(\sigma_s \Delta \eta_0)}{J_1(\sigma_s \Delta \eta_0)} J_1(\sigma_s \eta_0) - Y_1(\sigma_s \eta_0) \right]} \quad (22)$$

$$b_2 = \frac{J_1(\sigma\eta_0)}{J_0(\sigma\eta_0)} \frac{\frac{Y_1(\sigma_s\Delta\eta_0)}{J_1(\sigma_s\Delta\eta_0)} J_0(\sigma_s\eta_0) - Y_0(\sigma_s\eta_0)}{\varepsilon \left[\frac{Y_1(\sigma_s\Delta\eta_0)}{J_1(\sigma_s\Delta\eta_0)} J_1(\sigma_s\eta_0) - Y_1(\sigma_s\eta_0) \right]} \quad (23)$$

where $Y_j(\eta)$ is the Bessel function of the second kind of order j , $\sigma = \left(\frac{\nu_0}{\alpha_0} \right)^{1/2} = \text{Pr}^{1/2}$, $\sigma_s = \left(\frac{\nu_0}{\alpha_{s,0}} \right)^{1/2}$

and $\varepsilon = \frac{k_s\sigma_s}{k\sigma}$. The dimensional form of Eq.(21) was also given in [6], but, with some more complicated expression of coefficients. Substituting Eq.(14) and Eq.(21) in Eq.(20), and recalling the definitions of those dimensionless quantities Δ , ε , σ , σ_s and η_0 , we have:

$$\frac{1}{\text{Nu}} = \frac{\frac{\gamma-1}{2} - \left[\frac{1}{2} - \frac{1}{\eta_0} \frac{J_1(\eta_0)}{J_0(\eta_0)} \right] \phi}{\frac{\sigma\eta_0}{1-\sigma^2} \left[b_1 \frac{J_1(\sigma\eta_0)}{J_0(\sigma\eta_0)} - \sigma \frac{J_1(\eta_0)}{J_0(\eta_0)} \right] \phi - \frac{\gamma-1}{1-b_2} \frac{\sigma\eta_0 J_1(\sigma\eta_0)}{J_0(\sigma\eta_0)}} + \frac{1}{\varepsilon\sigma\sigma_s(\Delta^2-1)\eta_0^2} + \frac{1}{\sigma^2\eta_0^2} \quad (24)$$

where $\phi = \left(\frac{a}{\omega L} \right)^2 \frac{1}{T_0} \frac{dT_0}{dx} \frac{1}{p} \frac{\partial p}{\partial x}$ is a dimensionless quantity which depends only on axial position under the consideration of harmonic oscillation of pressure. Therefore, the value of the Nusselt number depends on thermal property parameters (σ , σ_s , ε , γ), geometrical parameter (Δ) and operation conditions parameters (η_0 , ϕ).

Fig.3 shows the variations of Nusselt number with respect to the dimensionless quantity ϕ when $R_1/\delta_0 = 1$ which were calculated based on the following conditions: (1) the fluid is Helium gas and the solid is stainless steel; (2) working pressure is 1Mpa and local temperature is 80K; (3) geometrical parameter Δ is assumed to be equal to 1.12, which is related to porosity of the porous medium. Under the considerations of temperature-dependant properties [7], we have $\sigma=0.876$, $\sigma_s=0.447$, $\varepsilon=86.469$, $\gamma=1.667$. As shown in Fig.3, there are different phase angles of Nusselt number with respect to the variation of quantities ϕ , which indicate that there is phase shift between heat flux and temperature differences.

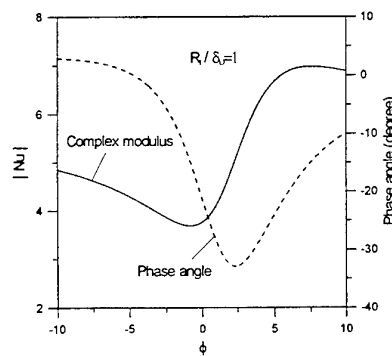


Fig.3 The variation of Nusselt number with respect to dimensionless quantity ϕ

CONCLUSION

In this paper, we have analyzed the transport phenomena in the porous medium subjected to a compressible oscillating flow by a capillary-tube model. The conclusions show that momentum transport of a compressible oscillating flow in a capillary-tube follows the Darcy law and the permeability has been theoretically determined. In addition, a theoretical expression of the Nusselt number has been obtained by analyzing the energy transport phenomenon. The value of the Nusselt number depends on thermal property parameters (σ , σ_s , ε , γ), the geometrical parameter (Δ) and operation conditions parameters (η_0 , ϕ). The local Nusselt numbers have different values when the flow has the same amplitudes but different directions.

ACKNOWLEDGEMENT

This work was supported by RGC grants # HKUST 709/95E and #HKUST6039/99E.

REFERENCE

1. L. S. Tong and A. L. London, 1957, Heat transfer and flow-friction characteristics of woven-screen and cross-rod matrices, *Trans ASME*, 1558-1570
2. M. Tanaka and I. Yamashita, 1990, Flow and heat transfer characteristics of the Stirling engine regenerator in an oscillating flow, *JSME International Journal*, Series II, v.33, no.2.
3. C. T. Hsu, H. L. Fu and P. Cheng, 1999, On pressure-velocity correlation of steady and oscillating flows in regenerator made of wire screens, *J.Fluid Engineering*, v.121, no.1, 52-56.
4. N.Rott, 1980, Thermoacoustics, *Adv.App.Mech*, v.20, p.135
5. G. W. Swift, 1988, Thermoacoustic engines, *J.Acoust.Soc.Am.*, v.84, p.1145.
6. J. H. Xiao, 1995, Thermoacoustic heat transport and energy transformations, Part 1: Formulation of the problem, *Cryogenic*, v.35, p.15 .
7. R.B.Scott, 1988, *Cryogenic engineering*. Met-Chen Research Inc..
8. M. Abramowitz and I. A. Stegun, 1965, *Handbook of mathematical functions with formulas, graphs, and mathematical tables*, Dover publication, Inc., New York.

ANALYSIS OF THE VALVE-TIMING EFFECT ON THE PERFORMANCE OF A 4.2K GIFFORD-MCMAHON REFRIGERATOR

Liang Zhang, Xiang-dong Xu and Ling-hui Gong
Cryogenic laboratory, Chinese Academy of sciences
P.O.Box 2711, Beijing, China 100080

Keywords: 4.2K, G-M refrigerator, valve-timing

ABSTRACT. A Gifford-McMahon Refrigerator based on the Simon expansion is a gas cryocooler, in which the helium is compressed at ambient temperature and expands at refrigerating temperature, from the view point of a thermodynamic cycle. This phenomena no longer exists in a 4.2K G-M refrigerator with the magnetic regenerative matrix in the cold regenerator, when the operating temperature reaches the liquid helium temperature, because of the unique features of the low temperature regenerator. The most helium expanding in the cold space is compressed in the void volume of the cold regenerator, and the compression heat becomes the main loss of the cooling capacity. Because the regenerator matrix with a limited specific heat can not absorb all the compression heat [1,2], which can't be avoided. In this condition, it is necessary to ensure that the helium, as far as possible, is compressed in the cold regenerator, not in the cold chamber, where no matrix. Owing to the existence of the flow resistance, the time for the build-up and come-down of the pressure in the cold chamber can not be neglected. Hence, it's certain that a part of helium is compressed in the cold chamber. In order to decrease this part of loss, the selection of the valve-timing is very important. Thus, the numeric simulation of the influence of the valve timing on a 4.2K Gifford-McMahon refrigerator is performed in this paper and the optimization of the valve timing is obtained.

1. INTRODUCTION

A Gifford-McMahon Refrigerator a gas cryocooler based on the Simon expansion. Owing to the discovery of the magnetic regenerator matrix at the end of eighties, the G-M refrigerator had made great progress. The no-load temperature of two-stage G-M refrigerator had reached 2.4 K, cooling capacity had reached 1.5W at 4.2 K[3,4]. In a common G-M refrigerator the helium is compressed at ambient temperature and expands at refrigerating temperature, according to the view of the thermodynamic cycle. This phenomena no longer exists in a 4.2K G-M refrigerator with the magnetic regenerative matrix in the cold regenerator, when the operating temperature reaches the liquid helium temperature. The working process of a 4.2K G-M refrigerator is far different from a common G-M refrigerator. Some research and analysis[1,2] had been made. The results show that most helium expanding in the cold space is compressed in the void volume of the cold regenerator and the compression heat becomes the main loss of the cooling capacity, because the regenerator matrix with a limited specific heat can not absorb all the compression heat. Owing to the existence of the flow resistance, the time for the build-up and come-down of the pressure in the cold chamber can not be neglected. In order to ensure that the helium, as far as possible, is compressed in the cold regenerator and expands in the cold chamber, the selection of the valve timing is very important. Hence, to understand the valve-timing on the performance of a 4.2k G-M refrigerator clearly is one of the key problems of a 4.2k G-M refrigerator. So, the numeric simulation of the influence of the valve-timing on a 4.2K Gifford-McMahon refrigerator is performed in this paper. The optimization of the valve timing is also obtained

2. THE NUMERICAL CALCULATION MODEL AND CONTROL EQUATIONS

Because of the complication of the working process of the regenerator, some simplifications are necessary. So we select a simplified numerical calculation model. The assumptions are given as:

1. the flow is one dimensional;
2. the longitudinal thermal conductivity in the regenerator is zero and the transverse thermal conductivity in the regenerator is infinite;
3. the wall effect is neglected;
4. the pressure drop along the regenerator is zero and the pressure change with time is linear.

Owing to the regenerator working at liquid helium temperature and the physical property of helium being far

away from the ideal gas, the helium in the void of the regenerator should be considered and the real gas state equation must be applied. According to the assumptions the control differential equations can be written as: the helium energy flow equation

$$\frac{\partial(\dot{M}h)}{\partial x} + \frac{\alpha A_\alpha}{\psi} (T_f - T_m) + \frac{\partial(\rho h - P)}{\partial t} = 0 \quad (1)$$

The matrix energy equation is

$$\alpha A_\alpha (T_f - T_m) - (1 - \psi) C_m \frac{\partial T_m}{\partial t} = 0 \quad (2)$$

The mass conservation equation is

$$\frac{\partial \dot{M}}{\partial x} + \frac{\partial \rho}{\partial t} = 0 \quad (3)$$

The real gas equation is

$$\rho = \rho(P, T_f) \quad (4)$$

3. THE NUMERICAL CALCULATION RESULTS AND DISCUSSION

According to the real working situation of a liquid helium temperature G-M refrigerator, the calculation parameters are given in Table 1.

Table 1. The calculation parameters

high pressure	1.9Mpa
low pressure	0.5Mpa
cold chamber temperature	4.2K
hot end temperature of regenerator	30.0K
porosity	0.4
volume ratio of regenerator to cold chamber	5.0
working period	1s
matrix in the regenerator	ErNi ₂

The pressure of the cold chamber, the displacement of the displacer vs the rotation angle of motor and the mass flow rate of the cold end of the regenerator are given as:

$$P = P(f) \quad (5)$$

$$S = S_0 [1 - \cos(f + f_0)] / 2 \quad (6)$$

$$\dot{M} = - \frac{\partial(S\rho)}{\psi \partial t} \quad (7)$$

where $f = 360t$; P is the pressure of the cold chamber; S is the displacement of the displacer; f is the rotation angle of motor; f_0 is the phase angle difference between the pressure and the displacement. $f_0 < 0$ expresses the 'ahead admission', that is, admission starts before the displacer reaches the bottom of the cylinder. $f_0 > 0$ expresses the 'delaying admission', that is, admission starts after the displacer leaves the bottom of the cylinder. Fig. 1 and 2 show the curves of P and S vs f . In Fig. 1 the curve is obtained by fitting the measured pressure in the cold chamber. From Fig. 1 we can see that the build-up process of pressure occupies about 40° region and the come-down process of pressure occupies about 70° region. Obviously, because of existence of the flow resistance of

the valve, the build-up and come-down process of the pressure of the cold chamber needs a period of time. Because the flow resistance of the valve during come-down process of pressure is greater than that during the build-up increasing process of pressure, the come-down process spends more time.

Using formulas (4), (5) and (7), the simultaneous differential equations (1), (2) and (3) can be solved by numerical methods. We calculate with different f_0 . A typical results of $f_0 = -20^\circ$ are shown in Fig.3-4. Fig. 3 presents the temperature distribution of the helium at regenerator and Fig. 4 gives the helium mass flow rate (\dot{M}) distribution of the helium per unit area at the porosity of regenerator with $f_0 = -20^\circ$. $\dot{M} > 0$ expresses the helium flowing from cold end to hot end while $\dot{M} < 0$ expresses the helium flowing from hot end to cold end. These curves are similar to that in literature[1,2].

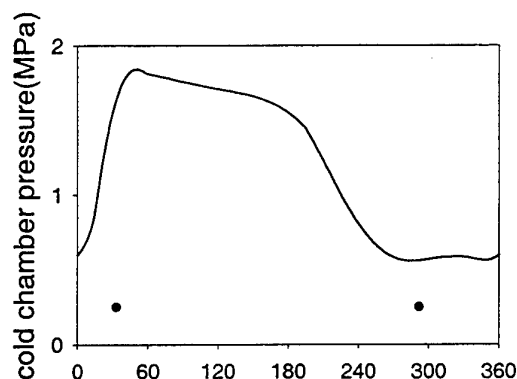


Fig. 1. The pressure of the cold chamber vs the rotation angle of motor

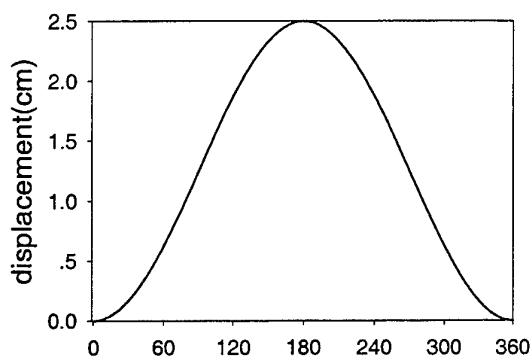


Fig. 2. The displacement of the displacer vs the rotation angle of motor

From Figure 3 we can see that the temperature distributions of the low temperature regenerator are obviously different from that of general regenerators. The first is that a low temperature platform appears at cold end. The second is the matrix temperature fluctuation is very large. This is mainly owing to that the physical properties of helium are far away from that of the ideal gas at low temperature and the disequilibrium of the enthalpy difference between the high pressure helium and the low pressure helium appears. Moreover, the volume specific heat of the matrix is less than that of helium. From Figure 4 we can see that the mass flow rate in the cold end is much larger than that in the hot end. This shows that the regenerator has 'respiration effect' and can store a large quantity of helium.

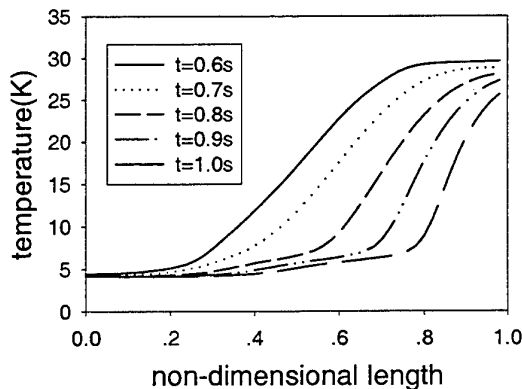
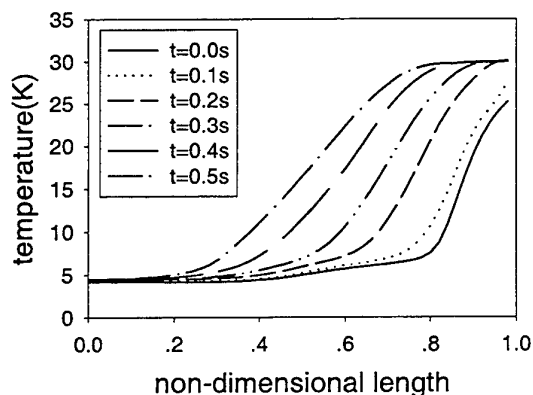


Fig. 3. The temperature distribution of the helium at regenerator

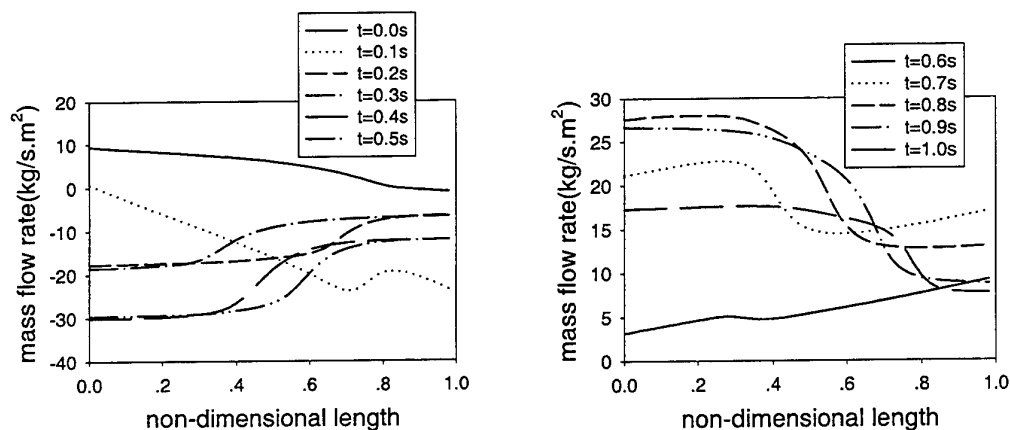


Fig. 4. The mass flow rate distribution of helium at the porosity of regenerator

The cooling capacity of the G-M refrigerator is calculated by following formula:

$$Q_c = Q_{pv} + H_{out} - H_{in} \quad (8)$$

where Q_{pv} ($Q_{pv} = P dV$) is the P-V work of the cold chamber, H_{out} is the enthalpy of the helium flowing out of cold chamber during a cycle, H_{in} is the enthalpy of the helium flowing into cold chamber during a cycle.

Figure 5 shows Q_{pv} and $(H_{out} - H_{in})$ vs f_0 . From Figure 5 we can see that Q_{pv} and $(H_{out} - H_{in})$ have a positive peak value with $f_0 = -20^\circ$ and a negative peak value with $f_0 = -30^\circ$ respectively.

Figure 6 shows the cooling capacity vs f_0 . It can be seen from Figure 6 that there are two positive peak values with $f_0 = -10^\circ$ and -40° . The cooling capacity for $f_0 = -10^\circ$ is a little greater than that for $f_0 = -40^\circ$. This is owing to the staggering peaks of the curves of P-V work and the enthalpy difference. The existence of two peaks will result in that the difference of the cooling capacities from $f_0 = 0^\circ$ to $f_0 = -50^\circ$ is less than 10%. For $f_0 < -50^\circ$ or $f_0 > 0^\circ$ the cooling capacity decreases quickly. Hence, for practical G-M refrigerator, the ahead phase angle (f_0) of the admission valve should be situated within $-50^\circ \sim 0^\circ$ region. From above results we can see that f_0 has important influence on the cooling capacity of the G-M refrigerator. Because the valve-timing has relation with f_0 , the valve-timing is important for the cooling capacity.

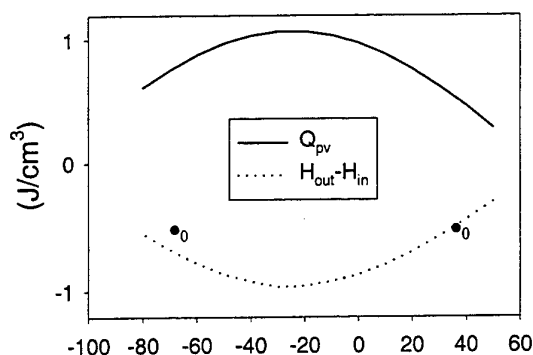


Fig. 5. Q_{pv} and $(H_{out} - H_{in})$ vs f_0

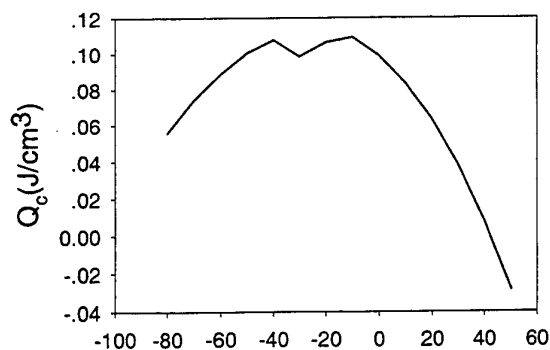


Fig. 6. The cooling capacity vs f_0

4. CONCLUSIONS

1. The curves of Q_{pv} and (Hout-Hin) vs f_0 have a positive peak value with $f_0 = -20^\circ$ and a negative peak value with $f_0 = -25^\circ$ respectively.
2. The curve of cooling capacity vs f_0 has two positive peak values at $f_0 = -15^\circ$ and -45° . This is mainly owing to the staggering peaks of the curves of the P-V work and the enthalpy difference.
3. For a practical G-M refrigerator, the ahead phase angle (f_0) of the admission valve should be situated within $-50^\circ \sim 0^\circ$ region. The optimal f_0 must exist and can be decided by tests.
4. Because the valve-timing has relation with f_0 , the valve-timing is important for the cooling capacity.

ACKNOWLEDGEMENT

This research was supported by the National Natural Science Foundation of China and the National Center for Research and Development on Superconductivity.

NOMENCLATURE

A_α	heat transfer area per unit volume of matrix
C_m	specific heat per unit volume of matrix
h	enthalpy of helium
\dot{M}	mass flow rate per unit area
P	pressure of helium
T_f	temperature of helium
T_m	temperature of matrix
α	heat transfer coefficient
ρ	density of helium
ψ	porosity of the regenerator

REFERENCES

1. C.S. Hong and X.D. Xu, On the thermodynamic Cycle of the Low Temperature G-M Refrigerator, *Cryogenics*, 34 Supplement 183-183 (1994)
2. X.D. Xu, L. Wang, L.H. Gong and L. Zhang, Analysis on the colder Regenerator of 4.2K G-M refrigerator, *Advances in Cryogenic Engineering*, 43B 1605-1610 (1998)
3. T. Inaguchi etc. : "Two-stage Gifford-McMahon Cycle Cryocooler Operation at about 2K", *Cryocoolers-6*, 2, 25-28 (1990)
4. T. Satoh etc. : "Development of 1.5W 4K G-M Cryocooler with Magnetic Regenerator Material" *Advances in Cryogenic Engineering*, 41 1631-1637 (1996)

H-MATRIX DESCRIPTION OF THE PERFORMANCE OF REGENERATOR

Qing Li, Wei Zhang, Fangzhong Guo

Cryogenic Laboratory, Huazhong University of Science and Technology

Wuhan 430074 P.R. China

Email: ymtian@mail.hust.edu.cn; Fax: 0086-27-8754 8737

Keywords: regenerator, regenerative heat engine, *H*-matrix

ABSTRACT. Basing on the active network modeling approach for regenerative heat engine, it is proposed that the energy conversion effect in regenerator can be modeled by analogy with transistor amplifier circuit. Following the method of network analysis, it is demonstrated that the thermoacoustic source term for a real regenerator in regenerative heat engine system can be identified experimentally with regenerator in system working under operational conditions. A performance description method for regenerator in regenerative heat engine system is proposed in the paper.

1. BACKGROUND

The longitudinal non-isotropic oscillation of fluid parcels along channels of regenerator with imposed temperature gradient causes meso-scale thermodynamic cycle to occur and thus convert part of the heat provided by the heat exchanger on the end of regenerator into work. This is the essence of the thermoacoustic theory of regenerator, it has recently been acknowledged more and more commonly [1, 2]. According to the conventional theory of regenerative heat engine, regenerator was treated as a recuperative heat exchanger and a series of computation procedure has been established taking heat exchanger efficiency as the only performance specification of regenerator. Following the viewpoint of thermoacoustic theory, it is clear that the recuperative modeling for regenerator can no longer be considered as adequate since regenerator is a device with energy conversion.

The authors have proposed [3, 4] the approach of active thermoacoustic network modeling for regenerative heat engines, as shown by Fig. 1, and have verified the existence of an active thermoacoustic source term by experiments shown in [5]. It has been revealed that beyond some threshold value of temperature difference imposed on regenerator, negative damping term has appeared really in the oscillation model of regenerator, this demonstrated clearly the existence of an active source term in network modeling, which means the conversion of heat to work. It is pointed out elsewhere in [6], that the coupling of the longitudinal pressure wave propagated by oscillating fluid and the transversal heat wave modulated by displacement oscillation of fluid causes thermoacoustic effect to occur. In fact the complete system of a regenerative heat engine may be treated as being composed of two subsystems, i.e. the acoustic field in the fluid existing in the channels of regenerator (flux subsystem) and the temperature field existing in the penetrating depth layer near the solid matrix wall of regenerator (source subsystem), see Fig. 2.

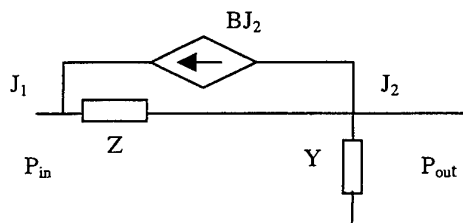


Fig. 1 Active thermoacoustic network

The approach basing on the analogy between electric circuit and fluid circuit has now been adopted more and more, but it is confined only for the description of the acoustic field in engine system (flux subsystem) by passive network. Recently there is no practical applicable engineering model to describe the thermoacoustic source term, i.e. the regenerator subsystem.

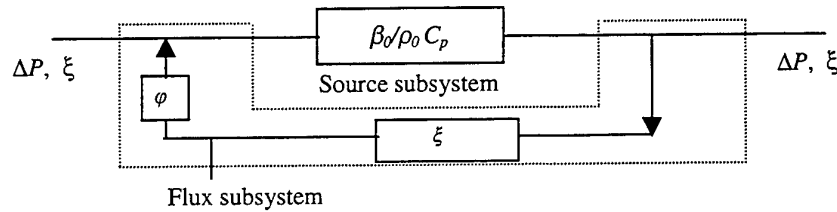


Fig. 2 Two subsystem in a Thermoacoustic heat engine system

2. DISPLACEMENT MODULATION MODELING FOR TRANSVERSAL HEAT WAVE

In fig. 3, plate 2 reciprocates harmonically along plate 1 with imposed axial temperature gradient, the transversal heat flux between plate 1 and 2 in direction perpendicular to the reciprocating motion in this case is

$$Q_{tr} = h\xi \nabla T \frac{1}{\sqrt{1+\phi^2}} \sin(\omega t + \phi) \quad (1)$$

which is a heat wave with a phase lag behind the longitudinal wave, the phase lag depends on the heat capacity ratio G of the two plates;

$$\phi = -\arcsin\left(\frac{1}{\sqrt{1+\phi^2}}\right) \quad (2)$$

$$\phi = \frac{h}{\omega G}, \quad \frac{1}{G} = \frac{1}{mc_2\rho_2} + \frac{1}{(1-m)c_1\rho_1} \quad (3)$$

This analysis demonstrates that with an imposed temperature gradient the relative longitudinal displacement can modulate a transversal heat wave with same frequency. It is the same mechanism for the fluid parcel to modulate a transversal heat wave when oscillating along the solid wall of matrix in regenerator with temperature difference across its two ends. The phase lag between the two waves depends on the heat capacity ratio G of fluid and matrix and the heat transfer rate h . It has been presented by a series of research reports[9,10] that the transversal diffusive wave is a complicated nonlinear process caused by wave dispersion and reflection. The coupling of the two waves causes the occurrence of thermoacoustic effect either to enhance the axial heat transport or to pump heat or to amplify the longitudinal wave, depending on the phase shift between two coupling waves.

Thus, the matrix-fluid interface in regenerator acts as a transversal heat wave modulator, which modulates the heat flux transported in longitudinal direction into transversal heat wave by means of the fluid parcels displacement driven by pressure wave, the mechanism can be shown schematically in Fig. 3 and Fig. 4.

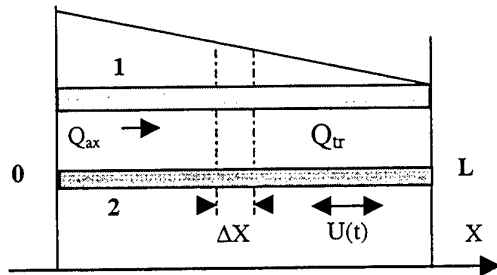


Fig. 3 Modulation of transversal heat wave



Fig. 4 Displacement modulation of Thermoacoustic source

3. FEEDBACK RELATIONSHIP BETWEEN REGENERATOR AND ACOUSTIC FIELD IN HEAT ENGINE SYSTEM

Obviously, there is a feedback relation between the flux (acoustic field in engine system) and the source (regenerator) subsystem, the feedback is realized by the isobaric thermal expansion coefficient of fluid β_0

$$\beta_0 = \left(\frac{\partial \rho}{\partial T} \right)_p$$

The transversal temperature difference ∇T acts on modifying the density of oscillating flow, which in coupling with its pressure oscillation under appropriate phase shift condition converts heat into work on amplifying acoustic field or pumping heat against temperature rise. Thus, the isobaric thermal expansion of fluid as a nonlinear link leads to the occurrence of parametric amplification, which causes self-excited oscillation of the fluid system. Thus parametric amplification is the key link to modulate the provided heat energy into wave energy, which in turn is absorbed by the oscillating system and thus maintain a self-sustained oscillation with the constant amplitude, phase and frequency. The detailed analysis about this feed-back relationship is presented elsewhere in [6], which is given by the source term in a transport equation

$$\begin{aligned} \frac{\partial p}{\partial x} &= -Z \cdot J \\ \frac{\partial J}{\partial x} &= -Y \cdot p + -\beta \cdot J \end{aligned} \quad (4)$$

with β - as a source parameter

$$\beta = \frac{f_k - f_\mu}{(1 - p_r)(1 - f_\mu)} \beta_0 e^{j\varphi} \frac{dT_0}{dx} \quad (5)$$

in which f_k, f_μ - cross distribution function of velocity and temperature.

4. H-MATRIX DESCRIPTION OF REGENERATOR

It is needed to model on the same network approach the coupling of transversal heat wave in penetration depth layer (i.e. regenerator) subsystem with the longitudinal pressure wave in oscillation fluid (acoustic field) subsystem.

It is well known that the transversal temperature difference between matrix and fluid which, by combining with the modulation model shown in Fig. 4, gives the block scheme for the transversal temperature wave modulation presented in Fig. 5.

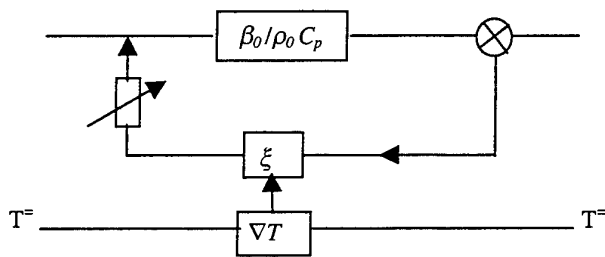


Fig. 5 The modulation of transversal temperature wave

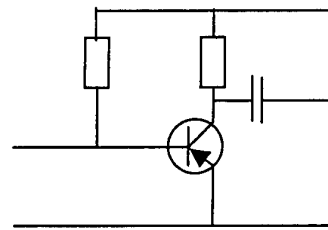


Fig. 6 Electric circuit of a common-emitter amplifier

The diffusion of ions on the PN-interface of a transistor can modulate the energy of the imposed direct current electric field into a wave of the same frequency with the provided signal and thus amplifies the later. By

comparing an electric circuit of common-emitter amplifier (fig. 6) with fig. 5, it can be found that they are the same in the sense of irreversible thermodynamics. Both are the conversion and transport of energy by means of nonlinear coupling of diffusion and oscillation phenomena and so both can be described by active network.

Active network can be characterized by various kinds of parameters, among which the so-called open loop impedance Z matrix has been adopted by [2] [3] for passive networks and also by the authors for modeling thermoacoustic resonance tube [7]. The result shows that it agrees well with reality for system with not very high frequency (lower than 10^2 hertz) and large diameter tubing. But in the case of higher frequency and small diameter tubing, the nonlinear character appears to be quite significant because of dispersion and wave reflection, the parameters should be determined experimentally. For easier parameter identification by experiments on system, H (hybrid) parameter is preferable.

According to the concept of network, the source term can be treated as a negative resistance and the self-sustained oscillation caused by the characteristics of the system itself can thus be described as a feedback oscillation. It has been derived that this negative resistance is a flux controlled flux source, i.e.

$$J(-R) = +X$$

The two-port network is shown by Fig. 7, the matrix equation of it is

$$\begin{bmatrix} J_1 \\ J_2 \end{bmatrix} = \begin{bmatrix} G_{11} & G_{12} \\ G_{21} & G_{22} \end{bmatrix} \begin{bmatrix} X_1 \\ X_2 \end{bmatrix} \quad (6)$$

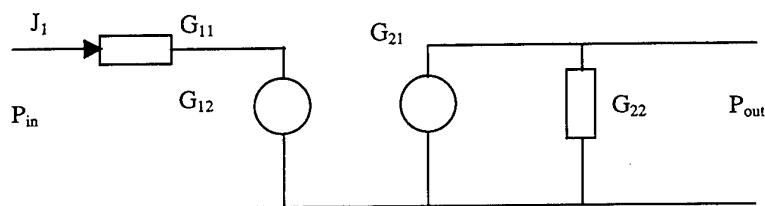


Fig. 7 Two-port network representation for flux controlled flux source

As for the thermoacoustic term βJ in (4), the theoretical values for the components in matrix should be

$$G_{11} = G_{12} = G_{21} = 0 \quad , \quad \text{and} \quad G_{22} = \beta \quad (7)$$

But for a real regenerator, the components G_{ik} can only be determined experimentally. For a network shown in Fig. 7, the input and output equations are

$$\begin{aligned} p_{in} &= f_1(J_1, p_{out}) \\ J_2 &= f_2(J_1, p_{out}) \end{aligned} \quad (8)$$

For small perturbations following relations can be written

$$\begin{aligned} dp_{in} &= \left. \frac{\partial p_{in}}{\partial J_1} \right|_{p_{out}} dJ_1 + \left. \frac{\partial p_{in}}{\partial p_{out}} \right|_{J_1} dp_{out} \\ dJ_2 &= \left. \frac{\partial J_2}{\partial J_1} \right|_{p_{out}} dJ_1 + \left. \frac{\partial J_2}{\partial p_{out}} \right|_{J_1} dp_{out} \end{aligned} \quad (9)$$

Which can be used for the definition of G_{ik} . The four components of the matrix are defined as:

$\left. \frac{\partial p_{in}}{\partial J_1} \right|_{p_{out}}$: Input impedance of regenerator under opened exit condition

$\left. \frac{\partial p_{in}}{\partial p_{out}} \right|_{J_1}$: Output-input pressure ratio of regenerator under closed entrance condition

$\left. \frac{\partial J_2}{\partial p_{out}} \right|_{J_1}$: Output conductance of regenerator under closed entrance condition

$\left. \frac{\partial J_2}{\partial J_1} \right|_{p_{out}}$: Output-input volumetric flow ratio of regenerator under opened exit condition

The most important component is the volumetric flow rate ratio, which represents the effect of heat-work conversion in regenerator by means of flux amplification factor. The ratio of output and input pressure reflects the friction loss in regenerator, while the input impedance and the output conductance characterize the required matching condition for coupling regenerator with heat engine system. The proposed description for the performance of regenerator is more reasonable for the thermoacoustic theory of regenerative heat engine. It can be identified by experiments in heat engine system. It can be identified by experiments in heat engine system with regenerator working under operational condition, so the performance factors determined by this way can reflect the real merit of regenerator in heat engine system. The results of experimental identification will be presented later.

5. CONCLUSION

A performance description for the regenerator in regenerative heat engine has been proposed. Basing on the active network concept, it, in combination with the thermoacoustic network modeling for regenerative heat engine presented in [6], constitutes a practical method for characterizing the merit of regenerator when working under operating conditions by experimental identification.

REFERENCES

1. G.W.Swift, Thermoacoustic engines, J.ASA. V84 1145, 1988.
2. J.H.Xiao, Thermoacoustic theory for cyclic flow regenerators, Cryogenics, V32, 895, 1992
3. X.H.Deng, Thermoacoustics Essence of Regenerator and the design of Thermoacoustic Engine, Ph.D, Thesis, Huazhong University of Science and Technology, 1994, China
4. F.Z.Guo, Flow characteristics of a cyclic Flow Regenerator, Cryogenics (1987) V27, 152
5. Y.Xiang, Parity Simulation of Thermoacoustic effect in regenerator of Stirling cryocooler, Cryogenics V35, 489, 1995
6. F.Wu., Active network modeling for regenerator of regenerative heat engine, report on SEE-2000, Hongkong, 2000
7. M.X.Francois, A Prototype of Thermoacoustic Prime mover, Limsi Report 1997, CNRS France
8. A.M.Fusco, Two-sensor power measurements in lossy ducts, J.ASA. V91. 2229, 1992
9. L.Bauwens, Thermoacoustics: Transient regimes and singular temperature profiles, Ph. of Fluids, V10, 807, 1998

DISPLACEMENT OF GAS IN PULSE TUBE OF PRT

Qing Li, Yurong Feng, Fangzhong Guo

Cryogenic Laboratory, Huazhong University of Science and Technology
Wuhan 430074 P. R. China

Email: ymtian@mail.hust.edu.cn; Fax: 0086-27-8754 8737

Keywords: displacement, pulse tube, pulse tube refrigerator

ABSTRACT. The role of pulse tube in PTR system is twofold, namely the thermodynamic and the dynamic aspects. The thermodynamic aspect determines the refrigeration mechanism of pulse tube, which in turn exerts dynamic influence on PTR system. The method proposed by Dr. de Boer has been developed to investigate the displacement of gas in pulse tube of a PTR system. The computational result and the discussion on it are presented here.

1. BACKGROUND

It is commonly acknowledged that in the pulse tube of a pulse tube refrigerator, there is a "gaseous piston" reciprocating in it. But this remains to be a concept only for qualitative analysis, because it is not easy to determine the length of this "gaseous piston". Meanwhile, it is now clear that this "gaseous piston" plays an important role in the governing mechanism of pulse tube refrigeration.

About the function of pulse tube in a pulse tube refrigerator system, there are two distinct explanations. Proceeding from thermoacoustic viewpoint; [1~3] pay attention mainly to its dynamic aspect as a phase regulator for establishing an appropriate acoustic field to match with the regenerator of the system; while [4~6] emphasize the thermodynamic aspect of the pulse-tube as a converter of heat to work and take note to its mechanism of refrigeration. More works have to be done before a comprehensive model of pulse tube can be settled.

Pulse tube works always in connection with regenerator and compression piston in a system, so it is important to find the interrelationship between pulse tube and other subsystems. For all types of regenerative heat engines, including the pulse-tube refrigerator, coupling between its subsystems is the key point for its good performance. For conventional regenerative heat engine, the coupling can be brought about by crank-shaft mechanism, for free-piston type machine, pneumatic or electromagnetic driving mechanism can be used. This means that for this type of stirling machine successful coupling can be achieved by dynamic way. But for the pulse-tube type with no movable displacer the coupling can only be realized by means of thermodynamic and acoustic parameter matching. In this case, coupling is determined firstly by thermodynamic equilibrium that in turn depends on the matching between the geometric dimensions of the system. These geometric parameters are the compression piston stroke X_p , the length of regenerator L_r , the length of heat exchangers L_h and L_c and the stroke of virtual movable plug X_c (see Fig 1). The displacement of gas in pulse tube reflects the result of this equilibrium.

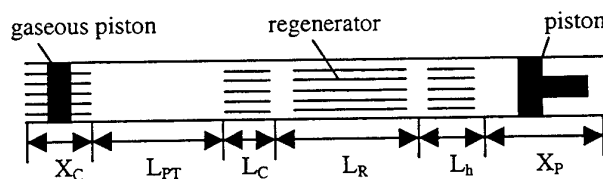


Fig 1 Geometry of PTR model

This paper presents some results of our computational work on the gas displacement in pulse tube, i.e. the motion behavior of the so-called buffer gas in pulse tube in relation to the dimensions of some main subsystems.

2. COMPUTATIONAL MODEL

A model of pulse tube refrigerator system is sketched in Fig 1. On one side of the pulse tube is the cold heat

exchange at temperature T_c , on the other side is a warm heat exchanger at temperature T_h . The warm heat exchanger is followed by a virtual plug piston with stroke X_c , that simulates the flow through orifice. The cold heat exchanger is followed by a regenerator, another heat exchanger at T_h and a tube linking with stroke X_p to the compressor piston. The cycle consists of following 4 steps: (see Fig.2).

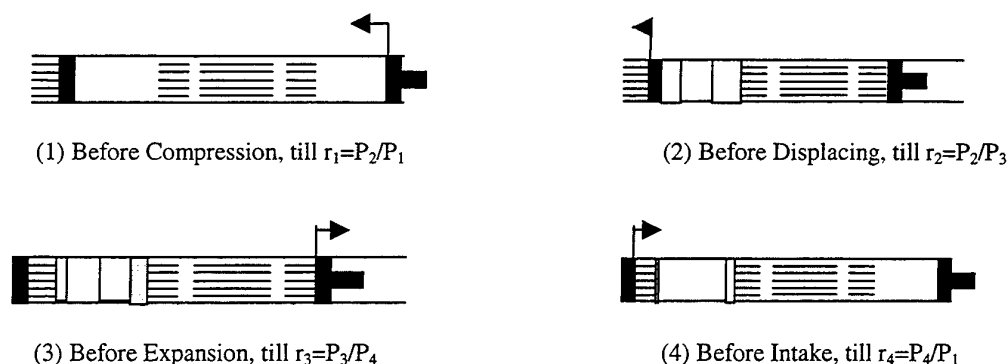


Fig 2 Operation steps of the model

1. Compression ,the compressor piston compresses the gas in the system, the pressure increases from P_1 to P_2 ;
2. Displacing, the virtual plug piston with stroke X_c moves to displace the gas into reservoir, the pressure drops to be P_3 ;
3. Expansion, the compressor piston expands the gas, the pressure decreases from P_3 till P_4 ;
4. Intake, the gas flows from reservoir decrease the pressure to P_1 .

In the computational model, the pressure ratio P_2/P_1 is considered as given input and is denoted by r_1 . The gas in the system is ideal, with constant specific heat and works in local isothermal condition in heat exchangers and regenerator. No dissipation is considered, so the pressure in system is taken to be uniform.

The longitudinal temperature distribution of gas can be used to describe the length of the buffer gas in pulse tube. As shown in Fig 3 the gas in pulse tube is composed of 3 parts: the cold part on the outlet of cold heat exchanger with its boundary x_c , the hot part on the inlet of hot heat exchanger with its boundary x_a and the constant temperature part (x_c-x_a). Under pressure variation dp , the gas element in pulse tube changes its volume adiabatically. The position of hot and cold part can be determined basing on the equilibrium method proposed by Dr. de Boer[5], The method has been developed for this computational investigation.

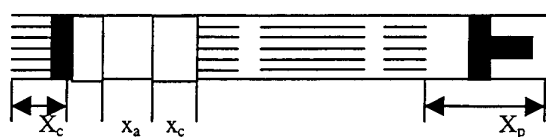


Fig 3 Displacement in PTR system

Among the above mentioned geometric parameters the compressor piston stroke X_p and the virtual plug piston stroke X_c are the two parameters, which influence the motion behavior of buffer gas mostly. Under fixed values of L_R , L_h , L_c , and presumed L_{PT} (taking L_{PT} as the reference for normalization), the influence of finite compressor piston stroke X_p on x_a and x_c can be determined through numerical iteration. The equilibrium of the computation can be checked by three conditions, namely

1. the agreement of the presumed value of L_{PT} with the required length of pulse tube under required value of X_p ;

2. the regression of temperature and pressure profile along cold heat exchanger to its starting state after step 4 for closing the cycle;
3. the conservation of mass in compression space by ensuring the mass balance in step1 (compression) and step2 (displacing).

3. DISCUSSION OF THE RESULT

The computation is carried out with normalized dimensions taking the pulse tube length as reference length. The parameters or the object for this investigation is presented in Table 1.

Table 1 The Dimension of PTR

Dimension \ Name	Pulse-tube	Regenerator	Piston X_p
Diameter(mm)	15	28	60
Length(mm)	146	100	

The influence of compression piston stroke X_p on the cold part of the buffer gas is shown in Fig 4. As shown in the figure, the boundary of cold part x_c is strongly effected by piston stroke X_p . The cold

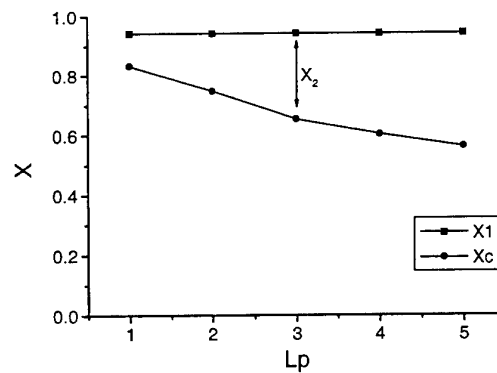


Fig 4 $x_1, x_c \sim X_p$ relation

part consists of two terms, the first is the gas expelled by compression piston during step 1 (the boundary of it is denoted by x_1 in Figure 5), and the second is the gas expelled by the virtual plug piston during step 2 (the boundary of it is denoted by x_2 in Figure 5). The temperature profiles of the gas column are also presented in the same figure. We can find in the figure that x_1 is not depending on X_p , this is naturally, because under other given geometric conditions, x_1 depends solely on pressure ratio r_2 (p_2/p_3), reflecting only the flow coefficient of orifice. About the boundary of the hot part of gas column in pulse tube x_a , the relation with X_p is shown in Fig 6. The relation of its component terms with X_p is also presented here. Component x_3 is caused by step 3, i.e. by the expansion motion of compression piston, while x_4 is caused by step 4, i.e. by the intake of gas by virtual plug piston. The combination of Fig 5 with Fig 6 gives a clear quantified picture of buffer gas oscillation in pulse tube (Fig 7), which is the key mechanism leading to the thermal hysteresis in pulse tube. This, according to the model given by [4], contributes to refrigeration. The required orifice flow for producing this thermal hysteresis is demonstrated by Figure 8 through the interrelation of X_c with pulse tube temperature distribution. Thus, a computational model with compression stroke X_p as given input has developed to demonstrate the result of thermodynamic equilibrium which is reflected pictorially by the length of buffer gas ($x_c - x_a$). Proceeding from thermodynamic viewpoint, buffer gas length should be minimized so as to produce high pressure ratio r_1 , which is the most important factor for good performance of refrigerator. Basing on this consideration, an optimal pulse tube length-compression piston stroke matching can be achieved using this computational model. The work is now in progressing and will be reported later.

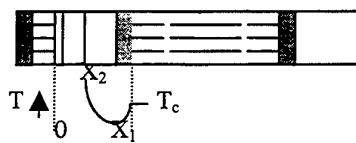


Fig.5 x_1 and x_2 as the boundary of cold par

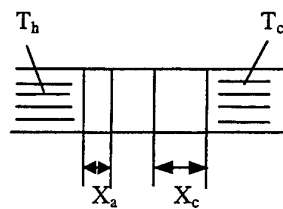


Fig 7 Gas buffer ($x_c - x_a$) in pulse tube

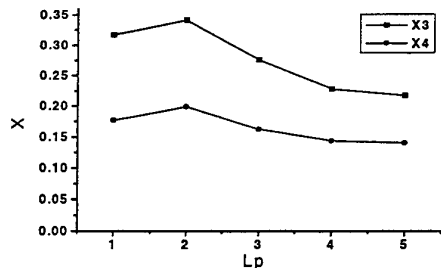


Fig 6 $x_3, x_4 \sim L_p$ relation

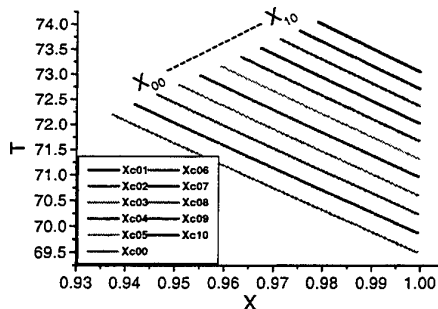


Fig 8 The temperature distribution as orifice flow change in pulse tube

4. CONCLUSION

A computational model has been developed and used successfully for investigating the dependence of gas displacement in pulse tube to compression piston stroke.

ACKNOWLEDGEMENT

The authors are grateful to Dr. de Boer for his very friendly advise.

REFERENCE

1. G.W.Swift, Acoustic recovery of lost power in pulse tube refrigerator, LA-UR-98-2031
2. A.Tominaga, Electronic analog of pulse-tube Refrigerator, Cryogenics (in Japanese), v31, No.5 1996
3. M.Kasuya, Work and heat flow in a pulse tube refrigerator, Cryogenics v31, Sept 1991
4. ML David, Theory of ideal orifice pulse tube refrigerator, Cryogenics, 1993, v33, No.2
5. P. C. T. De Boer, Heat removal in the orifice pulse-tube, Cryogenics, 1998, v38 No.3
6. P. Radebaugh, Pulse tube refrigeration, a new type of cryocooler, J.Appl, Phys(1987)26.v16

EXPERIMENTAL INVESTIGATION OF FRICTION CHARACTERISTICS OF INSTRUMENT BALL BEARINGS IN VACUUM AND AT LHe TEMPERATURES*

X. Z. Li, H. Yang, K. Cheng, Y.W. Liu, Y. Z. Wu

Department of Refrigeration and Cryogenics
Xi'an Jiaotong University, Xi'an 710049, China
Email: xzli@xjtu.edu.cn; Fax: (86-29)-266-8789

H. -D. Denner

Low Temperature Laboratory
Free University Berlin, Arnimallee 14, Berlin, Germany

Keywords: friction, ball bearing, thermal contact, cryogenics

ABSTRACT. The friction performance of precision instrument-size ball bearings at cryogenic temperatures are special important in designing space instruments which are need to be cooled to low temperatures during operation. The friction characteristics of ball bearings can be obtained by measuring the friction heat generated by the bearings. A reliable method for measuring the friction heat in vacuum and at liquid helium (LHe) temperatures is proposed in this paper. The experimental results for a stainless steel ball bearing with different rotating speeds, axial pre-loads and temperatures are presented. The friction heat generated at the bearing sample is found to be proportional to both rotating speed and axial pre-load and to be independent of temperature in the test range.

1. INTRODUCTION

Precision instrument-size ball bearings are widely used in space flight hardware. Their use includes basic spacecraft functions as solar-array drives, recording devices, antenna drive, attitude-control components and so on. For example, space infrared optical systems require bearings for scanning and positioning operations. As a consequence, performance of instrument ball bearings becomes very critical in designing space instruments. The friction characteristics of the bearings in vacuum and at liquid helium (LHe) temperatures is one of the most important cryogenic features for the bearings which are to be used in spaceborne devices being cooled to low temperatures during operation.

The purpose of this investigation was to obtain quantitative data of friction of instrument ball bearings in the vacuum and cryogenic environment analogous to the actual space conditions. The friction characteristics of bearings can be obtained by measuring the friction heat produced at the bearings. A reliable method for measuring the friction heat was put forward in the present work. In vacuum and at LHe temperature, a stainless steel ball bearing was experimental investigated with deferent rotating speeds, axial pre-loads and temperatures. The results are presented and discussed in this paper.

2. MEASUREMENT METHOD

When a ball bearing is rotating, heat will be generated due to friction. Therefore, the friction characteristics of the bearing can be evaluated by measuring the friction heat produced at the bearing. Consequently, a suitable method for measuring friction heat is required. In the present work, we make use of a special arrangement of the ball bearing sample and the unique features of thermal conductance of contact at cryogenic temperatures to carry out measurement of the friction heat.

Fig. 1 shows schematically the arrangement of the ball bearing sample. The bearing sample (4) is mounted in the bearing holder (3) and can only carry a purely axial mechanical load, which corresponds to the bearing's

* Project supported by the National Natural Science Foundation of China

work condition in space. An electric heater is mounted on the copper rod (5) in order to supply the desired heat flux to the sample. The temperatures T_o , T_{ho} of the outer race and the bearing holder are measured by the thermal resistors that are fixed directly on them. The temperature T_o is regarded as the reference temperature during the measurement. An actuating tube (6) connected both with a driving motor in the warm section of the set-up and with the copper rod, is used to transmit the rotating movement and axial pre-load F_a to the bearing sample. By this means, the rotating speed and axial pre-load can be easily varied. The vacuum chamber (1) is immersed into a liquid helium bath to get the desired LHe temperature environment for the sample. A temperature controller was used to adjust and keep reference temperature T_o by controlling the vapor pressure above the liquid helium bath.

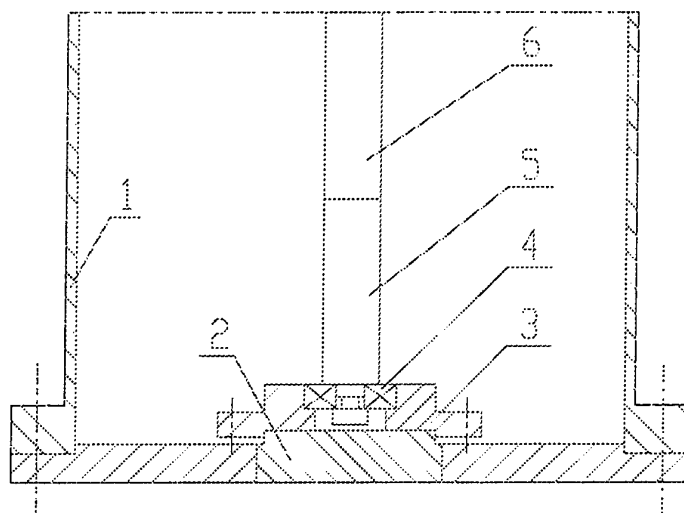


Fig. 1. Arrangement of the ball bearing sample: 1-vacuum chamber; 2-thermal link (copper); 3-bearing holder (copper); 4-ball bearing sample; 5-copper rod; 6-actuating tube.

As shown in Fig. 1, the out race of the bearing sample and the bearing holder compose a thermal contact. By calibrating the thermal conductance of the contact, the total heat flux, Q_{total} , across the contact can be easily determined as:

$$Q_{total} = h \cdot \Delta T \quad (1)$$

where h is thermal conductance, $\Delta T = T_o - T_{ho}$ is temperature difference across the contact. The total heat flux Q_{total} consists of the external heat flux Q_{ex} and the friction heat Q_{fr} . The external heat flux Q_{ex} is the sum of the heating power of the electrical heater and the heat leak due to conduction, which can be calculated. Therefore, the friction heat Q_{fr} can be finally determined as:

$$Q_{fr} = Q_{total} - Q_{ex} \quad (2)$$

3. RESULTS AND DISCUSSION

A dry stainless steel ball bearing (RMB, Biel, Switzerland, miniature bearing RV619-20/30 J613/83) was used as the measuring sample in this work. Its dimensions are as follows: inner diameter 6mm, outer diameter 19mm, ball diameter 3.175mm, and ball number 7.

3.1 Calibration of Thermal Conductance

The thermal conductance of the contact between the outer race and the holder was calibrated at three different temperatures as shown in Fig. 2. The slope of the straight line obtained by the least squares method is just the thermal conductance of the contact (i.e. $h = Q/\Delta T$) at the given reference temperature, while the intercept of the line on the x-axis gives the offset value of the thermal resistor at the same temperature. Fig. 3 displays the

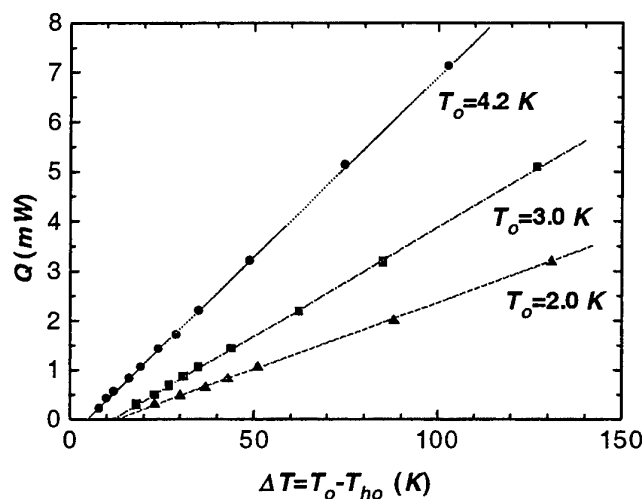


Fig. 2. Measurement of the thermal conductance of the contact between the outer race of the bearing and the bearing holder at various temperatures of the outer race.

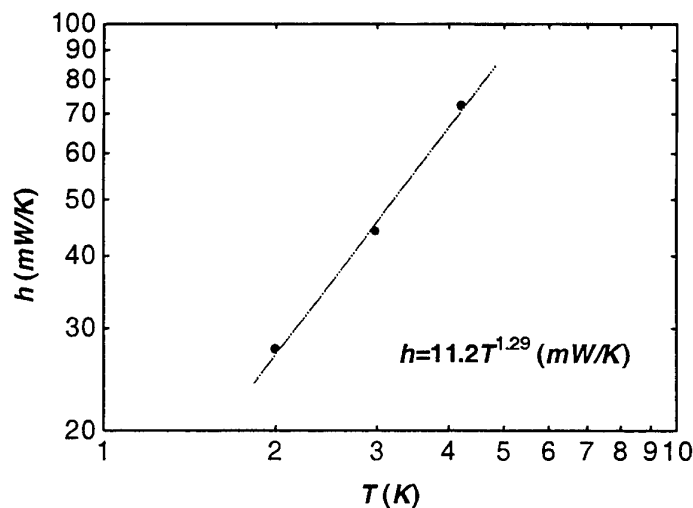


Fig. 3. The calibration result for the thermal conductance of the contact

calibration result. It can be seen from the figure that the result obeys general regularities of thermal contact. The calibrated thermal conductance is a power function of temperature and can be described as:

$$h = 11.2T^{1.29} \quad (3)$$

where h is in mW/K . This result is in reasonable agreement with the conductance values given in reference[1]. Therefore, the calibration results can be reliably used in calculating the total heat flux across the contact and the friction heat generated by bearing samples.

3.2 Results of Friction Heat

The friction heat as a function of the rotating speed n is measured by varying the rotating speed n to the values of 19.3, 38.4, 71.2 and 131rpm, while the reference temperature T_0 and the pre-load F_a are kept constant at $T_0 = 4.2\text{K}$ and $F_a = 18\text{N}$. Fig. 4 displays the friction heat Q_{fr} as a function of the rotating speed n . It can be seen that the friction heat is proportional to the rotating speed as we can expect. Based on the equation $Q_{fr} = \omega M$ (ω is the angular speed of rotation), the friction torque M is evaluated to be about $4 \times 10^{-4}\text{Nm}$ for this specific bearing. This value is of the same order as those given in references [2,3].

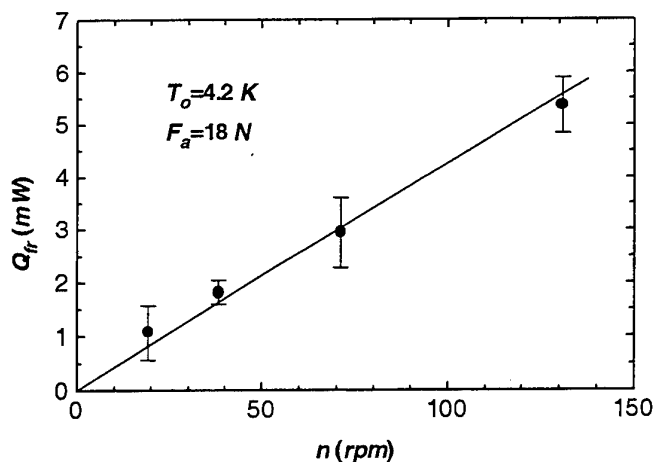


Fig. 4. Friction heat vs. rotating speed

The influence of the axial pre-load F_a on the friction heat is obtained by adjusting F_a to the values 18, 23, 28 and 33N at constant rotating speed $n = 71.2\text{rpm}$ and reference temperature $T_0 = 4.2\text{K}$. Fig. 5 shows the variation of the friction heat with the axial pre-load load. The friction heat is found to be approximately proportional to the mechanical pre-load.

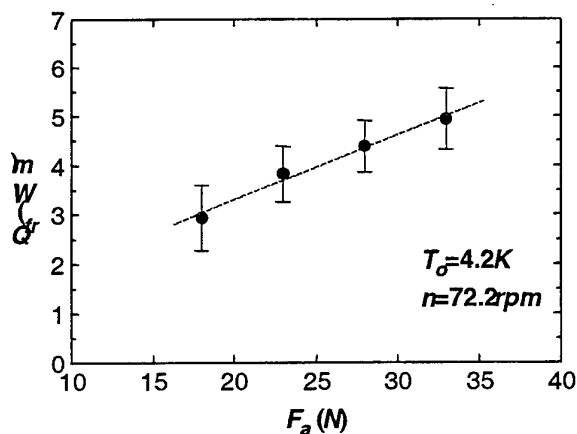


Fig. 5. Friction heat vs. axial mechanical load

The temperature dependence of the dynamic conductance is obtained by adjusting the reference temperature T_0 to 2.0, 3.0 and 4.2K, respectively, with the rotating speed n and the mechanical load F_a kept constant at $T_0 = 4.2\text{K}$ and $F_a = 18\text{N}$. The measuring results are shown in Fig. 6, indicating that within the range of helium temperature, the temperature has no visible influence on the friction heat.

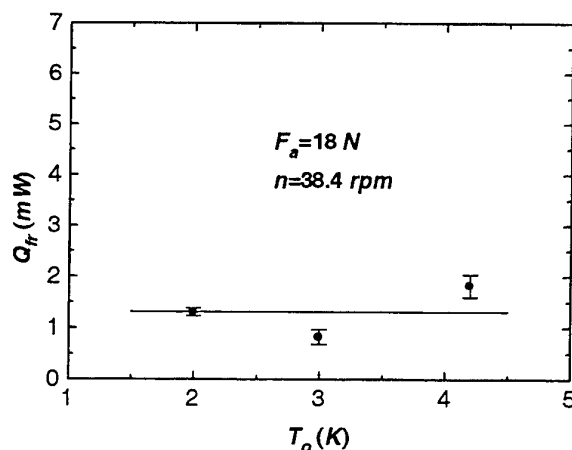


Fig. 6. Friction vs. reference temperature

4. CONCLUSIONS

A unique method for measuring friction heat generated at ball bearings in vacuum and at LHe temperatures is developed and the test shows that it is suitable and reliable in LHe temperature range. A precision instrument-size stainless steel ball bearing was experimentally investigated with different rotating speeds, axial pre-loads and LHe temperatures. The friction heat of the test bearing was found to be proportional to both the rotating speed and the axial pre-load and to be independent of temperature in the test range. The results can be expected to be of great technical interest as basic data for the use of the ball bearing in space cryogenic instruments.

REFERENCES

1. S.W. Van Sciver, M.J. Nilles, and J. Pfothner, Thermal and electrical contact conductance between metals at low temperatures, *Proc. Space Cryogenics Workshop*, Berlin, FRG(1984) 36-48.
2. O.A. Testard, Thermal contact through mechanical moving parts in low thermal budget optical cryogenic assemblies, *Cryogenics* (1987) 27 20-22.
3. K.T. Stevens, and M.T. Todd, Thermal conductance across ball bearings in vacuum, ESA report (1980).

ACTIVE NETWORK MODELING FOR REGENERATOR OF REGENERATIVE CRYOCOOLER

Feng Wu

Faculty of Physics
Wuhan Institute of chemical Technology
Wuhan 430074 P.R. China

Peigang Deng, Xiaohui Deng

Cryogenic Laboratory
Huazhong University of Science and Technology
Wuhan 430074 P.R. China

Keywords: network, regenerator, regenerative cryocooler

ABSTRACT. Basing on the analytical passive network modeling on the flow characteristic of an isothermal regenerator proposed before, an active network modeling for the regenerator with temperature gradient has been established proceeding from the progress of the theory of thermoacoustic refrigerator. The active source term of the modeling has been discussed. The thermally induced acoustic effect occurring in a regenerator with temperature gradient has been experimentally verified on particularly built regenerator experimental set-up.

1. INTRODUCTION

For a long time extensive studies have been conducted in order to provide a thorough understanding of the energy transport and conversion in a cyclic flow regenerator, which is an important part of regenerative heat engine (including prime mover and refrigerator). As a result, numerous technical papers, focusing on various aspects of the regenerator operations have been published in journals and conference proceedings. For regenerator working under pressure oscillation, these papers [1,2] dealing with regenerator as heat exchanger take no account of the effect of momentum conservation imposed by pressure oscillation. They are not able to explain the role of regenerator in the thermodynamic cycle of the regenerative heat engine system. Enlightened by the experimental fact of significant phase shift occurring in the cyclic flow through isothermal regenerator, a two port network with flow resistance, flow inductance and flow capacitance as its components has been proposed to describe the cyclic flow process in an isothermal regenerator. Proceeding from these points, following the progress of thermoacoustics [3-7], active network modeling for describing the thermoacoustic essence of the energy transport and conversion processes in a cyclic flow regenerator has been developed by degree [8-11] and experimentally verified by steps. The combination of thermoacoustic viewpoint with network theory is not only a more convenient tool for engineering consideration but also a way for better system structure analysis. The presented paper gives an overview on this way of network modeling together with its experimental verification and engineering application.

2. QUANTIFICATION OF PASSIVE ELEMENTS FOR PASSIVE NETWORK OF ISOTHERMAL REGENERATOR

According to irreversible thermodynamics, the causality of thermodynamic process may be described by "potential" and "flux". The choice of potential and flux is based on the displacement of the mass element of system, i.e. on the axiom of continuity [12]. Irreversible thermodynamics begins with the analysis on "displacement". Let G be a scalar of a field quantity of an arbitrary tensorial, we have

$$\frac{dG}{dt} = \left(\frac{\partial G}{\partial t} \right)_r + \bar{v} \cdot \nabla G \quad (1)$$

From equation (1) the convective variation $\bar{v} \cdot \nabla G$ due to the displacement of the mass element describes the flux of the field quantity G . It shows that the displacement is a current controllable parameter. The bond diagram [13] of a fluid system with pressure P and volumetric rate J is shown in Fig. 1, where C_F , R_F and L_F are the flow capacity, the flow resistance and the flow induction, respectively. Therefore, irreversible

thermodynamics is the basis of the network theory, which is recently extensively adopted in system dynamics. Thermodynamics and dynamics can be combined by network theory, which is able to describe the energy transportation in diffusion and wave propagation.

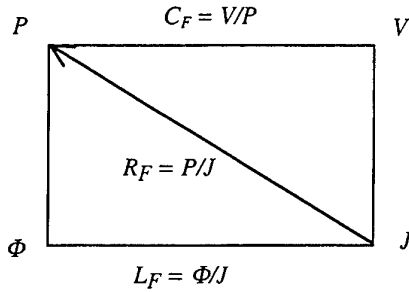


Fig. 1 The bond diagram of a fluid system

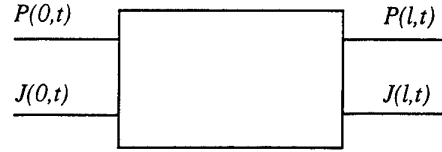


Fig. 2 A two-port network for regenerator

It has been discovered experimentally that the flow process in real regenerator has distinct wave propagation features, [6]. It is assumed that the flow in matrix is one-dimensional, the transfer matrix of cyclic flow in an isothermal regenerator can be found from the revised Darcy's law [6]:

$$\begin{bmatrix} P(l,t) \\ J(l,t) \end{bmatrix} = A \begin{bmatrix} P(0,t) \\ J(0,t) \end{bmatrix} \quad (2)$$

with
$$A = \begin{bmatrix} \text{ch}\lambda l & -Z_c \text{sh}\lambda l \\ -\frac{1}{Z} \text{sh}\lambda l & \text{ch}\lambda l \end{bmatrix}$$

where λ and Z_c denote the propagation coefficient and the characteristic reactance, respectively. Therefore, the cyclic flow in an isothermal regenerator can be treated as a two-port network component as shown in Fig. 2.

It is necessary to quantify the elements of the network for engineering application. The λ and Z_c both relate to the flow viscous resistance number $R_F = \alpha\mu/\pi r_0^2$, the flow inductive reactant number $L_r = \rho/\pi r_0$ and flow capacitance $C_F = \pi r_0^2/\rho R T_0$, where r_0 is the characteristic acoustic dimension of passage in matrix. In order to quantify the network model, the key point to the question is to determine r_0 correctly. For matrix with circular passages, it can be determined by taking the radius of the passage as r_0 . But for noncircular passages, r_0 can no longer be found basing on the premise of circular passage assumption. [14] was devoted to determine the characteristic acoustic dimension of matrix by experimental identification adopting its theoretical relation with the effective propagation velocity of sound within matrix as a model.

$$r_0 = \frac{2kc_1}{\omega} \sqrt{\frac{\mu k}{\omega}} \quad (3)$$

Where k and c_1 denote the wave number and the effective propagation velocity of sound within matrix. The test layout is shown schematically in Fig. 3, it is composed of pressure fluctuation generator, smoothening tube, two transducers and test section.

It is assumed that the length of the test section is L and the propagation time of sound with the matrix is Δt , then the effective sound velocity is

$$c_1 = L/\Delta t \quad (4)$$

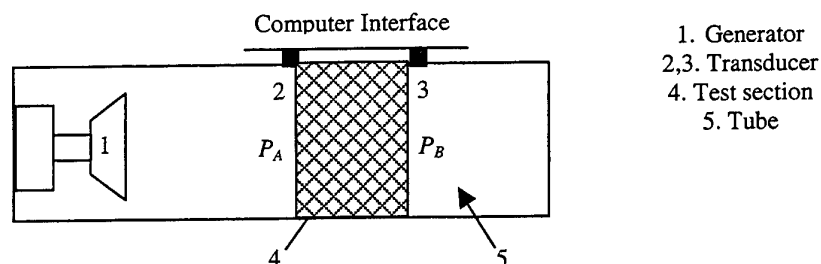


Fig. 3 Schematic of the test section

The propagation time Δt of sound from A to B can be determined by the cross-correlation function between pressure $P_1(t)$ and $P_2(t)$. To take account of the effect of reflection, $P_1(t)$ and $P_2(t)$ may be written as

$$P_1(t) = P_{1i}(t) + P_{1r}(t) \quad (5)$$

$$P_2(t) = P_{2i}(t) + P_{2r}(t) \quad (6)$$

Where i indicates incident wave and r indicates reflected wave. It has been found by analysis that the propagation time Δt of sound is the time corresponding to the first peak value of the cross-correlation function between the signal $P_1(t)$ and $P_2(t)$. While experiment, the computer recorded two transducers simultaneously, thus Δt can be measured. The sound velocity c_l and the characteristic dimension r_0 can be determined by equation (4) and (3). For regenerator with matrix made of 80-mesh phosphor bronze gauze the experimental value of r_0 is 1.156×10^{-4} m in the case with frequency of 19.5 Hz. The method has been verified further in [16].

3. ACTIVE THERMOACOUSTIC NETWORK MODELING FOR REGENERATOR WITH TEMPERATURE GRADIENT

For a real regenerator with longitudinal temperature gradient, longitudinal pressure oscillation propagates along the channels and a transversal oscillation of temperature difference penetrates into the interfacial region between fluid and solid wall of matrix. The passive network for an isothermal regenerator as mentioned above can only describe the sound field of the longitudinal wave, and cannot explain the transversal temperature wave. From the thermoacoustic point of view, in a regenerator the conversion between heat and work is essentially carried out by the coupling of the longitudinal pressure wave with a transversal heat wave via transversal heat diffusion in regenerator. The transversal heat wave (or transverse temperature wave) is modulated by the longitudinal displacement oscillation generated by the pressure wave propagation, [15]. It can be stated that there are two subsystems in a thermoacoustic heat engine system, among them subsystem 1 is related to the acoustic field in the passage of the regenerator which in turn depends on the wave propagation in heat engine system, while subsystem 2 is related to the heat penetration depth near the matrix solid wall. The former generates the acoustic field with required pressure-displacement phase shift depending on the geometrical constraint condition of the flow subsystem, the latter has the characteristic of active source under appropriate condition. The high performance of the regenerator relies on the optimal coupling between these two subsystems.

Starting from the basic conservation equation for an oscillating fluid system with known temperature gradient along with the state equation of fluid, it has been derived, [10], that under given boundary that this non-isotropic oscillation can be described by a transmission line equation with a source term in it:

$$\frac{\partial P}{\partial x} = -ZJ \quad (7)$$

With
$$Z = \frac{j\omega\rho_0}{A(1 - f_\mu)}$$

$$\frac{\partial J}{\partial x} = -YP + \beta J \quad (8)$$

$$\text{With } Y = \frac{j\omega}{\rho_0 C_0^2} [1 + (r-1)\bar{f}_k]$$

$$\beta = \frac{\bar{f}_k^* - \bar{f}_\mu}{(1-\sigma^2)(1-\bar{f}_\mu)} \beta_0 e^{j\theta} \frac{dT_0}{dx} \quad (9)$$

Where P and J indicate the spatial average of the pressure fluctuation and the volumetric flow rate, respectively, \bar{f}_μ denotes the section average of the distribution function, \bar{f}_k denotes the section average of the thermal conduction distribution function. Symbols \bar{f}_μ and \bar{f}_k reflect the geometric dimension of the passage whose scale is of order δ (penetration depth).

The term βJ related to the flux J is a feedback with β being a complicated nonlinear function describing the comprehensive effect of following factors, namely temperature gradient, thermodynamic properties of fluid (isobaric thermal expansion coefficient β_0 and the P_r number σ^2), acoustic field shift and geometric factor of passages. Thus, βJ is a current controllable current source, and β is the source parameter. This coincides with the result of deduction by thermodynamic consideration, since the thermodynamic micro-cycle occurring in the passage with temperature gradient is the result of coupling by the longitudinally propagating pressure wave and the transversal heat wave, which is modulated by the displacement of fluid parcels [15]. The transversal heat wave causes the variation of density of fluid parcels which can be described by thermal expansion coefficient β_0 and $\frac{dT_0}{dx_0}$. This variation in turn results in an increment of volumetric flow rate oscillation. So the transversal

heat wave results in a source of flux increment in acoustic field, i.e. current source. The source βJ and the admittance Y (YP) are in parallel in equation (8). Basing on equation (7) and (8), therefore, the equivalent network of a capillary tube in the K -th matrix is shown in Fig. 4. The active network of regenerator with temperature gradient consists of those networks shown in Fig. 4 connected in parallel and series.

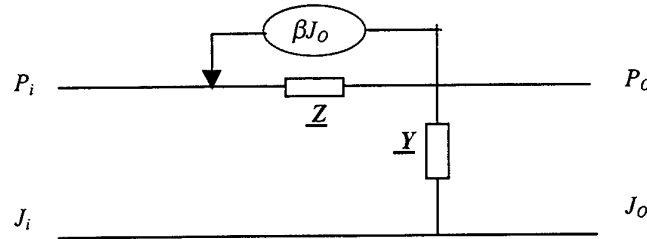


Fig. 4 Active network of a capillary tube with temperature gradient

It has been fixed in network theory, that for active network the impedance matrix of it should be non-positive real, this is naturally from thermodynamic point of view. And it has been proved [10], that behind some threshold value of source parameter β , the network determined by equations (7) and (8) turns to be active, i.e. with a non-positive real impedance matrix. Equation (9) shows that β is a complex function dominated by the angular frequency ω , the characteristic dimension r_0/δ_K , r_0/δ_μ (where δ_K and δ_μ are heat penetration depth and viscous penetration depth, respectively) under given temperature gradient and acoustic field phase shift. The role of characteristic dimension r_0/δ_K and r_0/δ_μ can be expressed through the diffusion relaxation times τ_K , viscous relaxation time τ_μ and acoustic characteristic time τ_a , which are defined as following

$$\tau_K = r_0 / \omega \delta_K \quad (9)$$

$$\tau_\mu = r_0 / \omega \delta_\mu \quad (10)$$

$$\tau_a = 2\pi / \omega \quad (11)$$

The ratio of τ_K and τ_μ is

$$\tau_K / \tau_\mu = \delta_\mu / \delta_K = \sigma^2 \quad (12)$$

In the thermoacoustic network description for regenerator the time τ_K leads by the heat penetration depth and the time τ_a leads by the sound field. According to the above discussion, it may be proved that the source parameter β is a function related to the ratio τ_K / τ_a . Whether a network is an active network can be determined by the coupling of the thermal relaxation time τ_K with the acoustic characteristic time τ_a under certain conditions. The good matching of the τ_K and the τ_a can make the network active. When the active source condition is satisfied, there is the optimum matching of the τ_K with τ_a corresponding to the maximum value of β . It makes the thermoacoustic performance of the regenerator best.

4. EXPERIMENT VERIFICATION ON THE EXISTENCE OF THERMOACOUSTIC SOURCE

The thermally induced acoustic effect occurring in a regenerator with a temperature gradient has been experimentally observed on a particularly built regenerator experimental set-up. A split Stirling cryocooler was retrofitted to be a regenerator setup with adjustable temperature difference imposed on regenerator. The motion of displacer with the tested regenerator is also controllable by a linear motor. The setup is shown schematically in Fig. 5 [11], in which the compressor can be out of operation during regenerator testing. By this way, the regenerator was working only under imposed temperature difference and the motion of displacer reflected the influence of the imposed temperature difference.

The motion of displacer was modeled by following linear oscillation equation [12],

$$M \cdot \ddot{x}_d + C_d \cdot \dot{x}_d + Kx_d = (p_g - p_a)A_{rod} + (p_w - p_c) \cdot (A_m \varepsilon + A_d + A_m) \quad (13)$$

where C_d denotes the damping factor of oscillation, K -rigidity of the spring supporting the displacer, p_w , p_c and p_g -measured in warm, cold and bound spaces, A -the concerned cross-section, known for tested cryocooler,. By means of coherence identification, the damping factor C_d of oscillation can be identified under operation conditions. It has been revealed that with the cold space temperature decreasing from room temperature to 77K, the identified C_d value gradually descended as shown in fig. 8, but turned to be rising abruptly when the cold space temperature was lower then some value. In order to find what has happened in the regenerator with the lowering of cold space temperature, experiments on specially built test layout have been carried out. The result is shown in Fig. 6 and Fig. 7.

When the imposed temperature difference ΔT is small, the amplitude of the pressure wave p_w in warm space is very small compared to p_c in cold space. During the

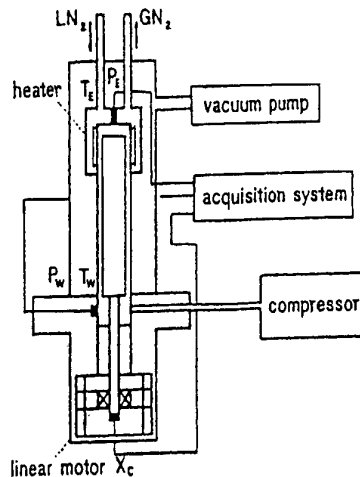


Fig. 5 Schematic of experimental setup

process of the longitudinal temperature difference ΔT changing from 0 to 110K, the phase difference between p_e and p_w reduced slowly from $\approx 90^\circ$ to 60° . Whereas the amplitudes of p_e and p_w obviously increased when ΔT attains the level of 120K, the phase difference between p_e and p_w abruptly turns to be zero and amplitude of p_w reduced. As ΔT continued to increase, the phase difference between p_e and p_w did not change obviously and the amplitude of these two pressure waves rose together.

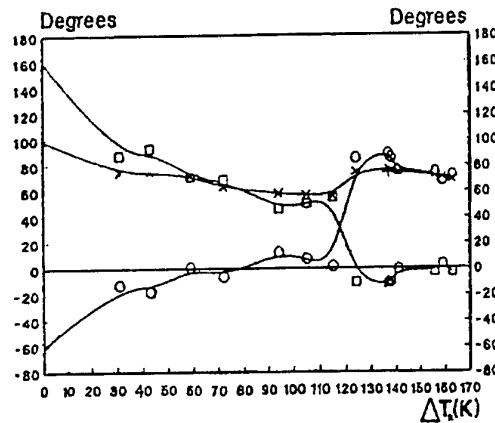


Fig. 6 Phase shift between X_d, P_E and P_W in terms of ΔT_R . $\square, P_E^P_W$; $\circ, P_W^X_d$; $\times, P_E^X_d$

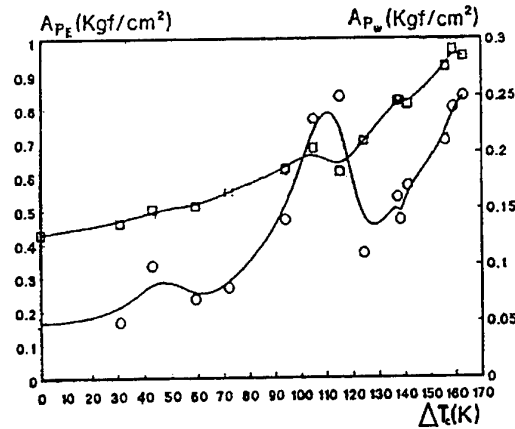


Fig. 7 Amplitude variation of P_E and P_W with ΔT_R . \square, A_{P_E} ; \circ, A_{P_W} (charging pressure = 11.0 Kg cm^{-2})

It has been demonstrated in [11], that the temperature gradient on the regenerator makes the regenerator active behind some threshold value and the regenerator began to generate work, which contributed to pressure amplification under the condition of a positive temperature gradient. The absorbed work was identified by model (10) as an increment of damping factor C_d in Fig. 8. Thus, the singular change of damping can be the evidence of heat to work conversion in regenerator.

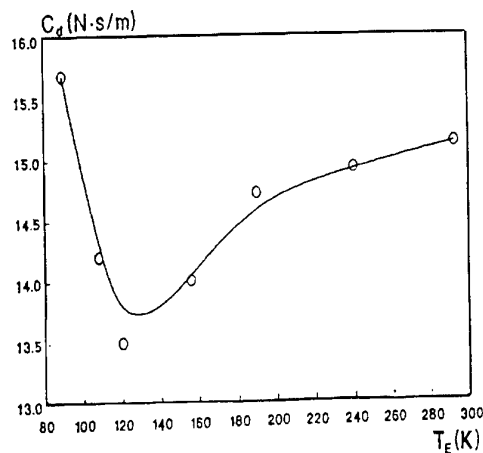


Fig. 8 Changing pattern of C_d with T_E

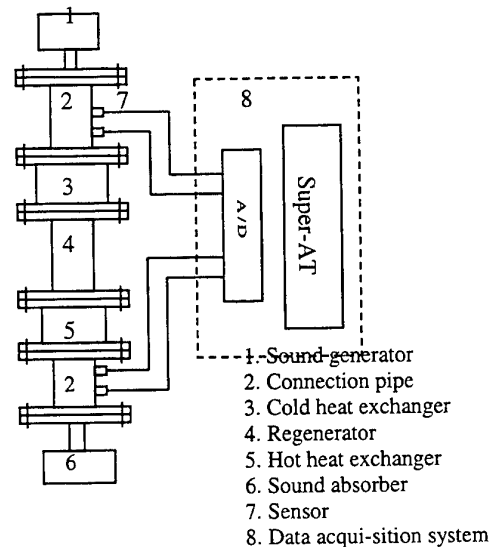


Fig. 9 Schematic of experimental Set-up

In order to verify this effect more directly, another experiment has been carried out [10]. The temperature gradient was maintained by the cold and hot heat exchanger on the ends of regenerator. The schematic of the

testing layout is shown in Fig. 9. The regenerator matrix with diameter in 34 mm, length in 50 or 100 mm, is made of 80 mesh phosphor bronze gauze. An adjustable temperature gradient $\frac{dT_0}{dx}$ (K/m) was exerted between the ends of the regenerator. The inlet and outlet pressure of the regenerator were measured and recorded by transient data acquisition system.

By fast Fourier-transform (FFT) the inlet and outlet pressure wave $P_1(t)$, $P_2(t)$ and $P_3(t)$, $P_4(t)$ can be described as $\tilde{P}_1(j\omega)$, $\tilde{P}_2(j\omega)$ and $\tilde{P}_3(j\omega)$, $\tilde{P}_4(j\omega)$. From this the amplitude ratio R_p of outlet pressure to inlet pressure can be obtained. Since the acoustic energy generated by thermoacoustic effect causes the amplification of pressure wave, so R_p can be used as an index indicating sound power generation.

By means of the transient data treatment mentioned above, the experimental of R_p related to the temperature gradient ($\frac{dT_0}{dx}$) and the frequency f have been obtained, and shown in Table 1, 2, 3.

Table 1 $L = 100\text{mm}$ $P_0 = 350\text{ kPa}$

$\frac{f}{R_p}$ $\frac{dT_0}{dx}$	10	14	18	21	24	29	34	38	43	47	52	61
0	.933	.761	.979	.835	.573	.476	.330	.726	.425	—	.533	.292
369	.909	.859	.694	.704	.713	.903	.751	.316	.533	—	.299	.355
630	—	.852	1.29	.878	.559	.812	.502	.490	.363	—	.361	.432
950	.655	1.00	.911	.956	.770	.593	.672	1.02	.866	—	.762	.487
1200	.933	.692	1.27	.847	.792	.507	.674	1.03	.692	—	.404	—
1550	.871	1.07	.725	.572	.425	.565	.658	.716	.612	.584	.485	.420

Table 2 $L = 50\text{mm}$ $P_0 = 350\text{ kPa}$

$\frac{f}{R_p}$ $\frac{dT_0}{dx}$	16	19	21	24	27	30	32	38	40	43	48	53
0	.980	—	.771	.531	.837	.847	.799	.693	—	.549	.750	.740
600	.939	1.89	1.35	1.74	1.70	1.69	1.44	.642	—	.600	.530	—
900	1.27	1.03	.776	.667	1.14	.974	.718	.775	.447	—	.811	—
1200	1.11	.688	1.28	.567	1.07	1.06	1.01	1.07	—	.990	—	.342
1500	1.15	.954	.909	1.11	—	.873	.878	.710	—	.544	.643	—
1800	1.05	1.03	.727	.442	2.09	.523	.639	.582	—	.464	—	.552
2100	1.02	.913	.884	.747	.890	.795	.834	.814	.720	.762	.916	—

Table 3 $L = 50\text{mm}$ $P_0 = 200\text{ kPa}$

$\frac{f}{R_p}$ $\frac{dT_0}{dx}$	16	19	21	24	27	30	32	38	40	43	48	53
0	—	.950	.920	.960	.541	.453	.810	.661	.716	.408	.369	—
620	1.32	.689	.379	1.65	.953	1.54	.566	.527	—	.569	—	.388
940	.704	.759	.798	.923	1.11	1.04	.743	.892	—	.703	—	.276
1220	.769	.691	.703	.612	2.38	1.08	1.05	.820	—	.490	.734	.442
1550	1.48	1.25	—	1.03	.614	.512	.372	.367	—	.441	.355	.593
1900	1.28	1.32	1.19	.708	.442	1.20	.792	1.08	—	.493	1.13	—
2350	2.07	2.44	2.25	2.16	.909	.864	.880	.715	—	.688	.817	.627

From Table 1, 2 and 3, it can be seen that on certain condition R_p is greater than 1 (the maximum experimental value of R_p is 2.44). It is shown that the regenerator has the capability to generate sound power, i.e. the regenerator is an active source component under appropriate condition. Those condition are controlled by the

source parameter β mentioned above.

5. CONCLUSIONS

- 1) The distributed parameter network model for flow characteristics of cyclic flow in an isothermal regenerator is passive, i.e. the isothermal regenerator has no thermoacoustic effect. The quantification of passive elements for network modeling of isothermal regenerator can be carried out by system identification basing on the experimental results.
- 2) The thermoacoustic network model of the regenerator with temperature gradient has been established basing on the conservative equations and irreversible thermodynamic principles. It is pointed out that the network model of the regenerator with a temperature gradient is active, and the active source component is discussed.
- 3) The thermoacoustic effect occurring in the regenerator with a temperature gradient has been verified experimentally, and the activity of regenerator under pressure oscillation conditions has been shown by experimental results.

REFERENCES

1. J. E. Coppage and A. L. London The periodic flow regenerator-A summary of design theory Trans, ASME Vol. 75, 1953
2. W. M. Koys and A. L. London Compact Heat Exchangers, 1964
3. D. O. Anderson Network Analysis and Synthesis, Prentice-hall, Inc. Englewood cliffs, New Jersey, 1973
4. A. Tominaga Thermodynamic aspects of thermoacoustic theory, Cryogenics, 35 (7), 1995
5. G.W.Swift Thermoacoustic engines, J Acoust Soc Am, 84 (4), 1988
6. F. Z. Guo Flow characteristics of a cyclic flow regenerator, Cryogenics, 1987, Vol. 27, 152-155
7. F.Z.Guo Network model of cyclic flow regenerator for Stirling cryocooler, 1990, Vol. 30, 199-205
8. J. H. Xiao and F. Z. Guo Analytical network on the flow and thermal characteristics of cyclic flow cryogenic regenerator, Cryogenics, 1988, 28
9. J. H. Xiao Thermoacoustic theory for cyclic regenerator, Part 1: fundament, Cryogenics, 1992, 32 (10)
10. X. H. Deng Thermoacoustic essence of regenerator and fundamental theory for design of thermoacoustic engine, PHD Thesis, Huazhong University of Science and Technology, China, 1994
11. Y. Xiang, B. Kuang and F. Z. Guo Parity simulation of thermoacoustic effect in regenerator of Stirling cryocooler, Cryogenics, 1995, 35 (8), 489-494
12. Istvan Gyarmati Non-equilibrium Thermodynamics, Berlin Heidelberg, New York, 1970
13. Y. L. Yao Irreversible Thermodynamics, Science Press, 1980
14. X. H. Deng Experimental identification of acoustic characteristic dimension of regenerator matrix, Cryogenic Engineering (in Chinese), 1993, No.6
15. Q. Li H-matrix Description of the performance of regenerator, Proc. of SEE-2000, Hongkong, 2000
16. B. Zhao Etude acoustique d'un regénérateur utilise dans une machine thermoacoustique, these de doctorat de l'universite Pierre et Marie Curie, 1997

R. Energy and Environment

A GRAND DESIGN OF ENERGY-EFFICIENT ELECTRIC VEHICLE WITH FUEL ECONOMY MORE THAN 100KM/LITER (CUTTING-EDGE TECHNOLOGIES TO MITIGATE URBAN AND GLOBAL WARMING)

Takeo S. Saitoh

Professor of Department of Aeronautics and Space Engineering,
Tohoku University, Sendai 980-8579, Japan
Phone : +81-22-217-6974; Fax : +81-22-217-6975
E-mail : saitoh@cc.mech.tohoku.ac.jp

Daigo Ando

TOYOTA Motor Corporation
1 Toyota-cho, Toyota 471-8571, Japan

Keywords: electric vehicle, energy utilization, urban warming, energy regeneration, energy-efficient vehicle

ABSTRACT. In this study, the authors concluded that a super energy-efficient vehicle (SEEV) with fuel economy more than 100km/liter could be possible with the present technology level. The new environmentally-compatible vehicle was designed to mitigate urban warming, air pollution and CO₂ emissions in the urban area. The authors evaluated optimal specifications of the new concept energy-efficient electric vehicle (EV) equipped with flywheel and photovoltaic (PV) cell and also reported the results of the running simulations for the proposed vehicle. The proposed SEEV will be very promising to mitigate urban and global warming, and to conserve fossil fuel consumption.

1. INTRODUCTION

Urban environment in mega-cities like Tokyo is getting worse and worse. For example, the concentration of NO₂ is still increasing and has risen gradually above the regulated level in Tokyo metropolitan area. The cause of aggravation in the urban environment can be mainly attributed to the increase of automobiles in this area. Another serious environmental issue is "urban warming (i.e. heat island)", which is caused by concentrated consumption of energy in the urban area.

In order to resolve the problems caused by the conventional vehicles which depend mostly on fossil fuels, we proposed an energy-efficient electric vehicle (SEEV), which runs about ten times more efficient than the conventional fossil fuel powered vehicles. According to our detailed computer simulations, principal factors which influence the vehicle performance are found to be (i) curb weight, (ii) aerodynamic design, (iii) regenerating system, (iv) utilization of photovoltaic cell, (v) energy source (for ex. night time electricity) and (vi) energy efficiency of drive system.

The similar project in line with this has been done at Hypercar Center of Rocky Mountain Institute [1]. They have been aiming at developing a conceptual car "Hyper car" with fuel economy about 60 km/liter. The electric power consumption rate was clarified via computer simulation under various running conditions, including community, and long-distance modes. We concluded that a super energy-efficient vehicle with fuel economy more than 100km/liter could be possible with the present technology level.

In this article, the new environmentally compatible vehicle was designed to mitigate urban warming, air pollution and CO₂ emissions in the urban area. Principal specifications for an optimal design will be clarified. We evaluated optimal specifications of the new concept energy-efficient EV equipped with flywheel and photovoltaic (PV) cell and also reported the results of the running simulations of the proposed vehicle. The proposed SEEV will be very promising in mitigating urban and global warming.

2. PROPOSAL OF ENVIRONMENTALLY-COMPATIBLE VEHICLE (SEEV)

In most cities, a great number of automobiles are in operation. For example, there are about 2,500,000 fleets

including passenger cars and trucks in Tokyo metropolitan area. Air polluting emissions (CO_2 , NO_x , SO_x , and CO etc.) exhausted from the automobiles are steadily increasing in the urban area. Further, it is considered that the increase in the CO_2 emissions has become one of the causes (20% in Japan) for the urban warming. Therefore, the Electric Vehicles (EVs) emitting no CO_2 , NO_x , and SO_x gases in the urban area are needed.

In this section, we will evaluate optimal specifications of the new concept hybrid EV equipped with flywheel and photovoltaic (PV) cell. We will also report the results of the running simulation of the proposed SEEV.

3. OPTIMAL DESIGN OF THE SEEV

Principal specifications of the SEEV are shown in Table 1 and a conceptual sketch is shown in Figure 1. These values are evaluated by considering the current specifications of each component.

Table 1 Optimal Specifications of Urban Friendly Vehicle

Weight (battery and driver are included)	[kg]	700
Drag coefficient		0.15
Frontal projected area	[m ²]	1.8
Coefficient of rolling resistance		0.005
Efficiency of fossil fuel powered engine *	[%]	35.7
Mechanical efficiency	[%]	63.6
Generating efficiency	[%]	66.7
Efficiency of motor	[%]	90
Charging/Discharging efficiency	[%]	90
Module efficiency of PV cell	[%]	16
Battery weight (Li-ion)	[kg]	100
Area of PV cell in running	[m ²]	1.8
Area of PV cell in parking		5.0

*Data with TOYOTA Prius

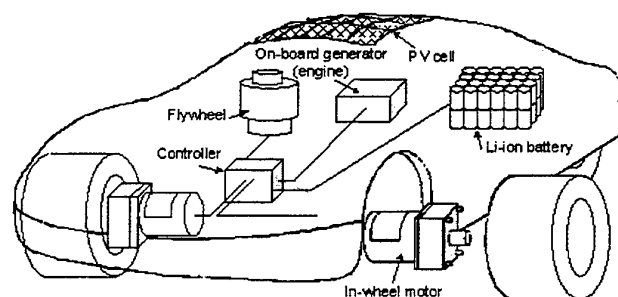


Fig. 1 Imaginary sketch of system of the SEEV

Figure 2 shows a comparison of power density and energy density of the flywheel, capacitor and batteries. Li-ion battery has the highest energy density among chemical batteries. On the other hand, the energy density of the flywheel (CFRP) is three times as high as Pb battery, which has been frequently used for the automobiles. The most noticeable feature of the flywheel is that it has a very fast charging rate compared with the conventional chemical batteries. It can restore more than 70 % of the total kinetic energy, while the other batteries can restore only about 10 %. If the flywheel (CFRP) were employed in the SEEV, it is expected that the weight of the battery can be reduced considerably.

For this reason, we consider the flywheel (CFRP) as one of the promising energy regenerating devices and confirm the validity of flywheel regenerative system for running experiment. Another energy source that is clean and environment-friendly energy is solar energy. PV cells were placed on the roof of the vehicle as shown in Fig.1. When ever the vehicle is parked, the area of PV module can be extended to collect as much energy as possible.

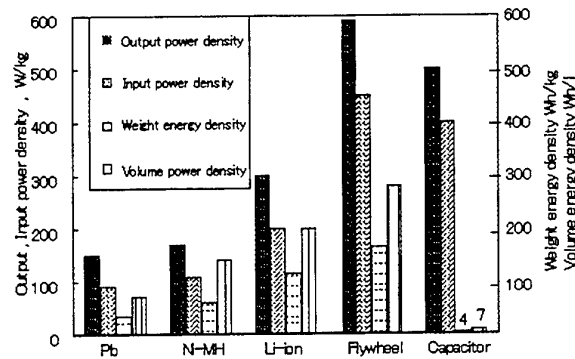


Fig. 2 Comparison of power and energy density of various batteries, flywheel, and capacitor

4. RUNNING SIMULATIONS

In running simulations of the SEEV, three running modes are selected; one is community drive mode; others are two long drive modes. The running simulations will indicate the availability of the energy regeneration and comparison of performance of SEEVs.

Definition Of Community Drive Mode, Long Drive Mode And Actual Drive Mode

Community drive mode. In order to validate the effectiveness of the flywheel and PV cell, the running simulations for daily use of the SEEV were performed by using the urban drive mode. In the urban area, there are many traffic signals, curves and up-and-down slopes. The Japanese test-driving mode (10 - 15 mode) shown in Figure 3 was employed as an urban drive mode. This mode has been developed for testing an actual running mode in the urban area and includes decelerating, accelerating, and stopping patterns.

Two driving periods are scheduled at the worker's commuter time in the morning and evening hours. During daytime, it is assumed that the SEEV is parked at a sunny place and is charged by the PV panel.

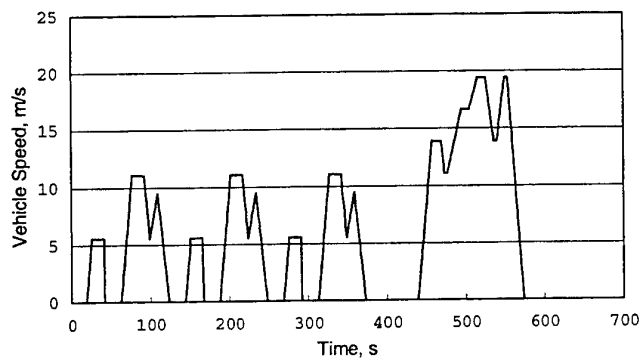


Fig. 3 Schedule of the community-drive mode (Japanese 10 - 15 mode)

Two driving periods are scheduled at the worker's commuter time in the morning and evening hours. During daytime, it is assumed that the UFV is parked at the sunny place and is charged by the PV panel.

Long drive mode. Time schedules of the long drive modes are shown in Figure 4. Long-drive modes consist of the long drive mode 1 (100km) and the long-drive mode2 (300km). Long drive mode 1 assumes that the SEEV runs only with battery. Long drive mode 2 assumes that the SEEV runs only with battery until 100km point. After this point, the SEEV is operated with the gasoline engine.

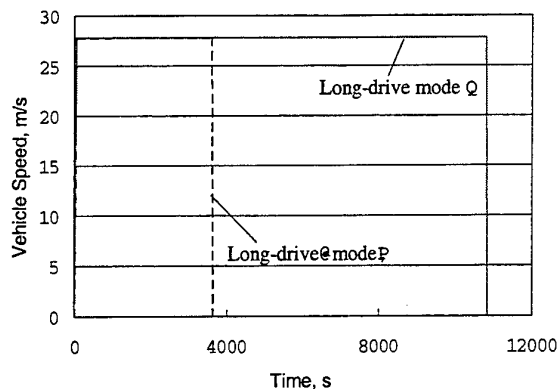


Fig. 4 Schedule of the long drive modes

Actual drive mode. In order to compare the actual drive mode and other drive modes (the community- and long-drive modes), a practical route was set in Sendai city area as shown in Figure 5. The total length is 11.4km. The actual average fuel consumption rate for this route was 13.8km/liter using a 1500cc gasoline powered passenger vehicle. The data will be used later for a comparison.

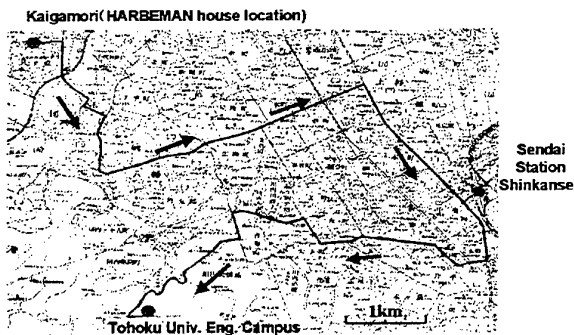


Fig. 5 Practical route (Sendai city)

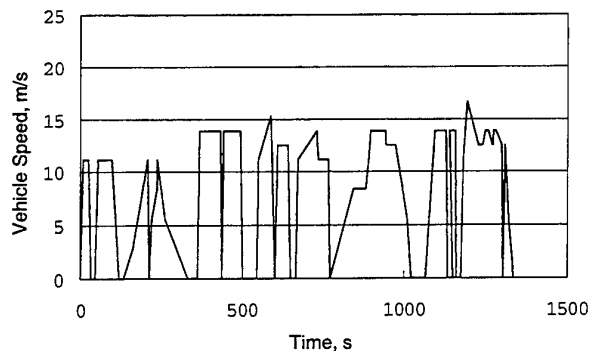


Fig. 6 Time variation of the actual drive mode

Result Of Running Simulation

Tables 2 and 3 show the simulation results for a community-drive mode and two long-drive modes with variations in PV cell area. From Table 3, we can expect unlimited mileage for the community-drive and the long-drive modes if we extend the area of PV cell installation.

Table 2 Comparison Among Various Drive Modes in Case of PV Cell Area of 1.8m²

Operation Fuel Consumption Rate and Transport Cost	Fuel Consumption Rate [km / liter]	Transport Cost [J / m ² kg]
Drive mode		
Community-drive mode*	188	0.09
Long-drive mode 1	65.8	0.24
Long-drive mode 2	54.3	0.29

*Japanese community drive mode (10 - 15 mode)

Daily driving distance in Japan : 20km/day.

Table 3 Comparison Among Various Drive Modes in Case of PV Cell Area of 5.0m²

Operation Fuel Consumption Rate and Transport Cost	Fuel Consumption Rate [km / liter]	Transport Cost [J / m ² kg]
Drive mode		
Community-drive mode*	Unlimited	0
Long-drive mode 1	unlimited	0
Long-drive mode 2	73.5	0.22

*Japanese community drive mode (10 - 15 mode)

Daily driving distance in Japan : 20 km/day.

Table 4 Results of Actual Drive Simulation (Summer)

Place	Sendai City		
Time and Weather condition	1994 7/4 sunny	1994 7/10 rainy	1994 7 average
Altitude difference, m	110.0	110.0	110.0
Distance, km	22.8	22.8	22.8
Consumed energy, kJ	4860	4860	4860
Consumed energy for heating and air conditioning, kJ	850.2	850.2	850.2
Regenerated energy, kJ	1457.6	1457.6	1457.6
Photovoltaic energy, kJ	6164.4	396.4	3682.6
Total energy, kJ	-1911.9	3856.2	570.0
Fuel Consumption Rate, km/l	-	65.7	444.6

For the long-drive mode, regeneration by flywheel is not considered since no regenerating break is available. These simulations show that the SEEV equipped with the flywheel and the PV cell has a high performance. As mentioned earlier in this article, the most important feature of the SEEV is apparently to be "zero emission vehicle", that is the vehicle does not produce pollutant gas emissions, and heat emissions in the urban area.

Table 5 Results of Actual Drive Simulation (Winter)

Place	Sendai City		
Time and Weather Condition	1994 1/2 sunny	1994 1/3 rainy	1994 1 average
Altitude difference, m	110.0	110.0	110.0
Distance, km	22.8	22.8	22.8
Consumed energy, kJ	4860	4860	4860
Consumed energy for heating and air conditioner, kJ	543.2	543.2	543.2
Regenerated energy, kJ	1457.6	1457.6	1457.6
Photovoltaic energy, kJ	2145.8	604.2	1796.0
Total energy, kJ	1799.8	3341.4	2149.5
Fuel Consumption Rate	140.8	75.8	117.9

Table 6 Improving Factors(%) in Future Electric Vehicle(SEEV)

Existing Hybrid Vehicle (PRIUS)	Commercially Available Electricity	PV Cell	Curb Weight	Aerodynamic Design (CdA)	Total
200	170	150	200	140	1430

Remarks (1) Japanese community-drive mode (10 - 15 mode)
 (2) Daily running distance: 20km
 (3) Electricity conversion efficiency at power plant: 40%
 (4) C_d : drag coefficient A: frontal area
 (5) "PRIUS" is Toyota's hybrid vehicle, which was put in Japanese market in December, 1997.

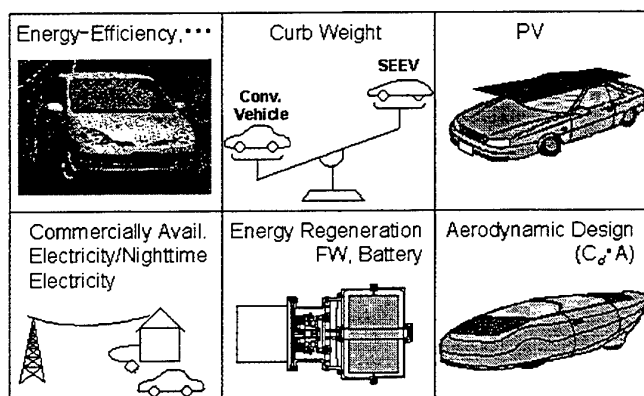


Fig. 7 Six improving factors for 100km/liter EV

Tables 4, and 5 show the simulation results for actual drive mode under various weather conditions. On a sunny summer day, energy produced by PV cells exceed the total consumed energy, thereby making it possible to run only with energy by PV cell. While, in rainy or winter days, energy produced by PV cells is not sufficient to run the vehicle without assistance from other energies. Fuel consumption rates are also shown in the lowest column in Tables 4 and 5.

Finally, in Table 6 (also see Fig. 7), improving factors (percent) for the ideal future vehicle are tabulated. For example, fuel consumption rate of existing hybrid vehicle (PRIUS) is twice (200%) the conventional gasoline powered vehicle with the same as efficient as curb weight and engine capacity.

5. CONCLUSION

In this article, the new environmentally compatible vehicle (SEEV) was designed and proposed to reduce urban warming, air pollution and CO₂ emissions in the urban area. Principal specifications of the SEEV were clarified. The following conclusions may be drawn from the present study.

1. By employing the flywheel system as energy regeneration and PV cells to gain solar energy, the electric power consumption of the SEEV can be reduced significantly in urban drive mode and the long-drive modes. Annual mean fuel consumption rate for the proposed SEEV will be at least ten times as efficient as the conventional fossil fueled vehicles.
2. The most important concept of the SEEV is "zero emission" in the urban area. In this respect, the SEEV is promising in the future urban traffic mode.
3. The proposed SEEV will be very promising to mitigate urban warming, global warming, and to conserve fossil fuel consumption.

REFERENCES

1. C.T. Moore, "Ultralight Hybrid Vehicles : Principles and Design", Proc. of EVS-13 Session 5A, 1996
2. J.G. Bitterly, Flywheel Technology Past, Present, and 21st Century Projections, *Proc. of IECEC*, pp.2312-2315, 1997.
3. TOYOTA Motor Corporation, Toyota Hybrid System, press information, 1997.
4. T. S. Saitoh and N. Yamada, "3-D Simulation of Urban Warming in Tokyo and Proposal of Air-cooled City Project", Proc. of ASME-JSME Joint Thermal Engineering Conference (1999).

IMPROVED MODELING OF URBAN WARMING AND NUMERICAL PROJECTION TO FUTURE URBAN ENVIRONMENT IN TOKYO

Takeo S. Saitoh

Professor of Department of Aeronautics and Space Engineering,
Tohoku University, Sendai 980-8579, Japan
Phone : +81-22-217-6974; Fax : +81-22-217-6975
E-mail : saitoh@cc.mech.tohoku.ac.jp

Noboru Yamada

Graduate student in Doctoral Course, Graduate School of Aeronautics
and Space Engineering, Tohoku University, Sendai 980-8579, Japan

Keywords: urban warming, urban heat island, microscopic modeling, porous media

ABSTRACT. This paper describes a microscopic modeling for urban surface layer, where a lot of various structures (i.e. building, bridge, pavement, and other facilities) exist. The authors found out a structural similarity between urban structure and porous media. Flow model and method of analysis in porous media were applied to the microscopic modeling for urban surface layer. First, 2-D numerical study and experimental verification were conducted on unsteady natural convection. Resultant model will be used for more precise 3-D computer simulation of urban warming and urban planning.

1. INTRODUCTION

In most cities, it is becoming evident that increase in energy consumption is causing environmental issues, including temperature rise in the urban atmosphere (urban warming or urban heat island), and air pollution. Recent computer projection of urban warming in Tokyo metropolitan area to the year 2030 indicated that the urban ambient temperature near Otemachi, heart of Tokyo, will exceed 43 degree Celsius (110 degree Fahrenheit) at 6 p.m. in the summer.

Horizontal scale of the urban warming in a huge city like Tokyo is about 50 ~ 100 km. In order to simulate such a large-scale problem by a numerical method, microscopic phenomena in the urban surface layer have been generally incorporated by a simplified modeling. For example, the effect of urban building structures has been considered by employing a roughness parameter in many past studies. This approach seems to be appropriate as long as we analyze large-scale phenomena. However, if we need to analyze small-scale or micro-scale phenomena, which are strongly influenced by building structures, existing coarse modeling and estimation employing such a roughness parameter are no longer valid. The most precise method should include the fine adaptive mesh division for accounting the shape of every building for accounting for configuration of buildings. However, it requires tremendous CPU time and is difficult to solve because there exist so many buildings even if a small-scale approach were adapted. Therefore, a new microscopic modeling, which reduces time and effort for the precise simulation, is required to accomplish the numerical analysis for the urban surface layer.

In the present study, a new microscopic modeling will be presented and 2-D numerical study and experimental verification for the urban surface layer was conducted. Validation of the proposed model was performed through a comparison between 2-D porous model and the experiment. However, the results of the experiment were omitted in this paper. Resultant model was used for the 3-D computer simulations of urban warming in Tokyo metropolitan area ca. 2030.

2. MODELING OF URBAN SURFACE LAYER

Similarity Between Urban Structure and Porous Media

Figure 1 shows three samples of actual urban structures (1 km \times 1 km) in the horizontal direction in Tokyo metropolitan area. From these samples, it is evident that various gaps formed by the arrangement of buildings and roads are complicatedly connected in the urban surface layer. There is a good similarity between urban structures and porous media as shown in Fig. 1. Actually, the definition of porous media could be appropriate for the urban structure. Therefore, it seems reasonable to assume a similarity between the urban structures and

the porous media. In this study, numerical modeling was founded on this assumption. In urban structures, structural characteristics varies according to the land-use in each area as shown in Fig. 1.

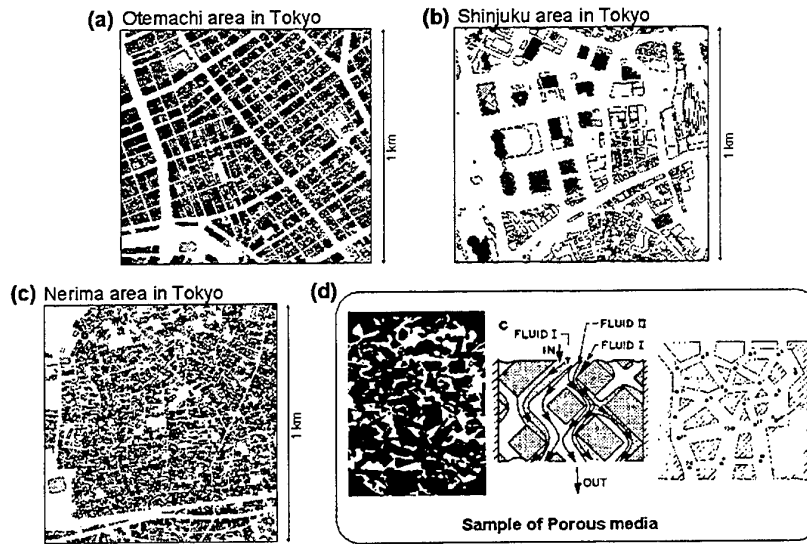


Fig.1 Samples of actual urban structure (Horizontal) (a), (b), (c): and porous media (d)

2-D Numerical Modeling

Due to a similarity between the urban structures and the porous media, model of "flow in porous media" has been developed in the field of Heat Transfer is applied to the modeling of the urban surface layer. In this modeling, the following points are incorporated:

1. Porosity in the urban surface layer has a spatial distribution. In the vertical direction, it increases in proportion to altitude, and it becomes unity in the edge of the urban structure.
2. Permeability in the vertical direction is much larger than that in the horizontal direction.
3. Flow is turbulent.

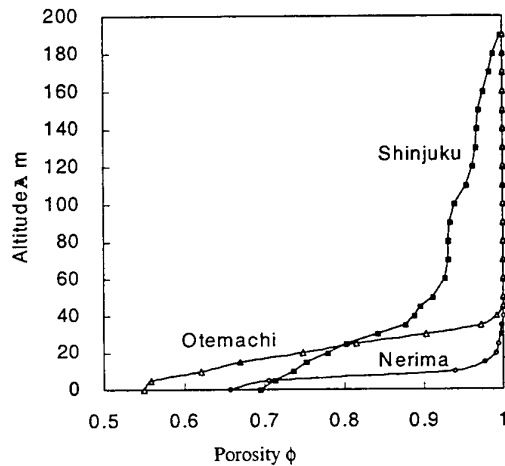


Fig. 2 Vertical profiles of porosity in Tokyo

Table 1 Conditions for the present simulation

Horizontal scale, x	2 km
Height of planetary boundary layer, z	2 km
High wall temperature, T_H	40 °C
Low wall temperature, T_C	20 °C
Temperature of the heated surface, T_S	30 °C
Temperature of the building surface, T_B	30 °C
Specific humidity	0.015
Concentration of CO_2	365 ppmv

Figure 2 shows vertical profiles of porosity ϕ in Tokyo metropolitan area. In order to obtain these profiles, the latest data of geographic information systems (GIS) provided by Tokyo Metropolitan Government were used. Three areas were selected for the present analysis. Otemachi is located at the heart of Tokyo. There exist a lot of

office buildings in this area. Shinjuku is a relatively new city center and there exist many skyscrapers. Nerima is a residential area located in suburban area.

In this study, the urban warming is simplified as a natural convection in stably stratified layer. First, validity of the numerical modeling is verified by performing 2-D computer simulations. In the present simulations, the effect of the urban structure is considered as a porous media over the heated surface. Figure 3 shows a simulation model, boundary conditions and initial temperature distribution. 50×50 grids were used for numerical computation.

The governing equations are basically the same as those of flow in porous media. Although validity of the turbulence model for flow through porous media has been argued and not well established yet, turbulent model proposed by Takatsu and Masuoka (1996) was used here in the present simulations. According to their turbulent model, in the process of deriving the governing equations by using the local volume-averaging technique, they consider the eddy viscosity (thermal conductivity) as the algebraic sum of the eddy viscosities (thermal conductivities) estimated from two types of vortices: (i) interstitial vortices of the order of the thickness of the gap width, which develop in micro-boundary layers between particles, and (ii) pseudo vortices of the order of the particle diameter, which reflect the forced distortion of flow due to interruption of the solid particles. The vorticity and velocity vectors were introduced to transform the 2-D Navier-Stokes and equation of continuity into a simple equation system without pressure term. The governing equations for volume-averaging values can be written under the Boussinesq approximation as follows.

Vorticity equations;

$$\begin{aligned} \frac{\partial \omega}{\partial t} + u \frac{\partial \omega}{\partial x} + w \frac{\partial \omega}{\partial z} = & \frac{\partial}{\partial x} \left(v_x \frac{\partial \omega}{\partial x} \right) + \frac{\partial}{\partial z} \left(v_z \frac{\partial \omega}{\partial z} \right) \\ & + \frac{\partial}{\partial x} \left(\frac{\partial v_x}{\partial x} \frac{\partial w}{\partial x} - \frac{\partial v_x}{\partial z} \frac{\partial u}{\partial x} \right) + \frac{\partial}{\partial z} \left(\frac{\partial v_z}{\partial x} \frac{\partial w}{\partial z} - \frac{\partial v_z}{\partial z} \frac{\partial u}{\partial z} \right) \\ & + \frac{\partial}{\partial z} \left(\phi \frac{\sigma v_{x,v}}{K_x} u \right) - \frac{\partial}{\partial x} \left(\phi \frac{\sigma v_{z,v}}{K_z} w \right) + Gr \frac{\partial T}{\partial x} \end{aligned} \quad (1)$$

Energy equations;

$$\begin{aligned} \frac{\partial T}{\partial t} + u \frac{\partial T}{\partial x} + w \frac{\partial T}{\partial z} = & \frac{\partial}{\partial x} \left(\kappa_x \frac{\partial T}{\partial x} \right) + \frac{\partial}{\partial z} \left(\kappa_z \frac{\partial T}{\partial z} \right) \\ & + \frac{1}{\rho C_p} \frac{S_B}{V_f} \left\{ h_z (T_B - T) + \epsilon \sigma_{stb} (T_B^4 - T^4) \right\} \end{aligned} \quad (2)$$

Equations of relationship between vorticity and velocity;

$$\frac{\partial^2 u}{\partial x^2} + \frac{\partial^2 u}{\partial z^2} = \frac{\partial \omega}{\partial z} \cdot \frac{\partial^2 w}{\partial x^2} + \frac{\partial^2 w}{\partial z^2} = \frac{\partial \omega}{\partial x} \quad (3)$$

In the Eq. (1), the fifth and sixth terms on the right-hand side are reduction terms, which are caused by the interstitial vortices. The coefficient of revision σ is assumed to be unity. In the Eq. (2), the third term on the right-hand side represents thermal radiation and heat transfer from the surface of the solid (i.e. urban structures). Local heat transfer coefficient h_z for the uniform wall temperature and band model for absorptivity ϵ of the concentration of CO₂ and H₂O were employed. S_B and V_f represent total surface area of buildings and total volume of gaps, respectively. σ_{stb} is Stefan-Boltzmann constant. Eddy diffusivities for momentum and heat were assumed to be 100 m²/s in the horizontal direction and 10 m²/s in the vertical direction. Furthermore, the interstitial diffusivity is assumed to be 1/10th of the pseudo diffusivity. Permeability K is generally expressed by the next equation.

$$K = c \frac{\phi^3}{(1-\phi)^2} d^2 \quad (4)$$

However, the order of nondimensional coefficient c , which is appropriate for the urban structure, is unknown. In this study, the order of the permeability c was varied and the results verified. d represents diameter of the particle which constructs porous media and was assumed to be 10 m.

2-D Simulation Results

Table 1 shows conditions and numerical values used for the present simulation. Simulation results were obtained until real time equals to 2 hours. Figure 4 shows the simulation results without urban structure (i.e. porous media). Figure 5, 6, 7, and 8 show the results when the permeability c and the height of urban structure H_p are varied. In all results, buoyancy plumes appear over the heated surface. Comparing these results with other ones, it is clear that the urban structures decrease the height of the convection and increases the ambient temperature. If we compare three results (Fig. 4., Fig. 5, and Fig. 6), we can see that the height of convection is inversely proportional to the permeability K . Furthermore, if we further compare the four results (Fig. 4, Fig. 6, Fig. 7, and Fig. 8), we can recognize that the height of convection is proportional to the height of urban structure. These phenomena can be ascribed to the effect of fifth and sixth terms in Eq. (1). The ambient temperature rise in the lower layer is strongly affected by the convection pattern. In addition, radiation and heat transfer from the surface of the urban structure cause the ambient temperature rise.

Finer Modeling and Simulation Results

The authors made the finer modeling than shown earlier and conducted simulation by using the above-mentioned model. Figure 9 shows a simulation model and boundary conditions. Conditions and numerical values for this simulation are the same as in Table 1. 100×100 grids were used for numerical computation. Figure 10 shows simulation results without urban structure. On the other hand, Figure 11 shows simulation results with urban structure. Here, it must be noted that the resultant figures are enlarged in the vertical direction and reference vectors are not equal in size. As compared with Fig. 10, isotherms and velocity vectors in Fig. 11 are quite different. The height of the convection in Fig. 11 is less than about 300 m, while in contrast, it is about 1 km in Fig. 10. Cells of the convection clearly appeared in Fig. 11. These cells strongly affect the ambient temperature increase. As a result, temperature increase over the urban structure amounts to more than 5 °C.

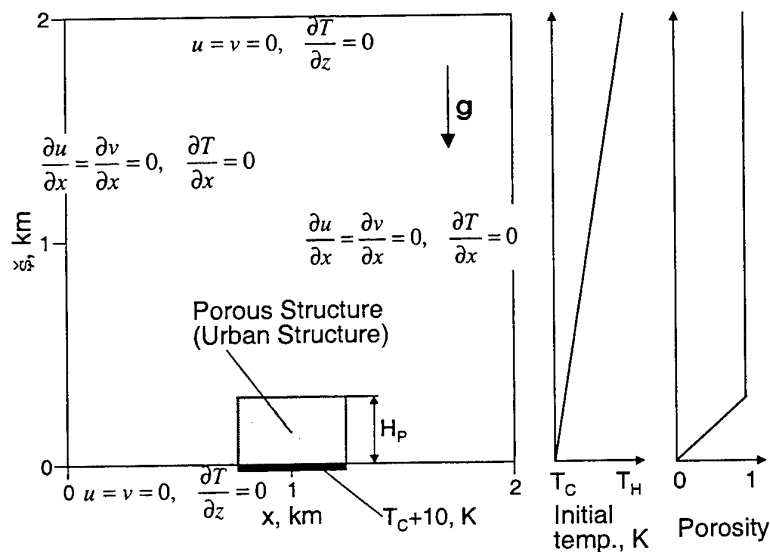


Fig. 3 2-D simulation model and boundary conditions

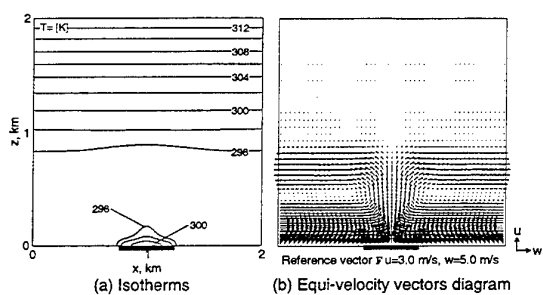


Fig. 4 Isotherms and velocity vectors
(without urban structure)

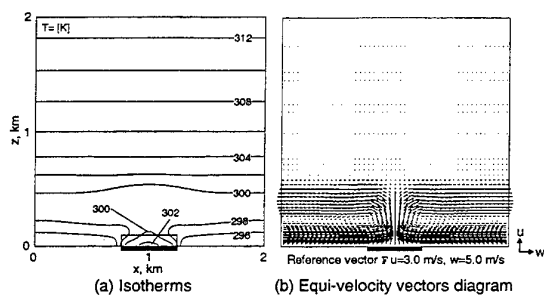


Fig. 5 Isotherms and velocity vectors
($c=100, H_p=100 \text{ m}$)

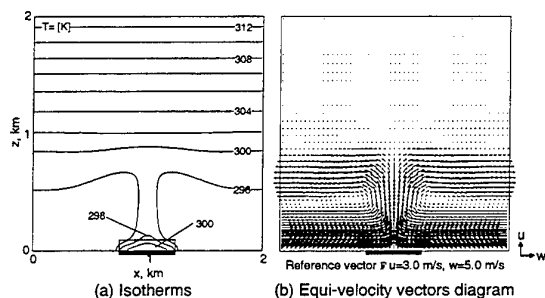


Fig. 6 Isotherms and velocity vectors
($c=1000, H_p=100 \text{ m}$)

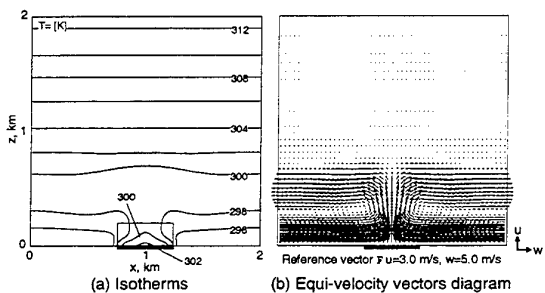


Fig. 7 Isotherms and velocity vectors
($c=1000, H_p=200 \text{ m}$)

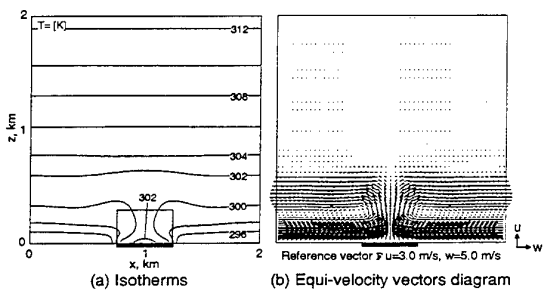


Fig. 8 Isotherms and velocity vectors
($c=1000, H_p=300 \text{ m}$)

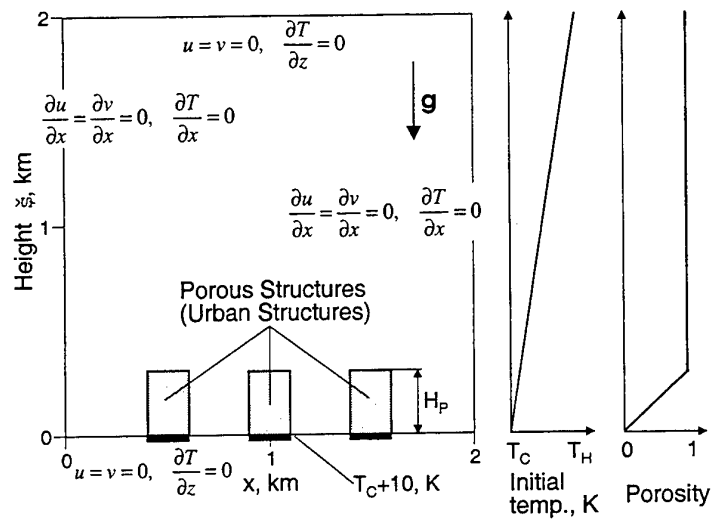


Fig. 9 2-D simulation model and boundary conditions

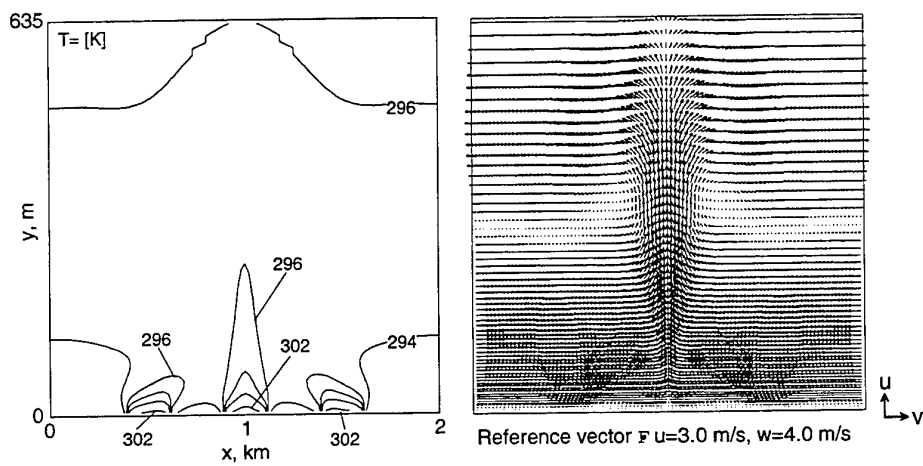


Fig. 10 Isotherms and velocity vectors (without urban structures)

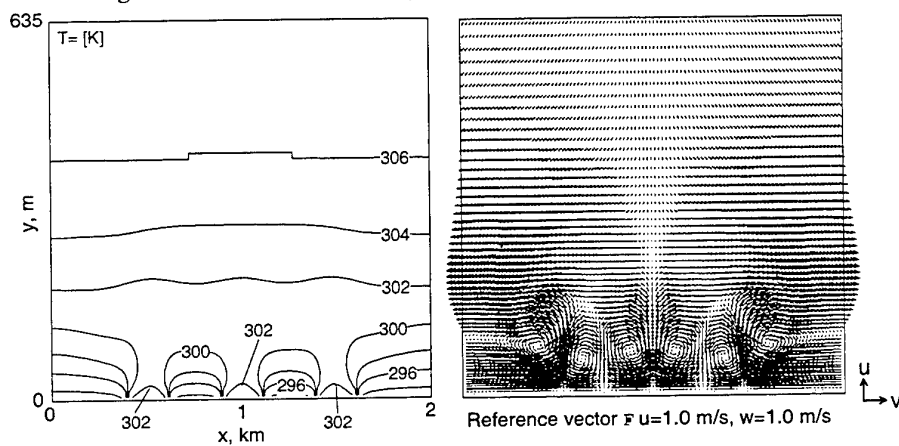


Fig. 11 Isotherms and velocity vectors ($c=100$, $H_p=100$ m)

3-D Numerical Modeling and Simulation Results

In this study, the authors tried to apply the present new modeling to 3-D computer simulation of urban warming. 3-D governing equations were introduced to transform the 3-D Navier-Stokes and equation of continuity into a simple equation system without pressure term just like 2-D governing equations. Details of 3-D governing equations were omitted for brevity in the present paper. Computational specifications and initial conditions were the same as that of 2-D computer simulation. Figure 12 shows a 3-D simulation model. The simulation was performed for the Tokyo metropolitan area covering 20×20 km with the center being located at the Imperial Palace. Spatial distribution of porosity was obtained by analysis of the latest GIS (Geographical Information System) data provided by Tokyo metropolitan government. Figure 13 shows the horizontal porosity distribution at $z=7.5$ m level.

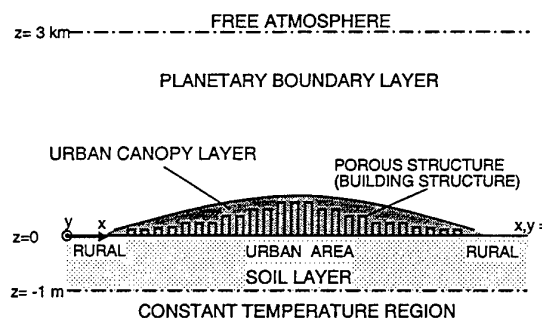


Fig. 12 3-D simulation model

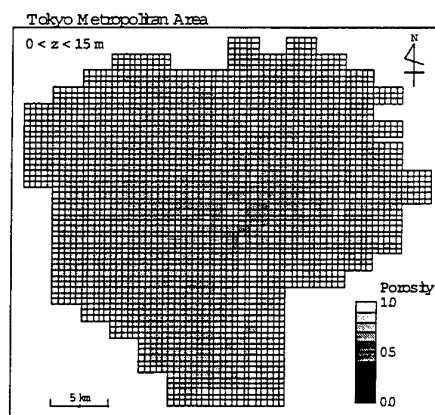


Fig. 13 Porosity distribution in Tokyo metropolitan area

The authors group previously performed a 3-D simulation for the Tokyo urban warming (Saitoh et al., 1996). According to their simulation results of urban warming in Tokyo metropolitan area ca. 2030, the maximum ambient temperature in the evening (18:00) at Otemachi, heart of Tokyo, will exceed 42°C . In the present simulation, their conditions of the future Tokyo were used. Figure 14 shows the ambient temperature distribution at near the surface in the evening in the summer. Figures 15 and 16 show the horizontal and vertical velocity vectors correspond to Fig.14, respectively. From these results, the validity of the new modeling was confirmed. Without the meteorological assumptions like the roughness parameter, the degree of resolution could be improved by using the new modeling. The authors suppose that the new modeling should verify its validity in the small-scale analysis.

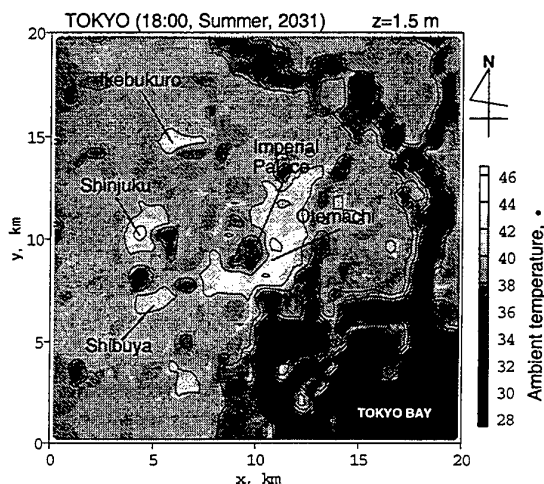


Fig. 14 Horizontal ambient temperature distribution at $z=1.5$ m in Tokyo metropolitan area ca. 2030

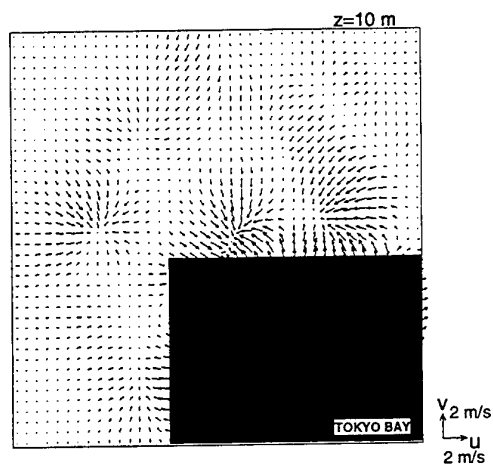


Fig. 15 Horizontal velocity vectors at $z=10$ m corresponding to Fig. 14

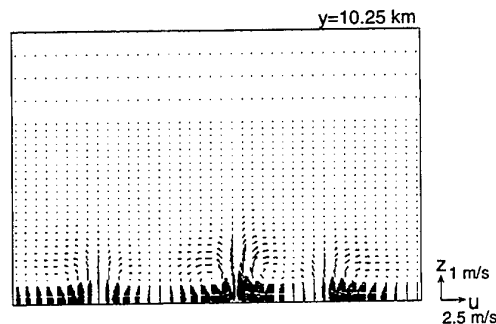


Fig. 16 Vertical velocity vectors at $y=10.25$ km

3. CONCLUSION

In this paper, a new microscopic modeling for the urban surface layer was presented. 2-D numerical simulation and experimental verification for the urban surface layer were conducted. Further, 3-D computer simulation was performed by using the new modeling. From the present study, the following conclusions may be drawn.

1. The authors found out a structural similarity between urban structure and porous structure. The modeling of the urban surface layer was done including this porous media flow.
2. The validity of the present model was verified by 2-D numerical simulation of unsteady natural convection, which simulates the urban warming. The effect of the urban structure was incorporated as porous media over the heated surface.
3. 3-D computer projection of Tokyo urban warming to 2030 was done via the proposed model.

REFERENCES

1. T. S. Saitoh, T. Shimada and H. Hoshi, "Modeling and Simulation of the Tokyo Urban Heat Island," *Atmospheric Environment* 30, 20, 3431-3442 (1996).
2. T. S. Saitoh and H. Hoshi, "Urban Warming in Tokyo Metro Area and Counterplan to Improve Future Environment," *Proc. of 28th IECEC'93*, 2, 887-892 (1993).
3. T. S. Saitoh, "Heat Island," Kodansha Publ. Co., Ltd (1997).
4. T. S. Saitoh and N. Yamada, "3-D Simulation of Urban Warming in Tokyo and Effect of Reduction of CO_2 Emissions," *Proc. of 33rd IECEC'98*, 364 (1998).
5. Y. Takatsu, T. Masuoka and T. Tsuruta, "Turbulence Model for Flow through Porous Media," *Trans. of the Japan Society for Mechanical Engineers*, B60, 571, 243-248 (1994).
6. J. C. Slattery, "Momentum, Energy and Mass Transfer in Continua," McGraw-Hill (1972).
7. F. A. L. Dullien, "Porous Media Fluid transport and Pore Structure," Academic Press (1979).
8. Japan Society of Mechanical Engineers, "JSME Data Book: Heat Transfer (4th edition)," Maruzen (1986).
9. Japan Society of Mechanical Engineers, "JSME Heat Transfer Handbook," Maruzen (1993).

INDOOR THERMAL ENVIRONMENT OF RESIDENTIAL BUILDINGS IN LARGE CITIES OF CHINA

Hiroshi Yoshino, Haihong Lou

Laboratory of Building Environmental Engineering

Department of Architecture & Building Science

Graduate School of Engineering, Tohoku University

Email: youshino@sabine.pln.archi.tohoku.ac.jp; Fax: (+81) 22-217-7886

Keywords: multi-family houses, indoor thermal environment, questionnaire survey, field measurement

ABSTRACT: Energy consumption of China increases rapidly due to recent economical development. That is one of major reasons of air pollution problem in large cities of China. Energy consumption of residential sector shares 40% of the total consumption and also increases. In residential buildings of developed countries, energy consumption used for space heating plays an important role in total residential energy consumption. Therefore, in order to estimate the future trend of residential energy consumption in China, it is necessary to understand the saturation level of space heating equipment and indoor thermal environment. However, there is no data available of these matters. Then, this paper deals with the space heating and indoor thermal environment of residential buildings in Shanghai and Beijing. The investigation has been done for 150 houses in winters of 1998 and 1999 by means of questionnaire and liquid crystal thermometers. Also, the temperature and humidity of 15 houses were measured by small data loggers with temperature and humidity sensors. The findings are as follows: 1) In Shanghai, the air conditioning unit is popularly used for space heating in 45% houses. One or two rooms of the house is only heated for about 4 hours in the evening. The indoor temperature of the houses was around 15°C and was stable during the measurement period due to thermal capacity of concrete structure. Occupant wears relatively heavy clothes in low temperature indoor environment. 2) In Beijing, the central space heating is popular and all rooms are heated in whole days. The room temperature is around 20°C.

1. INTRODUCTION

Energy consumption of China increases rapidly due to recent economical development. That is one of major reasons of air pollution problem in large cities of China. Energy consumption of residential sector shares 40% of the total consumption [1] and also increases. In residential buildings of developed countries, energy consumption used for space heating plays an important role in total residential energy consumption. Therefore, in order to estimate the future trend of residential energy consumption in China, it is necessary to understand the saturation level of space heating equipment and indoor thermal environment. However, there is no data available of these matters. Then we have investigated indoor temperature and humidity in multi-family houses in Shanghai and Beijing in winter in 1998 and 1999, respectively. The investigation consisted questionnaire survey (100 apartments in Shanghai and 40 apartments in Beijing) and fields measurement (6 apartments in Shanghai and 3 apartments in Beijing). This paper shows the results of investigation and analyzes the difference between Shanghai and Beijing. Shanghai and Beijing are belong to the transition heating zone and the central heating zone, respectively, which are classified by Chinese government.

2. QUESTIONNAIRE SURVEY

Outline of Questionnaire Survey

The name of cities, investigating period, number of respondents and outdoor environment during the investigation are showed in Table1. The indoor temperature is read and recorded using liquid crystal thermometers in a week continuously. The data of outdoor environment comes from the nearest meteorological observatory. The average temperature during the period of investigation is 9.2 in Shanghai, -3.6 °C in Beijing.

Method and Content of Questionnaire

For this investigation, we distributed questionnaire and liquid crystal thermometers to pupil in an elementary school and junior high schools. Pupils read to record the indoor temperature and their parents answered the questionnaire. Two pieces of liquid crystal thermometers attached on 5mm thickness form polystyrene board were distributed to each house, and pasted on the wall at 1 meter high over the floor in a bed room and a living room. The room temperature in the morning (6:30-8:30), midday (11:30-13:30) and evening (18:00-20:00) for a

week were recorded. The period of recording indoor temperature is from Dec. 27th, 1997 to Jan. 2nd, 1998 in Shanghai and from Jan. 12th to Jan. 18th, 1999 in Beijing. The contents of questionnaire are showed in Table 2.

Table 1. Outline of the Questionnaire Survey

City	Survey period	Subject for distribution (pupils)	Distributing number	Number of respondents	Number with temperature data	Outdoor conditions during the period
Shanghai	From 12/1997 to 1/ 1998	An elementary school and a junior high school	100	74	68	9.2 °C, 76%RH
Beijing	1/1999	A junior high school	40	36	36	-3.4 °C , 39%RH

Table 2. Contents of Questionnaire Survey

Thermal environment	Temperature of living room and bedroom in morning, midday and evening
Housing equipment	Space heating & cooling systems, household equipment
Life style	Period of heating, kind of clothing, methods for prevention of indoor air pollution and condensation, retrofitting of rooms
Building performance	Construction year, height of building, floor space, composition of rooms
Energy consumption	Consumption of gas and electricity on December
Occupant characteristics	Family structure, age of householder

Results of Questionnaire Survey

Characteristics of occupants. The ratio of households composed of one couple and one child is 80%. The number of apartments with two households is a little. The age of householder is between 40 and 50 years old in most cases.

Residential buildings. Figure 1 shows the view of apartments measured in Shanghai and Beijing. Residential buildings constructed during the past five years shares 50% in Shanghai and 18% in Beijing. And the old building over 15 years in Beijing is about 40%. Windows have single glazing and an insulation material is not used in construction. In Beijing, there are half apartments with double glazing windows. The floor space of apartments diversifies from 16m² to 88m² in Shanghai and 15m² to 98m² in Beijing. The average is 37.9m² and 44.3m², respectively.



Shanghai



Beijing

Fig. 1. The view of apartments measured in Shanghai & Beijing

The apartment with one or two bedrooms and one living room is 60% in Shanghai and 80% in Beijing. In some apartments, the bedroom is used for a living space. There are 40% apartments in Shanghai composed of just one room or two rooms. Even if there are both a bedroom and a living room, the bedroom is used for a living space in many cases because the living room is narrow and a television set is put in the bedroom.

Saturation level of household equipment except for space heating Figure 2 shows saturation level of household equipment except for space heating. Air cleaner, exhausting fan, kitchen hood with a fan, hot-water heater are popular. The saturation level of air cleaner is about 27% in Shanghai. The saturation level of gas hot-water heater is about 82% and 68% in Shanghai and Beijing, respectively. Though questionnaire doesn't include the question to the usage of gas range, a gas range is almost used in each apartment. The saturation level of kitchen hood with a fan is 90% and 65% in Shanghai and Beijing. And the exhausting fan is equipped in 42% apartments in Shanghai and 38% apartments of Beijing, and is mainly installed in bathroom.

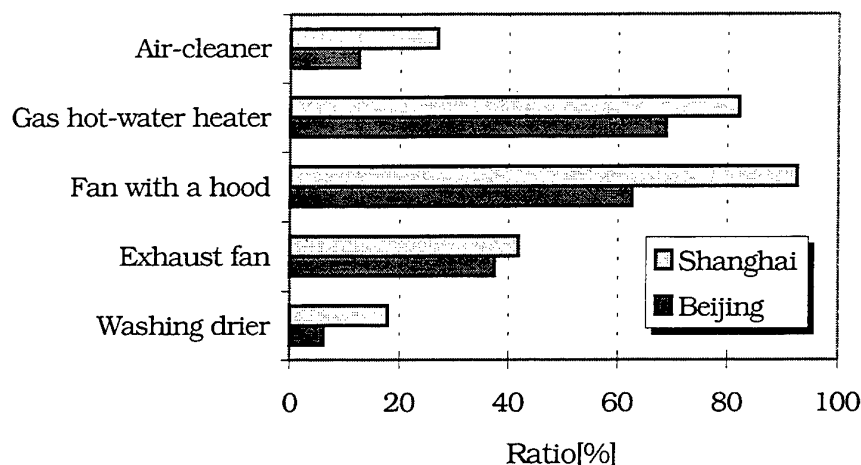


Fig. 2. The saturation level of household equipment except for space heating

Use of space heating. The space heating equipment used in apartment is showed in Fig.3. The air conditioning unit for both space heating and cooling, and electric infrared heater are popularly in Shanghai. But electric panel heater, electric warm-air heater, electric heater on foot and gas heater are used in some apartments. In most cases, air-conditioning units are installed in the bedroom. The electric portable infrared heater is used in different room. Electric warm-air heater is always hung on the wall in bathroom. On the other hand, in Beijing, the heating equipment used in Shanghai isn't popular because the radiators connected with district heating system are installed in each apartment. The electric infrared heater and the electric warm-air heater are also used for space heating if there is no radiator in a room.

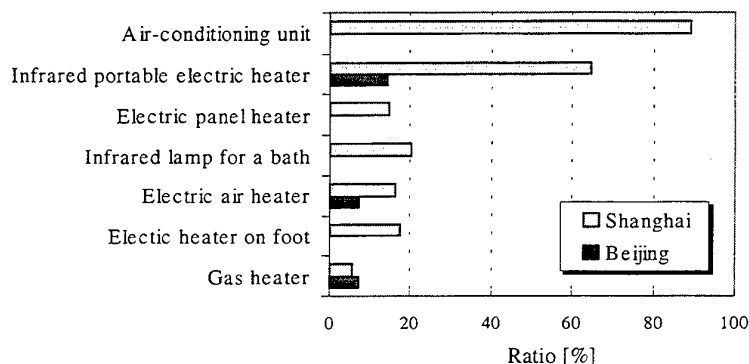


Fig. 3. The space heating equipment

The heating period is showed in Fig. 4. In Beijing, during four months from November to March, district heating system is operated. The energy source is coal. Small numbers of apartments are supplied with hot water in October this year. In Shanghai, the heating period is mainly from December to February. The hot water for space heating is supplied all day in Beijing. Figure 5 shows the heating hours in a day in Shanghai, that is only from 18:00 to 22:00. There are not many apartments that use space heating more than 5 hours. The reasons for this are such as 'the room is warm' and 'for saving fuel expenses'.

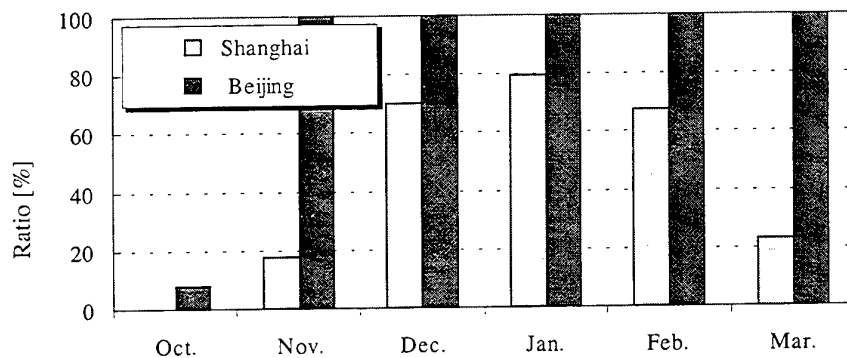


Fig. 4. The heating period

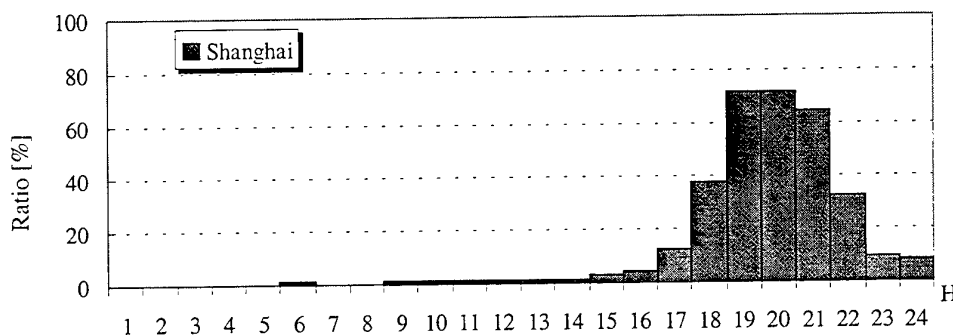


Fig. 5. The heating hours in a day

Indoor humidity sensation. Indoor humidity sensation is showed in Fig. 6. In Shanghai, the ratio of response of 'neutral' is nearly 70%, and that of 'feeling humid' is about 30%. In Beijing, the response of 'feeling dry' is more than 60%. At the field measurement in Shanghai, we found vapor condensation on the windows and sometimes on the wall. Due to questionnaire, mold growth appears in 2% apartments in Shanghai. There is no mold growth in Beijing.

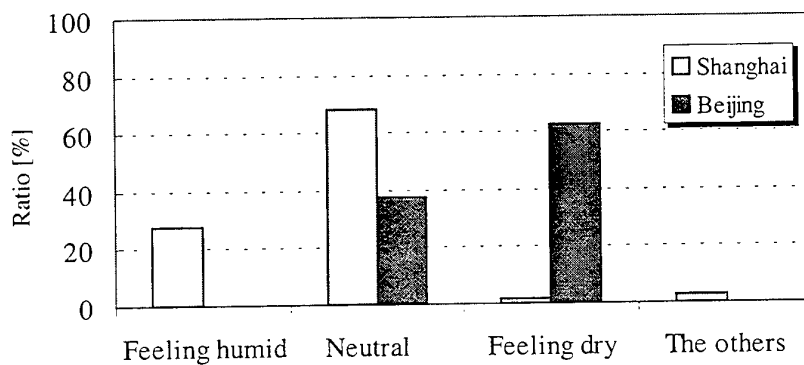


Fig. 6. The indoor humidity sensation

Indoor Temperature Measured by Liquid Crystal Thermometer

Bedroom temperature in the evening. We have used the data for analysis from 41 apartments where the temperature of living room and bedroom were recorded separately and the other 16 apartments where the bedroom is used for a living space in Shanghai. We have used the data of bedroom temperatures from 36 apartments in Beijing. Bedroom temperatures of each apartment in the evening were averaged for a week. Figure 7 shows the frequency distribution. Room temperature distributes from 18°C to 24°C in Beijing and from 10°C to 25°C in Shanghai. There are two rises which appear between 14°C and 18°C and between 22°C and 26°C in Shanghai. It is estimated that apartments with temperature between 14°C and 18°C was not heated, and the apartments between 22°C and 25°C was heated. According to questionnaire, most apartments keep low temperature without space heating in this period in Shanghai.

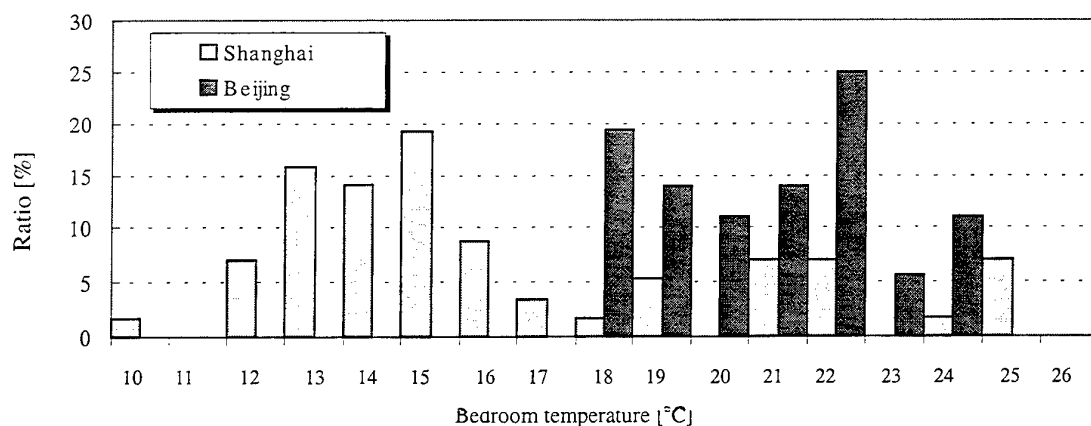


Fig. 7. The frequency distribution of bedroom temperature in the evening

Temperature of bedroom and living room. The average temperature and the standard deviation of bedroom and living rooms in morning midday and evening are showed in Fig. 8. The temperature of Beijing is 3°C to 7°C higher than that of Shanghai. The difference between two cities is caused by different type of space heating used. The bedroom temperature is higher than living room temperature in two cities. That is because families spend a lot of time in the bedroom.

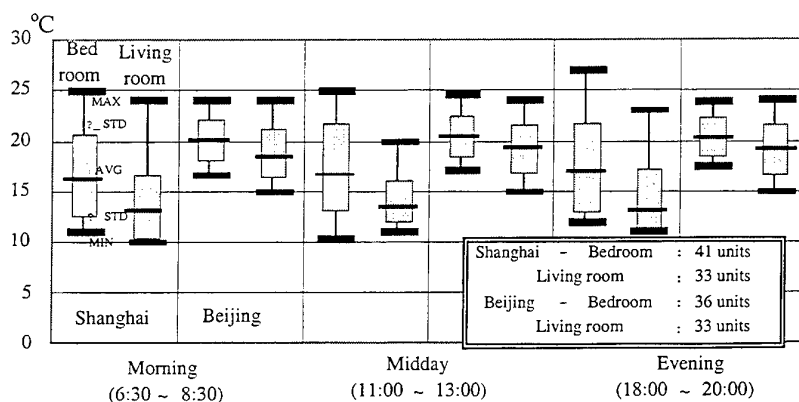


Fig. 8. The average and standard deviation of temperature in morning, midday and evening

Occupant's clothing. Figure 9 shows the relationship between indoor temperature and thermal insulation value of occupant's clothing (clo value), that was obtained by the response for question of kind of clothing. Comparing between two cities, clo insulation value is less and the indoor temperature is higher in Beijing. In the case of Shanghai, when indoor temperature is 14°C, the average of clo insulation value is about 1.4. According to the standard of ASHRAE55[2], when clo insulation value is 1.4, the operative temperature for thermal comfortability is 18°C. The actual room temperature is about 4°C lower than this standard.

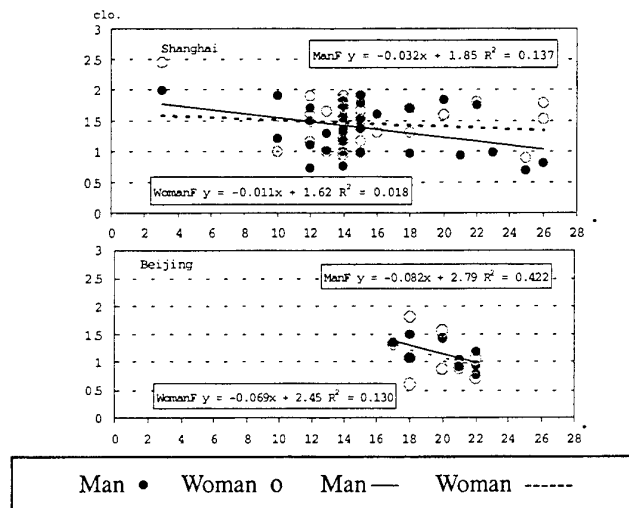


Fig. 9 The relationship between indoor temperature and thermal insulation value of occupant's clothing

3. FIELD MEASUREMENT OF INDOOR TEMPERATURE AND HUMIDITY IN MULTI-FAMILY HOUSES IN TWO CITIES

Description of Apartment for Measurement

Table 3 shows the summary of apartments and houses for measurement. The multi-family houses investigated in

Table 3. Summary of Houses Measured

	Houses	Structure of housing	Floor space [m ²]	Family structure	Space heating equipment	Outdoor environment
Shanghai	A	Thickness of outside wall: 35cm	23.8	Middle-aged couple + daughter	Air-conditioning unit	Average temperature: <u>10 °C</u>
	B		27.7	Middle-aged couple	Living room: air-conditioning unit	
	C		23.3	Old-aged couple	Electric heater	
	D	Inside wall: 25cm	41.2	Middle-aged couple	Bedroom: air-conditioning unit	Average relative humidity: <u>60%</u>
	E	Single glazing	56.0	Old-aged woman + daughter	Bedroom: air-conditioning unit	Rainy days: <u>12/31, 1/2, 1/4</u>
	F		50.8	Old-aged man + young couple + child	Living room: air-conditioning unit	
Beijing	M	Window of bedroom: double sashes	74.0	Old-aged couple + young couple	Bedroom and living room: air-conditioning Lavatory: electric warm-air heater	Average temperature: <u>-2.8 °C</u>
	O	Single glazing	98.0	Middle-aged couple + son	District heating system	Average relative humidity: <u>38%</u>
	P	Window of bedroom and kitchen: double sashes	45.0	Middle-aged couple + daughter	Lavatory and kitchen: radiators	

Shanghai are built from 1960s to 1990s, and are under 6 stories. The thickness of outside wall and inside wall is 35cm and 25cm, respectively. The windows have a single glazing. The houses investigated in Beijing are all high-rise buildings constructed after 1980s. The window has double sashes, which were retrofitted by occupants. The family structure is composed with one couple and one child or one couple with their parent. As floor space per person is very small, in some cases, there is a bedroom shared by one middle-aged couple and a matured child. Even though space heating apparatus is equipped in each apartment in Shanghai, it hadn't been used during the investigating period except Houses B, E and F in which occupants used space heating when feeling cold at one time. House plans of two apartments investigated are showed in Fig.10. In House C of Shanghai, the kitchen is shared with the adjacent apartment. The toilet is for common use in one story and there is no bathroom. In Beijing the radiator connected with district heating system is installed in all apartment houses including Houses M, O and P. There is no radiator in toilet in Houses M and O.

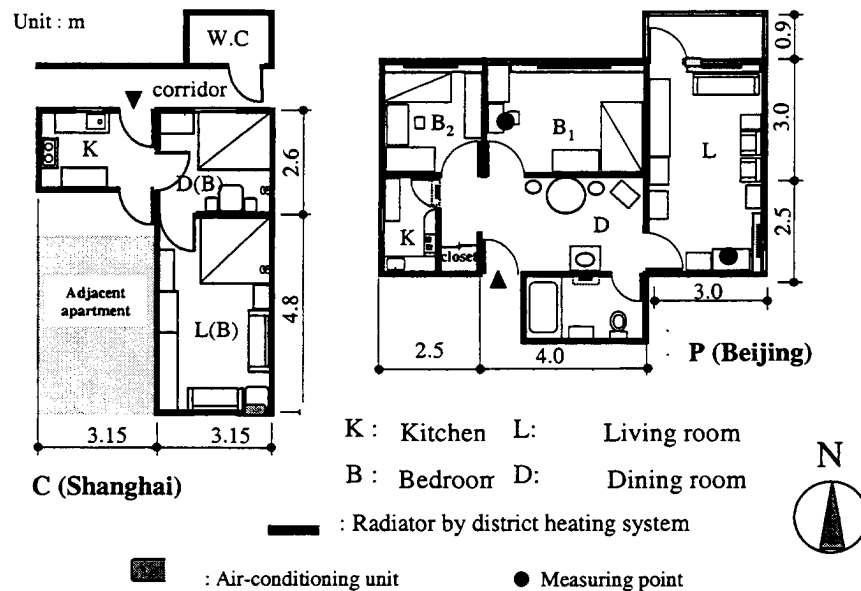


Fig. 10. House plans of two apartments

Method of Measurement

The period of measurement is from Dec.28th, 1997 to Jan.6th, 1998 in Shanghai, and from Jan.14th to Jan.19th, 1999 in Beijing. The compact data loggers with temperature and humidity sensors are fixed on the wall at 1 meter high over the floor in two rooms such as bedroom and living room. Data is recorded every 5 minutes in Shanghai and 30 minutes in Beijing.

Results of Measurement

Profile of temperature and humidity during a day. Figure 11 shows the profile of temperature and humidity, which were averaged at each hour during the measurement period. The room temperature of House C in Shanghai is stable between 12 °C and 14 °C even if the outdoor temperature changes. The temperature of living-bed room is at 14 °C and the temperature of dining room is low between 12-°C and 13 °C because the room faces the northern corridor open to the outside. The relative humidity is about 75%. The temperature of House P in Beijing is about 18 °C all day. The relative humidity is low between 10% and 30%. The reason why the temperature of two apartments doesn't change is due to the thermal capacity of reinforced concrete.

Relationship between indoor and outdoor temperatures. Using the average data of half an hour, the relationship between indoor and outdoor temperatures of House C and House P is showed in Fig.12. The change of indoor temperature is small compared with outdoor temperature. It is clear that the indoor temperature of House P in Beijing is higher than that of House C in Shanghai. Figure 13 shows the regression lines between bedroom and outdoor temperature of all houses investigated. The temperature of Houses M, O and P in Beijing that use district heating system are 5 °C to 10 °C higher than those in Shanghai. In Shanghai, the temperature of Houses A, D and C with no heating is lower than Houses B and E with space heating. Specially, the temperature of Houses A and D fall at 8 °C to 11 °C.

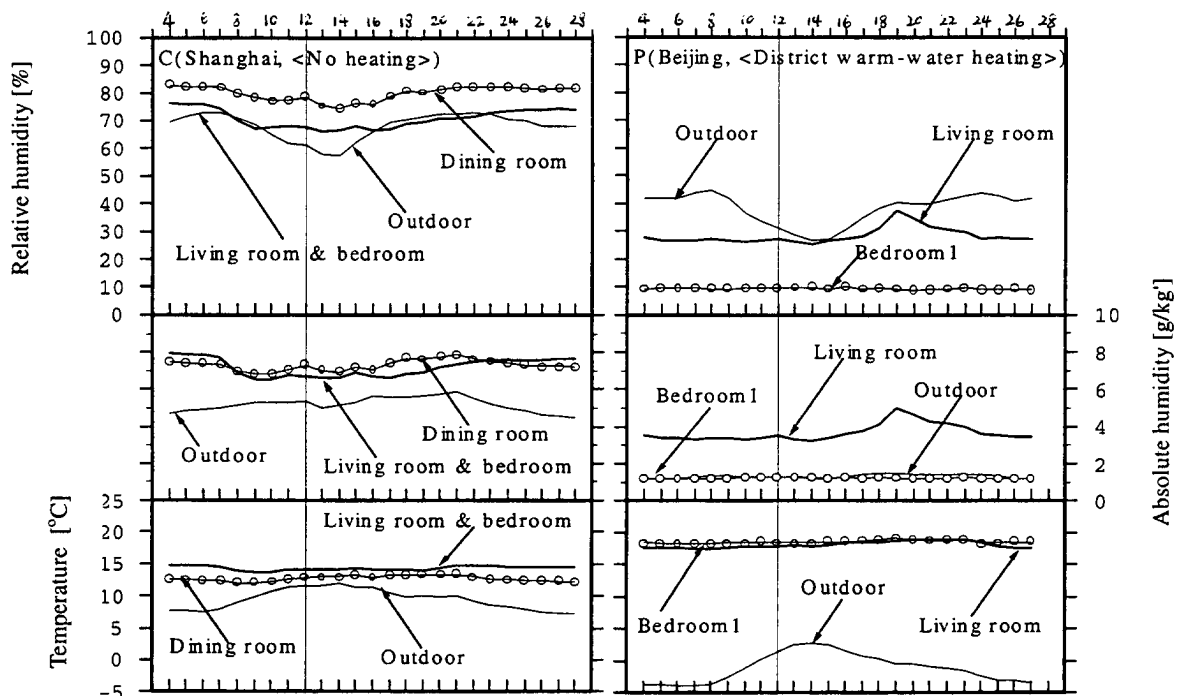


Fig. 11 The profile of temperature and humidity about House C and P

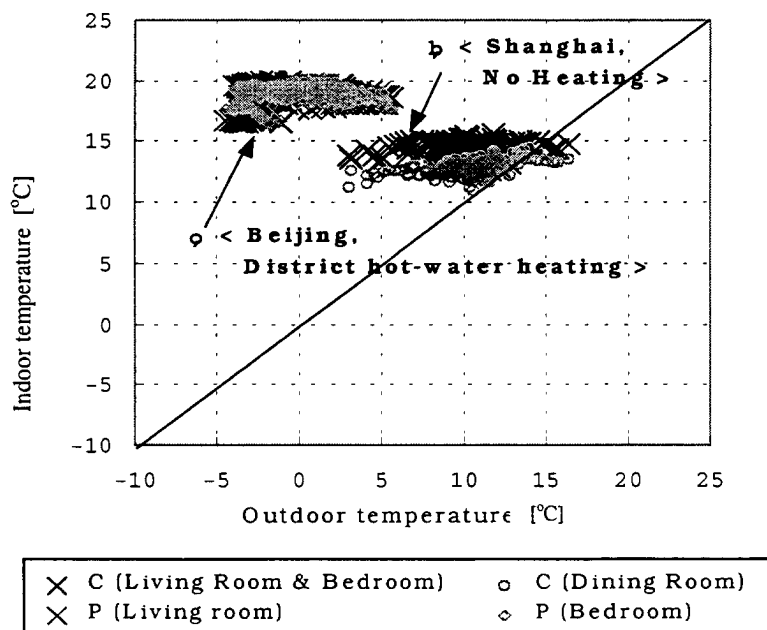


Fig. 12. The relationship between indoor and outdoor temperature about C & P

Indoor humidity Measurement results shows that indoor relative humidity is different between apartments in Shanghai and distributes from 55% to 85%. The absolute humidity is from 5g/kg' to 8g/kg' and a little higher than that of outdoor. Figure 11 shows that the absolute humidity of House C is about 8g/kg'. As the dew point temperature is estimated to be 10.5 °C, there is possibility of vapor condensation on the window surface and outside concrete wall surface without insulation. In fact, condensation was found in most cases at the visit to the apartments. The relative humidity of living room of House P in Beijing is 35% and the bedroom is lower than 10%.

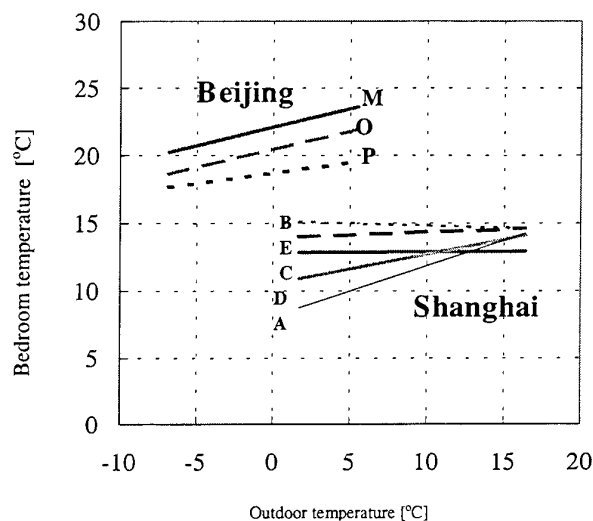


Fig. 13. The regression lines between bedroom and outdoor temperature of all apartments

4. CONCLUSIONS

- 1) In Shanghai, the air conditioning units are popularly used for space heating in 45% houses. One or two rooms of the house are only heated for about 4 hours in the evening. The indoor temperature of the houses were around 15 °C and was stable during the measurement period due to thermal capacity of concrete structure. Occupant wears relatively heavy clothes in low temperature indoor environment.
- 2) In Beijing, the central space heating is popular and all rooms are heated in whole days. The room temperature is around 20 °C. The energy sources are coal.
- 3) In Shanghai, energy consumption will increase in the future due to the need for comfortable thermal environment. In Beijing, the solid energy sources for space heating will change to liquid energy sources such as kerosene and natural gas.

REFERENCES

1. F. liu, "Energy Use and Conservation in China's Residential and Commercial Sector: Patterns, Problems, and Projects" Lawrence Berkeley Laboratory / University of California, (1993.7)
2. ASHRAE Standard 55-1992, "Thermal Environmental Conditions for Human Occupancy", American Society of Heating, Refrigerating and air-conditioning Engineers, Inc.

REAL TIME AND IN-SITU MEASUREMENT OF PARTICULATE EMISSIONS

Wang Nai-ning Yu Shi-min

College of Power Engineering

University of Shanghai for Science & Technology

E-mail: nnwang@public6.sta.net.cn, Fax: (021)-65682376

Keywords: pollution supervision, particulate emission, gas-solid flow, optical measurement, particle system

ABSTRACT. The supervision and determination of the mass concentration and size of the particulate matters in different industrial emissions are one of the most important problems faced now in China and in other countries. Several methods have been used for this purpose for a long time. Nevertheless, they can not meet all the modern requirements in environment control and give satisfactory results of measurements. In this paper, based on the light scattering theory, a novel method is presented, which is capable to make real time and on-line measurement of the mass concentration as well as the size of particulate matters in different industrial emissions. Theoretical analysis, computer simulation and experimental investigations are given and discussed.

1. INTRODUCTION

Particulate pollutants exist in many industrial emissions. They cause serious air pollution and negative influences on, such as, the human health, industrial production, organism growing, etc. This problem is particularly of great concern in China, because almost 75% energy are generated from the direct burning of coal. In the recent years, great efforts have been made by the government to reduce the amount of particulate matters exhausted to the atmosphere. In this instance it is very necessary and important to develop techniques and methods to monitor and/or measure continuously the mass concentration as well as the size of the particulate matters exhausted. Traditionally, this is done by the sampling method [1]. In this case, a small and representative amount of flue gas is extracted from the main flow and then transferred to a succeeding instrumentation, which separates the solid particles from the gas. The mass concentration and also the size of particulate matters can be determined. The sampling method is very simple in principle, but rather complicated in practical operation. It is time-consuming and strenuous, and often gives insufficient accuracy of the final results, especially when this is done by inexperienced operators.

Since the 70's, optical technique has been introduced, which is usually called opacity method[2]. In this case, a beam of light from a halogen lamp is passing through the flue gas to be measured and is attenuated by the suspended particles. The intensity of the transmitted (attenuated) light I is thus less than that of the incident light I_0 . The transmission of the light, or the ratio I/I_0 is then served as a measure to characterize the particle-burden in the gases. The main advantages of opacity method lie in its on-line and remote measurements. All optical parts, such as, the light sender and light detector are installed in places where the measurements are taken. No sampling is needed. Collected signals-incident and transmitted light intensities are sent to the ground and result of measurement, i.e. the ratio I/I_0 is immediately indicated in the control room. Nevertheless, there are also evident disadvantages which to a great extent compensate its advantages and limit its wide uses, because the results of measurements are ambiguous and indistinct. In fact, the ratio I/I_0 gives only a qualitative, but not a quantitative answer. One does not know the absolute values of particulate matters in flue gases. It is suggested by the producer that a calibration curve might be used to establish the correlation between the light transmission and mass concentration of particulate matters. It is well known that such a calibration is difficult and strenuous. Moreover, further investigation shows that mass concentration is not the only factor affecting the light transmission[3]. Owing to this reason, opacity method has found only limited uses in the pollution supervision.

In this paper, based on the light scattering theory, a novel method is presented which is capable to make non-intrusive, continuous and remote measurement of the mass concentration as well as the size of particulate matters in different industrial emissions.

2. BASIC PRINCIPLE AND METHOD

When a beam of light illuminates a particle, the light will be scattered in all directions in consequence of their

interaction. It is known as the light scattering. At the same time, the intensity of the transmitted light behind the particle will be attenuated (light extinction). Both the angular distribution of light intensities scattered by a particle and the resulted light extinction are in function of the light wavelength λ , the diameter of particle D and its refractive index m , and can be exactly calculated by the Mie theory. The principles of light scattering and light extinction are used in the study to determine simultaneously the mass concentration and size of the particulate matters in emissions. The general arrangement and optical system are shown in Fig.1. A He-Ne laser is used as the light source. The laser beam is collimated to pass through a flue gas or a particle-laden flow. The number concentration and mass concentration of the particulate matters and its diameter are expressed in terms of N , C and D , respectively. The distribution of light energy scattered by the particles F_i ($i=1,2,\dots,n$) are collected within several solid angles by a photo-detecting array located in the forward direction off the light axis, while the transmitted light intensity I is received by an another photo-detector located in a direct line with the incident laser beam just behind the medium. The measured F_i and I and also the incident light intensity I_0 are sent to a computer for data processing. The mass concentration and the diameter of the particulate matters are thus can be extracted from the signals by an inversion calculation.

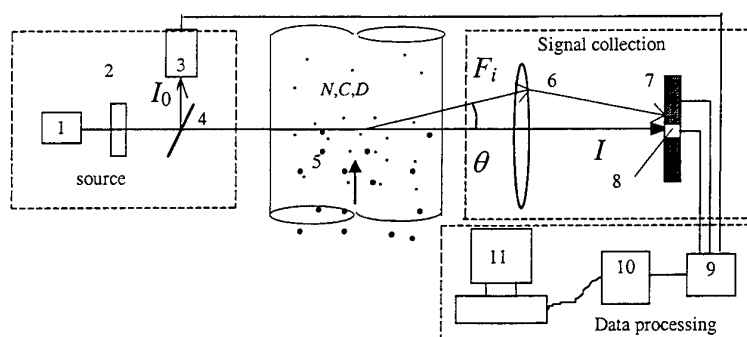


Fig.1 General arrangement

As mentioned above, the light scattering and also the light extinction are in function of refractive index of the particle. In practical conditions, the chemical compositions of particulate matters encountered in different emissions are quite different. For example, in the case of flue gases from thermal power stations, the particulate matters (ashes) are composed of many different materials, such as, SiO_2 , Fe_2O_3 , CaO , Al_2O_3 ,..... and of different weight percentages. Each composition has its own refractive index. It is therefore very difficult to know the real value of refractive index of particulate matters in every individual application. In order to overcome this difficulty, instead of Mie theory Fraunhofer diffraction is used in the study, which allows the distribution of scattered light intensities to be calculated without the reference to the refractive index of the particles. It is well known in the literature that Fraunhofer diffraction is the limiting case of Mie scattering and is valid when particles to be examined are large enough in comparison with the incident light wavelength. Theoretical analysis and numerical calculations show that when a He-Ne laser ($\lambda=0.6328\mu\text{m}$) is used and particles are larger than $2\mu\text{m}$, Fraunhofer diffraction gives almost the same results as the Mie scattering in the light scattering pattern calculation. Therefore, it would not result in any remarkable errors, if Fraunhofer diffraction is used in our study.

According to the Fraunhofer diffraction, the intensity of the scattered light by a spherical particle of diameter D at the angle of θ is given by

$$I(\theta) = I_0 \frac{\pi^2 D^4}{16\lambda^2 r^2} \left[\frac{2J_1(X)}{X} \right]^2 \quad (1)$$

where I_0 is the incident light intensity, r is the distance between the particle and detector, J_1 is the first-order spherical Bessel function, $X=\pi D \sin(\theta)/\lambda$. The multi-element photo-detecting array used to collect the distribution of scattered light energy may have different forms. In the case of rectangle, as shown in Fig.2, the scattered light energy falling on the i -element can be determined by

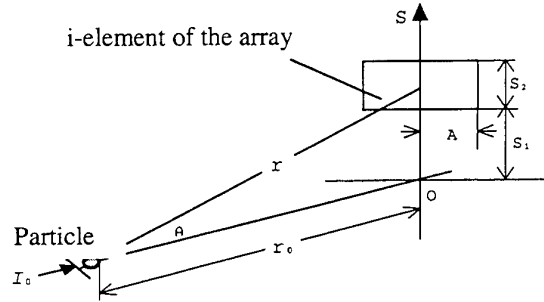


Fig.2 Scattered light energy collection

$$e_i = \frac{1}{2} I_0 D^2 \left\{ \int_{s_1}^{\sqrt{s_1^2 + A^2}} \arccos(s_1 / r) J_1^2 \left(\frac{\pi D r}{\lambda f} \right) ds + \int_{\sqrt{s_1^2 + A^2}}^{s_1 + s_2} \arcsin(A / r) J_1^2 \left(\frac{\pi D r}{\lambda f} \right) ds \right. \\ \left. + \int_{s_1 + s_2}^{\sqrt{(s_1 + s_2)^2 + A^2}} \arcsin(A / r) J_1^2 \left(\frac{\pi D r}{\lambda f} \right) ds \right\} \quad (2)$$

For a monodisperse particle system of diameter D , the total scattered light energy received will be

$$E_i = N \cdot e_i \cdot v \quad (3)$$

where N is the number concentration of particles and v is the volume of the measuring zone. In the case of polydisperse particle system $[N_j, D_j]$, the total scattered light energy will be the sum of all contributions by different particles.

$$e_i = \frac{1}{2} I_0 v \sum_j N_j D_j^2 \left\{ \int_{s_1}^{\sqrt{s_1^2 + A^2}} \arccos(s_1 / r) J_1^2 \left(\frac{\pi D r}{\lambda f} \right) ds + \int_{\sqrt{s_1^2 + A^2}}^{s_1 + s_2} \arcsin(A / r) J_1^2 \left(\frac{\pi D r}{\lambda f} \right) ds + \int_{s_1 + s_2}^{\sqrt{(s_1 + s_2)^2 + A^2}} \arcsin(A / r) J_1^2 \left(\frac{\pi D r}{\lambda f} \right) ds \right\} \quad (4)$$

The left sides of Eq.4 are known from the measurements and the geometric dimensions of the photo-detecting array are also known from the producer. The particle size and its distribution can be thus determined by an inversion calculation. It should be pointed out that the constant $I_0 v$ in Eq.4 can be omitted in the normalized data processing.

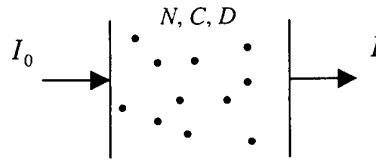


Fig.3 Light extinction

After determining the size of particles, the mass concentration of particulate matters can be further determined from the light extinction by the Lambert-Beer formula, which is expressed in the following form (Fig.3)

$$I / I_0 = e^{-\tau L} \quad (5)$$

where I_0 and I are the intensities of incident and transmitted light, L is the length of the light path and τ is the

turbidity of the medium, which can be determined by

$$\tau = \frac{\pi}{4} \sum_j D_j^2 N_j K_e \quad (6)$$

where K_e is the extinction coefficient. In the case of Fraunhofer diffraction, i.e. when particles are larger than $2\mu\text{m}$, extinction coefficient is a constant $K_e=2$. The weight fraction of particle D_j is

$$w_j = \frac{\rho}{6} \pi D_j^3 N_j \quad (7)$$

where ρ is the specific weight of the particulate matters. After substituting Eq.6 and Eq.7 into Eq.5, the mass concentration of particulate matters C can be expressed by

$$C = \frac{\rho \ln(I_0/I)}{3 \sum_j w_j / D_j} \quad (8)$$

The incident and transmitted light intensities I_0 and I are known from the measurements.

3. COMPUTER SIMULATION AND NUMERICAL CALCULATION

In order to verify the correctness and effectiveness of this method and the programmed inversion algorithm, comprehensive computer simulation and numerical calculation are performed. A two-parameter Rosin-Rammler particle size distribution function is used in the study, which can be expressed by

$$R(D) = \exp[-(D/X)^N] \quad (9)$$

where X and N are characteristic diameter and size distribution parameter, respectively. The weight fraction of diameter D_j is

$$W_i = [R(D_j + 1) - R(D_j)] \times 100\% \quad (10)$$

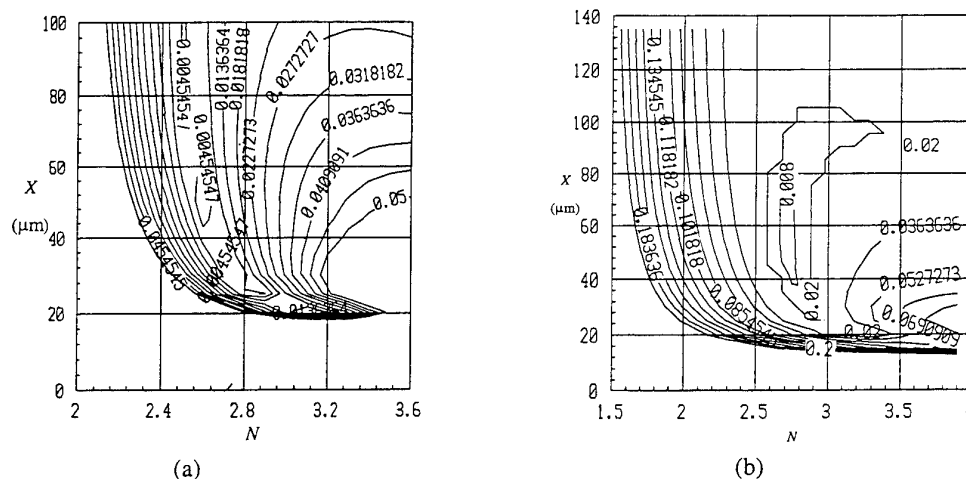


Fig.4 Error contour

As an example, Fig.4(a) gives the error contour of the inversion calculations, which is defined as the minimum of the differences between the theoretically calculated and measured light energy in all elements of the photo-detecting array. The preset two parameters are $X=50\mu\text{m}$, $N=2.6$ and the scattered light energy are collected

within $1^\circ/2^\circ, 2^\circ/3^\circ, 3^\circ/4^\circ, 4^\circ/5^\circ, 5^\circ/6^\circ, 6^\circ/7^\circ, 7^\circ/8^\circ$ and $8^\circ/9^\circ$ ($j=8$), respectively.

Evidently, the final result agrees with the preset value. Further investigations are made when certain errors are occurred in the scattered light energy measurements. Fig.4b shows the same error contour, but $+4\%$, -4% , errors are alternately existed in the light energy measurements. It is clear from the figure that the final result agrees still very well with the preset values. Table 1 gives some quantitative results of the numerical calculations. The preset values of X and N are $4.0\mu\text{m}$ and 1.5 , $9.5\mu\text{m}$ and 2.4 , $33\mu\text{m}$ and 3.0 , $85\mu\text{m}$ and 2.5 , respectively. Case 1 in Table 1 denotes that there are alternatively $+1.5\%$, -1.5% , errors in the scattered light energy measurements. Case 2 denotes $+3\%$, while case 3 and 4 -3% and $+5\%$ errors in all scattered light energy measurements. In all cases, the final errors in the particle size determination due to the errors in the scattered light energy measurements are generally less than 5% . It should be pointed out that with the modern data collecting systems it is not difficult to limit the errors in the scattered light energy measurements within $3\sim 5\%$. It can be thus concluded that the presented method is able to give reliable and accurate results

Table 1 Some Results of Numerical Calculations

Preset values		$X(\mu\text{m})$	4.0	9.5	33	85
		N	1.5	2.4	3.0	2.5
		$D_{32}(\mu\text{m})$	1.49	6.21	24.37	57.08
Case 1	Calculated values	$X(\mu\text{m})$	4.23	9.02	31.45	81.45
		N	1.56	2.41	3.19	2.48
		$D_{32}(\mu\text{m})$	1.53	5.99	23.83	55.42
	Error in $D_{32}(\%)$		2.7	-3.5	2.2	-2.9
Case 2	Calculated values	$X(\mu\text{m})$	4.16	9.36	34.01	84.31
		N	1.45	2.52	3.01	2.47
		$D_{32}(\mu\text{m})$	1.44	6.32	25.15	57.19
	Error in $D_{32}(\%)$		-3.4	1.8	3.2	0.2
Case 3	Calculated values	$X(\mu\text{m})$	3.97	9.29	32.93	86.39
		N	1.51	2.34	3.11	2.51
		$D_{32}(\mu\text{m})$	1.50	5.97	24.69	58.15
	Error in $D_{32}(\%)$		0.6	-3.9	1.3	1.6
Case 4	Calculated values	$X(\mu\text{m})$	4.31	9.38	31.56	87.19
		N	1.44	2.48	2.98	2.48
		$D_{32}(\mu\text{m})$	1.43	6.27	23.26	58.26
	Error in $D_{32}(\%)$		-4.0	1.1	-4.6	2.1

3. EXPERIMENTAL STUDY

Based on the theoretical analysis, a prototype has been constructed, which is in tubular form, as shown in Fig.5. There is a slot in the front of the probe body, which serves as the measuring zone. The whole probe is inserted in places where measurements should be taken. The particle-laden flow to be measured passes the slot perpendicularly. A laser diode is used as the light source. The laser beam passes the slot axially, where the light

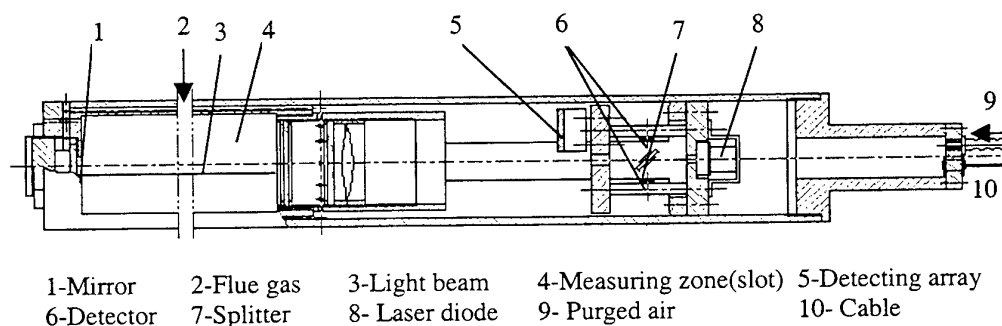


Fig.5 General arrangement of the probe

interacts with the particles. The light scattering and light extinction are occurred. Purged air is conducted to prevent the possible pollution or sedimentation of particles on the surfaces of optical elements. First experiments are carried out in laboratory conditions. The monodisperse polystyrene latex spheres are used as the Standard Reference Material. An optical cell is filled with purified water, in which the latex spheres are added. The cell is then put in the light path of the probe. Altogether 3 latex spheres are measured, whose nominal diameters are known from the supplier. Table 2 summarizes the results of measurements. The errors are generally less than 5%, which lies within the scope of supplier's deviation. Table 3 shows the repeated measurements of the 9.88 μm latex spheres. The reproducibility is also considered to be very well.

Table 2 Measurement Results of Latex Spheres

Nominal diameter(μm)	9.88	37.0	75.0
Measured diameter(μm)	9.69	35.62	72.89
Error(%)	1.9	3.7	2.8

Table 3 Repeated Measurements of 9.88 μm Latex Sphere

No.	1	2	3	4	5	6	7	Average
$D(\mu\text{m})$	9.49	9.43	9.64	9.81	9.83	9.83	9.81	9.69

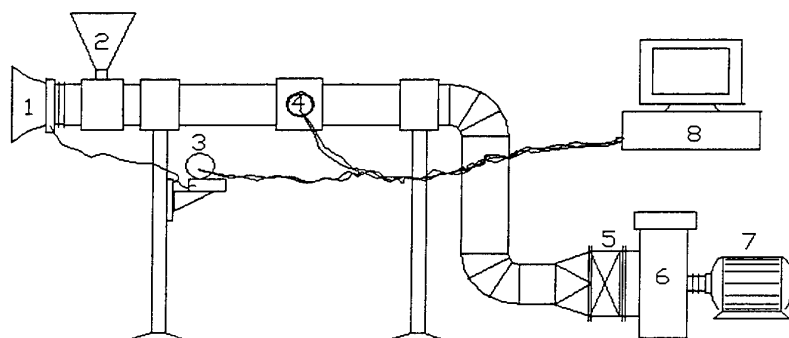


Fig.6 Measurement in particle-laden flows

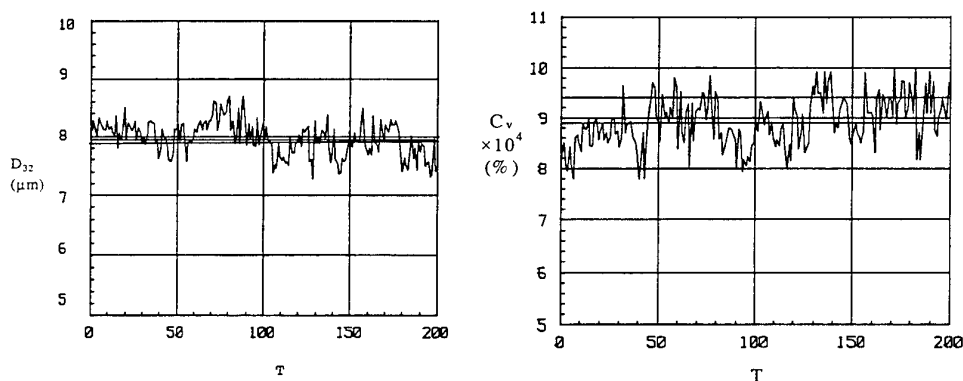


Fig.7 Results of measurements

The probe is then used to make simulating measurements in particle-laden flows, as shown in Fig.6. Samples to be measured are added in at place 2, whose sizes are known. Its mass concentration can be controlled or regulated by the air flow and the amount of added samples. The probe is inserted at place 4. Fig.7 gives some results of the continuous measurements. Although two curves are to some extent oscillate, but their mean values (solid lines in the figures) are in good agreement with the preset testing conditions. For example, the average diameter of the added sample D_{32} and its mass concentration (in volume) in these experiments are 8.04 μm and

9.40×10^{-4} , while the measured values are $7.94 \mu\text{m}$ and 8.91×10^{-4} . The deviations are 1.2% and 5.2%, respectively. Further investigations will be made in the field tests later.

REFERENCE

1. Fundamentals of Air Pollution, second edition, Academic Press, Inc. London. (1984).
2. P. Martin and G. Müller, Optical In-situ Smoke Spot Number Measuring. Vulkan Verlag, Essen. (1993).
3. S.M. Yu, A Study to the Continuous and In-situ Measurement of Particulate Matters in Emissions, Ph.D. Dissertation, University of Shanghai for Science and Technology, (1999).

APPLICATION OF PHOTOENERGY ON OXIDATION OF TOXIC NITRITE ION AND HYDROGEN GENERATION USING THE RUTILE FORM OF TiO_2/Ti PHOTOELECTRODE

Chih-Cheng Sun

Department of Chemical Engineering
The Yung-Ta Industrial Commercial College

Tse-Chuan Chou

Department of Chemical Engineering
The National Cheng Kung University
Email : tcchou@mail.ucku.edu.tw ; Fax : (886)-6-2366836

Keywords: photoelectrochemical oxidation, photocurrent efficiency, nitrite ion, titanium dioxide

ABSTRACT. Immobilized TiO_2 powder on a conductive supports exhibits interesting electrochemical and photoelectrochemical properties. TiO_2 supported on Ti plate, TiO_2/Ti , was used as working electrode, and Pt, Ti and graphite were used as counter electrode. The morphology of TiO_2 on the Ti plate is rutile form. Experimental results indicate that the rutile form of TiO_2/Ti film electrode has excellent photoactivity by applying a bias potential and photoenergy simultaneously. The toxic nitrite ion was destroyed on the TiO_2/Ti electrode. Furthermore, the hydrogen generation on the counter electrode also occurred simultaneously during this photoelectrochemical reaction. The rates of both the nitrite ion oxidation and the hydrogen generation are mainly promoted by the applied potential and power of photoenergy. The photocurrent efficiency can be calculated from the measurement of photocurrent and the rate of nitrite ion removal. The photocurrent efficiency of nitrite ion oxidation was 33~40% at a pH of about 7. The photoefficiency of nitrite ion oxidation and hydrogen generation are about 16 and 40 %, respectively. It may be a suitable method for water purification and hydrogen energy generation simultaneously using solar energy.

1. INTRODUCTION

Photoenergy is an inexhaustible energy from the nature and is potential to apply in many areas. A photocatalytic process with photoenergy has been recognized as a useful method for the detoxification of pollutants in both air and water [1-4]. The photocatalytic reaction has been studied since the discovery of photolysis of water using TiO_2 as a photocatalyst [5]. Recently, the applications of photocatalytic techniques have been extensively discussed [6-11].

TiO_2 is the most attractive photocatalyst for decreasing pollutants and purifying both water and air [6,12,13]. The semiconductor photocatalyst, TiO_2 , is excited by photoenergy, such as solar energy. The excited-electrons and holes on the TiO_2 surface have potential to carry out the photocatalytic oxidation and reduction reactions. For the oxidation of pollutants in aqueous streams, numerous investigations have attempted to develop the supported TiO_2 film catalyst [7-11,14-15]. Immobilized TiO_2 powder on a conductive supports exhibits interesting electrochemical and photoelectrochemical properties. For a TiO_2 film coated electrode, the anatase form is the commonly used photocatalyst [16], because the anatase form has a higher photoactivity than the rutile form. In order to maintain the anatase form of TiO_2 film, the calcination temperature of the TiO_2 film is held lower than 500 °C for the preparation of a TiO_2 film coated electrode [17-20]. However, the adhesion of the anatase form of TiO_2 films and the phenomena of applying high bias potential on these film electrodes has seldom been mentioned. In general, increasing the calcination temperature increases the adhesion of the TiO_2 film onto the substrate [17-19]. The adhesion of the rutile form of TiO_2 film onto the Ti substrate may be better than that of the anatase form. For the practice view, the adhesion of TiO_2 film is significant to endure bias potential, especially high bias potential, in electrochemically assisted photocatalytic reactions. A photoelectrochemical reaction using applying bias potential on the rutile form of a TiO_2 coated film electrode is interesting.

Nitrite ion is a toxic material in wastewater or fish breeding water. The toxicity of nitrite ion threatens the life of aquatic species immediately, when the concentration is higher than the 0.10 ppm limiting level. Previous investigators have examined the feasibility of oxidizing nitrite ion by supplying oxygen in an aqueous solution

using different semiconductor powders as photocatalysts [21-23]. A photocatalytic reaction of nitrite ion oxidation in brine, which contains 1~3 % NaCl, using the rutile form of TiO₂ film electrode by applying high electric field was not found.

In this work, the photoelectrochemical oxidation of nitrite ion in a NaCl aqueous solution using the rutile form of a TiO₂/Ti film electrode was systematically studied. The effect of light power, applying bias potential and pH value on both the reaction rate and photocurrent efficiency of nitrite ion oxidation were also studied.

2. EXPERIMENTAL SECTION

Preparing TiO₂/Ti Electrode

A Ti plate with a 30 cm² surface area was etched by a 18 M of hydrogen chloride at 90°C for 2 hours and then washed with distilled water in an ultrasonic bath. The treated Ti plate was dried in an oven at 100°C for 30min, and then immersed in a suspension solution containing 2.00 g of TiO₂ (Degussa P25) in a 20 ml 10% TiCl₄ and 90% ethanol. When immersed pretreated Ti plate to the TiO₂ suspension solution, the coated TiO₂ film was formed. The TiO₂ film contained TiO₂ particles (Degussa P25), which surrounded with entrained TiCl₄ solution. The coated TiO₂ film was dried at a constant moisture air, the entrained TiCl₄ solution on this film would hydrolyse to form titanium hydroxide. Then, the TiO₂ film was calcinated at 650°C for 2 hours. The TiO₂ coated Ti electrode was prepared. Finally, the structure of the TiO₂ coated plate was analyzed by X-ray diffractometer.

Measurement of Current on TiO₂/Ti Electrode

The desired NaCl concentration and volume of the electrolyte were prepared and added into the divided cell. The prepared TiO₂/Ti plate was used as the working electrode, and Pt, Ti and graphite were used as counter electrode. The experimental apparatus set up was described previously [24]. The current was measured by applying a bias potential and irradiation simultaneously on the working electrode, and was recorded by an EG&G 273A potentiostat/galvanostat with a 270 Electrochemical Analysis System. All potentials were specified to the reference electrode, Ag/AgCl/saturated KCl aqueous solution, prepared in our laboratory. The irradiation light was supplied by a supper-high-pressure Hg(Xe) lamp (Oriel) which was operated at different powers by adjusting power supply output.

Photoelectrochemical Oxidation of Nitrite Ion

The desired nitrite ion concentration was added into a 200ml 1~3% NaCl electrolyte, which was deoxygenated by nitrogen gas in the reactor. This reactor is the same used for the current measurements. The photocatalytic oxidation of nitrite ion was carried out by simultaneously applying both irradiation and a bias potential. Samples were periodically taken with a pipette from the reactor and, then were analyzed. According to the APAH testing method [25], the nitrite ion concentration was determined by a Jasco UV-vis spectrophotometer (Jasco) at a wavelength of 543 nm, a color reagent was added to the sample by the NEDA(N-1-Naphthyl ethylene diamine dihydricchloride) colorimetric method. The pH values were determined using a pH meter.

Photocurrent Efficiency of Nitrite ion Oxidation

The photocurrent efficiency of nitrite ion photoelectrochemical oxidation (η) is defined as

$$\eta = \frac{(\text{Mole of nitrite ion oxidation during a period of a run}) \times 2}{\text{Faradays of photocurrent passed during the same period of a run}}$$

$$= \frac{2 \left([\text{NO}_2^-]_0 - [\text{NO}_2^-]_t \right) V_l}{\left(\frac{I_p \times t}{F} \right) / 96500} \quad (1)$$

Where $[\text{NO}_2^-]_0$ and $[\text{NO}_2^-]_t$ are the nitrite ion concentrations at the initial time and time t , respectively. I_p is the photocurrent, and V_l is the volume of reaction solution. The η value is based on the photocurrent measured from the TiO₂/Ti electrode. The number "2" of the multiplier in the numerator of Eq. (1) represents two mole of hole required to oxidize one mole of nitrite ion in photoelectrochemical oxidation.

Photoefficiency of Nitrite ion Oxidation

The photoefficiency of nitrite ion photoelectrochemical oxidation (ϕ_1) is defined as

$$\phi_1 = \frac{\text{nitrite ion oxidation rate}}{\text{incident photons rate}} \quad (2)$$

Photoefficiency of Hydrogen Generation

The photoefficiency of hydrogen photoelectrochemical generation (ϕ_2) is defined as

$$\phi_2 = \frac{\text{hydrogen generation rate}}{\text{incident photons rate}} \quad (3)$$

3. RESULTS AND DISCUSSION

Properties of TiO₂/Ti Electrode

Fig. 1 shows the X-ray diffraction (XRD) spectra of the Ti plate, TiO₂ powder (Degussa P25) and TiO₂ film on the titanium plate calcinated at 650 °C. The peaks at $2\theta = 25.5$ and 48.0° in the spectrum of TiO₂ are easily identified as the crystal of anatase form, whereas the crystal peaks at $2\theta = 27.6$ and 54.5° are also easily identified as the crystal of rutile form. After the TiO₂ coated Ti plate was calcinated at 650°C, the adhesion of TiO₂ film on the Ti plate is fine, and the peak of the anatase form disappears, only the peak of rutile form remains. This indicates that all of the crystals on this TiO₂ coated film electrode transfer from the anatase to the rutile form. In order to maintain fine adhesion of TiO₂ film on the Ti plate, the calcination temperature higher than 650 °C is needed in our manufacturing procedure.

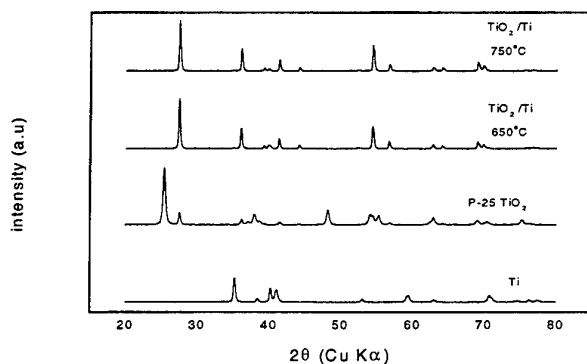


Figure 1. XRD spectra of Ti plate, TiO₂ powder (Degussa P25) and TiO₂/Ti electrode.

Photoelectrochemical Properties of TiO₂/Ti Electrode

Fig. 2 shows that increasing the applying bias potential from 0.00 to 4.00 volts (vs. Ag/AgCl) increases the current density from 0.34 to 2.65 mA/cm² under irradiation on the TiO₂/Ti electrode in a 0.51 M NaCl solution. Without irradiation on this TiO₂/Ti electrode, no current, i.e. dark current, was measured by applying bias potential in a range from 0.00 to 4.00 volts as shown in Fig.2. In this electrochemically promoted photocatalysis, the current was contributed from the TiO₂ photocatalyst on the TiO₂/Ti electrode, the TiO₂ was excited by the incident photons. Because no dark current occurred, the current measured from the TiO₂/Ti electrode can be considered as photocurrent. Even a high positive potential was applied on this TiO₂/Ti electrode, purely electrochemical reaction did not occur, which was an important side effect on TiO₂/SnO₂/glass electrode [19]. Fig. 2 also shows the effect of applying bias potential on the photoefficiency of hydrogen generation (ϕ_2).

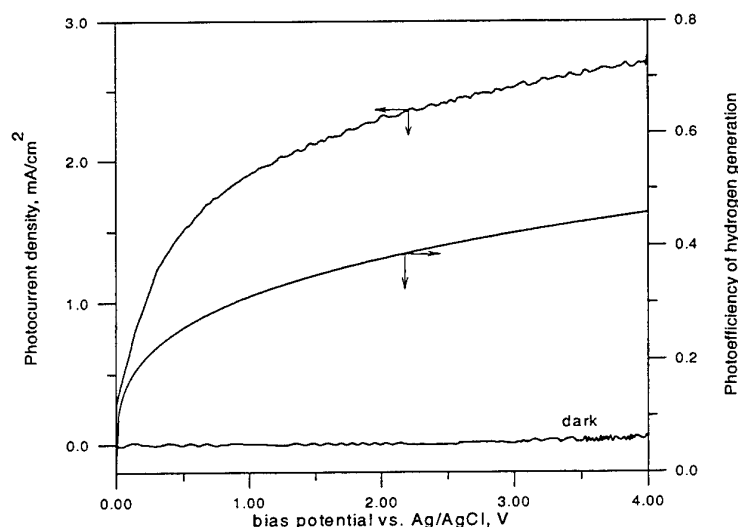
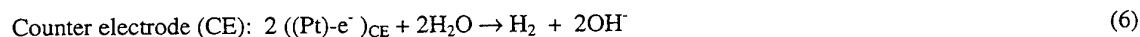
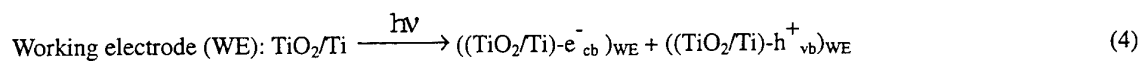


Figure 2. Effect of applying bias potential on both the photocurrent density and photoefficiency of hydrogen generation (ϕ_2): working electrode, $7.06 \text{ cm}^2 \text{ TiO}_2/\text{Ti}$; counter electrode, $4.5 \text{ cm}^2 \text{ Pt}$; temperature, 30°C ; agitation rate, 250 rpm; potential vs. Ag/AgCl; electrolyte, 0.51 M NaCl, $\text{pH}_i=5.50$; light power, 400W.

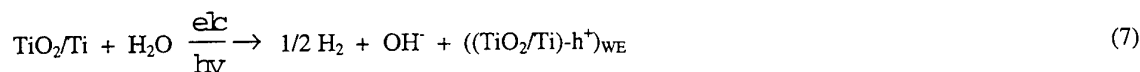
Photoelectrochemical Mechanism on TiO_2/Ti Electrode

Applying an anodic bias potential to a working electrode provides a potential gradient within the photocatalyst film to efficiently drive away the photogenerated holes and electrons at opposite directions [10-11,14-15,18-19]. From the experimental data of the photocurrent measurements, the mechanism of our device on the TiO_2/Ti working electrode and the Pt counter electrode by the applying bias potential can be expressed by Eqs. (4) to (6).



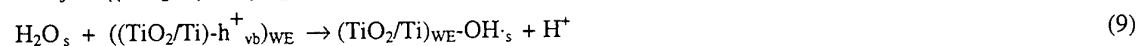
Where the subscripts cb and vb denotes the conduction and valence band of the photocatalyst, respectively, and WE and CE denote the working and counter electrode, respectively.

Total reaction:



The schematic illustration of photooxidation of nitrite ion and generation of hydrogen by applying bias potential on the working electrode are illustrated as Fig. 3. Eqs. (4) to (5) indicate that the applying bias potential makes more available holes for nitrite ion oxidation on the working electrode. Eq. (6) indicates that the photo-electrons induce the reduction reaction, and generate H_2 and OH^- on the counter electrode [26]. Eq. (7) is a combination of Eqs. (4) to (6), indicating that the applying bias potential promotes photoactivity of the rutile form of TiO_2 film, and makes more available holes on the electrode for the photocatalytic oxidation reaction.

The holes on the TiO_2/Ti electrode react with the OH^- anion or H_2O molecules adsorbed on the TiO_2 surface, i.e. OH^-_s and H_2O_s , to generate the OH free radical [22].



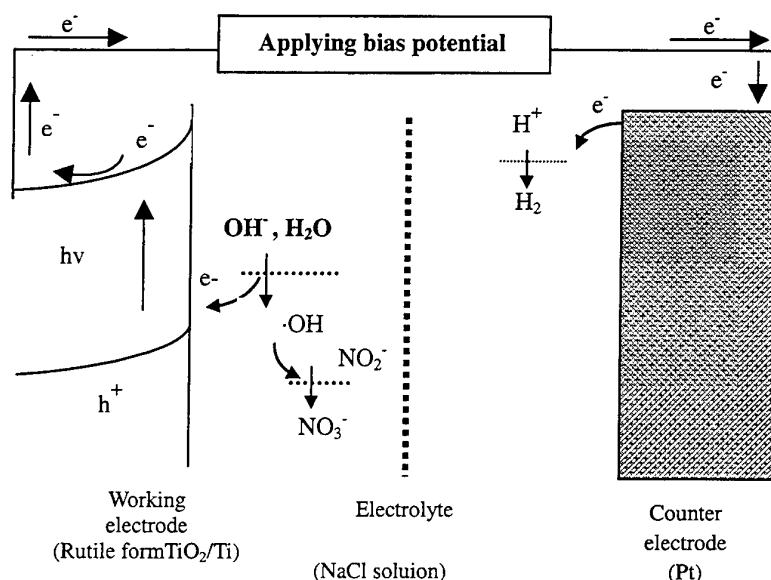
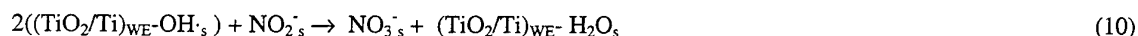
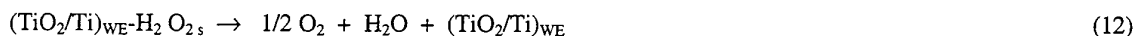
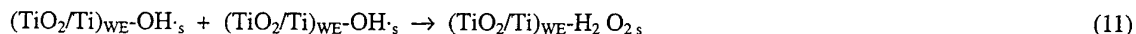


Figure 3. Schematic illustration of photooxidation of nitrite ion and photogeneration of hydrogen by applying bias potential on the working electrode (vs. Ag/AgCl).

The generated OH free radical is used to oxidize the nitrite ion adsorbed on the TiO₂ surface, i.e. NO₂⁻_s [22,23]



Eq. (10) is the main reaction of this photocatalytic oxidation reaction. In addition, the OH free radical on the TiO₂ surface of the TiO₂/Ti electrode may combine to generate oxygen or lose its activity at adsorbate [21,22].



Besides the main reaction, Eq. (11) to (13) are the side reactions of this nitrite ion oxidation.

Effect of Applying Bias Potential

Fig. 4 shows the effect of applying bias potential on the reaction rate of nitrite ion oxidation and hydrogen generation. Increasing the applying bias potential from 0.00 to 2.00 V (vs. Ag/AgCl), the reaction rate of nitrite ion oxidation increased from 3.05 to 7.60 μmole/(ℓ min). Further increasing the bias potential from 2.00 to 4.00 V, the reaction rate increased slowly from 7.60 to 8.10 μmole/(ℓ min) as shown in Fig. 4. The applying bias potential significantly promotes the reaction rate, but has a limitation of promotion when the applying bias potential is higher than 2.00 V (vs. Ag/AgCl). In addition, Fig. 4. also shows that increasing the applying bias potential from 0.00 to 4.00 V (vs. Ag/AgCl) increased the hydrogen generation rate from 0.75 to 5.81 μmole/min. Therefore, applying bias potential enhances the reaction rates of nitrite ion oxidation and hydrogen generation. Fig. 5 shows the photocurrent efficiency (η) and photoefficiency (Φ₁) of nitrite ion oxidation.

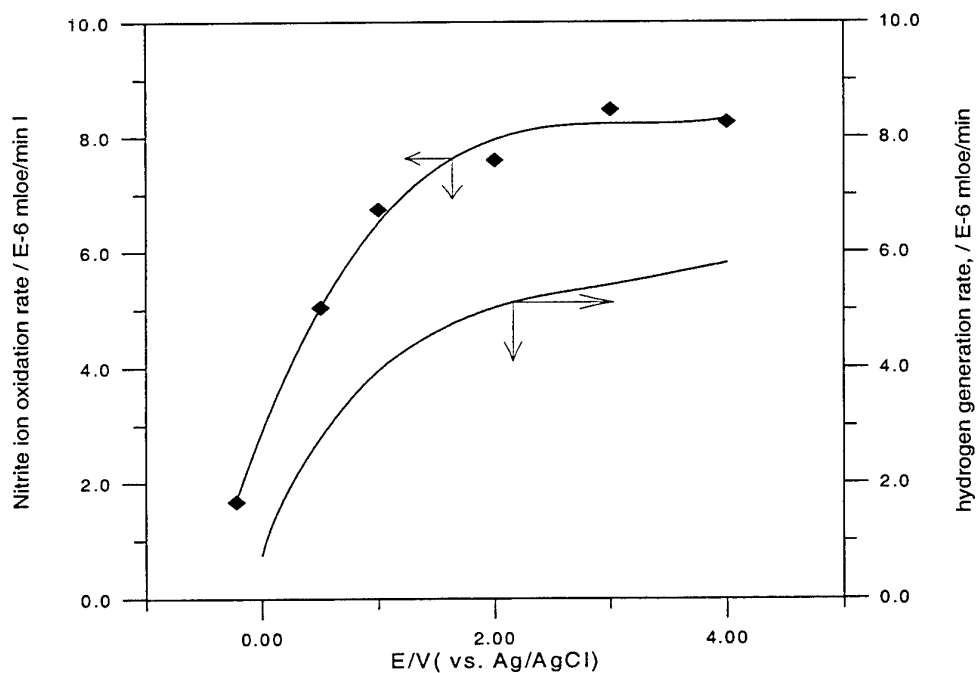


Figure 4. Effect of applying bias potential on both the initial reaction rates of nitrite ion oxidation and hydrogen generation. initial nitrite ion concentration, 20 ppm; temperature, 30°C; agitation rate, 250 rpm; electrolyte, 0.51 M NaCl, pH_i=5.50; light power, 400W.

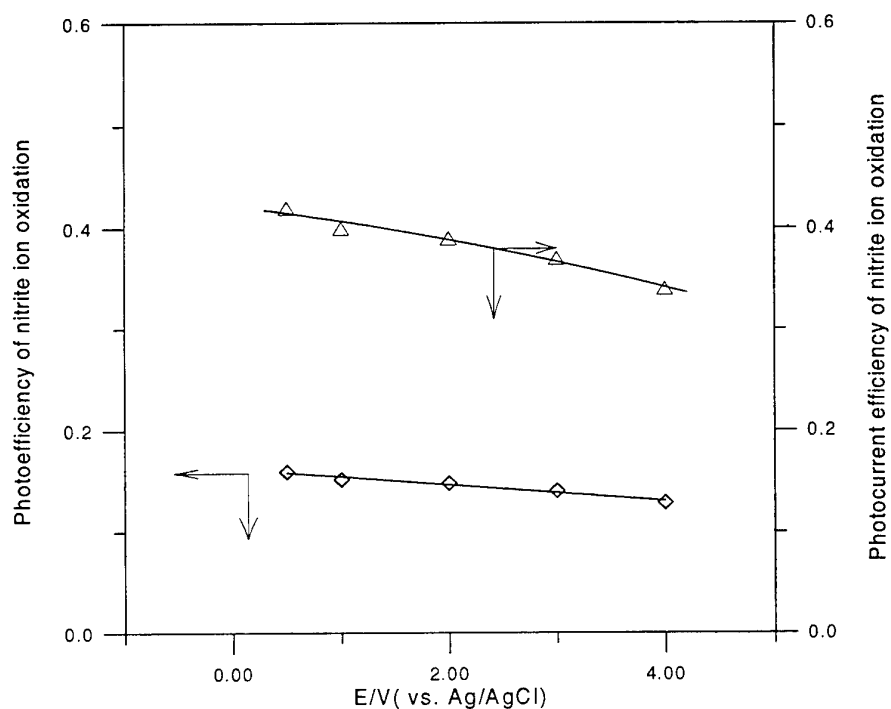


Figure 5. Effect of applying bias potential on both the photocurrent efficiency (η) and the photoefficiency (ϕ_i) of nitrite ion oxidation. initial nitrite ion concentration, 20 ppm; temperature, 30°C; agitation rate, 250 rpm; electrolyte, 0.51 M NaCl, pH_i=5.50; light power, 400W.

Effect of Light Power

Increasing the light power from 360 to 640 watts increases the reaction rate of nitrite ion oxidation from 6.56 to 10.48 $\mu\text{mole}/(\ell \text{ min})$, and increases the hydrogen generation rate from 3.95 to 6.03 $\mu\text{mole}/\text{min}$ as shown in Fig. 6. In general, a higher light power generates more holes and electrons. Both the nitrite ion oxidation rate and hydrogen generation rate are enhanced by the generated holes and electrons.

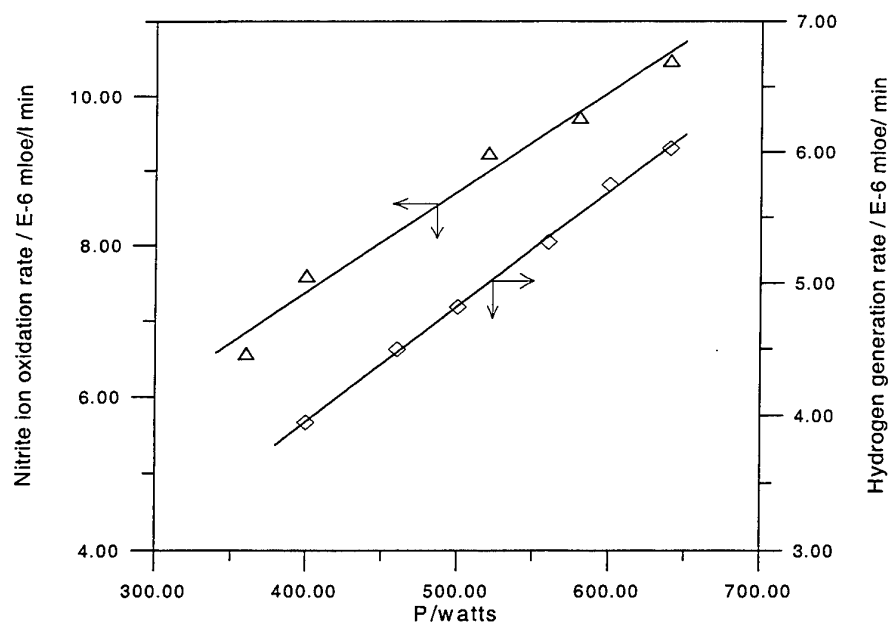


Figure 6. Effect of light power on the initial reaction rate of nitrite ion oxidation and the hydrogen generation rate: initial nitrite ion concentration, 20 ppm; temperature, 30°C; agitation rate, 250 rpm; potential, 2.00 vs. Ag/AgCl; electrolyte, 0.51 M NaCl, $\text{pH}_i=5.50$.

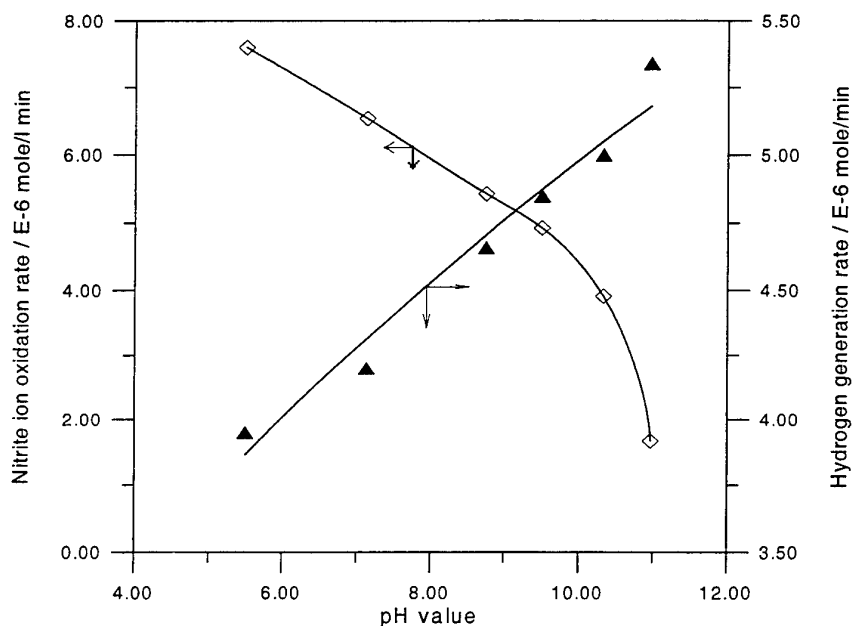


Figure 7. Effect of pH on both the initial reaction rate of nitrite ion oxidation and hydrogen generation rate. Initial nitrite ion concentration, 20 ppm; temperature, 30°C; potential, 2.00 vs. Ag/AgCl; agitation rate, 250 rpm; potential, 2.00 vs. Ag/AgCl; electrolyte, 0.51M NaCl; light power, 400W.

Effect of pH

Increasing the pH from 5.50 to 11.00 decreases the reaction rate from 7.60 to 1.67 $\mu\text{mole}/(\ell \text{ min})$ as shown in Fig. 7. When the pH is larger than 10.30, the reaction rate decreases sharply. In addition, the hydrogen generation rate increased from 3.95 to 5.34 $\mu\text{mole}/\text{min}$ when the pH was increased from 5.50 to 11.00, as shown in Fig. 7. Therefore, under basic conditions, the reaction rate of nitrite ion oxidation decreases sharply, but the hydrogen generation rate still increases.

4. CONCLUSIONS

The photocatalytic oxidation of nitrite ion in a NaCl aqueous solution can be electrochemically promoted by applying bias potential on the rutile form of a TiO_2 film electrode. The applying bias potential promotes the photoactivity of the rutile form of TiO_2/Ti electrode, and enhances the photocurrent density, the photoefficiency of hydrogen generation. The photoelectrochemical oxidation rate of nitrite ion is promoted by increasing both the light power and applying bias potential, and is decreased by increasing the pH. The maximum value of the photocurrent efficiency of nitrite ion oxidation was about 40%, indicating that more than 50 % of the OH free radicals lose its activity on the surface of the TiO_2 photocatalyst. The photocurrent efficiency of nitrite ion oxidation decreased slowly with increased applying bias potential. Using the value of photocurrent efficiency of nitrite ion oxidation, the oxidation rate of the nitrite ion can be evaluated by photocurrent measurement only.

ACKNOWLEDGEMENT

The support of National Science Council of the Republic of China, National Chung Kung University and Yung-Ta Industrial Commercial College are acknowledged

REFERENCES

1. M.R. Hoffmann, S.T. Martin, W. Choi and D.W. Bahnemann, *Chem. Rev.* v.95, pp. 69-96 (1995).
2. M. Andrew, H.D. Richard and W. David, *Chem. Soc. Rev.* pp. 417-425 (1993).
3. A. Hagfeldt and M. Gratzel, *Chem. Rev.* v.95, pp. 49-68 (1995).
4. P.V. Kamat, *Chem. Rev.* v. 93, pp.267-300 (1993).
5. A. Fujishima and K. Honda, *Nature* v.238, pp. 37- 38 (1972).
6. K. Rajeshwar, *J. Appl. Electrochem* v.25, pp. 1067-1082 (1995).
7. M. Butterfield, P.A. Christensen and C.R. Howarth, *J. Appl. Electrochem* v.27, pp. 385-395 (1997).
8. G.P. Lepore, L. Persand and C.H. Langford, *J. Photochem. Photobiol. A. Chem* v.98, pp.103-111 (1996).
9. H. Tada and H. Hon, *J. Electrochem. Soc.* v.142, pp. 3438-3443 (1995).
10. K. Vinodgopal and P.V. Kamat, *Chemtech.* April, pp. 18-22 (1996).
11. I.M. Butterfield, P.A. Christensen, T.P. Curtis and J. Gunlazuardi, *Wat. Res* v.31, pp.675 (1997).
12. L.C. Chen and T.C. Chou, *Ind. Eng. Chem. Res* v.32, pp.1520-1527 (1993).
13. L.C. Chen and T.C. Chou, *Ind. Eng. Chem. Res* v.33, pp. 1436 (1994).
14. K. Vinodgopal, S. Hotchandani and P.V. Kamat, *J. Phys. Chem* v.97, pp. 9040-9044 (1993).
15. K. Vinodgopal, U. Stafford, K.A. Gray and P.V. Kamat, *J. Phys. Chem* v.98, pp. 6797-6803 (1994).
16. R.I. Bickle, T.G. Carreno, J.S. Lees, L. Palmisano and J.D. Richard Tilley, *J. Solid. State. Chem* v.92, pp.178-190 (1991).
17. J. Augustynski, *Electrochimica. Acta* v.38, pp. 43-46 (1993).
18. D. H. Kim and M. A. Anderson, *Environ. Sci. Technol* v.28, pp. 479-483 (1994).
19. D. H. Kim, M. A. Anderson and W. A. Zeltner, *J. Environ. Engng* August, pp. 590-594 (1995).
20. Y. Hori, A. Bandoh and A. Nakatsu, *J. Electrochem. Soc.* v.137, pp. 1155-1161 (1990).
21. Y. Hori and N.S. Suzuki, *Chem. Lett* pp. 1429 (1985).
22. Z. Antonio and X. Domenech, *J. Mol. Catal* v.70, pp. 343-349 (1991).
23. A. Milis, J. Peral and X. Domenech, *J. Mol. Catal* v.87, pp. 67-74 (1994).
24. C.C. Sun and T.C. Chou, *Ind.Eng.Chem.Res* v.37, pp. 4207-4214 (1998).
25. APHA, Standard Method for the Examination of Water and Wastewater, 17 th Ed., Methods 4500-NO-B, pp.4-1129~4-131, Washington, D.C. (1989).
26. N.N. Rao and S. Dube, *Int. J. Hydrogen Energy* v.21, pp. 95-98 (1996).

S. Combustion and Fire

NO_x AND CO EMISSIONS OF METHANE/AIR FILTRATION COMBUSTION WAVES

J.P. Bingue, A.V. Saveliev, A.A. Fridman and L.A. Kennedy

Department of Mechanical Engineering,

University of Illinois at Chicago,

Chicago, IL 60607

Email: lkennedy@uic.edu; Fax: (312) 996-8664

Keywords: combustion, filtration combustion, porous media, pollutant emissions

ABSTRACT. Emission characteristics of the filtration combustion waves freely propagating in an inert packed bed are studied experimentally. The waves were formed under filtration of lean and ultra-lean methane/air mixtures with equivalence ratios from 0.25 to 0.9 and filtration velocities from 10 to 40 cm/s. Downstream (superadiabatic) and upstream (underadiabatic) propagation of filtration combustion waves was observed depending from experimental conditions. Stabilized by intensive heat transfer in the traveling wave, the combustion temperature shows only small variation (100 to 200 K) over the range of the equivalence ratios studied. The NO_x and CO emissions are found to be very low throughout ultra-lean region ($\phi < 0.5$). In this area, NO_x levels are lower than 4 ppm and CO levels are below 10 ppm. The NO_x concentration grows with equivalence ratio, while faster filtration velocities correspond to higher NO_x levels. Measured CO emissions are only slightly influenced by experimental conditions at the equivalence ratios below 0.8. More complex behavior is observed for $\phi > 0.8$. In this region the experimental data shows rapid increase in CO concentrations after critical equivalence ratio, which is found to be lower for high filtration velocities.

INTRODUCTION

Stringent emission regulations imposed special requirements on the combustion technologies for the new millennium. This fosters the development of novel combustion techniques [1]. Among other concepts, combustion in a porous media offers a possible technological breakthrough, providing the basis for development of more efficient combustion systems with low and ultra-low pollutant emissions. The applications of porous combustion developed for the last years include porous radiant burners (see, for example, porous media combustor-heaters [2,3], porous burners for pollution control [4,5], and reverse-flow filtration burners [6,7,8])

The filtration combustion of gaseous mixtures in porous media differs significantly from the homogeneous flames or normal fluidized beds. This difference is attributed to following main factors: (1) the highly developed inner surface of the porous medium results in the efficient heat transfer between gas and solid; (2) turbulent structure of the gas flow through porous media increases effective diffusion and heat transfer in the gas phase. These factors ensure stable combustion over a wide range of filtration velocities, equivalence ratios, and power loads.

Effectively arranged heat transfer from the reacting gas to the porous media and from the porous media to the surroundings decreases peak flame temperatures, thus providing the basis for reduced NO_x formation. In the porous radiant burner, the strong emission of thermal radiation from the solid matrix provides an energy sink from the combustion zone. In the surface combustor-heater system the heat is transferred from the hot combustion gases and the porous matrix to a system of cooling tubes embedded directly in the porous combustion zone.

The stationary and transient systems are the two major design approaches commonly employed in porous burners. The former is widely used in radiant burners and surface combustor-heaters. Here, combustion zone is stabilized in the finite element of porous matrix by the imposed boundary conditions. However, in unrestricted uniform porous media, the combustion zone is usually unsteady and can freely propagate as a combustion wave in the downstream or upstream direction. Strong interstitial heat transfer results in a low degree of thermal non-equilibrium between gas and solid. These conditions correspond to the low-velocity regime of filtration gas combustion, according to classification given by Babkin [9]. The relative displacement of the combustion zone results in positive or negative enthalpy fluxes between the reacting gas and solid carcass. As a result, observed combustion temperatures can be significantly different from the adiabatic predictions and are controlled mainly

by the reaction chemistry and heat transfer mechanism. The upstream wave propagation results in the underadiabatic combustion temperatures [10] while the downstream propagation of the wave leads to the combustion in superadiabatic regime with temperatures much in excess of the adiabatic one [11]. Superadiabatic combustion significantly extends conventional flammability limits to the region of ultra-low heat content mixtures. The principles of transient filtration combustion is practically realized in several burner geometries, including linear reactors, moving bed reactors, and reciprocal-flow burners. The modern applications of transient porous burners include combustion of low-calorific fuels, VOC emissions control with possible waste-to-heat recovery [7], and fuel reforming in the ultra-rich superadiabatic flames [12,13].

While there is a number of studies devoted to the emissions of stabilized porous burners, the data on emission characteristics of unrestricted filtration combustion waves are limited. These data can be as important for development of practical porous media burners as emission characteristics of laminar flames in homogeneous combustion.

In the present work the emission characteristics of the one-dimensional combustion waves formed under filtration of methane/air mixtures in an inert packed bed are studied experimentally. Resulting CO and NO_x emissions were measured over a wide range of equivalence ratios and gas velocities for lean underadiabatic and ultra-lean superadiabatic combustion waves.

EXPERIMENTAL SETUP

Filtration combustion waves were initiated in a linear packed bed reactor. The linear reactor was a quartz tube with an internal diameter 38 mm. The tube contained a uniform packed bed of 3-mm diameter spherical alumina particles. The diagnostic part of the reactor is 45-cm long. To minimize heat losses, the outer reactor wall was covered with a 5-cm thick high-temperature insulation layer. Additional 2-mm thick layer of insulation was used to cover inner wall of the tube. This layer was used to minimize possible effects of the packed bed - tube interface. The insulation of the tube ensures low temperature gradients across the combustion zone, providing essentially one-dimensional structure of the combustion waves. The small internal diameter of the reactor is selected to suppress development of inclination instabilities, experimentally observed for downstream propagating waves [14].

Combustion mixtures were composed from dried air and 97% pure methane. A system of mass flow controllers (Model 1179A, MKS Inc.) was used to independently control the air to fuel ratio and total gas flow rate. The accuracy provided by the controller system was better than 3% for all experimental runs conducted. The mixing chamber was used to ensure uniform gas composition at the reactor entrance. The gas mixture was introduced in the reactor through the distribution grid at the reactor bottom.

The composition of the combustion products were measured at the reactor exit. The gas was continuously sampled by an inert ceramic probe positioned radially 3 cm into the packed bed and connected to a sampling pump. Sampled gases were dried and directed to in-line NO_x and CO analyzers. Chemiluminescence NO-NO₂-NO_x analyzer (Model 42H, Thermo Environmental Instruments, Inc.) and infrared CO analyzer (Model 867, Beckman Inc.) were used to record emission levels. Both analyzers were calibrated using span CO and NO gases before each experimental run.

The temperature measurements were conducted by a set of S-type thermocouples inserted with staggered junctions in a multibore ceramic tube. The tube was centrally positioned along the reactor axis. Additional side thermocouples were radially inserted in the packed bed. Their junctions were located close to the reactor wall. These thermocouples were used to control uniformity of radial temperature distribution. Signals from thermocouples and analyzers were continuously digitized and stored by the PC-based data acquisition system. During the experiments, the combustion wave was initiated at the reactor outlet. Then upstream propagation was recorded. As the wave reached the reactor bottom, the experimental conditions were adjusted to a required setting and the downstream propagating wave was recorded on the reverse run.

RESULTS AND DISCUSSION

The properties of filtration combustion waves formed in the combustion reactor were studied experimentally in

the range of equivalence ratios $0.25 < \phi < 0.95$ and filtration velocities from 10 to 40 cm/s. The time-dependent temperature profiles were recorded and further processed to infer peak combustion temperatures (T_c) and wave velocities (u_w).

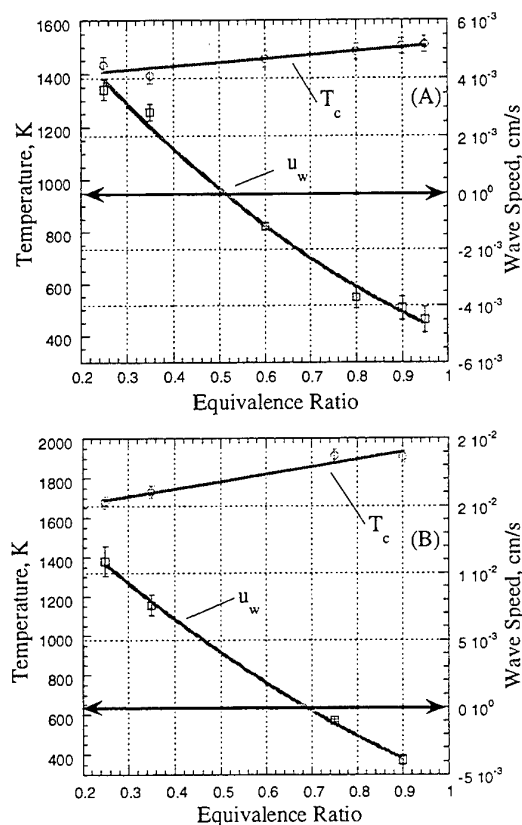


Fig. 1. Peak temperatures and propagation velocities of the combustion waves formed in the 3-mm alumina packed bed under filtration of lean methane/air mixtures. Filtration velocity (a) 12 cm/s and (b) 36 cm/s mixtures.

Figure 1 shows data obtained for filtration velocities of 12 cm/s and 36 cm/s. These experimental conditions correspond to the lower and upper limit of the studied flow rates. Due to the wave displacement in the packed bed, the combustion temperature (Fig. 1) remains practically constant with variation of equivalence ratio. For filtration a velocity 12 cm/s, the combustion temperature is equal to 1420 K at equivalence ratio $\phi = 0.25$ (Fig 1a.). Combustion temperatures slightly grow with the increase of fuel content, reaching 1520 K at an equivalence ratio $\phi = 0.9$. Thus, the overall temperature variation is close to 100 K for more than a threefold increase of the fuel content in the mixture. It is found, that an increase in the gas velocity leads to higher combustion temperatures. Relative to that obtained for a filtration velocity of 12cm/s, combustion temperatures were higher by almost 400 K for a filtration velocity 36 cm/s (Fig. 1b). The temperatures for equivalence ratios 0.25 and 0.9 are respectively 1700 K and 1900 K. The maximum temperature variation observed (~ 200 K) remains small in comparison with the variation of the heat content in the supplied methane/air mixture. Overall, the experimental are respectively 1700 K and 1900 K. The maximum temperature variation observed (~ 200 K) remains small in comparison with the variation of the heat content in the supplied methane/air mixture. Overall, the experimental data show that temperature dependence from equivalence ratio is well approximated as a linear function

While the combustion temperature varies insignificantly in the lean and ultra-lean region, the propagation of the combustion wave changes drastically with the fuel content. These include both velocity and direction of propagation. For filtration velocity of 12 cm/s and an equivalence ratio $\phi = 0.25$, the combustion wave propagates downstream with a velocity $u_w = 4 \times 10^{-3}$ cm/s. Downstream propagation causes positive heat recirculation from preheated porous body, allowing excess-enthalpy combustion in so-called superadiabatic regime. The superadiabatic propagation is observed over the range of equivalence ratios from 0.25 to 0.5. The wave velocity decreases as the fuel content increases, approaching zero at $\phi \approx 0.5$. The direction of propagation changes for $\phi > 0.5$ and the wave propagates upstream at higher equivalence ratios. During upstream travel the portion of the combustion heat release is consumed to preheat the upstream packed bed layers and overall combustion temperatures can be significantly less than adiabatic. The wave accelerates as the equivalence ratio increases and reaches a propagation velocity $u_w = 4 \times 10^{-3}$ cm/s at $\phi \approx 0.9$.

For a filtration velocity of 36 cm/s, the region of downstream (superadiabatic) propagation is extended to the range of equivalence ratios $0.25 < \phi < 0.7$. Conversely, the region of upstream propagation is narrowed to equivalence ratios $\phi > 0.7$. The shift of the transition point to the higher equivalence ratios is mainly due to the

rise in the combustion temperatures at higher gas velocities. The increase in the gas velocity from 12 to 36 cm/s induces almost a threefold increase in the combustion wave velocity at $\phi = 0.25$. However, the velocities of the waves traveling upstream at an equivalence ratio 0.9 remain close to $u_w = 4 \cdot 10^{-3}$ cm/s.

The overall relation between the combustion temperature, gas mixture filtration velocity and the velocity of wave propagation is well illustrated by heat balance equation of the filtration wave [11].

$$u/v_f = K (1 - \Delta T_a / \Delta T_c) \quad (1)$$

where K is the constant depending from the porosity and heat properties of the packed bed, ΔT_a is the adiabatic temperature rise and ΔT_c is the peak temperature rise in the combustion wave. The heat balance can be extended to the case of lateral heat losses, introducing the effective coefficient for heat exchange with surroundings [11]. Equation (1) shows that when the fuel concentration and hence adiabatic temperatures T_a are very small, the combustion wave velocity is positive and close to the thermal wave velocity. When the fuel concentration is increasing but $\Delta T_a < \Delta T_c$, the wave propagates downstream with the velocity decreasing to zero. Standing wave exists when ΔT_a is equal to ΔT_c .

As the fuel content rises further, the adiabatic temperature exceeds the combustion temperature. The left term in Eq. (1) becomes negative and the wave propagates upstream with the absolute velocity value increasing with equivalence ratio. Experimentally recorded combustion temperatures are presented in Fig. 2 along with calculated adiabatic temperatures of the filtered mixtures. Combustion temperatures significantly exceed adiabatic values at ultra-lean conditions. With an increase of the equivalence ratio, the gap narrows and at a certain point the temperature becomes equal. This critical point is $\phi = 0.5$ for filtration velocity 12 cm/s, and $\phi = 0.72$ for $v_f = 36$ cm/s. Figure 1 shows that these conditions correspond to the change in the direction of the combustion wave propagation.

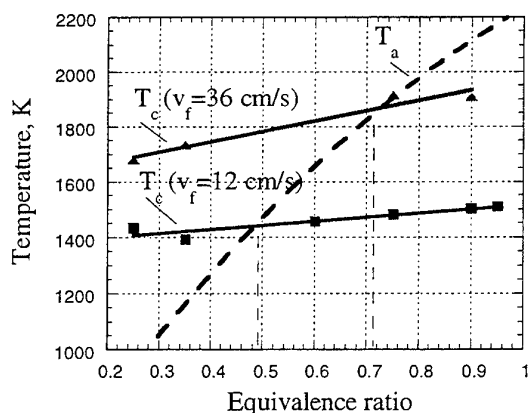


Fig. 2. Peak combustion wave temperatures versus equivalence ratio. Filtration velocities of methane/air mixtures are 12 and 36 cm/s. Adiabatic combustion temperature is given for reference.

It is worth noting also (see Fig. 2), that in superadiabatic regime the temperatures can be enhanced by as much as 700 K, while in the underadiabatic region the temperatures can be reduced by almost the same value. According to Eq. (1), the velocity of the filtration wave is directly proportional to the gas velocity if the combustion temperature is constant. However, the combustion temperature also rises with the gas velocity in order to sustain the complete combustion at reduced residence times. This causes characteristic non-linear dependence of wave velocity from the gas flow rate. The combustion temperature rise cause additional acceleration of the combustion wave propagating at superadiabatic regime ($\phi = 0.35$, Fig. 3). More complicated dependence is observed for underadiabatic propagation. The combustion wave at equivalence ratio 0.9 initially accelerates, reaching the maximum absolute value at $v_f = 12$ cm/s (Fig. 3). Further increase of the gas velocity slows the wave down. Finally, the direction of the wave propagation can be reversed at high flow rates, increasing combustion temperature above adiabatic value [10]. In the range of filtration velocities studied, the

wave reversal was observed in the range of equivalence ratios from 0.5 to 0.7.

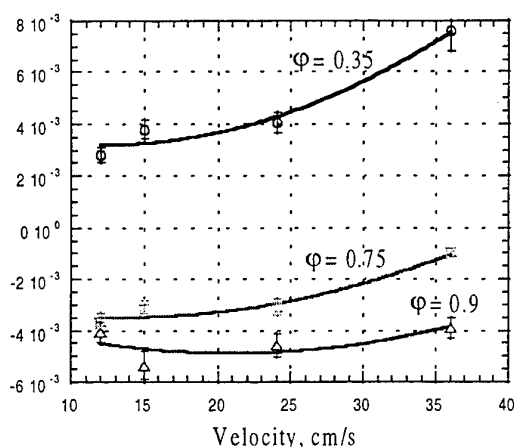


Fig. 3. Combustion wave velocities as a function of gas filtration velocity.

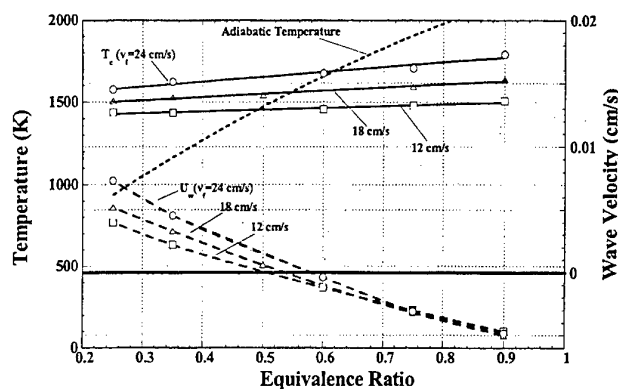


Fig. 4. Combustion wave temperature and velocity, Filtration velocity = 12, 18, 24 cm/s

NO_x and CO emissions were monitored continuously during the experimental runs. It was found that measured NO_x concentration was quite independent from the wave position along the reactor length. The CO level was slightly increased with the wave approaching the reactor exit. For this reason, the reported emission measurements were collected for the wave positions at least 15 cm upstream from the exit.

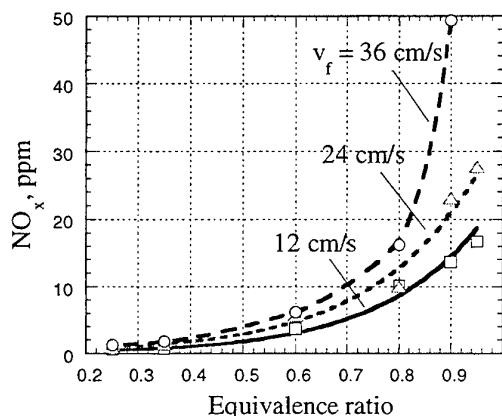


Fig. 4. Measured NO_x emissions versus equivalence ratio of methane/air mixtures filtered with gas velocities 12, 24, and 36 cm/s.

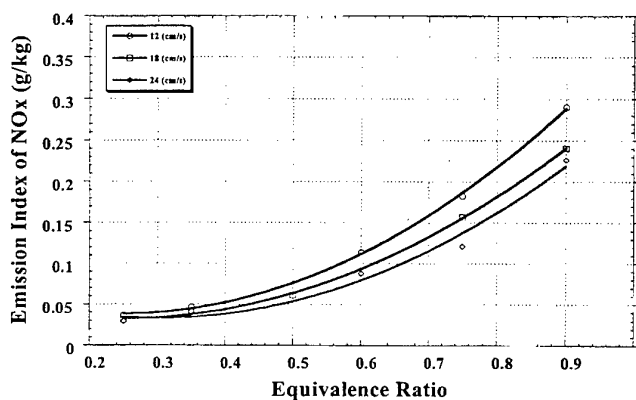


Fig. 5. Emission index of NO_x , Filtration velocity = 12, 18 and 24 cm/s

Figure 4 shows NO_x concentrations obtained at experiments with filtration velocities 12, 24, and 36 cm/s. It was observed that NO_x concentration rises with an increase in ϕ for all studied filtration velocities. Typically, the NO_x emissions are very low (0.5 to 4 ppm) in the region of ultra-lean equivalence ratios $\phi < 0.5$. The NO_x levels measured for different filtration velocities at $\phi = 0.25$ are very close and fall within the experimental error, despite the combustion temperatures differing by almost 400 K. Significant difference is observed at high equivalence ratios. At $\phi = 0.9$, NO_x level increases to 14 ppm for a filtration velocity $v_f = 12$ cm/s while NO_x concentration rises more rapidly at filtration velocity 36 cm/s, reaching 50 ppm at $\phi = 0.9$. This effect can be related to the high combustion temperatures obtained at higher filtration velocities and the influence of the Zeldovich NO mechanism. Concentrations of NO_x below 10 ppm were observed for all superadiabatic combustion regimes. Overall, the equivalence ratio is the strongest factor affecting the NO_x emission levels. It

should be noted that for $\phi < 0.7$, NO emissions were < 10 ppm. The emission index of NO_x increases with equivalence ratio. The characteristic values for $v_f = 12$ cm/s are 0.05 g/kg ($\phi = 0.25$) and 0.35 g/kg ($\phi = 0.95$). Figure 5 presents the NO_x emission index. For filtration velocities of 12, 18 and 24 cm/s, the emission index is 0.04 g/kg at $\phi = 0.25$ within experimental resolution. At $\phi = 0.9$, the NO_x index rises to 0.23 g/kg at $v_f = 12$ cm/s to 0.29 g/kg at $v_f = 24$ cm/s.

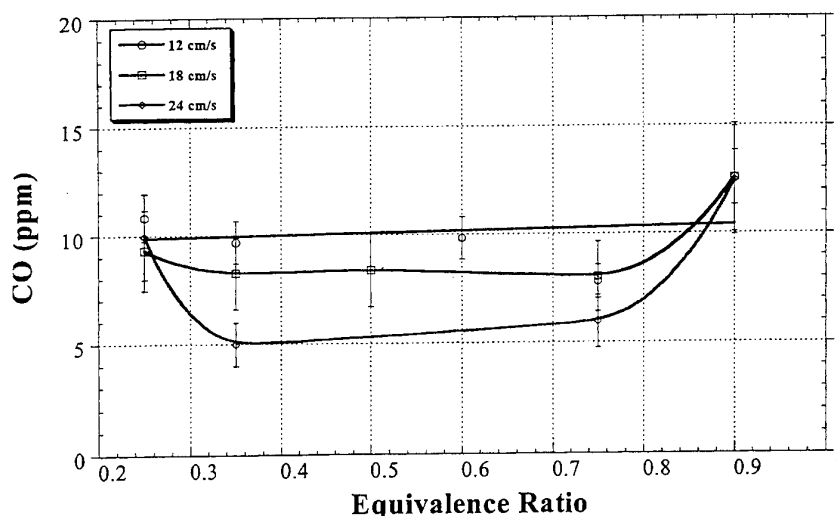


Fig. 6. CO emission levels as a function of equivalence ratio. Filtration velocities of methane/ air mixtures are 12, 24, and 36 cm/s.

Observed CO levels are low and never exceed 15 ppm (Fig. 6). For filtration velocity $v_f = 12$ cm/s, CO remains practically constant at about 10 ppm over the equivalence ratio $0.25 < \phi < 0.9$. At a filtration velocity 24 cm/s, the CO level remains fairly constant at 5-6 ppm for equivalence ratios $0.3 < \phi < 0.75$. The rise for $\phi > 0.75$ is consistent with predictions. At $\phi = 0.25$ for $v_f = 24$ cm/s, the extinction limit was approached and could account for the increase in CO.

CONCLUSIONS

Emission characteristics of the filtration combustion waves freely propagating in an inert packed bed were examined. The waves were formed under filtration of lean and ultra-lean methane/air mixtures with equivalence ratios from 0.25 to 0.9 and filtration velocities from 10 to 40 cm/s. Downstream (superadiabatic) and upstream (underadiabatic) propagation of filtration combustion waves was observed depending from experimental conditions. Stabilized by intensive heat transfer in the traveling wave, the combustion temperature shows only small variation (100 to 200 K) over the range of the equivalence ratios studied.

The NO_x and CO emissions are found to be very low ($\text{NO}_x < 4$ ppm, $\text{CO} < 10$ ppm) throughout the ultra-lean region ($\phi < 0.5$). Ultra-low emission characteristic of superadiabatic combustion is beneficial for its application in the pollution control and low-calorific fuel burning. It is found that NO_x concentration and emission index grow with equivalence ratio, while faster filtration velocities correspond to higher NO_x levels. Overall, the equivalence ratio is the strongest factor affecting the NO_x emission levels through its influence on the combustion wave velocity and temperature. Measured CO emissions are only slightly influenced by experimental conditions at equivalence ratios below $\phi < 0.8$.

ACKNOWLEDGEMENTS

The authors wish to acknowledge the support of the National Science Foundation through grant # 9812905 and the support of the Air Liquide Corp.

NOMENCLATURE

K	constant	v_f	filtration velocity
T_a	adiabatic temperature	u_w	wave velocity
T_c	combustion temperature	ϕ	equivalence ratio

REFERENCES

1. L.A. Kennedy, A.A. Fridman, A.V. Saveliev; Transient Filtration Combustion, Proc Mediterranean Combustion Symposium. (1999)
2. T.W. Tong, S.B. Sathe, Heat Transfer characteristics of Porous Radiant Burners, *J. of Heat Transfer*, Vol. 113, pp. 423-429. (1991).
3. M.D. Rumminger, R.W. Dibble, N.H. Heberle, Crosley D.R.. Gas Temperature Above a Porous Radiant Burner : Comparison of Measurements and Model Predictions, *26th Symposium (1996) (International) on Combustion*, The Combustion Institute, Pittsburgh, pp. 1755-1762.
4. M.J. Khinkis, W. Kunc, T.Y. Xiong, Experimental Evaluation of a High Efficiency Surface Combustor-Heater Concept with Low Pollutant Emissions, *AFRC 1989 International Symposium*, Short Hill, New Jersey, pp. 1 -21. (1989).
5. A.A. Mohamad, R. Viskanta, S. Ramadhyani, Numerical Predictions of Combustion and Heat Transfer in a Packed bed with Embedded Coolant Tubes, *Combustion Science and Technology*, Vol. 96, pp. 387-407. (1994).
6. D. Trimis, F. Durst, Combustion in a Porous Medium - Advances and Applications, *Combustion Science and Technology*, Vol. 121, pp. 153-168. (1996).
7. K. Hanamura, R. Echigo, S.A. Zhdanok, Super Adiabatic Combustion in Porous Media, *International Journal of Heat and Mass Transfer*, Vol. 36, pp 3201-3209. (1993).
8. M.K. Drayton, A.V. Saveliev, L.A. Kennedy, A.A. Fridman, Y.-E. Li., Syngas Production Using Superadiabatic Combustion of Ultra-Rich Methane-Air Mixtures, *27th Symposium (International) on Combustion*, The Combustion Institute, Pittsburgh, pp. 1361-1367. (1998)
9. V.S. Babkin, Filtration Combustion of Gases. Present State of Affair and Prospects, *Pure and Applied Chemistry*, Vol. 65, pp. 335-344. (1993).
10. Laevskii, M. Yu, V.S. Babkin, Filtration Combustion of Gases, in *Propagation of Heat Waves in Heterogeneous Media*, Ed. Yu. Matros, p. 108-145, Nauka, Novosibirsk. (1982).
11. S. Zhdanok, L.A. Kennedy, G. Koester, Superadiabatic Combustion of Methane Air Mixtures under Filtration in a Packed Bed, *Combustion and Flame*, Vol. 100, pp. 221-231. (1995).
12. L.A. Kennedy, A.A. Fridman, A.V. Saveliev, Superadiabatic Combustion in Porous Media: Wave Propagation, Instabilities, New Type of Chemical Reactor, *Fluid Mechanic Research*, Vol. 22, pp. 1-26. (1995).
13. S.S. Minaev, S.I. Potytnyakov, V.S. Babkin, Combustion Wave Instability in the Filtration Combustion of Gases, *Combustion Explosion and Shock Waves*, Vol. 30, pp. 306-310. (1994).

ACCELERATION OF FLAMES AND TRANSITION FROM DEFLAGRATION TO DETONATION DUE TO THE INFLUENCE OF HIGHLY BLOCKING OBSTACLES

C. Gerlach*, A. Eder, M. Jordan, F. Mayinger

Lehrstuhl A für Thermodynamik

Technische Universität München, Germany

Email: gerlach@thermo-a.mw.tum.de; Fax: +49 89 289-16218

Keywords: combustion, hydrogen, jet-ignition, DDT, optical measurement-techniques

ABSTRACT. Obstacles in the path of a flame lead to a significant increase of the turbulence in the expansion flow in front of the flame and therefore, have a strong influence on the combustion process itself. The present paper deals with the aspect of flame quenching due to the turbulence induced by one highly blocking obstacle in hydrogen-air mixtures and the resulting acceleration of the flame. In case of sensitive mixtures it is possible to obtain a transition from the deflagrative to the detonative combustion mode (DDT). Several experiments were performed in facilities of different dimension in order to investigate the physical phenomena for the jet ignition behind the obstacle. Non-intrusively optical measurement techniques were used to obtain information on the flow field, the turbulence intensity in the expansion flow directly in front of the flame, and the structure of the flame itself.

1. INTRODUCTION

The combustion of hydrogen/air mixtures can lead to high pressure loads depending on the mode of combustion either deflagrative or detonative. In case of a hydrogen release during a hypothetical accident in a closed building, fast combustion processes have to be avoided under all circumstances, as their corresponding high pressure loads can endanger the integrity of a building. The objective of this work is to help the understanding of the combustion process influenced by highly blocking obstacles, which simulate two connected rooms e.g. by a door or a window. The difference of the density of hot burned and cold unburned gas leads to an expansion flow in front of the flame. This expansion flow can be highly turbulent due to the interaction with obstacles like grids, tubes or walls with openings, even at low hydrogen concentrations. Since Damköhler [1] it is well known that large scale eddies tend to bend the flame and thereby increase the effective flame surface, which results in an acceleration of the flame. On the other hand, small scale eddies increase the heat and mass transfer in the preheating zone of the flame, which results in a thickening of the reaction zone and a higher reaction rate. Nevertheless, at a very high level of turbulence, the mass transfer due to the gas fluctuations in the preheating zone leads to an increasing heat loss and therefore to a local quenching or even total extinction of the flame.

2. EXPERIMENTAL FACILITIES

The basic phenomena of flame quenching for deflagrative combustion in highly turbulent jet flows were performed at two different scaled facilities, the *Large View*-facility (L.VIEW) at the University of Pisa (677 x 677 x 3000 mm) and the *Pulsed Flame Generator* (PuFlaG) (diameter $d=72$ mm, length $l=8$ m) at the Technical University of Munich. The facilities consist of two chambers, which are divided by a wall with a central orifice. Using different insets, the diameter of the orifice can be varied. Before ignition, both chambers are filled with the same hydrogen-air mixture. A more detailed description of these two facilities can be found in [2].

The Hot-Jet Explosion Tube at the Technical University of Munich was designed to perform DDT experiments with the corresponding high pressure loads. It consists of an acceleration section with a diameter $d_1=200$ mm and a length of $l_1=4$ m and a DDT-section with a diameter $d_2=600$ mm and a length of $l_2=4$ m that are connected by an orifice (see Fig. 1). Geometry and diameter of the orifice can be varied by changing the obstacle plate.

For the application of optical measurement techniques all facilities are equipped with optically accessible sections. In case of the L.VIEW-facility the whole front and upper side is made out of glass to get a full insight into the combustion process over the two chambers.

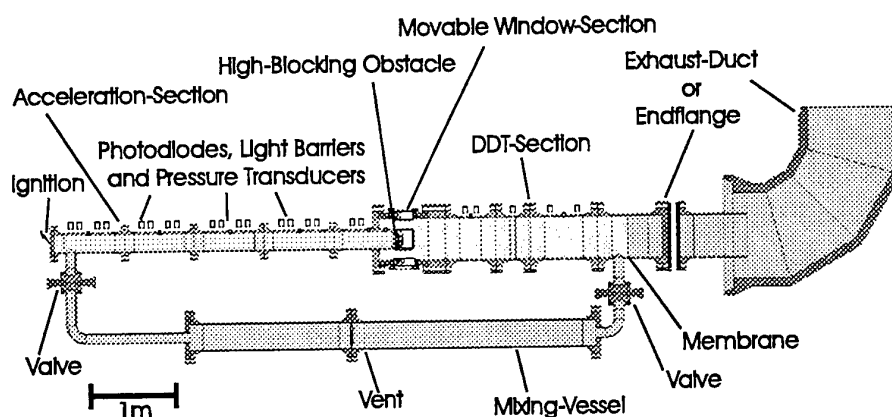


Figure 1: Schematic sketch of the hot-jet explosion tube.

3. MEASUREMENT TECHNIQUES

Optical Measurement Techniques

For the investigation of turbulent combustion processes, both, the chemical reaction as well as the turbulent flow field in front of the flame have to be determined with a high accuracy in time and in space. Therefore, optical measurement techniques are often used as they work inertialess and non-intrusively. Nevertheless, to investigate turbulent combustion processes, a combination of several measurement techniques is needed. Within this program, the flame propagation at the large scale experiments was recorded by means of an intensified high-speed video-camera simultaneously with the measurement of the turbulent flow-field directly in front of the flame by means of a Laser-Doppler-Velocimeter. In the small scale experiments, the flame propagation was visualised by means of the Schlieren-technique. The detailed flame-structure and the characteristic size of the eddies in the area of flame quenching was determined by means of the Laser-induced Predissociation Fluorescence.

High-speed video records. A digital high-speed video-camera was used for the recording of the flame propagation. For the present investigations a maximum repetition rate of 9.000 frames/s was used. As the light of the combustion process is too weak to be detected by the camera, a two stage image intensifier consisting of a Multiple-Channel-Plate and an Inverter-Diode was adapted to the system.

Schlieren technique. With the Schlieren-technique, the integral density gradient through the depth of the test section was visualised. In combination with the high-speed video-camera mentioned above, the flame propagation and the global structure of the flame was determined with a very high resolution in time.

Laser-Doppler-Velocimetry. The measurement of the flow velocity and the turbulence in front of the flame was performed by means of the Laser-Doppler-Velocimetry. With this technique, the velocity of tracer particles, which have to be added to the flow, can be determined in a measurement volume with a repetition-rate of several kHz in two directions simultaneously. Aerosols of a NaCl-solution with a mean diameter of $2.2 \mu\text{m}$ were used as tracer particles, which ensure a high tracking ability.

Laser-induced Predissociation-Fluorescence (LIPF). Applying this technique, selected radicals (e.g. OH^-) are excited by a high energy KrF excimer-laser ($\lambda=248 \text{ nm}$), within a two-dimensional light-sheet with a thickness of 0.3 mm and an exposure time of 17 ns . The answering signal of the radicals can be detected by means of an intensified CCD-camera perpendicular to the excitation. As the Laser-induced Predissociation-Fluorescence is species specific and the intensity of the scattered light is many orders of magnitudes stronger than those achieved by other light-scattering techniques (e.g. Raman-spectroscopy), it is a very important tool for detailed flame diagnostics.

Conventional Measurement Techniques

Several conventional transducers are used in the facilities to obtain information about pressure, temperature, as well as shock and flame velocities. Pressure records are made by means of fast piezoelectric pressure transducers and give detailed information about the maximum loads to the walls and the velocity of shock waves. The flame velocities are determined by means of UV-sensitive photodiodes that are positioned along the tubes. The UV-sensitivity is very important to detect the light emission of the reaction zone, which is limited to the UV wavelengths.

In the Hot-Jet explosion tube laser diode light barriers are used in addition to determine flame velocities due to the density gradients caused by the flame temperature.

4. EXPERIMENTAL RESULTS AND DISCUSSION

In Fig. 3, a representative experiment, which was performed at the L.VIEW-facility with a hydrogen concentration of 10.6 Vol.-% H_2 in air and a blockage ratio of $BR=99.2\%$, is shown. After the ignition in the left bottom corner of the first chamber, the flame burns under laminar conditions. As soon as the flame front reaches the influence of the obstacle, it is strongly accelerated. When the flame passes the orifice, the high turbulence intensities in the turbulent jet lead to quenching effects, resulting in an extinction of the flame in the second chamber behind the orifice. Nevertheless, after a delay time of 0.38 s the gas mixture in the second chamber is ignited. The exact ignition delay as well as the resulting high flame velocities were measured by means of the intensified high-speed video camera. Depending on the hydrogen concentration and the blockage ratio direct ignition, ignition after a certain delay (up to 1 s), and flame quenching without ignition in the second chamber can be identified.

The maximum pressure loads, that were measured inside the second chamber of the L.VIEW-facility (Fig. 2), depend on the blockage ratio and the hydrogen concentration, too. Furthermore, with an increasing blockage ratio of the obstacle the velocity of the jet increases, which can lead to a quenching of the flame (e.g. 11 Vol.-% H_2 in air, $BR=98.8\%$) when it passes the obstacle.

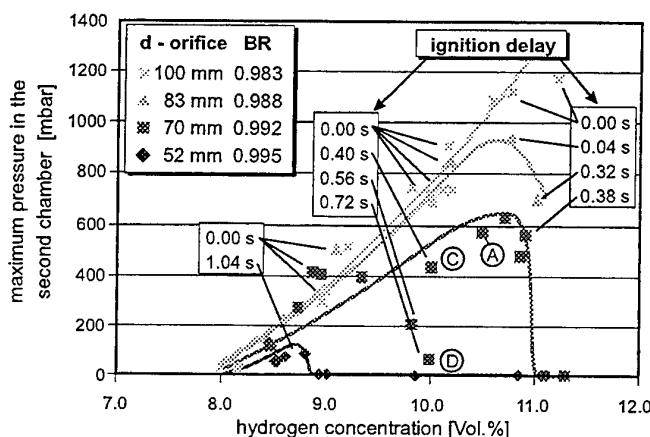


Figure 2: Pressure in the 2nd chamber of the L.VIEW-facility at various hydrogen concentrations and different orifice diameters.

The ignition follows after a delay, as shown in Fig. 3. As the rupture disk, which closes the facility at the right side of the experiment (see Fig. 3), usually breaks, before the flame reaches the obstacle, unburned gas of the first chamber is replaced by hot combustion products, that are blown through the orifice. After the ignition, the leaner mixture in the second chamber, compared to the direct ignition, leads to a decreasing pressure release. At blockage ratios higher than 99.2 %, the flame can also be extinguished totally without any ignition in the second chamber at all (in Fig. 2 this is indicated by a pressure of 0 mbar).

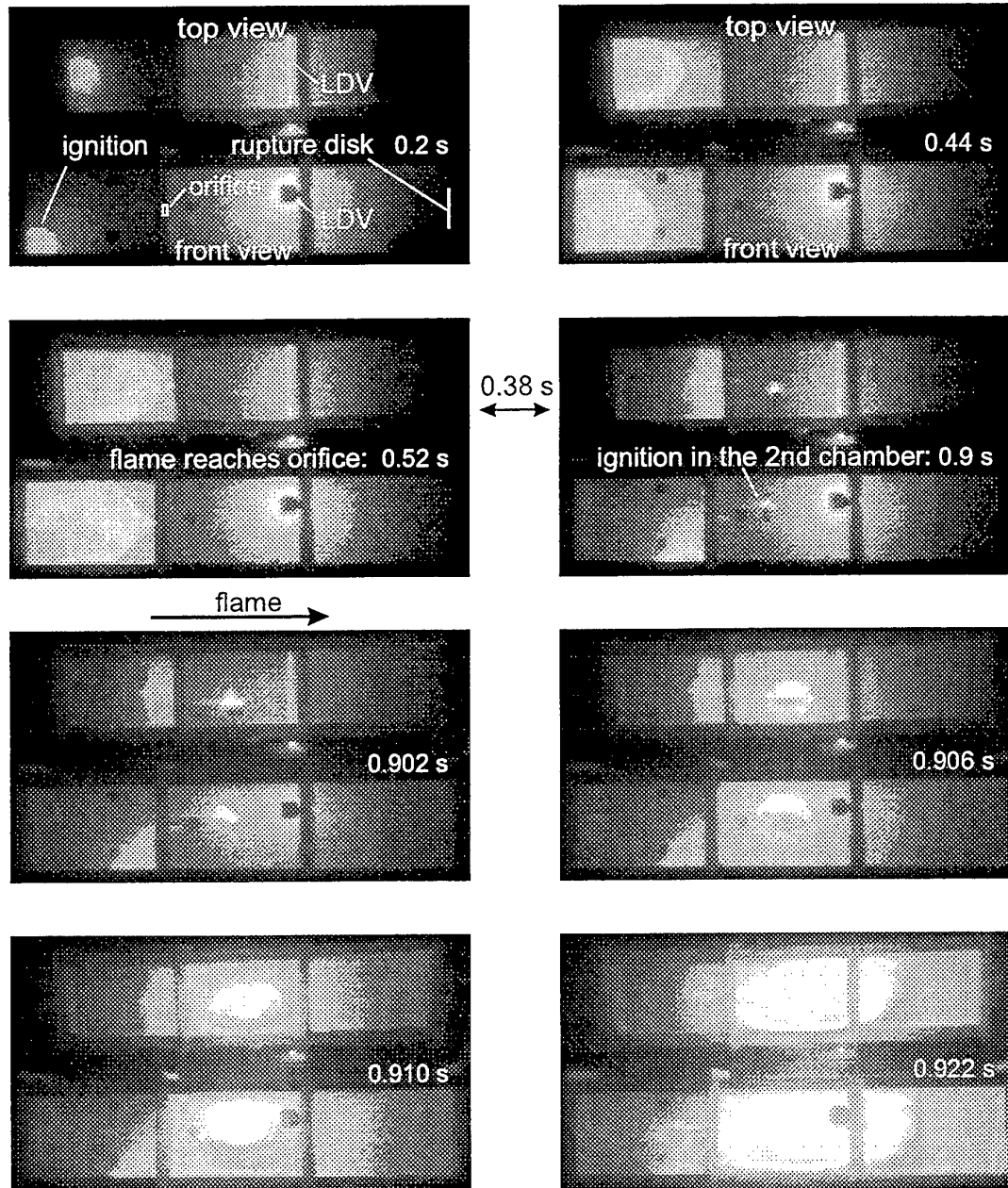


Figure 3: Representative experiment on jet ignition at the L.VIEW-facility with a hydrogen concentration of 10.6 Vol.-% and an orifice diameter of 70 mm. After the flame reaches the orifice, it is quenched for 0.38 s, before the ignition in the second chamber takes place.

Flame Quenching

In the literature, the flame quenching at highly blocking ratios is discussed by a number of authors (e.g. [3], [4], [5]). Regarding to Abdel-Gayed et al. [5] flame quenching takes place, if the product of the Karlovitz flame stretch factor Ka and the Lewis number Le exceeds a value of 1.5. The Lewis number, which is defined as the ratio between the thermal and the molecular diffusivity, of under-stoichiometric hydrogen-air flames can be regarded to have a constant value of approximately 0.35 [3]. The Karlovitz flame stretch factor is not easy to determine, therefore, the criteria of Abdel-Gayed has to be modelled with

$$Ka = 0.157 \frac{u'_{rms}}{s_l^2} \left(\frac{\nu}{L}\right)^{0.5} \quad (1)$$

to

$$0.157 \frac{u'_{rms}}{s_l^2} \left(\frac{\nu}{L}\right)^{0.5} \cdot Le > 1.5 \quad (2)$$

The fluidynamical parameters for this criteria were determined by means of laser-optical measurement techniques. The turbulence intensity u'_{rms} was measured directly in front of the flame in the quenching area by means of the Laser-Doppler-Velocimeter. The integral length scale of the flow field can be estimated to approximately 1/4 of the orifice diameter [6]. Data for the laminar flame velocity s_l was taken out of the literature [7].

In Fig. 4, the product of Ka and Le is shown as a function of the hydrogen concentration. The different values of $Ka \cdot Le$ for the same concentration of hydrogen derive from the usage of various orifice diameters. The area of direct ignition in the second chamber is separated from the areas of ignition after a certain delay and flame extinction without ignition at all.

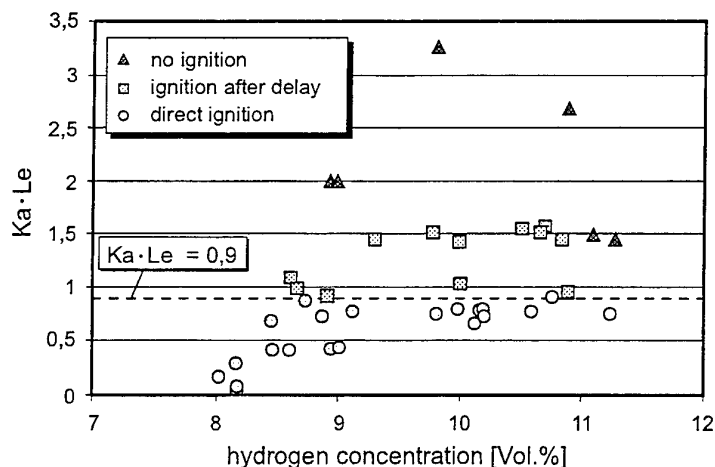


Figure 4: Product of Ka and Le for various hydrogen concentrations at the L.VIEW-facility.

Nevertheless, the flame quenching occurs at $Ka \cdot Le > 0.9$, which is clearly below the value of Abdel-Gayed et al.. This can be explained by the fact that the criteria of Abdel-Gayed was derived from measurements in a homogenous and isotropic flow field. In case of a turbulent jet, this assumption can be expected at the earliest 40-50 orifice diameters behind the opening [8].

Turbulent Burning Velocity In The Second Chamber

The turbulent flame acceleration has been investigated by many authors (e.g. [9 - 11]). A correlation between selected turbulence parameters and the turbulent burning velocity was suggested by Beauvais [12]:

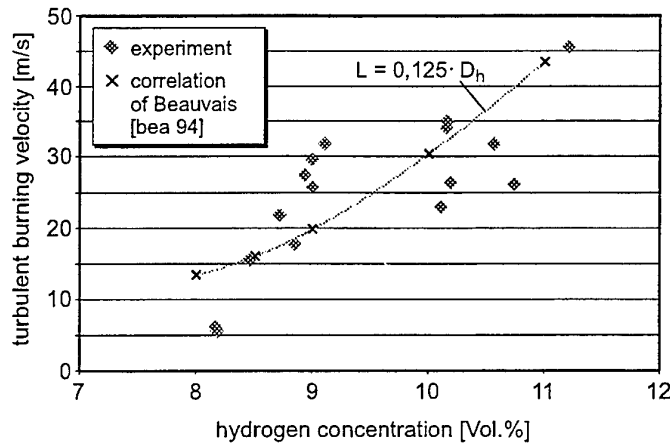


Figure 5: Comparison between the measured turbulent burning velocity at the L.VIEW-facility at direct ignition in the second chamber and correlation of Beauvais [12].

$$\frac{s_t}{s_l} = 1 + b \left[\sqrt{\frac{L}{\delta_l}} \left(\sqrt{\frac{u'_{rms}}{s_l} + 1} - 1 \right) - 0.026 Le \left(\frac{u'_{rms}}{s_l} \right)^2 \right] \quad (3)$$

The scale of the facility is taken into account by the integral length scale L . Due to the high turbulence intensities, that were measured in front of the flame in the middle of the second chamber at the L.VIEW-facility, local quenching effects have to be expected, as it is described by Griffiths and Barnard [3]. In the correlation of Beauvais, those quenching effects are taken into consideration in a quenching term as a function of u'_{rms} .

The turbulence intensity directly in front of the flame in the middle of the second chamber could be measured by means of the applied LDV-system, simultaneously with the measurement of the flame velocity by means of the intensified high-speed video-camera.

Due to the irregular structure of the flame after the ignition in the second chamber, the integral length scale could not be determined. Therefore, data out of the literature was taken ($L \approx 0.125 \cdot$ hydraulic diameter of the chamber) [13].

In Fig. 5 the comparison between the measured turbulent burning velocity in case of a direct ignition without delay and the correlation of Beauvais is shown. A good agreement could be achieved by adapting the correlation factor b to a value of $b = 0.53$. With the same value of b , a good agreement could be found with the data of other authors ([5, 11]).

In case of a ignition delay, as shown in Fig. 3 the resulting high flame velocity cannot only be explained by the high turbulence intensity. During the ignition delay, burned gas is blown through the orifice, where it is mixed with the unburned gas. Together with the burned gas, also free radicals and atoms, which have not totally recombined behind the flame, are mixed with the unburned gas. After the ignition in the second chamber, this leads to a decrease of the chemical induction time and therefore to an increasing burning velocity. This flame accelerating mechanism by radicals in a burned jet has been investigated in detail by Oppenheim et al. [14].

Flame Structure

The flame structure was visualised by measuring the two-dimensional OH-radical distribution in the small-scale PuFlaG-facility by means of the Laser-induced Predissociation Fluorescence. This measurement technique could not be applied to the large-scale experiments, because of the limited pulse energy of the available lasers and the necessary dimension of the optical components.

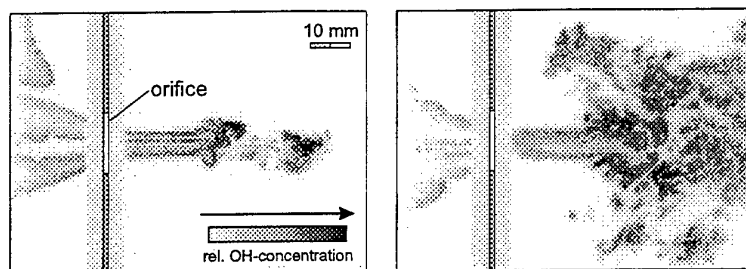


Figure 6: Flame structure (OH-radical distribution) during ignition and combustion in the second chamber.

These measurements show that in case of a direct ignition the combustion is initiated from several ignition kernels. At a later stage, the leading flame contour, which was observed during the combustion in the first chamber, is replaced by a volumetric reaction.

In the Hot-Jet explosion tube higher concentrations of hydrogen in air were investigated (up to stoichiometric mixtures). In a sensitive mixture the fast volumetric reaction due to the turbulent quenched jet can cause a coupling of the flame front to the shock wave and propagate further as a detonation.

In Fig. 7 the pressure records and the corresponding flame velocities of an exemplary DDT-experiment in the Hot-Jet explosion tube are shown.

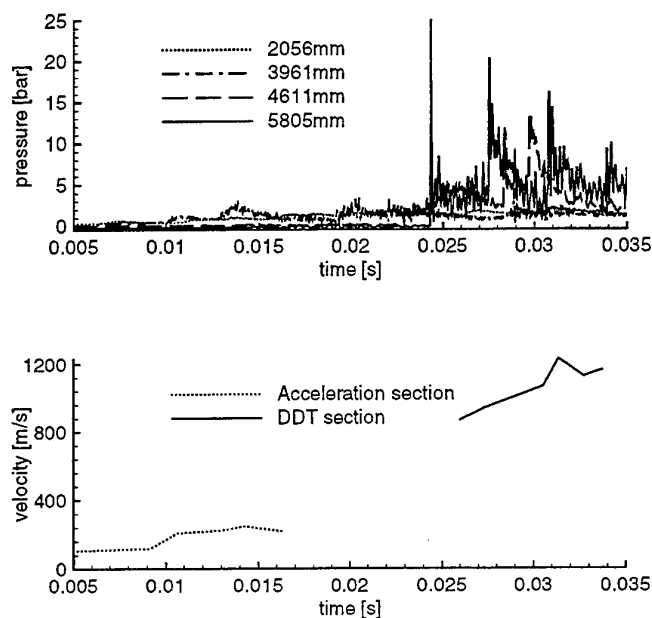


Figure 7: Pressure records and flame velocity (photodiodes) of a transition to a detonation in the DDT section of the Hot-Jet explosion tube (24 Vol.-% H_2 in air, round opening, BR=90 %, pressure transducers 2056 mm and 3916mm are positioned in the acceleration section, 4611 mm and 5805 mm in the DDT section).

The flame velocity increases in the acceleration section up to 300 m/s. After the jet-ignition of the gas mixture in the second chamber the flame propagates with a detonative burning velocity of 1200 m/s. The occurrence of a DDT depends on the flame velocity in the acceleration section, the geometry of the orifice and, of course, the mixture composition. In case of a round opening with a blockage ratio of BR=90 % a DDT was observed at concentrations of hydrogen in air above approximately 19 Vol.-% in air.

5. CONCLUSION

The basic mechanisms that describe the behaviour of turbulent flames influenced by highly blocking obstacles have been shown. Extinction of a hydrogen flame in the jet has to be taken into account at concentrations far above the flameability limit of the mixture. A criteria for the flame quenching could be given depending on the hydrogen concentration, the turbulence intensity and the integral length scale. In case of a delayed ignition in the second chamber, that was observed at some configurations, the flame velocities were much higher than expected. This could be explained by the increased sensitivity of the mixture in the second chamber due to the amount of radicals, which were produced during the combustion in the first chamber and transported through the orifice during the time of ignition delay. It has been shown, that at higher concentrations of hydrogen in air a DDT can occur. For the validation of quantitative criteria for the DDT induced by jet ignition further experiments are performed in the Hot-Jet explosion tube.

ACKNOWLEDGEMENT

It is gratefully acknowledged that the work presented in this paper has been supported by the German Ministry of Economics and Technology (BMWi) and the European Commission.

REFERENCES

1. G. Z. Damköhler, *Angewandte Physikalische Chemie*, 46, pp. 601 (1940)
2. M. Jordan et al., *FISA-97*, Luxembourg, EC, pp. 340-349 (1997)
3. J. F. Griffiths, J. A. Barnard, *Flame and Combustion*, Blackie Academic. (1995)
4. R. G. Abdel-Gayed, D. Bradley, *Combustion and Flame* Vol. 62, pp. 61-68 (1995)
5. R. G. Abdel-Gayed, D. Bradley, *Combustion and Flame*, Vol. 76, pp. 213-218 (1989)
6. M. Berman, Sandia Laboratories report, SAND84-0689 (1984)
7. M. Jordan, *Zündung und Verbrennung von vorgemischten, turbulenten Freistrahlen*, Dissertation, TU München (1999)
8. G. Comte-Bellot, S. Corrsin, *Journal of Fluid Mechanics* Vol. 25, pp. 657-683 (1966)
9. G. W. Koroll, R. K. Kumar, E. M. Bowles, *Combustion and Flame* Vol. 94, pp. 330-340 (1993)
10. N. Peters, *Cours sur la combustion turbulent*, Institute de l'Ecole Normale Supérieure, Paris (1997)
11. N. Ardey, *Struktur und Beschleunigung turbulenter Wasserstoff-Luft-Flammen in Räumen mit Hindernissen*, Dissertation, TU München (1998)
12. R. Beauvais, *Brennverhalten vorgemischter, turbulenter Wasserstoff-Luft-Flammen in einem Explosionsrohr*, Dissertation, TU München (1994)
13. R. P. Lindstedt, V. Sakthithran, *Combustion and Flame* Vol. 114, pp. 469-483 (1998)
14. A. K. Oppenheim et al., *Society of Automotive Engineers*, paper: 780637 (1979)

RESEARCHES ON THE IGNITION REGULATION OF THE PULVERIZED COAL-AIR FLOW IN A TUBE

Zhijun Zhou * Junhu Zhou Qiang Yao Xinyu Cao Kefa Cen

Institute for Thermal Engineering, Zhejiang University
Hangzhou, P. R. China

Email: zhouzj@hotmail.com Fax: 0086-571-7951616

Keywords: pulverized coal, ignition model, ignition test

ABSTRACT. An experimental method and a theoretical model to study the ignition of the pulverized coal-air flow in a tube are introduced. The situation of the tube ignition is similar to the practical engineering process, so the method has some advantages over the other methods. Several typical coals are used in our experiments. The coal concentration, the air flow velocity, the tube wall temperature and the heat flux of the tube wall surface are controlled and adjusted in the experiments. The experimental results are in full agreement with the calculated results of the model.

1. INTRODUCTION

The ignition research of pulverized coal can be traced back to 150 years ago, but a deep comprehension for the ignition mechanics is made only in recent decades. During about one century's time, people thought that the ignition always happened in gas phase, which meant the ignition was due to the ignition of volatile in coal. Howard and Essenhigh(1967) [1] proved that the ignition was most likely to begin from solid particles especially the finest particles through calculation and analysis. Soon afterwards Thomas(1968) [2] provided direct evidence of heterogeneous ignition with high-speed photography. In 70's, Juntger(1976-1977) [3] inspected the ignition process and the condition of the ignition pattern transition with the pulverized coal particle size and the heating rate in details experimentally. He advanced a uni-ignition pattern theory.

There are many kinds of experimental methods and equipment to study ignition regulation. In early times, the main widely used equipment were Greenwald vertical tube test furnace, Wheeler horizontal tube thermal coil igniter test furnace and Hartman test furnace [4]. The critical energy of ignition source during ignition was measured. Because of different pulverized coal concentration, flow pattern, particle size distribution, it was difficult to obtain the accurate results. In 50's, Gassel and Lebmann [5] adopted the method to study the ignition of single coal particle. Single particle ignition is easy to be realized in experiments and easy to be analyzed in theory. However, ignition temperature is not only a parameter of substance but also related to the practical ignition conditions. Therefore it is inappropriate to use the results of single particle in practical engineering. In modern research, thermobalance, ignition index furnace, droptube furnace and the other special equipment are used to analyze the ignition and combustion performance of coal [6]. The data of thermobalance are that of packed pulverized coal heated slowly, so it is quite different from the combustion condition of practical pulverized coal-air flow and it can only distinguish the coal combustibility by comparison.

The experimental conditions of droptube furnace are similar to that of the practical boilers. The heating rate of particles is very high. The active energy and frequency factor were expected to be calculated from single particle experimental data of droptube furnace [7]. Because the actual temperature in the particles reaction zone is difficult to be determined, there is a large temperature difference from the real particle temperature of E and N based on the central temperature of particle. Ignition index furnace [8] simulate the pulverized coal ignition condition of actual pulverized coal furnace and estimate the ignition degree, ignition distance, combustion efficiency with the reaction index of coal. It is more precise than proximate analysis of coal and thermobalance. When it is used to test the easy-fired coal type, there will be a large deviation. Reaction index only can be used to distinguish the combustibility of the coal relatively.

The ignition of coal under actual conditions is always a group ignition, which means an ignition of whole pulverized coal-air flow in hot environment. The group ignition is largely different from single particle ignition because of the mutual effect on particles. When a group ignition happens, the temperature and gas composition in the space vary greatly. A method to make pulverized coal-air flow through a heated tube continuously is introduced here and the ignition point is defined where the air flow temperature is higher than the wall surface

temperature at the same axial position. This method tries to simulate the actual combustion equipment and determine the ignition temperature, ignition time and the minimum ignition power. The data are similar to that of engineering and suitable for many kinds of coal type. Therefore, researches on the ignition regulation of the pulverized coal-air flow in a tube are of great significance in directing the design and operation of pulverized coal burner.

2. TEST FACILITY

The test facility includes: the air and pulverized coal supply system, one dimension ignition equipment, the furnace and the measurement system, which are shown in Figure 1.

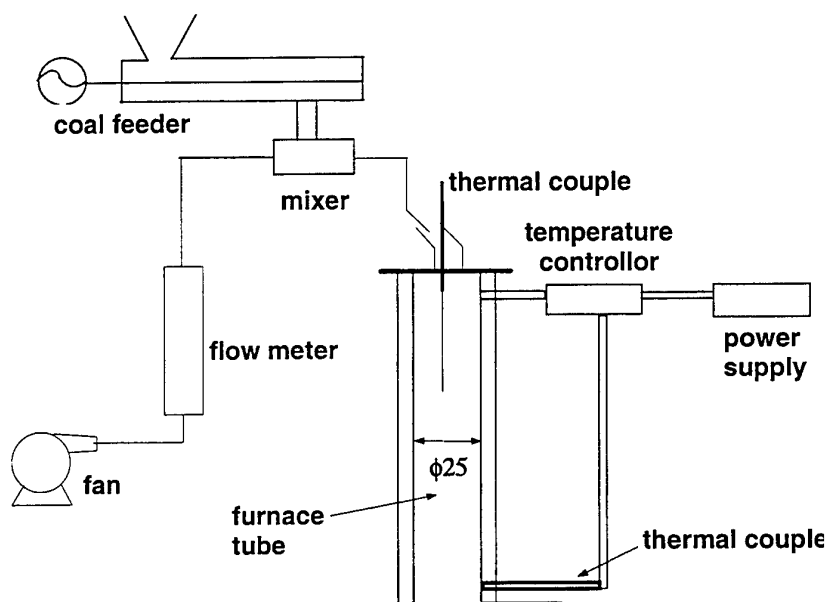


Fig.1. Test Facility

2.1 Air and Pulverized Coal Supply System

The air and pulverized coal system includes: pulverized coal feeder, air supply system and air-pulverized coal mixer. The pulverized coal is fed by the spiral feeder whose capability is 5~45kg/h. At the outlet of the feeder, the pulverized coal is mixed with air and blown into the furnace. The pulverized coal-air flow concentration can be adjusted by adjusting the coal flow and the air flow.

2.2 One Dimension Ignition Equipment

There is a porcelain tube the diameter of which can be adjusted from 25mm to 40mm and the length of which is 600mm in this equipment. A refractory layer is installed at the outside of the tube. Between the refractory layer and the tube, there is a heating wire the power of which can be adjusted from 0 to 7KW.

2.3 Furnace

The furnace is a vertical pulverized coal fired test channel, and its heat release rate is 0.3MW. The flue gas is exhausted from the chimney.

2.4 Measurement System

The main test data are temperatures. The temperatures are measured by thermocouples and a data collector. In order to measure the wall temperature, several thermocouples are buried in the furnace wall. One of them is connected with the temperature controller to control the highest temperature of the wall. The others are connected with the data collector, so the variation of the temperature can be recorded continuously. The flame temperature is measured with the dichromatic pyrometer through the observe ports in the furnace. The type of the dichromatic pyrometer is TR-RIT. Its measurement range is 800~1600°C. The shortest measurement distance is 500mm. The smallest measurement area is 5*5mm². The air flow temperature in the tube is measured with different methods according to the diameter. When the diameter of the tube is larger than 40mm, PtL-Pt thermocouple is adopted and there is a porcelain protection shell around it. The thermocouple is put into

a stainless steel tube. There is a graduation on it. It is stretched into the porcelain tube during the test and can be moved up and down to measure the temperature at different points. To the tube whose diameter is below 40mm, several NiCd-NiSi thermocouples are buried in the center of the tube cross the wall. The distance between them is 70mm.

2.5 Test Conditions

In order to study the ignition characteristics of the pulverized coal-air flow in the tube, Datong coal, Changguang coal and Liugiao blend coal are employed in the test. The proximate analysis of the test coals are listed in table 1. Different pulverized coal concentrations and flow velocities are also adopted to determine the relationship between the pulverized coal concentration and the minimum ignition power and that between the flow velocity and the ignition temperature. The wall temperature is adjusted for the inspecting of the relation of the wall temperature and the ignition.

Table 1. Proximate Analysis of the Test Coals (%)

Ingredient	Mad	Aad	Vad	Cad
Datong coal	3.18	26.84	25.81	44.17
Changguang coal	2.15	34.69	25.35	37.45
Liugiao blend coal	1.49	25.80	13.34	59.37

3. THEORETICAL MODEL

In order to inquire into the ignition process theoretically, mathematical model is adopted to simulate the physical and chemical process of the ignition in the tube. The quantitative relation of parameters and the ignition can be determined.

The ignition of pulverized coal-air flow in the tube is a heat and mass-transferring problem of gas-solid multi-phase flow in the tube. The ignition of pulverized coal-air flow in the tube, is actually the process of pulverized coal-air flow ignition near the wall surface and then the combustion flame expanding to all the cross section. For the acquisition of the ignition under different conditions, the flow velocity and the temperature at the outlet of the ignition tube, the following assumptions are made.

3.1 Basic Assumptions

3.1.1 The fluid in the tube is treated as single phase fluid. There is no velocity difference between the pulverized coal and the air, and the particles do not affect the velocity and turbulent characteristic of the gas.

3.1.2 The velocity distribution in the tube is calculated approximately according to the 1/7 power regulation of developed turbulence in the tube.

3.1.3 The effect of turbulence to the combustion rate is neglected. The combustion reaction of volatile and that of carbon can be expressed with average Arrhenius equation.

3.1.4 The particles have uniform diameter, and they are evenly distributed at the same cross section.

3.1.5 The micro body radiation heat transfer is calculated with average radiation length method of the radiation heat transfer between the gas and the wall.

3.1.6 The boundary is assumed as the fixed heat flux condition.

3.2 Basic Equation

Velocity distribution

This is a problem of stable turbulence developed section in one dimension tube. Under medium Reynolds number, the velocity distribution can be expressed approximately with 1/7 power regulation. At last, the equation can be got as followings:

$$u^+ = 8.74(y^+)^{1/7}, \text{ where, } u^+ = \frac{u}{u_\tau}, y^+ = \frac{yu_\tau}{\nu}, y = r_0 - r$$

Turbulent viscosity

The turbulence in the tube is not even and there are boundary layer and main flow zone. It can be expressed as followings:

viscous boundary layer: $\varepsilon_m \approx 0 \quad (0 \leq y \leq 5)$

transition boundary layer $\epsilon_m \approx \frac{(y^+ - 5)}{.5} \cdot \nu \quad 5 \leq y^+ \leq 30$

turbulent core zone : $\epsilon_m = \frac{0.4r_0^+}{6} \left[1 - \left(\frac{r}{r_0}\right)^2\right] \left[1 + 2\left(\frac{r}{r_0}\right)^2\right] \quad y^+ > 30$

Temperature distribution

When the axial heat conductance is neglected, the energy equation of the fluid in the tube can be expressed as:

$$\frac{\partial}{\partial t} (\rho_m \nu C_m T) = \frac{1}{r} \frac{\partial}{\partial r} [r \rho_m C_m (a + \epsilon_h) \frac{\partial T}{\partial r}] + S_T$$

Species equation

The conservation equation of oxygen and volatile can be expressed as one united equation. When axial diffusion is neglected,

$$\frac{\partial}{\partial x} (\rho_m U f_i) = \frac{1}{r} \frac{\partial}{\partial r} \left[r \rho_m (D_i + \epsilon_s) \frac{\partial f_i}{\partial r} \right] + S_i$$

Source item of energy S_T and source item of each species S_i

(1) In the energy equation, the source item S_T includes reaction heat of volatile, reaction heat of fixed carbon at the surface and radiation heat absorbency,

$$S_T = S_{vc} + Q_r$$

Where, S_{vc} is the reaction heat, $S_{vc} = W_v \times q_v + W_c f_b q_c$

Q_r is the radiation heat absorbed by each fluid micro body in the tube, and it can be acquired according to the average mass of the body.

(2) Species of volatile

$$S_v = n \times \frac{\pi}{6} d_p^3 \rho_p V_f - W_v$$

(3) Species of oxygen (including the reaction mass of volatile and that of carbon)

$$S_{ox} = -(LW_v + \frac{32}{12} W_c f_b)$$

Boundary condition

Energy equation: Where $x=0$, $T=T_0$

Species of volatile: Where $x=0$, $f_v=0$

Species of oxygen: Where $x=0$, $f_{ox} = 0.23 \frac{1}{C+1}$

Near the wall surface, it accords with heat flux condition

$$q = \lambda_m \left. \frac{\partial T}{\partial r} \right|_{r=r_0} + Q_f$$

Specification of the substances

$$\text{gas phase density: } \rho_a = \rho_{a0} + n \cdot \frac{\pi}{6} d_p^3 \rho_p V_f$$

$$\text{particle density } \rho_p = \rho_{p0} - \rho_{p0} V_f - W_c \frac{6}{d_p}$$

$$\text{mixture density } \rho_m = \rho_a + n \cdot \frac{\pi}{6} d_p^3 \rho_p$$

$$\text{mixture specific heat } C_m = \frac{C_a}{1+C} + \frac{C \cdot C_p}{1+C}$$

Average

$$\text{average density } \overline{\rho_m} = \left(\int_0^r 2\pi r \rho_m dr \right) / (\pi r_0^2)$$

$$\text{average temperature } \overline{T} = \left(\int_0^r 2\pi r \rho_m C_m T dr \right) / \left(\pi r_0^2 \overline{\rho_m} C_m \right)$$

$$\text{average velocity } \overline{U_m} = \left(\int_0^r 2\pi r \rho_m U dr \right) / (\pi r_0^2 \overline{\rho_m})$$

Ignition criterion

Ignition can be determined where there is a sudden change of temperature in the whole cross section for the ignition in the tube with constant heat flux.

4. COMPARISON OF THE EXPERIMENTAL RESULTS AND PREDICTED RESULTS

4.1 The Determination of Ignition Point

The ignition characteristic of coal is not only related to the characteristic of fuel itself, but also to the environmental parameter. The ignition point is defined where sudden temperature change takes place here. The temperature at which the sudden change begins is the ignition temperature, as shown in Figure 2.

Theoretical model calculation adopts same heat flux assumption. After calculation, the cross section temperature distribution and average temperature distribution along the length are obtain and shown in Figure 3 and Figure 4. Comparing the test curves in Figure 4 and Figure 2, it shows that the calculation results have the same general trend to test results. This shows that the calculation is reasonable.

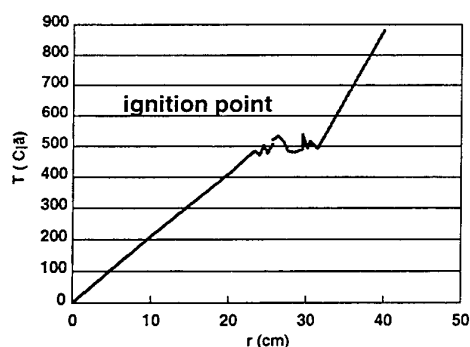


Fig.2. Sudden temperature change curve

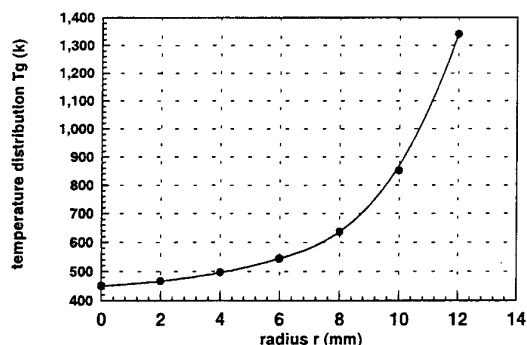


Fig.3. Air flow temperature distribution of ignition cross section

4.2 The Relationship between Pulverized Coal Concentration and the Ignition

Because the ignition is closely related to the pulverized coal concentration and high concentration pulverized coal can stabilize ignition, the pulverized coal ignition in the tube under different pulverized coal concentrations are studied. As shown in Figure 5, there is a best concentration corresponding to the smallest

ignition distance. When the pulverized coal concentration is below this value, the ignition distance can be shortened along with the rising of the concentration. When the pulverized coal concentration is higher than this value, the ignition distance begins to get longer. When the pulverized coal concentration increases, the ignition temperature drops obviously. As shown in Figure 6, when the concentration increases from 0.2 to 1.2, the ignition temperature drops from 650°C to 560°C. In addition, it is observed that the minimum power which the ignition needs gets larger when the concentration increases. When the concentration is below 0.6, the ignition power varied not obviously. But when the concentration is higher than 0.6, the ignition power increases greatly along with the increasing of concentration. If the ignition power is replaced with the power of each unit medium heat capacity, there is a minimum ignition power. The concentration which is corresponding with the minimum ignition power of $\phi 25$ mm tube is 0.5–0.8kgc/kg. When the tested coals are Changguang coal, Pindinshan coal and Huainan coal, the experimental results are similar to it. The results of $\phi 60$ tube are shown in Figure 8. The best ignition concentration is 0.8 ~1.0kgc/kg.

The model predicted results produce the same conclusions as the experimental results. The best concentration varies with the increasing of the tube diameter. This is because the ignition is close to boundary layer ignition when the diameter of the tube is large, so the ignition will be more difficult. It needs more volatile to be volatilized and ignited, and the flame can spread to the center of the tube. Higher pulverized coal concentration can ensure more volatile to draw out.

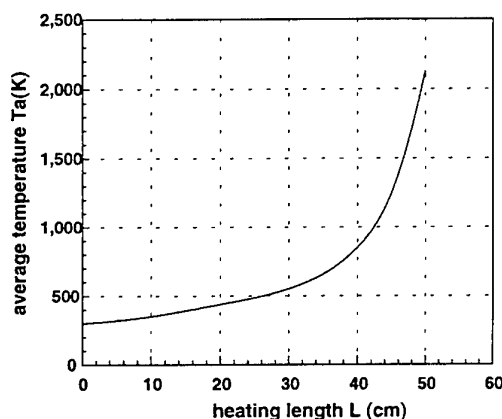


Fig.4. Air flow temperature distribution along the tube length

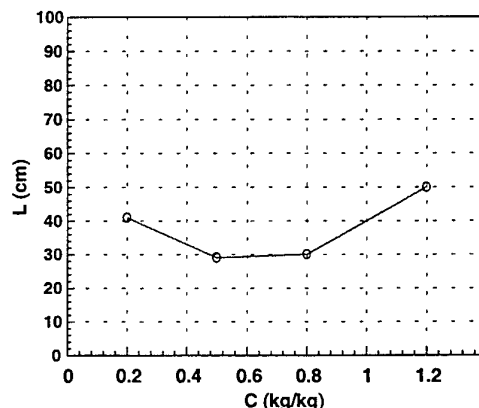


Fig.5. The relationship between the PC concentration and ignition distance

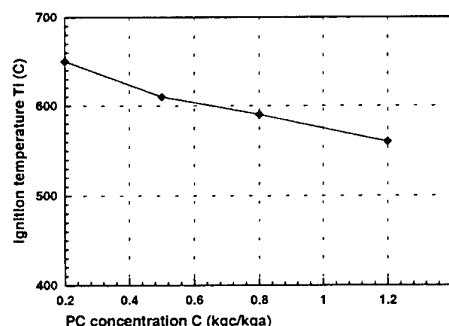


Fig. 6 The relationship between PC concentration and ignition temperature

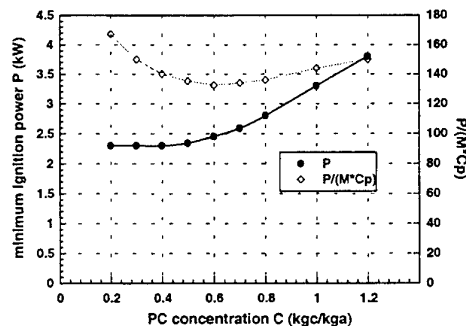


Fig.7 The minimum ignition power of different PC concentration in $\phi 25$ tube

4.3 The Relationship between Air Flow Velocity and Ignition

The increasing of air flow velocity does no good to ignition. The ignition distance is lengthened with the increasing of air flow velocity, although the ignition temperature keeps the same, as shown in Figure 9. When the air flow velocity increases, according to the calculation, the ignition distance is lengthened quickly even if the ignition fails. This is because the air flow velocity is high and the heating period of air flow is too short. The

predicted results are shown in Figure 10. Comparing the test curve in Figure 9, the calculation accords with the experimental results.

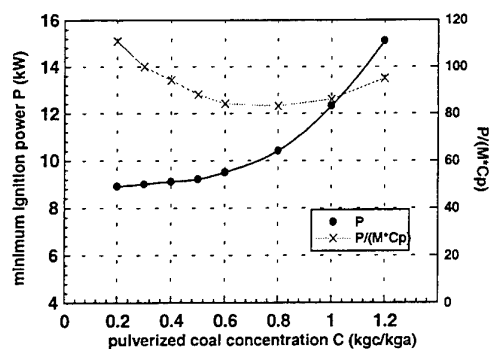


Fig.8. The minimum ignition power of different PC concentration in $\phi 25$ tube

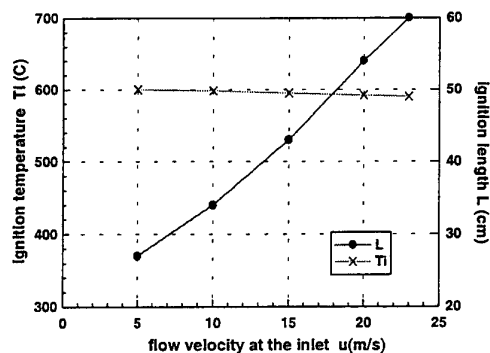


Fig. 9. The ignition temperature and ignition distance under different velocity

4.4 Ignition Power

The increase of wall surface temperature actually means the increase of ignition power. This brings the ignition position forward. When the primary air flow is 26.5kg/h and the pulverized coal concentration is 0.5, the relationship between the ignition distance and the wall surface temperature is shown in Figure 11.

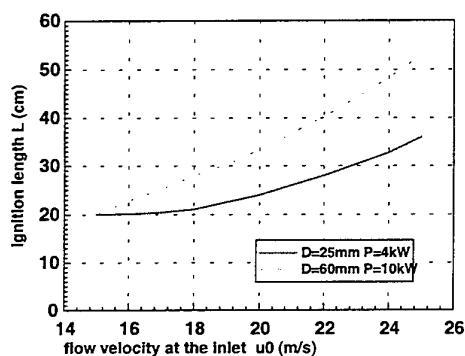


Fig.10. Ignition distance under different velocities

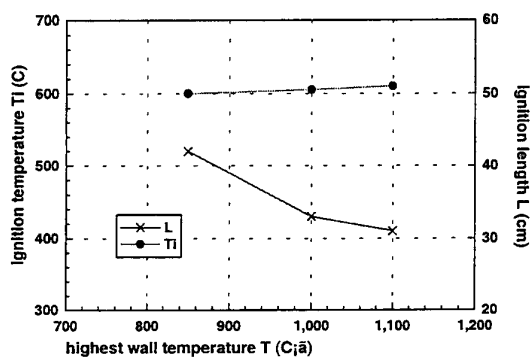


Fig.11. Ignition temperature and ignition distance under different temperature

5. CONCLUSION

1. Ignition temperature is not only related to the substance specifications, but also to the actual conditions. Researches on the ignition in the tube which simulates the actual pulverized coal ignition conditions can provide reliable parameter as ignition temperature and the smallest ignition power for the design of pulverized coal burners.
2. Ignition in the tube experiments show that the wall surface temperature will be higher when the heating heat flux increases. The ignition level of pulverized coal air flow will also increase, but the range is rather small. The flow velocity does not affect the ignition temperature obviously. Ignition distance will decrease greatly along with the increasing of heating heat flux, the increasing of temperature and the decreasing of flow velocity. Pulverized coal concentration can affect the ignition temperature and ignition distance obviously.
3. The model of ignition in the tube is reasonable, and it can reflect the ignition mechanism under different conditions. Its prospect of ignition temperature with different heating conditions, different particle size, different pulverized coal concentration, different volatile content is correct, and the predicted results are in good agreements with the experimental results.

NOMENCLATURE

$U\tau$: shearing velocity
 ν : air movement viscosity
 r_0 : tube diameter
 ρ_m : the mixture density
 C_m : specific heat of mixture
 a : temperature conductance coefficient
 ϵ_h : thermal disperse coefficient of turbulence
 WV : reaction rate of volatile
 WC : reaction rate of carbon
 f_b : the surface area of carbon in one unit volume
 C_a : average specific heat of air
 C_p : average specific heat of particles
 q_V : heat value of volatile
 q_C : heat value of carbon
 Q_r : the radiation heat absorbed by each fluid micro body in the tube
 Q_f : the convection heat transfer

REFERENCES

1. J. B. Howard and R. H. Essenhigh, 11th. Int. Symp. On Combustion, 399-408 (1967).
2. G. R. Thomas, J. J. Harris and D. G. Evans, Combustion and Flame 12:391-393 (1968).
3. H. Juntgen, EPE, Vol XII, NO3-4, 1976-77.
4. R. H. Essenhigh etc., Ignition of coal particles: A review, Combustion and Flame, 72:3-30 (1989).
5. V. S. Gururajan. etc., Mechanisms for the ignition of Pulverized coal particles, Combustion and Flame, 81:1990.
6. C. Y. Chen, Research on the judgment of the ignition and combustion stability of the fuel, boiler technology, 1993.4 (in Chinese).
7. Wu Yi, Research on the ignition dynamics of coal-water-slurry and pulverized coal, degree thesis (1988) (in Chinese).
8. Xian Institute of Thermal Power Engineering, Measurements of the ignition temperature of pulverized coal-air mixture, report (1990) (in Chinese).

THEORETICAL AND EXPERIMENTAL STUDY OF THE PERFORMANCE OF INTUMESCENT FIRE-RETARDANT MATERIALS

F. B. Cheung

Department of Mechanical and Nuclear Engineering
Pennsylvania State University, University Park, PA 16802
Email: fxc4@psu.edu; Fax: (814) 863-4261

J. H. Koo

Institute for Environmental and Industrial Science
Southwest Texas State University, San Marcos, TX 78666

Y. C. Shih and B. C. Yang

Energy & Resource Laboratories
Industrial Technology Research Institute, Hsinchu, Taiwan

Keywords: fire-retardant materials, intumescent process, thermochemical behavior

ABSTRACT. The characteristics of three intumescent fire-retardant materials were examined in a controlled laboratory environment by performing a series of small-scale propane-fired furnace tests. The protective performance of these materials over a selected range of conditions was determined based on the ASTM E119 temperature-time curve for fire tests of building and materials. The objective was to provide a complete set of data needed to validate a new mechanistic model. The latter was developed specifically to predict the thermochemical behavior of intumescent materials when subjected to intensive thermal attack, taking full account of the energy consumption during the intumescent reaction, the temperature range of the tumescent phase, and the effect of thermochemical expansion. Numerical calculations were made to predict the thermal response of the intumescent materials under consideration. Comparisons of the numerical results with the experimental data indicate that the temperature-time history of the substrate temperature can be realistically predicted by choosing an adequate pseudo latent heat for the intumescent reaction over an appropriate range of the tumescent temperatures. The results also indicate that thermochemical expansion plays an important role in the intumescent process.

1. INTRODUCTION

Intumescent fire-retardant materials have been used in military weapon/structural systems as well as commercial/residential buildings as thermal barriers to protect various substrates from intensive thermal attack due to fires. Most intumescent materials are made of polymer composites and include five major components. These components are the carbonific agent, acid source, nitrogen source, spumific agent, and binder. In applications, the intumescent materials are sprayed directly onto the surfaces of the substrates. The sprayed material is then adhere and harden in the same manner as paint to form a fire-protection coating. When the coating temperature is increased beyond a threshold point, a chemical reaction would initiate, causing the coating to enlarge several times its original thickness, thereby forming an insulating blanket to protect the substrate against heat penetration.

Small-scale experiments have been conducted in laboratory environments to characterize the protective performance of intumescent coatings by measuring the time history of the substrate temperature [1-5]. In most cases, the intumescent process can be divided into three sequential phases. These are the preheat phase, the tumescent phase, and the post-tumescent phase. In the preheat phase, the substrate temperature is below the threshold point and the heat transfer is dominated by conduction. The temperatures of both the virgin coating and the substrate tend to increase rather rapidly in the preheat phase. In the tumescent phase, the threshold point is approached and the intumescent reaction would take place in the coating over a range of temperatures. Owing to the energy consumption of the intumescent reaction and the swelling of the coating, the substrate temperature rises very slowly in this phase. Toward the end of the intumescent reaction, the coating completely turns into a char layer. In the post-tumescent phase, both the substrate and the char temperatures rise rapidly again. As a result, the temperature-time curve of the substrate resembles a bending curve, which is one of the characteristics

of intumescent coatings. This special feature of the coating behavior needs to be properly simulated in predicting the thermal response of intumescent coatings.

A number of theoretical models have been developed by previous investigators to describe the thermal response of intumescent coatings [6-13]. A critical review of these models is given in [11]. Owing to the similarities between high-temperature ablatives and intumescent materials [10, 12], the same models derived to predict the thermal behavior of ablatives have often been used to predict the behavior of intumescent coatings in the past. Most existing models, however, fail to predict the bending behavior of intumescent coatings that occurs in the tumescent phase. The only exceptions are the models of Buckmaster et al. [9] and Shih et al. [13], where the intumescent reaction was successfully treated as analogous to a phase change process. Buckmaster et al. [9] assumed that the intumescence occurs at a very thin zone or front and the temperature of the front is kept at a constant value, equal to the temperature of intumescence. Shih et al. [13] generalized the model proposed by Buckmaster et al. by considering the intumescence to occur over a range of temperatures. They employed the enthalpy method along with the use of a pseudo-latent heat to obtain better predictions of the thermal response of intumescent coatings, particularly the bending behavior in the tumescent phase.

In this study, small-scale tests were performed on three intumescent materials under carefully controlled laboratory conditions to obtain the temperature-time histories of the intumescent materials. The data were used to further validate the mechanistic model proposed by Shih et al. [13] and to determine the importance of thermochemical expansion on the intumescent process. The latter was not reported in the work of Shih et al. [13].

2. EXPERIMENTAL WORK

A propane-fired furnace was employed in this study to provide a combustible environment for the testing of the intumescent materials under consideration. The furnace was a metal enclosure having the dimensions of 0.61-m long, 0.46-m wide, and 0.46-m tall. The inside of the metal enclosure was lined with firebricks and Fiberfax Duraboard in order to isolate the furnace from the ambient environment and to retain heat within the enclosure. The furnace was equipped with two venturi air-mixed propane burners, one mounted on each end of the enclosure. The burners were adjustable in the impingement angle and flow rate of the air-propane mix. The test sample was positioned inside the furnace such that both burners were aiming at the surface of the sample. With this setup, the furnace provided direct flame impingement on the test sample. Thermocouple portholes were located around the exposed test samples to monitor surface temperatures of the test samples. Previous studies [4,5] have demonstrated that the propane-fired testing method is the recommended method to simulate fires.

The test samples were 7.6 cm by 7.6 cm steel plates coated with three intumescent materials having two film thicknesses of 1.59 mm and 3.18 mm. To prepare for a run, the selected sample was placed on an elevated Fiberfax Duraboard bed that allowed the sample thermocouples to be routed through the combustion zone. The flame temperature could reach 1,650 K. By adjusting the flame impingement angle and the gas flow rate, the total heat flux at the sample surface could be controlled, which varied from approximately 60 to 570 kW/m² in this study. The backside temperature of each sample was collected during each test. Post-test analysis includes mass loss, maximum expansion, thermal margin, and surface structures using scanning electron microscope (SEM). Since the major objective of this study was to validate the mechanistic model of Shih et al. [13], only the data on the thermal response of the intumescent materials were examined and analyzed.

Three intumescent fire-retardant materials, i.e., #477 Epoxy, Formula FRL-1 and FIREX-2390, were used to form the protective coatings on the steel-plate samples in this study. The substance #477 is a two component, fire protective epoxy coating for interior, exterior, and marine applications. It dries to a smooth semi-gloss finish that is highly durable and resistant to most chemicals. This substance is formulated to meet military specifications and carries the Underwriters Laboratories certification for flame retardant products. FRL-1, on the other hand, is a one component water-based latex flat paint formulated by Fire Research Laboratory. FIREX is a two-component mixture of liquid polymer and epoxide containing polysulfid polymer, epoxy resin, amorphous silica, toulaine, alumino-silicate fiber, and inorganic filler. All three intumescent coatings are suitable for steel, aluminum, sheet metal, plaster, wood, or other substrates. The samples coated with each of these three intumescent materials were tested in the propane-fired furnace over a selected range of conditions to characterize their protective performance and to obtain their temperature-time histories.

3. THEORETICAL MODEL

Intumescent Process

Figure 1 shows schematically the three sequential phases of the intumescent process in progress. When an intumescent coating is exposed to intensive thermal attack, the initial heat transfer mode in the preheat phase is dominated by heat conduction in the virgin material, as shown in Fig. 1a. The temperature of the intumescent coating increases continuously in time under the influence of the external heat input. As the temperature of the coating reaches the threshold point at the onset of the tumescent phase, a thin intumescent zone begins to form in the coating, as shown in Fig. 1b. The intumescent reaction, which may include thermochemical decomposition, thermochemical expansion, and solid-liquid, liquid-vapor and solid-vapor phase changes, occurs within the intumescent zone. A considerable amount of gases will be given off from the intumescent zone to blow and expand the softened but viscous solid into foam-like substance, thus leading to a significant swelling of the coating. As heating continues, the intumescent zone gradually moves inward, leaving residue char behind. In the post-tumescent phase, shown in Fig. 1c, the entire coating becomes a porous char structure.

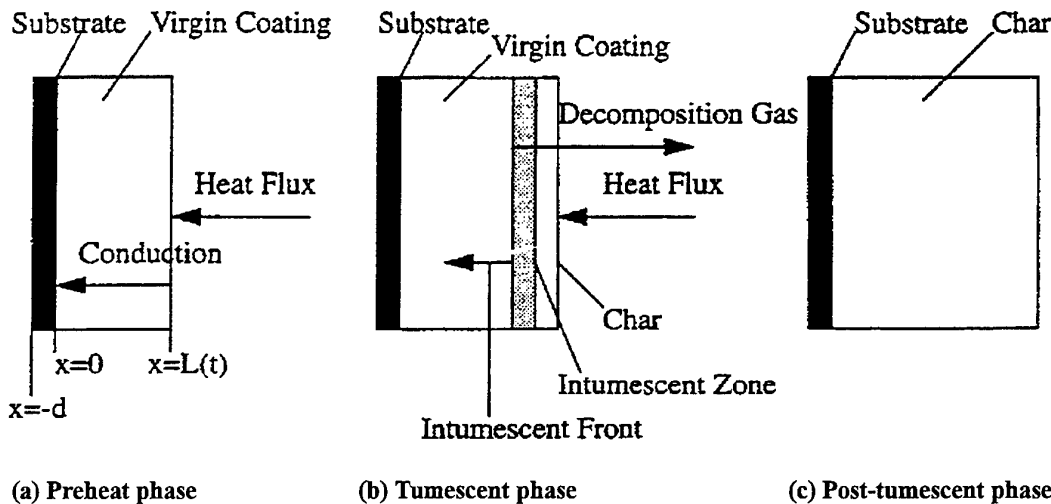


Fig. 1. Schematic of the three sequential phases of the intumescent process.

Governing Equations

In formulating the model, the intumescent reaction is treated as a phase change process over a finite temperature range. The effect of the energy consumption due to the intumescent reaction is incorporated in the model by the use of a pseudo latent heat. The conservation equations of mass for the solid and gas phases in the intumescent coating are expressed by

$$\frac{\partial \bar{\rho}_s}{\partial t} = \dot{\rho}_s \quad (1)$$

$$\frac{\partial \bar{\rho}_g}{\partial t} + \frac{\partial}{\partial x} (\hat{\rho}_g \bar{u}_g) = \dot{\rho}_g \quad (2)$$

$$\dot{\rho}_g = -\dot{\rho}_s \quad (3)$$

where ρ is the density, u the velocity, x the spatial coordinate, and t the physical time. The subscripts "s" and "g" refer to the solid and gas phases, respectively, whereas the superscript " \wedge " and " $-$ " refer to the apparent quantity and the volume-averaged quantity, respectively [12]. Under the assumption of local thermal equilibrium for the solid and gas phases, the energy equation for an intumescent coating can be written as [12]

$$\frac{\partial}{\partial t}(\bar{\rho}_g h_g + \bar{\rho}_s h_s) = \frac{\partial}{\partial x} \left[(\bar{k}_g + \bar{k}_s) \frac{\partial f^{\pm}}{\partial x} \right] - \frac{\partial}{\partial x} (\bar{\rho}_g \bar{u}_g h_g) - Q \frac{\partial \bar{\rho}_s}{\partial t} \quad (4)$$

where h is the enthalpy, k the thermal conductivity, and Q the heat of decomposition. Equation (4) can be simplified by using equation (2) as

$$\bar{\rho}_s \frac{\partial h_s}{\partial t} = \frac{\partial}{\partial x} \left[(\bar{k}_g + \bar{k}_s) \frac{\partial T}{\partial x} \right] - \bar{\rho}_g \bar{u}_g \frac{\partial h_g}{\partial x} - Q \frac{\partial \bar{\rho}_s}{\partial t} + (h_g - h_s) \frac{\partial \bar{\rho}_s}{\partial t} \quad (5)$$

In order to implement the enthalpy method [12] to predict the intumescent reaction occurring over a finite temperature range, equation (5) is rewritten as

$$\bar{\rho}_s \frac{\partial h_s}{\partial t} = \frac{\partial}{\partial x} \left(\frac{\bar{k}_s}{C^*} \frac{\partial h_s}{\partial x} \right) + \frac{\partial}{\partial x} \left[\frac{\bar{k}_s}{C^*} \frac{\partial}{\partial x} (h^* - h_s) \right] \quad (6)$$

$$h^* = C^* (T - T_0) \quad (7)$$

where C is the specific heat. One of the advantages of using equation (6) is that the enthalpy of solid phase can be solved implicitly. In deriving equation (6), the thermal conductivity of the gas phase is ignored as it is small compared with that of the solid phase. Also, the transpiration cooling of the gas phase on the right side of second term is ignored. The heat loss Q of thermochemical decomposition is dropped because it is only important in the temperature range of the intumescent reaction. In addition, the last term of equation (5) is neglected because the heat transfer mode is dominated by conduction outside the intumescent zone. Note that the specific heat of the intumescent coatings under consideration does not vary appreciably as supported by experimental data. Therefore, the specific heat of the intumescent coating C_s is assumed to be constant and C^* is set to be C_s in the proposed model. Because the purpose of this model is to predict the behavior of the solid phase, the behavior of the gas phase, such as the pressure and velocity fields, will not be solved.

Enthalpy Function

To complete the modeling of the intumescent coating, the solid enthalpy needs to be defined properly. The intumescent reaction usually occurs at a finite temperature range ΔT . If the intumescent reaction is analogous to the phase change process that takes place over a temperature range, the relation between the solid temperature and enthalpy can be defined as follows:

$$T_s = T_0 + \frac{h_s}{C_s} \quad \text{if } h_s < h_1 \quad (8)$$

$$T_s = T^* + \left(\frac{h_s - h_1}{h_2 - h_1} \right) \Delta T \quad \text{if } h_1 \leq h_s \leq h_2 \quad (9)$$

$$T_s = T_0 + \frac{h_s - \Delta H_s}{C_s} \quad \text{if } h_s > h_2 \quad (10)$$

where h_1 and h_2 are defined by

$$h_1 = C_s (T^* - T_0) \quad (11)$$

$$h_2 = C_s (T^* + \Delta T - T_0) + \Delta H_s \quad (12)$$

In the above expressions, ΔH_s is the pseudo latent heat across the temperature range ΔT , which account for the heat loss during the intumescent reaction. When the temperature range ΔT is very small, the slope of h - T curve in this temperature range becomes very large, and the phase change process is quite similar to that occurring at a

particular temperature. The present model can be used to predict the intumescent reaction occurring at both cases of narrow and wide temperature ranges.

Boundary Conditions

Referring to Fig. 1, the boundary conditions at the substrate/coating interface ($x=0$) and at the surface ($x=L$) of the intumescent coating can be expressed by

$$\rho_p C_p d \frac{dT_p}{dt} = \bar{k}_s \frac{\partial T_s}{\partial x} \quad x=0 \quad (13)$$

$$\bar{k}_s \frac{\partial T_s}{\partial x} = q'' \quad x=L \quad (14)$$

where q'' is the input heat flux and L the thickness of the coating. The input heat flux employed in the small-scale furnace tests is used for the value of q'' in the numerical calculations. Meanwhile, the thermophysical properties of the intumescent coating measured by Chaboki et al. [2] are employed. The solid specific heat does not vary appreciably, so that it is kept at 2000 J/kg in this study. The above system of equations is solved numerically using the iteration scheme outlined in [12].

4. RESULTS AND DISCUSSION

Typical temperature-time histories measured in the experiments are shown in Fig. 2. For each of the three intumescent coatings, the temperature was observed to rise rather rapidly in the initial stage, corresponding to the preheat phase of the intumescent process. As the threshold point was approach, the temperature rose relatively slowly throughout the tumescent phase. Toward the end of the intumescent process, i.e., in the post-tumescent phase, the temperature began to rise rapidly again. The bending behavior, which is one of the characteristic features of intumescent materials, was most obvious for the case of FIREX-2390. On the other hand, it was less obvious for the case of FRL-1 as can be seen from the figure. For #477 Epoxy, the bending behavior was quite obvious. However, the temperature decrease beyond 500s was unexpected. This could be due to experimental error or it could be caused by excessive heat loss in the later stage of the run. In view of the results presented in Fig. 1, it was decided that the data for FIREX-2390 would be most reliable and useful for the purpose of model validation. Another reason for using the experimental data for this particular intumescent material in the numerical calculations was that its thermophysical properties were relatively well established [2].

Numerical predictions of the thermal response of FIREX-2390 have been performed using the experimental conditions as the input quantities. The numerical results are compared with the experimental data to validate the model as shown in Figs. 3 to 5. Figure 3 depicts the effect of the pseudo latent heat on the history of the substrate temperature. The results presented in this figure are for the case of a coating thickness of 1.59 mm. The numerical values are obtained by assuming the range of tumescent temperatures to be 50°C. The pseudo latent heat is treated as a parameter and its value is chosen to be one to four times of the heat of decomposition. By comparing the numerical results with the experimental data, it is evident that the bending behavior in the tumescent phase can be simulated by the use of the pseudo latent heat. The bending behavior is best simulated when the pseudo latent heat is approximately three times larger than the heat of decomposition. It should be noted that the optimal value of the pseudo latent heat depends on the range of tumescent temperatures for the intumescent process under consideration.

Figure 4 depicts the effect of the range of tumescent temperatures on the history of the substrate temperature for FIREX-2390. The thickness of the coating is 3.18 mm whereas the pseudo latent heat is equal to three times the heat of decomposition. The range of tumescent temperatures is treated as a parameter in the numerical calculations, varying from 10°C to 200°C. By comparing the numerical results with the experimental data, the optimal value is found to be 50°C. The use of this value gives rise to the best simulation of the bending behavior of the temperature-time curve, as shown in the figure. Evidently, by using adequate values for the pseudo latent heat and the range of tumescent temperatures, the thermal response of an intumescent material can be realistically simulated by the present model. For FIREX-2390, the optimal value for the pseudo latent heat is found to be three times the heat of decomposition and the range of tumescent temperatures is 50°C. Using

these particular values, the thermal responses for various thicknesses of the coating can be correctly predicted, as can be seen from Figs. 3 and 4.

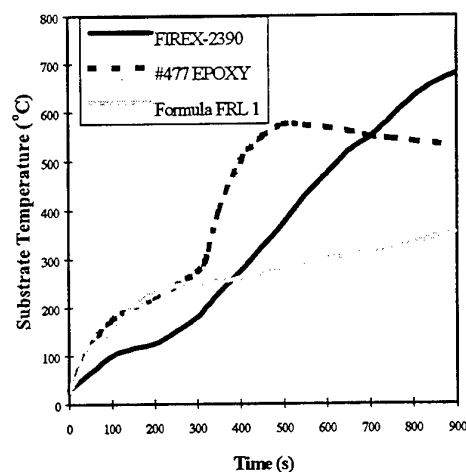


Fig. 2. Typical temperature-time histories observed for the three coatings

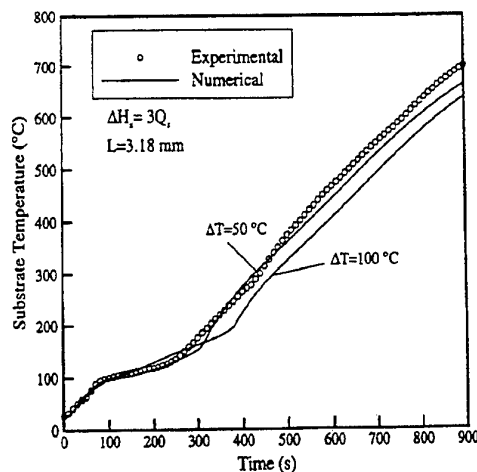


Fig. 4. Comparison of the model with data: effect of tumescent temperature range

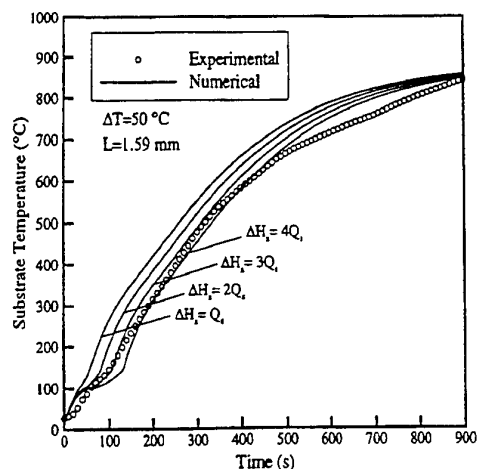


Fig. 3. Comparison of the model with data: effect of the pseudo latent heat

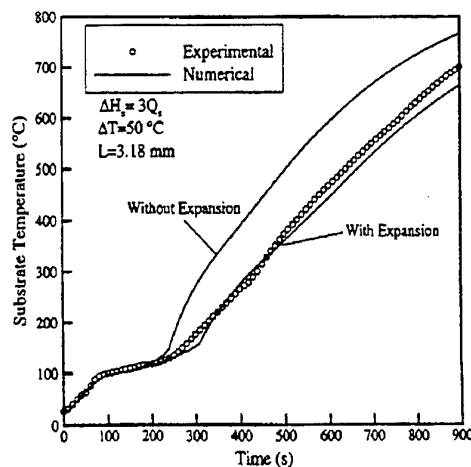


Fig. 5. Comparison of the model with data: effect of thermochemical expansion

Note that the model predictions shown in Figs. 3 and 4 have already accounted for the thermochemical expansion of the coating material during the intumescent process. It is desired to determine quantitatively the importance of the thermochemical expansion effect. This can be done by repeating the numerical calculations without accounting for the thermochemical expansion effect. Figure 5 depicts the effect of thermochemical expansion on the thermal response of FIREX-2390 having the thickness of 3.18 mm. In preparing this figure, the pseudo latent heat is set equal to three times the heat of decomposition whereas the range of tumescent temperatures is fixed at 50°C. When the effect of thermochemical expansion is ignored, the numerical results significantly over-predict the measured value. The differences between the predicted and the measured values can not be compensated by the pseudo latent heat and the range of tumescent temperatures employed in the numerical calculations. Evidently, the thermochemical expansion of the coating has an important effect on the intumescent process and should be adequately accounted for in the model.

5. CONCLUSIONS

Based upon the experimental evidence and the numerical results obtained in this study, the following conclusions can be made:

1. The bending behavior of the temperature-time curve represents a characteristic feature of intumescent materials when attacked by high-temperature sources such as fires. This characteristic behavior needs to be adequately simulated in predicting the thermal response of an intumescent coating.
2. The energy consumption during the intumescent process can be simulated using an adequate pseudo latent heat for the intumescent reaction over an appropriate range of tumescent temperatures.
3. By employing the optimal values for the pseudo latent heat and the range of tumescent temperatures, the thermal response of a given intumescent coating can be realistically simulated. These optimal values appear to be independent of the coating thickness.
4. The thermochemical expansion of the coating material plays an important role in the intumescent process. As a result, the effect of thermochemical expansion should be adequately accounted for in modeling the intumescent process.

REFERENCES

1. J. H. Koo, M. J. Kneer and M. J. Miller, *JANNAF Propulsion Systems Hazards Subcommittee Meeting*, CPIA Pub. 562, pp. 225-240 (1991).
2. A. Chaboki, M. J. Kneer, M. E. Schneider and J. H. Koo, *ASME HTD* Vol. 170, pp. 1-9 (1991)
3. M. J. Kneer, J. H. Koo, M. J. Miller and M. E. Schneider, *31st Aerospace Science Meeting and Exhibit*, AIAA-93-0840, (1993).
4. J. H. Koo, M. J. Miller, and M. J. Kneer, *Proceedings of the Joint Technical Meeting*, The Combustion Institute, pp. 601-605 (1993).
5. J. H. Koo, P. S. Ng and F. B. Cheung, *Journal of fire Research*, Vol. 15, pp. 488-504 (1997).
6. D. E. Caliosro, S. R. Riccitiello, K. J. Clark and A. B. Shimizu, *Journal of Fire & Flammability*, Vol. 6, pp. 205-221 (1975).
7. C. E. Anderson and D. K. Wauters, *International Journal of Engineering Science*, Vol. 22, No. 7, pp. 881-889 (1984).
8. C. E. Anderson, J. Dziuk, W. A. Mallow and J. Buckmaster, *Journal of Fire Sciences*, Vol. 3, pp. 161-194 (1985).
9. J. Buckmaster, C. E. Anderson and A. Nachman, *International Journal of Engineering Science*, Vol. 24, No. 3, pp. 263-276 (1985).
10. B. C. Yang, "A Theoretical Study of Thermochemical Erosion of High-Temperature Ablatives," *Ph.D. Dissertation*, The Pennsylvania State University, University Park, PA (1992).
11. Y. C. Shih, F. B. Cheung and J. H. Koo, *33rd Aerospace sciences Meeting and Exhibit*, AIAA-95-0257 (1995).
12. Y. C. Shih, "Thermochemical Ablation of High-Temperature Thermal Insulation Materials," *Ph.D. Dissertation*, The Pennsylvania State University, University Park, PA (1997).
13. Y. C. Shih, F. B. Cheung and J. H. Koo, *Journal of fire Research*, Vol. 16, pp. 46-71 (1998).
14. ASTM E119-88, *Standard Test Methods for Fire Tests of Building Construction and Materials*, American Society for Testing & Materials (ASTM), Philadelphia, Pennsylvania, USA (1988).

EXPERIMENTAL OBSERVATION OF FAST DEFLAGRATIONS AND TRANSITION TO DETONATIONS IN HYDROGEN-AIR-MIXTURES

A. Eder*, C. Gerlach, F. Mayinger

Lehrstuhl A für Thermodynamik

Technische Universität München, Germany

Email: eder@thermo-a.mw.tum.de; Fax: +49 89 289-16218

Keywords: hydrogen safety, supersonic combustion, DDT, optical measurement-techniques

ABSTRACT. The present paper reports on experimentally obtained results of fast propagating deflagrations, the transition-process from deflagration to detonation, and detonations in hydrogen-air mixtures. These combustion phenomena are investigated by means of various sophisticated optical and conventional measurement-techniques like the Laser-induced Predissociation Fluorescence, which, in particular, gives a new insight into the understanding of these supersonic combustion-modes. Focus is put on the regime of the lean detonation-limit, depending on both, the mixture-composition and the dimension of the test-facility. For this limit criteria of empirical character have been applied for hydrogen-safety considerations until now. This study reports that a transition into a detonation of a fast-propagating flame is possible for leaner mixture-compositions as they are covered in the empirical criterion down to the theoretical detonation limit of the test-facility. It was observed that a detonation is not the most dangerous combustion mode. For mixture-compositions between the theoretical and the empirical detonation limit, it is as well possible that the flame propagates as a supersonic deflagration with the same velocity as the leading shock-wave. The peak-pressure of this combustion mode can be more than two-times higher compared to that of a detonation.

1. INTRODUCTION

After a possible failure of any hydrogen infrastructure at industrial or, in future, civil sites, freely propagating flame-fronts are very likely to arise due to both, the low required ignition-energy and the wide ignition-range (4 – 75 Vol.%) of hydrogen-air mixtures. The pressure-load of the combustion depends strongly on its mode, either deflagrative or detonative. In case of a subsonic deflagration of a hydrogen-air mixture, a structure of a building can withstand the pressure rise of the combustion process. Although a direct ignition of a detonation is very unlikely due to the required high energy-source, an at first slow deflagration can turn into a detonation – referred to as DDT –, with a peak pressure-rise of more than 100 bar, which can endanger the integrity of a building structure. The transition mechanisms are roughly divided into the following categories:

- The focusing of a precursor shock-wave,
- local explosions resulting from re-ignition of partially quenched volumes (hot-jet ignition), and,
- the exceeding of a critical flame speed due to a turbulent flame-acceleration.

The exceeding of a critical flame-speed, which is discussed in the present paper, has been investigated by many authors. Already Urtiev and Oppenheim [1] showed in 1966 by means of the classical Schlieren-Cinematography that for this transition mode four sub-categories can be distinguished: the onset of a detonation between flame and shock, the onset at the flame-front, the onset at the shock-front, and the onset at a contact discontinuity, where two shock-waves coalesce ahead of the flame. Nevertheless, for the prediction of these transition-modes, only very conservative criteria have been set up, yet. This must be attributed to the fact that for the detailed investigation of this highly transient combustion-phenomenon with propagation-velocities of up to 2000 m/s, sophisticated measurement-techniques have to be applied.

For many years this phenomenon has been investigated in detail by means of conventional measurement techniques like pressure-transducers and photo-diodes. But only the combination of conventional measurement-techniques with modern optical methods allows a deep insight into this physical process. Optical measurement methods are very suitable for the investigation of these combustion processes. Since they work non-intrusively and inertia-less they do not influence the combustion-process. This aspect is very important, especially for the investigation of the interaction of a shock-wave and its following flame-front. The experimentally determined data with a very high resolution in time and in space are very important for the validation of computational tools,

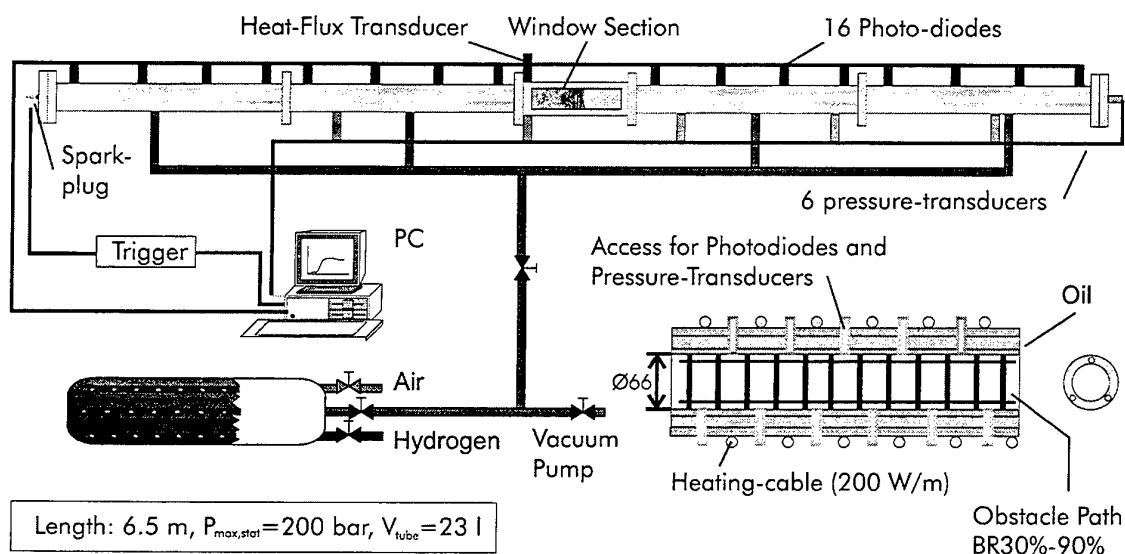


Figure 1: Schematic sketch of the test facility

simulating these phenomena. The detailed modeling of the transition-process is not a primary goal for hydrogen-safety considerations. Furthermore, the fast deflagrations have to be simulated with a high accuracy and, if the conditions for a detonation are reached, a detonation code can be used for further calculations. Therefore, it is very important to investigate the fast-propagating deflagrations up to the transition to the detonation in detail for the understanding and the determination of characteristic criteria for this combustion-phenomenon.

2. EXPERIMENTAL APPARATUS

The experiments are carried out in an explosion tube which facilitates the application of modern laser-optical measurement-techniques as well as conventional measurement-techniques. This section describes the geometry and the set-up of the test facility and shows the application of various measurement-techniques for the investigation of the deflagration to detonation transition process.

Explosion Tube

The explosion-tube has a length l of 6.5 m, an inner diameter d of 66 mm, and a design-pressure of 200 bar (see Fig. 1). It consists of four segments with a length of 1.5 m each and a window section which allows an optical access to the explosion tube over a length of 300 mm. The window-section can be placed at any position in-between the segments or at the tube-ends so that all stages of the combustion-process can be investigated. The gas-composition is determined by the method of partial pressures. The tube has a coaxial shape with oil between the inner and outer tube-walls. Heating cable allow a variation of the temperature of the initial gas-mixture of up to 200° C and, therefore, facilitate the investigation of the influence of steam on the flame-propagation. The ignition is provided by means of a spark-plug.

Turbulence promoting obstacles facilitate an acceleration of the flame. The acceleration itself can be varied by both, using obstacles of different blockage ratios BR (in this case 30-90%) as well as varying the spacing between the obstacles l_{SP} and the total length of the obstacle path L_{OP} . As the focus for the present study is put on the transition process in an unobstructed area, the window-section was positioned in the middle of the tube and a maximum length of 3 m for the obstacle path was used. All applied obstacle-configurations are summarized in Table 1.

Table 1: Applied Obstacle-Configurations for the Turbulent Flame-Acceleration

Configuration	BR	l_{SP} [mm]	L_{OP} [m]	Configuration	BR	l_{SP} [mm]	L_{OP} [m]
1	30%	185	1	6	60%	185	3
2	30%	185	2	7	60%	95	1
3	60%	35	1	8	60%	95	2
4	60%	185	1	9	90%	185	2
5	60%	185	2	10	without obstacles		

Optical Measurement Techniques

Schlieren technique. The classical Schlieren Technique, which was first described by Toepler [2] in 1867 is used to record both, the global flame propagation process by means of visualizing the density gradients between the unburned mixture and the exhaust-gas, as well as the propagation of precursor shock- and pressure-waves. The quantitative evaluation of the Schlieren-images is almost impossible as only integral images through the whole depth of the combustion chamber can be recorded. But in order to get an idea of the strength of the density-gradients, the Schlieren-wedge can be replaced by a color or a gray-scale slide. Depending on the strength of the gradient, each gradient can be assigned to a unique color/gray-scale on the resulting image, which is recorded by means of a fast-shutter, color-CCD Camera (Resolution 1280×1024 pixel). Therefore, it is possible to get a good imagination of the density-gradient field of a detonation-front or of the space between the leading shock-wave and the flame-front with this technique. Nevertheless, the Schlieren-technique allows no distinction between the flame front and the exhaust gas. Therefore, the Laser-induced Predissociation Fluorescence is applied to the combustion process, too.

Laser-induced predissociation fluorescence. The Laser-induced Predissociation-Fluorescence (LIPF) is a very accurate measurement method in order to visualize the location of the reaction zone with a very high spatial resolution. Combustion-radicals are an intermediate product of the fuel-air reaction. In the case of hydrogen-combustion, OH-radicals indicate the exact position of the flame-front. By choosing an appropriate laser-wavelength, these radicals are excited to a higher electronic energy state. The fluorescence can be observed by the transition from an excited electronic state to a lower state. The radicals are excited within a lightsheet with a thickness of less than 1 mm in order to visualize thin layers of the flame [3,4]. By using an excimer laser running with KrF as laser medium and emitting light with a wavelength of 248 nm, the excitation of the OH-radicals appears. The pulse duration of the laser is 17 ns, the lifetime of the OH-radicals in the excited state ranges between 10^{-10} and 10^{-5} sec [5], which facilitates to visualize the combustion process in a "frozen" state. The fluorescence appears frequency-shifted at a wavelength of 295 – 304 nm. Both, additional fluorescence signals and Rayleigh scattering are tuned out by means of appropriate filters. The emitted fluorescence signal of the excited radicals can be observed by an intensified CCD camera. The obtained images contain information about the shape of the flame and the local radical concentration.

Conventional Measurement Techniques

The explosion tube is equipped with a standard conventional instrumentation of 16 photodiodes which are sensitive to ultraviolet light for a precise detection of the position of the flame-front. The pressure is recorded by means of 6 piezoelectric pressure-transducers (five along the tube-axis side-on and one head-on in the end-flange). In addition, a transducer measuring the heat-flux to the side-walls is positioned right in front of the window-section and opposite to a pressure-transducer. The measurement-principle of this transducer is based on the thermo-electrical effect of oblique superconductor-layers. For a detailed description of this measurement principle refer to the specialized literature of Langfellner et al. [8] or to the producing company¹.

¹FORTECH HTS Ltd., Germany

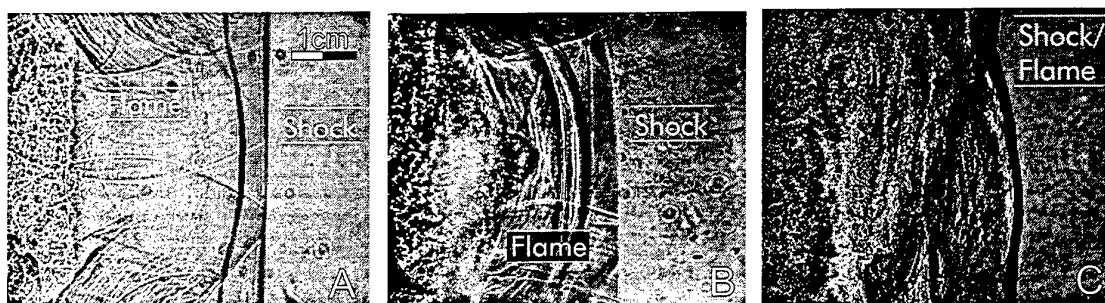


Figure 2: Schlieren images of a fast-deflagration (A), the transition from deflagration to detonation (B), and a detonation (C) [6,7]

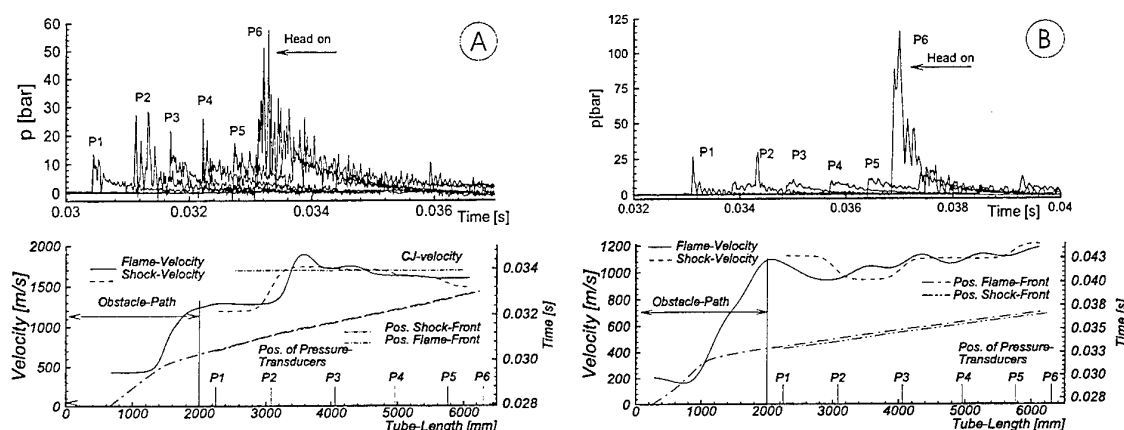


Figure 3: Propagation of a flame/shock-system with DDT for a 17.5 Vol.% H₂ in Air mixture (left) and without DDT for a 17 Vol.% H₂ in Air mixture (right), Obstacle-Configuration #2. P1-P5: pressure-transducers side-on, P6: pressure-transducer head-on.

3. RESULTS AND DISCUSSION

For the different geometrical conditions, which are listed in Table 1, the DDT-spot was adjusted to the optical section of the explosion tube by varying the composition of the initial-mixture. The mode of combustion is determined by applying the Schlieren-Technique. In Fig. 2, a comparison of a fast-deflagration just prior to the DDT, the moment of the transition, and a detonation is shown. In case of a fast-deflagration, the flame-front is propagating into a system of transversal and reflected shock-waves, which are generated by the leading main shock-wave. For this propagation mode it was possible to accelerate the flame up to a velocity of about 1000 m/s right behind the obstacle-path. Depending on the mixture-composition the flame decelerated to a subsonic speed and decoupled from the shock-wave or propagated further with that constant velocity. In this study as well as in the work of Chan et al. [9] and Brehm [10] it was found that the flame-front and the shock-front propagate with a constant distance up to spot at which the transition occurs, as shown in Fig. 2B. The flame-front is closing up in the middle of the tube to the shock-front and ignites it so that it propagates further as a detonation wave (Fig. 2C).

The typical traces of the flame- and the shock-velocity along the tube-length for this process are shown in Fig. 3A. The shock-wave and the flame-front propagate with an identical velocity and constant distance for a length of 1 m behind the obstacle-path before the transition to the detonation occurs. The velocity-data are derived by the time-dependency of the location of the shock/flame-front, which are shown in Fig. 3, too. The maximum propagation velocity of a stable detonation is the Chapman-Jouguet (CJ) Detonation-Velocity. In this case the

flow-velocity behind the detonation-front is equal to the local velocity of sound and, therefore, no disturbance can reach the reaction-front. With this information, it is possible to calculate the CJ-velocity for the frictionless propagation. In Fig. 4, the CJ-Detonation-velocity in dependence on the mixture composition, calculated with the chemical equilibrium solver *Stanjan* [11] is shown.

It is of interest to note that after the transition in Fig. 3A the detonation-front propagates approximately with the Chapman-Jouguet (CJ) Detonation velocity although many authors observed that the CJ-velocity can only be reached in tubes with a greater diameter (about 5 times greater compared to the diameter of this test-facility) due to the friction loss in the smaller tubes. The pressure-records in Fig. 3A are in a range as they are expected to be for a detonation.

Nevertheless, the pressure-load obtained by a detonation is *not* the maximum load of the investigated hydrogen-air combustion modes. It has as well been observed that the flame accelerates up to a velocity which is high enough for the onset of a detonation, but no transition occurs, as shown in Fig. 3B. Furthermore, the shock- and the flame-front propagate – as described above – with constant velocity and distance up to the tube-end. The head-on pressure is – in this case – twice as high compared to that of the detonation shown in the example of Fig. 3A.

In order to determine criteria for the occurrence of this very dangerous combustion mode, both, the maximum head-on pressure as well as the respective averaged flame-speed in the last section of the tube ($x_{tube} = 5 - 6.5\text{m}$) were evaluated for experiments with the obstacle-configurations #1-9 (see Table 1). The detonation-cellwidth λ is often used for the determination of conservative criteria for the decision whether a detonative combustion mode is possible or not. The detonation cell-width is a characteristic measure of the reactivity of the mixture. It can only be determined by means of experiments where the trajectories generated by the triple-point (Mach stem) of the leading and transversal shock-waves are "printed" on a smoked foil within the explosion tube. Selected data found in literature [12,13] for the cell-size for hydrogen-air mixtures are shown in Fig. 5.

The theoretical detonation limit for a circular tube is that the tube-diameter is greater than the detonation-cellwidth of the initial-mixture divided by π [14]. Very often, the criterion $d > \lambda$ is applied as a conservative criterion. This criterion is of empirical character and was obtained by means of various measurements in tubes of 5 – 30 cm in diameter. In Fig. 6, the dependency of the maximum head-on pressure on the mixture-composition as well as the mean flame speed in the last tube section for the obstacle-configurations # 1-9 is shown. It can be seen that a detonative combustion mode *is*, as well as the deflagrative mode, possible for initial hydrogen-air mixtures within the range $d \leq \lambda \leq d \cdot \pi$, which is in this case 15.8 – 19.3 Vol.% H_2 in Air. The correlation of

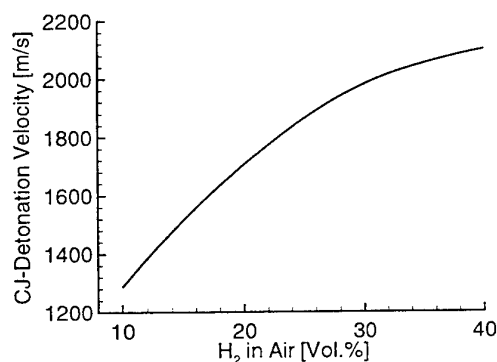


Figure 4: Chapman-Jouguet Detonation Velocity for dry H_2 -Air mixtures ($p = 1$ bar, $T = 293$ K), calculated with the Chem. Equilibrium Solver *Stanjan*

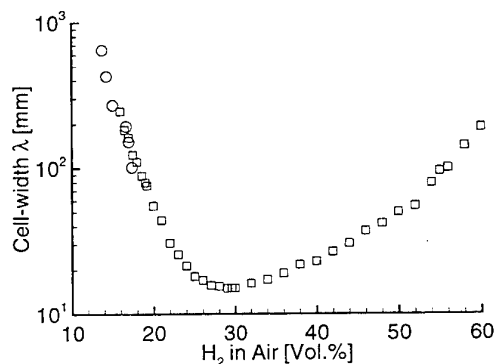


Figure 5: Detonation cell-width for dry H_2 -Air mixtures ($p = 1$ bar, $T = 293$ K), experimental data from Guirano et al. [12] (square symbol) and Tieszen et al. [13] (round symbol)

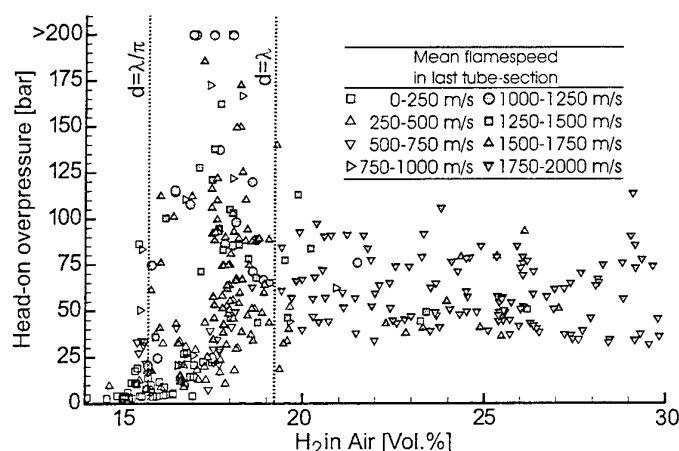


Figure 6: Dependency of the head-on pressure on the mixture-composition as well as the mean flame speed in the last tube section, obstacle-configurations #1-9.

the head-on pressure, mixture-composition, and flame-speed in Fig. 6 shows in addition that the occurrence of experiments with maximum head-on pressures of more than 200 bar can be limited to this mixture-range. For these experiments the flame-front propagates – like in the example shown in Fig. 3 – with a velocity of about 1000 m/s, which is considerably lower than the propagation-speed of a detonation.

Table 2: Classification of Combustion Modes

Condition	Combustion Mode	max. pressure
$d < \lambda/\pi$	Deflagration	25 bar
$d \leq \lambda \leq d \cdot \pi$	Deflagration	25 bar
	Detonation	150 bar
	"Fast Deflagration"	> 200 bar
$d > \lambda$	Detonation	100 bar

The application of the heat-flux transducer facilitates the assignment of each experiment to the specific combustion phenomenon. A comparison of the heat-fluxes to the side-walls for a detonation and a fast deflagration which is coupled to the leading shock wave is shown in Fig. 7. It can be seen that the shock-induced ignition of a detonation initiates a heat-flux, which is about 7-times higher compared to that of a deflagration. Furthermore, it is possible to detect the distance between the leading shock-wave and the reaction-zone. The comparison shows that in the case of a fast deflagration the shock-wave is directly, but with a discrete distance followed by the reaction-zone. The classification of combustion modes in dependence of tube-diameter and detonation cell-width for flames which accelerate up to their specific maximum flame speed by means of adequate turbulence promoting obstacles is summarized in Table 2.

By means of the Laser-induced Predissociation Fluorescence it is possible to get a detailed understanding for the observed combustion-phenomena. In Fig. 8, both, the visualization of the shock-structure by means of the Schlieren-Technique as well as the distribution of the OH-radicals taken by means of LIPF behind the obstacle path (obstacle configuration #6) are shown. Right behind the shock-wave, the formation of OH-radicals starts. The flame is, therefore, propagating into a preconditioned mixture of elevated pressure and temperature. Due to the high flow-velocities and the resulting high turbulence-fluctuations behind the shock-wave, the flame itself has a wrinkled structure and is distributed into separated but coherent reacting zones. Jordan et al. [15] showed that the existence of OH-radicals has an enormous influence on the burning-velocity of a hydrogen-air flame.

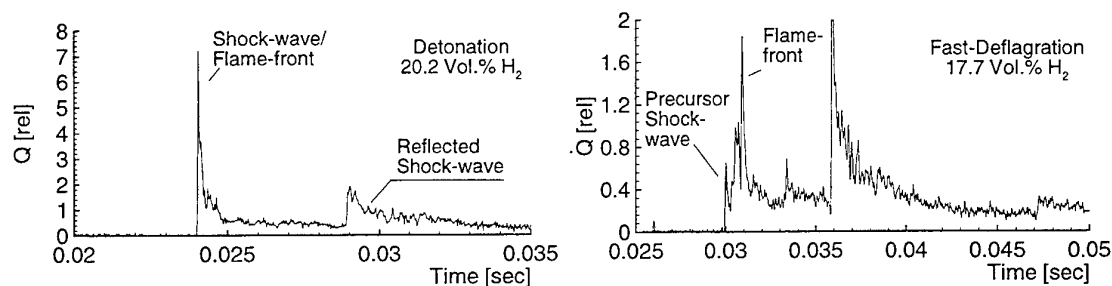


Figure 7: Heat-flux to the side-walls for a detonation (left) and a fast-deflagration (right). Obstacle-Configuration #9, $t = 0$ s corresponds to ignition.

This could be one reason for the occurrence of the high head-on pressure-peaks [16]. The leading shock wave is reflected at the tube-end and due to the high temperature and pressure after the shock-reflection, the whole volume of preconditioned mixture starts simultaneously to react.

A comparison of a fast-propagating deflagration, a near-limit detonation with an initial gas composition of $d < \lambda$ and a detonation with $d > \lambda$ is shown in Fig. 9. The flame-structure of the fast propagating flame is like in the example shown above wrinkled which leads to an increased surface of the flame. Therefore, more hydrogen per unit time is consumed which facilitates a flame-propagation of 650 m/s. The total flame-thickness is about 2.5 cm. The structure of a propagating detonation is often described with the one-dimensional model of Zeldovich, Döring and von Neumann (ZND-model). The ZND-model describes the detonation wave as a shock wave, immediately followed by a reaction zone (i.e., the flame). The thickness of this zone is given by the reaction rate. By linking this model to a chemical equilibrium-solver like *Chemkin-II* [17], it is possible to calculate the OH-radical distribution of a detonation-wave and, therefore, to compare the LIPF-measurement with this calculations. The LIPF-measurements show that the application of the ZND-model are only valid for detonations with an initial mixture with the condition $\lambda < d$. As shown in Fig. 9C, the mixture starts simultaneously to react in a parallel line to the leading shock-wave. Due to the high temperatures after the detonation, the mole-fraction of OH in the oxygen-nitrogen-steam mixture is still very high (about 40% of the maximum OH-concentration in the main reaction zone according to ZND-calculations for a 20 Vol.% hydrogen-air detonation). In case of a detonation in a mixture with the condition $d \leq \lambda \leq d \cdot \pi$, the one-dimensional model is no longer valid. Although the flame propagates like in the richer mixture with the specific CJ-Detonation-velocity, the reaction-zone has an unsymmetrical, three-dimensional shape. The reaction starts at single spots behind the shock-wave rather than simultaneously in a parallel line behind the shock-wave, but the heat-release of the reaction-zone is still high enough and close enough to the shock wave, so that it can propagate as a detonation wave with constant velocity.

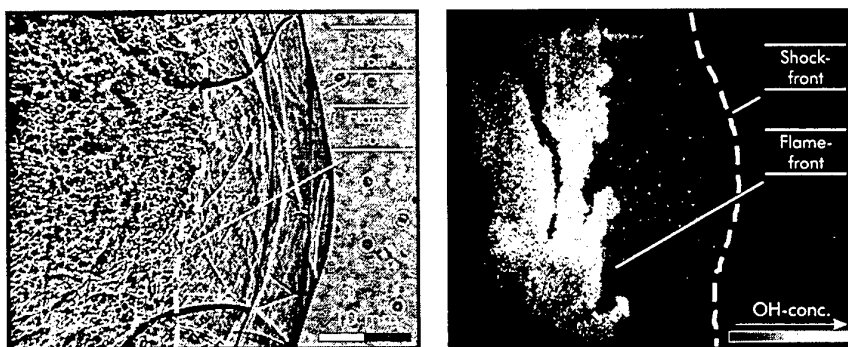


Figure 8: Shock-/flame-structure of a Fast-Deflagration, Obstacle-Configuration #6, 17.2 Vol.% H₂ in Air. Left figure taken with Schlieren, right figure taken with LIPF

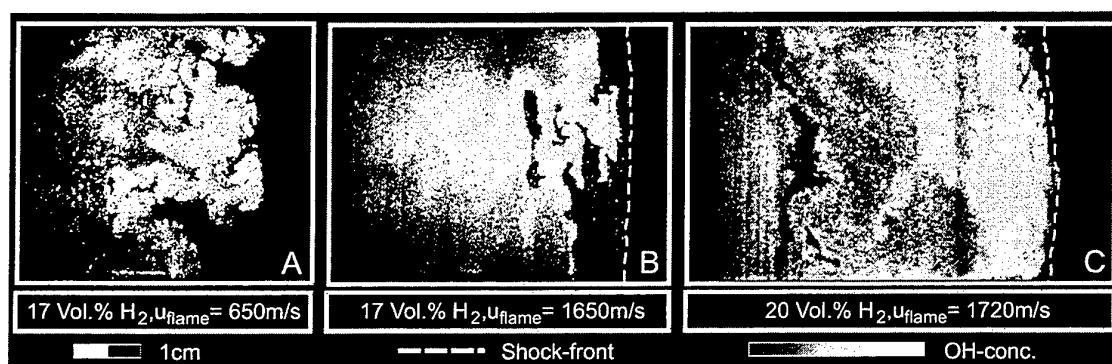


Figure 9: OH-Radical-Distribution of a deflagration (A), a near-limit detonation with $\lambda > d$ (B), and a detonation with $\lambda < d$ (C), taken with LIPF.

4. CONCLUSIONS

The combination of optical and conventional measurement-techniques facilitates the understanding of the highly transient combustion-phenomena of fast-deflagrations and detonations. In order to determine quantitative criteria for the transition process from the deflagrative to the detonative combustion-mode or the occurrence of abnormal high pressure-peaks for fast deflagrations, the results shown in this study have to be put in their proper place among all studies which have been carried out in this field yet. The results determined by various authors in facilities of different geometry and scale deviate sometimes to a very high extend. The goal for the future is, therefore, to develop a tool for the numerical simulation of these phenomena, which is not depending on the geometrical boundary-conditions as the dominating input-parameter. One dominant parameter – especially for the simulation of combustion-phenomena – is the correct modeling of the heat-flux to the confining walls of the combustion process, which has an essential influence on the propagation-velocity of the flame and, therefore, the pressure rise. The qualitative traces of the heat-flux have been shown in this paper for the described combustion modes. These data will be evaluated in a quantitative way, too, which shall serve as an essential input-parameter for numerical codes simulating these phenomena.

ACKNOWLEDGEMENT

It is gratefully acknowledged that the work presented in this paper has been supported by the German Ministry of Economics

REFERENCES

1. P.A. Urtiev and A.K. Oppenheim, *Proc. Roy. Soc.*, v. A295, pp.13-28 (1966).
2. A. Toepler, *Poggendorfer Annalen*, v. CXXXI (1867).
3. F. Mayinger *Optical Measurement Techniques*, Springer-Verlag Berlin (1994).
4. A. Eder, B. Edlinger, M. Jordan, and F. Mayinger, "Investigation of the Transient Flame Development using a Combination of Advanced Optical Measurement Techniques", *Proceedings of the 8th Int. Symposium on Flow Visualization*, ISBN 0-9533991-09, Sorrento, Italy (1998).
5. A. Eckbreth, *Laser diagnostics for combustion and temperature species*, 2nd ed., rev. and updated, Combustion & Science Technology Book Series, v. 3, Gordon and Breach Science Publishers, Amsterdam, The Netherlands (1996).
6. A. Eder and M. Jordan, *Applications and Potentials of Optical Measurement Techniques for the Investigation of Transient Combustion Phenomena*, In D. Mewes and M. Lehner (eds.) *Applied Optical Measurements*, Springer Verlag Heidelberg, Germany, (1984).
7. C. Gerlach, A. Eder, M. Jordan, N. Ardey, and F. Mayinger, *Advances in Understanding of Flame Acceleration for the Improving of Combustion Efficiency*. In S. Kakac, A.E. Bergles, F. Mayinger,

- and H. Yüncü (eds.), Heat Transfer Enhancement of Heat-Exchangers, Kluwer Academic Publishers, Dordrecht, ISBN 0-7923-5637-3 (1999).
8. H. Langfellner, G. Kremb, A. Schnellbögl, J. Betz, K.F. Renk, and W. Prettl, *Appl. Phys. Lett.* 60(4), American Institute of Physics (1992).
 9. C.K. Chan, W.A. Dewit, and G.W. Koroll, "Criteria for Transition from Deflagration to Detonation in H₂-Air-Steam Mixtures", *Proceedings of the International Seminar on Heat and Mass Transfer in Severe Reactor Accidents*, ISBN: 1-56700-059-2 (1995).
 10. N. Brehm, *A contribution to the phenomenon Deflagration-Detonation* (in German). PhD-Thesis, Technische Universität München (1987).
 11. W.C. Reynolds, *The element potential method for chemical equilibrium analysis: Implementation in the interactive program STANJAN*. Technical Report, Stanford University, Dept. of Mech. Engng. (1986).
 12. C.H. Guirano, R. Knystautas, J.H.S. Lee, W.B. Benedick, and M. Berman, "Hydrogen-air detonations", *Proc. of the 19th Int. Symp. Combustion*, pp. 583-590 (1982).
 13. S.R. Tieszen, M.P. Sherman, W.B. Benedick, J.E. Shepherd, R. Knystautas, and J.H.S. Lee, *Prog. Astronaut. Aeronaut.*, vol. 106, pp 205-219 (1986).
 14. S.R. Tieszen, M.P. Sherman, W.B. Benedick, and M. Bermann, *Detonability of H₂-Air-Dilutant Mixtures*, Technical Report SAND-85-1263, Sandia National Lab., USA (1987).
 15. M. Jordan, N. Ardey, and F. Mayinger "Effect of the molecular and turbulent transport on flame acceleration within confinements.", *Proc. of the 11th International Heat Transfer Conference*, Kjongju, Korea (1997).
 16. A. Eder, C. Gerlach, and F. Mayinger, "Determination of Quantitative Criteria for the Transition of Deflagration to Detonation (DDT) in H₂/H₂O/Air-Mixtures", *Proc. of the 22nd Intern. Symp. on Shock Waves*, London, UK (1999).
 17. R.J. Kee, F.M. Rupley, and J.A. Miller, *Chemkin-II: A Fortran chemical kinetics package for the analysis of gas-phase chemical kinetics*, Technical Report SAND89-8009, Sandia National Laboratories, USA (1989).

THE GEOMETRIC APPEARANCE OF THE COUNTERFLOWING PREMIXED FLAME UNDER HIGH TURBULENT INTENSITY

Yiqian Xu, Hongmin Yang, Yong Liu, Weimin Ma and Fan Gu

Thermoenergy Engineering Research Institute

Southeast University, Nanjing, China

Email: yiqnxu@seu.edu.cn; Fax: (086)-025-7714489

Keywords: high turbulent intensity, counterflowing combustion, fractal characteristics, local curvature

ABSTRACT. The counterflowing flame is a novel combustion manner with plenty of advantages for the researches on local characteristics of combustion under intensive turbulence. Using the laser tomography technology and the digital imaging processing technique, the experimental studies on the fine geometric characteristics of turbulent counterflowing premixed flame were carried out under various experimental conditions, such as Reynolds number, bulk strain, equivalence ratio and the ratio of counterflowing momentum. The velocity aspects near the counterflowing interface were measured by PIV technology in cold condition and the strain rates of tangent velocity were acquired to describe the influence of gradient of velocity on combustion. The special appearance of twin flame was discovered which resulted from the interaction between the vortex and the flame. Using the extracted fronts of flame, some discontinuous cusps and holes on the wrinkled boundaries were found in our experiments and this was thought to predict the extinction in local region under high turbulent intensity. Furthermore, Applying the fractal theory, the nonlinear fractal characteristics of the counterflowing flame fronts were investigated and it seems that there may be some relations between the fractal dimension and the turbulent intensity.

1. INTRODUCTION

The geometric structure of the premixed flame is significant to the research on the propagation and the stability in the combustion. The theory of wrinkled laminar flamelet in turbulent combustion proposed in 1940's by Damkohler [1] has been accepted to be the common basis to the research on the propagation of flame. The assumption of the influence on the flame front resulted from the interaction between the Taylor type's large scale vortex and the Kolmogorov type's small scale vortex predicted the process of turbulent transport and the energy dissipation. The successful application of this theory encouraged many researchers to turn their interests on the structure of combustion. Boyer [2] studied the combustion under high turbulent intensity and found that the fronts of flame were too complex to be described using the traditional geometric theory; Sung [3] analyzed the evolution of 2-D flame surface under the spatially periodic flow fields theoretically using the G-equation and the analytical solution revealed some interesting characteristics of the geometry and propagation of the flame, including the formation of cusps and their inner structure; Furukawa [4] examined the wrinkled scale of propane-air turbulent premixed flame and explored the dependence of the wrinkle scale on the characteristics of turbulence, burner size and mixture ratio. He found the average scale of a lean flame is larger than those of the near stoichiometric and rich flames, the smallest wrinkle scale of turbulent flame is in the range of 0.75-1.0mm which is much larger than the Kolmogorov scale of turbulence in the non-reacting flow.

The counterflowing flame is a novel combustion manner with plenty advantages for the researches on local characteristics of combustion under intensive turbulence and whose proposal is based on the theory of laminar flamelets. The counterflowing flame is stagnating one and the intensive reaction zone is confined in a thin zone whose position can be regulated easily. On the other hand, the counterflowing flame is a alternative type of lift-off combustion. Compared with traditional jet flame, the sudden extinction under lower turbulent intensity needn't to be worried about. Kostiuk [5] introduced this type of combustion in the research on turbulent reacting stream, found out special structure and the extinction happened while the Karlovitz number with 1 scales. N.Darabiha [6] acquired the chemical structure distribution of the laminar flame with strain rate through numerical simulation using the detailed chemical mechanism of the reaction of C_3H_6 and the air, meanwhile, deduced the critical stretch ratio for predicting the extinction of the laminar flame.

Historically, it was difficult to measure the flame areas and structure in highly turbulent flows because of the absence of suitable techniques. The available methods, including Schlieren and Shadowgraph, suffered from

the scattering light errors which restricted the use in quantitative analysis. The two-dimensional imaging techniques --- LT (Laser Tomography Technique), combined the novel laser technique and the digital imaging processing technique, solved the problems satisfactorily. The successful applications of the fractal theory to many complex natural phenomena encouraged us to introduce it to describe and analyze the counterflowing flame structure. Although the structure of the counterflowing flame has been studied formerly, how to describe the fine geometric appearance quantitatively is still a fresh fields and the applications of the fractal theory in the analysis of the counterflowing flame are also seldom known.

According to above ideas, this paper consisted of four parts as follows: At first, the laser tomography technique and the procedure of experiments were briefly introduced ; Secondly, several parameters used to describe the counterflowing flame and their calculating methods were proposed; Thirdly , some appearances of flame and the imaging processing results were presented; At the end of the paper, the theory of fractal and their application in counterflowing flame were introduced .

2. EXPERIMENTS

The burner of counterflowing combustion is similar to the traditional Bunsen's burner. In order to regulate the diameter of exit, the front part of burners are refitted to be disassembled. Figure 1 shows the configuration of counterflowing flame. The exit of burner are made of steel tube with double walls, the diameter of exit are 8mm or 4mm, The diameter of the holes in the perforated plate ,which is used to generate turbulence , is 1.5mm. The burner are aligned horizontally in case of the damage of burner. This arrangement of burner is suitable on condition that the jet velocity is high enough to ignore the effect of buoyancy. The air is supplied by air-compressor and fully mixed with the fuels (propane) in the premixing vessel, and then ejected from the perforated plate. The maximum exit velocity can reach 50m/s at which speed the stability of combustion can't be ensured on the traditional jet burner at all.

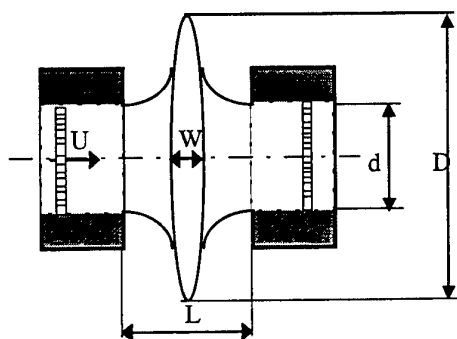
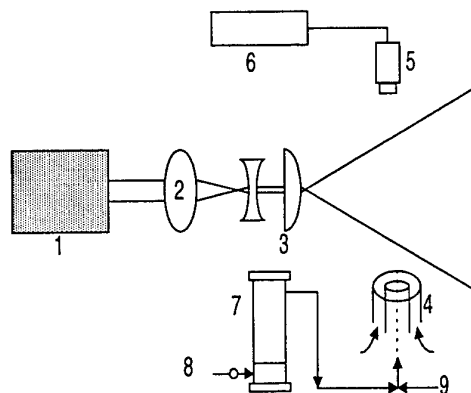


Fig.1. Configuration of counterflowing combustion



1. laser 2. focus lens 3. cylindrical lens 4. burner 5. CCD
6. recorder 7. seeded particles feeder
8. fluidized air 9. fuel

Fig.2. Schematic of laser measuring system

The principle of laser tomography technique [7] is described as shown in Figure 2. The particles tracing scheme was applied. The reactants are uniformly seeded with the small white MgO particles whose sizes range from 3 to 5 μm . The seeded particles are transported to the premixing vessel through a small scale fluidized bed and the concentration of particle can be controlled by regulating the fluidized air volume. When the white MgO particles are exposed in the laser light sheet, they can scatter the laser light according to the Mie scattering principle and then identify the intersection image of flow fields. The laser device used in the experiments are Nd-YAG laser, output power can be controlled from 1W to 10W continuously. The wavelength of output light is 532nm and the diameter of light beam is about 4mm. The focus lens set can transform the beam to 0.5~1.0mm at the tested region. The laser sheet are produced by a set of cylindrical lens. Because of the boundary effect of lens, the intensity of laser sheet are not homogeneous. The size of collected image is 40mm \times 40mm and it is acceptable to

think there isn't influence on the image quality. In order to distinguish the two different streams, the seeded particles is only added in one burner.

The part of image collection consists of the intensified CCD camera and video recorder. The interference filter for the camera matched to the wavelength of the laser is equipped ahead of CCD. The signal of video is stored in the tape and can be processed in the image information extracting system. The video card used in this experiment is VideoStar of the Diamond Company. The VideoStar video card can: (1) supply three channel video signals i/o; (2) PAL, NTSC and SECAM optional; (3) capture the sequence of video by 320 pixel×240 pixel×24 bit dimension and 25 fps(PAL) or 30 fps(NTSC or SECAM) and compresses the video by Motion JPEG method and save it as AVI (Audio Video Interleaved) format file.

Table 1. Bulk stretch, jet velocity and space between two exits

BS*	L(mm)20	30	40
$U_g(\text{m/s})$	800 (A1)	533 (A4)	400 (A8)
10	1000 (A2)	667 (A5)	500(A9)
15	1500 (A3)	1000(A6)	750(A10)
20	×	1333(A7)	1000(A11)
30	×	×	1500(A12)

BS* is Bulk Strain

Table 2. (L=30mm) Diameter of exit

Re	d(mm) 4	8
$U=8(\text{m/s})$	2348 (B1)	4696 (B5)
10	2935 (B2)	5870 (B6)
15	4402 (B3)	8805 (B7)
20	5870 (B4)	11740 (B8)

Table 3. Asymmetric Condition

State	U_{Left}	U_{Right}
C1	15	10
C2	20	10

The PIV system is based on the above laser tomography system and supported by the specially developed software. The traditional method[8] of double pulses exposure is applied for the measurement of lower velocity fields, in other word, find out the matching point pairs in two continuous frames. The method for measuring high velocity fields was improved here. As we know, the exposure time of CCD camera can be change in the range from 1/60 to 1/10000 s, if the exposure time was prolonged properly and the image of particles with high speed can be symbolized by a trailing line on the frame. By extracting the trailing line the velocity of the particles can be decided.

3. SEVERAL DESCRIBING PARAMETERS

Local curvature of flame:

$$H = ((d^2x/ds^2)^2 + (d^2y/ds^2)^2)^{1/2} \quad (1)$$

Local curvature of flame describes the alternation of geometrical structure on the flame surface and can be used to quantify the effects of sharp bugles and holes which seems to be connected with the local extinction characteristics of flame. The local curvature of flame can be acquired from the digital boundary curve of flame front. The definition of the curvature is showed as formula (1), where y and x are the orthogonal coordinate in PIV image, and s is a coordinate measurement along the flame front. s(x) and s(y) are computed according to the formula of discrete arc length. The central difference is used to compute the derivatives of x(s) and y(s). The sign of curvature used here assigns positive values to regions which are convex to the reactants.

The above method is traditional one and if we use the digital imaging processing technique to get the curves of flame's fronts, the coordinates are some integers. The derivative calculated with those coordinates will be finite values and can't symbolize the various characteristics of curves. According to the theory of pattern recognition, a new approach is proposed here to solve above problem. The procedure to realize this method is related as follows and the schematic is shown as Fig.3.

If we want to acquire the curvature at point O, (1) Connect point O with the forward point N and the backward point A, B, C, D, E, F; (2) Calculate the angles between the line ON and OA, OB, OC, OD, OE, OF; (3) Search the minimum value of those angles; (4) Calculate the tangent value of the minimum angle and let it to be the curvature at point O.

The strain rate of velocity in cold condition:

$$S_{tt} = d(u_{\text{tangent}}) / ds \quad (2)$$

The strain rate of velocity describes the influence of the velocity gradient at the jet boundary on the local stretch of flame. The local strain rate is defined using the PIV data at adjacent points along the flame coupled with the local flame orientation information. Flame orientation is defined by the tangent line at the flame surface which borders the PIV velocity vector location. The strain rate at each point is calculated using centered differences of local tangent velocities.

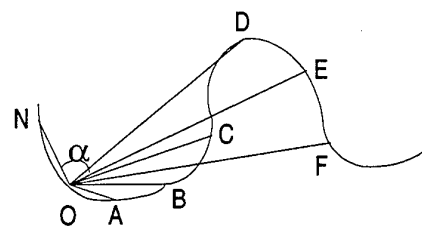


Fig. 3 Schematic of method to calculate curvature

Bulk stretch :

$$a = \frac{2U}{L} \quad (3)$$

The bulk stretch symbolizes the bulk velocity gradients in the counterflowing flame. The axial velocity decrease from the exit velocity U to zero in a short distance L. The velocity gradient in this streams is so high that it play a important role to affect the structure of flames.

4.THE ANALYSIS OF COUNTERFLOWING STREAM IN COLD CONDITIONS

Figure 4 shows the velocity vectors near the interface of two streams when the ratio of momentum of two streams is 1.0. The size of flow fields is 40mm×40mm and the interrogation area is about 1.0mm×1.0mm. The direction of particle movement is changed from horizon to vertical after the interaction of two streams, the similarity of momentum of two streams causes the symmetry structure. Furthermore, we can also find that the velocity at the interface increases sharply and the component of velocity in horizontal direction is near zero. The local strain rate of tangent velocity at the boundary is showed in Figure 5. The graph reveals the random

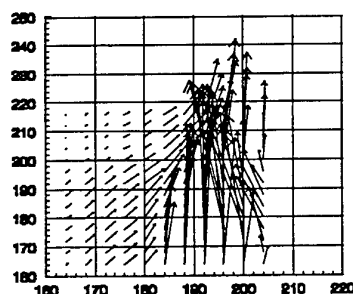


Fig. 4 Local velocity field (M1:M2=1)

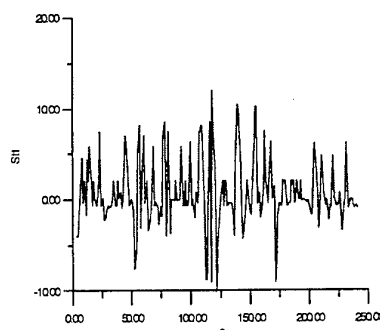


Fig. 5 The local strain rate of tangent velocity (State A3)

fluctuation of the values . This feature is more prominent under the flows with greater turbulent intensity. The higher speed is, the greater fluctuation range of the local strain rate of tangent velocity is.

5. ANALYSIS OF STRUCTURE IN COUNTERFLOWING PREMIXED FLAME

The structure characteristics of flame reflects the state of combustion directly. The flamelet theory has connected the laminar combustion with the turbulent combustion and solved the propagation of turbulent flame successfully, so the researches on the flame structure have been emphasized in recent years. The structures of counterflowing flame possess its special feature — The flame is compressed into a thin disk and the turbulent flame brush consists of twin thin wrinkled flames back-to-back to each other. Because of the short distance between these two flames, the stretch is much higher. The diverse twin flame boundaries were acquired by image processing technology which were shown in Figure 6 in which (a) is the result under symmetry condition. The complexity of two curves is less difference and there are some little twists on the boundaries; (b) is the result under asymmetry condition. The left curve is more complex than the right one and there are many little cusps and holes on it. Since the bulk stretch is not much greater, the distance between two flame isn't closer; (c) and (d) are the situations of the flames with higher bulk strain and the two boundaries are compressed closer and closer. There are obvious sharp cusps and holes at certain points of curves and the probability of those discontinuous points shows tendency to increase with the increasing of the jet velocity.

Figure 7 is the local curvature of flame boundary, s is a coordinate measurement along the flame fronts. From those figures we can conclude that the local curvature reflects the complexity and the changing of flame fronts. There are small scale fluctuations along the flame fronts, intensive changes occur at local position. The curve shows in (a) reveals that there are large scale fluctuation at the beginning of flame front whose effects will influence the surrounding flame and extend to near regions. Several peaks existing in the curve of the graph (b) indicate that there are some large scale discontinuous segments on the flame fronts.

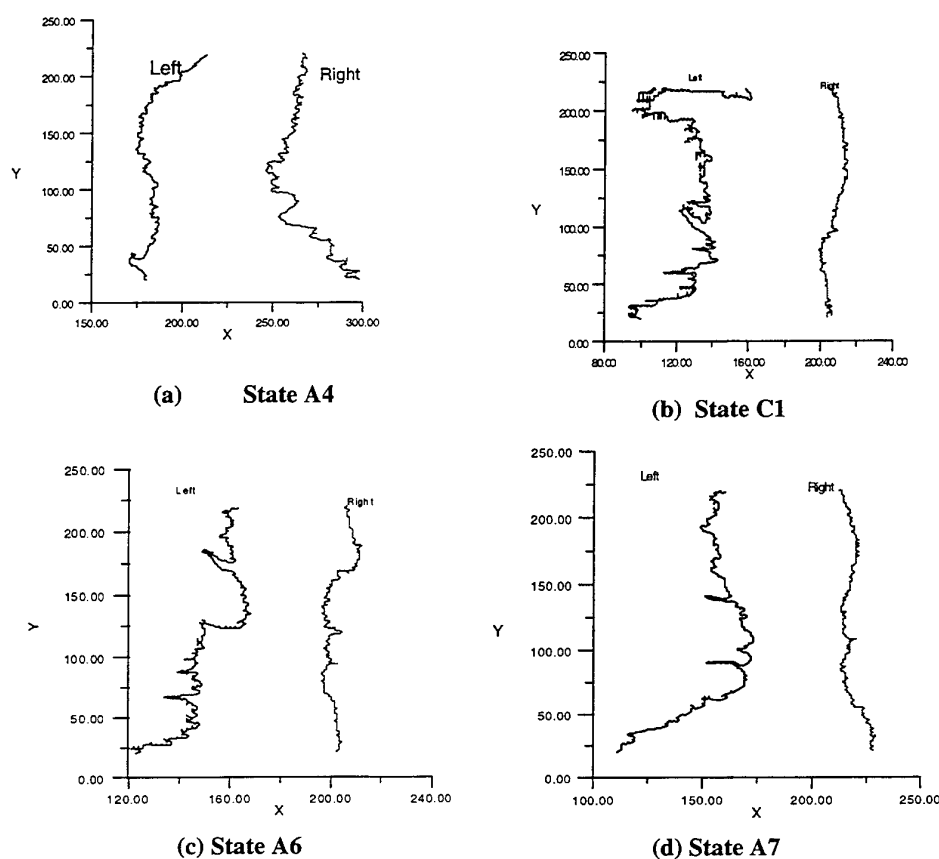
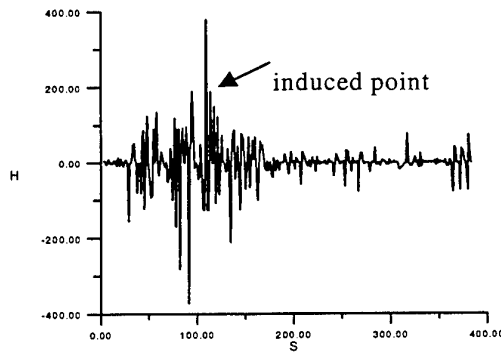
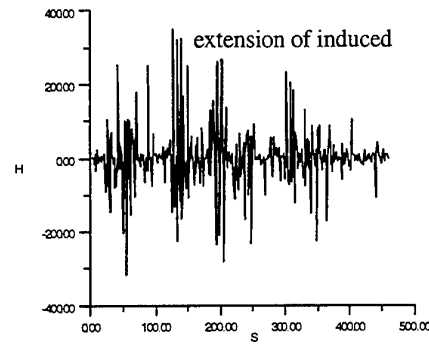


Fig. 6 The twin structure of counterflowing flame



(a) State A4



(b) State A7

Fig.7 The local curvature of flame fronts

6. THE APPLICATION OF THE FRACTAL THEORY IN THE COUNTERFLOWING PREMIXED FLAME

The fractal theory [9] is an important branch of the non-linear science and give a method to characterize the extremely complex geometric objects which can not be described using traditional Euclidean geometric theory. Fractals are objects that display self-similarity over a wide range of scales. Consider a rough curve or surface, if we use methods with different resolution to measure it, we can get different measuring results. According to fractal theory, the measured parameters of a object will increase as the resolution is increased (scale of measurement, ϵ , is increased) and if the objects has self-similarity at all levels of resolution ϵ , the increasing of measuring parameters will accord with a power law relationship. Due to self-similarity, two fractal dimension D_2 , D_3 can be defined according to the measured object and there should be a relation between them: $D_3 = D_2 + 1$. The fractal dimension D_3 of the surface of an object in three dimension is 1 greater than the fractal dimension D_2 of the boundary of a two-dimensional cross-section of the same object.

The conventional fractal dimension is defined using the space filling method [10]. Define $\Lambda(\epsilon)$ is the measured length of curves using the ϵ scale resolution. We have formula as follows:

$$\Lambda(\epsilon) \propto \epsilon^{1-D_2} \quad (4)$$

So, $1-D_2$ can be estimated as the slope of the line relating $\log[\Lambda(\epsilon)]$ to $\log(\epsilon)$.

In this paper, the new calculating method based on measure theory was proposed. As we know, the length L with 1 dimensional measure, A is surface with 2 dimensional measure and V is the volume with 3 dimensional measure, we obtain:

$$L \propto A^{1/2} \propto V^{1/3} \quad (5)$$

extend this relation to the parameter P with D_3 dimensional measure:

$$L \propto A^{1/2} \propto V^{1/3} \propto P^{1/D_3} \quad (6)$$

$$D_3 = 2 \frac{\log[P(T_i)]}{\log[A(T_i)]} \quad (7)$$

Here, the D_3 can be defined as a fractal dimension and the value is between 2~3 because the object described is surface.

Using the conventional fractal analysis method, the fractal characteristics of the curves extracted from the fronts of counterflowing flame have been examined. For the purpose of increasing the range of measuring scale, the CCD camera was zoom in a small region and the minimum resolution of the images could reach 0.01mm between two pixels. After rearranging the data of the measured length with different scale in a log-log coordinates, the data points accorded with the linear distribution obviously. Applying the linear fitting algorithm, the slope of the line relating $\log[L(\epsilon)]$ to $\log(\epsilon)$ could be acquired easily and the fractal dimension $D2$ could also be obtained.

If we investigated the cross-section image of the flame obtained from LT technique, it was easy to get the perimeters of the curves extracted from the fronts of the flame and the areas enclosed by the boundaries. Rearranging the data of perimeters and the areas according to the formula (7) in a log-log coordinates, the data points were fitted with a line very well and the maximum error of fitting didn't exceed 1.5%. So, a conclusion could be drawn from above fact that the turbulent counterflowing flame possessed the fractal nature and the fractal dimension $D3$ obtained from this method is between 2.05~2.3.

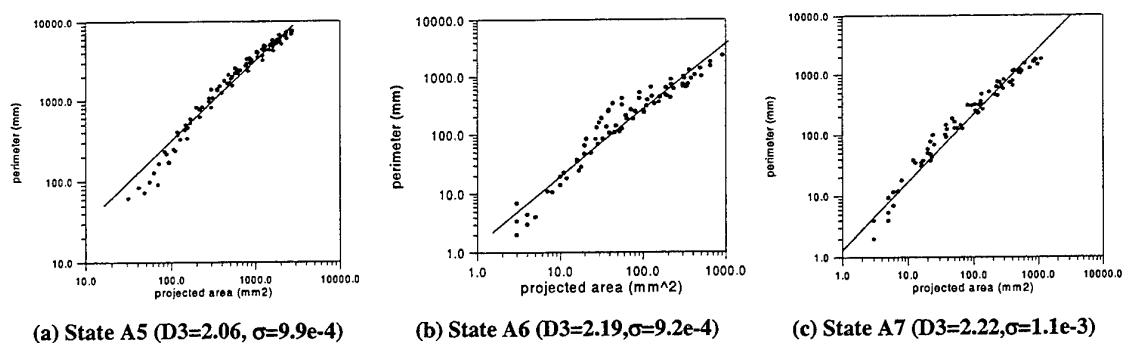


Fig.8 The fractal analysis based on measure theory

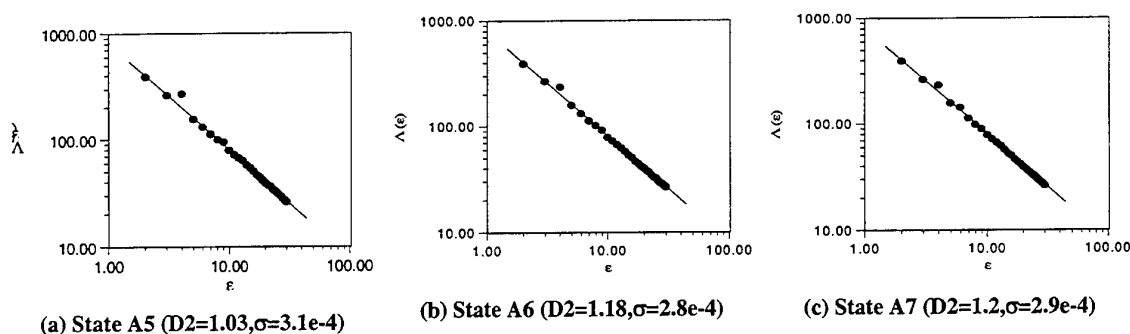


Fig.9 The fractal analysis based on space filling method

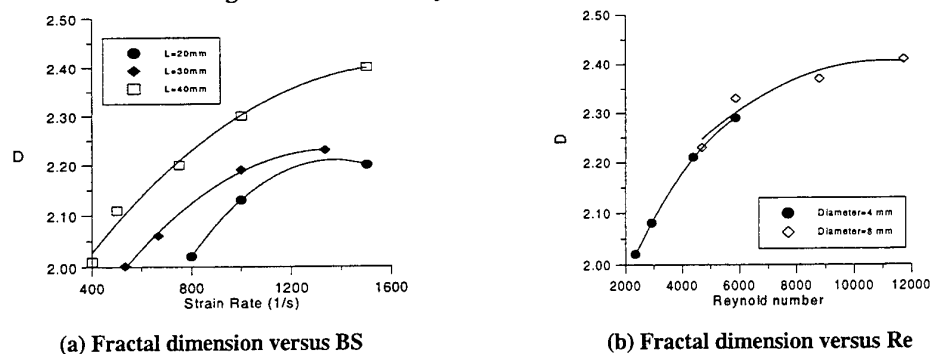


Fig. 10 Relation between fractal dimension and the bulk strain, Reynold number

Compared with the fractal dimensions calculated with above two approaches , there was a relation between the two fractal dimensions described as follows:

$$D_3 \approx D_2 + 1 \quad (8)$$

With the increasing of the bulk strain in the turbulent counterflowing streams, the appearances of flame became more and more complex and the fractal dimensions revealed the tendency of increasing. The increasing is accordance with nonlinear laws.

The fronts of flame are consisted of vortexes and vortex tubes with various scales which distribute in the reaction zone randomly. They interact under high intensive turbulent stress. the large scale vortexes distort the fronts of flames and the small scale ones which are contained in the large scale structures influence the transports of molecules scale and destroy the surface structures of large scale vortexes. The similarity of mechanism of interaction determined the self-similarity of flame structure. This may be a reasonable explanation to the fractal nature of the counterflowing flame.

7. CONCLUSIONS

1. We proposed the local curvature of flame's fronts and strain rate to describe the combustion characteristics of counterflowing flames quantitatively.
2. The strain rate of tangent velocity computed using the PIV data exhibited the effect of flow on the flames.
3. Using the laser tomography technique we observed the structure of the twin flame fronts and extracted the digital boundary curves applying the imaging processing technique. These curves revealed the extremely wrinkled structure. The local curvature of flame boundaries showed discontinuous and changed sharply at certain points. With the increasing of exit velocity, the sharp fluctuations of data extended outward from the inducing points.
4. Applying the fractal theory, the geometric fractal characteristics of the counterflowing flames was investigated. Two kinds of fractal analysis approaches based on space filling and measure analysis respectively were introduced to examine the fractal dimension, the results fulfilled the relation $D_3 = D_2 + 1$. with the increasing of the bulk strain , the fractal dimension increased according to the nonlinear laws and a reasonable explanation to this fact was proposed.

REFERENCES

1. G. Damkohler, Ze. Elektroch, 46:601-652 (1940). (English Translation NACA TM 1112, 1947).
2. L. Boyer, "Laser Tomographic Method for Flame Front Movement Studies", Combustion and Flame, v.39, pp.321-340 (1980).
3. C.J. Sung, "Analytic Description of the Evolution of Two-Dimensional Flame Surface", Combustion and Flame, v.107, pp.114-124 (1996).
4. J. Furukawa and K. Maruta, "Flame Front Configuration of Turbulent Premixed Flames", Combustion and Flame, v.112, pp.293-301 (1998).
5. L.W. Kostiuk and K.N.C. Bray, "Premixed Turbulent Combustion in Counterflowing Streams", Combustion Science and Technology, v.64, pp.233-241 (1989).
6. N. Darabiha and S.M. Candel, "Extinction of Strained Premixed Propane-Air Flames with Complex Chemistry", Combustion Science and Technology, v.66, pp.267-285 (1988).
7. L.P. Chin and R.S. Tankin, "Vortical Structures in a 2-D vertical Bluff-Body Burner", Combustion Science and Technology, v.80, pp.207-229 (1991).
8. R. J. Adrian, "Particle imaging techniques for experimental fluid mechanics", Annual Review of Fluid Mechanics, ASME, v.23, pp. 261-304 (1991).
9. B. B. Mandelbrot, The Fractal Geometry of Nature. Freeman W H, 1982.
10. Z. Mantzaras, "Fractal and Turbulent Premixed Engine Flames", Combustion and Flame, v.24, pp.1001-1008 (1989).

NEW CONCEPTS AND TEST PROCEDURES IN THE ASSESSMENT OF HAZARDS DUE TO SPONTANEOUS HEATING OF TRANSPORTED COMBUSTIBLE SOLIDS

J.C. Jones

Department of Engineering
University of Aberdeen

E-mail: j.c.jones@eng.abdn.ac.uk; Fax: Int + 44 1224 272497

Keywords: spontaneous heating, solid fuels, Frank-Kamenetskii theory

ABSTRACT. The author has pursued a major appraisal of test procedures for propensity to spontaneous heating, such as that issued by IMCO, which are used to determine whether a particular material such as a coal is safe to be shipped. An extensive body of published work has resulted. The current tests involve the heating at 140°C of a sample of the subject material and monitoring of the central temperature. The Frank-Kamenetskii (F-K) model of thermal ignition is invoked, on the basis of which critical behaviour at an ambient temperature of 140°C in the sample size used in the test is equivalent to criticality at 50 °C in a 3m cube shipping hold. There is the flaw that this calculated equivalence of critical ambient temperatures for the small and large assemblies involves assumption of a particular value of the activation energy of the reaction, and because in the F-K model the activation energy appears in an exponential, small uncertainties in it are 'blown up'. The current test procedures are frequently applied in total ignorance of the activation energy of the material under examination. Accordingly the author has developed a means of estimating the activation energy of any particular subject material by a simple extension of the current test. For the longer term, a move away from 'critical ignition temperature' towards 'heat-release rate at criticality' is recommended as a quantity upon which to focus when assessing hazards.

1. INTRODUCTION

Background to the Problem

Throughout the industrial era, spontaneous heating has been a difficulty in coal-utilising enterprises, for example power generation [1,2]. Losses resulting include the coal itself and man hours spent on extinguishment. There is also the possibility that once there has been ignition there will be fire spread, endangering property and life. Ignition of coal on board ship is particularly dangerous. The primary reason for coal spontaneous heating is the reaction of the coal with atmospheric oxygen. Secondary influences, capable of exacerbating the primary effect, include creation of new surface by breakage during handling; newly created surface is more reactive than weathered surface. Other secondary factors are pyrite (FeS_2), present as a mineral in some coals, which reacts with moist air to release heat which can accelerate the primary self-heating due to atmospheric oxidation. Moisture can also promote self-heating under certain conditions. This is especially true of low-rank coals such as lignites. Water entering the pores of such materials wets the internal surface and in so doing releases 'heat of wetting', which, like heat released by the oxidation of pyrite, can accelerate the primary process. In areas of the world where lignites are mined on a large scale, such as the La Trobe Valley in southern Australia, it is 'folklore' that a stockpile is more likely to self-heat on a damp day than on a very dry one.

Less mature coals such as lignites are more susceptible to spontaneous heating than those more advanced along the coalification sequence, such as bituminous coals and anthracites. Recalling that coal is derived from vegetation by a sequential process characterised by increase in the proportion of carbon and decrease in the proportion of oxygen, the difference is primarily due to the intrinsic chemical nature of the organic coal substance. Industrially important materials other than coals which display self-heating include solid coal derivatives such as briquettes and chars. Activated carbons, such as are used as adsorbents or decolourising agents, and cellulosic materials such as sawdust, coconut waste, rice husks and sugar cane residue, have a very significant tendency to self-heat. Fibre materials such as wool and cotton also display spontaneous heating, and here again moisture is a potential accelerating influence. During the early years of the 20th century the New

Zealand wool industry suffered great losses through spoilage of shipments of wool by charring due to self-heating [2].

2. THE CURRENTLY USED TEST PROCEDURE

Details of the Current Test

By the early 'seventies there had been incidences of spontaneous combustion of carbonaceous materials on board ship which necessitated the introduction of a standard test to distinguish materials which are safe to ship from those which are not. The development work was done at the Fire Research Station in England, and led by P.C. Bowes. There was also input from the activated carbon industry. The seminal work is described and explained in Bowes' well-known book [3]. Figure 1, in the box below, outlines the test procedure.

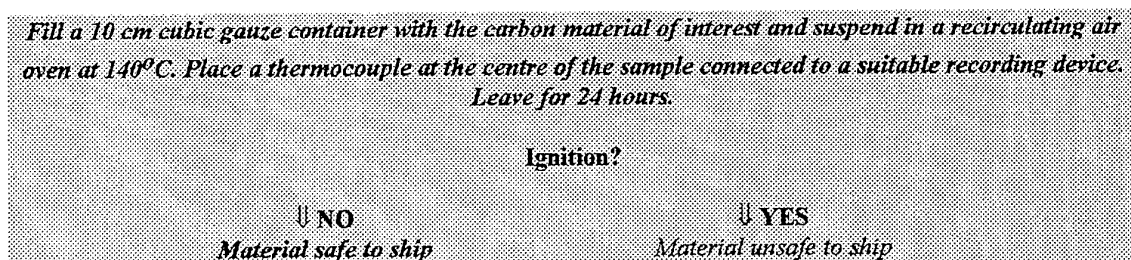


Fig. 1. Outline of the Current Standard Test Procedures for Judging the Shipping Safety of a Carbonaceous Material

The test has been authorised by IMCO and issued in draft form by ISO. Results from it might be required to stand up in law in the follow-up to a case of spontaneous combustion and losses caused by it.

The Theoretical Basis

Bowes focused on the Frank-Kamenetskii (F-K) model of thermal ignition, for a detailed coverage of which the reader is referred elsewhere [4]. This applies to reactions with large exothermicity, an Arrhenius dependence of reaction rate on temperature and purely conductive heat transfer within the reacting medium. The boundary condition is that at the outside surface the temperature remains at ambient even after there has been a significant degree of self-heating manifest as an internal temperature rise. Such a system will display one of two sorts of behaviour: *ignition* (supercritical behaviour) with temperatures rising to hundreds of degrees above that of the surroundings and total destruction of the fuel; or *failure to ignite* (subcritical behaviour), in which the temperature at the centre of the assembly reaches, at most, a few tens of K above the surroundings. It comes out of the F-K analysis that the condition distinguishing the two is expressible in terms of the Frank-Kamenetskii (F-K) critical parameter δ , which has the nature of a dimensionless form of the heat-release rate at ambient temperature:

$$\delta = \frac{r_0^2 E Q \sigma A \exp(-E/RT_0)}{kRT_0^2} \quad (1)$$

where T_0 = ambient temperature (K), r_0 = reactant dimension (m), E = activation energy (J mol^{-1}), k = thermal conductivity ($\text{W m}^{-1} \text{K}^{-1}$), A = pre-exponential factor (s^{-1}), σ = bulk density (kg m^{-3}) and R the gas constant ($8.314 \text{ J K}^{-1} \text{ mol}^{-1}$). The condition for an ignition is that δ should exceed a critical value, i.e., $\delta > \delta_{\text{crit}}$. If this inequality is not fulfilled there will be no ignition. For a cubic assembly the value of δ_{crit} is 2.57 with r_0 equal to the half-width. Bowes et al. reasoned along the following lines. They equated δ_{crit} for a 10 cm cube to δ_{crit} for a 3 m cube (2.57 in each case), and insert T_0 for the 3 m cube = 311 K (38°C). Shipping stows for such things as activated carbons are commonly 3m cube, and 38°C is as hot as such a stow will get purely by heat transfer from the surroundings, even if the vessel enters tropical waters. The equation becomes in effect a transcendental one for T_0 for the 10 cm cube, which gave the result that $(T_0)_{\text{crit}}$ for the 10 cm basket is 413K

(140°C). Criticality in a 10 cm cube at 413K is therefore equivalent to criticality in a shipping hold at 311K, and that is why the temperature of 140°C was adopted as the oven (in effect, ambient) temperature in the standard tests.

The Flaw in the Current Test

The alert reader will have recognised that in equating the critical F-K parameter for the two assemblies - 10 cm cube and 3 m cube - and solving for one of the critical temperatures, Bowes et al. would have needed to assume a value for the activation energy, since this appears in an exponential so does not cancel. Moreover, precisely because it is in an exponential uncertainties in it 'blow up' and have disproportionate effects on the calculated critical ambient temperature for the test-sized assembly. The assumed value is 77 kJmol⁻¹, or 90 kJmol⁻¹ if an extra margin of safety is built in by using 50°C instead of 38°C for the shipping temperature. *If the activation energy is outside this range or unknown the test is not reliable.* In fact the test is usually applied in total ignorance of the activation energy. Although the test is focused on a 3m cube, the author's impression is that this has to some extent been lost sight of in related industries and that a test result where a 10 cm cube does not ignite in an oven at 140°C is taken to signify a material free of spontaneous heating hazards at ordinary storage temperatures.

3. EXTENSIONS OF AND IMPROVEMENTS TO THE CURRENT TEST PROCEDURE

Determination of the Activation Energy

It was pointed out with some emphasis in the previous section that the difficulty with the current test is its unjustifiable use of a single activation energy for any material to which the test might be applied. Such activation energies are of course obtainable, in the following way. Equation 1 rearranges to:

$$\ln\{\delta_{crit}(T_o)_{crit}^2 / r_o^2 \sigma\} = \ln\{EQA/Rk\} - E/R(T_o)_{crit} \quad (2)$$

Clearly $(T_o)_{crit}$ is the value of the oven temperature corresponding to the critical condition ($\delta = 2.57$, if a cubic assembly) and can be experimentally determined by taking samples of the material of interest and carrying out tests at different oven temperatures. The mean of the lowest oven temperature at which there is ignition and the highest at which there is failure to ignite is $(T_o)_{crit}$, and this can be obtained to +/- 2 K or better. If this is done for different sizes of sample, say cubic containers ranging from 4 cm side to 10 cm side, $(T_o)_{crit}$, r_o data pairs are obtained and a plot of $\ln\{\delta_{crit}(T_o)_{crit}^2 / r_o^2 \sigma\}$ against $1/(T_o)_{crit}$ yields E from the slope. This has been done for numerous materials including coals and carbons, sawdust, milk powder and cereal substrates; for a review see reference [5]. This however involves a week or so of oven operation, and there might not be enough of the subject material to spare to carry out the required number of tests, so it is not a suitable basis of a routine standard test. Accordingly, the present author has developed and implemented a simple extension of the current test which enables a good estimate of the activation energy of the subject material to be obtained from a *single* $(T_o)_{crit}$, r_o data pair [6,7,8]. Its theoretical basis is as follows.

The temperature history of a sample in an oven heating test has three distinct parts. Initially it is warming up to oven temperature, there being heat transfer from oven to substrate. Later the sample is releasing heat by reason of its oxidation and this results in transfer from substrate to oven. In between there is a short time during which the sample is approximately uniform at oven temperature and there is heat transfer in neither direction. At this stage the rate of temperature rise is a direct measure of the sample's heat-release and, indeed, easily converted to a heat release rate simply by multiplying by the heat capacity. The heat release rate so formulated can be equated to the same rate expressed in terms of the Arrhenius parameters:

$$QA\exp[-E/R(T_o)] = c[dT/dt]_o \quad (3)$$

where $[dT/dt]_o$ = rate of temperature rise at the stage where the sample reaches oven temperature (Ks⁻¹) and c the heat capacity (J kg⁻¹K⁻¹), other symbols as previously defined. If tests at a range of oven temperatures, spanning and subcritical and supercritical outcomes, are performed and a plot prepared of $\ln[dT/dt]_o$ against

$1/T_0$ clearly E is obtainable from the slope and A is also available given suitable values of k and c . This, though interesting and novel, is no less time-consuming than using baskets of different sizes and plotting according to Equation (2) as outlined above. However, if conditions are critical in the F-K sense, Equation 3 becomes:

$$QA\exp[-E/R(T_0)_{crit}] = c\{[dT/dt]_0\}_{crit} \quad (4)$$

Substituting into the expression for δ_{crit} :

$$\delta_{crit} = \frac{r_0^2 E \sigma c [(dT/dt)_0]_{crit}}{kR(T_0)_{crit}^2} \quad (5)$$

Rearranging:

$$[(T_0)_{crit}/r_0]^2 \times [kR/\sigma c \{[dT/dt]_0\}_{crit}] = E \quad (6)$$

Now the quotient in the first pair of square brackets on the right of Equation 5 is directly calculable from a data pair, and $\{[dT/dt]_0\}_{crit}$ can be measured from the recorder traces using the mean of the values for the two experiments bracketing the critical ambient temperature. The density σ is of course known, and k and c can be reliably estimated for materials such as coals. A value for E can therefore be obtained from one criticality data point, and this is on a time scale suitable for adaptation into a routine standard test.

The single-point method was applied [6] to two Scottish bituminous coals the activation energies of which were, in an independent series of tests, also determined [9] by the multi-point method based on Equation 3. Results from the two approaches are summarised in Table 2 below.

Table 1. Single- and Multi-point the Activation Energies of Combustion of Two Scottish Coals

	Single-point value [6]/kJ mol ⁻¹	Multi-point value [9]/kJ mol ⁻¹
Coal A	66	54±5
Coal B	68	74±4

In the single-point determination the rates of temperature rise when the sample had reached oven temperature were measured by hand, and literature values for k and c were used (see below). Nevertheless, it is clear that the approach gives a reasonable estimate which can of course be refined by better values for k and c and more precise measurement of the rate of temperature rise. Even a 'rough and ready' determination without such refinements gives a value adequate as a basis of judgement as to whether the activation energy is in the range to which the standard IMCO test applies, 77-90 kJ mol⁻¹ as we have seen. Clearly it is not for either coal, and a calculated adjustment is possible in the following way.

Adjustment of the Test Conditions for Activation Energies Other Than the Assumed One

Consider coal B, and use the single-point value of E of 68 kJ mol⁻¹. If a coal or carbon having this value of E were critical in a 3m cube at 50°C - the hypothetical state of affairs at the centre of the IMCO test - at what temperature will it be critical in a 10 cube? Equating δ_{crit} for the two:

$$1.5^2 \exp(-68000/323R)/323^2 = 0.05^2 \exp(-68000/RT_0)/T_0^2 \quad (7)$$

where T_0 is the required quantity. Solving by trial and error gives a value of 459K (186°C) for T_0 . Hence, had the test been applied in the standard way, with the oven at 140°C, there would have been a negative result but this would not truly have signified safety since the critical ambient temperature in a 10 cm cube thermally equivalent to criticality in a 3m cube at 50°C is much higher than 140°C. *Had the test been applied in ignorance of the activation energy it would have erred on the dangerous side.* With larger activation energies than that assumed in the test the result will err on the safe side, but perhaps so much so as to be quite

misleading. Let us suppose that a substrate to which the test is applied has an E value of 120 kJ mol^{-1} , a value well within the range for carbonaceous materials. Equation 7 becomes:

$$1.5^2 \exp(-120000/323R)/323^2 = 0.05^2 \exp(-120000/RT_0)/T_0^2 \quad (8)$$

which gives $T_0 = 384.5^\circ\text{C}$ (111.5°C), hence for a material with this E value the standard test temperature is grossly too high.

Once the activation energy has been calculated from substitution of the criticality data points into Equation 6, an estimate of the pre-exponential factor can be obtained from Equation 1. Also from Equation 1, the size of assembly which would be critical at the storage or transportation temperature of interest can then be calculated. The recommended procedure (6) is as spelt out in Figure 2, below.

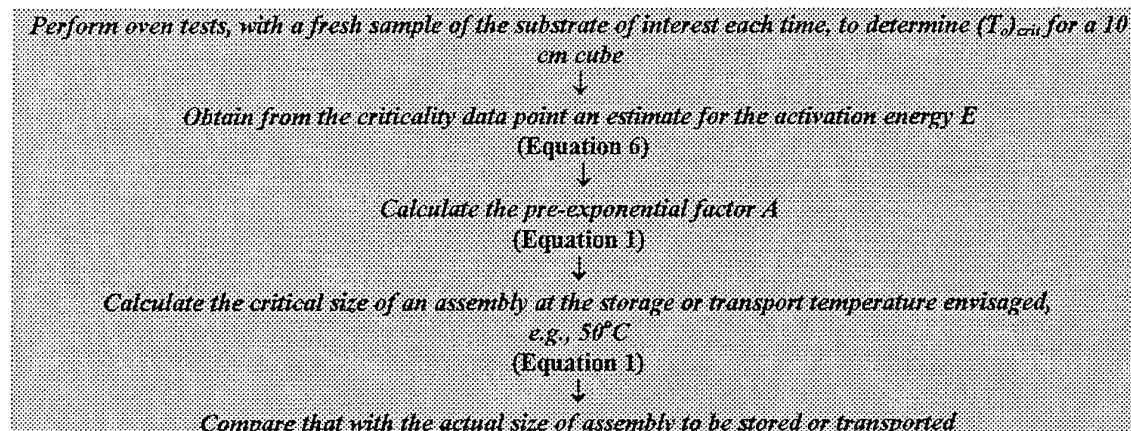


Figure 2. Revised procedure for testing of coals and carbons for shipping hazards

Note that whereas the current test is focused on one particular storage size, a 3 m cube, the revised test is subject to no such restriction; any actual sample size can be compared with that shown to be critical at the storage temperature. Values of the heat capacity and thermal conductivity are required, and 'general purpose' values from such sources as *Perry's Chemical Engineers' Handbook* will usually suffice. The author recommends the following 'general purpose' values which he has himself obtained from the literature and used in calculations of this sort.

Table 2. Recommended Generic Values of the Quantities required for Implementation of the Test Procedure

	Heat capacity $c/ \text{J kg}^{-1}\text{K}^{-1}$	Thermal conductivity $k/ \text{W m}^{-1}\text{K}^{-1}$
Crushed bituminous coal	1200	0.14
Powdered activated carbon	1300	0.06
Crushed lignite	1400	0.4

More precise values might be obtainable for particular substrates. A value of the exothermicity of about 25 MJ kg^{-1} is usually accurate enough for any of the above types of substrates.

Difficulties with Extension to Cellulosic Materials

Importantly, this approach is not recommended for cellulosic materials such as sawdust. It has been found [8] that for these $[dT/dt]_0$ measurements are erratic because of local reactivity variations within the sample.

The Role of Times to Ignition

A great deal has been said in this section about the unreliability of the current test procedure. Why then has it continued to find wide acceptance over so many years? In the activated carbon industry in particular there has

been reliance on it and there have been no incidences of fires during transportation of materials deemed, on the basis of the test, to be safe.

The present author has examined this question closely and concluded that the reason is to found in consideration of ignition times [10]. For a quantity of a coal or an activated carbon large enough to fill a 3 m cube volume the times to ignition, which depend upon the degree of supercriticality at assembly, can be several tens of days and therefore much longer than the storage or transportation time. It has therefore probably happened that a material wrongly classified as safe according to the standard test has arrived at its destination without incident because the journey time was significantly shorter than the time to ignition.

4. A NEW TEST PROCEDURE USING MICROCALORIMETRY

The Concept of Heat-Release Rate at Criticality

The oven heating test, both in its current form and the improved form described herein, involves ignition temperature as the quantity on the basis of which safety or hazard is assessed. A more logical quantity upon which to base a test is heat-release rate at criticality. For a substrate conforming to F-K conditions this is quite simply:

$$q = Q A \exp[-E/R(T_0)_{\text{crit}}] = \{\delta_{\text{crit}} k R [(T_0)_{\text{crit}}]^2\} / (\sigma E r_0^2) \quad (9)$$

where $(T_0)_{\text{crit}}$ is the critical ambient temperature and q (units W kg^{-1}) is the heat-release rate at criticality. Re-expressing Equation 9 without the intermediate step gives:

$$q = \{\delta_{\text{crit}} k R [(T_0)_{\text{crit}}]^2\} / (\sigma E r_0^2) \quad (10)$$

This quantity is relatively insensitive to uncertainties in E because this quantity does not appear in an exponential; the exponential is taken care of by the fact that conditions are critical and δ_{crit} is incorporated. Hence it is possible, for particular substrates, to work out the heat-release rate at criticality at various temperatures and sizes. For example, an activated carbon conforming to the hypothetical conditions of the traditional standard test, viz.:

$$(T_0)_{\text{crit}} = 50^\circ\text{C} \text{ (323K)}$$

$$r_0 = 1.5 \text{ m}$$

$$E = 90 \text{ kJ mol}^{-1}$$

$$k = 0.06 \text{ W m}^{-1}\text{K}^{-1}$$

$$\sigma = 500 \text{ kg m}^3$$

⇓

$$q = 10^{-3} \text{ W kg}^{-1}$$

Values can clearly be adapted for different substrates, sizes and temperatures.

Implementation by Microcalorimetry

To measure the heat-release rate of a material at say 50°C requires use of a microcalorimeter. At the University of Aberdeen such an instrument has been used to assess the spontaneous heating propensity of substances including activated carbons [12], coals of various rank, sawdust, graphite and hydrocarbon wax [13, 14].

The procedure is very simple. The instrument, which can operate at any temperature between just above room and 90°C is set at whatever value of T_0 is of interest. A known weight of the subject material is placed in a steel ampoule, with air in the reference ampoule. The two ampoules are allowed an hour to equilibrate thermally with the instrument before being lowered into the measuring position, and the heat-release rate (in μW) is displayed digitally at the instrument as well as being recorded on hard copy. The heat-release rate

divided by the weight in kg of the sample is the rate per kg, and this can be compared with q , and a judgement made as to whether the material is safe to ship under the conditions of r_o , T_o that went into the calculation of q .

For example, imagine that a 200 mg sample of an activated carbon at 50°C gave a reading of 7 μ W. Is this safe to ship in a 3m shipping stow? The rate of heat release per kg is clearly:

$$(7 \times 10^{-6}) / (200 \times 10^{-6}) \text{ W kg}^{-1} = 0.035 \text{ W kg}^{-1} > q$$

and the material is quite *unsafe* to ship in that size of container. In what size of container would it be safe at this temperature? Putting $q = 0.035 \text{ W kg}^{-1}$ and inserting this together with the other quantities relevant to an activated carbon gives $r_o = 0.3$, signifying a cube of 0.6 m side, a bulk volume of about 220 litre.

Clearly this approach is more soundly based than the current oven heating test and also very flexible in that different temperatures and sizes can be inserted into Equation 9 and the resulting q value compared with the experimental value of the heat-release rate per kg. It has the further merit of being quite rapid: one measurement of the sort outlined is about half a day's work with a modern microcalorimeter.

The Campaign to Launch the Approach

The author, as well as having published this approach in the peer-reviewed literature, has visited the company who manufactured the microcalorimeter which has been at his disposal and lectured to their applications chemists. The company published an applications note [15] on this, which is intended to introduce the idea to current users of microcalorimeters. One obvious issue is that whereas the oven heating test is relatively very inexpensive to set up, a microcalorimeter represents a major capital asset which, for example, a company involved in transporting coal and currently using the oven heating test could not necessarily be expected to make. However whereas a microcalorimeter can operate across a wide temperature range, a single-temperature instrument would be sufficient for routine testing based on the principles outlined herein and this, if developed, would eliminate much of the cost disadvantage. There have been discussions with the company along these lines.

5. CONCLUDING REMARKS

The significant weakness in the current standard test due to the assumption of a single activation energy for all applicable substances was actually not unknown to the original developers of the test [3], but its far-reaching effects were not recognised. In spite of its wide acceptance the test is actually close to being useless, and the long ignition times in stockpile or shipping hold samples have, in the view of the present author, obscured the unreliability of the test, as discussed above.

This paper brings together seminal work all of which has been published in the peer-reviewed literature over the last couple of years which provides an extension to the existing test and the basis of a whole new one. It is hoped that the opening years of the 3rd millennium will see these benefits transferred to related industries, especially coal-utilising industries and manufacturers of carbon products. The author will be pleased to receive enquiries.

REFERENCES

1. R.T. Haslam and R.P. Russell *Fuels and their Combustion* McGraw-Hill (1926).
2. J.C. Jones *Chemistry in Australia* v. 65 Issue no 2, page 3 (1998).
3. P.C. Bowes *Self-Heating: Evaluating and Controlling the Hazards* Elsevier (1984).
4. J.C. Jones *Combustion Science: Principles and Practice* Millennium Books (1993).
5. J.C. Jones *Proceedings of the 24th International Conference on Fire Safety* 179-190 (1997).
6. J.C. Jones *Fuel* v. 77 1677-1678 (1998).
7. J.C. Jones *Proceedings of the 27th International Conference on Fire Safety* 57-64 (1999).
8. J.C. Jones *Fuel* v. 78 507-508 (1999).
9. J.C. Jones, P.S. Chiz, R. Koh, J. Matthew *Fuel* v 75 1755-1757 (1996).

10. J.C. Jones *Journal of Loss Prevention in the Process Industries* - in press.
11. J.C. Jones *Journal of Loss Prevention in the Process Industries* - submitted for publication.
12. J.C. Jones *Journal of Loss Prevention in the Process Industries* v. 11 407-411 (1998).
13. J.C. Jones *Journal of Loss Prevention in the Process Industries* v. 12 183-185 (1999).
14. J.C. Jones *Proceedings of the 27th International Conference on Fire Safety* 57-64 (1999).
15. J.C. Jones *Applications Note 22026 Thermometric AB, Sweden* (1998).

TRIFLUORO METHYL IODIDE (CF₃I) AS A HALON 1301 REPLACEMENT FOR FUEL TANK INERTION APPLICATIONS

Juan A. Vitali

Chief, Fire Research Group
Survivability and Safety Division – AFRL/VACS
Fire Research – Air Base Technology – AFRL/MLQC
U.S. Air Force Research Laboratory
1901 Tenth St, Bldg 63, Suite 18
Wright Patterson AFB, OH 45433
Email: Juan.Vitali@va.wpafb.af.mil; Fax: (937)-255-2237

Steven R. Vanhorn

ASC/YPVF (F-16 System Program Office)
Lead Flight Equipment Engineer
1981 Monahan Way
Wright- Patterson AFB, OH 45433 USA
Email: VANHORSR@ypmail.wpafb.af.mil; Fax: (937) 255-4948

Keywords: Halon 1301, explosion suppression, ozone depletion, Montreal Protocol, CF₃I, Halon Replacement

ABSTRACT. The search for a replacement to the highly effective and safe Halon 1301 agent has yielded the development of CF₃I, its iodine analog, as a safe, and equally efficient replacement for explosion mitigation applications in military aircraft. Live fire tests conducted by the USAF yielded protection to standard offensive small weapons threats to the fuel tank of the F-16 weapon system equivalent to that of Halon 1301 systems. CF₃I is a drop-in replacement for the F-16 fuel inertion system thus reducing the retrofit cost of implementation.

1. INTRODUCTION

Historically, fuel fire explosion has been a major cause of aircraft losses in combat. To increase survivability, various techniques are used to reduce the vulnerability of the aircraft's fuel system to this significant threat effect. The F-16 weapon system relies on Halon 1301 to provide fuel cell inerting to protect the fuel system from explosions due to combat threats. Halon, the worst known ozone depleting chemical, has been eliminated as part of an international agreement to cease man-made production of these type chemicals. A ban on production that went into effect in 1994 has left only existing stocks of Halon available to support halon use in essential applications such as aircraft fire and explosion suppression systems. As a result, all F-16s are dependent on a finite amount of halon available from Department of Defense stocks. However, these stocks may become useless as there are currently on going preliminary discussions among some countries to ban the use of halon altogether.

A review of the F-16 fuel cell inerting technical characteristics and the overall fuel cell ullage inerting issues have resulted in a preliminary set of F-16 fuel cell explosion suppression system requirements (Reference 1). The review also highlighted information voids in baseline data that preclude immediate definition or specification of an optimum approach to replacement of the current Halon inerting system. Therefore, a test program was conducted to (1) help determine the F-16 fuel "bare" system vulnerability behavior, (2) confirm (and quantify) the performance of the current F-16 halon inerting system and (3) perform preliminary testing of candidate new alternative fire suppression systems.

A test series was planned to describe the F-16 fuel tank explosion suppression replacement and baseline characterization tests required to allow development of alternative approaches to the current F-16 Halon 1301 fuel tank inerting system. The test series was conducted to collect data to evaluate the vulnerability of the F-16 fuel system due to ballistic threat induced fuel/air vapor explosions in the fuel tank ullages. The ullage explosion test series was conducted using Air Force Research Laboratory (AFRL) W-Tank to simulate sections of F-16 internal fuselage A1 and F1 fuel tanks and F-16 wing fuel tanks. Explosion-initiation threats typically encountered by the F-16 while on user-specified missions were utilized in the ballistic tests. The test article

contained JP-8 or JP-8+100 fuel heated to a temperature and filled to a level defined by the 10% fuel state of the representative mission profile. Three major technical objectives addressed in this test program were:

1. What level of protection does the current halon system provide against fuel system ullage fire/explosions compared to no inerting protection at all?
2. What level of protection do alternative fire/explosion suppression candidates provide?
3. What alternative fire/explosion suppression candidates should be investigated in more detail in follow-on testing?

2.SYSTEM DEVELOPMENT

The F-16 aircraft has the capability to inert fuel tanks using Halon 1301. This system is shown in schematically in Figure 1(Reference 2). The system consists of a halon tank reservoir, a halon flow control valve, solenoid operated shutoff valves and associated plumbing, electrical wiring and switches. The halon reservoir is located in the wheel well area for easy access and rapid turnaround. The volume of halon reservoir is specified at a maximum of 340 cubic inches and the reservoir is pressurized by the vapor pressure of the halon, which varies from 560 psi at 150 °F to 17 psi at -40 °F. A 400 watt heater is installed to maintain reservoir pressures. A window with a ball float is incorporated into the reservoir tank to provide a liquid level indication at 235 cubic inches volume without the need for aircraft or ground electrical power. The reservoir also contains an integral pressure relief valve to relieve reservoir pressure at 600 psi, a threaded refill port with a zero leak valve for servicing and a quick disconnect at the outlet port. The halon reservoir is mounted in the aircraft with locator pins and can readily be removed during the combat turnaround and replaced with a fully serviced unit. This can be accomplished simultaneously with aircraft refueling.

Upon selection of "Tank Inerting" on the fuel control panel in the cockpit, the halon system is activated. Electrical signals are provided to the halon shutoff valve located in the vent tank to allow halon to flow to the fuel tanks, to the initial inert solenoid valve to open and to the internal tank vent and pressure control valve to reduce internal aircraft pressure. An airflow within the tanks is produced as the internal tank pressure is reduced from roughly 5.5 psig to 2.0 psig and air is vented overboard. This assists in the distribution of halon gas throughout the vapor space above the fuel. The initial inert valve opens for 20 seconds to permit a quick dump of halon into the forward, aft, and internal wing tanks on the F-16. An inert atmosphere at proper regulated valves as fuel is consumed or the aircraft changes altitude. The fuel absorbs some of the halon supplied to the tanks. This is replaced by a continuous bleed of halon through an orifice in the vent tank plumbing.

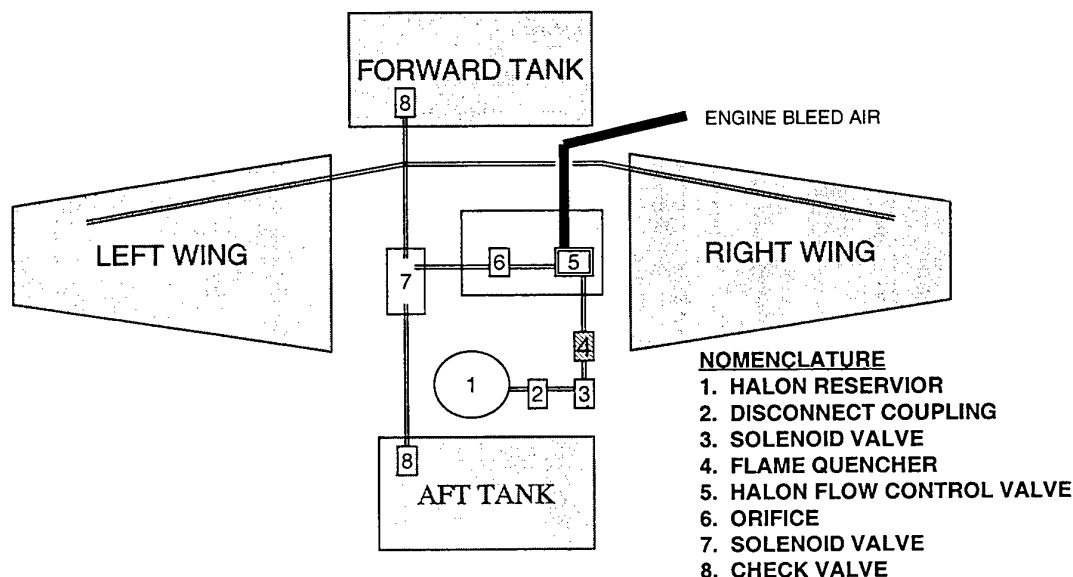


Figure 1: F-16 Inertion system schematic

In the unlikely event that fuel or fumes should leak backwards into the reservoir and be ignited by the heater, it was theorized that a fire could prorogate to the aircraft fuel tanks. In order to protect against this possibility, a flame arrestor is installed in the reservoir outlet line.

3. DEVELOPMENT TEST AND ANALYSIS

A comprehensive test and analysis program was planned to develop alternates candidates to halon 1301 for fuel inerting. The data from the government test will aid the F-16 airframe contractor to complete Engineering Manufacturing Development of the preferred candidate. The contractor's integration work will include materials compatibility tests and studies, solubility characteristics in JP-8 and JP-4, and engine component tests. The focus of the government test program was live munitions testing.

In today's dynamic all changing global environment, the F-16 aircraft may encounter a variety of conventional (non-nuclear) terminal threat weapons. During its operational life, these threats may include both surface-to-air types and may be present at both high and low altitudes. The terminal threat weaponry the F-16 might encounter includes the latest state-of-the-art technology air-to-air and surface-to-air ballistic weapons (guns), guided missiles and directed energy weapons (DEW). Desert Storm experiences for the F-16 highlight the growing missile threat while close air support mission means surface-to-air guns are potential threats. Therefore, the threats used in the test series were missile warheads and anti-aircraft artillery (AAA). DEW threats were not examined.

The ballistic threats and guided missiles can be divided into three major categories by weapon type: high explosive (HE) projectiles, non-explosive or armor piercing projectiles and HE missile warheads (fragments). The HE incendiary (HEI) AAA threats were not a focus due to limited budget of this test program. Tests were performed using 12.7mm armor piercing incendiary (API) projectile, 23mm API, 110-grain missile fragments, 150-grain missile fragments, and 300-grain missile fragments.

The tests simulate the case of an F-16 in an air-to-ground close air support mission. This mission is representative of F-16 experience in Dessert Storm. The mission was used to design and size the current halon inerting system, and is the scenario used for previous vulnerability analyses and live fire tests for the F-16 weapon system.

Fuel and ullage temperature is a critical parameter, which drives the ullage fuel/air ratio. The F-16 fuel system is designed to operate in temperature ranges from -65 °F to +160 °F. Fuel temperature at threat impact is dependent on the temperature of the fuel at take-off. The fuel temperature on the ground is dependent upon the ambient temperature of the day (i.e., a cold day or a hot day). The flight altitude and duration will alter this initial temperature. The fuel temperatures selected for ullage testing, (105 °F, 125 °F, 145 °F, and 165 °F) based upon likely flight conditions for the selected mission profile. Previous AFRL test data for B-1 program office (Reference 3) showed JP-8 fuel experienced very little pressure increases below 105 °F (leaner fuel vapor volume percent).

The fuel system vent and pressurization system is designed to keep internal pressure between 4.7 and 6.4 pounds per square inch gage (psig) for normal operations and between 1.0 and 3.0 psig or between 5.5 and 7.2 psi absolute (psia) for combat conditions. The ullage pressure was evaluated at approximately 3.0 psig, which is a representative pressure maintained by the F-16 for the selected mission profile. An equivalent stoichiometric ullage fuel/air mixture for the given fuel temperature and ullage pressure was used for testing. A fan was located inside the tank to ensure an even fuel/air mixture of the ullage.

The ullage test article consists of a 100-gallon rectangular tank (W-Tank), which simulates the basic configuration of an F-16 fuselage fuel tank (Figure 2). The tank measures 20 inches from front wall to back wall and 38 inches wide and high. The JP-8 ullage test article will contain a four-inch fuel level measured from the bottom of the W-Tank. The impact location on the target striker plate is 16 inches above this level. The striker plates used in the test were removable, representative of the F-16 wing and fuselage skin thickness, varying from 0.125 inches to 0.500 inches thick. The tank has window ports for external viewing by various cameras. The aircraft internal fuel level state is assumed to be 10 %, which leaves ullage volumes in the F-16 fuel tanks. JP-8 and JP-8+100 fuel was used in testing as is the case in the operational F-16 aircraft.

Airflow would have a small effect on the severity of an ullage explosion. The small entrance holes caused by the threats used the ullage test series do not allow significant airflow to enter the test article and significantly change the fuel/ air ratio. The pressure exerted on the test article by the airflow would be insignificant compared to the internal pressure associated with a fuel/ air explosion. Damage areas, including metal skin that would protrude into the airflow, should not be increased. Based on this information, airflow was not applied to the test article.

Test instrumentation was kept to a minimum with some redundancy. Thermocouples were used to acquire temperature data of the fuel and ullage. Piezoelectric pressure transducers were used to acquire pressure data and characterize fast response shock wave phenomena associated with an explosion. Pressure and temperature time histories and fuel/air vapor in the W-Tank were collected to characterize the ignition event. In addition, the temperature – time histories and video footage were examined for indications of a sustained fire following the impact event. Flash detectors indicated the time of the flash from a fragment impact incendiary functioning for an API projectile. Gun brakes paper over the target and a light screen between the muzzle and target were used to measure the projectile/ fragment velocity. Prior to each test, the amount of agent was measured using partial pressure into the tank and a sample was obtained in a Tedlar Sampling Bag. The Tedlar sampling bags were analyzed by the University of Dayton Research Institute using a gas chromatograph with flame ionization detection sampling analysis technique.

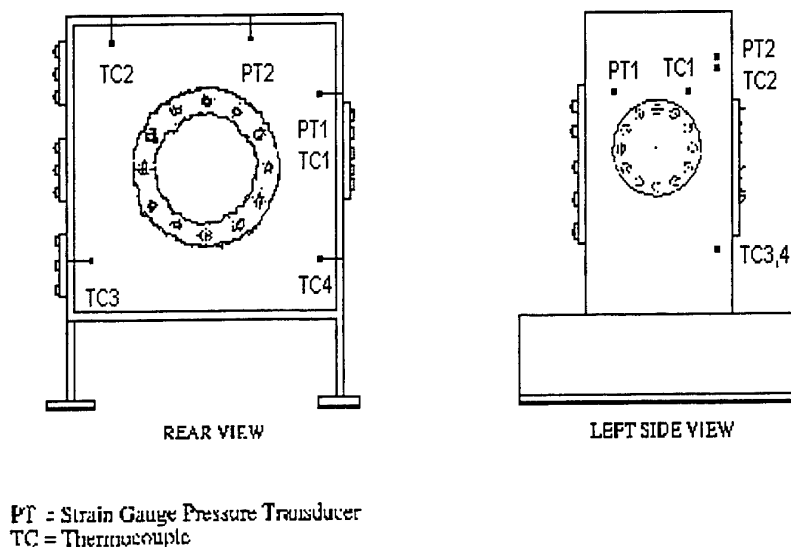


Figure 2: W-Tank schematic

The test program consisted of over 250 shots between all candidate alternative agents including C_2F_5H (HFC-125), C_3F_8 (FC-218), and CF_3I , as well as baselining CF_3Br (Halon 1301). This data will be used by F-16 airframe contractor to characterize the survivability and vulnerability of the F-16 aircraft using an alternate agent. The preferred agent based on testing to date and environmental friendliness is CF_3I .

The sensitivity of the CF_3I agent in JP-8 fuel to temperature is shown in Figure 3. The temperature peaks near the stoichiometric temperature of JP-8. All previous verification testing was completed with JP-4 fuel (Reference 4, 5). JP-8 is flammable at higher temperatures than JP-4. This is one reason why JP-8 is considered safer for operations such as ground refueling.

Generally, a fuel/air mixture will react if an ignition source, such as 12.7mm API, is introduced into a mixture. The rate of energy release by the reaction will be dependent on the fuel/air ratio and the temperature of the ignition source. In our test series the fuel/air ratio, which is described in the following formula was kept relatively constant.

$$F/A = \frac{(\text{Volume percent of fuel})(\text{Molecular weight of fuel})}{(\text{Volume percent of air})(\text{Molecular weight of air})}$$

A reaction in a fuel/air mixture whose fuel/air ratio is stoichiometric will consume all the reactants as the 125 °F test points shows. If a reaction occurs in a lean fuel/air mixture, less than stoichiometric, there is an excess of oxygen that must be heated to the product temperature by the heat generated by the reaction (Reference 6). The 105 °F test points results are such a case. In a reaction of rich fuel/air ratio, greater than stoichiometric, there is an excess of fuel vapor that will not react. This is because insufficient oxygen is present. The energy release is less again, resulting in a final temperature less than stoichiometric, as is the 165°F test points. The maximum final temperature actually occurs at a fuel/air just rich of stoichiometric because of the differences in specific heats of combustion products that occur. As a result, final temperatures and pressures will be dependent on the fuel/air ratio of the mixture. At fuel/air near the lean and rich flammability limits, modest pressure rises, less than 10 psi, were experienced while for fuel/air ratios near stoichiometric, the pressure was above 20 psi.

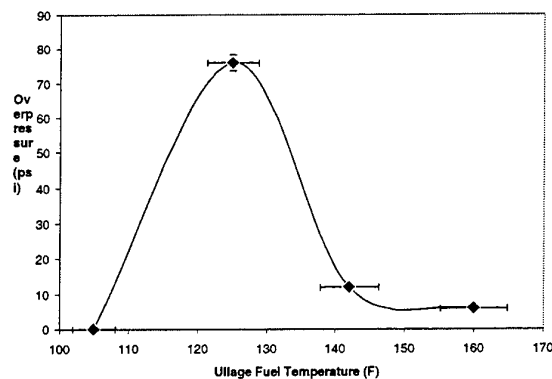


Figure 3: Temperature sensitivity
CF₃I Concentration: 7%, 0.250 Inch Panel, Threat: 12.7mm

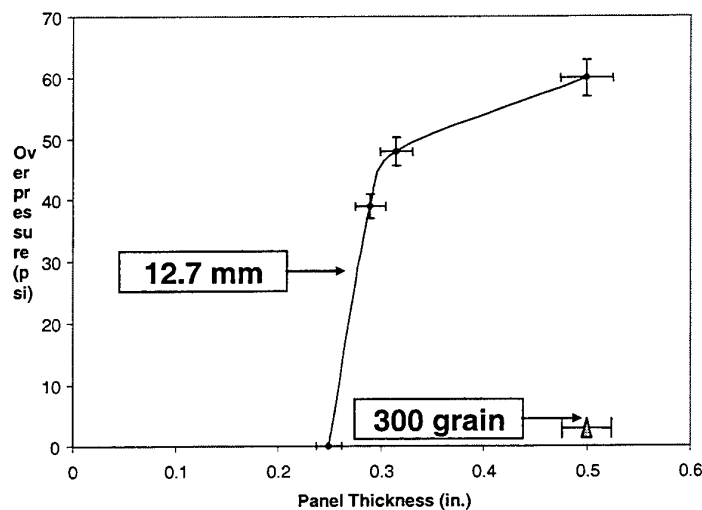


Figure 4: Panel thickness sensitivity
CF₃I Concentration: 8%, Ullage Temperature 125 °F, Threat: 12.7 mm and 300 grain

The sensitivity to panel thickness shown in Figure 4, is dependant on the threat. This again will be a function of the fuel/ air mixture to react with the ignition source, e.g.: the thermal energy deposited by a ballistic threat. The

thermal energy deposited by the ignition source was affected by the size of the fragment, the velocity of the fragment, and the thickness of the ullage tank wall striker plate. The test data would suggest that the concentration of energy that a 12.7mm has a greater chance of obtaining a stoichiometric ratio than that of a 300-grain missile fragment. The velocity of the 12.7mm was about 2500 feet per second (fps), while the 300 grain missile fragment was about 5500 fps.

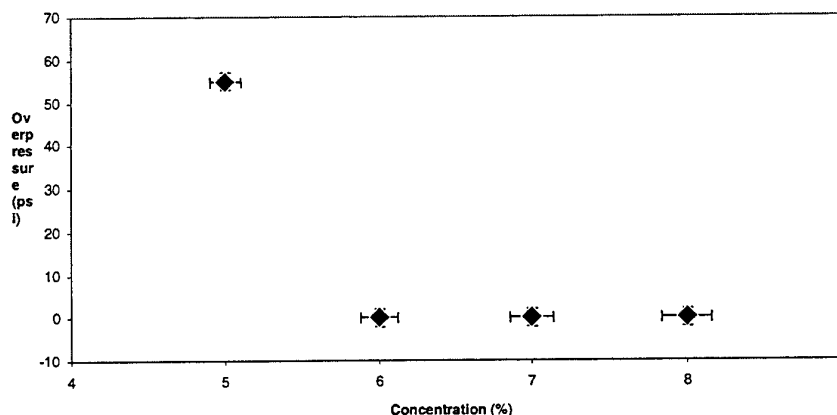


Figure 5: Concentration sensitivity
Ullage Temperature: 125 °F, 0.500 inch panel, Threat: 300 grain

The sensitivity to concentration is again related to the fuel/air mixture and thermal energy. Figure 5 shows for the given test point that stoichiometric mixture is possible below 6% concentration. Above 6% concentration, the amount of agent increases the molecular weight of air creating a lean stoichiometric mixture and a modest pressure rise less than 10 psi.

4. SUMMARY/CONCLUSIONS

The technical objectives of the test program were met. An agent is required to protect from overpressure. Using the original threats of the JP-4 verification at a concentration of 5%, the baseline agent of Halon 1301 prevented an overpressure in JP-8. Alternative suppression agents were characterized for live munitions. Preliminary analysis indicates CF₃I will be able to replace Halon 1301 with minor airframe system modifications. The F-16 airframe contractor is continuing to refine this analysis to an Engineering Manufacturing Development status. CF₃I offers an environmentally friendly answer to fire suppression for the F-16, while working within existing airframe requirements and specifications.

REFERENCES

1. S. Van Horn, F-16 Fuel Tank Explosion Suppression System Replacement Characterization Test With the W-Tank, March 1997.
2. J. Klien, The F-16 Halon Tank Inerting System, AIAA Aircraft Systems and Technology Conference, August 1981.
3. J.P. Haas, B-1 Live Fire Test and Evaluation Program: JP-8 Characterization Development Test Report, May 1997.
4. General Dynamics Corporation, Compatibility of F-16 Fuel Tank Materials with Halon 1301, ECDM # 122, January 1977.
5. General Dynamics Corporation, F-16A Fuel Subsystem F-16 No.7 (FSD A-6) Aircraft Fuel Tank Inerting System Functional Tests After Modification of the 16VP018 Halon Flow Control Valve, August 1978.
6. White Paper by Andrew Pascal, October 1995.

TWA800 FUEL TANK COMBUSTION AND EXPLOSION MIXTURES

Floyd A. Wyczalek

FW Lilly Inc.

155 S. Williamsbury Road, Bloomfield Hills MI 48301 USA

Email: 75467.2677@compuserve.com; Fax: (248)-646-9585

Keywords: fuel tank, air fuel ratio model, combustion, explosion, ignition energy

ABSTRACT. This project identified atmospheric conditions under which a Boeing model 747-131 fixed wing jet aircraft empty center wing tank (CWT), containing a residual fuel loading of 3 kg/m^3 , about 200 liters of aviation kerosene (JetA Athens refinery), could form hazardous air/fuel mixtures. The issues are limited to explosion safety concerns for certificated fixed wing jet aircraft in scheduled passenger service. It is certain a combustible mixture does not exist in a fuel tank containing Jet-A fuel at ambient temperatures below 38°C (100°F), the lean limit flash point (LFP) at sea level. Nevertheless, this study identified six unlikely, but possible critical conditions which may permit combustible mixtures to exist within jet aircraft fuel tanks. The scope is limited to concerns relating to fixed wing jet aircraft. It is further limited to a review of scientific literature from 1950 to present time, which defined the thermodynamic and minimum ignition properties of aviation gasoline and commercial jet fuels; and, comparison with new thermodynamic data for JetA Athens fuel, released by National Transportation Safety Board (NTSB) in December 1997 [1]. This paper demonstrates that USAF Wright Air Development Center and US Bureau of Mines published comprehensive evaluations of potential hazards relating to jet aircraft fuel tanks as early as 1952 [2].

1. INTRODUCTION

The history of the last hours of Trans World Airlines, Inc., Flight 800 Boeing 747-131, N93119 fueled with low volatility kerosene type JetA in Athens, Greece, arrival New York Kennedy 17 July 1997, departure for Paris, essentially empty center fuel tank of 50 m^3 (12980 gallons) containing about 200 liters (52 gallons) of Athens refinery JetA fuel, exploding 11 minutes after takeoff at 4176 m (13700 ft) altitude, 12 km (8 miles) South of East Moriches, New York, 17 July 1997 NTSB Docket SA-516 [1].

The analysis is based on a mathematical model shown by Wyczalek and Suh [3] to estimate the air-fuel mass ratios (AFR) as a function of fuel saturation temperature (boiling points at various pressures). JetA aviation fuel is a mixture of a wide range of the heavier kerosene like hydrocarbon (HC) molecules with a relatively wide band of ASTM D86 distillation temperatures as shown by Wyczalek and Suh [3] and Sagebiel et al [4]. Consequently, the properties of three single component hydrocarbon (HC) liquid fuels: hexane, octane, naphthalene, published by Marks [5]; are included to serve as reference standards. Furthermore, the properties of JP6 jet fuel and aviation kerosene, both multiple HC species fuels published by Zabetakis et al [6], were included to relate the new JetA sample test data to historical 1952 scientific data on jet fuels.

Further, air/fuel ratios from about 2 to 1 rich flammability limit (RFL) through about 35 to 1 lean flammability limit (LFL) are ignitable for gasoline and jet fuel [7]. The temperature 38°C at one atmosphere sea level, is specifically defined as lean limit flash point for JetA fuel. A composite plot of air/fuel mass ratio vs. saturation temperature, RFL and LFL, define a zone of potentially hazardous air-fuel vapor mixtures.

The scope of this paper is limited to: relating the new JetA Athens refinery test data to the zone of flammability for jet aircraft fuels as functions of pressure and temperature; and, to correlating the model AFR for JetA fuel to AFR test data obtained during a series of 1997 emulation flight tests reported by Sagebiel et al exhibit 20G in NTSB-DCA-96-MA-070 [4]. 6/15/99 8:50 AM

2. AIR FUEL RATIO MODEL

The air-fuel ratio (AFR) model is an application of Dalton's Law of partial pressures which states that modal composition of a multi component gas mixture and/or vapor mixture is proportional to the distribution of partial pressures and molecular weights of the components [8].

We can assume saturated fuel vapor approaches perfect gas behavior and apply the perfect gas law to relate pressure, volume, temperature and mole fraction. This is based on the observation of van der Waals that at low pressures the reduced properties: reduced pressure and reduced temperature, of vapors and gases approximate the perfect gas equation [8-10].

For example, the single component hydrocarbon (HC) naphthalene $C_{10}H_8$ molecular weight 128, has a carbon number and molecular weight similar to JetA fuel. Since, naphthalene reduced pressure, defined as partial pressure divided by critical pressure 40.5 bar, equals 0.0025 almost zero; and, reduced temperature, ambient temperature divided by critical temperature 748.4° Kelvin (K) equals 0.416 also a small value, the deviation from perfect gas behavior for naphthalene, and by inference for JetA, also may be considered negligible [10].

When we assume that JetA fuel-air mixtures can be treated mathematically as a perfect gas, the fuel input values required are: JetA fuel saturation vapor pressure and temperature relationship, plus, mean effective molecular weight of JetA fuel, as shown by Wyczalek and Suh [3], Sagebiel et al [4], and Shepherd et al [11]. Since flight TWA800 was fueled with JetA fuel from the Athens refinery in Greece, which is a multi-component liquid with a wide range of HC molecules, these properties must be obtained by laboratory tests of Athens JetA samples.

Fig. 1 shows the hydrocarbon component spectrum for aviation kerosene (LAXJetA), equivalent to but not Athens refinery JetA, in terms of percent abundance based on Gas-Chromatograph Mass Spectrometer studies at California Institute of Technology (CIT), by Sagebiel et al [4]. Shepherd et al [11] specifically tested Athens JetA fuel samples, and reported a typical carbon number of 9 to 10, a mean effective molecular weight of about 132 and an average hydrogen-carbon (H/C) ratio of about 1.8, in NTSB exhibit 20G [4]. Further, Shepherd [11] reported fuel vapor pressure vs saturation temperature for LAXJetA at loading of 3 kg/m³ and 400 kg/m³. Finally, the Athens JetA air-fuel vapor-mixture temperature at the final moment of the TWA800 event was needed to relate the AFR model directly to flight TWA800. Fig. 2 illustrates the center wing tank (CWT) temperature-time history from NTSB exhibit 23F [1], during a series of nine TWA800 emulation flights of a Boeing 747-121, test takeoffs were from New York Kennedy Airport July 1997.

As examples, Fig. 2 shows the temperature profiles for three of the nine thermocouples mounted in the CWT during this flight emulation test series. The upper curve is the highest temperature profile recorded and shows a

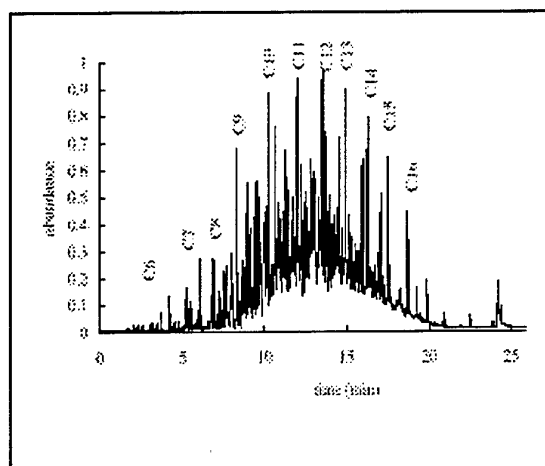


Fig. 1 LAXJetA fuel hydrocarbon component distribution plotted vs carbon number

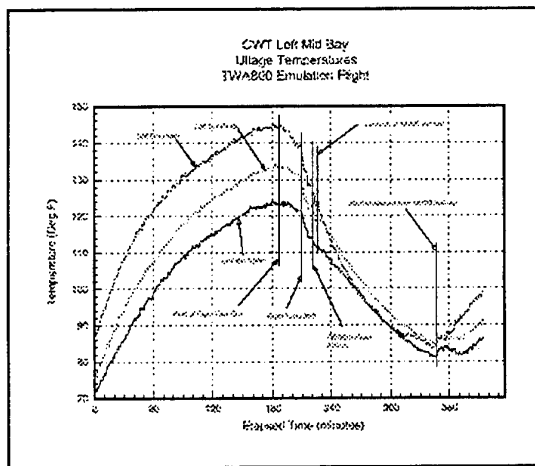


Fig. 2 Center wing tank ullage temperature °F vs time history for three thermocouples

temperature of about 88° F (31° C) at time zero, representing the time the fatal Athens-New York flight arrived NY Kennedy airport. At start of flight test taxi, 187 minutes later, the CWT left mid bay ullage temperature (temperature of clearance air-fuel vapor mixture above the liquid fuel), was about 145° F (63° C), at flight test

liftoff, 210 minutes, temperature was 136° F (58° C), and finally, at TWA800 event altitude 11 minutes later at time 221 minutes, the CWT clearance space above the fuel, (ullage) temperature was 127° F (53° C) [1].

3. FUEL VAPOR PRESSURE PROPERTIES

California Institute of Technology (Caltech) (CIT), Explosion Dynamics Lab., Shepherd et al [11], measured saturated vapor properties of LAXJetA aviation kerosene at the normal fuel loading factor of 400 kg fuel/m³ of tank volume, and also at 3 kg/m³. The lower 3 kg/m³ value is believed to be the fuel loading factor in the center wing tank (CWT) of flight TWA800 at the time of the explosion event. Temperature 38° C (100° F) is the JetA lean limit flash point at sea level, and, 49° C (120° F) is believed to be the CWT ullage air fuel mixture temperature at the time of the TWA800 event, Fig. 2.

Prior to these CIT measurements, literature on HC fuel saturation properties had not reported effects of fuel loading factor on vapor pressure of fuels. Caltech has shown that fuel loading factor has a significant effect on the vapor pressures recorded, and consequently, validity of the AFR model.

Fig. 3 compares the CIT LAXJetA400 test data denoted by the "X" symbol, a multi component hydrocarbon (HC) fuel, to three single component HC fuels: hexane denoted by the "+" symbol, octane denoted by the "diamond" symbol, and naphthalene denoted by the "O" symbol, which serve as a reference framework. Furthermore, the decades old 1962 data for aviation kerosene denoted by the "box" symbol, Zabetakis et al [6], published by the US Bureau of Mines, is also plotted as a tie-in with historical data. The LAXJetA400 data denoted by the "X" symbol is coincident with part of the Zabetakis data for aviation kerosene denoted by the "box" symbol. The LAXJet400 code denotes data obtained at a fuel tank JetA fuel loading factor of 400 kg/m³. Elsewhere the LAXJetA3 code denotes data obtained at a fuel tank JetA loading factor of 3 kg/m³.

This coincidence of old and new aviation kerosene vapor pressure data, although reassuring, is unusual, in view of the differences between modern and decades old petroleum feed stock and refinery equipment and operating parameters.

4. PREDICTABILITY OF AFR MODEL

Fig. 4 shows air-fuel mass ratio (AFR) in grams of dry air /gram of fuel vapor vs. temperature in °C. Since we have shown in a preceding paragraph that the air-fuel vapor mixtures within the ambient pressure and temperature range essentially approximate perfect gas behavior, the perfect gas equation $PV=nRT$ applies, where: n =moles, $R=0.08207$ liter-atm/mole-°K [3]. This simplification results in an effective AFR model. As an example, the AFR is modeled at each temperature by multiplying the ratio of partial pressure of air/partial vapor pressure of fuel, times, the ratio of molecular weight of air/molecular weight of fuel.

As an example, the predicted ARF based on the CIT LAXJetA400 vapor pressure data "X" symbol, covers the AFR range from about 10 to 1 rich to beyond 40 to 1 lean, and the temperature range from about 32° C (90° F) to about 66° C (150° F). Fig. 2 has previously shown that the air-fuel vapor ullage temperature exceeded 120° F (49° C) in the left mid bay of the center wing tank (CWT), during the Boeing 747-121 flight emulation tests conducted by the NTSB in July 1997 [1].

At sea level, Fig. 4 predicts an AFR of 19 to 1 at the temperature of 49° C (120° F), based on the CIT LAXJetA400 vapor pressure test data. Furthermore, LAXJetA400 AFR values are in a range between single component reference fuels: octane "diamond" and naphthalene "O" symbols, which validate sea level behavior of LAXJetA400 at the 400 kg/m³ fuel loading factor.

5. LABORATORY AND FLIGHT TEST DATA CORRELATION

Fig. 5 illustrates effect of altitude on AFR at a fuel loading factor of 3 kg/m³, as predicted by the mathematical AFR model shown by Wyczalek and Suh [3]. As examples, the model shows a dot curve at sea level, a solid curve at 14000 ft (4267 m) for the TWA800 event altitude, a dash-dot curve at 30000 ft (9144 m), and a dash curve at 40000 ft (12192 m).

An example of test data correlation with the AFR mathematical model, Caltech test data "X" symbols in Fig. 5 for LAXJetA3 aviation kerosene at a fuel loading factor of 3 kg/m^3 , was corrected to partial pressure of air at 4267 m altitude, see 1962 US Standard Atmosphere in Marks [10], to demonstrate correlation with the curve predicted by the AFR model at 4267 m, solid curve plot. Similar plots were made to validate correlation at seal level, 9144 m, and 12192 m altitudes.

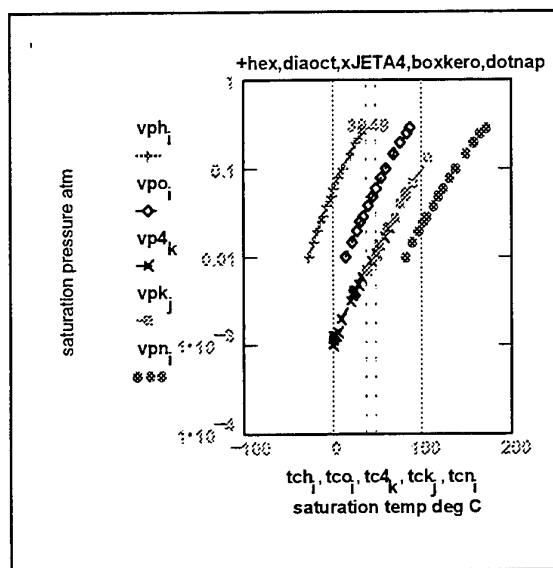


Fig. 3 Saturation pressure in atm vs saturation temperature degrees Centigrade

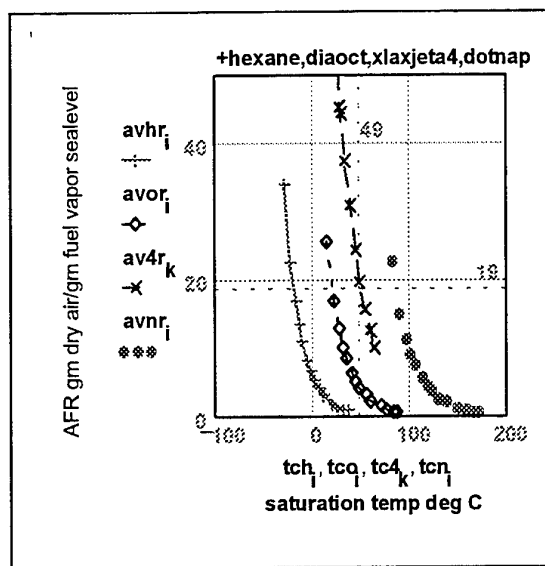


Fig. 4 Air-fuel ratio model at sea level for 400 kg/m^3 fuel loading and classic single component HC reference fuels

Included in Fig. 5 are nine flight test AFR data points, "o" symbol, obtained with Athens JetA at a 3 kg/m^3 fuel loading during NTSB TWA800 flight emulation, Sagebiel et al [4]. AFR for three center wing tank ullage samples are shown at sea level, three points at 3048 m (10000 ft), and three points at 4267 m (14000 ft). Three sea level points are just above the model sea level AFR dotted line curve. The three 4267 m points are tangent to the 4267 m model AFR solid line curve.

6. MINIMUM IGNITION ENERGY FOR JETA SAMPLES

Fig. 6 shows minimum ignition energy in milli-Joules vs air fuel ratio for LAXJetA fuel at the two fuel loading factors of 200 kg/m^3 shown by the "x" symbol and 3 kg/m^3 shown by the "o" symbol, in comparison to historical ignitability for butane, "diamond" symbols, C_4H_{10} from 1952 Zabetakis data [2]. These two sets of new JetA ignition energy data bracket the historical data for butane.

Although Shepherd et al [11] plotted JetA minimum ignition energy against temperature $^{\circ}\text{C}$, we converted the "o" symbol 3 kg/m^3 temperature data to equivalent "o" symbol air-fuel ratio by entering the temperature axis of Fig. 5 for the 3 kg/m^3 loading at sea level. The 200 kg/m^3 ignition test data denoted by the "x" symbol was similarly converted to "x" symbol AFR points with an AFR plot at a 300 kg/m^3 loading, since AFR data at 200 kg/m^3 was not available at this point in time.

This unorthodox expedient of correlating 200 kg/m^3 and 300 kg/m^3 data was adopted on a tentative basis, because of the limited test points available at the time of the NTSB hearings in December 1997. Further testing is expected to be on-going to improve resolution, Shepherd et al [11].

Fig. 6 shows minimum ignition energy depends on fuel loading. For example, at a given AFR, ignition energy values are lower at 3 kg/m^3 than for a 200 kg/m^3 loading. This result is the reverse of our expectations. Hopefully, tests to resolve this issue are on-going.

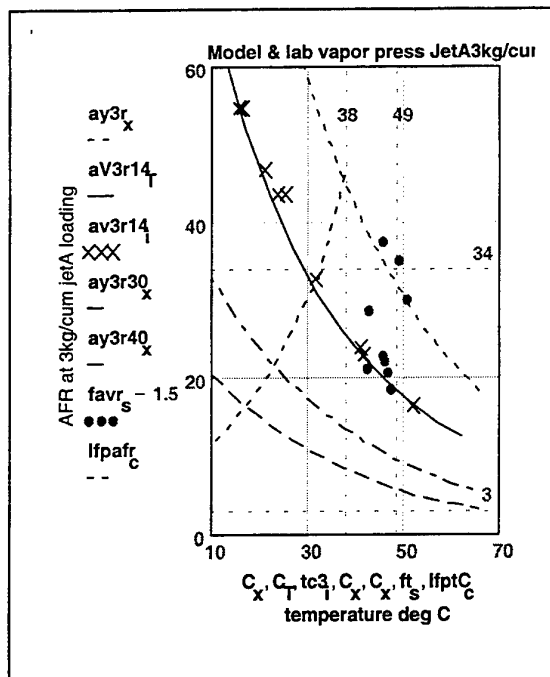


Fig. 5 Correlation of laboratory and flight test data with mathematical model shows effect of altitude on air fuel ratio

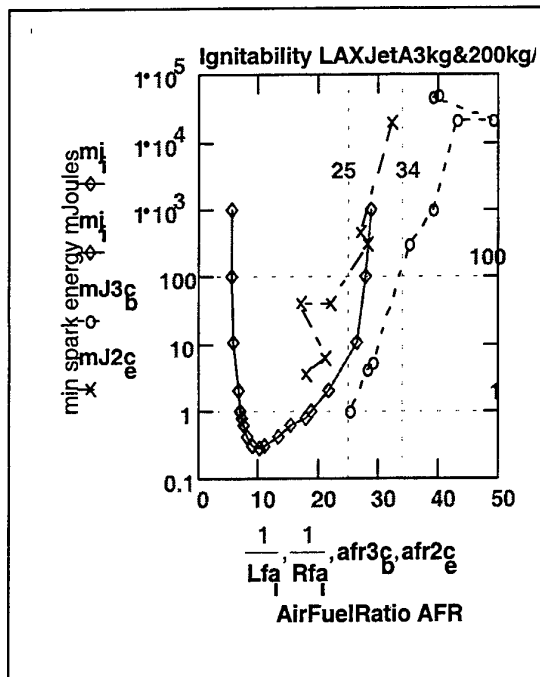


Fig. 6 Minimum ignition energy in milli-Joules vs air fuel ratio for JetA fuel

7. CONCLUSIONS

This evaluation of NTSB TWA800 emulation flight test data [1] and laboratory test data which defines the fuel saturated vapor - temperature properties, air-fuel vapor mixture ratios, and minimum ignition energy of JetA aviation kerosene and Athens JetA fuel samples, led to the following conclusions regarding air-fuel mixtures in the fuel tank clearance volume, of a Boeing model 747-121 jet aircraft:

1. In the case of so called empty jet aircraft fuel tanks containing about 3 kg fuel/m³ tank volume, residual JetA aviation kerosene, the head space air-fuel vapor mixture is normally too lean to propagate a flame at ambient temperatures below the lean flammability limit of 38°C (100°F) [2,3,11],
2. Conversely, when the temperature of the air-fuel vapor within the ullage space is above the lean limit flash point temperature of 38° C (100° F) at sea level, and below the rich flammability limit temperature of 93° C (200°F), then, the air-fuel vapor mixture may be potentially hazardous [3,4,11].
3. Within the lean limit and rich limit temperature flammability boundaries stated in conclusions [1] and [2], these flammability boundaries decrease with increasing altitude, and, In accord with Murphy's Principle and Jung's Synchronicity Principle, six critical factors occurred In a synchronous combination which led to the fuel tank explosion of TWA800 [3,12,13].
4. These critical factors are: one, a fuel temperature of about 49° C (120° F); two, a lean limit flash point of 38° C (100°F) at sea level for the JetA Athens refinery fuel which crossed over into the flammable zone for JetA fuel; three, the reduced atmospheric pressure at 4176 m (13700 ft) altitude which drove the air-fuel mixture further into the flammable zone, NTSB 23F [1-4,12,13].

5. And further, four, an air-fuel ratio of about 35 to 1; five, the very low electrostatic spark energy levels ranging from 1 to 100 milli-Joules which may ignite an air-fuel vapor mixture within the flammable AFR zone from 2 to 1 rich through 40 to 1 lean; and, six, the common and familiar household electrostatic spark, which may exhibit energy levels as high as 15 mJ, exceeding the minimum ignition energy levels reported for wide ranges of air-hydrocarbon vapor mixtures, including JetA [2,3,11-13].

REFERENCES

1. NTSB Docket SA-516 (1997), "Flight Test Results: TWA800 Emulation Flight", *NTSB Docket SA-516 exhibit 23Fpg8, pg9 of 38 is fig2*, 7 Dec 1997, Baltimore, MD.
2. M.G. Zabetakis, et al (1952), "Research on the Flammability characteristics of Aircraft Fuels", Wright Air Development Center, Tech report 52-35 supplement 4, 85 pp.
3. F.A. Wyczalek, & C.M. Suh, (1997). "Fuel Tank Combustible Mixtures - New Lessons Learned", 32nd *IECEC Proceedings, paper 97004 AIChE*, Honolulu, Hawaii, 3-7 August 1997.
4. J.C. Sagebiel, et al (1997) "Sampling and Analysis of Vapors from the Center Wing Tank of a Test Boeing 747-100 Aircraft" Desert Research Institute, U of Nevada Reno, *NTSB Docket SA-516 exhibit 20G*, 7 Dec 1997, Baltimore, MD.
5. L.S. Marks', (1990), *'Mechanical Engineers Handbook' ninth ed, Thermodynamic Saturation Temp Properties of hexane, octane, naphthalene, diphenyl pp4-57 to 4-60*, McGraw Hill.
6. M.G. Zabetakis, et al (1962), "Review of Fire and Explosion Hazards of Flight Vehicle Combustibles", flash point, rich limit, spontaneous ignition temperatures, and saturated vapor vs temp characteristics of JP6 in air. pp58-59 *US Bureau of Mines, info circular 8137*, 80pp.
7. M.G. Zabetakis, et al (1965), "Flammability Characteristics of Combustible Gasses and Vapors", gasoline lean limit=48g/m³, rich limit=360g/m³ at 298°K, *US Bureau of Mines, Bulletin 627*, Washington DC.
8. L.S.Marks', (1941), *'Mechanical Engineers Handbook' 4th ed, Dalton's Law , Avagadro's Law p378, van der Waals p311* McGraw-Hill.
9. E.B. Millard, (1953), *'Physical Chemistry for Colleges', 7th ed, units, standards ch 1 pp19-21, properties of substances in gases state ch 4, perfect gas eq of state p89*, McGraw-Hill.
10. L.S. Marks', (1996), *'Standard Handbook for Mechanical Engineers' tenth ed, Petroleum and Other Liquid Fuels pp7-1 to 7-14; Specifications for Aviation Gasoline pp7-13; Aeronautics chap 11.4 US Std Atm p11-60, saturation properties of HC pp4-53 to 4-56, van der Waals p4-8, critical propertied p4-51* McGraw Hill.
11. J.E. Shepherd, et al (1997), "Jet A Explosion Experiments: Laboratory Testing", Caltech CIT, *NTSB Docket SA-516 exhibit 20Dpg67, pg74 of 75 is fig1*, 7 Dec 1997, MD.
12. F.A. Wyczalek, (1998). "TWA800 Fuel Tank Flammability- Analytical Investigation", *IEEE Aerospace and Electronics Systems Magazine*, v13 n1, pp 16-19, Jan 1998.
13. F.A. Wyczalek, (1998). "Computer Modeling Applied to TWA800 Fuel Tank Forensic Issues", *CEC - Computers in Engineering Conf, Proceedings*, Atlanta, GA.

SECTION TEMPERATURE FIELD RECONSTRUCTION FROM FLAME IMAGES USING ALGEBRAIC RECONSTRUCTION TECHNIQUE

Fei Wang Yong Chi Chengye Wei Zengyi Ma Jianhua Yan Gang Hu Kefa Cen

Department of Energy Engineering

Zhejiang University, P.R. China

Email: itpe@sun.zju.edu.cn; Fax: 86-571-7951616

Keywords: algebraic iterative, reconstruction, image processing, temperature field

ABSTRACT. In the study of measurement for the flame temperature field, using the method of image processing, how to reconstruct three-dimensional temperature field from two-dimensional accumulative images of the flame is very important. In this paper, combining with the principles of sector scanning Computer Tomography (CT) and flame radiant transfer equation, the controlling equation of the radiation intensity which decay with projective paths is deduced. After dividing a flame section into $M \times N$ grids, temperature and radiant extinction coefficient distribution be solved by iterations to discrete equations simultaneously using Algebraic Reconstruction Technique (ART). Experiment research is proceeding using this method on a burner mixed coal and oil, possible error and improvable direction is also discussed.

1. INTRODUCTION

In the study of combustion, the temperature field is very important for combustion diagnosis and boiler control, but it is difficult for existing techniques to measure three-dimension temperature distribution of the flame accurately. In recent years, many researchers who used computer image processing technique and optical tomography technique, have made some progress in determining combustion situation and temperature level. It appears that Japan applied image processing technique to flame monitoring was first applied in Japan. FIRS (Flame Image Recognition System) developed by Hitachi Research Lab, which was applied to HIACS-3000 system, can obtain the distribution of the flame temperature and the NO_x concentration combustion [1]. OPTIS (Optical Image Flame Scanner) of Mitsubishi Corp. improved the sensitivity and detecting capability of the system to the flame by using the optical image sensor. It can be used to distinguish shape of the flame and determine stableness of the flame [2]. DIMAC (Digital Monitoring and Analysis of Combustion), developed by IVO (Imatran Voima Oy) Corp. in Finland, can help to improve the efficiency of combustion, reduce the amount of aided oil and lower the oxygen concentration in the exit of the boiler [3]. In China, Zhou [4] calculated 2-dimensional temperature field from the flame radiant energy distribution by using a temperature referring point, and gave a method to reconstruct 3-dimensional temperature field [5]. Xu [6] developed a image processing system, which reflected combustion situation in boiler. It has been used in several power plants [6]. Wang [7] studied stableness of the combustion and detection of the flame [7]. Yan [8] reconstructed a temperature field using improved algebraic iteration technique. In addition to these, Electric Power Research Institute of America [9] and CE Corp. also carry out studies on how to detect and monitor the combustion by using image technique. Most of research mentioned above concerned only combustion diagnosis, three-dimensional temperature distribution was studied seldom, which is a difficult point in this research.

This paper deduces the relation between space radiant intensity and accumulative grey value according to radiation transfer equation and optical specificity of the camera system. Section temperature distribution is reconstructed from the projection using Algebraic Reconstruction Techniques (ART). Experimental results and numerical analog analysis have also been given.

2. TEMPERATURE RECONSTRUCTION

2.1 The Principle of Computer Tomography (CT)

The invention of CT technique is a revolution for medicine and other related area whose principle and method also fit to the reconstruction of flame temperature field. Taking X-ray CT for instance, it detects the cross-section of the body using very thin X-ray. The intensity of the X-ray which crosses the body is inversely proportional to exponent of the integral of the medium absorption coefficient along the ray. So, the line integral of the absorption coefficient can be worked out if the logarithm to the base of the intensity of the X-ray has been calculated, as shown in Figure 1.

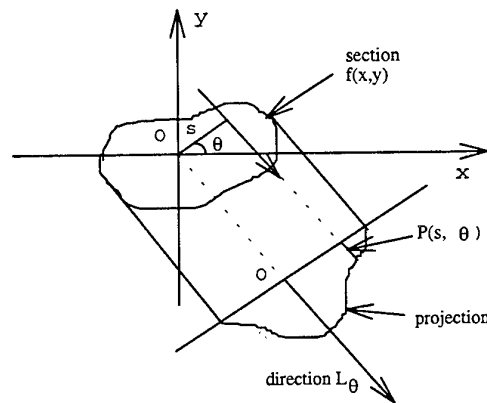


Fig. 1. Section and projection

$I_\theta(s)$ indicates 1-dimensional distribution of the X-ray intensity in L_θ direction, I_0 indicates the intensity of the incident X-ray, $P(s, \theta)$ represents the integral of θ direction, if :

$$P(S, \theta) = \ln\{I_0 / I_\theta(S)\} \quad (1)$$

hence, there is a relationship between $P(s, \theta)$ and the absorption coefficient of the section:

$$P(S, \theta) = \int_{L_{s\theta}} f(x, y) dl \quad (2)$$

the right part of the equation represents the integral value along the path $L_{s\theta}$.

In Equation (2), $f(x, y)$ is the indeterminate distribution function, $P(s, \theta)$ is the value that we can measure directly, so, we should solve $f(x, y)$ from Equation (2). This is reconstruction image from the projection. In medical CT technology, many effective methods have been advanced to figure out $f(x, y)$, such as anti-matrix method, iteration method, converse projection method, FFT method, convolution, and Radon integral.

2.2 Controlling Equations of Radiant Transfer

The basic principle of three-dimension temperature field calculation from the flame image is the same as those of image reconstruction from the projection in CT. Information captured by camera is the accumulative of radiation of every point along the ray's direction. In order to reconstruct three dimension temperature distribution, it is very important to clarify that how the radiant intensity transmits to camera target.

The flame radiant transfer in pulverized coal boiler is the result of interaction of emission, absorption and scatter of gas and particle. The radiant transfer equation, Which describes change of the radiant intensity in position \vec{r} along direction \vec{s} , can be in the form of [11]:

$$dI(\vec{r}, \vec{s}) / d\vec{s} = -(k_g + k_p + \delta_{sp})I(\vec{r}, \vec{s}) + k_g I_{bg}(\vec{r}) + k_p I_{bp}(\vec{r}) + \delta_{sp} / 4\pi \int_{4\pi} I(\vec{r}, \vec{s}') \phi(\vec{s}, \vec{s}') d\omega' \quad (3)$$

in this equation, k_g and k_p is the radiant absorption coefficient of gas and particle respectively, I_{bg} and I_{bp} is the blackbody radiant intensity of gas and particle, δ_{sp} is scatter coefficient of particle, ϕ is phase function.

Reference [12] analyzed how to simplify the radiant transfer equation when it is used in image processing. Neglecting radiation of gas and effect of scatter, simplified radiant transfer equation is:

$$dI(\vec{r}, \vec{s}) / d\vec{s} = -k_p I(\vec{r}, \vec{s}) + k_p I_{bp}(\vec{r}) \quad (4)$$

The section for measurement is divided into grid, δs_p is the selected wavelength, Equation (4) is integrated in every single grid, we can obtain:

$$I_{o\lambda} = I_{i\lambda} e^{-ks} + I_{b\lambda} (1 - e^{-ks}) \quad (5)$$

in this equation, s is the distance of the ray in the grid, k is radiant damping coefficient, $I_{o\lambda}$ and $I_{i\lambda}$ is respectively radiant intensity of out of and into the grid, $I_{b\lambda}$ is the blackbody radiant intensity of the grid.

To a ray as describing in Figure 2, accumulative radiant intensity obtained by CCD along that ray can be calculated and reorganized:

$$P = I_{w\lambda} e^{-(k_1 s_1 + k_2 s_2 + \dots + k_m s_m)} + I_{b\lambda 1} (1 - e^{-k_1 s_1}) e^{-(k_2 s_2 + \dots + k_m s_m)} + I_{b\lambda 2} (1 - e^{-k_2 s_2}) e^{-(k_3 s_3 + \dots + k_m s_m)} + \dots \quad (6)$$

$$+ I_{b\lambda i} (1 - e^{-k_i s_i}) e^{-(k_{i+1} s_{i+1} + \dots + k_m s_m)} + \dots + I_{b\lambda m} (1 - e^{-k_m s_m})$$

in the above equation, $I_{w\lambda}$ is radiant intensity emitted by the wall of boiler, P is the accumulative radiant intensity along ray number j .

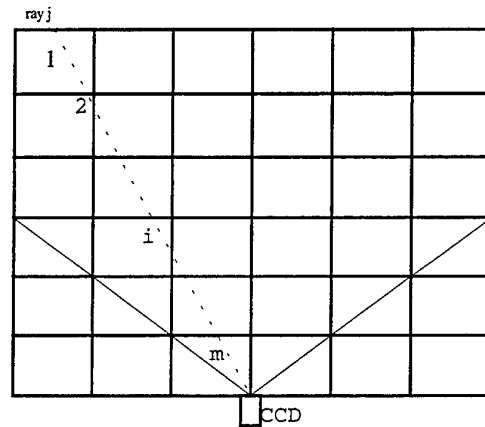


Fig 2. Projection of the radiant intensity

The temperature of the wall is further low than that of the flame, so effect of the wall is neglected. Simplified Equation (6) is:

$$P_j = \sum_i A_{i,j} I_{b\lambda i} \quad (7)$$

i is the ordinal number of the grid ($i=1,2,\dots,m$), m is the amount of the grid along number j ray, j is the ordinal number of rays, $A_{i,j}$ is weight number,

$$A_{i,j} = (1 - e^{-k_i s_{i,j}}) e^{-(k_{i+1} s_{i+1,j} + \dots + k_m s_{m,j})} \quad (8)$$

According to Plank law, we can obtain:

$$T_i = c_2 / \lambda \ln [c_1 / (\lambda^5 \pi I_{b\lambda i}) + 1] \quad (9)$$

2.3 Optical Transformation Relation of Camera System

In Equation (6), P is accumulative radiant intensity which arrive at camera target. In the system of image

processing, We apply color Charge Coupled Devices (CCD) camera to grab flame image. Because of the effect of camera's flare stop, whose function is to diminish garbage ray, only radiation from those positions which satisfy specific optical geometric relation can be accumulated and compose of the flame image. After radiation passes by optical systems and arrive at the target of CCD, it is transformed to grey value G by electrooptical device in camera. Assumed medium between flame and camera have no absorption to radiation. Some elements, such as absorption of optical filter, optical transfer loss and electrooptical transform efficiency, must be considered. According to mention above, the relation of P and G can be formed:

$$G = C P \quad (10)$$

C is response of the whole optical system, its value is obtained by experimental calibration. Equations (7)-(10) compose of the controlling function of three-dimension reconstruction from flame image.

2.4 ART Reconstruction Algorithm

In Equation (7), $A_{i,j}$ is a coefficient related with temperature $T_{i,j}$, so equation is non-linear. Algebraic Reconstruction Techniques (ART) especially fits to the situation such as three-dimension reconstruction from flame image, where projective data is not complete. The principal process of ART is: assumed a initial radiant intensity distribution $I^{(0)}$ firstly, calculate the first approximate radiation $I^{(1)}$ according to $I^{(0)}$, then calculate the secondary approximate radiation $I^{(2)}$ according to $I^{(1)}$, continue like this until given condition is satisfied. A correction $\Delta I^{(k)}$ is needed when calculating $I^{(k+1)}$ according to $I^{(k)}$. $\Delta I^{(k)}$ only consider the effect of the projection of one ray, the corrected radiation is also limited to those grids who are passed by this ray. The next ray is considered in the next time. Anyway, the projection of only one ray is considered when correcting each time, and radiation of those grids who passed by that ray are corrected. Reference [14] demonstrated mathematical basis of ART.

ART iteration process to solve temperature field is:

$$I_k^{(n)} = I_k^{(n-1)} + A_{ij} \left(p_j - \sum_{i=1}^m A_{ij} I_k^{(n-1)} \right) / \sum_{i=1}^m A_{ij}^2 \quad (11)$$

If initial value $I_i^{(0)}$ ($i=1, 2, \dots, m$) is given, the solution that satisfy specific demand can be gotten by iteration.

2.5 Radiant Damping Coefficient

In Equation (6), radiant damping coefficient in each grid is not constant, it is associated with temperature distribution in the boiler, distribution of particle and gas and combustion condition. Neglecting the effect of scatter of the particle, according to Reference [15], radiant damping coefficient of coal combustion is:

$$k_i = 0.32 + 0.28 \times \exp(-T_i/1135) \quad (12)$$

In the process of iteration, k is carried out due to temperature distribution in each step, till given condition is satisfied.

3. EXPERIMENTAL EQUIPMENT

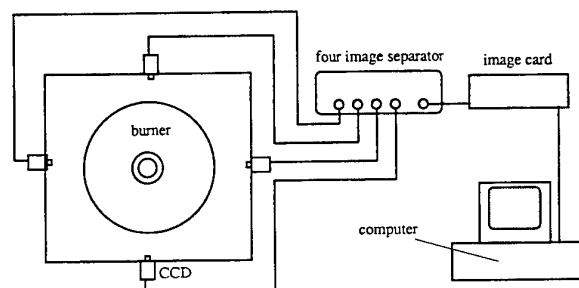


Fig. 3. Experimental system

Experimental system mainly consist of oil and coal mixing burner, CCD camera, four-image separator, image processing card and computer (as shown in Figure 3).

The flame comes from the burner, whose given coal rate is variable. The size of the section for measuring is $750\text{mm} \times 750\text{mm}$. CCD camera is placed in the middle of every side. In the front of camera, each there is an optical filter whose wavelength is 560nm , in order to obtain single wavelength image of the flame. The four-image separator combines four images into one image to be dealt with simultaneously.

4. EXPERIMENTAL RESULTS

Figure 4 is projective image of the flame in four CCD, the section is divided into 15×15 grids, the real size of each grid is $50\text{mm} \times 50\text{mm}$. The given coal rate is 1.44 kg/h . The reconstruction result is shown in Figure 5 where the unit is K.

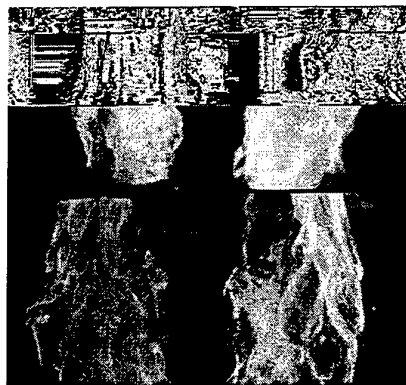


Fig. 4. Image of the flame

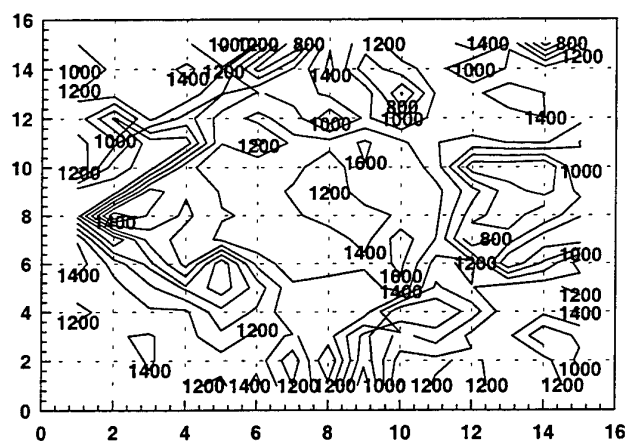


Fig. 5. Temperature field of the measuring section

5. ERROR ANALYSIS

5.1 Numerical Analogy

It is important is to observe the distribution of temperature field when diagnosing combustion. The propose of numeral analogy is to inspect whether ART method can reflect the set temperature distribution accurately. Numerial analog calculation to 5×5 grids shows that error from temperature calculation using ART method is no large than 50 degree. The set temperature distribution can be reconstructed well, and the solution is not

affected by the change of initial value, that shows good convergence of this method. To accelerate convergence, it is taken as constraint condition to iterate that the temperature value is not negative and the range of temperature is in 20-2000K, this can promote the rate of calculation. Table 1 and Table 2 are the set temperature field and the result of analog calculation respectively.

Table 1. Set Temperature Field (unit: K)

1273	1273	1273	1273	1273
1473	1473	1473	1473	1473
1673	1673	1673	1673	1673
1873	1873	1873	1873	1873
2073	2073	2073	2073	2073

Table 2. Result of Calculation(unit: K)

1299	1288	1300	1254	1281
1505	1479	1492	1496	1486
1686	1688	1694	1683	1687
1890	1892	1896	1895	1886
2094	2093	2091	2107	2106

Temperature measurements used in industrial site for combustion diagnosis, temperature distribution is continuous and non-mutable. If proper constraint condition according to prior information is selected, we can obtain the satisfactory result.

5.2 Comparison With Measurement

In order to see the accuracy of the calculated temperature value, we place four thermal couples to measure temperature in the measuring section of the flame, whose position are shown in Figure 6. The calculated temperature and the measured temperature are shown in Figure 7:

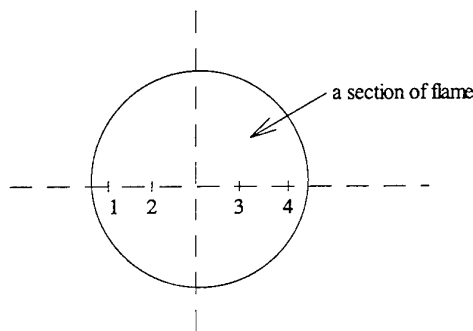


Fig. 6. The position of thermal couple

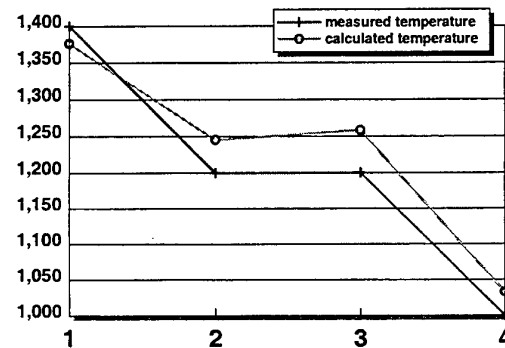


Fig. 7. Calculated and measured temperature

From Fig.7, we can see that absolute uncertainty between calculated and measured temperature is about 50 degree. But because the responsive rate of the therm couple was slow, to trace the change of the temperature of some point is impossible.

6. CONCLUSION

This paper develops a method to reconstruct the section temperature field of the flame captured by CCD camera with ART, then measures its temperature distribution in a test burner. This non-contact method do not need referring optical source and referring measured temperature point, it has important current significance to combustion diagnosis and temperature detecting. Because the equation is non-linear, the calculated resolution of ART and exact resolution exist some error when the number of the unknown is large. But numerical analog calculation and measurement demonstrate that error can be controlled under 50 degree if proper constraint condition is selected, and distribution of temperature can reflect accurately, this is acceptable for application in industrial site. The further research is to select better iterative algebraic to promote the accuracy of the result.

REFERENCES

1. W. Liu, Chinese Electric Power, v.10, pp.58-61 (1993).
2. Z. Shu et.al, Information of Thermal Engineering Automation, v.1, pp.32-35 (1993).
3. S.Collins, Power, v.10, pp.75-78 (1993).
4. H. Zhou et.al, Proceedings of the CSEE, v.15, pp.295-300 (1995).
5. H. Zhou et.al, Proceedings of the CSEE, v.17, pp.1-4 (1997).
6. W. Xu et.al, Chinese Electric Power, v.10, pp.41-44 (1994).
7. Y. Zou et.al, Boiler Technique, v.11, pp.8-13 (1997).
8. D. Yan et.al, Proceedings of the Optics, v.16, pp.1296-1300 (1996).
9. L.J.Muzio D.Eskinazi and S.F.Green, Power Engineering, v.11, pp.49-52 (1989).
10. W. X. Lu, *Medical Image Processing*, Higher Education Press. (1985).
11. J.J.Miles et.al, Proceedings of SPIE, v.3056, pp.20-32 (1997).
12. F. Xue et.al, "Experimental Study of Flame Section Measurement Using Radiant Image Method", *Proceedings of the Chinese Combustion Symposium*, v.2, pp.68-72, edited by Chinese Engineering Thermal Physics Association (1998).
13. S. Yang, *Heat Transfer*, Higher Education Press. (1992).
14. G.T. Herman and Lent A, Computers in Biology and Medicine, v.6, pp.273-274 (1976).
15. C. Zheng and Z. Liu, Optical Property and Radiant Transfer of Dispersive Medium, Huazhong Science and Technology University Press. (1996).

EXPERIMENTS AND OBSERVATIONS OF INTERACTION OF WATER MIST WITH POOL FIRES

Wang Xishi Liao Guangxuan Yao Bin Fan Weicheng

State Key Laboratory of Fire Science

University of Science & Technology of China

Email: wxs@ustc.edu.cn; Fax: 086-0551-3601669

Wu Xiaoping

Department of Mechanics & Mechanical Engineering

University of Science & Technology of China

Email: xpwu@ustc.edu.cn; Fax: 086-0551-3601248

Keywords: interaction, water mist, pool fire, thermal field isogram

ABSTRACT. In order to investigate the interaction of water mist with pool fires, a series of measurements and observations were conducted. Fire source is a small-scale circular stainless steel pan with heptane, ethanol and kerosene. The radiation spectra of the flames were measured by a monochromator system and the radiant heat flux were obtained by a thermogage before and after the application of water mist. At the same time, a Thermal Video System (TVS) was used to visualize the thermal field of the flame. These results show that in the case of heptane and ethanol, the flames was suppressed to less scale and the temperature and radiant heat flux decreased rapidly due to fuel surface cooling, oxygen displacement and heat radiant attenuation of the application of water mists. But in the case of kerosene, the results are different from the previous one. For instance, at the beginning of the injection of water mists, the kerosene flame was enhanced to larger scale, temperature and the radiant heat flux increased. These results maybe caused by more soot particles which were produced during the combustion of kerosene flame, because the particles can influence the penetration of mists into the plume and arrival at the fuel surface.

1 INTRODUCTION

Since the first version of the Montreal Protocol was introduced in 1987, it has become a beacon of international commitment to protecting the earth's ozone layer from further damage by chlorinated fluorocarbons (CFC's). This commitment has driven almost a decade of testing to develop alternative fire suppression technologies to replace the chlorine- or bromine-based gaseous fire suppressants known as Halons. In addition, some traditional and chemical agents were found to be a danger to personnel due to toxicity and asphyxiation. However, water mist which has been defined as sprays of water droplets of 30 to 300 μ m in volumetric mean diameters [1], is not associated with such dangers to ozone layer and people in occupied areas. And it was regarded as not only a suitable and effective method, but also a way to avoid the cost problem [2]. Therefore, the use of water mists for fire extinguishment and control is currently receiving a considerable attention as one of the potential methods for Halon 1301 replacement [3-8]. And some studies on the application to the water mists in practical fires, such as aircraft cabin, military radar, computer rooms, communication equipment cabinets and shipboard space, have been performed, especially in Canada, Britain and American Navies [9].

However, the combustion characteristics, such as the radiant spectra, radiant heat flux and the thermal field on the interaction of water mist with flame, especially pool fires, are still limited in study. And indeed, the designer of a water mist system must understand how fuel type, fire location, fire growth rate, ventilation and degree of obstruction, affect the ability of the mist to extinguish a fire. Obviously, in order to optimize design of water mists system, the understanding of the interaction between water sprays and fires is very important. Therefore, a series of measurements and observations were performed to investigate the interaction of water mist with pool fires of heptane, ethanol and kerosene. The flame radiation spectra, radiation heat flux and thermograms before and after the application of water mist were measured and visualized by a monochromator system, thermogage and Thermal Video System (TVS), separately. Some K-type thermal couples of 0.5mm diameter were arrayed along the centerline and radius of the flame to measure the temperature which can be used to calibrate the TVS. And the experiment results show that the interaction mechanisms of water mist with kerosene flame are different from heptane and ethanol, these will be further discussed in the proceeding text.

2 EXPERIMENTAL APPARATUS

The experiments and observations were performed with small-scale pool fires of heptane, ethanol and kerosene respectively. The configuration of apparatus is given in Fig.1.

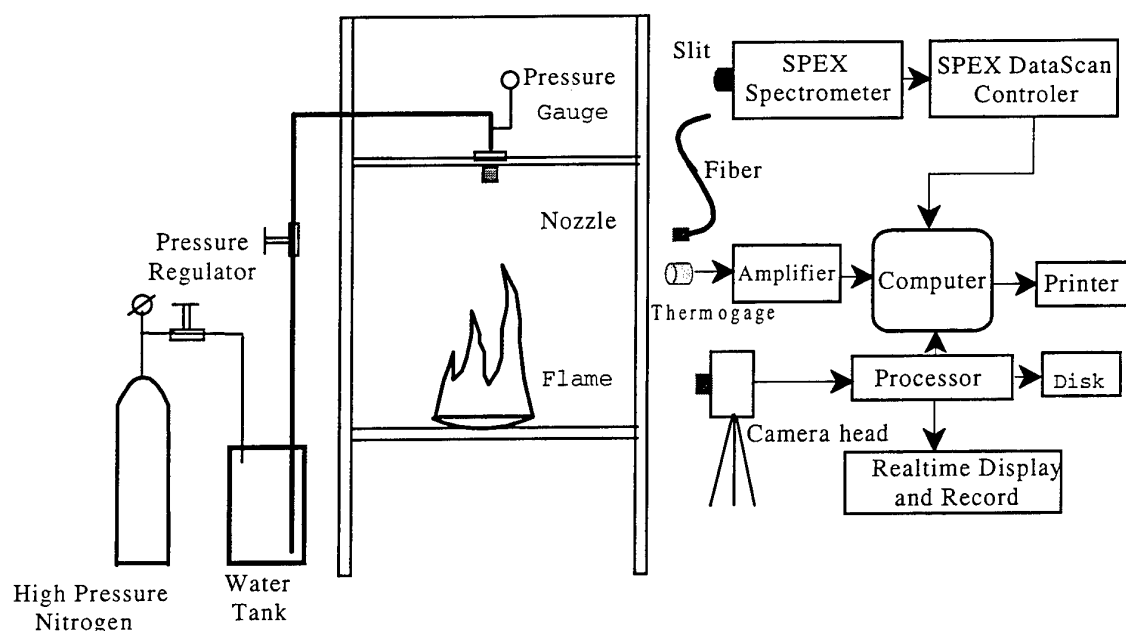


Fig.1 Schematic of the experimental apparatus

The fuel sample was contained in a circular stainless steel pan, with height of 10mm and inner diameter of 150mm. The pool was mounted on a steel stand 600mm above the ground to minimize the effects of surrounding ground surfaces on the behavior of the fire. A downward-directed pressure nozzle was positioned on a square steel plate 300mm over the fuel sample. Combined with the water tank, high pressure Nitrogen, the water can be crushed into millions of water sprays which is called water mist. The nozzle operated at pressure of 0.5Mpa which can be altered by adjusting the pressure regulators according to different requirements. The water sprays were injected into the pool fire downward directly, the relative flow rate was nearly 1.0ml/s.

The 340s monochromator system and a thermal video system were used to measure the radiant spectra and visualize the thermal field of the flame before and after the injection of water mist, respectively. Their specifications were given in Table 1 and Table 2.

Table 1 Specifications of 340s Monochromator (With the 1200gr/mm Grating)

Focal length (mm)	220 (input) /340 (output)
Dispersion (nm/mm)*	2.5
Resolution (nm)*	0.15
Aperture (f/n)	4
Accuracy (nm)	±0.1
Scan Disk	Stepped Driver
Mechanical length (nm)*	200-1000

* The dispersion, resolution and mechanical length will be changed as the different gratings are used*

Some K-type thermal couples of 0.5mm diameter were arrayed along the centerline and radius to calibrate the TVS. The radiant heat flux of the flame, with and without the application of water mist, was also measured by a thermogage which full scale output range is 0 ~ 5 Watts per cm² to 0 ~ 5000 Watts per cm². It's response time

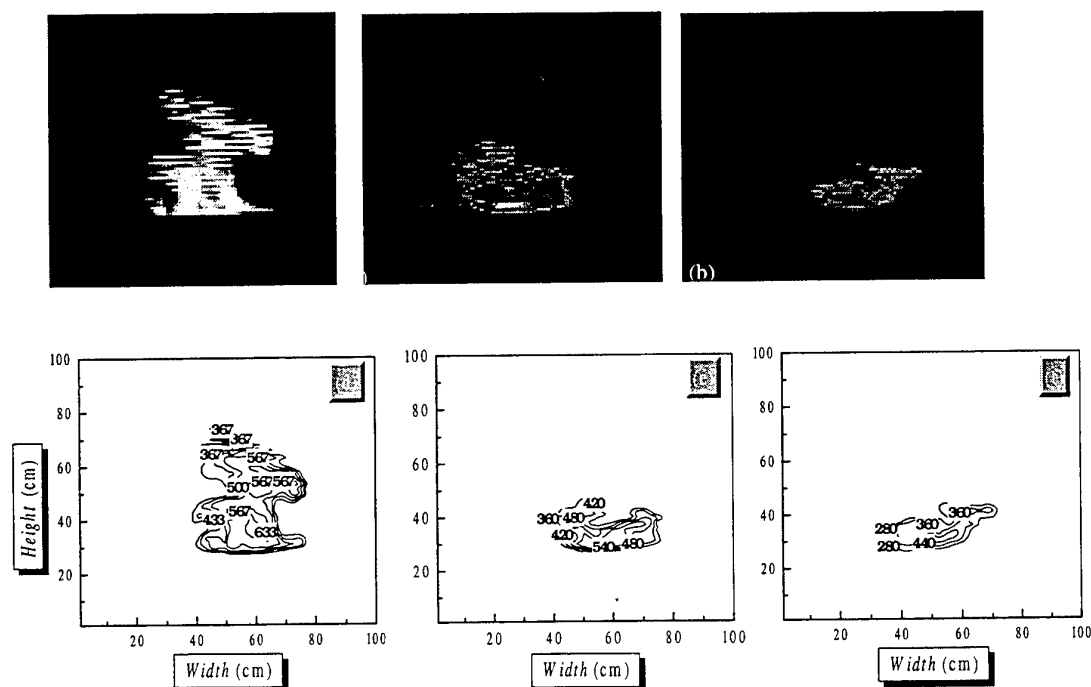
and sensitivity varies with the range, and the response time can be as small as 1.5 milliseconds. The thermogage sensors were designed for 10 millivolts maximum output. All of the systems begin to acquire data after the automatic ignition started, and the fire was allowed to burn for 100 seconds to make quasi-steady burning before the spray injection. All the raw data were saved and processed automatically by computer.

Table 2 Specifications of TVS-2000ST

FOV	15°(H)×10°(V)
Focus Distance	20cm~∞
Scan Speed	30 Frames/Second
Detector	InSb 10 elements
Temperature Range	-20°C ~2000°C
Coolant	Stirling Cooling
Emissivity setting	From 1.00 to 0.10 (0.01 step)
Output Signal	RGB analog video signal, NTSC or PAL signal
External Control	GPB, RS-232C, Trigger signal
Accuracy	Full scale±0.4%

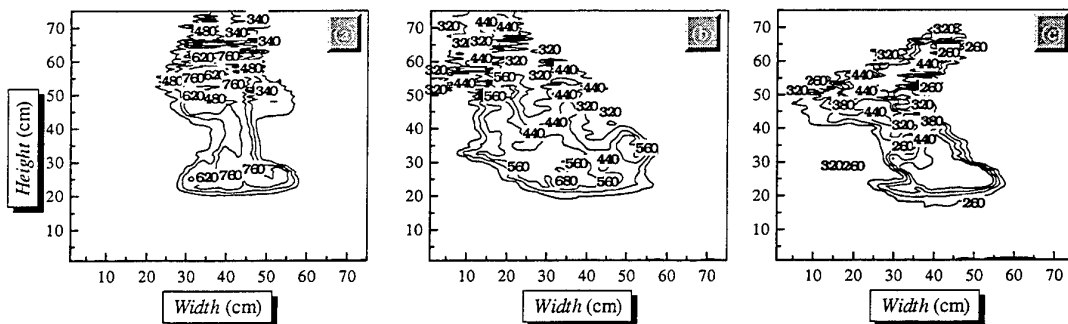
3 RESULTS AND DISCUSSION

Fig.2 shows the thermograms (a, b and c) and thermal field isograms (d, e and f) of ethanol flame with and without the application of water mist. Fig 3 only shows the thermal field isograms of heptane flame, it's thermograms, similar to the previous one, were omitted in order to save the paper length. It is obvious that the flames were suppressed to less scale and the temperature decreased rapidly due to the application of mist, and after about 60s , the temperature decreased below the boiling point, and then the fires were extinguished quickly.



(a) and (d), without the interaction of water mist, (b) and (e), with the interaction of water mist after 40s and (c),(f), after 56s;

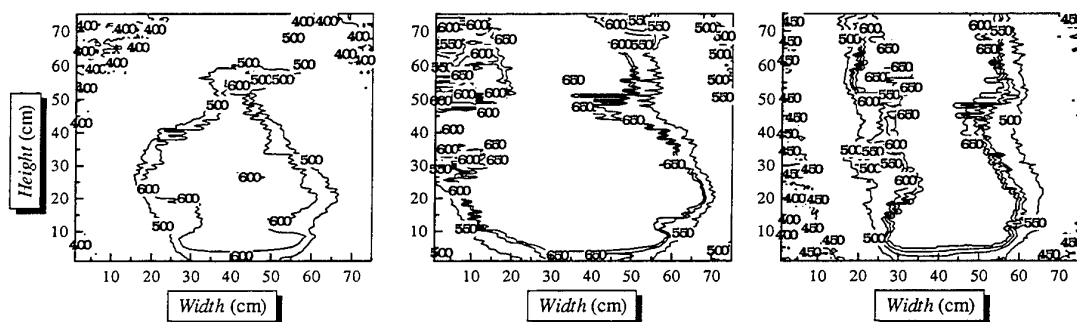
Fig.2 Thermograms and thermal field isograms of ethanol flame



(a) without the interaction of water mist, (b) with the interaction of water mist after 40s and (c) after 56s;

Fig.3 Thermal field isograms of heptane flame

However, Fig.4 shows some different results on the interaction of kerosene pool fire with water mist. From the thermal field isograms, we can see, at the beginning of the injection of water mists, the kerosene flame was enhanced to larger scale and temperature was higher, even after 60s, the flame remained larger and the temperature was remain higher. It's radiant heat flux increased a lot when the water mist injection started, then decreased slowly till the fire was extinguished (see Fig.5). These cases indicate that the interaction mechanisms of kerosene pool fire are different from the previous two cases.



(a) without the interaction of water mist, (b) with the interaction of water mist after 30s and (c) after 60s;

Fig.4 Thermal field isograms of kerosene flame

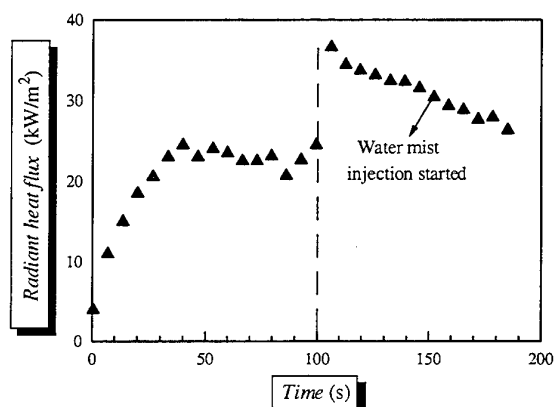


Fig.5 Radiant heat flux of kerosene flame before and after the application of water mist

According to these results, some interaction mechanisms of water mist with pool fires can be inferred. In the cases of heptane and ethanol pool fires, water mist suppressed and extinguished them through cooling, heat radiant attenuation and oxygen displacement, and the former two are obviously shown in Fig.2 and Fig.3, the effects of water mist on flame through oxygen displacement are shown in Fig.6 explicitly. For instance, the middle and strong absorption spectra of O_2 , such as 0.579, 0.688, and 0.762 μm vanished after the application of water mist. Fig.6 also shows many changes of combustion components of the flame due to the effects of the water mist. But in the case of kerosene, combustion was enhanced at the beginning of the application of water mist, this indicates that the interaction mechanisms of flame with water mist are different from heptane and ethanol which maybe mainly caused by the soot production. It is well know that more soot particles can be produced during the combustion of kerosene flame, which can influence the penetration of sprays into the plume and arrival at the fuel surface. Therefore, not only is there little water sprays can arrival at the fuel surface and cool it, but can much water mist enhance combustion through evaporation expansion which reinforces gas fuel and oxygen mixture and changes the chain reactions, especially, following reaction may occur during this process



where the first term is water vapor and the second term is hot residue carbon of combustion.

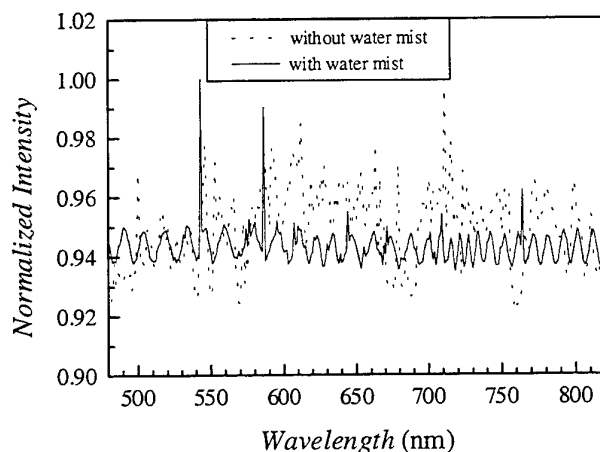


Fig.6 Radiant spectra of ethanol flame before and after the application of water mist

Of course, there are some problems and limitations which should be solved in further studies. Firstly, in order to measure the flame thermal field distribution accurately by the TVS, the flame emissivity should be determined initially. In fact, it is a difficult problem to solve till now. In our experiments, only some thermocouples were used to calibrate the data of TVS because our purpose is not to measure the temperature distribution itself, but to visualize it's changes after the application of water mist. Secondly, expounding of the flame radiant spectra is limited because of the lacking of corresponding standard datum.

4 CONCLUSION

A series of measurements and visualizations were performed in pool fires with heptane, ethanol and kerosene to investigate the interaction of flame with water mist. In the cases of heptane and ethanol pool fires, water mist suppressed and extinguished them quickly through cooling, oxygen displacement and heat radiant attenuation. But in the case of kerosene, combustion was enhanced at the beginning of the application of water mist due to the hot soot particles, this phenomenon shows that effective spray flux densities arriving at the fuel surface is a important factor in kerosene fire suppression and extinction. Future work will consider 1) variations of the combustion components 2) modeling based on experiments.

ACKNOWLEDGMENTS

The authors appreciate the support of the Natural Science Foundation of China (NSFC) (Code: 59876038) and vice professor Qin Jun for his help and benefit suggestions of our experiments.

REFERENCES

1. K. A. Notarianni, P. E., "Water Mist Fire Suppression System", Proceeding of Technical Symposium on Halon Alternatives, Society of Fire Protection Engineers and PLC Education Foundation, pp.57-64, Knoxville, TN(1994).
2. R. L. Alpert., "Incentive for Use of Misting Spray as a Fire Suppression Flooding Agent", Proceedings of Water Mist Fire Suppression Workshop, pp.31-36, Edited by A. N. Kathy and H. J. Nora(1993).
3. A. Jones and P. F. Nolan, J. Loss Prev. Process Ind, Vol. 8, pp.17-22(1995).
4. J. R. Mawhinney, "The role of fire dynamics in design of water mist fire suppression systems", Proc. the Seventh International Fire Science and Engineering Conference, pp. 415-424, Cambridge England(1996)
5. Grosshandle, et al, "Suppression within a simulated computer cabinet using an external water spray", Annual Conference of Fire Research: Abstracts, NISTIR 5499, pp. 75-76, National Institute of Standards and Technology, Gaithersburgh(1994).
6. B. Yao, W. C. Fan and G. X. Liao, "Experimental study on the interaction of water mists with fires in the Confined Space", Symposium on Fire Science and Technology, Singapore(1998).
7. M. B. Kim, et al, Fire safety Journal, Vol.27, pp.37-48(1996).
8. B. Downie, C. Polymeropoulos and G. Gogos, Fire Safety Journal, Vol.24, pp.359-381(1995).
9. J. R. Mawhinney, P. Eng, "Engineering Criteria for Water Mist Fire Suppression System", Proceedings of Water Mist Fire Suppression Workshop, pp.37-73, Edited by A. N. Kathy and H. J. Nora(1993).

Authors Index to Volumes 1-4

Ahmad, G.E.	751	Cen, K.F.	1586
Ahn, J.	212	Cen, K.F.	1603
Ahn, Y.	557	Chai, L.H.	343
Akisawa, A.	759	Chan, A.M.C.	408
Akisawa, A.	1145	Chan, C.K.	1508
Allcock, H.R.	1483	Chan, C.K.	1515
Altraide, A.	191	Chandratilleke, T.T.	191
Amazouz, M.	917	Chang, L.J.	1002
Amazouz, M.	1084	Chazly, N.E.	826
An, E.	355	Chen, C.T.	636
An, E.	367	Chen, D.Z.	1595
Anderson, R.	1033	Chen, G.H.	910
Ando, D.	1226	Chen, G.H.	1048
Antohi, C.	866	Chen, G.J.	588
Aoki, H.	748	Chen, G.Y.	1553
Aoyama, S.	843	Chen, H.P.	1496
Aoyama, S.	852	Chen, J.	1397
Arlabosse, P.	923	Chen, M.J.	1581
Asano, H.	1122	Chen, Q.H.	379
Asano, H.	1438	Chen, T.K.	393
Assassa, G.M.R.	766	Chen, T.K.	416
Baba, A.	1710	Chen, X.	270
Bae, S.C.	1153	Chen, Y.	1427
Bai, Q.	521	Chen, Y.	1433
Bai, W.D.	1703	Chen, Y.	1632
Bartoli, C.	247	Chen, Z.H.	355
Behnia, M.	873	Chen, Z.H.	367
Benali, M.	917	Chen, Z.H.	598
Benali, M.	1412	Chen, Z.Q.	505
Benning, L.	1483	Chen, Z.Q.	529
Bhattacharyya, S.	1353	Cheng, K.	1212
Bi, Q.C.	393	Cheng, P.	505
Bi, Q.C.	438	Cheng, P.	529
Bingue, J.P.	1266	Cheng, P.	1192
Bockhorn, H.	1573	Cheng, X.H.	1728
Boral, A.A.	888	Cheng, Y.C.	1476
Borisov, I.	422	Cheung, C.S.	1397
Borzenko, V.I.	512	Cheung, F.B.	888
Bossi, L.	239	Cheung, F.B.	1289
Buchner, H.	1573	Chi, Y.	1333
Bull, S.R.	18	Chi, Z.H.	1586
Cai, J.Y.	416	Chiu, H.H.	1640
Cai, S.	1651	Cho, H.K.	384
Cannon, A.M.	1483	Choi, M.	1532
Cao, X.Y.	1281	Chou, C.S.	474
Cao, X.Y.	1603	Chou, T.C.	1257
Cao, Z.H.	1651	Chow, A.	680
Carrere-Gee, C.	923	Chua, H.T.	1145
Casey, R.T.	1524	Chung, B.T.F.	581
Cen, K.F.	1281	Chung, J.D.	1532
Cen, K.F.	1333	Chung, K.C.	636
Cen, K.F.	1566	Chung, S.K.	229

Ciocan, V.	866	Garner, S.D.	1007
Cote, R.	1084	Gavotti, N.	539
Cui, W.Z.	379	Gerlach, C.	1273
Cui, Y.B.	1662	Gerlach, C.	1296
Cunnington, G.R.	613	Goldstein, R.J.	206
Da Veiga, V.R.	1114	Gong, L.H.	1198
Dai, X.W.	1632	Gopinath, A.	1170
Davis, S.B.	1686	Gori, F.	239
Deeb, S.E.	826	Grandum, S.	860
Deng, P.G.	1217	Groll, M.	708
Deng, X.H.	1217	Groll, M.	957
Denner, H.D.	1212	Groll, M.	1130
Díaz, G.	940	Gu, F.	1305
Ding, L.S.	650	Gu, Z.Z.	1651
Dong, Y.X.	980	Guo, F.Z.	1203
Druck, H.	740	Guo, F.Z.	1208
Du, D.X.	658	Guo, T.M.	588
Du, D.X.	665	Guo, X.F.	1433
Du, J.H.	490	Guo, X.Q.	588
Dubble, E.H.	1007	Guo, X.S.	1566
Duluc, M.C.	127	Guo, Y.C.	1508
Eder, A.	1273	Guo, Y.C.	1515
Eder, A.	1296	Guo, Z.	658
Eisen, S.	1366	Guo, Z.Y.	118
El-Kotb, M.	826	Guy, C.	1412
Elphick, I.G.	408	Hahne, E.	740
Eschenbacher, J.F.	262	Hamada, K.	843
Fagguani, S.	247	Han, B.	206
Fan, M.X.	1566	Han, P.	270
Fan, W.C.	1340	Han, X.	1603
Fedkin, M.V.	1483	Hara, T.	1178
Fei, Q.	1002	Haruki, N.	695
Feng, B.	1560	Haruki, N.	723
Feng, Y.	1208	Haruki, N.	852
Feng, Z.	643	Haruki, N.	1138
Feng, Z.X.	1646	Hatabaka, M.	288
Fiebig, M.	598	Hawladar, M.N.A.	451
Francois, M.X.	127	He, K.X.	680
Francois, M.X.	1164	Hein, D.	1347
Fridman, A. A.	96	Hetsroni, G.	72
Fridman, A.A.	1266	Hetsroni, G.	255
Fu, H.L.	497	Hiller, G.	1677
Fu, X.Y.	1033	Hirashima, M.	564
Fudym, O.	923	Hirata, M.	57
Fujii, I.	1540	Hirata, Y.	628
Fujii, T.	1122	Hisazumi, Y.	1122
Fujii, T.	1438	Ho, C.J.	881
Fujioka, K.	628	Hoffmann, S.	1573
Fujita, Y.	521	Hofmann, M.A.	1483
Fujiyoshi, M.	1404	Holden, C.	680
Fushimi, J.	399	Honda, T.	1546
Gale, T.K.	1686	Horibe, A.	695
Ganzha, V.L.	688	Horibe, A.	723
Gao, X.	1566	Horibe, A.	852

Horibe, A.	1138	Kashiwagi, T.	759
Hosatte, S.	1084	Kashiwagi, T.	1145
Hoshi, A.	796	Kato, Y.	1546
Hsiau, S.S.	474	Katsuta, M.	1153
Hsieh, S.S.	1015	Kaviany, M.	32
Hsu, C.T.	505	Kawaguchi, Y.	716
Hsu, C.T.	731	Kellam, E.C.	1483
Hu, G.	1333	Kennedy, L.A.	96
Hu, W.	279	Kennedy, L.A.	1266
Huang, J.	1002	Khalatov, A.	422
Huang, S.H.	821	Khattab, N.	826
Huang, X.	355	Kida, T.	1138
Huang, X.	367	Kim, M.	557
Huang, X.Y.	497	Kim, M.O.	384
Hugron, I.	1412	Kim, M.S.	965
Hui, C.K.P.	1090	Kim, Y.J.	295
Hussien, H.M.S.	751	Kimura, M.	843
Hwang, I.J.	295	Kimura, T.	1540
Hwang, Y.W.	965	Klein, H.P.	1130
Hyuga, T.	521	Komiya, A.	873
Ichimiya, K.	184	Koo, J.H.	1289
Inaba, H.	695	Koyama, S.	445
Inaba, H.	723	Kudra, T.	917
Inaba, H.	852	Kuge, K.	1546
Inaba, H.	1138	Kumagai, S.	399
Inada, T.	860	Kuo, J.T.	474
Inatomi, Y.	302	Kurosaki, Y.	84
Ipek, O.	778	Kuwahara, K.	149
Ishizuka, M.	321	Kuwahara, K.	445
Iwai, H.	161	Kuznetsov, A.V.	896
Izumi, M.	399	Kwan, M.K.	731
Jang, K.J.	1015	Kwanka, K.	1347
Jebali, F.	127	Ladevie, B.	482
Jegla, Z.	1624	Ladevie, B.	923
Jeong, U.C.	295	Lam, W.C.	1404
Jerbi, F.J.	1164	Lazarescu, C.D.	866
Jiang, X.J.	1586	Lecomte, D.	923
Jiang, Y.	788	Lee, B.D.	650
Jiang, Y.	804	Lee, J.S.	212
Jiang, Y.	1059	Lee, L.	1098
Jiang, Y.	1066	Lee, S.C.	613
Joko, M.	262	Lee, T.H.	384
Jones, J.C.	1313	Lee, T.S.	1581
Jordan, M.	1273	Lee, T.S.	1640
Jung, I.S.	212	Leong, K.C.	497
Kage, H.	932	Leung, D.Y.C.	1427
Kakimoto, K.	302	Leung, D.Y.C.	1553
Kalabin, E.V.	328	Leutz, A.	759
Kameda, K.	1138	Li, B.Q.	1433
Kaneda, M.	302	Li, B.Q.	1722
Kang, Y.B.	788	Li, C.F.	255
Kang, Y.B.	804	Li, G.H.	1615
Kang, Y.M.	430	Li, H.B.	1433
Kasagi, N.	972	Li, H.P.	270

Li, J.	335	Ma, W.M.	1305
Li, M.	1728	Ma, Z.	581
Li, P.W.	716	Ma, Z.Y.	1333
Li, Q.	1203	Machida, K.	843
Li, Q.	1208	Madadnia, J.	349
Li, Q.Y.	1615	Makino, T.	604
Li, R.	355	Malysenko, S.P.	512
Li, R.Y.	367	Mandel, H.	740
Li, X.Z.	1212	Martiny, M.	221
Li, Y.D.	1420	Maruyama, S.	873
Li, Z.	658	Matsuno, Y.	932
Li, Z.W.	1388	Matsushita, M.	843
Li, Z.Y.	177	Mayinger, F.	1273
Li, Z.Z.	1603	Mayinger, F.	1296
Li, Z.Z.	1646	Mayinger, F.	1366
Liang, J.T.	1184	Mayinger, F.	1379
Liao, G.X.	1340	Mbarawa, M.	1524
Liao, H.Q.	1722	McClain, R.L.	940
Lin, F.	1388	Mei, Y.G.	980
Lin, G.T.	821	Meng, X.Z.	459
Lin, H.H.	821	Meng, X.Z.	1159
Lin, J.Y.	1041	Mertz, R.	708
Lin, R.	1360	Mertz, R.	957
Lin, W.Y.	1508	Mettawee, E.S.	766
Linak, W.P.	1686	Meyer, J.P.	1076
Ling, S.C.	1446	Meyer, J.P.	1105
Liu, B.M.	451	Meyer, J.P.	1114
Liu, C.	373	Mi, J.	1609
Liu, C.Y.	497	Miller, A.	1033
Liu, D.C.	1496	Milton, B.E.	1524
Liu, H.	1420	Mo, J.	680
Liu, H.C.	1640	Mohamad, M.A.	751
Liu, H.T.	1468	Morford, R.V.	1483
Liu, X.G.	1651	Morin, M.	1412
Liu, Y.	1305	Mosyak, A.	72
Liu, Y.	1615	Mosyak, A.	255
Liu, Y.F.	1591	Mujumdar, A.S.	910
Liu, Y.P.	1595	Mujumdar, A.S.	932
Liu, Y.W.	1212	Murayama, Y.	1546
Liu, Z.L.	1360	Mutaf-Yardimci, O.	96
Liu, Z.T.	1397	Nagayama, G.	672
Liu, Z.Y.	1054	Nakabe, K.	262
Lloyd, A.C.	138	Nakamura, S.	1715
Lorenzine, M.	247	Nakata, T.	695
Lou, H.	1241	Nathan, G.J.	1609
Lu, G.Q.	1192	Negishi, K.	564
Lu, S.S.	860	Neo, E.C.	161
Lu, Y.Z.	1054	Ng, K.C.	1145
Lubiez, J.V.	1164	Ng, M.L.	1476
Luo, W.H.	1566	Nguyen, T.H.	349
Luo, Y.	416	Nguyen, T.V.	1453
Luo, Y.H.	393	Nie, J.H.	177
Luo, Z.Y.	1566	Nigmatulin, R.	110
Lvov, S.N.	1483	Nishio, S.	360

Nobuchika, K.	695	Schmidt, B.	708
North, M.T.	573	Scholz, K.H.	1500
Novellani, M.	466	Schulz, A.	221
Nursubyakto	191	Seames, W.S.	1686
Ofner, B.	1366	Sen, M.	940
Ogura, H.	932	Serizawa, A.	643
Oido, K.	628	Shao, H.	279
Oka, M.	813	Sharkawy, A.E.	826
Okada, S.Y.	604	Sheen, P.J.	949
Olaru, I.	866	Shen, B.X.	1496
Oliveira, A.A.M.	32	Sheng, X.L.	650
Ooyatsu, N.	1710	Shevtsov, S.	422
Osa, N.	445	Shi, M.H.	905
Ota, T.	199	Shiah, S.W.	888
Ozoe, H.	288	Shih, Y.C.	1289
Ozoe, H.	302	Shimogori, M.	1710
Pacheco-Vega, A.	940	Shoji, M.	335
Paitoonsurikarn, S.	972	Shu, Z.D.	1703
Pan, Y.K.	910	Smid, J.	474
Pao, H.P.	1446	So, R.M.	169
Park, G.	557	Soudarev, A.	1500
Park, G.C.	384	Stehlik, P.	1624
Park, G.C.	430	Stubington, J.F.	1662
Park, K.S.	1532	Stubington, J.F.	1669
Peng, X.F.	343	Sugimoto, K.	1438
Petit, P.J.	1076	Sugiyama, T.	1024
Polasek, F.	539	Sumathy, K.	774
Poslushny, G.	1500	Sun, C.C.	1257
Precht, P.	1379	Sun, C.Y.	588
Qiu, J.R.	1560	Sun, G.J.	1586
Qiu, Y.	980	Sun, H.	650
Que, X.C.	279	Sun, J.Y.	1041
Quitard, M.	482	Sun, L.S.	1728
Raghavan, G.S.V.	1090	Sun, S.J.	1404
Ramsden, V.	349	Sun, X.X.	1728
Ren, B.Z.	1002	Suzuki, A.	759
Ro, S.T.	965	Suzuki, H.	1024
Rong, S.X.	588	Suzuki, K.	161
Rozenblit, R.	72	Suzuki, K.	262
Sadhal, S.S.	229	Suzuki, Y.	972
Saenger, M.	1677	Swanepoel, W.	1105
Saha, B.B.	1145	Swift, G.W.	2
Saito, T.	84	Syred, N.	422
Saitoh, T.S.	796	Tadrist, L.	466
Saitoh, T.S.	1226	Tagawa, T.	288
Saitoh, T.S.	1233	Tagawa, T.	302
Sanchez, J.G.	1098	Tagishi, A.	1715
Santini, R.	466	Takahashi, K.	873
Sato, K.	695	Takarayama, N.	1710
Sato, M.	748	Takeguchi, S.	1153
Satoh, I.	84	Tan, G.H.	881
Saveliev, A.V.	96	Tanaka, H.	360
Saveliev, A.V.	1266	Tao, W.Q.	177
Saxena, S.C.	688	Tian, F.J.	1433

Tomiyama, S.	695	Wu, J.	1560
Toriyama, K.	184	Wu, X.P.	1340
Trinh, E.H.	229	Wu, Y.Z.	1212
Tsai, H.H.	474	Wyczalek, F.A.	1327
Tsai, Y.C.	1015	Xiang, J.	1728
Tsuchimoto, N.	1438	Xiao, L.Q.	835
Tsuruta, T.	672	Xin, M.D.	379
Vanhorn, S.R.	1321	Xing, K.Q.	373
Vesely, S.	1500	Xiong, F.	701
Vigneault, C.	1090	Xiong, Z.H.	1632
Vinogradov, E.	1500	Xu, B.Y.	1427
Vitali, J.A.	1321	Xu, S.S.	1657
Wakabayashi, H.	604	Xu, X.D.	1198
Wako, Y.	748	Xu, X.F.	1566
Wang, A.L.T.	1669	Xu, X.Y.	1433
Wang, B.X.	343	Xu, Y.Q.	1305
Wang, B.X.	490	Yabe, A	716
Wang, B.X.	665	Yabe, A	860
Wang, C.Y.	1460	Yabe, T.	1153
Wang, D.Q.	459	Yamada, N.	1233
Wang, F.	1333	Yamagishi, F.	695
Wang, J.	598	Yamanaka, T.	1024
Wang, J.C.	680	Yamashita, T.	1438
Wang, J.F.	1048	Yan, J.H.	1333
Wang, L.B.	980	Yan, W.M.	949
Wang, N.N.	1250	Yan, W.P.	1591
Wang, Q.H.	1560	Yan, Z.D.	1397
Wang, Q.W.	177	Yang, B.C.	821
Wang, S.	118	Yang, B.C.	1289
Wang, S.P.	835	Yang, D.	1566
Wang, X.	905	Yang, H.	1212
Wang, X.	1122	Yang, H.M.	1305
Wang, X.	1489	Yang, K.	199
Wang, X.S.	1340	Yang, K.T.	940
Wang, Y.	1646	Yang, L.W.	1184
Wang, Z.G.	459	Yang, S.M.	310
Wang, Z.G.	1159	Yang, X.L.	1433
Wang, Z.N.	701	Yao, B.	1340
Watanabe, C.	445	Yao, Q.	1281
Watanabe, M.	335	Ye, X.H.	270
Wei, C.Y.	1333	Yeh, C.L.	1640
Wei, Q.D.	1651	Yin, X.L.	1427
Wei, X.J.	1483	Yokota, K.	1546
Wendt, J.O.L.	1686	Yokota, M.	852
Weng, L.C.	1640	Yokoya, S.	335
Werther, J.	1677	Yong, Y.P.	1651
Whitaker, S.	482	Yoshikawa, H.	199
Willers, E.	1130	Yoshino, H.	1241
Wittig, S.	221	Yoshizawa, Y.	1546
Wong, H.	621	You, L.X.	1468
Wu, C.Z.	1427	Yu, B.F.	459
Wu, C.Z.	1632	Yu, B.F.	1159
Wu, F.	1217	Yu, C.J.	1566
Wu, G.T.	1002	Yu, H.L.	355

Yu, H.L.	367	Zhu, N.	316
Yu, J.	445	Zhu, W.X.	1184
Yu, S.M.	1250	Zhu, Y.Q.	804
Yu, W.P.	905	Zhu, Y.X.	788
Yu, X.L.	1397	Zhu, Y.X.	1059
Yue, D.T.	1002	Zou, Z.Q.	1728
Yun, Y.	1703	Zubkov, P.T.	328
Zakharov, Y.	1500	Zuo, Z.J.	573
Zeng, D.L.	373	Zuo, Z.J.	1007
Zhang, G.	379		
Zhang, H.	621		
Zhang, H.	701		
Zhang, H.S.	1595		
Zhang, H.X.	1048		
Zhang, J.W.	1603		
Zhang, L.	1198		
Zhang, L. Winston	989		
Zhang, L.Z.	1066		
Zhang, L.Z.	1560		
Zhang, S.H.	1489		
Zhang, S.Z.	1048		
Zhang, W.	1203		
Zhang, X.	860		
Zhang, X.L.	355		
Zhang, X.S.	997		
Zhang, Y.	910		
Zhang, Y.	1646		
Zhang, Y.H.	980		
Zhang, Y.P.	788		
Zhang, Y.P.	804		
Zhang, Y.P.	1059		
Zhang, Y.P.	1066		
Zhang, Z.J.	490		
Zhao, C.Y.	169		
Zhao, L.F.	1489		
Zhao, L.J.	910		
Zhao, T.S.	438		
Zhao, T.S.	529		
Zhao, Z.L.	1427		
Zheng, J.X.	393		
Zheng, L.	1360		
Zheng, Q.G.	1703		
Zhou, H.	1586		
Zhou, J.	379		
Zhou, J.	1694		
Zhou, J.H.	1281		
Zhou, J.M.	1615		
Zhou, J.S.	1566		
Zhou, L.P.	997		
Zhou, Q.T.	701		
Zhou, T.H.	1468		
Zhou, X.Y.	1483		
Zhou, Y.	1184		
Zhou, Z.J.	1281		